INTER- AND INTRA-SUBJECT VARIABILITY IN BRAIN IMAGING AND DECODING

EDITED BY: Tzyy-Ping Jung, Corey J. Keller, Junhua Li, Yuan-Pin Lin, Masaki Nakanishi, Johanna Wagner, Chun-Shu Wei, Wei Wu and Yu Zhang

PUBLISHED IN: Frontiers in Human Neuroscience, Frontiers in Neuroscience and Frontiers in Computational Neuroscience

frontiers Research Topics

frontiers

ISSN 1664-8714
ISBN 978-2-88974-087-1
DOI 10.3389/978-2-88974-087-1

About Frontiers

Frontiers is more than just an open-access publisher of scholarly articles: it is a pioneering approach to the world of academia, radically improving the way scholarly research is managed. The grand vision of Frontiers is a world where all people have an equal opportunity to seek, share and generate knowledge. Frontiers provides immediate and permanent online open access to all its publications, but this alone is not enough to realize our grand goals.

Frontiers Journal Series

The Frontiers Journal Series is a multi-tier and interdisciplinary set of open-access, online journals, promising a paradigm shift from the current review, selection and dissemination processes in academic publishing. All Frontiers journals are driven by researchers for researchers; therefore, they constitute a service to the scholarly community. At the same time, the Frontiers Journal Series operates on a revolutionary invention, the tiered publishing system, initially addressing specific communities of scholars, and gradually climbing up to broader public understanding, thus serving the interests of the lay society, too.

Dedication to Quality

Each Frontiers article is a landmark of the highest quality, thanks to genuinely collaborative interactions between authors and review editors, who include some of the world's best academicians. Research must be certified by peers before entering a stream of knowledge that may eventually reach the public - and shape society; therefore, Frontiers only applies the most rigorous and unbiased reviews.
Frontiers revolutionizes research publishing by freely delivering the most outstanding research, evaluated with no bias from both the academic and social point of view. By applying the most advanced information technologies, Frontiers is catapulting scholarly publishing into a new generation.

What are Frontiers Research Topics?

Frontiers Research Topics are very popular trademarks of the Frontiers Journals Series: they are collections of at least ten articles, all centered on a particular subject. With their unique mix of varied contributions from Original Research to Review Articles, Frontiers Research Topics unify the most influential researchers, the latest key findings and historical advances in a hot research area! Find out more on how to host your own Frontiers Research Topic or contribute to one as an author by contacting the Frontiers Editorial Office: frontiersin.org/about/contact

INTER- AND INTRA-SUBJECT VARIABILITY IN BRAIN IMAGING AND DECODING

Topic Editors:
Tzyy-Ping Jung, University of California, San Diego, United States
Corey J. Keller, Stanford University, United States
Junhua Li, University of Essex, United Kingdom
Yuan-Pin Lin, National Sun Yat-sen University, Taiwan
Masaki Nakanishi, University of California, San Diego, United States
Johanna Wagner, University of California, San Diego, United States
Chun-Shu Wei, National Chiao Tung University, Taiwan
Wei Wu, South China University of Technology, China
Yu Zhang, Lehigh University, United States

Citation: Jung, T.-P., Keller, C. J., Li, J., Lin, Y.-P., Nakanishi, M., Wagner, J., Wei, C.-S., Wu, W., Zhang, Y., eds. (2022). Inter- and Intra-subject Variability in Brain Imaging and Decoding. Lausanne: Frontiers Media SA.
doi: 10.3389/978-2-88974-087-1

Table of Contents

frontiers in Computational Neuroscience

EDITORIAL
published: 29 November 2021
doi: 10.3389/fncom.2021.791129

Editorial: Inter- and Intra-subject Variability in Brain Imaging and Decoding

Chun-Shu Wei[1,2,3]*, *Corey J. Keller*[4], *Junhua Li*[5], *Yuan-Pin Lin*[6,7], *Masaki Nakanishi*[8], *Johanna Wagner*[8], *Wei Wu*[4], *Yu Zhang*[9] *and Tzyy-Ping Jung*[1,8]*

[1] Department of Computer Science, National Yang Ming Chiao Tung University, Hsinchu, Taiwan, [2] Institute of Education, National Yang Ming Chiao Tung University, Hsinchu, Taiwan, [3] Institute of Electrical and Control Engineering, National Yang Ming Chiao Tung University, Hsinchu, Taiwan, [4] Department of Psychiatry and Behavioral Sciences, Stanford University, Stanford, CA, United States, [5] School of Computer Science and Electronic Engineering, University of Essex, Colchester, United Kingdom, [6] Institute of Medical Science and Technology, National Sun Yat-sen University, Kaohsiung, Taiwan, [7] Department of Electrical Engineering, National Sun Yat-sen University, Kaohsiung, Taiwan, [8] Institute for Neural Computation, University of California, San Diego, San Diego, CA, United States, [9] Department of Bioengineering, Lehigh University, Bethlehem, PA, United States

Keywords: human variability, neuroimaging, brain decoding, brain-computer interface, EEG, MEG, fMRI, fNIRS

Editorial on the Research Topic

Inter- and Intra-subject Variability in Brain Imaging and Decoding

Pervasive and elusive human variability, both across and within individuals, poses a major challenge in interpreting and decoding human brain activity. Individual differences in brain anatomy and function contribute to inter-subject variability. A variety of factors may contribute to intra-subject variability, including neural processing, brain activity non-stationarity, neurophysiological mechanisms, and certain unknown factors.

Studies have recently focused on embracing variability rather than disregarding it. By focusing on variability, they have improved insights into individual differences and cross session variations, enabling precise mapping and decoding of functional brain areas based on individual variability and similarity. For instance, transfer learning techniques have enhanced brain decoding performance by dealing with variations in data collected from different subjects over a wide range of sessions and days. The applicability of a neurophysiological biometric is determined by its manifest inter-subject variability and minimal intra-subject variability. As a result, questions arise about how to observe, analyze, and model inter- and intra-subject variability, what researchers might gain or lose from this variability, and how to cope with the variability in brain imaging and decoding.

This Research Topic emphasizes the need to account for both inter- and intra-subject variability in brain imaging and decoding. The present collection contains an expanded overview of related fields and can shed light on future endeavors in those fields. We highlight three domains in this editorial that emerge from the sixteen contributions of this topic:

(1) Characterizing inter- and intra-subject variability in neural observations
(2) Analyzing and assessing the variability of neural data
(3) Methods for eliminating inter- and intra-subject variability in brain imaging and decoding

Our editorial cannot fully encapsulate all the details and depth of this Research Topic. As such, we encourage you to peruse these articles to gain a fuller understanding of the research field of brain imaging and decoding.

1. Characterizing inter- and intra-subject variability in neural observations

OPEN ACCESS

Edited and reviewed by:
Si Wu,
Peking University, China

***Correspondence:**
Chun-Shu Wei
wei@nycu.edu.tw
Tzyy-Ping Jung
tpjung@ucsd.edu

Received: *08 October 2021*
Accepted: *13 October 2021*
Published: *29 November 2021*

Citation:
Wei C-S, Keller CJ, Li J, Lin Y-P, Nakanishi M, Wagner J, Wu W, Zhang Y and Jung T-P (2021) Editorial: Inter- and Intra-subject Variability in Brain Imaging and Decoding. Front. Comput. Neurosci. 15:791129. doi: 10.3389/fncom.2021.791129

A collection of contributions exhibits a wide range of characteristics of inter- and intra-subject variability in various types of neural observations including sensorimotor electroencephalographic (EEG) pattern, cerebral metabolism, clinical neuromarkers, brain structure, etc. Ma et al. assessed the cerebral structural changes associated with the effect of chronic pain on empathy, and identified multiple structural brain abnormal pathways connected to anterior insula in a population of patients suffering from chronic lower back pain. Shen and Lin showed that emotional responses exhibited salient intra- and inter-individual differences and considerably modulated the spatio-spectral EEG oscillations. Such EEG variability may lead to a great challenge for the development of a generalized emotion-classification model for real-life applications.

The presence of inter- and intra-subject variability has a significant impact on the findings in neurobiological studies. Sundar et al. investigated whether or not functional connectivity can be integrated to reduce the variability of absolute values of the cerebral metabolic rate of glucose (CMRGlc) and showed that functional connectivity among six major brain networks was not suited for standardization of CMRGlc values. Cai et al. measured the interaction effect on frontal-striatum-thalamus by rs11146020 and rs3813296 from GRIN1 and GRIA2 genes in first-episode negative schizophrenia patients. Their results suggested a modulation on the glutamic frontal-striatum-thalamus pathway by rs11146020 and rs3813296 gene polymorphism. According to the findings, patients with different genotypes have different neuroimaging characteristics on causality connections and structural characteristics in the frontal-striatum-thalamus pathway, implying the importance of personalized clinical interventions.

The performance of using brain-computer interfacing (BCI) systems varies greatly across subjects. Saha and Baumert addressed an important issue of varying neurophysiological processes in sensorimotor rhythms over time and across subjects. They found that time-variant and individualized neurophysiological characteristics could have a significant impact on BCI performance. Lee et al. applied a dynamic causal modeling method to study how motor networks measured by EEG during the resting state could predict the performance of motor imagery. They discovered a significant difference in the connectivity strength from the supplementary motor area to the right dorsolateral prefrontal cortex between the low- and high-performance groups. These findings advanced the understanding of the inefficiency of BCI and the prevention of ineffective use of BCI.

2. Evaluation and assessment of the variability in neural data

Following the papers that characterize inter- and intra-subject variability in neural observations, another set of papers focuses on evaluating and assessing the variability in their neural data. Goodman et al. assessed the stability of a mildly stress-inducing math calculation task to evaluate its usability in clinical trials aimed at reducing stress responses. They found good stability in most of the functional magnetic resonance imaging (fMRI) measures performed twice, 13 weeks apart. The authors measure and show significant test-retest reliability of neuronal activation and physiological responses associated with acute psychosocial stress using Montreal Imaging Stress Tasks. Wriessnegger et al. evaluated inter-individual differences in event-related desynchronization/synchronization (ERD/S) patterns during sports motor imagery. The correlation distance of ERD/S values in six region-of-interests between pairs of participants was used to assess inter-individual differences. Mikkelsen et al. addressed the variability between EEG recordings collected in lab and at home locations. Thanks to the emergence of wearable EEG devices, EEG data collection could be performed outside the lab. They concluded that while an experimental environment can affect the quality of EEG data, the effect is smaller than the natural inter-individual variances. The data is thus valid to use from an experimental perspective. The findings would encourage researchers to collect EEG measurements at home.

3. Methods for obviating inter- and intra-subject variability in brain imaging and decoding

The last group of contributions sheds light on techniques for obviating inter- and intra-subject variability in analyses of brain imaging and/or decoding brain activities. Yang et al. proposed a neural network with error feedback to improve the stability of neural signal decoding, which is critical for the performance of brain-machine interfaces. The results showed that using an evolutionary network with error feedback could improve decoding stability significantly, compared to either the same network without error feedback. Xu et al. addressed the problem of variability across EEG datasets, which led to a model generalization in EEG classification. To address the aforementioned issue, a pre-alignment strategy, in which covariance matrices were aligned, was proposed to mitigate the variability problem. The alignment used in the study effectively reduced the variability across EEG datasets and improved the performance of cross-dataset classification. The comparison results demonstrated that this strategy could be promising for improving EEG classification accuracy across datasets.

Liang and Liu studied how emotions perceived from whole-person (all facial and body parts included) stimuli could be decoded using motion-sensitive areas. Results revealed that emotions could be successfully decoded based on the activation patterns in dorsal motion-sensitive areas. Furthermore, results from the cross-subject classification analysis showed that motion-sensitive areas supported the classification of individual emotion representation across subjects. Their findings provide new evidence for the involvement of motion-sensitive areas in emotion decoding, and they also suggested that there exists a common emotion code in the motion-sensitive areas across individual subjects. Kanoga et al. presented an automatic artifact reduction technique based on independent low-rank matrix analysis (ILRMA), which was compared to independent component analysis (ICA) and independent vector analysis (IVA) on a public EEG dataset containing various BCI paradigms. The results suggested that ILRMA has the potential to achieve higher discriminability than ICA and IVA for BCIs.

Nonetheless, the presence of variability in brain imaging/decoding gives rise to a new class of techniques that leverage the variability to gain insight into their neural data. Wang et al. proposed a novel method using individual template-based multivariate synchronization index and adaptive

threshold strategy for high-speed SSVEP-BCI. Trinh et al. investigated the use of task-induced intra-subject variability of resting-state EEGs for the classification and early detection of individuals with mild cognitive impairment (MCI) and Alzheimer's disease (AD). The results showed that the between-run spectral power similarity/variability could provide better performance than single-run resting-state EEGs. Qiao et al. used machine-learning approaches to extract biomarkers from resting EEG signals and identify the differences between major depression disorder (MDD) and healthy control (HC) groups.

AUTHOR CONTRIBUTIONS

C-SW: coordinated the writing process and proposed the structure of the article. All authors contributed equally to the editing process.

FUNDING

This work was supported by the Ministry of Science and Technology of Taiwan (MOST 109-2222-E-009-006-MY3, 109-2221-E-110-009-MY3), the Higher Education Sprout Project of the National Yang Ming Chiao Tung University and Ministry of Education of Taiwan, the US Army Research Laboratory (W911NF2120154), the US National Science Foundation (CBET-1935860), the US National Institute of Mental Health (R01MH126639 and R01MH129018), Burroughs Wellcome Fund (Career Award for Medical Scientists), a gift to UC San Diego from The Swartz Foundation (Sag Harbor, NY), the National Natural Science Foundation of China (61806149), and the Guangdong Basic and Applied Basic Research Foundation (2020A1515010991).

Conflict of Interest: The authors declare that the research was conducted in the absence of any commercial or financial relationships that could be construed as a potential conflict of interest.

Publisher's Note: All claims expressed in this article are solely those of the authors and do not necessarily represent those of their affiliated organizations, or those of the publisher, the editors and the reviewers. Any product that may be evaluated in this article, or claim that may be made by its manufacturer, is not guaranteed or endorsed by the publisher.

frontiers in Human Neuroscience

ORIGINAL RESEARCH
published: 30 October 2019
doi: 10.3389/fnhum.2019.00366

Challenge for Affective Brain-Computer Interfaces: Non-stationary Spatio-spectral EEG Oscillations of Emotional Responses

*Yi-Wei Shen and Yuan-Pin Lin**

Institute of Medical Science and Technology, National Sun Yat-sen University, Kaohsiung, Taiwan

Electroencephalogram (EEG)-based affective brain-computer interfaces (aBCIs) have been attracting ever-growing interest and research resources. Whereas most previous neuroscience studies have focused on single-day/-session recording and sensor-level analysis, less effort has been invested in assessing the fundamental nature of non-stationary EEG oscillations underlying emotional responses across days and individuals. This work thus aimed to use a data-driven blind source separation method, i.e., independent component analysis (ICA), to derive emotion-relevant spatio-spectral EEG source oscillations and assess the extent of non-stationarity. To this end, this work conducted an 8-day music-listening experiment (i.e., roughly interspaced over 2 months) and recorded whole-scalp 30-ch EEG data from 10 subjects. Given the large size of the data (i.e., from 80 sessions), results indicated that EEG non-stationarity was clearly revealed in the numbers and locations of brain sources of interest as well as their spectral modulation to the emotional responses. Less than half of subjects (two to four) showed the same relatively day-stationary (source reproducibility >6 days) spatio-spectral tendency towards one of the binary valence and arousal states. This work substantially advances the previous work by exploiting intra- and inter-individual EEG variability in an ecological multiday scenario. Such EEG non-stationarity may inevitably present a great challenge for the development of an accurate, robust, and generalized emotion-classification model.

Keywords: affective brain-computer interface, EEG, intra-individual difference, inter-individual difference, independent component analysis

OPEN ACCESS

Edited by:
Vasil Kolev,
Institute of Neurobiology (BAS), Bulgaria

Reviewed by:
Ahmet Ademoglu,
Boğaziçi University, Turkey
Pekcan Ungan,
Koç University, Turkey

***Correspondence:**
Yuan-Pin Lin
yplin@mail.nsysu.edu.tw

***Specialty section**:*
This article was submitted to Brain-Computer Interfaces, a section of the journal Frontiers in Human Neuroscience

Received: *30 July 2019*
Accepted: *27 September 2019*
Published: *30 October 2019*

Citation:
Shen Y-W and Lin Y-P (2019) Challenge for Affective Brain-Computer Interfaces: Non-stationary Spatio-spectral EEG Oscillations of Emotional Responses. Front. Hum. Neurosci. 13:366. doi: 10.3389/fnhum.2019.00366

INTRODUCTION

Electroencephalogram (EEG)-based affective brain-computer interfaces (aBCIs) have been attracting ever-growing interest and research resources. The aBCI represents an external device with a capacity for emotional awareness based on its interaction with a user's emotional responses. Recent availability of user-friendly wearable EEG sensing technologies and their market profitably bring laboratory-oriented aBCI research closer to practical applications in multidisciplinary domains such as NeuroMarketing, NeuroRehabilitation, and NeuroGaming. To this end, an embedded framework in aBCI that enables the accurate and reliable recognition of emotional

states of interest from time-varying, spatio-spectral EEG oscillations is of tremendous interest. Considerable work has been carried out to develop a machine learning framework to this end. The leveraged framework typically combines signal processing, feature engineering, and feature classification (Lin et al., 2010b; Jenke et al., 2014; Zheng, 2017; Xing et al., 2019). This research in machine-learning has rapidly progressed and contributed to our understanding of EEG oscillation modeling underlying emotional responses in general.

Nonetheless, the brain often switches between different operational modes while engaging in a task in realistic environments (Lance et al., 2015). This may be attributed to changes in several behavioral and/or psychophysiological states such as attention, stress, anxiety, or sleep quality. For an individual, the task-relevant EEG oscillations of interest may change on a daily basis, especially in emotional perception and experience. The EEG patterns are thus likely to be different on different days, considered to be reflective of inter-day non-stationarity or intra-individual variability. Some work has focused on empirically assessing such day-to-day variability and its negative impact on machine-learning proficiency in affective computing (Chai et al., 2017; Lin et al., 2017; Liu et al., 2018). In other words, the same emotion across days tended to be more widely scattered than the data clusters of different emotions within the same day (Lin et al., 2015). Such inter-day non-stationarity inevitably makes emotion prediction by a pre-trained emotion-aware model more difficult given the discrepancy between EEG distributions from different days. Until now, recent endeavors have focused on integrating advanced signal processing techniques or additional data calibration (Chai et al., 2017; Lin et al., 2017; Liu et al., 2018) to tackle this intra-individual variability, though the proposed scenario or the corresponding improvements still remain limited in their ability to perform robust predictions.

In addition, substantial non-stationary EEG correlates of emotional responses also exist between individuals, reflective of, namely, inter-individual non-stationarity or inter-individual variability. Due to intrinsic differences in personality, culture, gender, educational background, and/or living environment, individuals may have distinct behavioral and/or neurophysiological responses even while perceiving the same event. They are thus not likely to share common EEG distributions corresponding to the same emotional states, meaning that the performance of a generic machine-learning model will either be compromised or fail for certain individuals. Some related work has explored the negative impact of inter-individual non-stationarity on affective computing (Lin et al., 2010b; Soleymani et al., 2012; Lin and Jung, 2017; Li et al., 2019; Xing et al., 2019). In other words, a subject-independent model (i.e., in which learning has been carried out on the aggregated data of all available individuals) did not exclusively outperform a subject-dependent counterpart due to the increased amount of training data. Taken together, EEG non-stationarity (intra- and inter-individual counterparts) represents a great challenge to the development of an accurate, robust, and generalized emotion-classification model, and thereby considerately hinders the practical applicability of an aBCI to a realistic environment.

While most work has searched for better cross-day or cross-individual prediction by means of novel signal processing and machine learning frameworks, less effort has been directed at pinpointing the fundamental nature of the non-stationary EEG oscillations underlying emotional responses across both days and individuals. This work is thus devoted to using a data-driven blind source separation method, i.e., independent component analysis (ICA), to exploit emotion-relevant spatio-spectral EEG source oscillations and assess the extent of the non-stationarity in terms of the spatial configuration of cortical sources and the statistical properties of their tempo-spectral activities. To this end, this work conducted an 8-day music-listening experiment (i.e., roughly interspaced over the course of 2 months) and recorded whole-scalp 30-ch EEG data from a group of 10 subjects. This big dataset (80 sessions) allowed us to systematically investigate intra- and inter-individual EEG non-stationarity through source-level analysis. The empirical outcomes of this work not only advance previous work in EEG neuroscience that focused on single-day/-session recordings (Lin et al., 2010a; Rogenmoser et al., 2016) and sensor-level analysis (Schmidt and Trainor, 2001; Sammler et al., 2007; Daly et al., 2014), but also empirically demonstrate how challenging it is to deploy a robust emotion-aware analytical infrastructure given ecological EEG non-stationarity.

MATERIALS AND METHODS

Participants

Ten healthy subjects (six males, four females; age 23.3 $\pm$ 0.82 years) participated in an 8-day music-listening experiment interspaced over the course of 2 months (approximately once per week with an average time interval of 7.94 $\pm$ 1.76 days). All subjects were undergraduate or graduate students in the College of Engineering or Science. They had not received professional training on musicology or musical instruments and were thus considered to be non-musicians. They read and signed a consent form prior to the longitudinal experiment, which was approved by Human Research Protections Program of the local ethics committee. All subjects completed the entire eight-session experiment even though they were allowed to voluntarily withdraw at any time. The experiment facilitated an EEG analysis of emotional responses from a total of 80 day-sessions.

Experimental Design and Procedure

Prior to the music-listening experiment, all subjects were asked to provide a list of their favorite songs which, in their daily life, are able to emotionally arouse them. They were instructed, following the 2D valence-arousal emotion model (Russell, 1980), to select five songs from each of the four emotion quadrants (i.e., positive valence–high arousal, negative valence–high arousal, negative valence–low arousal, and positive valence–low arousal states) and further extract from each song a 60-s excerpt for use in the EEG-recording experiment. In order to avoid startling effects, the beginning and end of each excerpt were each faded in and out over the course of 10 s. The finalized 60-s song highlights were confirmed by each subject prior to the experiment. In addition,

along with a self-selected set per subject, this study randomly recruited extra four excerpts (one per quadrant) from other subjects to form his/her music procedure. This was intended to explore the relationship between familiarity and emotional responses in a longitudinal experiment, though this was not the analytical focus of this study.

The 24 song excerpts from each subject were separated into six four-trial blocks. Each block contained an excerpt for each emotional quadrant in random order. Each trial began with a 30-s resting phase followed by a 60-s music listening phase and ended with a self-reported rating task. In the rating task, subjects were required to rate songs on a five-point scale of emotional valence (from negative to positive), emotional arousal (from calm to excited), preference (from dislike to like), and familiarity (from never heard to knew well) based on what they had felt on each day. They did not necessarily assign the same scores as those assigned previously or as those provided in the selection of the songs. The experimental protocol was entirely self-paced such that each subject decided the amount of rest time before proceeding to the next trial or block. The music-listening experiment took place in a dimly lit room. The subjects were instructed to remain seated, keep their eyes closed (an auditory cue for every self-rating task), minimize their body movements, and fully attend to the song excerpts played through speakers during the entire experiment. Each subject listened to his/her unique set of 24 60-s songs in a shuffled order on each of the 8 days.

EEG Acquisition

EEG signals were recorded using a 36-channel EEG system (Neuroscan, Compumedics Ltd., Abbotsford, VIC, Australia). The 30 scalp electrodes were placed according to the International 10–20 system, with the linked mastoids (average of A1 and A2) and forehead as reference and ground sites, respectively. Four auxiliary electrodes were also placed to monitor electrooculogram (EOG) activity (two for above and below the left eye and another two on the outer canthi). All electrode impedance values were kept below 15 kΩ for better signal quality. EEG signals were sampled at 500 Hz and in a bandwidth of 1–100 Hz with a 60 Hz notch filter to remove powerline contamination.

Exploring Stationary Spatio-spectral EEG Oscillations

The adopted analytical framework included a number of steps to explore stationary spatio-spectral EEG oscillations of emotional responses for the 8-day dataset of each subject, including artifact suppression, ICA and clustering, and statistical assessment of emotional valence and arousal states. Data analysis and visualization were performed using the open source EEGLab toolbox/scripts (Delorme and Makeig, 2004) and MATLAB functions/scripts (The Mathworks, Inc., Natick, MA, USA). Details of technical procedures and implementation are provided below.

EEG data of each single-day session were band-passed filtered to 1–50 Hz to suppress low-frequency drifts and high-frequency artifacts. Artifact subspace reconstruction (ASR; Kothe and Jung, 2015) was then used to compensate for high-variance artifacts from the filtered EEG signals (Mullen et al., 2015; Artoni et al., 2017; the user-defined threshold was set to 5 standard deviations in this study), followed by a visual inspection to ensure data quality prior to the subsequent ICA analysis. Given the available 80 sessions (10 subjects × 8 sessions), only ∼1% on average (within a range of 0.1%–7%) of data from a single-day session was removed prior to further analysis.

The preprocessed single-day EEG data was submitted to ICA separately to parse the multichannel signals into independent components (ICs) via an extended infomax ICA algorithm. To localize the sources of the decomposed ICs, a single-dipole source model best fitted to the IC's scalp projection was calculated using a boundary element head model (BEM) based on the MNI brain template (Montreal Neurological Institute, MNI, Montreal, QC, Canada) implemented using the DIPFIT routine (Oostenveld and Oostendorp, 2002). Among the 30 derived ICs (four EOG and two reference channels excluded), this study evaluated scalp maps, spectral profiles, single dipole-fitting efficiency (explaining >85% of variance of the IC scalp map, as in Onton and Makeig, 2006), and within-brain dipole locations to retain cortical brain sources yet discard stereotyped non-cortical artifactual counterparts (e.g., eye movements, sporadic muscle tensions) prior to further analysis. The above ICA procedures and screening criteria are commonly used in other studies (Delorme et al., 2012; Wagner et al., 2016). On average, 88.50 ± 16.28 cortical ICs were retained in each subject in the 8-day dataset (11.20 ± 1.96 ICs per single-day session). Next, to assess stationary spatio-spectral sources across days, a *K*-means clustering algorithm was used to categorize similar ICs across 8 days into distinct IC clusters for each individual based on the attributes of their power spectral densities, scalp maps, and 3D dipole locations. ICs with distance values more than 3 standard deviations from the mean of their cluster centroids were relocated to another suitable one or classified as outliers. Such a semi-automatic IC clustering procedure allowed for the aggregation of neurophysiologically interpretable brain sources featuring homogeneous scalp maps and spectral profiles, thereby facilitating the assessment of their stationarity over the course of multiple days. This work adopted two objective measurements, namely dipolarity (Delorme et al., 2012) and reproducibility, to quantify both how well dipolar brain sources of interest were exploited on each single day and how frequently they emerged across days. The dipolarity value in this study represented the percentage of data variance accounting for a single dipole-fitting of the IC scalp map. The higher the dipolarity value, the more dipolar and prone to neurophysiological assessment of the brain source. Reproducibility was intuitively defined as the percentage of day sessions yielding the same dipolar ICs. In other words, a dipolar IC with 100% reproducibility means it is present in each of the 8 days.

In order to further assess spectral correlations between the derived ICs and emotional responses in distinct frequency bands, the short-time Fourier transform with a 50% overlapped 2-s Hamming window was used to estimate their spectrograms. The spectra were then grouped into five typical bands, namely delta (1–3 Hz), theta (4–7 Hz), alpha (8–13 Hz), beta (14–30 Hz),

and gamma (31–50 Hz) bands. Each logarithmic band-power time series belonging to a 60-s music excerpt was normalized by subtracting the mean power and dividing by the standard deviation of its preceding 30-s resting phase, followed by the single-trial baseline normalization manner in Grandchamp and Delorme (2011).

Statistical Assessment of Spatio-spectral Oscillations vs. Emotional States

This work attempted to exploit stationary spatio-spectral EEG correlates of emotional responses. All neurophysiological and behavioral responses regarding self-reported valence and arousal ratings were evaluated across multiple days for each individual. To this end, the 60-s band-specific spectral time series of the grouped ICs were categorized according to their assigned dichotomized valence (positive vs. negative) and arousal (high vs. low) states and assessed for whether there was a set of relatively day-stationary spatio-spectral oscillations modulated by emotional responses. The dichotomization was determined by setting a threshold at the middle of the five-point rating scale, i.e., <3 for negative valence/low arousal and >3 for positive valence/high arousal labels. This may have led to an imbalance in the classification of samples according to this binary classification scheme in each daily session. This work thus employed an unpaired t-test to assess the relationship across days between 8-day spatio-spectral EEG oscillations and emotional responses in each individual. For the daily association, a non-parametric permutation test was adopted since the limited 24 dichotomized trials per day may not comply with the assumption of a parametric approach. The permutation was done by iteratively shuffling the labels (n = 20,000) over trials and computing the test statistic, forming a distribution of test statistic values under the null hypothesis. Statistical assessment was then conducted by comparing the observed test statistic value (without shuffled data) against the distribution of null-hypothesis test statistic values. This work further stressed the behavior of emotion response-categorized EEG oscillations on each day as a reference.

RESULTS

Behavioral Ratings

Figure 1 depicts the daily self-reported ratings of 10 subjects while participating in the 8-day music-listening experiment. The dichotomization (=3) on the five-point scale of valence and arousal states led to averaged trials of 10.70 ± 0.25 vs. 11.30 ± 0.44 (positive vs. negative valence) and of 12.40 ± 0.47 vs. 9.40 ± 0.58 (high vs. low arousal) for each day session, and corresponded to a total of 85.70 ± 12.70 vs. 90.70 ± 18.57 and 114.50 ± 28.30 vs. 56.70 ± 34.35 for binary valence and arousal classes on average, accounting for eight sessions in each individual. However, the data of two subjects who happened to assign fewer labels with low arousal over the course of the eight sessions (<mean-standard deviation) were excluded from the arousal analysis. As can be seen, according to the unpaired t-test, the valence ratings differed significantly between positive and negative outcomes on each day session ($p < 0.01$). All eight sessions resulted in mean scores of 4.49 ± 0.08 and 1.69 ± 0.04 for positive and negative states, respectively. On the other hand, daily high arousal ratings were consistently higher than the low ones ($p < 0.01$), yielding 8-day mean ratings of 4.45 ± 0.05 and 1.68 ± 0.05 for high and low arousal states, respectively. The derived 8-day EEG trials and their self-reported binary labels from 10 subjects facilitated the subsequent exploratory assessment of (non)stationary spatio-spectral EEG dynamics of emotional responses.

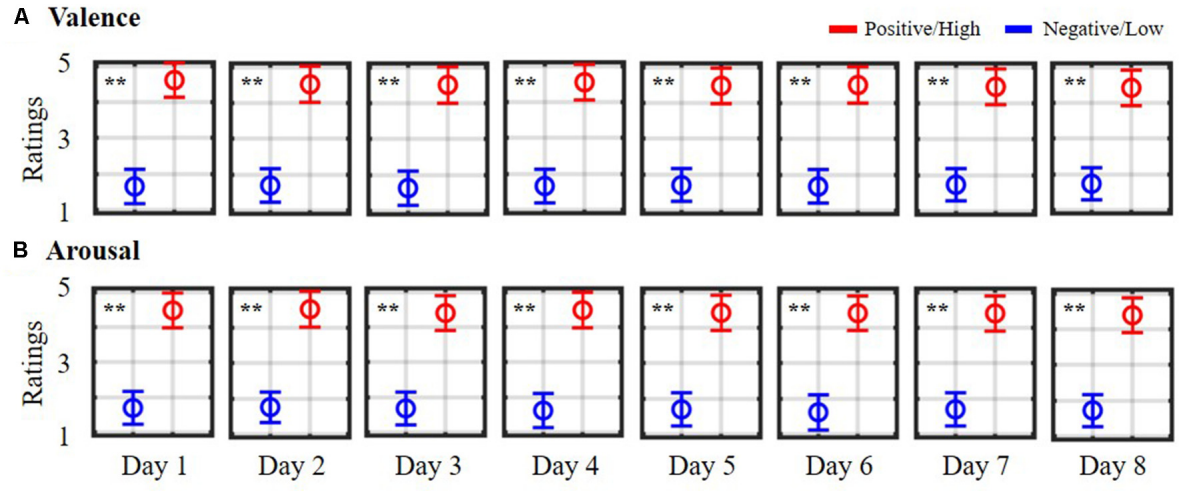

FIGURE 1 | Daily self-reported ratings of emotional **(A)** valence and **(B)** arousal states. Ratings were summarized from 10 subjects participating in an 8-day music-listening experiment. The symbols are color-coded according to the adopted dichotomized threshold (= 3) in the five-point scale. Red symbols (>3) indicate positive valence/high arousal ratings, whereas blue symbols (<3) indicate negative valence/low arousal ratings. ** Indicates a statistical significance of $p < 0.01$.

Demonstrating Day-Stationary Spatio-spectral EEG Oscillations and Their Associations With Emotional Responses From a Representative Subject

Figure 2 illustrates the neurophysiologically plausible IC clusters commonly exploited in the 8-day dataset from a representative subject. Nine ICs appeared to be relatively reproducible across days (reproducibility >75%, at least 6 of 8 days) and returned high estimated single-dipole brain sources (dipolarity >91%) that were spatially located in left frontal, frontal central, right frontal, left sensorimotor, central midline, right sensorimotor, left occipital, superior parietal, and right occipital brain regions. Each aggregated IC cluster corresponded to similar characteristics in terms of their logarithmic spectral profiles and 3D dipole source locations on the MNI brain template. Among them, the three frontal clusters and central midline cluster demonstrated a major peak in the theta band, and the others demonstrated a prominent alpha peak, in which the sensorimotor and superior parietal counterparts accompanied a minor beta peak.

Figure 3 explores the association of the spectral oscillations of the nine exploited IC clusters with the binary valence states from the same representative subject (as shown in **Figure 2**). The cross-day outcome was summarized by leveraging the trials of all eight sessions together to benchmark the within-day counterpart. As shown in **Figure 3A**, the cross-day analysis demonstrated that four spatio-spectral oscillations were significantly altered according to positive vs. negative valence ($p < 0.05$), consisting of central midline beta, right frontal alpha, and frontal central beta and gamma bands. A valence-irrelevant outcome of right occipital alpha ($p = 0.869$) was also provided in the last row as a technical control. As can be seen, after the eyes-closed baseline, the state-wise spectral time series notably diverged from one another over the course of the 60-s excerpt. The negative valence led to a major drop in central midline beta and right frontal alpha ($p < 0.01$) and a marginal drop in frontal central beta ($p = 0.049$), whereas the positive valence

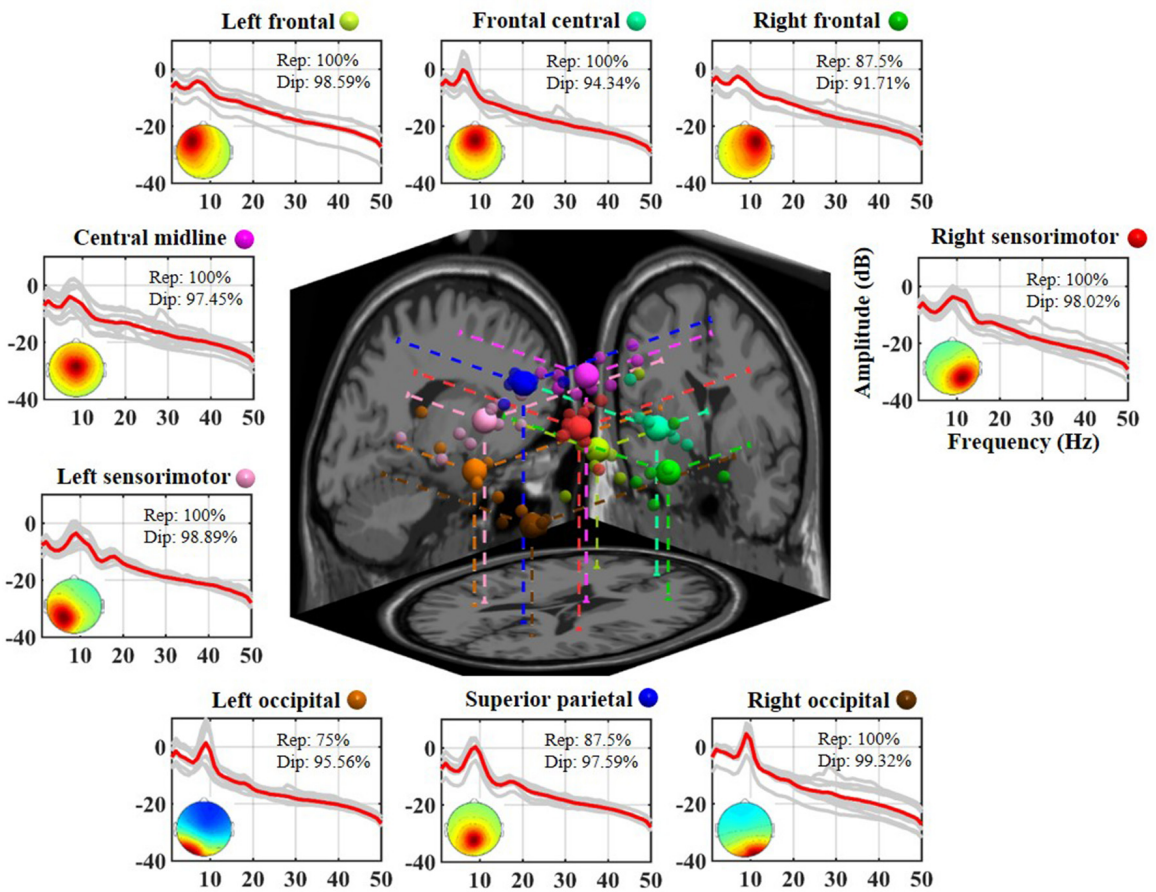

FIGURE 2 | Eight-day cortical source reproducibility from a representative subject. Each surrounding subplot refers to an aggregated independent component (IC) cluster. Averaged and individual IC log-power spectra (dB) are plotted in red and gray lines, respectively, and the corresponding mean scalp maps of clusters are superimposed. Rep and Dip indicate reproducibility and mean dipolarity per IC cluster, respectively. The centered subplot represents a 3D overview of the equivalent dipole locations of the nine clusters and their projections onto the MNI brain template. Dots in the same color represent the ICs grouped into the same cluster, in which bigger dots represent the cluster centroids.

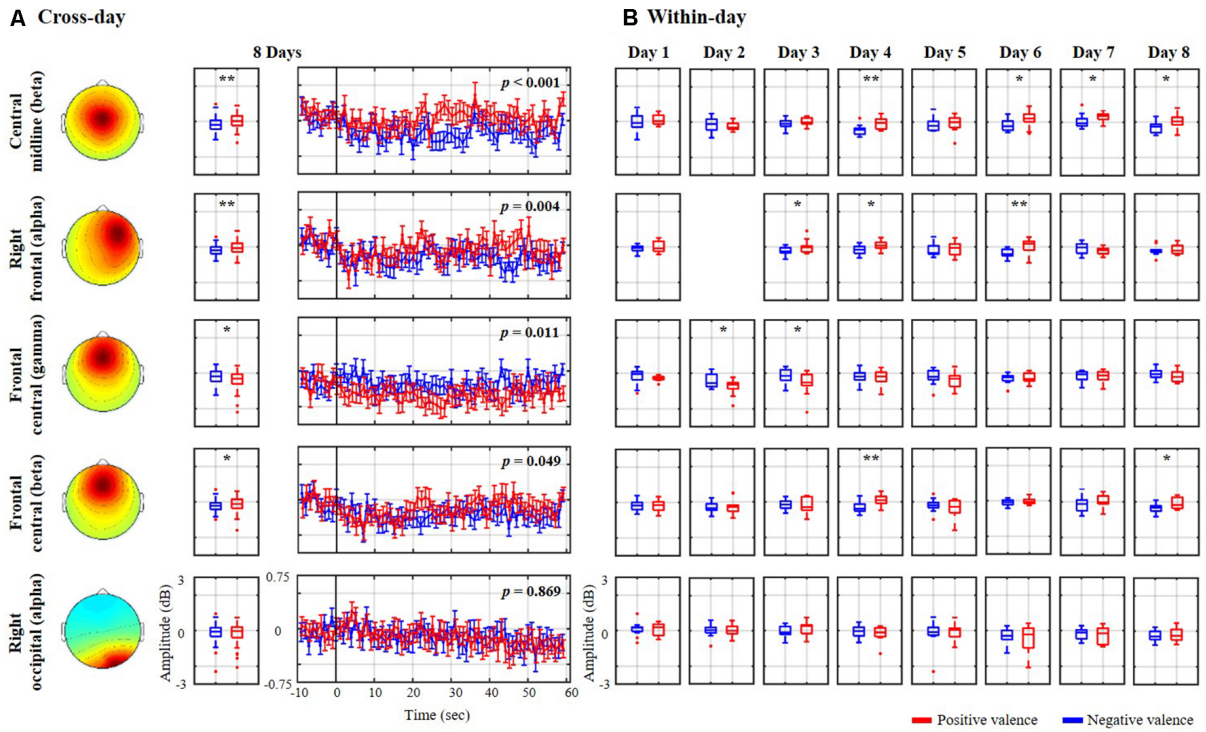

FIGURE 3 | Valence-relevant spatio-spectral oscillations using **(A)** cross-day and **(B)** within-day analyses from the same representative subject shown in **Figure 2**. The cross-day analysis led to four meaningful spatio-spectral oscillations from the nine IC clusters. The insignificant right occipital alpha in the last row was also provided as a technical control. Red and blue profiles represent the spectral oscillations associated with a positive and negative valence, respectively. * and ** refer to a statistical significance of $p < 0.05$ and $p < 0.01$, respectively.

accompanied a gamma decrease over the frontal central region ($p < 0.05$). Moreover, the cross-day analysis reflected a similar spectral tendency for most single days that were obtained by the within-day analysis. However, certain days happened to present reciprocal or distinctive outcomes. Taking the central midline beta as an example, 5 of 8 days (days 3, 4, 5, 6, and 8) exhibited a consistent decrease in negative compared to positive valence (days 4, 6, and 8 with $p < 0.05$), on day 2 there was a tendency towards a drop in positive valence, on day 7 positive valence tended to increase, and on day 1 spectral distinction was barely re-established. Such discrepancies in the cross- and within-day analysis more or less emerged in the other three informative spatio-spectral oscillations of interest from this representative subject. As the technical benchmark, the cross-day outcome of the right occipital alpha did reflect a common tendency towards indistinguishable spectral profiles on each individual day.

Figure 4 further demonstrates the validity of the exploited emotional valence-relevant spatio-spectral oscillations on the initial five-point scale from the same representative subject, as shown in **Figures 2**, **3**. With respect to the baseline, the spatio-spectral fluctuations of interest tended to be statistically modulated by the rating scale. Stronger negative ratings resulted in accentuated power attenuation in central midline beta ($r = 0.26$, $p < 0.01$), right frontal alpha ($r = 0.25$, $p < 0.01$), and frontal central beta ($r = 0.16$, $p = 0.05$) frequencies. In contrast, stronger positive ratings were linked to attenuated frontal central gamma deterioration ($r = -0.21$, $p < 0.01$). According to the empirical demonstration on the representative subject, this work as such applied the cross-day ICA analytical framework to each of the 10 subjects separately, exploring inter-subject commonality of the relatively day-stationary spatio-spectral EEG oscillations associated with emotional responses.

Exploring the Inter-subject Commonality of the Day-Stationary Spatio-spectral EEG Oscillations and Their Associations With Emotional Responses

Figure 5 summarizes the dipolarity and reproducibility of the exploited 8-day aggregated nine IC clusters from 10 subjects. Each IC cluster yielded a mean dipolarity of >94.28%, and their grand mean dipolarity was 95.99 ± 1.04%, indicating their neurophysiological adequacy for the sequential spectral assessment of emotional responses. In contrast, mean reproducibility in the nine clusters varied from 60.89 ± 28.36% (in the left occipital cluster) to 88.57 ± 10.98% (in the frontal central cluster) and the grand mean reproducibility was 76.03 ± 10.40%. In the worst-case scenario, some of them happened to be completely absent from distinct subjects, such as in the right frontal, central midline, left sensorimotor, left

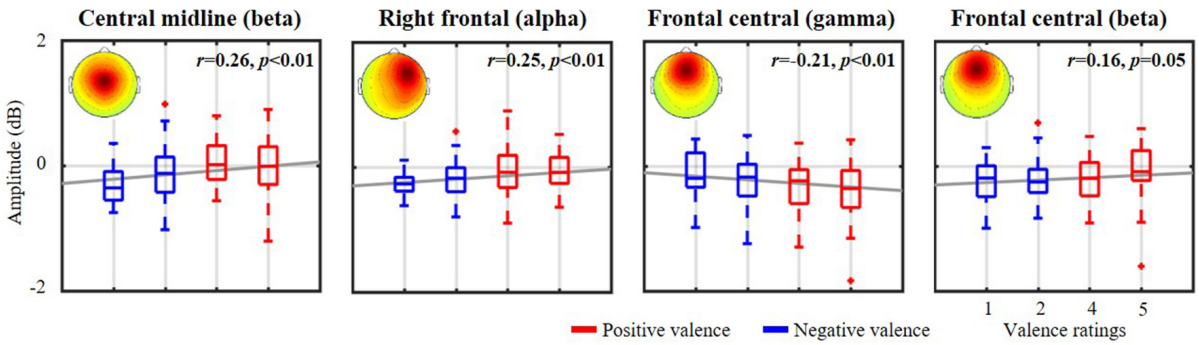

FIGURE 4 | The relationship between valence-relevant spatio-spectral oscillations and self-reported ratings from the same representative subject shown in **Figures 2**, **3**. The five-point scale of emotional valence was divided into two groups corresponding to scores below and above 3. Red and blue profiles represent positive (>3, more positive) and negative valences (<3, more negative), respectively. The gray lines depict the linear relationship as assessed by linear regression analysis. The mean scalp maps of the informative IC clusters are superimposed on each subplot.

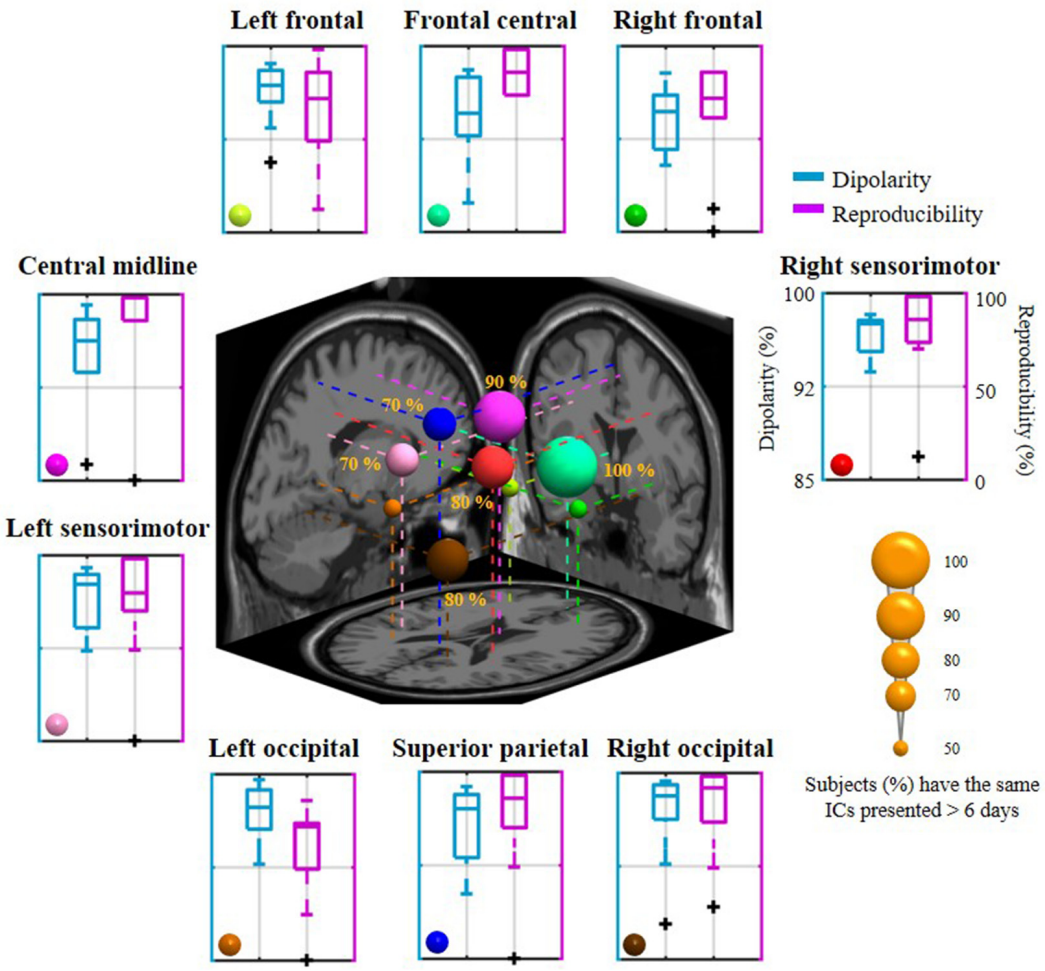

FIGURE 5 | The mean dipolarity and reproducibility of the 8-day aggregated nine IC clusters for 10 subjects and their inter-subject commonality. Each surrounding subplot refers to the mean of an IC cluster summarized across subjects. The centered subplot represents a 3D overview of the dipole centroids of the nine clusters and their projections onto the MNI brain template, where the dipole size was scaled by the inter-subject commonality of the relatively day-stationary ICs (the percentage of subjects with consistently the same IC appeared in 6 of 8 days).

occipital, and superior parietal sources (extreme outliers are shown in the boxplot). In order to evaluate the commonality of relatively day-stationary ICs for most subjects, this work defined a criterion by empirically counting ICs that were consistently present at least over the course of N days in the 8-day recording setting. N was set to six in this work due to the resultant nine-cluster mean reproducibility (i.e., 75% represents 6 of 8 days). Given the 6-day criterion, the inter-subject commonality (i.e., the percentage of the recruited 10 subjects with the same ICs over 6 days) was found to vary from 50% to 100%. The frontal central source was presented for each subject (100%), followed by the central midline source (90%), the right sensorimotor and the right occipital sources (80%), the left sensorimotor and the superior parietal sources (70%). The remaining three sources located in the left and right frontal regions and the left occipital regions had lower commonality (50%). The mean inter-subject commonality for the nine clusters was 71.11 ± 18.33% with cross-day reproducibility >6 days. The discernible cluster-to-cluster reproducibility and their inter-subject commonality reflected the non-stationarity of IC sources for each day and for each subject.

Figure 6 shows how the relatively day-stationary, subject-common ICs behaved in accordance with the emotional responses and whether they demonstrated the same spectral tendency towards the same binary state. Two main findings are mapped onto the MNI brain template in **Figure 6A**, including the percentage of subjects with the same ICs whose spectral oscillation statistically differed between the two binary states ($p < 0.05$) and the percentage of subjects with the same spatio-spectral tendency towards one of the two binary states ($p < 0.05$). The use of a large and more solid dipole means that analogous day-stationary spatio-spectral EEG correlates of an emotional state can be seen across more subjects. The Talairach coordinates of the centroids of the dipole distribution for each IC cluster and the relatively stationary outcomes for each emotion category are represented in **Table 1**. In general, the valence category yielded a higher inter-subject commonality for the spatio-spectral association across days. Four of 10 subjects similarly possessed central midline beta oscillations that significantly differed between the two binary states (i.e., the same emotion-related IC: 40%). They further led to more beta suppression for the negative valance compared

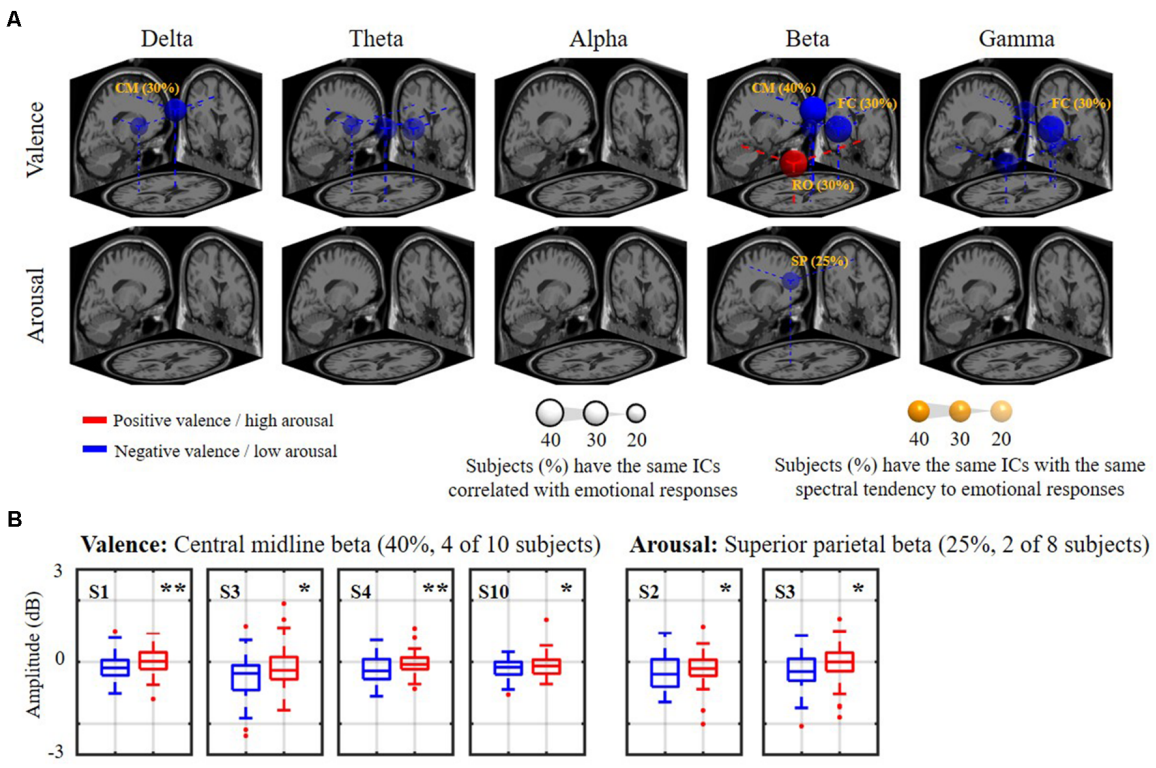

FIGURE 6 | The relatively day-stationary, subject-common spatio-spectral oscillations in response to the binary valence and arousal states. Panel **(A)** refers to a 3D overview of emotion-relevant IC cluster centroids and their projections onto the MNI brain template (FC: frontal central, CM: central midline, RO: right occipital, SP: superior parietal). Sphere size was scaled to indicate the percentage of subjects with the same day-stationary IC significantly related to emotional responses ($p < 0.05$), and transparency further represents the percentage of subjects with the same spectral tendency towards an emotional label of the target ICs (annotated %). Only results above 20%, i.e., with at least two subjects in common, are shown. Red and blue colors represent the power suppression associated with positive valence/high arousal and negative valence/low arousal states, respectively. Panel **(B)** demonstrates valence and arousal outcomes with the highest inter-subject commonality. * and ** refer to a statistical significance of $p < 0.05$ and $p < 0.01$, respectively. Two subjects with highly imbalanced labels were excluded from the arousal analysis.

TABLE 1 | Major day-stationary independent component (IC) clusters and their inter-subject commonalty to the binary valence and arousal states.

Emotional category	Source	Talairach coordinates			BA	Band power	Subjects (%) with the same emotion-related IC (>6 days)	Label	Subjects (%) with the same spatio-spectral tendency
		x	*y*	*z*					
Valence	Frontal central	0	52	6	10	Beta	40	Negative	30
						Gamma	40		30
	Central midline	3	1	49	6	Beta	40	Negative	40
						Delta	30		30
	Right occipital	20	−56	−6	19	Beta	40	Positive	30
Arousal	Superior parietal	3	−42	58	5	Beta	25	Low	25

The percentage of subjects with the same relatively day-stationary spatio-spectral oscillations correlated with the binary states and with the same tendency towards one of the binary states are identified.

to the positive counterpart (i.e., spatio-spectral tendency: 40%), as shown in **Figure 6B**. The negative valence also manifested the suppression in central midline delta power and frontal central beta and gamma power (i.e., spatio-spectral tendency: 30%). In addition, the positive valence tended to be associated with more right occipital beta suppression (30%). Other spatio-spectral tendencies typically had less commonality (20%). Unlike the valence outcome, the arousal category had worse inter-subject commonality. Only two of eight subjects (25%) were found to have similar superior parietal beta suppression in low arousal compared to high counterpart. Other spatio-spectral oscillations behaved quite inconsistently across individuals (<20%, with no consensus found between two subjects).

DISCUSSION

This work explored the extent of intra- and inter-individual EEG non-stationarity associated with emotional responses using the data-driven approach of an ICA. For the analysis of the 8-day EEG sessions of 10 subjects, an ICA-based analytical framework was conceived to identify the neurophysiologically interpretable spatio-spectral source oscillations for each single-day session, exploit their statistical link to the dichotomized emotional states, and assess the (non)stationary emotion-related EEG patterns along days and their inter-subject commonality. Results indicated substantial salient EEG non-stationarity in the numbers and locations of brain sources of interest as well as their spectral modulations to the emotional responses. However, this work did not attempt to disentangle the underlying neural mechanisms driving such vivid non-stationarity; rather, it sought to empirically demonstrate how clearly they emerge through source-level analysis. Leveraging neuroscience and machine-learning approaches, previous studies have yielded many important insights regarding affective computing, yet they mostly focused on single-day analysis given a group of subjects. This work substantially advanced the previous work by addressing the EEG non-stationarity in an ecologically valid multiday scenario that is considered to be a great challenge to the development of a robust, accurate, and generalized aBCI model for realistic applications.

Integrity of the ICA for Exploring (Non)stationary Sources

In this work, we used ICA to parse scalp channel data into spatially fixed and temporally independent sources and evaluate their association with emotional responses. Unlike channel-level analysis which may be compromised by volume conduction (Jung et al., 2000; Onton and Makeig, 2006), the ICA algorithm theoretically isolates cortical and non-cortical source signals, such as muscle tension and eye movements, from the spontaneous signal mixtures recorded from the scalp sensors. Once the respective best-fitting equivalent dipoles of the derived ICs have been localized, the source-level outcomes enable a better understanding of brain source-specific neural oscillations and their behavior over time and across individuals. Nevertheless, the number of resolved ICs is the same as the number of sensors used to record the signal mixtures. Using a limited number of sensors is not likely to fully reflect the underlying sources, which could be unlimited (Onton and Makeig, 2006). In addition, among the decomposed sources, only a few of them, with homogeneous scalp maps, within-brain dipoles, and meaningful spectral oscillations, explain the relatively large data variance of the signals, potentially leading to more neurophysiologically accessible associations. The remaining ones, which either have stereotypical artifacts or low-energy non-dipolar scalp maps, are less relevant and can be omitted. The analytical rationale of an ICA has been successfully demonstrated for the analysis of various phenomena using different numbers of scalp channels (e.g., 32–250), such as motor imagery (Wang et al., 2012), motion sickness (Chuang et al., 2012), music appreciation (Cong et al., 2013; Lin et al., 2014), walking locomotion (Wagner et al., 2016; Artoni et al., 2017), stress level (Schlink et al., 2017), and affective state (Onton and Makeig, 2009; Rogenmoser et al., 2016; Banaei et al., 2017). Comparing previously reported IC outcomes in terms of the number of cortical ICs vs. the number of channels, e.g., 5–15 ICs with 31 channels (Onton and Makeig, 2006), 8–15 ICs (mean: 11.2) with 32 channels (Wang et al., 2012), 12–29 ICs (mean: 20.3) with 128 channels (Banaei et al., 2017), 15–25 (mean: 18.4) with 248 channels (Gramann et al., 2010), and 9–31 ICs (mean: 16.0) with 250 channels (Onton and Makeig, 2009), this work, yielding an average of 11.20 ± 1.96 interpretable cortical ICs from 30-channel EEG signals across 80 single sessions, was

deemed acceptable. Moreover, the meaningful brain ICs derived from this work were all located in frontal, central, sensorimotor, parietal, and occipital regions of the cortex, consistent with previous findings (Onton and Makeig, 2006; Chen et al., 2010; Lin et al., 2014; Rogenmoser et al., 2016; Wagner et al., 2016; Banaei et al., 2017; Schlink et al., 2017), regardless of the channel set up used. No ICs located in deeper sub-cortical regions were resolved. This may be attributed to the fact that scalp EEG signals are less sensitive to neural activation stemming from deep subcortical structures. This work therefore cannot draw any conclusions on whether deeper structurers behave more (non)stationarily compared to the explored cortical ICs, especially for limbic and paralimbic areas involved in emotion processing revealed by other neuroimaging modalities, such as functional magnetic resonance imaging (fMRI) and positron emission tomography (PET; Blood et al., 1999; Phan et al., 2002; Trost et al., 2015). Accordingly, this issue needs to be taken into account during the interpretation of the stationary EEG sources in the present work.

From the 8-day EEG signals of 10 subjects, each subject returned an 8-day average of 88.50 ± 16.28 cortical ICs, from which was assessed which ICs were relatively reproducible across the 8 days. Nine aggregated cortical IC clusters located in frontal (left, right, and central), central midline, sensorimotor (left and right), superior parietal, and occipital (left and right) regions showed an average 8-day reproducibility of 76.03 ± 10.40 (min: 60.89 ± 28.36, max: 88.57 ± 10.98%) over 10 subjects (mean dipolarity: 95.99 ± 1.04%, see **Figure 5**). In other words, the nine identified ICs appeared at least, on average, for four (50%) and six (75%) of the 8 days. In an attempt to further quantify inter-subject commonality across the 10 subjects (as reflected in an IC present over 6 days, i.e., with a reproducibility >75%), 5 to 10 subjects possessed the same distinctive relatively day-stationary sources with a mean inter-subject commonality of 71.11 ± 18.33%. In all subjects, the frontal central source could be repeatedly seen on at least 6 days. If the criterion for cross-day reproducibility became more stringent (not presented in Results), the range and mean of inter-subject commonality considerably decreased towards the value reached at 8 days (7 days: 20%–90% (mean: 54.44 ± 23.51%), 8 days: 0%–70% (33.33 ± 22.91%). Among these cross-day criteria, the central midline source, rather than the frontal central source, was found relatively stationary across days and individuals (6 days: 90%, 7 days: 90%, and 8 days: 70% vs. 6 days: 100%, 7 days: 70%, and 8 days: 40%, respectively). Such varied cluster-to-cluster reproducibility indicated that the cortical EEG sources of interest behaved distinctly across multiple days, precisely considered to reflect intra-individual non-stationarity. The absence of the ICs on certain single-day sessions may be in part due to the source origins whose projected signals were neither strong nor distinct enough to be detected at the scalp and subsequently resolved by ICA (Onton et al., 2006). Previous EEG-ICA studies mostly assessed task-related spatio-spectral EEG oscillations by summarizing single-day analyses from a group of subjects (Onton and Makeig, 2006; Chen et al., 2010; Gramann et al., 2010; Chuang et al., 2012; Wang et al., 2012; Lin et al., 2014; Rogenmoser et al., 2016; Wagner et al., 2016; Banaei et al., 2017; Schlink et al., 2017). Less effort was invested in the issue of intra-individual differences across EEG sources. We believe that the qualitative IC outcomes from the 8-day sessions in this work have provided an opportunity to better understand EEG non-stationarity.

Intra- and Inter-individual Differences in Spatio-spectral Correlates of Emotional Responses

Even though the nine cortical IC clusters were significantly compromised by EEG non-stationarity, some remained relatively consistent across days and individuals in response to the dichotomized emotional states (see **Figure 6** and **Table 1**), especially in the valence category. Four of 10 subjects possessed the central midline source (BA 6, premotor cortex) on 6 of the 8 days, accompanying the beta suppression with the negative valence. Other outcomes included negative valence-induced beta and gamma suppression over the frontal central region (BA 10, anterior prefrontal cortex), negative valence-induced delta suppression over the central midline region, and positive valence-induced beta suppression over the right occipital region (BA 19, visual cortex), as derived from three subjects. In contrast, only two of eight subjects (2 of 10 subjects were excluded due to highly imbalanced labels) showed beta suppression in the superior parietal region (BA 5, superior parietal lobule) in low arousal. To the best of our knowledge, this work represents the first attempt to extract information from spatio-spectral EEG oscillations of emotional responses in the context of a longitudinal experiment (i.e., in the form of 8-day music-listening recordings interspaced over 2 months, roughly once per week). Due to a lack of direct evidence, the obtained outcomes were related to previous single-day work in terms of the localized brain regions and spectral oscillations. A meta-analysis study (Phan et al., 2002) that aggregated the findings of emotional activation from 55 PET and fMRI studies summarized the role of medial prefrontal cortex in emotional processing (reported by at least 40% of the included studies), which may support our findings on frontal central ICs. Further, it is plausible that emotional states reached during exposure to consonant music stimulate the additional drive of the motor system (Sammler et al., 2007; Lin et al., 2014). Several neurophysiological studies have also found that some music-modulated brain activity intervenes in emotion processing (Blood et al., 1999; Khalfa et al., 2005). Similarly, our results demonstrated informative IC sources located around the premotor cortex. Posterior (parietal and occipital) regions have been reported to be associated with emotional affect and intensity (Heller, 1993; Schmithorst, 2005), which may explain the engagement of parietal and occipital sources in this work. Engagement of multiple brain sources was ecologically true since music-induced emotion was accompanied by a rich involvement of reward, memory, self-reflective, and sensorimotor processes and engaged distributed brain networks across both cortical and subcortical regions (Trost et al., 2015). In contrast, with regards to the distinguishable spectral

oscillations, most of them were seen in the beta band (frontal central, central midline, superior parietal, and right occipital regions), with fewer in the delta (central midline region) or gamma (frontal central region) bands. Previous EEG findings may provide partial support to these findings, notably those related to prefrontal beta and gamma asymmetry in valence (Daly et al., 2014), parietal beta asymmetry for motivation and emotion (Schutter et al., 2001), and widespread delta synchronization for music processing (Bhattacharya and Petsche, 2005). However, this work did not replicate certain representative spectral outcomes, such as fronto-midline theta enhancement for the positive valence (Sammler et al., 2007; Lin et al., 2010a) or frontal alpha asymmetry for valence distinction (Schmidt and Trainor, 2001; Davidson, 2004). Frontal central theta was sparsely observed in two subjects (yet did not result in an augmentation in positive valence), while frontal alpha modulation was only seen in the representative subject (see **Figures 3**, **4**). This may be partly attributed to inter-day variability due to changes in mental states over the course of a multiday recording, such as in the form of mental fatigue modulating the lower frequency power of delta, theta, and alpha bands (Lal and Craig, 2002).

With regards to the within- vs. cross-day analysis of the representative subject (see **Figure 3**), it may be that the emotion-discriminative sources analyzed in the cross-day analysis could have been absent, and their spectral associations to the binary states could have behaved either reciprocally or even indiscriminately on certain days. Such day-to-day spectral variability was similar to findings using peripheral bio-signals (Picard et al., 2001) and in other EEG-related topics (Christensen et al., 2012). The underlying mechanisms of this cross-day discrepancy remain unclear based on this study's outcomes, but could be partly attributed to the physiological modulation of behavioral and mental states, such as attention, stress, anxiety, and sleep quality. Previous EEG studies have reported that these factors indeed somehow modulate tasked-related EEG patterns. For example, neurophysiological correlates of mental fatigue differed between sleep-deprived and well-rested controls (Ahn et al., 2016), spectral oscillations fluctuated according to attentional demands (Wang et al., 2018), and acute stress affected the cognitive ability of brain-computer interface control (Garcia et al., 2019). It is reasonable to conclude that each of the aforementioned factors and their plausible interactions more or less concurrently confound the EEG patterns, leading to non-stationarity on different days. As such, exploring inter-subject commonalty for the relatively day-stationary sources is presumably more challenging. Given the criterion for IC's cross-day reproducibility (>6 of 8 days), only a few subjects demonstrated same day-stationary ICs with a significant relationship to emotional responses (valence: 3–4 of 10 subjects, arousal: two of eight subjects). The inter-subject commonality more or less deteriorated if the same spectral tendency was involved (see **Table 1**). Previous neuroimaging studies have proven that individual differences associated with morphological differences in brain anatomy (e.g., gray and white matter volume), exhibiting a wide range of basic and higher cognitive functions (Kanai and Rees, 2011). The distinctive brain structures and functional patterns involved may serve as a useful source of information to study their links to human personality, behavior and cognition (Kanai and Rees, 2011; Liu et al., 2019). Particularly, personality is considered a dominant factor contributing to individual differences in emotion perception and experiences (Eysenck, 1998) and regulation strategies (Gross and John, 2003). These data could thus serve as a physiological indicator, for example, to correlate with stress resilience (Brouwer et al., 2015) and emotional states (Subramanian et al., 2018). In addition, recent work has demonstrated that the EEG variability was considerably larger across individuals than across repeated sessions. Such inter-subject variability may be increased while engaging in a more cognitive-oriented task (Melnik et al., 2017). In contrast, with regards to the ICA, the non-identical cortical and subcortical brain volumes likely make the size and/or orientation of EEG sources quite variable. Therefore, all individuals may not contribute the same ICs located in brain regions of interest (Onton and Makeig, 2006). Taken together with intra-individual variability, this low inter-subject commonality for the same tendency of day-stationary spatio-spectral correlates of psychophysiological emotional responses seems reasonable and realistic.

Negative Impact of Nonstationary Spatio-spectral Oscillations to aBCI

This work has empirically demonstrated strong intrinsic intra- and inter-individual variability in emotional responses using source-level analysis. The numbers and locations of EEG sources of interest and their discriminative spectral profiles were found to be different across days and individuals. As such, EEG signals recorded from the scalp may be more substantially different from one another since they consist of linear mixtures projected from multiple non-stationary cortical sources (in addition to non-cortical artifactual sources). This source-to-channel projection may explain why the inter-day data clusters of the same emotion had more variability more than the inter-emotion data clusters within one day, as revealed by the channel-level analysis (Lin et al., 2015). Our exploratory findings also demonstrate why the day-independent (Chai et al., 2017; Lin et al., 2017; Liu et al., 2018) and subject-independent (Soleymani et al., 2012; Li et al., 2018, 2019) emotion prediction scenarios (i.e., a single generic model works on multiple days or on multiple subjects) were more challenging than their day-dependent and subject-dependent counterparts. Accordingly, this work highlights an urgent need to incorporate typical machine-learning frameworks with advanced signal processing [e.g., robust principal component analysis (Lin et al., 2017) stationary subspace analysis (Kaltenstadler et al., 2018)] and model calibrating steps (Chai et al., 2017; Liu et al., 2018; Li et al., 2019) to obviate the negative interference of discrepant EEG distributions across sessions obtained on different days or from different individuals. Furthermore, alternative to leveraging a unique model for the prediction of different days or individuals, future effort can be devoted to evaluate an ensemble learning framework (Chuang et al., 2014) that generates multiple classifiers to learn distinctive EEG distributions of emotional responses and strategically combines

their multiple decisions. Thus, effectively monitoring/alleviating the EEG non-stationarity and adapting an existing model(s) accordingly will facilitate the translation of laboratory-oriented demonstrations to real-life aBCI applications.

CONCLUSION

This work exploratorily demonstrated the extent of intra-individual and inter-individual EEG non-stationarity associated with emotional responses using the data-driven approach of an ICA. To this end, this work conducted an 8-day music-listening experiment (i.e., roughly interspaced over 2 months) and recorded whole-scalp 30-ch EEG data from a group of 10 subjects. Results from this large dataset (i.e., 80 sessions) indicated substantial EEG non-stationarity in the numbers and locations of brain sources of interest as well as their spectral modulations to emotional responses. Only less than half of subjects (two to four) demonstrated the same relatively distinct day-stationary (source reproducibility >6 days) spatio-spectral tendency towards one of the binary emotion states. Since previous works mostly focused on single-day/-session recordings and sensor-level analysis, this work substantially advances the work of these previous studies by exploiting EEG non-stationarity in an ecological multiday scenario. This is considered a great challenge to the development of a robust, accurate, and generalized aBCI model aimed at realistic applications.

DATA AVAILABILITY STATEMENT

The datasets for this manuscript are not publicly available at this moment because the data recording is ongoing for more subjects. Future requests to access the datasets should be directed to the corresponding author.

ETHICS STATEMENT

The studies involving human participants were reviewed and approved by Human Research Protection Program of Kaohsiung Medical University, Taiwan. The patients/participants provided their written informed consent to participate in this study.

AUTHOR CONTRIBUTIONS

Y-WS conducted the experiments, analyzed the data, and wrote the corresponding parts of the article. Y-PL conceived and supervised the experiments and data analysis and wrote and revised the article.

FUNDING

This work was supported in part by the Ministry of Science and Technology, Taiwan, under Grant MOST 106-2628-E-110 -002-MY3.

REFERENCES

Ahn, S., Nguyen, T., Jang, H., Kim, J. G., and Jun, S. C. (2016). Exploring neuro-physiological correlates of drivers' mental fatigue caused by sleep deprivation using simultaneous EEG, ECG, and fNIRS data. *Front. Hum. Neurosci.* 10:219. doi: 10.3389/fnhum.2016.00219

Artoni, F., Fanciullacci, C., Bertolucci, F., Panarese, A., Makeig, S., Micera, S., et al. (2017). Unidirectional brain to muscle connectivity reveals motor cortex control of leg muscles during stereotyped walking. *Neuroimage* 159, 403–416. doi: 10.1016/j.neuroimage.2017.07.013

Banaei, M., Hatami, J., Yazdanfar, A., and Gramann, K. (2017). Walking through architectural spaces: the impact of interior forms on human brain dynamics. *Front. Hum. Neurosci.* 11:477. doi: 10.3389/fnhum.2017.00477

Bhattacharya, J., and Petsche, H. (2005). Phase synchrony analysis of EEG during music perception reveals changes in functional connectivity due to musical expertise. *Signal Process.* 85, 2161–2177. doi: 10.1016/j.sigpro.2005.07.007

Blood, A. J., Zatorre, R. J., Bermudez, P., and Evans, A. C. (1999). Emotional responses to pleasant and unpleasant music correlate with activity in paralimbic brain regions. *Nat. Neurosci.* 2, 382–387. doi: 10.1038/7299

Brouwer, A., van Schaik, M. G., Korteling, J. E., van Erp, J. B. F., and Toet, A. (2015). Neuroticism, extraversion, conscientiousness and stress: physiological correlates. *IEEE Trans. Affect. Comput.* 6, 109–117. doi: 10.1109/taffc.2014.2326402

Chai, X., Wang, Q. S., Zhao, Y. P., Li, Y. Q., Liu, D., Liu, X., et al. (2017). A fast, efficient domain adaptation technique for cross-domain electroencephalography(EEG)-based emotion recognition. *Sensors* 17:E1014. doi: 10.3390/s17051014

Chen, Y. C., Duann, J. R., Chuang, S. W., Lin, C. L., Ko, L. W., Jung, T. P., et al. (2010). Spatial and temporal EEG dynamics of motion sickness. *Neuroimage* 49, 2862–2870. doi: 10.1016/j.neuroimage.2009.10.005

Christensen, J. C., Estepp, J. R., Wilson, G. F., and Russell, C. A. (2012). The effects of day-to-day variability of physiological data on operator functional state classification. *Neuroimage* 59, 57–63. doi: 10.1016/j.neuroimage.2011.07.091

Chuang, S. W., Ko, L. W., Lin, Y. P., Huang, R. S., Jung, T. P., and Lin, C. T. (2012). Co-modulatory spectral changes in independent brain processes are correlated with task performance. *Neuroimage* 62, 1469–1477. doi: 10.1016/j.neuroimage.2012.05.035

Chuang, C. H., Ko, L. W., Lin, Y. P., Jung, T. P., and Lin, C. T. (2014). Independent component ensemble of EEG for brain-computer interface. *IEEE Trans. Neural Syst. Rehabil. Eng.* 22, 230–238. doi: 10.1109/TNSRE.2013.2293139

Cong, F. Y., Alluri, V., Nandi, A. K., Toiviainen, P., Fa, R., Abu-Jamous, B., et al. (2013). Linking brain responses to naturalistic music through analysis of ongoing EEG and stimulus features. *IEEE Trans. Multimedia* 15, 1060–1069. doi: 10.1109/tmm.2013.2253452

Daly, I., Malik, A., Hwang, F., Roesch, E., Weaver, J., Kirke, A., et al. (2014). Neural correlates of emotional responses to music: an EEG study. *Neurosci. Lett.* 573, 52–57. doi: 10.1016/j.neulet.2014.05.003

Davidson, R. J. (2004). What does the prefrontal cortex "do" in affect: perspectives on frontal EEG asymmetry research. *Biol. Psychol.* 67, 219–233. doi: 10.1016/j.biopsycho.2004.03.008

Delorme, A., and Makeig, S. (2004). EEGLAB: an open source toolbox for analysis of single-trial EEG dynamics including independent component analysis. *J. Neurosci. Methods* 134, 9–21. doi: 10.1016/j.jneumeth.2003.10.009

Delorme, A., Palmer, J., Onton, J., Oostenveld, R., and Makeig, S. (2012). Independent EEG sources are dipolar. *PLoS One* 7:e30135. doi: 10.1371/journal.pone.0030135

Eysenck, H. (1998). *Dimensions of Personality*. Piscataway, NJ: Transaction Publishers.

Garcia, L., Zak, M., Grenier, C., Hanrio, S., Henry, D., Randriamanantena, R., et al. (2019). "Is stress state an important factor in the BCI-P300 speller performance?," in *Advances in Computational Intelligence*, eds I. Rojas, G. Joya and A. Catala (Cham: Springer International Publishing), 442–454.

Gramann, K., Gwin, J. T., Bigdely-Shamlo, N., Ferris, D. P., and Makeig, S. (2010). Visual evoked responses during standing and walking. *Front. Hum. Neurosci.* 4:202. doi: 10.3389/fnhum.2010.00202

Grandchamp, R., and Delorme, A. (2011). Single-trial normalization for event-related spectral decomposition reduces sensitivity to noisy trials. *Front. Psychol.* 2:236. doi: 10.3389/fpsyg.2011.00236

Gross, J. J., and John, O. P. (2003). Individual differences in two emotion regulation processes: implications for affect, relationships, and well-being. *J. Pers. Soc. Psychol.* 85, 348–362. doi: 10.1037/0022-3514.85.2.348

Heller, W. (1993). Neuropsychological mechanisms of individual differences in emotion, personality, and arousal. *Neuropsychology* 7, 476–489. doi: 10.1037/0894-4105.7.4.476

Jenke, R., Peer, A., and Buss, M. (2014). Feature extraction and selection for emotion recognition from EEG. *IEEE Trans. Affect. Comput.* 5, 327–339. doi: 10.1109/taffc.2014.2339834

Jung, T. P., Makeig, S., Humphries, C., Lee, T. W., Mckeown, M. J., Iragui, V., et al. (2000). Removing electroencephalographic artifacts by blind source separation. *Psychophysiology* 37, 163–178. doi: 10.1017/s0048577200980259

Kaltenstadler, S., Nakajima, S., Müller, K., and Samek, W. (2018). Wasserstein stationary subspace analysis. *IEEE J. Sel. Top. Signal Process.* 12, 1213–1223. doi: 10.1109/jstsp.2018.2873987

Kanai, R., and Rees, G. (2011). The structural basis of inter-individual differences in human behaviour and cognition. *Nat. Rev. Neurosci.* 12, 231–242. doi: 10.1038/nrn3000

Khalfa, S., Schon, D., Anton, J. L., and Liegeois-Chauvel, C. (2005). Brain regions involved in the recognition of happiness and sadness in music. *Neuroreport* 16, 1981–1984. doi: 10.1097/00001756-200512190-00002

Kothe, C. A. E., and Jung, T. P. (2015). *Artifact Removal Techniques with Signal Reconstruction*. United States Patent Application.

Lal, S. K. L., and Craig, A. (2002). Driver fatigue: electroencephalography and psychological assessment. *Psychophysiology* 39, 313–321. doi: 10.1017/s0048577201393095

Lance, B. J., Touryan, J., Wang, Y.-K., Lu, S.-W., Chuang, C.-H., Khooshabeh, P., et al. (2015). "Towards serious games for improved BCI," in *Handbook of Digital Games and Entertainment Technologies*, eds R. Nakatsu, M. Rauterberg and P. Ciancarini (Singapore: Springer), 1–28.

Li, X., Song, D. W., Zhang, P., Zhang, Y. Z., Hou, Y. X., and Hu, B. (2018). Exploring EEG features in cross-subject emotion recognition. *Front. Neurosci.* 12:162. doi: 10.3389/fnins.2018.00162

Li, Y., Zheng, W., Wang, L., Zong, Y., and Cui, Z. (2019). From Regional to Global Brain: A Novel Hierarchical Spatial-Temporal Neural Network Model for EEG Emotion Recognition. *IEEE T AFFECT COMPUT.* doi: 10.1109/TAFFC.2019.2922912

Lin, Y. P., Duann, J. R., Chen, J. H., and Jung, T. P. (2010a). Electroencephalographic dynamics of musical emotion perception revealed by independent spectral components. *Neuroreport* 21, 410–415. doi: 10.1097/wnr.0b013e32833774de

Lin, Y. P., Wang, C. H., Jung, T. P., Wu, T. L., Jeng, S. K., Duann, J. R., et al. (2010b). EEG-based emotion recognition in music listening. *IEEE Trans. Biomed. Eng.* 57, 1798–1806. doi: 10.1109/TBME.2010.2048568

Lin, Y. P., Duann, J. R., Feng, W. F., Chen, J. H., and Jung, T. P. (2014). Revealing spatio-spectral electroencephalographic dynamics of musical mode and tempo perception by independent component analysis. *J. Neuroeng. Rehabil.* 11:18. doi: 10.1186/1743-0003-11-18

Lin, Y. P., Hsu, S. H., and Jung, T. P. (2015). "Exploring day-to-day variability in the relations between emotion and EEG signals," in *Foundations of Augmented Cognition: 9th International Conference, AC 2015, Held as Part of HCI International 2015, Los Angeles, CA, USA, August 2-7, 2015, Proceedings*, eds D. D. Schmorrow and C. M. Fidopiastis (Cham: Springer International Publishing), 461–469.

Lin, Y. P., Jao, P. K., and Yang, Y. H. (2017). Improving cross-day EEG-based emotion classification using robust principal component analysis. *Front. Comput. Neurosci.* 11:64. doi: 10.3389/fncom.2017.00064

Lin, Y. P., and Jung, T. P. (2017). Improving EEG-based emotion classification using conditional transfer learning. *Front. Hum. Neurosci.* 11:334. doi: 10.3389/fnhum.2017.00334

Liu, S., Chen, L., Guo, D., Liu, X., Sheng, Y., Ke, Y., et al. (2018). Incorporation of multiple-days information to improve the generalization of EEG-based emotion recognition over time. *Front. Hum. Neurosci.* 12:267. doi: 10.3389/fnhum.2018.00267

Liu, W., Kohn, N., and Fernández, G. (2019). Intersubject similarity of personality is associated with intersubject similarity of brain connectivity patterns. *Neuroimage* 186, 56–69. doi: 10.1016/j.neuroimage.2018.10.062

Melnik, A., Legkov, P., Izdebski, K., Kärcher, S. M., Hairston, W. D., Ferris, D. P., et al. (2017). Systems, subjects, sessions: to what extent do these factors influence EEG data? *Front. Hum. Neurosci.* 11:150. doi: 10.3389/fnhum.2017.00150

Mullen, T. R., Kothe, C. A. E., Chi, Y. M., Ojeda, A., Kerth, T., Makeig, S., et al. (2015). Real-time neuroimaging and cognitive monitoring using wearable dry EEG. *IEEE Trans. Biomed. Eng.* 62, 2553–2567. doi: 10.1109/tbme.2015.2481482

Onton, J., and Makeig, S. (2006). Information-based modeling of event-related brain dynamics. *Prog. Brain Res.* 159, 99–120. doi: 10.1016/s0079-6123(06)59007-7

Onton, J., and Makeig, S. (2009). High-frequency broadband modulations of electroencephalographic spectra. *Front. Hum. Neurosci.* 3:61. doi: 10.3389/neuro.09.061.2009

Onton, J., Westerfield, M., Townsend, J., and Makeig, S. (2006). Imaging human EEG dynamics using independent component analysis. *Neurosci. Biobehav. Rev.* 30, 808–822. doi: 10.1016/j.neubiorev.2006.06.007

Oostenveld, R., and Oostendorp, T. F. (2002). Validating the boundary element method for forward and inverse EEG computations in the presence of a hole in the skull. *Hum. Brain Mapp.* 17, 179–192. doi: 10.1002/hbm.10061

Phan, K. L., Wager, T., Taylor, S. F., and Liberzon, I. (2002). Functional neuroanatomy of emotion: a meta-analysis of emotion activation studies in PET and fMRI. *Neuroimage* 16, 331–348. doi: 10.1006/nimg.2002.1087

Picard, R. W., Vyzas, E., and Healey, J. (2001). Toward machine emotional intelligence: analysis of affective physiological state. *IEEE Trans. Pattern Anal. Mach. Intell.* 23, 1175–1191. doi: 10.1109/34.954607

Rogenmoser, L., Zollinger, N., Elmer, S., and Jancke, L. (2016). Independent component processes underlying emotions during natural music listening. *Soc. Cogn. Affect. Neurosci.* 11, 1428–1439. doi: 10.1093/scan/nsw048

Russell, J. A. (1980). A circumplex model of affect. *J. Pers. Soc. Psychol.* 39, 1161–1178. doi: 10.1037/h0077714

Sammler, D., Grigutsch, M., Fritz, T., and Koelsch, S. (2007). Music and emotion: electrophysiological correlates of the processing of pleasant and unpleasant music. *Psychophysiology* 44, 293–304. doi: 10.1111/j.1469-8986.2007.00497.x

Schlink, B. R., Peterson, S. M., Hairston, W. D., König, P., Kerick, S. E., and Ferris, D. P. (2017). Independent component analysis and source localization on mobile EEG data can identify increased levels of acute stress. *Front. Hum. Neurosci.* 11:310. doi: 10.3389/fnhum.2017.00310

Schmidt, L. A., and Trainor, L. J. (2001). Frontal brain electrical activity (EEG) distinguishes valence and intensity of musical emotions. *Cogn. Emot.* 15, 487–500. doi: 10.1080/0269993004200187

Schmithorst, V. J. (2005). Separate cortical networks involved in music perception: preliminary functional MRI evidence for modularity of music processing. *Neuroimage* 25, 444–451. doi: 10.1016/j.neuroimage.2004.12.006

Schutter, D. J. L., Putman, P., Hermans, E., and Van Honk, J. (2001). Parietal electroencephalogram β asymmetry and selective attention to angry facial expressions in healthy human subjects. *Neurosci. Lett.* 314, 13–16. doi: 10.1016/s0304-3940(01)02246-7

Soleymani, M., Lichtenauer, J., Pun, T., and Pantic, M. (2012). A multimodal database for affect recognition and implicit tagging. *IEEE Trans. Affect. Comput.* 3, 42–55. doi: 10.1109/t-affc.2011.25

Subramanian, R., Wache, J., Abadi, M. K., Vieriu, R. L., Winkler, S., and Sebe, N. (2018). ASCERTAIN: emotion and personality recognition using commercial sensors. *IEEE Trans. Affect. Comput.* 9, 147–160. doi: 10.1109/taffc.2016.2625250

Trost, W., Frühholz, S., Cochrane, T., Cojan, Y., and Vuilleumier, P. (2015). Temporal dynamics of musical emotions examined through intersubject

synchrony of brain activity. *Soc. Cogn. Affect. Neurosci.* 10, 1705–1721. doi: 10.1093/scan/nsv060

Wagner, J., Makeig, S., Gola, M., Neuper, C., and Muller-Putz, G. (2016). Distinct β band oscillatory networks subserving motor and cognitive control during gait adaptation. *J. Neurosci.* 36, 2212–2226. doi: 10.1523/JNEUROSCI.3543-15.2016

Wang, Y. K., Jung, T. P., and Lin, C. T. (2018). Theta and alpha oscillations in attentional interaction during distracted driving. *Front. Behav. Neurosci.* 12:3. doi: 10.3389/fnbeh.2018.00003

Wang, Y. J., Wang, Y. T., and Jung, T. P. (2012). Translation of EEG spatial filters from resting to motor imagery using independent component analysis. *PLoS One* 7:e37665. doi: 10.1371/journal.pone.0037665

Xing, X., Li, Z., Xu, T., Shu, L., Hu, B., and Xu, X. (2019). SAE+LSTM: a new framework for emotion recognition from multi-channel EEG. *Front. Neurorobot.* 13:37. doi: 10.3389/fnbot.2019.00037

Zheng, W. M. (2017). Multichannel EEG-based emotion recognition *via* group sparse canonical correlation analysis. *IEEE Trans. Cogn. Dev. Syst.* 9, 281–290. doi: 10.1109/tcds.2016.2587290

Conflict of Interest: The authors declare that the research was conducted in the absence of any commercial or financial relationships that could be construed as a potential conflict of interest.

frontiers in Computational Neuroscience

MINI REVIEW
published: 21 January 2020
doi: 10.3389/fncom.2019.00087

Intra- and Inter-subject Variability in EEG-Based Sensorimotor Brain Computer Interface: A Review

Simanto Saha and Mathias Baumert**

School of Electrical and Electronic Engineering, The University of Adelaide, Adelaide, SA, Australia

Brain computer interfaces (BCI) for the rehabilitation of motor impairments exploit sensorimotor rhythms (SMR) in the electroencephalogram (EEG). However, the neurophysiological processes underpinning the SMR often vary over time and across subjects. Inherent intra- and inter-subject variability causes covariate shift in data distributions that impede the transferability of model parameters amongst sessions/subjects. Transfer learning includes machine learning-based methods to compensate for inter-subject and inter-session (intra-subject) variability manifested in EEG-derived feature distributions as a covariate shift for BCI. Besides transfer learning approaches, recent studies have explored psychological and neurophysiological predictors as well as inter-subject associativity assessment, which may augment transfer learning in EEG-based BCI. Here, we highlight the importance of measuring inter-session/subject performance predictors for generalized BCI frameworks for both normal and motor-impaired people, reducing the necessity for tedious and annoying calibration sessions and BCI training.

Keywords: electroencephalography, brain computer interface, sensorimotor rhythms, transfer learning, inter-subject associativity

OPEN ACCESS

Edited by:
Chun-Shu Wei,
National Chiao Tung University, Taiwan

Reviewed by:
Bradley Jay Edelman,
School of Medicine, Stanford University, United States
Po-Chih Kuo,
Massachusetts Institute of Technology, United States
Yu-Kai Wang,
University of Technology Sydney, Australia

****Correspondence:***
Simanto Saha
simanto.saha@ieee.org
Mathias Baumert
mathias.baumert@adelaide.edu.au

Received: *21 October 2019*
Accepted: *16 December 2019*
Published: *21 January 2020*

Citation:
Saha S and Baumert M (2020) Intra- and Inter-subject Variability in EEG-Based Sensorimotor Brain Computer Interface: A Review. Front. Comput. Neurosci. 13:87. doi: 10.3389/fncom.2019.00087

1. INTRODUCTION

Brain computer interfaces (BCI) exploiting sensorimotor rhythms (SMR) have shown promise for both the improvement of motor performance in normal subjects and the rehabilitation of motor function in patients (Dobkin, 2007; Wang and Jung, 2011). The SMR can be elicited by motor imagery (MI) that shares common neurophysiological mechanisms with overt motor execution (ME), the former being more convenient for BCI users who cannot perform an overt ME task due to some degree of motor disability (Jeannerod, 1995; Lotze and Halsband, 2006; Zich et al., 2015; Vyas et al., 2018). ME supplements the MI-based motor learning process for people with intact cognitive functions (Allami et al., 2008; Ruffino et al., 2017).

Since the motor learning processes differ across individuals (Herzfeld and Shadmehr, 2014; Wu et al., 2014), significant inter-subject variability in motor behavior is anticipated that manifests in the task-specific electrical activities in the cortico-subcortical networks (Seghier and Price, 2018). Consequently, the cortical activity observed in electroencephalogram (EEG) varies across subjects during MI, impeding its utility for BCI applications (Saha et al., 2017b). A study has suggested that time-variant brain functions cause unreliable EEG signatures with poor reproducibility even within a particular subject (Meyer et al., 2013). Such inter-session, intra-subject variability together with even larger inter-subject variability confounds BCI using SMR. This review discusses how inter-session and inter-subject performance predictors could potentially augment transfer learning to improve SMR-based BCI performance while reducing calibration efforts significantly.

2. SENSORIMOTOR DYNAMICS AND BCI

2.1. Motor Learning Process and Brain Function

Motor variability due to variability in human kinematic parameters, e.g., force field adaptation, speed and trajectory, and motivational factors such as level of user engagement, arousal and feelings of competence, necessary for performing a motor task is an integral part of the motor learning process (Duarte and Reinkensmeyer, 2015; Úbeda et al., 2015; Edelman et al., 2019; Faller et al., 2019). Such variability does not necessarily represent noise contents only, but may potentially be a manifestation of motor and perceptual learning processes. Motor variability may augment reinforcement-based motor learning (Herzfeld and Shadmehr, 2014; Wu et al., 2014; Singh et al., 2016). Individuals with higher motor variability may learn a skill faster than individuals with lower motor variability (Wu et al., 2014; Singh et al., 2016). The EEG patterns associated with motor variability could therefore partly explain intra-individual variability in SMR-based BCI (Bradberry et al., 2010; Úbeda et al., 2015; Ostry and Gribble, 2016). Furthermore, structural and functional differences between subjects are associated with motor learning process, which might explain the motor learning variability (Tomassini et al., 2011). On the other hand, motor variability could be leveraged to augment the motor learning and rehabilitation (Krakauer, 2006; Singh et al., 2016). A study has demonstrated that alterations in EEG signatures due to motor training are dependent on intra- and inter-subject variability (Jochumsen et al., 2017).

2.2. Motor Imagery vs. Motor Execution

Motor imagery is the kinesthetic anticipation of corresponding overt ME without producing an actual motor output. Jeannerod stated that MI is functionally equivalent to its ME counterpart (Jeannerod, 1995). More specifically, MI is related to the preparation of ME and represents meaningful neurophysiological dynamics of human motor functions (Zich et al., 2015). Consequently, both MI and ME share common sensorimotor areas such as primary motor area (M1), supplementary motor area (SMA) and premotor cortex (PMC) (Jeannerod, 1995; Lotze and Halsband, 2006; Zich et al., 2015).

The neurophysiology underlying MI may differ in healthy people and patients with motor-impairing conditions (Lotze et al., 2001). MI-based BCI may augment the motor learning process in healthy subjects (Ruffino et al., 2017). In patients with impaired motor functions, MI is often the only viable option to drive rehabilitative BCI due to users' inability to perform overt ME (Jackson et al., 2001; Lotze and Halsband, 2006). The individuality and severity of motor impairments impact the underlying neurophysiology, for example, post-stroke neurophysiology relies on the lesion locations (Niazi et al., 2013). Studies are essential to further delineate the roles of MI and ME in motor learning or relearning for both healthy and impaired subjects to refine the design of BCI for supplementing the motor learning process.

2.3. Neuroplasticity and BCI-Driven Motor Rehabilitation

Rehabilitative BCI designs either attach neural prostheses to the impaired upper/lower limb or restimulate the damaged synaptic networks. In either case, the idea is to exploit and promote neural plasticity (Dobkin, 2007; Wang et al., 2010). The plastic characteristics of the brain are created by the time-variant behavior of the synapses within complex neural networks, first illustrated by Hebb, 1949 (Brown and Milner, 2003). The motor learning process and associated variability promote plasticity in the sensorimotor networks and adjust both motor and perceptual skills (Ostry and Gribble, 2016). This inherent plasticity is exploited by BCI systems to rehabilitate impaired motor functions (Dobkin, 2007). Ruffino et al. demonstrated that MI-based mental training can contribute to corticospinal plasticity (Ruffino et al., 2017). This might lead to BCI-driven rehabilitation systems for stroke and spinal cord injury patients (Niazi et al., 2013; Müller-Putz et al., 2014). Recent studies showed that BCI skill acquisition and associated physiological changes may improve BCI performance in both patients and healthy users (Perdikis et al., 2018; Edelman et al., 2019). Complex or cognitively entertaining tasks that require greater user engagement or motivation can compensate for intra- and inter-subject variability, leading to enhanced BCI learning in adverse operating conditions (Perdikis et al., 2018; Edelman et al., 2019; Faller et al., 2019; Li et al., 2019).

BCI-driven prostheses can extend the degree of freedom of users with motor impairments. The success of BCI control and rehabilitation depends on the user's capacity to modulate the intact neural ensembles (Dobkin, 2007). Substantial changes in neural substrates that were observed following closed-loop BCI-driven motor learning of prosthesis control provide evidence of neuroplasticity (Orsborn et al., 2014). In stroke patients, post-rehabilitation electromyographic recordings showed increased activity in the paretic finger following BCI-driven rehabilitation using an orthosis, which exhibits improvement in neuromuscular coherence for movement control (Ramos-Murguialday et al., 2013). Furthermore, BCI-driven proprioceptive feedback-based and functional electrical stimulation-based rehabilitation strategies could reinforce motor control (Zhao et al., 2016; Darvishi et al., 2017; Selfslagh et al., 2019).

The structural and functional changes in neural substrates induced by MI-based training with transcranial direct current stimulation or transcranial magnetic stimulation provide further evidence for the induction of neuroplasticity that is essential for motor recovery (Hong et al., 2017; Johnson et al., 2018). Because the induction of plasticity by rehabilitation varies across subjects (Leamy et al., 2014; Vallence et al., 2015), subject-specific training sessions may be required. Since the neurophysiology associated with SMR dynamics varies between individuals, quantification of variability in healthy user groups could be beneficial first step that may guide the interpretation of altered neurophysiology in diverse conditions of motor-impairment (Müller-Putz et al., 2014).

3. BRAIN TOPOGRAPHY AND BCI PERFORMANCE PREDICTORS

3.1. Intra- and Inter-subject Variability in Brain Topography

The functional relevance of brain topographical variability with the anatomical boundaries is still not fully understood; however, significant structure-function correspondences may be derived at the aggregate level (Honey et al., 2009, 2010). Smith et al. delineated structural differences, suggesting that the number of folds and thickness of the cortex could be associated with whole-brain functional networks (Smith et al., 2019). Furthermore, inter-subject variability in topography occurs due to subject-specific cognitive style and strategy to perform a task over time (Seghier and Price, 2018), which could augment the underlying learning processes, e.g., motor and perceptual learning (Krakauer, 2006; Baldassarre et al., 2012; Herzfeld and Shadmehr, 2014; Wu et al., 2014; Singh et al., 2016).

Intra- and inter-subject variability can be explained by scale-dependent brain networks in spatial, temporal and topological domains (Betzel and Bassett, 2017; Betzel et al., 2019). For example, diversity in spatial organization of the brain networks can be investigated either at cellular or system level. The sources of intra- and inter-subject variability in brain dynamics may be identifiable using multi-scale analysis tools (Betzel et al., 2019) although the interpretation of brain connectivity networks at different scales may not be straightforward (Raichle, 2009).

Integrating intrinsic brain activities (i.e., resting state activities) into BCI design could offer experimental and methodological advantages for scrutinizing task-specific brain dynamics (Northoff et al., 2010). While it has been argued that the brain is primarily reflexive, responding according to external stimuli/environmental demand, the brain also performs many intrinsic functions including signal acquisition, maintenance, and interpretation (Raichle, 2009, 2010). Supporting the critical role of intrinsic brain activity, it consumes 20% of the body's energy (Clarke, 1999). Thus, understanding the role of resting EEG might supplement BCI performance (Northoff et al., 2010; Suk et al., 2014; Morioka et al., 2015).

3.2. BCI Performance Predictors

Around 15–30% users are inherently unable to produce task-specific signature robust enough to control a BCI (Blankertz et al., 2009; Vidaurre and Blankertz, 2010). The underlying causes of this BCI illiteracy are not well-understood; however, diverse psychological and neurophysiological predictors appear to be associated with BCI performance (Blankertz et al., 2009; Vidaurre and Blankertz, 2010; Jensen et al., 2011; Hammer et al., 2012; Ahn and Jun, 2015; Jeunet et al., 2015; Reichert et al., 2015; Zhang et al., 2015; Acqualagna et al., 2016; Vasilyev et al., 2017; Sannelli et al., 2019).

Cognitive and neurological factors including functions and anatomy along with emotional and mental processes give rise to intra- and inter-subject variability affecting the performance of SMR-based BCI (Wens et al., 2014; Reichert et al., 2015; Zhang et al., 2015; Acqualagna et al., 2016; Betzel and Bassett, 2017; Vasilyev et al., 2017; Seghier and Price, 2018; Betzel et al., 2019; Smith et al., 2019). Time-variant cognitive factors such as fatigue, memory load, attention and reaction time modulate instantaneous brain activity, and can cause inconsistent SMR-based BCI performance (Hammer et al., 2012; Ahn and Jun, 2015; Fox et al., 2015; Jeunet et al., 2015; Darvishi et al., 2018; Sannelli et al., 2019). Furthermore, users' characteristics such as lifestyle, gender, and age can influence BCI performance (Ahn and Jun, 2015). Kasahara et al. illustrated that a neuroanatomical feature i.e., gray matter volume is associated with SMR-based BCI performance (Kasahara et al., 2015).

The structural and functional differences may characterize dynamic baseline activities manifested in resting-state network (RSN) dynamics. RSNs represent large-scale spatiotemporal structures exhibiting intrinsic brain activities that are thought to be functionally relevant (Deco et al., 2011). Studies have shown intra- and inter-subject variability in sensorimotor RSN, which may have implications for BCI performance variability (Jensen et al., 2011; Wens et al., 2014; Reichert et al., 2015; Zhang et al., 2015; Acqualagna et al., 2016; Vasilyev et al., 2017). It has been hypothesized that SMR-based BCI performance predictor is reliable for people who display strong resting EEG amplitudes (Blankertz et al., 2010; Suk et al., 2014; Sannelli et al., 2019). **Table 1** shows a list of intra- and inter-subject BCI performance predictors.

4. TRANSFER LEARNING

4.1. Covariate Shift and Transfer Learning

Transfer learning techniques originating from the field of machine learning have been adopted to compensate BCI systems for inter-subject and inter-session variability of EEG feature distributions (Fazli et al., 2015; Jayaram et al., 2016). A key idea is to regularize BCI model parameters for covariate shift adaptation. Covariate shift occurs when distributions of training and test data differ significantly although their conditional distributions may remain unchanged (Krusienski et al., 2011). **Figure 1** schematically illustrates the idea of covariate shift when the training and test data distributions are different. The underlying time-variant and subject-specific brain dynamics depends on associated psychological and neurophysiological factors (Blankertz et al., 2009; Vidaurre and Blankertz, 2010; Jensen et al., 2011; Hammer et al., 2012; Ahn and Jun, 2015; Jeunet et al., 2015; Reichert et al., 2015; Zhang et al., 2015; Acqualagna et al., 2016; Vasilyev et al., 2017; Sannelli et al., 2019) and cause covariate shift in EEG-derived feature distributions (Krusienski et al., 2011; Fazli et al., 2015; Jayaram et al., 2016).

The earliest attempts to overcome inter-session variability include preliminary training sessions to enhance the user's ability to modulate brain signals robust enough to control BCI (Wolpaw et al., 1991; Wolpaw and McFarland, 1994; Birbaumer et al., 1999). The training sessions required for users are tedious and inconvenient. Therefore, machine learning-based BCI models were introduced to reduce individual training session for each BCI use, in which a model has to be calibrated based on the data at the beginning of each session (Ramoser et al., 2000; Blankertz et al., 2002). Recent studies have proposed SMR-based BCI without any session- and subject-specific calibration utilizing the

TABLE 1 | Intra- and inter-subject BCI performance predictors.

Study	Subject*	Task type	Task description	Predictor
Edelman et al. (2019)	68	MI, Rest	LH, RH, LH+RH (Continuous cursor or robotic arm control)	User engagement
Faller et al. (2019)	40	Visuo-motor	Virtual reality-based plane control	Arousal
Sannelli et al. (2019)	80	MO, ME, MI	MO: LH, RH, Foot ME: LH, RH, RF MI: LH, RH, RF	Tiredness, imagination strength, motivation, uneasiness
Saha et al. (2019)	5	MI	RH, RF	Cortical regions of interest
Perdikis et al. (2018)	2 (SCI)	MI	LH, RH, LH+RH, LF+RF, Rest	Mutual learning (parameters derived from interface-application, BCI output, and EEG)
Darvishi et al. (2018)	10	MI	LH, RH	Reaction time
Jochumsen et al. (2017)	47	ME	Palmar grasp	Motor training (laparoscopic surgery training using a simulator)
Saha et al. (2017a)	5	MI	RH, RF	Optimal Channels
Saha et al. (2017b)	9	MI	LH, RH, LF+RF, Tongue	
Úbeda et al. (2015)	5	ME	Continuous Cursor control	Kinematic parameters, i.e., speed, trajectory
Jeunet et al. (2015)	18	Mental Imagery	Motor: LH Non-motor: mental rotation and mental subtraction	Personality and Cognitive Profile; Neurophysiological markers, including parietal θ-power and frontal and occipital α-power
Kasahara et al. (2015)	30	MI	LH, RH (Finger-thumb opposition)	Gray matter volume
Morioka et al. (2015)	51	Visuo-spatial attention task	Attend-left or Attend-right	Resting EEG
Suk et al. (2014)	83	Attention task	LH, RH, Foot	
Hammer et al. (2012)	83	MI	LH, RH, RF	Visuo-motor coordination, ability to concentrate

**Subjects were healthy unless specified otherwise; SCI, spinal cord injury; MI, motor imagery; ME, motor execution; MO, motor observation; LH, left hand, RH, right hand; LF, Left Foot; RF, right foot.*

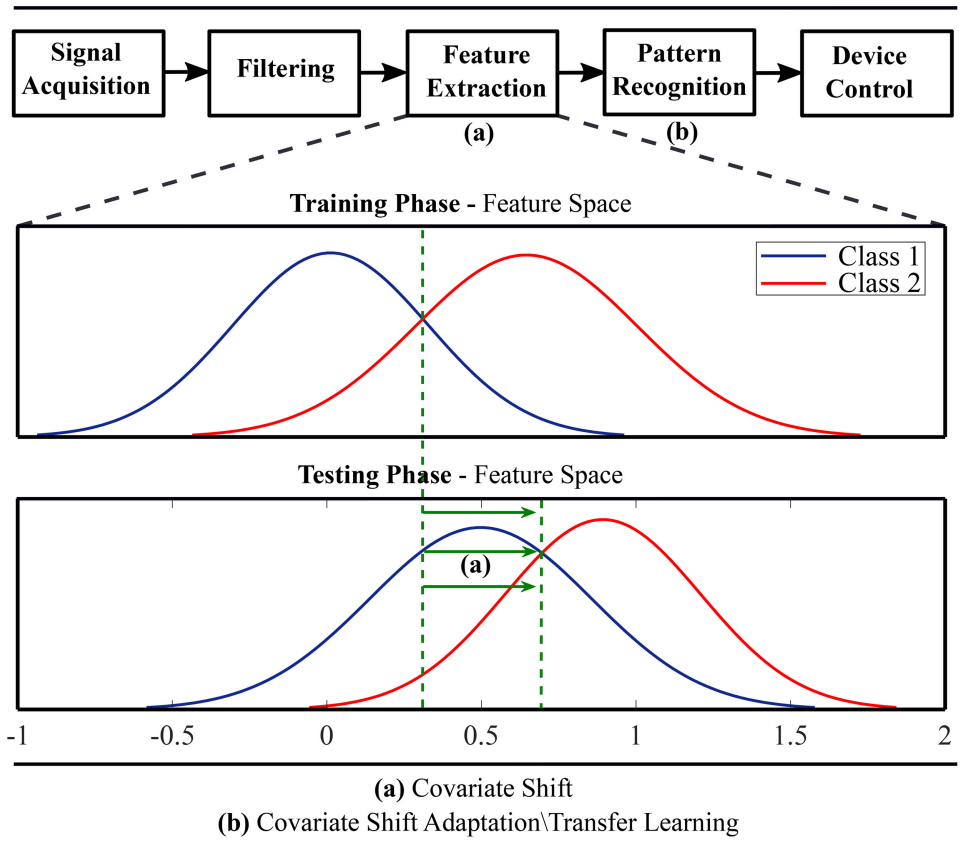

FIGURE 1 | A schematic illustration of covariate shift in the feature space and application of transfer learning methods for covariate shift adaptation.

concept of transfer learning (Kang et al., 2009; Li et al., 2010; Lu et al., 2010; Niazi et al., 2013; Kang and Choi, 2014; Fazli et al., 2015; Lotte, 2015; Jayaram et al., 2016; Saha et al., 2017a,b, 2019; Fahimi et al., 2018; He and Wu, 2019).

4.2. The Concept of Inter-subject Associativity

Most of the existing transfer learning approaches are based on regularization or inter-session/subject transfer of model parameters, indirectly transferring knowledge pertaining to the sources of intra- and inter-subject variability (Samek et al., 2013; Lotte, 2015). Many works on transfer learning for SMR-based BCI proposed the use of a very few training samples from the target subject (Kang et al., 2009; Lu et al., 2010; Kang and Choi, 2014; Fahimi et al., 2018; He and Wu, 2019). Recent studies have utilized resting EEG from the target subject incorporated into transfer learning model before proceeding to the actual experiment (Suk et al., 2014; Morioka et al., 2015). While time and effort for building those models could be significantly reduced, they still require training session. Others have recently demonstrated the feasibility of inter-subject BCI models without any training trial from the target subject (Saha et al., 2017a,b, 2019). However, the performance requires to be improved significantly prior to real-life use of such BCI systems.

A transfer learning method is worthwhile if the subjects share non-stationarities that can be modeled in an inter-subject context, but ineffective if the subjects exhibit unlike non-stationarities (Samek et al., 2013). The term *inter-subject associativity* refers to potential inter-subject BCI performance predictors, which could be incorporated into BCI design to augment transfer learning (Kang and Choi, 2014; Wronkiewicz et al., 2015; Saha et al., 2017a,b, 2019). Source-space analysis for detecting inter-subject associative EEG channels can improve SMR-based BCI performance (Wronkiewicz et al., 2015; Saha et al., 2017a, 2019). For example, the classification accuracies for two different subject pairs are $90.36 \pm 5.59\%$ and $63.21 \pm 8.43\%$, respectively, suggesting not both subject pairs can be used to achieve a good performance (Saha et al., 2019).

A set of generalized BCI frameworks would be more feasible to implement as compared to a common BCI framework for all users. Because, it is evident to observe significant inter-subject variability in EEG signals (Saha et al., 2017b). Successful quantification of *inter-subject associativity* may suggest clustering of subjects, each cluster having subjects with EEG signal

characteristics that are similar or can be interpreted in an inter-subject context. Considering the increasing volume of EEG-BCI databases, it may become feasible to quantify the exact sources of inter-subject/session variability as well as indicators of inter-subject associativity allowing to reduce training sessions to a minimum (Lotte, 2015). Recent advances in deep learning methods demonstrate a potential application that alleviates intra- and inter-subject variability in BCI settings (Chiarelli et al., 2018; Fahimi et al., 2018). Meanwhile, recent studies suggest that the quantification of *inter-subject associativity* could be equally important to increase the efficacy of exclusively machine learning-based transfer learning strategies for covariate shift adaptation (Kang et al., 2009; Kang and Choi, 2014; Wronkiewicz et al., 2015; Saha et al., 2017b, 2019; Perdikis et al., 2018).

5. CONCLUSION

Intra- and inter-subject variability is undeniable due to time-variant factors related to the experimental setting and underlying psychological and neurophysiological parameters. Besides the extensive use of transfer learning methods for the covariate shift adaptation, many recent works sought to find suitable psychological and neurological predictors for BCI performance. The assimilation of such predictors into a subject independent context may reduce or eliminate the tedious session or subject-specific training by supplementing the performance of existing transfer learning methods. However, collecting *a priori* information related to BCI performance predictors could be challenging. Inter-subject topographical associativity characterized by resting EEG could provide a viable alternative solution to reduce the calibration time to a minimum (Northoff et al., 2010; Suk et al., 2014; Morioka et al., 2015) assuming we understand the significance of intrinsic brain activities, i.e., resting EEG signals, and the role of RSN topographies on SMR-related brain functions.

AUTHOR CONTRIBUTIONS

SS conceived the idea, prepared the figure and table, and wrote the first draft. MB reviewed and commented on the manuscript. SS and MB read and approved the final manuscript.

REFERENCES

Acqualagna, L., Botrel, L., Vidaurre, C., Kübler, A., and Blankertz, B. (2016). Large-scale assessment of a fully automatic co-adaptive motor imagery-based brain computer interface. *PLoS ONE* 11:e0148886. doi: 10.1371/journal.pone.0148886

Ahn, M., and Jun, S. C. (2015). Performance variation in motor imagery brain–computer interface: a brief review. *J. Neuroscience Methods* 243, 103–110. doi: 10.1016/j.jneumeth.2015.01.033

Allami, N., Paulignan, Y., Brovelli, A., and Boussaoud, D. (2008). Visuo-motor learning with combination of different rates of motor imagery and physical practice. *Exp. Brain Res.* 184, 105–113. doi: 10.1007/s00221-007-1086-x

Baldassarre, A., Lewis, C. M., Committeri, G., Snyder, A. Z., Romani, G. L., and Corbetta, M. (2012). Individual variability in functional connectivity predicts performance of a perceptual task. *Proc. Natl. Acad. Sci. U.S.A.* 109, 3516–3521. doi: 10.1073/pnas.1113148109

Betzel, R. F., and Bassett, D. S. (2017). Multi-scale brain networks. *Neuroimage* 160, 73–83. doi: 10.1016/j.neuroimage.2016.11.006

Betzel, R. F., Bertolero, M. A., Gordon, E. M., Gratton, C., Dosenbach, N. U., and Bassett, D. S. (2019). The community structure of functional brain networks exhibits scale-specific patterns of inter-and intra-subject variability. *NeuroImage* 202:115990. doi: 10.1016/j.neuroimage.2019.07.003

Birbaumer, N., Ghanayim, N., Hinterberger, T., Iversen, I., Kotchoubey, B., Kübler, A., et al. (1999). A spelling device for the paralysed. *Nature* 398:297.

Blankertz, B., Curio, G., and Müller, K.-R. (2002). "Classifying single trial eeg: towards brain computer interfacing," in *Advances in Neural Information Processing Systems*, eds T. G. Dietterich, S. Becker, and Z. Ghahramani (Vancouver: MIT Press), 157–164.

Blankertz, B., Sanelli, C., Halder, S., Hammer, E., Kübler, A., Müller, K.-R., Curio, G., et al. (2009). Predicting bci performance to study bci illiteracy. *BMC Neurosci.* 10(Suppl. 1):P84. doi: 10.1186/1471-2202-10-S1-P84

Blankertz, B., Sannelli, C., Halder, S., Hammer, E. M., Kübler, A., Müller, K.-R., et al. (2010). Neurophysiological predictor of smr-based bci performance. *Neuroimage* 51, 1303–1309. doi: 10.1016/j.neuroimage.2010.03.022

Bradberry, T. J., Gentili, R. J., and Contreras-Vidal, J. L. (2010). Reconstructing three-dimensional hand movements from noninvasive electroencephalographic signals. *J. Neurosci.* 30, 3432–3437. doi: 10.1523/JNEUROSCI.6107-09.2010

Brown, R. E., and Milner, P. M. (2003). The legacy of donald o. hebb: more than the hebb synapse. *Nat. Rev. Neurosci.* 4, 1013–1019. doi: 10.1038/nrn1257.

Chiarelli, A. M., Croce, P., Merla, A., and Zappasodi, F. (2018). Deep learning for hybrid eeg-fnirs brain–computer interface: application to motor imagery classification. *J. Neural Eng.* 15:036028. doi: 10.1088/1741-2552/aaaf82

Clarke, D. D. (1999). "Circulation and energy metabolism of the brain," *Basic Neurochemistry: Molecular, Cellular, and Medical Aspects*, eds G. J. Siegel, B. W. Agranoff, and R. W. Albers (Philadelphia: Lippincott-Raven), 637–670.

Darvishi, S., Gharabaghi, A., Boulay, C. B., Ridding, M. C., Abbott, D., and Baumert, M. (2017). Proprioceptive feedback facilitates motor imagery-related operant learning of sensorimotor β-band modulation. *Front. Neurosci.* 11:60. doi: 10.3389/fnins.2017.00060

Darvishi, S., Gharabaghi, A., Ridding, M. C., Abbott, D., and Baumert, M. (2018). Reaction time predicts brain–computer interface aptitude. *IEEE J. Trans. Eng. Health Med.* 6, 1–11. doi: 10.1109/JTEHM.2018.2875985

Deco, G., Jirsa, V. K., and McIntosh, A. R. (2011). Emerging concepts for the dynamical organization of resting-state activity in the brain. *Nat. Rev. Neurosci.* 12:43–56. doi: 10.1038/nrn2961

Dobkin, B. H. (2007). Brain–computer interface technology as a tool to augment plasticity and outcomes for neurological rehabilitation. *J. Physiol.* 579, 637–642. doi: 10.1113/jphysiol.2006.123067

Duarte, J. E., and Reinkensmeyer, D. J. (2015). Effects of robotically modulating kinematic variability on motor skill learning and motivation. *J. Neurophysiol.* 113, 2682–2691. doi: 10.1152/jn.00163.2014

Edelman, B., Meng, J., Suma, D., Zurn, C., Nagarajan, E., Baxter, B., et al. (2019). Noninvasive neuroimaging enhances continuous neural tracking for robotic device control. *Sci. Robot.* 4:eaaw6844. doi: 10.1126/scirobotics.aaw6844

Fahimi, F., Zhang, Z., Goh, W. B., Lee, T.-S., Ang, K. K., and Guan, C. (2018). Inter-subject transfer learning with end-to-end deep convolutional neural network for eeg-based bci. *J. Neural Eng.* 16:026007. doi: 10.1088/1741-2552/aaf3f6

Faller, J., Cummings, J., Saproo, S., and Sajda, P. (2019). Regulation of arousal via online neurofeedback improves human performance in a demanding sensory-motor task. *Proc. Natl. Acad. Sci. U.S.A.* 116, 6482–6490. doi: 10.1073/pnas.1817207116

Fazli, S., Dähne, S., Samek, W., Bießmann, F., and Mueller, K.-R. (2015). Learning from more than one data source: data fusion techniques for sensorimotor rhythm-based brain–computer interfaces. *Proc. IEEE* 103, 891–906. doi: 10.1109/JPROC.2015.2413993

Fox, K. C., Spreng, R. N., Ellamil, M., Andrews-Hanna, J. R., and Christoff, K. (2015). The wandering brain: meta-analysis of functional neuroimaging studies of mind-wandering and related spontaneous thought processes. *Neuroimage* 111, 611–621. doi: 10.1016/j.neuroimage.2015.02.039

Hammer, E. M., Halder, S., Blankertz, B., Sannelli, C., Dickhaus, T., Kleih, S., et al. (2012). Psychological predictors of smr-bci performance. *Biol. Psychol.* 89, 80–86. doi: 10.1016/j.biopsycho.2011.09.006

He, H., and Wu, D. (2019). Transfer learning for brain-computer interfaces: a euclidean space data alignment approach. *IEEE Trans. Biomed. Eng.* doi: 10.1109/TBME.2019.2913914. [Epub ahead of print].

Hebb, D. O. (1949). *The Organization of Behavior, Vol. 65.* New York, NY: Wiley.

Herzfeld, D. J., and Shadmehr, R. (2014). Motor variability is not noise, but grist for the learning mill. *Nat. Neurosci.* 17, 149–150. doi: 10.1038/nn.3633

Honey, C., Sporns, O., Cammoun, L., Gigandet, X., Thiran, J.-P., Meuli, R., et al. (2009). Predicting human resting-state functional connectivity from structural connectivity. *Proc. Natl. Acad. Sci. U.S.A.* 106, 2035–2040. doi: 10.1073/pnas.0811168106

Honey, C. J., Thivierge, J.-P., and Sporns, O. (2010). Can structure predict function in the human brain? *Neuroimage* 52, 766–776. doi: 10.1016/j.neuroimage.2010.01.071

Hong, X., Lu, Z. K., Teh, I., Nasrallah, F. A., Teo, W. P., Ang, K. K., et al. (2017). Brain plasticity following mi-bci training combined with tdcs in a randomized trial in chronic subcortical stroke subjects: a preliminary study. *Sci. Rep.* 7:9222. doi: 10.1038/s41598-017-08928-5

Jackson, P. L., Lafleur, M. F., Malouin, F., Richards, C., and Doyon, J. (2001). Potential role of mental practice using motor imagery in neurologic rehabilitation. *Arch. Phys. Med. Rehabil.* 82, 1133–1141. doi: 10.1053/apmr.2001.24286

Jayaram, V., Alamgir, M., Altun, Y., Scholkopf, B., and Grosse-Wentrup, M. (2016). Transfer learning in brain-computer interfaces. *IEEE Comput. Intell. Magaz.* 11, 20–31. doi: 10.1109/MCI.2015.2501545

Jeannerod, M. (1995). Mental imagery in the motor context. *Neuropsychologia* 33, 1419–1432.

Jensen, O., Bahramisharif, A., Oostenveld, R., Klanke, S., Hadjipapas, A., Okazaki, Y. O., et al. (2011). Using brain–computer interfaces and brain-state dependent stimulation as tools in cognitive neuroscience. *Front. Psychol.* 2:100. doi: 10.3389/fpsyg.2011.00100

Jeunet, C., NKaoua, B., Subramanian, S., Hachet, M., and Lotte, F. (2015). Predicting mental imagery-based bci performance from personality, cognitive profile and neurophysiological patterns. *PLoS ONE* 10:e0143962. doi: 10.1371/journal.pone.0143962

Jochumsen, M., Rovsing, C., Rovsing, H., Cremoux, S., Signal, N., Allen, K., et al. (2017). Quantification of movement-related eeg correlates associated with motor training: a study on movement-related cortical potentials and sensorimotor rhythms. *Front. Hum. Neurosci.* 11:604. doi: 10.3389/fnhum.2017.00604

Johnson, N., Carey, J., Edelman, B., Doud, A., Grande, A., Lakshminarayan, K., et al. (2018). Combined rtms and virtual reality brain–computer interface training for motor recovery after stroke. *J. Neural Eng.* 15:016009. doi: 10.1088/1741-2552/aa8ce3

Kang, H., and Choi, S. (2014). Bayesian common spatial patterns for multi-subject eeg classification. *Neural Networks* 57, 39–50. doi: 10.1016/j.neunet.2014.05.012

Kang, H., Nam, Y., and Choi, S. (2009). Composite common spatial pattern for subject-to-subject transfer. *IEEE Signal Process. Lett.* 16, 683–686. doi: 10.1109/LSP.2009.2022557

Kasahara, K., DaSalla, C. S., Honda, M., and Hanakawa, T. (2015). Neuroanatomical correlates of brain–computer interface performance. *Neuroimage* 110, 95–100. doi: 10.1016/j.neuroimage.2015.01.055

Krakauer, J. W. (2006). Motor learning: its relevance to stroke recovery and neurorehabilitation. *Curr. Opin. Neurol.* 19, 84–90. doi: 10.1097/01.wco.0000200544.29915.cc

Krusienski, D. J., Grosse-Wentrup, M., Galán, F., Coyle, D., Miller, K. J., Forney, E., et al. (2011). Critical issues in state-of-the-art brain–computer interface signal processing. *J. Neural Eng.* 8:025002. doi: 10.1088/1741-2560/8/2/025002

Leamy, D. J., Kocijan, J., Domijan, K., Duffin, J., Roche, R. A., Commins, S., et al. (2014). An exploration of eeg features during recovery following stroke–implications for bci-mediated neurorehabilitation therapy. *J. Neuroeng. Rehabil.* 11:9. doi: 10.1186/1743-0003-11-9

Li, Q., Lu, Z., Gao, N., and Yang, J. (2019). Optimizing the performance of the visual p300-speller through active mental tasks based on color distinction and modulation of task difficulty. *Front. Human Neurosci.* 13:130. doi: 10.3389/fnhum.2019.00130

Li, Y., Kambara, H., Koike, Y., and Sugiyama, M. (2010). Application of covariate shift adaptation techniques in brain–computer interfaces. *IEEE Trans. Biomed. Eng.* 57, 1318–1324. doi: 10.1109/TBME.2009.2039997

Lotte, F. (2015). Signal processing approaches to minimize or suppress calibration time in oscillatory activity-based brain–computer interfaces. *Proc. IEEE* 103, 871–890. doi: 10.1109/JPROC.2015.2404941

Lotze, M., Flor, H., Grodd, W., Larbig, W., and Birbaumer, N. (2001). Phantom movements and pain an fmri study in upper limb amputees. *Brain* 124, 2268–2277. doi: 10.1093/brain/124.11.2268

Lotze, M., and Halsband, U. (2006). Motor imagery. *J. Physiol. Paris* 99, 386–395. doi: 10.1016/j.jphysparis.2006.03.012

Lu, H., Eng, H.-L., Guan, C., Plataniotis, K. N., and Venetsanopoulos, A. N. (2010). Regularized common spatial pattern with aggregation for eeg classification in small-sample setting. *IEEE Trans. Biomed. Eng.* 57, 2936–2946. doi: 10.1109/TBME.2010.2082540

Meyer, M. C., van Oort, E. S., and Barth, M. (2013). Electrophysiological correlation patterns of resting state networks in single subjects: a combined eeg–fmri study. *Brain Topography* 26, 98–109. doi: 10.1007/s10548-012-0235-0

Morioka, H., Kanemura, A., Hirayama, J.-I., Shikauchi, M., Ogawa, T., Ikeda, S., et al. (2015). Learning a common dictionary for subject-transfer decoding with resting calibration. *NeuroImage* 111, 167–178. doi: 10.1016/j.neuroimage.2015.02.015

Müller-Putz, G. R., Daly, I., and Kaiser, V. (2014). Motor imagery-induced eeg patterns in individuals with spinal cord injury and their impact on brain–computer interface accuracy. *J. Neural Eng.* 11:035011. doi: 10.1088/1741-2560/11/3/035011

Niazi, I. K., Jiang, N., Jochumsen, M., Nielsen, J. F., Dremstrup, K., and Farina, D. (2013). Detection of movement-related cortical potentials based on subject-independent training. *Med. Biol. Eng. Comput.* 51, 507–512. doi: 10.1007/s11517-012-1018-1

Northoff, G., Duncan, N. W., and Hayes, D. J. (2010). The brain and its resting state activity-experimental and methodological implications. *Progress Neurobiol.* 92, 593–600. doi: 10.1016/j.pneurobio.2010.09.002

Orsborn, A. L., Moorman, H. G., Overduin, S. A., Shanechi, M. M., Dimitrov, D. F., and Carmena, J. M. (2014). Closed-loop decoder adaptation shapes neural plasticity for skillful neuroprosthetic control. *Neuron* 82, 1380–1393. doi: 10.1016/j.neuron.2014.04.048

Ostry, D. J., and Gribble, P. L. (2016). Sensory plasticity in human motor learning. *Trends Neurosci.* 39, 114–123. doi: 10.1016/j.tins.2015.12.006

Perdikis, S., Tonin, L., Saeedi, S., Schneider, C., and Millán, J. d. R. (2018). The cybathlon bci race: successful longitudinal mutual learning with two tetraplegic users. *PLoS Biol.* 16:e2003787. doi: 10.1371/journal.pbio.2003787

Raichle, M. E. (2009). A paradigm shift in functional brain imaging. *J. Neurosci.* 29, 12729–12734. doi: 10.1523/JNEUROSCI.4366-09.2009

Raichle, M. E. (2010). Two views of brain function. *Trends Cognit. Sci.* 14, 180–190. doi: 10.1016/j.tics.2010.01.008

Ramoser, H., Muller-Gerking, J., and Pfurtscheller, G. (2000). Optimal spatial filtering of single trial eeg during imagined hand movement. *IEEE Trans. Rehabil. Eng.* 8, 441–446. doi: 10.1109/86.895946

Ramos-Murguialday, A., Broetz, D., Rea, M., Läer, L., Yilmaz, Ö., Brasil, F. L., et al. (2013). Brain–machine interface in chronic stroke rehabilitation: a controlled study. *Ann. Neurol.* 74, 100–108. doi: 10.1002/ana.23879

Reichert, J. L., Kober, S. E., Neuper, C., and Wood, G. (2015). Resting-state sensorimotor rhythm (smr) power predicts the ability to up-regulate smr in an eeg-instrumental conditioning paradigm. *Clin. Neurophysiol.* 126, 2068–2077. doi: 10.1016/j.clinph.2014.09.032

Ruffino, C., Papaxanthis, C., and Lebon, F. (2017). Neural plasticity during motor learning with motor imagery practice: Review and perspectives. *Neuroscience* 341, 61–78. doi: 10.1016/j.neuroscience.2016.11.023

Saha, S., Ahmed, K. I., Mostafa, R., Khandoker, A. H., and Hadjileontiadis, L. (2017a). Enhanced inter-subject brain computer interface with associative sensorimotor oscillations. *Healthcare Technol. Lett.* 4, 39–43. doi: 10.1049/htl.2016.0073

Saha, S., Ahmed, K. I. U., Mostafa, R., Hadjileontiadis, L., and Khandoker, A. (2017b). Evidence of variabilities in eeg dynamics during motor imagery-based multiclass brain–computer interface. *IEEE Trans. Neural Syst. Rehabil. Eng.* 26, 371–382. doi: 10.1109/TNSRE.2017.2778178

Saha, S., Hossain, M. S., Ahmed, K., Mostafa, R., Hadjileontiadis, L., Khandoker, A., et al. (2019). Wavelet entropy-based inter-subject associative cortical source localization for sensorimotor BCI. *Front. Neuroinform.* 13:47. doi: 10.3389/fninf.2019.00047

Samek, W., Meinecke, F. C., and Müller, K.-R. (2013). Transferring subspaces between subjects in brain–computer interfacing. *IEEE Trans. Biomed. Eng.* 60, 2289–2298. doi: 10.1109/TBME.2013.2253608

Sannelli, C., Vidaurre, C., Müller, K.-R., and Blankertz, B. (2019). A large scale screening study with a smr-based bci: Categorization of bci users and differences in their smr activity. *PLoS ONE* 14:e0207351. doi: 10.1371/journal.pone.0207351

Seghier, M. L., and Price, C. J. (2018). Interpreting and utilising intersubject variability in brain function. *Trends Cognit. Sci.* 22, 517–530. doi: 10.1016/j.tics.2018.03.003

Selfslagh, A., Shokur, S., Campos, D. S., Donati, A. R., Almeida, S., Yamauti, S. Y., et al. (2019). Non-invasive, brain-controlled functional electrical stimulation for locomotion rehabilitation in individuals with paraplegia. *Sci. Rep.* 9:6782. doi: 10.1038/s41598-019-43041-9

Singh, P., Jana, S., Ghosal, A., and Murthy, A. (2016). Exploration of joint redundancy but not task space variability facilitates supervised motor learning. *Proc. Natl. Acad. Sci. U.S.A.* 113, 14414–14419. doi: 10.1073/pnas.1613383113

Smith, S., Duff, E., Groves, A., Nichols, T. E., Jbabdi, S., Westlye, L. T., et al. (2019). Structural variability in the human brain reflects fine-grained functional architecture at the population level. *J. Neurosci.* 39, 6136–6149. doi: 10.1523/JNEUROSCI.2912-18.2019

Suk, H.-I., Fazli, S., Mehnert, J., Müller, K.-R., and Lee, S.-W. (2014). Predicting BCI subject performance using probabilistic spatio-temporal filters. *PLoS ONE* 9:e87056. doi: 10.1371/journal.pone.0087056

Tomassini, V., Jbabdi, S., Kincses, Z. T., Bosnell, R., Douaud, G., Pozzilli, C., et al. (2011). Structural and functional bases for individual differences in motor learning. *Human Brain Mapp.* 32, 494–508. doi: 10.1002/hbm.21037

Úbeda, A., Hortal, E., Iáñez, E., Perez-Vidal, C., and Azorín, J. M. (2015). Assessing movement factors in upper limb kinematics decoding from eeg signals. *PLoS ONE* 10:e0128456. doi: 10.1371/journal.pone.0128456

Vallence, A.-M., Goldsworthy, M. R., Hodyl, N. A., Semmler, J. G., Pitcher, J. B., and Ridding, M. C. (2015). Inter-and intra-subject variability of motor cortex plasticity following continuous theta-burst stimulation. *Neuroscience* 304, 266–278. doi: 10.1016/j.neuroscience.2015.07.043

Vasilyev, A., Liburkina, S., Yakovlev, L., Perepelkina, O., and Kaplan, A. (2017). Assessing motor imagery in brain-computer interface training: psychological and neurophysiological correlates. *Neuropsychologia* 97, 56–65. doi: 10.1016/j.neuropsychologia.2017.02.005

Vidaurre, C., and Blankertz, B. (2010). Towards a cure for bci illiteracy. *Brain Topography* 23, 194–198. doi: 10.1007/s10548-009-0121-6

Vyas, S., Even-Chen, N., Stavisky, S. D., Ryu, S. I., Nuyujukian, P., and Shenoy, K. V. (2018). Neural population dynamics underlying motor learning transfer. *Neuron* 97, 1177–1186. doi: 10.1016/j.neuron.2018.01.040

Wang, W., Collinger, J. L., Perez, M. A., Tyler-Kabara, E. C., Cohen, L. G., Birbaumer, N., et al. (2010). Neural interface technology for rehabilitation: exploiting and promoting neuroplasticity. *Phys. Med. Rehabil. Clinics* 21, 157–178. doi: 10.1016/j.pmr.2009.07.003

Wang, Y., and Jung, T.-P. (2011). A collaborative brain-computer interface for improving human performance. *PLoS ONE* 6:e20422. doi: 10.1371/journal.pone.0020422

Wens, V., Bourguignon, M., Goldman, S., Marty, B., De Beeck, M. O., Clumeck, C., et al. (2014). Inter-and intra-subject variability of neuromagnetic resting state networks. *Brain Topography* 27, 620–634. doi: 10.1007/s10548-014-0364-8

Wolpaw, J. R., and McFarland, D. J. (1994). Multichannel eeg-based brain-computer communication. *Electroencephal. Clin. Neurophysiol.* 90, 444–449.

Wolpaw, J. R., McFarland, D. J., Neat, G. W., and Forneris, C. A. (1991). An eeg-based brain-computer interface for cursor control. *Electroencephal. Clin. Neurophysiol.* 78, 252–259.

Wronkiewicz, M., Larson, E., and Lee, A. K. (2015). Leveraging anatomical information to improve transfer learning in brain–computer interfaces. *J. Neural Eng.* 12:046027. doi: 10.1088/1741-2560/12/4/046027

Wu, H. G., Miyamoto, Y. R., Castro, L. N. G., Ölveczky, B. P., and Smith, M. A. (2014). Temporal structure of motor variability is dynamically regulated and predicts motor learning ability. *Nat. Neurosci.* 17, 312–321. doi: 10.1038/nn.3616

Zhang, R., Yao, D., Valdés-Sosa, P. A., Li, F., Li, P., Zhang, T., et al. (2015). Efficient resting-state eeg network facilitates motor imagery performance. *J. Neural Eng.* 12:066024. doi: 10.1088/1741-2560/12/6/066024

Zhao, X., Chu, Y., Han, J., and Zhang, Z. (2016). Ssvep-based brain–computer interface controlled functional electrical stimulation system for upper extremity rehabilitation. *IEEE Trans. Syst. Man Cybernet. Syst.* 46, 947–956. doi: 10.1109/TSMC.2016.2523762

Zich, C., Debener, S., Kranczioch, C., Bleichner, M. G., Gutberlet, I., and De Vos, M. (2015). Real-time eeg feedback during simultaneous eeg–fmri identifies the cortical signature of motor imagery. *Neuroimage* 114, 438–447. doi: 10.1016/j.neuroimage.2015.04.020

Conflict of Interest: The authors declare that the research was conducted in the absence of any commercial or financial relationships that could be construed as a potential conflict of interest.

frontiers in Neuroscience

ORIGINAL RESEARCH
published: 25 March 2020
doi: 10.3389/fnins.2020.00252

Fully Integrated PET/MR Imaging for the Assessment of the Relationship Between Functional Connectivity and Glucose Metabolic Rate

*Lalith Kumar Shiyam Sundar[1], Shahira Baajour[2], Thomas Beyer[1], Rupert Lanzenberger[3], Tatjana Traub-Weidinger[4], Ivo Rausch[1], Ekaterina Pataraia[5], Andreas Hahn[3], Lucas Rischka[3], Marius Hienert[3], Eva-Maria Klebermass[4] and Otto Muzik[6]**

[1] QIMP Team, Center for Medical Physics and Biomedical Engineering, Medical University of Vienna, Vienna, Austria, [2] Department of Psychiatry and Behavioral Neurosciences, Wayne State University School of Medicine, Detroit, MI, United States, [3] Department of Psychiatry and Psychotherapy, Medical University of Vienna, Vienna, Austria, [4] Division of Nuclear Medicine, Department of Biomedical Imaging and Image-guided Therapy, Medical University of Vienna, Vienna, Austria, [5] Department of Neurology, Medical University of Vienna, Vienna, Austria, [6] Department of Pediatrics, Wayne State University School of Medicine, Detroit, MI, United States

OPEN ACCESS

Edited by:
Junhua Li,
University of Essex, United Kingdom

Reviewed by:
Xi-Nian Zuo,
Institute of Psychology (CAS), China
Rocco Marchitelli,
Inserm U1000, France
Jorge Jovicich,
University of Trento, Italy

***Correspondence:**
Otto Muzik
otto@pet.wayne.edu

Specialty section:
This article was submitted to Brain Imaging Methods, a section of the journal Frontiers in Neuroscience

Received: *02 October 2019*
Accepted: *06 March 2020*
Published: *25 March 2020*

Citation:
Shiyam Sundar LK, Baajour S, Beyer T, Lanzenberger R, Traub-Weidinger T, Rausch I, Pataraia E, Hahn A, Rischka L, Hienert M, Klebermass E-M and Muzik O (2020) Fully Integrated PET/MR Imaging for the Assessment of the Relationship Between Functional Connectivity and Glucose Metabolic Rate. Front. Neurosci. 14:252. doi: 10.3389/fnins.2020.00252

In the past, determination of absolute values of cerebral metabolic rate of glucose (CMRGlc) in clinical routine was rarely carried out due to the invasive nature of arterial sampling. With the advent of combined PET/MR imaging technology, CMRGlc values can be obtained non-invasively, thereby providing the opportunity to take advantage of fully quantitative data in clinical routine. However, CMRGlc values display high physiological variability, presumably due to fluctuations in the intrinsic activity of the brain at rest. To reduce CMRGlc variability associated with these fluctuations, the objective of this study was to determine whether functional connectivity measures derived from resting-state fMRI (rs-fMRI) could be used to correct for these fluctuations in intrinsic brain activity. Methods: We studied 10 healthy volunteers who underwent a test-retest dynamic [18F]FDG-PET study using a fully integrated PET/MR system (Siemens Biograph mMR). To validate the non-invasive derivation of an image-derived input function based on combined analysis of PET and MR data, arterial blood samples were obtained. Using the arterial input function (AIF), parametric images representing CMRGlc were determined using the Patlak graphical approach. Both directed functional connectivity (dFC) and undirected functional connectivity (uFC) were determined between nodes in six major networks (Default mode network, Salience, L/R Executive, Attention, and Sensory-motor network) using either a bivariate-correlation (R coefficient) or a Multi-Variate AutoRegressive (MVAR) model. In addition, the performance of a regional connectivity measure, the fractional amplitude of low frequency fluctuations (fALFF), was also investigated. Results: The average intrasubject variability for CMRGlc values between test and retest was determined as (14 ±8%) with an average inter-subject variability of 25% at test and 15% at retest. The average CMRGlc value (umol/100 g/min) across all networks was 39 ±10 at test and increased slightly to 43 ±6 at retest. The R, MVAR and fALFF coefficients showed relatively large test-retest variability in comparison to the inter-subjects variability, resulting in poor reliability

(intraclass correlation in the range of 0.11–0.65). More importantly, no significant relationship was found between the R coefficients (for uFC), MVAR coefficients (for dFC) or fALFF and corresponding CMRGlc values for any of the six major networks. Discussion: Measurement of functional connectivity within established brain networks did not provide a means to decrease the inter- or intrasubject variability of CMRGlc values. As such, our results indicate that connectivity measured derived from rs-fMRI acquired contemporaneously with PET imaging are not suited for correction of CMRGlc variability associated with intrinsic fluctuations of resting-state brain activity. Thus, given the observed substantial inter- and intrasubject variability of CMRGlc values, the relevance of absolute quantification for clinical routine is presently uncertain.

Keywords: resting-state fMRI, Cerebral metabolic rate of glucose, integrated PET/MRI, glucose metabolic rate variability, standardization of psychological state, real-time fMRI

INTRODUCTION

Pioneering studies in the early days of PET imaging have demonstrated the potential of absolute quantification of glucose metabolic rate using [18F]-labeled deoxy-glucose (FDG) (Lammertsma, 2017). Absolute quantification studies typically mandate lengthy dynamic imaging protocols, along with the measurement of arterial blood samples (Schmidt and Turkheimer, 2002). Due to the complexity associated with the imaging protocols and surprisingly large inter- and intra-subject variability (in the range of 15–25%) of the cerebral metabolic rate of glucose (CMRGlc) (Chang et al., 1987; Tyler et al., 1988; Camargo et al., 1992), absolute quantification studies have not been clinically viable.

Under normal physiological conditions, the brain derives most of its energy from glucose metabolism (Raichle and Mintun, 2006). The observed substantial variability of glucose metabolic rate was mostly unexpected, especially as it was shown that changes in moment-to-moment energy demands may contribute as little as 0.5–1% to the total energy budget (Raichle and Mintun, 2006). This implies that intrinsic brain activity may be an important factor in terms of overall brain function. It is believed that this intrinsic activity is an expression of recurrent excitatory and inhibitory connections between and within layers of the cerebral cortex that are fundamental to the operation of local cortical circuits (Haider et al., 2006).

Currently the underlying factors that give rise to the observed variability in intrinsic brain activity are unknown. However, it has been speculated that it might be an expression of fluctuations in vigilance and conscious awareness, which is strongly tied to electrical and chemical signaling at neuronal synapses (Fukunaga et al., 2008). Thus, the brain's intrinsic energy consumption, as measured using FDG-PET imaging might be closely linked to the function of neural regulatory networks that underlie affective and cognitive processes. These processes are known to be associated with the hemodynamic response that can be studied based on spontaneous oscillations captured during resting-state fMRI (rs-fMRI) (Logothetis et al., 2001). With the advent of fully integrated PET/MR imaging (PET/MRI), both CMRGlc, as well as rs-fMRI can be acquired contemporaneously, paving the way for the study of the relationship between moment-to-moment blood flow changes and longer-lasting states of brain energy consumption. Here, we investigate whether a relationship exists between CMRGlc values and the functional connectivity between major nodes within the larger brain network. Such a relationship would allow standardization of CMRGlc values to a subject's resting-state intrinsic activity, which may provide a means to decrease test-retest variability of CMRGlc values and may improve the relevance of absolute quantification of glucose metabolic rates in clinical routine.

MATERIALS AND METHODS

Subjects

Ten healthy volunteers (27 ± 7 years, 5M/5F) were included in this study. The study was approved by the Ethics Committee of the Medical University of Vienna (EK1960/2014) and was performed in accordance with the Gandavia and Tovella (1964), including current revisions. Volunteers were deemed to be healthy based on their medical history, physical examinations, and vital signs. Written informed consent was obtained from all the subjects before the examinations.

PET/MR Imaging Protocol

This study was part of an ongoing project with the goal to validate methodology that allows the determination of an accurate image-derived arterial input function (AIF) (Sundar et al., 2019). All volunteers underwent test-retest examinations (mean time difference = 17 ± 44 days) in a fully integrated PET/MR system (Siemens Healthineers Biograph mMR, Erlangen, Germany). Examinations were conducted in the afternoon and subjects were asked to keep their eyes open and to relax without thinking of anything in particular.

Subjects were fasted for at least 6 h prior to the PET imaging procedure. Before each scan, blood glucose levels (mmol/l) were measured and a venous line was established for the injection of the FDG tracer. In addition, an arterial line was established in the contra-lateral arm of the subjects for manual arterial blood sampling. After positioning the subject in the PET/MR

system with the brain in the field-of-view (FOV), a 60-min PET list-mode acquisition was initiated simultaneously with an intravenous injection of (352 ± 66 MBq, 5.2 MBq/kg) FDG administered manually as a slow bolus over 40 s.

Parallel to the PET data acquisition, multiple MR sequences were acquired: a T1-w MR sequence (TR: 2200 ms, TI: 778 ms, TE: 3 ms, flip-angle = 13°, FOV: 256 mm × 256 mm, 256 axial slices of thickness = 1.0 mm, matrix = 256 × 256, scan-time = 5 min 22 s) for anatomical localization as well as a rs-fMRI sequence (TR: 2.44 s, TE: 29 ms, FOV: 256 mm × 256 mm, acquisition matrix: 128 × 128, 36 axial slices, voxel dimensions: 2 mm × 2 mm × 3 mm, 170 images for a total of 7 min). The fMRI sequence was initiated at 30 min post injection of the FDG tracer to match the linear component of the Patlak-transformed time-activity curves (see below). In addition, sparsely sampled MR navigators (2D EPI 3.0 mm × 3.0 mm × 3.0 mm voxels, 64 × 64 matrix, 36 slices, TE = 30 ms, TR = 3000 ms) were interleaved between clinical MR sequences with the following time intervals: 0, 2.5, 5, 7.5, 10, 14, 17, 21, 26, 33, 38, 42, 44, and 50.5 min post-injection.

Following the PET/MR examination, the controls were moved to the PET/CT for a low-dose CT scan (120 kVp, 50 mAs) of the brain. The PET list-mode data was re-binned into a dynamic frame sequence (24 × 5 s, 1 × 60 s, 1 × 120 s, 11 × 300 s) and was reconstructed (Siemens e7 tools) into a 344 × 344 × 127 matrix (voxel size 2.08 mm × 2.08 mm × 2.03 mm) using the ordinary Poisson ordered subset expectation-maximization (OP-OSEM) 3D algorithm (3 iterations, 21 subsets, 2 mm Gaussian filter). Brain attenuation correction was performed using a CT-derived mu-map (Carney et al., 2006), which was co-registered to the navigator image volumes, yielding dynamic AC-maps along with scatter correction.

Blood Sampling

To obtain the AIF, blood samples were collected manually at different time points (24 × 5 s, 1 × 60 s, 1 × 120 s, 1 × 300 s, 1 × 600 s, 2 × 1200 s post injection) from the radial artery. The blood sampling was performed manually using vacuum test tubes via an arterial cannula fitted with an adapter. Before every arterial sample, the line was flushed with 5 mL sodium chloride solution to prevent clotting and sampling stagnant blood. To avoid dilution of the actual sample, a 1 mL of discard was drawn followed by the sampling of the arterial blood sample. Whole-blood radioactivity concentrations were measured using a gamma counter (PerkinElmer, 2480 Automatic Gamma counter, Wizard23). To obtain the AIF, whole blood samples were centrifuged to separate the plasma component, followed by the measurement of radioactivity in the plasma.

MR-Driven Motion Correction

Sparsely sampled MR navigators interleaved between MR sequences were used to perform motion correction of PET images (Keller et al., 2015). The initial navigator (Nav-0) was considered as the reference volume, and all subsequent navigators (Nav-1 to Nav-13) were rigidly aligned to Nav-0 using SPM 12 (Wellcome Trust Center for Neuroimaging, UCL), yielding a set of motion vectors (MV-1 to MV-13, three translations, and three rotation parameters). A correspondence between the MR navigators and PET emission data was assumed based on the least temporal difference between the MR navigator acquisition time and the PET frame mid-scan time. To account for spatial misalignment between the static CT-derived AC map and the PET emission data, the inverse of the MVs (iMVs) were applied to the AC map, which resulted in a set of motion-corrected AC maps (MoCo-AC). The obtained MoCo-AC maps were then employed for reconstruction of the dynamic PET emission data using the Siemens e7 tools.

PET Quantification

Motion vectors (MVs) derived from the MR navigators were applied to the corresponding PET frames, resulting in motion-corrected PET frames (MoCo-PET). Following the spatial alignment, a voxel-wise Patlak graphical analysis (lumped constant, LC = 0.65) (Wu et al., 2003) was performed using time-activity curves derived from MoCo-PET frames in combination with the sampled AIF. The analysis was performed using an in-house developed Matlab tool (Matlab R2018a, MathWorks, United States) that generated parametric images representing the CMRGlc in units of umol/100 g/min. To be specific, a linear function was fitted to the Patlak-transformed data, including data from 25 min p.i. until the end of the study (8 data points). The resulting slope was then multiplied with the subject's plasma glucose level (umol/L) and divided by the LC (**Supplementary Figure S2**).

fMRI Preprocessing

The fMRI images were analyzed using SPM12 (Wellcome Department of Cognitive Neurology, Institute of Neurology, London, United Kingdom). In all analyses, the first four images were discarded to account for echo planar imaging (EPI) equilibration effects (Haacke, 2014). The remaining images in the sequence were realigned to correct for head movements, corrected for slice timing, and subsequently spatially normalized based on the transformation matrix derived between the co-registered (to the mean EPI image) T1-weighted image and the MNI template brain. The images were then smoothed spatially with a 3D Gaussian kernel of 6 mm FWHM and re-sampled (2 mm × 2 mm × 2 mm).

fMRI Time Series Extraction

A subset of six pair-wise nodes was selected for our analysis [see Supplementary Figure S3 in Biswal et al. (2010)]. These nodes are defined by their peak coordinates and correspond to the following major networks: the default mode network (DMN) including the medial prefrontal cortex (MPFC, MNI coordinates [0/60/−6]) and the posterior cingulate cortex (PCC, MNI [3/−42/27]), the R/L executive network connecting the right/left superior frontal gyrus (SFG, MNI [±30/21/51]) with the right/left inferior parietal lobe (IPL, MNI [±48/−57/42]) within each hemisphere, the salience network connecting the L and R anterior insula cortex (AIC, MNI [−36/18/3] ↔ [42/15/−3]), the attention network connecting the L and R IPL (MNI [−54/−30/42] ↔ [42/−36/48]) and the sensory-motor cortex connecting the L and R superior

central sulcus (MNI [−57/−9/33] ↔ [60/−9/33]). For each peak location, the time series of all voxels within a radius of 6 mm were averaged. These averaged time-series were then used to determine both the directed and undirected functional connectivity (FC) between pair-wise nodes constituting the selected networks (**Figure 1**). Specifically, the directed functional connectivity (dFC) model is well suited for assessing (possibly) asymmetrically directed interactions between any nodes in any class of network with quantifiable dynamics (Granger, 1969; Bressler and Seth, 2011; Friston, 2011). Moreover, in order to assess local functional connectivity (which characterizes the extent of temporal coherence between neighboring voxels) we also calculated the fractional amplitude of low frequency fluctuations (fALFF). This measure of local connectivity has been shown to be associated with brain activity (Yu-Feng et al., 2007; Zhou et al., 2010).

Undirected Functional Connectivity Analysis

Undirected functional connectivity (uFC) analysis was performed using previously published methods (Whitfield-Gabrieli and Nieto-Castanon, 2012). Segmentation of structural (T1-w) images was performed and the resulting gray matter and cerebrospinal fluid (CSF) images were co-registered with the functional (T2-w) scans. The BOLD signals from white matter and CSF masks as well as the motion regressors were set as confounds, using the default orthogonal time series. The temporal confounding factors were then regressed from the BOLD time series at each voxel and the residual time series' were band-pass filtered (0.01–0.1 Hz) to eliminate low frequency drifts. ROI time series' were extracted by averaging across all the voxels within each individual ROI. Finally, uFC between two regions was computed using a zero-lagged bivariate-correlation *R*-value), estimating the linear association between two BOLD signals.

Directed Functional Connectivity Analysis

Directed Functional Connectivity was estimated using Multi-Variate AutoRegressive (MVAR) models. These models provide a measure of the causal influence of each anatomical node on every other node in the network and are equivalent to Granger Causality (GC) (Granger, 1969). In brief, GC relies on the notion of "prediction" to generate influences regarding "causality." A constituent "X" within a complex dynamic system exerts a "causal" effect on another constituent "Y" within the system if the predictability of "Y" decreases when "X" is removed from the set of all possible causative variables. The most typically used framework relies on auto-regressive models (Bressler and Seth, 2011). Thus, the MVAR model was used to estimate the strength of the causal influence between nodal pairs (A, B: A → B, B → A), with the model coefficient encoding the magnitude of this strength (Bressler and Seth, 2011; Tang et al., 2012; Asemi et al., 2015; Diwadkar et al., 2017; Morris et al., 2019). The number of previous time points in the model that was used to estimate the current time point was restricted to one (Tang et al., 2012), since network interactions at time scales that are proximate to the cognitive neuro-dynamics of the brain networks are in the time range of milliseconds (Singh, 2012).

All modeling was performed using specifically written scripts (R software suite). For each nodal pair (A, B) two MVAR coefficients were estimated for each subject characterizing the direction of the pair (A → B and B → A). Thus, each participant contributed 24 coefficients to the group level analyses (6 pairs from 12 nodes; two directions for each pair over the test and retest conditions).

Fractional Amplitude of Low Frequency Fluctuations Analysis

Fractional amplitude of low frequency fluctuations (Zou et al., 2008) is defined as the power within the low-frequency range (0.01–0.08 Hz) divided by the total power in the entire detectable frequency range and is calculated for the time course of each voxel within a ROI. These values were averaged to yield one regional value for the 10 nodes. The rationale for using this measure is based on the assumption that slow fluctuations in activity are a fundamental feature of the resting brain, and their presence is crucial for determining correlated activity between brain regions that constitute resting state networks.

Multimodal Analysis

In order to determine the relationship between CMRGlc and functional connectivity of major brain networks (**Figure 1**), CMRGlc values were derived from the same coordinate locations as were used for the fMRI data analysis. Specifically, parametric images representing CMRGlc were co-registered with the corresponding T1-w images and following spatial normalization of the T1-w images to MNI space using DARTEL (Diffeomorphic Anatomic Registration Through Exponentiated Lie algebra) software, these normalization parameters were also applied to parametric CMRGlc images. Thereafter, CMRGlc values were extracted from spheres with a 6 mm radius centered at the same location as was used for the extraction of the fMRI time series. Next, CMRGlc values obtained from the 12 nodes were averaged separately for each network, yielding for each subject six network-specific regional CMRlc values for both the test ($rCMRGlc_{tst}$) and retest ($rCMRGlc_{retst}$) condition. A correlation analysis was then performed in order to determine whether the magnitude of the uFC (expressed by Pearson's R coefficients), dFC (expressed by the MVAR coefficients) of local connectivity (characterized by fALFF) is predictive of CMRGlc values at rest and retest conditions. In case of a significant correlation between CMRGlc values and the R/MVAR/fALFF coefficients (COEF), these coefficients could be applied to account for CMRGlc variability by adjusting the retest CMRGlc values to the psychological state during the test condition as

$$CMRGlc'_{retest} = CMRGlc_{retest} \times \left[COEF_{test} / COEF_{retest}\right] \quad (1)$$

where $CMRGlc'_{retest}$ represents the adjusted glucose metabolic rate.

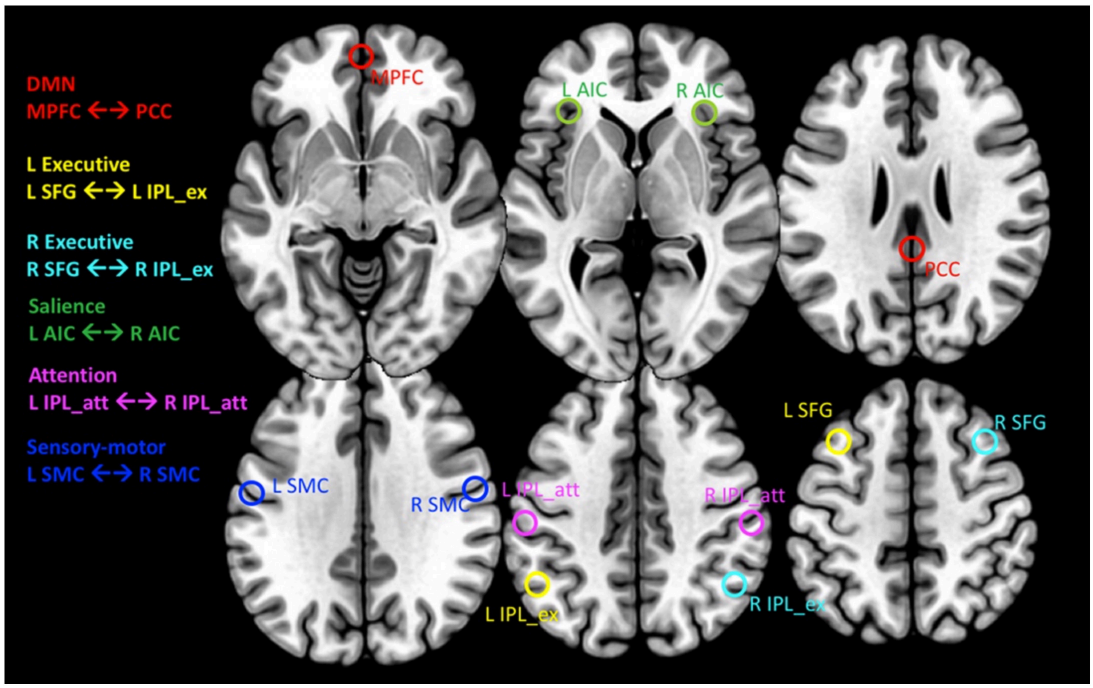

FIGURE 1 | Transaxial planes showing the location of spherical regions in MNI space from where the CMRGlc values and rs-fMRI time series' were extracted. For MNI coordinates of regions, see text. Red: default mode network (DMN) connecting the medial prefrontal cortex (MPFC) with the posterior cingulate cortex (PCC). Yellow and Cyan: L/R Executive networks, connecting the L/R superior frontal gyrus (SFG) with the anterior portion of the inferior parietal lobe (IPL_ex), respectively. Green: salience network connecting the R/L anterior insular cortex (AIC). Magenta: attention network connecting the L and R posterior portion of the inferior parietal lobe (IPL_att). Blue: sensory-motor cortex connecting the L and R sensory motor cortex (SMC).

Statistical Analysis

Descriptive statistics was used to characterize the average and the variance of outcome measures (CMRGlc values, R, MVAR, and fALFF coefficients) determined at test and retest condition for the six major networks. Moreover, the test-retest repeatability of each outcome measure was assessed using the two-way random effects model intraclass correlation coefficient [ICC (2,1)]. To determine whether there is a significant difference with respect to outcome measures across time and network, a (2 × 6) repeated measures ANOVA was applied, where the two within-subjects factors represent time with 2 levels (test, retest) and networks with 6 levels (DMN, Salience, L/R Executive, Attention, Sensory-motor). All tests were performed 2-sided and a p-value of <0.05 was assumed to represent significance. Pearson's correlation was used in order to assess whether a significant correlation exists between CMRGlc values and the R or MVAR coefficients. For correlation analyses, individual values were transformed to z-scores prior to correlation computation. Statistical analysis was performed using SPSS version 25 (SPSS, Inc.).

TABLE 1 | CMRGlc values determined for the test (Test) and retest (Retest) condition in each of the six major brain networks.

Network	Test (COV) CMRGlc (umol/100 g/min)	Retest (COV) CMRGlc (umol/100 g/min)	Intrasubject variability
DMN	41 ± 10 (24)	45 ± 6 (12)	14 ± 8
L executive	41 ± 11 (24)	44 ± 8 (17)	14 ± 8
R executive	40 ± 10 (26)	42 ± 7 (16)	13 ± 7
Salience	41 ± 10 (25)	45 ± 6 (13)	14 ± 9
Attention	36 ± 9 (26)	39 ± 6 (12)	15 ± 8
Sensory-motor	35 ± 8 (24)	37 ± 6 (12)	15 ± 8
Average	39 ± 10 (25)	43 ± 6 (15)	14 ± 8

The coefficient of variation (COV = mean/SD) is provided in brackets. "Average" represents the overall mean derived from all nodes across all subjects.

RESULTS

Cerebral metabolic rate of glucose values at rest and retest condition obtained for the six major networks are shown in **Table 1**. The average intrasubject variability between rest and retest was determined as (14 ±8%) with an average inter-subject variability of 25.4% at rest and 15.1% at retest, representing a trend toward a significant decrease in variability during retest (F = 2.7, p = 0.08). The intraclass correlation coefficient (ICC) for CMRGlc values determined in the six networks was in the range of 0.68–0.78, indicating a moderate agreement between the two time points. The average CMRGlc value over all networks was (39 ±10) umol/100 g/min at test and increased slightly to (43 ±6) umol/100 g/min at retest (p = 0.11) (**Figure 2**). As expected, the repeated measures ANOVA showed a highly significant main effect for the network variable (p < 0.001),

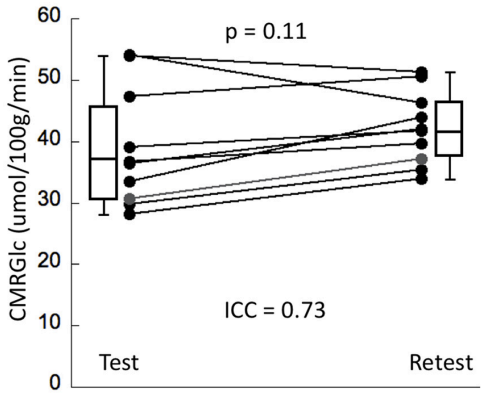

FIGURE 2 | The panel displays whole brain CMRGlc values at test and retest condition (N = 10). Although the average CMRGlc value across the two conditions is similar, the variability is decreased during the retest condition (see **Table 1**).

indicating significant differences of CMRGlc values in the individual networks. Despite the significant differences in absolute CMRGlc values between test and retest condition, the ratio between CMRGlc values in individual regions was preserved across the two time points (as verified by a non-significant (time × network) interaction of $p = 0.47$).

Reliability of Functional Connectivity Measures

The R coefficients at test and retest conditions for all six networks are shown in **Figure 3A**, indicating a relatively large test-retest variability in comparison to the between-subjects variability. This was reflected in the poor network ICC values that were determined in the range of 0.11–0.36. Nevertheless, the repeated measures ANOVA showed a non-significant effect both with respect to the main effect for time ($p = 0.95$) as well as for the (time × network) interaction ($p = 0.89$). A similar result was determined for the MVAR coefficients (**Figure 3B**). The network ICC values were determined in the range 0.14–0.55, with the repeated measures ANOVA again showing a non-significant time effect ($p = 0.71$) and (time × network) interaction ($p = 0.67$). For both analyses, the highest overall connectivity was determined for the Sensory-motor network ($R = 0.97$ and MVAR = 0.59 for uFC and dFC, respectively) while the DMN displayed lowest connectivity ($R = 0.88$ and MVAR = 0.41). Finally, the network ICC values for the fALFF parameter were determined in the range of 0.33–0.65 with a non-significant time ($p = 0.92$) and (time × region) interaction effect ($p = 0.87$) based on a repeated measures ANOVA.

Relationship Between CMRGlc and Functional Connectivity

No significant correlation was found between corresponding CMRGlc values and either of the R, MVAR or fALFF coefficients for any of the six major networks. Correlation analysis showed a very poor correlation between CMRGlc values and R coefficients with an r^2 value of <0.02 for all individual networks. A similar result was determined for the MVAR coefficients characterizing dFC for all networks and directions as well as for the fALFF parameter. **Figure 4** shows representative correlation graphs between CMRGlc values and the R, MVAR and fALFF coefficients collapsed over all six networks, demonstrating the absence of any meaningful correlation between functional connectivity measures and regional CMRGlc. Accordingly, application of (Eq. 1) did not improve the reproducibility of CMRGlc values between test and retest conditions. The variability of adjusted CMRGlc values was either similar (13 ±6% vs 13 ±8%, sensory-motor cortex) or was significantly worse (24 ±18% vs 16 ±10%, DMN network) as compared to the measured CMRGlc values.

Figure 5 provides representative CMRGlc images of two subjects with good reproducibility across time (<5% difference in whole brain CMRGlc values) and two subjects with poor reproducibility (>15% difference) together with the corresponding MVAR coefficients for the three selected networks. Although the changes in absolute CMRGlc values differ between the two groups, changes in functional connectivity (as characterized by the MVAR coefficient) between test and retest condition are similar, as indicated in the figure for the DMN and Sensory-motor network. The poor agreement between temporal changes in whole brain CMRGlc values and changes in the MVAR coefficient in two representative brain networks can be clearly appreciated.

DISCUSSION

The main result of our study is the absence of a relevant relationship between absolute metabolic rate of glucose values and measures of functional connectivity in six major brain networks (**Figure 4**). Our results indicate that functional connectivity between major network nodes (as quantified using R, MVAR or fALFF coefficients derived from rs-fMRI) is not suited for standardization of CMRGlc values with respect to the subject's intrinsic network activity (**Figure 5**). Thus, given the substantial intra- and intrasubject variability of glucose metabolic rate, the usefulness of absolute quantification in clinical routine remains to be determined.

The current study confirms the poor test-retest reliability of functional connectivity measures reported in recent literature (Noble et al., 2019). These investigators performed a meta-analytic estimate of the reliability of fMRI based functional connectivity in 44 studies, stating an overall poor ICC of 0.29 (95% CI = 0.23–0.36). One potential reason for the observed low ICC of functional connectivity measures is the relatively large intra-subject variability compared to a comparatively low inter-subject variability (see **Figure 3**).

Moreover, our results both complement and extend the findings of a recent study (Parker and Razlighi, 2019) that demonstrates that consistent and robust deactivations in task-based fMRI studies can be significantly altered without causing any changes in their overlapping intrinsic functional connectivity. These authors present compelling evidence for a disassociation between task-evoked deactivations

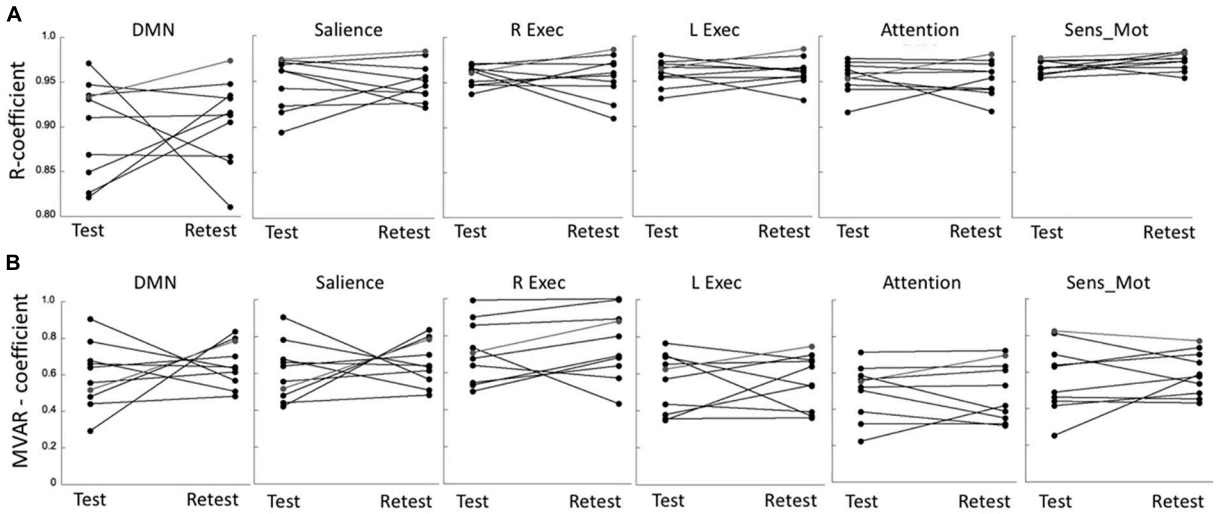

FIGURE 3 | (A) Test-retest values of R coefficients in six major networks: Default Mode network (DMN), Salience network (Salience), R/L Executive network (R Exec/L Exec) and Attention network (Attention) and Sensory-motor network (Sens_Mot). **(B)** Corresponding test-retest values of MVAR coefficients in the same six major networks. R, bivariate-correlation coefficient; MVAR, Multi-Variate Auto-Regressive model coefficient.

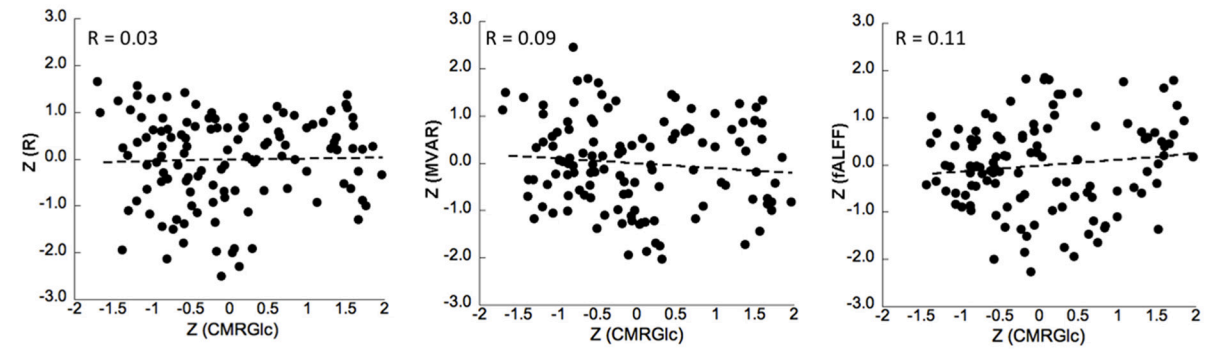

FIGURE 4 | Correlation between z-transformed CMRGlc values and z-transformed R (left), MVAR (middle) and fALFF (right) coefficients for all subjects in six networks at test and retest conditions. The *R*-value represents the Pearson's correlation coefficient between the measures. R, bivariate-correlation coefficient; MVAR, Multi-Variate Auto-Regressive model coefficient; fALFF, fractional amplitude of low frequency fluctuations.

and functional connectivity, both extracted from the same DMN regions. Moreover, they demonstrate that task-based deactivations are more closely related to task performance than is functional connectivity. Based on this data the authors conclude that functional connectivity represents a distinct and ongoing neuro-physiological process whose coherence and magnitude is not altered by task-performance, but is taking on a more basic role in the hierarchical functional architecture of the brain.

Recent studies have demonstrated that task-related changes in brain activity levels are associated with changes in glucose consumption (Riedl et al., 2014; Jamadar et al., 2019), presumably due to altered energy demand of the underlying synaptic transmission processes. Using simultaneous acquisition of both FDG-PET and fMRI data, these investigators have shown a close relationship between task-based functional connectivity and local glucose metabolism in the visual network, consistent with results obtained in non-simultaneously acquired data (Di and Biswal, 2012; Tomasi et al., 2017). Thus, as CMRGlc is closely tied to task-performance, our results showing a poor correlation between glucose metabolic rate and non-task based functional connectivity, directly corroborate Parker and Razlighi (2019) interpretation. Finally, our results are also in partial agreement with a study by Marchitelli et al. (2018), who set out to investigate the coupling between FDG tracer uptake and intrinsic functional activity in both patients (Alzheimer Disease) and a control group. These investigators showed only a modest across-subjects correlation between FDG tracer uptake and intrinsic functional activity, indicating that the variability observed with functional connectivity measures is at least as large as the variability of glucose consumption. Thus, both studies indicate that functional connectivity measures cannot provide added information that could be used to account for the observed physiological variability in glucose metabolic rate.

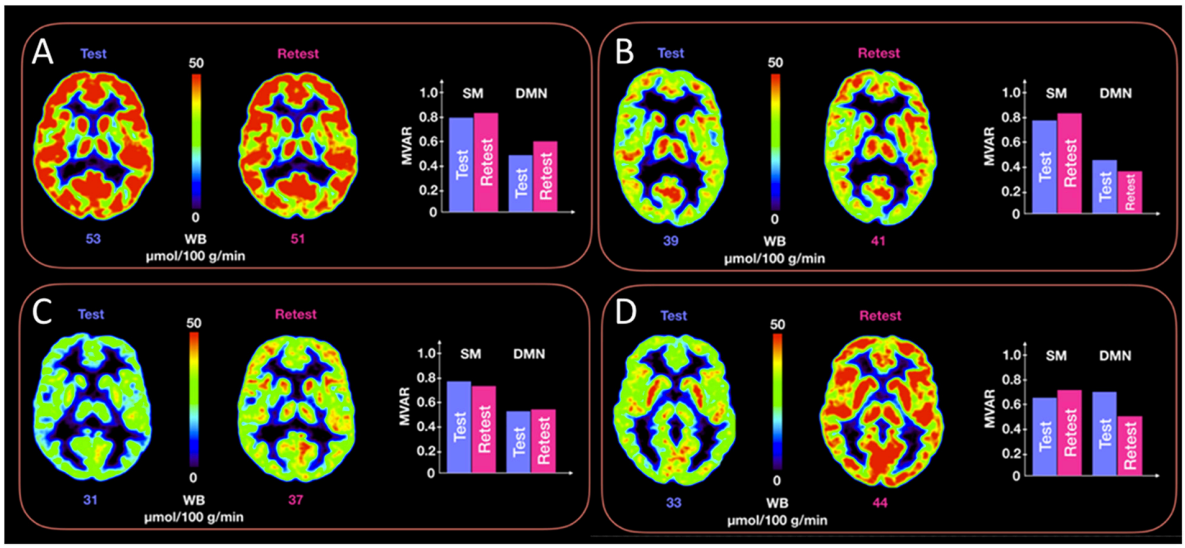

FIGURE 5 | Representative CMRGlc images with low (top row, panels **A,B**) and high (bottom row, panels **C,D**) test-retest variability. Each of the four panels **(A–D)** corresponds to a different subject at rest and retest condition. Each panel renders a trans-axial cross-section through the subject's brain at the level of the caudate head obtained at rest and retest condition, together with bar graphs representing test-retest changes in MVAR coefficients for the DMN and Sensory-motor (SM) networks. The figure demonstrates a similar distribution of MVAR coefficient changes for subjects with low (top row) and high (bottom row) CMRGlc variability across time. WB, whole brain values.

Physiological Variability of CMRGlc Values

Fully quantitative assessment of CMRGlc provides valuable and detailed information about the regional metabolic state of brain tissue, but this advance in methodology brings its own set of issues that need to be carefully considered. Early studies that have investigated absolute CMRGlc in control subjects have revealed a surprisingly large physiological variability that was in the range of 15–25%, even for large regions and the same subject being scanned only a few days apart (Camargo et al., 1992; Schaefer et al., 2000). Our own data confirms these earlier findings (**Figure 2**). Consequently, in the absence of improved data acquisition or analysis protocols that are able to standardize the resting-state metabolism of the subjects, sensitivity to detect areas of significantly increased or decreased CMRGlc will be relatively low, requiring about 30% deviations from baseline (Sundar et al., 2019). This compares unfavorably with the visual assessment of regional asymmetries between homotopic brain areas, which can be quite easily detected at the 10% level (Niimura et al., 1999). Thus, in order to improve the relevance of absolute quantification in clinical applications, standardization of the subjects' resting-state activity will be mandatory. Unfortunately, it is currently unclear how such a standardization could be achieved.

Our previous work showed that the observed physiological variability does not correlate with the time duration between the two PET scans (Sundar et al., 2019), suggesting that variability is not due to a slow drift of brain metabolism across time, but appears to be an inherent characteristic of the underlying neural network. This effect has been extensively studied in the context of the DMN, originally proposed by Raichle et al. (Gusnard et al., 2001; Raichle and Snyder, 2007). The DMN displays fluctuation of brain activity during times when a subject is not performing any task but is left in an "idle" state. These fluctuations are believed to be the result of unconstrained, spontaneous cognition - daydreams or, more technically, stimulus-independent thoughts (McGuire et al., 1996; Mason et al., 2007), which recently led to the realization that a truly "resting" state of the brain probably does not exist (Gusnard et al., 2001). Moreover, such a state is in general undefined as various neural processes that are currently uncontrollable are likely to contribute to the observed variability in CMRGlc. As a case in point, our data suggests that higher-order brain networks (such as the DMN and R/L executive networks) show higher temporal variability than does the sensory-motor network. A possible reason for this surprising finding might be the fact that intrinsic flexibility in these high-order brain networks in combination with complex between-network interactions (Calhoun et al., 2014) may increase their sensitivity to transient environmental factors that play an important role in the mental state of a patient. In contrast, the functional connectivity within the sensory-motor system is relatively independent of transient factors and as a result, might more stably reflect the baseline state of the brain.

Temporal Relationship Between CMRGlc and rs-fMRI

In order to calculate CMRGlc values, dynamic PET data over an extended time period (∼60 min) is acquired. Moreover, to derive CMRGlc values from such data, a three-compartment model (consisting of a vascular, intracellular and metabolic compartment) is applied. Analysis of such a compartmental model indicates that after ∼25 min post injection a dynamic equilibrium is reached between the compartments which, under

resting conditions, is maintained until the end of the study (∼60 min). The presence of such a dynamic equilibrium suggests that during this time the CMRGlc is unchanged and can be therefore uniquely identified from the data. This assumption is well supported by the observation that the Patlak-transformed dynamic time-activity curves display a linear behavior during the dynamic equilibrium phase, allowing a simplified analysis based on linear fitting. Thus, it appears reasonable to assume that during dynamic equilibrium the functional EPI data should also reflect a stable network configuration commensurate with the measured CMRGlc values (see **Supplementary Figure S1** in the **Supplementary Material**).

Neurovascular Coupling

It is reasonable to assume that resting-state glucose is physiologically related to baseline neural activity as well as to resting cerebral blood flow (Attwell and Iadecola, 2002). Although rs-fMRI is considered to represent an indirect measure of neural activity in specified neural networks, several issues prevent a straightforward application of rs-fMRI derived parameters to yield information about overall energy consumption in these networks.

Firstly, the mechanisms underlying neurovascular coupling and neuronal function are still not completely understood (Leithner and Royl, 2014). For example, it is not fully understood what function moment-to-moment changes in blood flow serve. The delivery of oxygen and glucose are indeed an important factor, but the availability of reserves (i.e., unextracted oxygen in circulating blood and glucose and glycogen in astrocytes) make a simple relationship unlikely. Possible other mechanisms that have been proposed are the removal of excess lactate produced during an increase in activity or the adjustment of the acid-base/ionic balance of the tissue. However, these mechanisms do not lend themselves easily to a transparent relationship with functional connectivity.

Secondly, established measures of local connectivity such as Regional Homogeneity (ReHo, Zang et al., 2004) and fractional Amplitude of Low Frequency Fluctuations (fALFF, Zou et al., 2008) represent local variables closely related to small (<3%) moment-to-moment regional blood flow changes, but not to absolute blood flow values (which can be non-invasively measured using 15O-water PET imaging). Both these parameters have been shown to correlate with local FDG uptake (Tomasi et al., 2013; Aiello et al., 2015; Savio et al., 2017; Rajkumar et al., 2018), but a relationship with absolute glucose metabolic rates could not be demonstrated.

Finally, Zuo et al. (2012) defined a direct connectivity (DC) parameter which provides a measure of information flow within a network. DC is a local measure of functional connectivity that indexes the number of direct connections for a given node and is calculated as the Pearson's correlation coefficient between remote voxels (Buckner et al., 2009). Conceptually, a node has high DC if it has numerous direct connections to other nodes and such a node would be expected to be more active than a node with low DC. Surprisingly, DC has been shown to correlate poorly with FDG tracer uptake (Aiello et al., 2015), corroborating our results. Our findings suggest that fluctuations in blood flow measured with rs-fMRI are superimposed on a much larger blood flow baseline that cannot be assessed using fMRI measures. However, it is this (unknown) blood flow baseline, that determines overall energy consumption in the brain (Sokoloff, 1980).

PET/MR: The Sum Is Greater Than Its Parts

In accordance with the finding that task-based deactivations are more closely related to task performance than is functional connectivity (Parker and Razlighi, 2019), it is reasonable to assume that a subject's psychological state could be influenced by performing a specific task. There is evidence that task-related psychological states in different patients are more similar than during resting state (Duara et al., 1987). These investigators have demonstrated that by involving the subjects in a picture preference test during the FDG uptake period decreases the variability of CMRGlc values by 60–80%. Interestingly, the same task performed in mild to moderately demented patients (with Mini-Mental-State >15) did not result in any appreciable decreases of CMRGlc variability, indicating that subjects need to have a certain level of engagement with the performed task in order to achieve standardization.

Obtaining a measure of task performance might be an excellent parameter that can be used to characterize a particular psychological state. In this context, combined PET/MRI methodology might provide a highly efficient means to monitor task performance by taking advantage of advanced fMRI protocols. For example, a real-time fMRI (rt-fMRI) neurofeedback protocol could be applied to regulate the psychological state of the subjects under study (Caria et al., 2012; Weiskopf, 2012; Sulzer et al., 2013; Gerin et al., 2016). In fact, numerous studies have established the effectiveness of the rt-fMRI neurofeedback approach in being able to change the activity of specific brain regions and even to improve emotion regulation through the willful increase of prefrontal control over the amygdala complex (Young et al., 2017; Mehler et al., 2018; Sorger et al., 2018; Watanabe et al., 2018). Thus, although speculative, a protocol that uses an rt-fMRI neurofeedback paradigm during the FDG uptake period could generate a very similar psychological state in the studied subjects, potentially resulting in excellent temporal reproducibility of PET-derived CMRGlc values.

Study Limitations

There are several possible issues associated with our study that deserve mentioning. Our study includes a relatively low number of participants (N = 10) that were, however, imaged in a test/retest design. As such, our data includes 20 measurements, allowing assessment of both between- and within-subjects effects. Moreover, standardization of MRGlc values to psychological state will need to be applied to individual measurements, rendering statistical averages of lesser importance. Another possible limitation is the relatively heterogenous time difference between the test/retest imaging sessions, with a mean time difference between scans being 17 ± 44 days (range 3 days to 2 months). However, our previous analysis (Sundar et al., 2019) showed no significant correlation between test/retest differences in MRGlc values and the length of time separating the two acquisitions

(R^2 = 0.03). These results suggest that time effects are most likely not responsible for the observed variability in the observed MRGlc values. Finally, we observed a relatively large (but not statistically significant) decrease in inter-subject variability from the test to the retest condition (from 25% to 15%). This decrease in CMRGlc variability represents a confound that might be due to increased familiarity of the subjects with the imaging procedure at the second scan, thereby decreasing uncertainty and anxiety levels. It is conceivable that the so generated expectations allowed the subjects to enter a state of mind that was conducive to the task ahead, in essence standardizing their psychological state and resulting in decreased CMRGlc variability. Although speculative, this observation supports our notion that exerting influence over a subject's psychological state might be effective in decreasing CMRGlc variability.

Future Directions

In future studies we expect to build upon the results presented herein. In particular, we will seek to combine the current approach with various metrics that focus on local functional connectivity for the purpose of CMRGlc standardization, such as regional homogeneity (ReHo), ALFF as well as a more systematic investigation of the potential of an independent component analysis (ICA) for this purpose. All these measures have been shown to possess excellent test-retest reliability (Zuo and Xing, 2014), leaving open the possibility that a hybrid approach that takes into account both long distance as well as local functional connectivity measures might provide a means to significantly decrease test-retest variability of glucose metabolic rates.

CONCLUSION

Although high expectations have been pinned upon the absolute glucose metabolic rates in a clinical setting, these have not been matched by the results of fully quantitative FDG-PET imaging due to the large intra- and intersubject variability. Presumably, this variability appears to be caused by changes in patients' intrinsic brain activity, of which the underlying mechanisms are currently poorly understood and as a result are being inadequately controlled for. Our attempt to standardize glucose metabolic rates based on functional connectivity measures determined within six major brain networks was unsuccessful, rendering the clinical relevance of absolute quantification of cerebral glucose metabolism uncertain at present.

DATA AVAILABILITY STATEMENT

All datasets generated for this study are included in the article/**Supplementary Material**.

ETHICS STATEMENT

The studies involving human participants were reviewed and approved by the Ethics Committee of the Medical University of Vienna (EK1960/2014). The patients/participants provided their written informed consent to participate in this study.

AUTHOR CONTRIBUTIONS

All authors made substantial contributions to conception and design, and/or acquisition of data, and/or analysis, and interpretation of data; participated in drafting the article or revising it critically for important intellectual content; and gave final approval of the version to be submitted and any revised version.

FUNDING

This work was supported by the Austrian Science Fund KLI482-B31.

ACKNOWLEDGMENTS

We gratefully acknowledge the support of NVIDIA Corporation with the donation of the Titan Xp GPU used for this research. We also would like to thank Bernd Pichler, Tudor Mihai Ionescu, and Kristina Herfert from Werner Siemens Imaging Center for their constructive inputs and feedback.

SUPPLEMENTARY MATERIAL

The Supplementary Material for this article can be found online at: https://www.frontiersin.org/articles/10.3389/fnins.2020.00252/full#supplementary-material

REFERENCES

Aiello, M., Salvatore, E., Cachia, A., Pappata, S., Cavaliere, C., Prinster, A., et al. (2015). Relationship between simultaneously acquired resting-state regional cerebral glucose metabolism and functional MRI: a PET/MR hybrid scanner study. *Neuroimage* 113, 111–121. doi: 10.1016/j.neuroimage.2015.03.017

Asemi, A., Ramaseshan, K., Burgess, A., Diwadkar, V. A., and Bressler, S. L. (2015). Dorsal anterior cingulate cortex modulates supplementary motor area in coordinated unimanual motor behavior. *Front. Hum. Neurosci.* 9:309. doi: 10.3389/fnhum.2015.00309

Attwell, D., and Iadecola, C. (2002). The neural basis of functional brain imaging signals. *Trends Neurosci.* 25, 621–625. doi: 10.1016/s0166-2236(02)02264-6

Biswal, B. B., Mennes, M., Zuo, X. N., Gohel, S., Kelly, C., Smith, S. M., et al. (2010). Toward discovery science of human brain function. *Proc. Natl. Acad. Sci. U.S.A.* 107, 4734–4739. doi: 10.1073/pnas.0911855107

Bressler, S. L., and Seth, A. K. (2011). Wiener-granger causality: a well established methodology. *Neuroimage* 58, 323–329. doi: 10.1016/j.neuroimage.2010.02.059

Buckner, R. L., Sepulcre, J., Talukdar, T., Krienen, F. M., Liu, H., Hedden, T., et al. (2009). Cortical hubs revealed by intrinsic functional connectivity: mapping, assessment of stability, and relation to Alzheimer's disease. *J. Neurosci.* 29, 1860–1873. doi: 10.1523/JNEUROSCI.5062-08.2009

Calhoun, V. D., Miller, R., Pearlson, G., and Adali, T. (2014). The chronnectome: time-varying connectivity networks as the next frontier in fMRI data discovery. *Neuron* 84, 262–274. doi: 10.1016/j.neuron.2014.10.015

Camargo, E. E., Szabo, Z., Links, J. M., Sostre, S., Dannals, R. F., and Wagner, H. N. Jr. (1992). The influence of biological and technical factors on the variability of global and regional brain metabolism of 2-[18F]fluoro-2-deoxy-D-glucose. *J. Cereb. Blood Flow Metab.* 12, 281–290. doi: 10.1038/jcbfm.1992.38

Caria, A., Sitaram, R., and Birbaumer, N. (2012). Real-time fMRI: a tool for local brain regulation. *Neuroscientist* 18, 487–501. doi: 10.1177/1073858411407205

Carney, J. P., Townsend, D. W., Rappoport, V., and Bendriem, B. (2006). Method for transforming CT images for attenuation correction in PET/CT imaging. *Med. Phys.* 33, 976–983. doi: 10.1118/1.2174132

Chang, J. Y., Duara, R., Barker, W., Apicella, A., and Finn, R. (1987). Two behavioral states studied in a single PET/FDG procedure: theory, method, and preliminary results. *J. Nucl. Med.* 28, 852–860.

Di, X., and Biswal, B. B. (2012). Alzheimer's disease neuroimaging initiative. Metabolic brain covariant networks as revealed by FDG-PET with reference to resting-state fMRI networks. *Brain Connect.* 2, 275–283. doi: 10.1089/brain.2012.0086

Diwadkar, V. A., Asemi, A., Burgess, A., Chowdury, A., and Bressler, S. L. (2017). Potentiation of motor sub-networks for motor control but not working memory: Interaction of dACC and SMA revealed by resting- state directed functional connectivity. *PLoS One* 12:e0172531. doi: 10.1371/journal.pone.0172531

Duara, R., Gross-Glenn, K., Barker, W. W., Chang, J. Y., Apicella, A., Loewenstein, D., et al. (1987). Behavioral activation and the variability of cerebral glucose metabolic measurements. *J. Cereb. Blood Flow Metab.* 7, 266–271. doi: 10.1038/jcbfm.1987.62

Friston, K. J. (2011). Functional and effective connectivity: a review. *Brain Connect.* 1, 13–36. doi: 10.1089/brain.2011.0008

Fukunaga, M., Horovitz, S. G., de Zwart, J. A., van Gelderen, P., Balkin, T. J., Braun, A. R., et al. (2008). Metabolic origin of BOLD signal fluctuations in the absence of stimuli. *J. Cereb. Blood Flow Metab.* 28, 1377–1387. doi: 10.1038/jcbfm.2008.25

Gandavia, B., and Tovella, A. (1964). Declaration OF Helsinki. *Med. J. Aust.* 22, 320–321.

Gerin, M. I., Fichtenholtz, H., Roy, A., Walsh, C. J., Krystal, J. H., Southwick, S., et al. (2016). Real-Time fMRI neurofeedback with war veterans with chronic PTSD: a feasibility study. *Front. Psychiatry* 7:111. doi: 10.3389/fpsyt.2016.00111

Granger, C. W. J. (1969). Investigating causal relations by econometric models and cross-spectral methods. *Econometrica* 37, 424–438. doi: 10.2307/1912791

Gusnard, D. A., Raichle, M. E., and Raichle, M. E. (2001). Searching for a baseline: functional imaging and the resting human brain. *Nat. Rev. Neurosci.* 2, 685–694. doi: 10.1038/35094500

Haacke, M. E. (2014). *Magnetic Resonance Imaging: Physical Properties and Sequence Design*, 2nd Edn. Hoboken, NJ: John Wiley & Sons.

Haider, B., Duque, A., Hasenstaub, A. R., and McCormick, D. A. (2006). Neocortical network activity in vivo is generated through a dynamic balance of excitation and inhibition. *J. Neurosci.* 26, 4535–4545. doi: 10.1523/JNEUROSCI.5297-05.2006

Jamadar, S. D., Ward, P. G., Li, S., Sforazzini, F., Baran, J., Chen, Z., et al. (2019). Simultaneous task-based BOLD-fMRI and [18-F] FDG functional PET for measurement of neuronal metabolism in the human visual cortex. *Neuroimage* 189, 258–266. doi: 10.1016/j.neuroimage.2019.01.003

Keller, S. H., Hansen, C., Hansen, C., Andersen, F. L., Ladefoged, C., Svarer, C., et al. (2015). Motion correction in simultaneous PET/MR brain imaging using sparsely sampled MR navigators: a clinically feasible tool. *EJNMMI Phys.* 2:14. doi: 10.1186/s40658-015-0118-z

Lammertsma, A. A. (2017). Forward to the past: the case for quantitative PET imaging. *J. Nucl. Med.* 58, 1019–1024. doi: 10.2967/jnumed.116.188029

Leithner, C., and Royl, G. (2014). The oxygen paradox of neurovascular coupling. *J. Cereb. Blood Flow Metab.* 34, 19–29. doi: 10.1038/jcbfm.2013.181

Logothetis, N. K., Pauls, J., Augath, M., Trinath, T., and Oeltermann, A. (2001). Neurophysiological investigation of the basis of the fMRI signal. *Nature* 412, 150–157. doi: 10.1038/35084005

Marchitelli, R., Aiello, M., Cachia, A., Quarantelli, M., Cavaliere, C., Postiglione, A., et al. (2018). Simultaneous resting-state FDG-PET/fMRI in Alzheimer disease: relationship between glucose metabolism and intrinsic activity. *Neuroimage* 176, 246–258. doi: 10.1016/j.neuroimage.2018.04.048

Mason, M. F., Norton, M. I., Van Horn, J. D., Wegner, D. M., Grafton, S. T., and Macrae, C. N. (2007). Wandering minds: the default network and stimulus-independent thought. *Science* 315, 393–395. doi: 10.1126/science.1131295

McGuire, P. K., Paulesu, E., Frackowiak, R. S., and Frith, C. D. (1996). Brain activity during stimulus independent thought. *Neuroreport* 7, 2095–2099.

Mehler, D. M. A., Sokunbi, M. O., Habes, I., Barawi, K., Subramanian, L., Range, M., et al. (2018). Targeting the affective brain-a randomized controlled trial of real-time fMRI neurofeedback in patients with depression. *Neuropsychopharmacology* 43, 2578–2585. doi: 10.1038/s41386-018-0126-5

Morris, L. S., Kundu, P., Costi, S., Collins, A., Schneider, M., Verma, G., et al. (2019). Ultra-high field MRI reveals mood-related circuit disturbances in depression: a comparison between 3-Tesla and 7-Tesla. *Transl. Psychiatry* 9:94. doi: 10.1038/s41398-019-0425-6

Niimura, K., Muzik, O., Chugani, D. C., Shen, C., and Chugani, H. T. (1999). [11C]flumazenil PET: activity images versus parametric images for the detection of neocortical epileptic foci. *J. Nucl. Med.* 40, 1985–1991.

Noble, S., Scheinost, D., and Constable, R. T. (2019). A decade of test-retest reliability of functional connectivity: a systematic review and meta-analysis. *Neuroimage* 203:116157. doi: 10.1016/j.neuroimage.2019.116157

Parker, D. B., and Razlighi, Q. R. (2019). Task-evoked negative BOLD response and functional connectivity in the default mode network are representative of two overlapping but separate neurophysiological processes. *Sci. Rep.* 9:14473. doi: 10.1038/s41598-019-50483-8

Raichle, M. E., and Mintun, M. A. (2006). Brain work and brain imaging. *Annu. Rev. Neurosci.* 29, 449–476. doi: 10.1146/annurev.neuro.29.051605.112819

Raichle, M. E., and Snyder, A. Z. (2007). A default mode of brain function: a brief history of an evolving idea. *Neuroimage* 37, 1083–1090. doi: 10.1016/j.neuroimage.2007.02.041

Rajkumar, R., Farrher, E., Mauler, J., Sripad, P., Regio Brambilla, C., Rota Kops, E., et al. (2018). Comparison of EEG microstates with resting state fMRI and FDG-PET measures in the default mode network via simultaneously recorded trimodal (PET/MR/EEG) data. *Hum. Brain Mapp.* doi: 10.1002/hbm.24429 [Epub ahead of print].

Riedl, V., Bienkowska, K., Strobel, C., Tahmasian, M., Grimmer, T., Förster, S., et al. (2014). Local activity determines functional connectivity in the resting human brain: a simultaneous FDG-PET/fMRI study. *J. Neurosci.* 34, 6260–6266. doi: 10.1523/JNEUROSCI.0492-14.2014

Savio, A., Funger, S., Tahmasian, M., Rachakonda, S., Manoliu, A., Sorg, C., et al. (2017). Resting-state networks as simultaneously measured with functional MRI and PET. *J. Nucl. Med.* 58, 1314–1317. doi: 10.2967/jnumed.116.185835

Schaefer, S. M., Abercrombie, H. C., Lindgren, K. A., Larson, C. L., Ward, R. T., Oakes, T. R., et al. (2000). Six-month test-retest reliability of MRI-defined PET measures of regional cerebral glucose metabolic rate in selected subcortical structures. *Hum. Brain Mapp.* 10, 1–9. doi: 10.1002/(sici)1097-0193(200005)10:1<1::aid-hbm10>3.0.co;2-o

Schmidt, K. C., and Turkheimer, F. E. (2002). Kinetic modeling in positron emission tomography. *Q. J. Nucl. Med.* 46, 70–85.

Singh, K. D. (2012). Which "neural activity" do you mean? fMRI, MEG, oscillations and neurotransmitters. *Neuroimage* 62, 1121–1130. doi: 10.1016/j.neuroimage.2012.01.028

Sokoloff, L. (1980). Local cerebral energy metabolism: its relationship to local functional activity and blood flow. *Bull. Schweiz. Akad. Med. Wiss.* 36, 71–91.

Sorger, B., Kamp, T., Weiskopf, N., Peters, J. C., and Goebel, R. (2018). When the brain takes 'BOLD' steps: real-time fMRI neurofeedback can further enhance the ability to gradually self-regulate regional brain activation. *Neuroscience* 378, 71–88. doi: 10.1016/j.neuroscience.2016.09.026

Sulzer, J., Haller, S., Scharnowski, F., Weiskopf, N., Birbaumer, N., Blefari, M. L., et al. (2013). Real-time fMRI neurofeedback: progress and challenges. *Neuroimage* 76, 386–399. doi: 10.1016/j.neuroimage.2013.03.033

Sundar, L. K., Muzik, O., Rischka, L., Hahn, A., Rausch, I., Lanzenberger, R., et al. (2019). Towards quantitative [18F]FDG-PET/MRI of the brain: automated MR-driven calculation of an image-derived input function for the non-invasive determination of cerebral glucose metabolic rates. *J. Cereb. Blood Flow Metab.* 39, 1516–1530. doi: 10.1177/0271678X18776820

Tang, Y., Wang, L., Cao, F., and Tan, L. (2012). Identify schizophrenia using resting-state functional connectivity: an exploratory research and analysis. *Biomed. Eng. Online* 11:50. doi: 10.1186/1475-925x-11-50

Tomasi, D., Wang, G. J., and Volkow, N. D. (2013). Energetic cost of brain functional connectivity. *Proc. Natl. Acad. Sci. U.S.A.* 110, 13642–13647. doi: 10.1073/pnas.1303346110

Tomasi, D. G., Shokri-Kojori, E., Wiers, C. E., Kim, S. W., Demiral, ŞB, et al. (2017). Dynamic brain glucose metabolism identifies anti-correlated cortical-cerebellar networks at rest. *J. Cereb. Blood Flow Metab.* 37, 3659–3670. doi: 10.1177/0271678X17708692

Tyler, J. L., Strother, S. C., Zatorre, R. J., Alivisatos, B., Worsley, K. J., Diksic, M., et al. (1988). Stability of regional cerebral glucose metabolism in the normal brain measured by positron emission tomography. *J. Nucl. Med.* 29, 631–642.

Watanabe, T., Sasaki, Y., Shibata, K., and Kawato, M. (2018). Advances in fMRI real-time neurofeedback. *Trends Cogn. Sci.* 21, 997–1010. doi: 10.1016/j.tics.2018.05.007

Weiskopf, N. (2012). Real-time fMRI and its application to neurofeedback. *Neuroimage* 62, 682–692. doi: 10.1016/j.neuroimage.2011.10.009

Whitfield-Gabrieli, S., and Nieto-Castanon, A. (2012). Conn: a functional connectivity toolbox for correlated and anticorrelated brain networks. *Brain Connect.* 2, 125–141. doi: 10.1089/brain.2012.0073

Wu, H. M., Bergsneider, M., Glenn, T. C., Yeh, E., Hovda, D. A., Phelps, M. E., et al. (2003). Measurement of the global lumped constant for 2-deoxy-2-[18F]fluoro-D-glucose in normal human brain using [15O]water and 2-deoxy-2-[18F]fluoro-D-glucose positron emission tomography imaging. A method with validation based on multiple methodologies. *Mol. Imaging Biol.* 5, 32–41. doi: 10.1016/s1536-1632(02)00122-1

Young, K. D., Siegle, G. J., Zotev, V., Phillips, R., Misaki, M., Yuan, H., et al. (2017). Randomized clinical trial of real-time fMRI amygdala neurofeedback for major depressive disorder: effectson symptoms and autobiographical memory recall. *Am. J. Psychiatry* 174, 748–755. doi: 10.1176/appi.ajp.2017.16060637

Yu-Feng, Z., Yong, H., Chao-Zhe, Z., Qing-Jiu, C., Man-Qiu, S., Meng, L., et al. (2007). Altered baseline brain activity in children with ADHD revealed by resting-state functional MRI. *Brain Dev.* 29, 83–91. doi: 10.1016/j.braindev.2006.07.002

Zang, Y., Jiang, T., Lu, Y., He, Y., and Tian, L. (2004). Regional homogeneity approach to fMRI data analysis. *Neuroimage* 22, 394–400. doi: 10.1016/j.neuroimage.2003.12.030

Zou, Q.-H., Zhu, C.-Z., Yang, Y., Zuo, X.-N., Long, X.-Y., Cao, Q.-J., et al. (2008). An improved approach to detection of amplitude of low-frequency fluctuation (ALFF) for resting-state fMRI: fractional ALFF. *J. Neurosci. Methods* 172, 137–141. doi: 10.1016/j.jneumeth.2008.04.012

Zhou, Y., Wang, K., Liu, Y., Song, M., Song, S. W., and Jiang, T. (2010). Spontaneous brain activity observed with functional magnetic resonance imaging as a potential biomarker in neuropsychiatric disorders. *Cogn. Neurodyn.* 4, 275–294. doi: 10.1007/s11571-010-9126-9

Zuo, X. N., Ehmke, R., Mennes, M., Imperati, D., Castellanos, F. X., Sporns, O., et al. (2012). Network centrality in the human functional connectome. *Cereb. Cortex* 22, 1862–1875. doi: 10.1093/cercor/bhr269

Zuo, X.-N., and Xing, X.-X. (2014). Test-retest reliabilities of resting-state FMRI measurements in human brain functional connectomics: a systems neuroscience perspective. *Neurosci. Biobehav. Rev.* 45, 100–118.

Conflict of Interest: The authors declare that the research was conducted in the absence of any commercial or financial relationships that could be construed as a potential conflict of interest.

frontiers in Computational Neuroscience

ORIGINAL RESEARCH
published: 31 March 2020
doi: 10.3389/fncom.2020.00022

Inhibition of Long-Term Variability in Decoding Forelimb Trajectory Using Evolutionary Neural Networks With Error-Correction Learning

*Shih-Hung Yang[1], Han-Lin Wang[2], Yu-Chun Lo[3], Hsin-Yi Lai[4,5], Kuan-Yu Chen[2], Yu-Hao Lan[2], Ching-Chia Kao[6], Chin Chou[7], Sheng-Huang Lin[8,9], Jyun-We Huang[1], Ching-Fu Wang[2], Chao-Hung Kuo[2,10,11] and You-Yin Chen[2,3]**

[1] Department of Mechanical Engineering, National Cheng Kung University, Tainan, Taiwan, [2] Department of Biomedical Engineering, National Yang Ming University, Taipei, Taiwan, [3] The Ph.D. Program for Neural Regenerative Medicine, College of Medical Science and Technology, Taipei Medical University, Taipei, Taiwan, [4] Key Laboratory of Medical Neurobiology of Zhejiang Province, Department of Neurology of the Second Affiliated Hospital, Interdisciplinary Institute of Neuroscience and Technology, Zhejiang University School of Medicine, Hangzhou, China, [5] Key Laboratory of Biomedical Engineering of Ministry of Education, College of Biomedical Engineering and Instrument Science, Qiushi Academy for Advanced Studies, Zhejiang University, Hangzhou, China, [6] Research Center for Information Technology Innovation, Academia Sinica, Taipei, Taiwan, [7] Department of Regulatory & Quality Sciences, University of Southern California, Los Angeles, CA, United States, [8] Buddhist Tzu Chi Medical Foundation, Department of Neurology, Hualien Tzu Chi Hospital, Hualien, Taiwan, [9] Department of Neurology, School of Medicine, Tzu Chi University, Hualien, Taiwan, [10] Department of Neurosurgery, Neurological Institute, Taipei Veterans General Hospital, Taipei, Taiwan, [11] Department of Neurological Surgery, University of Washington, Seattle, WA, United States

OPEN ACCESS

Edited by:
Chun-Shu Wei,
National Chiao Tung University, Taiwan

Reviewed by:
Eric Bean Knudsen,
University of California, Berkeley, United States
Ting Zhao,
Howard Hughes Medical Institute (HHMI), United States

***Correspondence:**
You-Yin Chen
irradiance@so-net.net.tw

Received: *20 November 2019*
Accepted: *04 March 2020*
Published: *31 March 2020*

Citation:
Yang S-H, Wang H-L, Lo Y-C, Lai H-Y, Chen K-Y, Lan Y-H, Kao C-C, Chou C, Lin S-H, Huang J-W, Wang C-F, Kuo C-H and Chen Y-Y (2020) Inhibition of Long-Term Variability in Decoding Forelimb Trajectory Using Evolutionary Neural Networks With Error-Correction Learning. Front. Comput. Neurosci. 14:22. doi: 10.3389/fncom.2020.00022

Objective: In brain machine interfaces (BMIs), the functional mapping between neural activities and kinematic parameters varied over time owing to changes in neural recording conditions. The variability in neural recording conditions might result in unstable long-term decoding performance. Relevant studies trained decoders with several days of training data to make them inherently robust to changes in neural recording conditions. However, these decoders might not be robust to changes in neural recording conditions when only a few days of training data are available. In time-series prediction and feedback control system, an error feedback was commonly adopted to reduce the effects of model uncertainty. This motivated us to introduce an error feedback to a neural decoder for dealing with the variability in neural recording conditions.

Approach: We proposed an evolutionary constructive and pruning neural network with error feedback (ECPNN-EF) as a neural decoder. The ECPNN-EF with partially connected topology decoded the instantaneous firing rates of each sorted unit into forelimb movement of a rat. Furthermore, an error feedback was adopted as an additional input to provide kinematic information and thus compensate for changes in functional mapping. The proposed neural decoder was trained on data collected from a water reward-related lever-pressing task for a rat. The first 2 days of data were used to train the decoder, and the subsequent 10 days of data were used to test the decoder.

Main Results: The ECPNN-EF under different settings was evaluated to better understand the impact of the error feedback and partially connected topology. The experimental results demonstrated that the ECPNN-EF achieved significantly higher daily

decoding performance with smaller daily variability when using the error feedback and partially connected topology.

Significance: These results suggested that the ECPNN-EF with partially connected topology could cope with both within- and across-day changes in neural recording conditions. The error feedback in the ECPNN-EF compensated for decreases in decoding performance when neural recording conditions changed. This mechanism made the ECPNN-EF robust against changes in functional mappings and thus improved the long-term decoding stability when only a few days of training data were available.

Keywords: brain machine interfaces, neural decoding, error feedback, evolutionary algorithm, recurrent neural network

INTRODUCTION

Brain machine interface (BMI) technology converts the brain's neural activity into kinematic parameters of limb movements. This allows controlling a computer cursor or prosthetic devices (Kao et al., 2014; Slutzky, 2018), which can greatly improve the quality of life. Intracortical BMIs have used microelectrodes implanted in the cortex to decode neural signals. These signals have then been converted into motor commands to control an anthropomorphic prosthetic limb, thereby restoring natural function (Collinger et al., 2013; Roelfsema et al., 2018).

The decoder was the most crucial component of a BMI; it modeled the functional mapping between neural activities and kinematic parameters (e.g., movement velocity or position), and assumed that this functional mapping was time-invariant (i.e., a stationary statistical assumption) (Kim et al., 2006). However, under real neural recording conditions, there existed a high degree of within- and across-day variability (Simeral et al., 2011; Perge et al., 2013, 2014; Wodlinger et al., 2014; Downey et al., 2018) that prevented satisfaction of the stationary statistical assumption. This variability consisted of the relative position of the recording electrodes—and surrounding neurons, electrode properties, tissue reaction to electrodes, and neural plasticity—and might affect the functional mapping between neural activities and kinematic parameters (Jackson et al., 2006; Barrese et al., 2013; Fernández et al., 2014; Salatino et al., 2017; Michelson et al., 2018; Hong and Lieber, 2019). The variability in neural recording conditions resulted in unstable long-term decoding performance and led to frequent decoder retraining (Jarosiewicz et al., 2013, 2015).

Conventional decoder retraining required the subject to periodically perform a well-defined task to collect new training data for preventing model staleness (Jarosiewicz et al., 2015). This manner may lead to additional training time before the BMI can be used. Traditional linear neural decoders did not need frequent retraining but possessed limited computational complexity to deal with neural recording condition changes owning to linear properties (Collinger et al., 2013). It is known that the newly encountered neural recording conditions in chronic BMI systems have some commonality with past neural recording conditions (Chestek et al., 2011; Perge et al., 2013; Bishop et al., 2014; Nuyujukian et al., 2014; Orsborn et al., 2014). Therefore, computationally powerful non-linear decoders were proposed to learn a diverse set of neural-to-kinematic mappings corresponding to various neural recording conditions collected over many days before BMI use (Sussillo et al., 2016). This approach avoided BMI interruption by keeping model parameters fixed during BMI use and made BMI inherently robust to changes in neural recording conditions by exploiting the similarities between newly encountered and past neural recording conditions. Therefore, the BMIs were trained with several days of data in order to learn various neural recording conditions and achieve stable long-term decoding. However, they heavily relied on the huge training data where a large training set may not be available for both non-human primates and rodent models.

The limited training data have become an issue for BMI application in long-term performance. A chronic inflammatory reaction results in neural signal loss and decrease in quality over time (Chen et al., 2009). Also, the number of implanted electrodes is limited by the size of the neural nuclei in the rodent brain. Therefore, limited neurons and limited recording times lead to limited training data.

Rodent models with small numbers of implanted electrodes have been widely used to investigate state-of-the-art neural prostheses. Previous studies have demonstrated the decoding performances of various methods at the motor cortex (Zhou et al., 2010; Yang et al., 2016), somatosensory cortex (Pais-Vieira et al., 2013), and hippocampus (Tampuu et al., 2019) in rodent models. The results indicated that good decoding methods should be considerably more robust to small sample sizes caused by limited neurons or limited recording times. In general, a limited amount of training data made traditional decoding methods inaccurate, because they usually required a large number of neurons to achieve desirable levels of

Abbreviations: MI, brain machine interface; ECPNN-EF, evolutionary constructive and pruning neural network with error feedback; NN, neural network; RNN, recurrent neural network; ESN, echo-state network; TDNN, time-delay neural network; EA, evolutionary algorithm; ECPA, evolutionary constructive and pruning algorithm; CBP, cluster-based pruning; ABSS, age-based survival selection; BPTT, backpropagation through time; ECPNN-EFWC, ECPNN-EF only with CBP; ECPNN-EFWA, ECPNN-EF only with ABSS; RNN-EF, fully-connected RNN with error feedback; ECPNN, ECPNN-EF without error-correction learning; PCNN, partially connected NN; FCNN, fully connected neural network.

performance. Furthermore, small amounts of data have made modern decoding methods unreliable, because their increasing model complexities required a large amount of training data (Glaser et al., 2017). Whether the BMIs could deal with the scenario in which only a few days of training data were available is unknown. This motivated us to develop a neural decoder that could learn from limited training data based on rodent models.

In time-series prediction applications, neural networks (NNs) usually employed prediction error as an additional input of the networks. This has been proven to yield superior performance compared with that without error feedback (Connor et al., 1994; Mahmud and Meesad, 2016; Waheeb et al., 2016). The error feedback determined the difference between the network output and the target value. This information could provide the network with information concerning previous prediction performance and might thereby guide the network to accurate prediction. In a feedback control system, the output signal was fed back to form an error signal, which was the difference between the target and actual output, in order to drive the system. Using feedback could reduce the effects of model uncertainty (Løvaas et al., 2008). Furthermore, feedback control could cope with trial-to-trial variability caused by complex dynamics or noise in motor behavior (Todorov and Jordan, 2002). Based on the contemporary physiological studies in the human cortex (Miyamoto et al., 1988), a feedback motor command has been used as an error signal for training an NN (Kawato, 1990). One study hypothesized that the user intended to directly move toward the target when using BMI. This study fitted the neural decoder by estimating user's intended velocity which was determined from target position, cursor position, and decoded velocity (Gilja et al., 2012). A recent study took into account how the user modified the neural modulation to deal with the movement errors caused by neural variability in the feedback loop (Willett et al., 2019). Their framework simulated online/closed-loop dynamics of an intracortical BMI and calibrated its decoder by an encoded control signal, which was the difference between target position and cursor position. The encoded control signal using target position was first transformed into neural features which were then mapped to a decoded control vector for updating decoder output, i.e., cursor velocity. This motivated us to introduce an error feedback into a neural decoder for dealing with the variability in neural recording conditions because the error feedback might compensate for the changes in neural recording conditions. Then, the neural decoder did not need retraining and was expected to be robust to various neural recording conditions when only using a few days of training data.

Several characteristics make NNs computationally powerful decoders in BMIs. First, an NN with a sufficient number of hidden neurons can approximate any continuous function (Hornik et al., 1989). This makes an NN well-suited to learn the functional mapping between neural activity and kinematic parameters. Second, several types of NNs can successfully control motor movement in BMIs. These include recurrent NN (RNN) (Haykin, 1994; Shah et al., 2019), echo-state network (ESN) (Jaeger and Haas, 2004), and time-delay NN (TDNN) (Waibel et al., 1989). RNNs have feedback connections that are capable of processing neural signal sequences. Their feedback loop is applicable to system dynamics modeling and time-dependent functional mapping between neural activity and kinematic parameters (Haykin, 1994). ESN was developed as an RNN that only trains connections between the hidden neurons and the output neurons for a simple learning process (Jaeger and Haas, 2004). TDNNs are feedforward NNs with delayed versions of inputs that implement a short-term memory mechanism (Waibel et al., 1989). Of these NNs, RNNs are highly accurate in BMI applications (Sanchez et al., 2004, 2005; Sussillo et al., 2012; Kifouche et al., 2014; Shah et al., 2019). Therefore, the present work designed an RNN with error feedback as the neural decoder.

Because the performance of an NN relied heavily on its network structure, structure selection is a crucial concern. An NN with an excessively large architecture may overfit the training data and yield poor generalization. Furthermore, it often exhibited rigid timing constraints. By contrast, an NN with an excessively small architecture may underfit the data and fail to approximate the underlying function. The four most frequently used algorithms to determine a network's architecture are constructive, pruning, constructive-pruning, and evolutionary algorithms (EAs). Constructive algorithms (Kwok and Yeung, 1997) began with a simple NN and then increased the number of hidden neurons or connections to that network in each iteration. However, an oversized network may be constructed due to inappropriate stopping criterion. In other words, the matter of when to stop constructing networks lacked consensus. The pruning algorithm (Reed, 1993) began with an oversized NN and then removed insignificant hidden neurons or connections iteratively. However, it was difficult to initially determine an oversized network architecture for a given problem (Kwok and Yeung, 1997). The constructive-pruning algorithm (Islam et al., 2009; Yang and Chen, 2012) combined both a constructive algorithm and pruning algorithm to build an NN. Starting with the simplest possible structures, the NN was first constructed using a constructive algorithm and then removed trivial hidden neurons or connections by using a pruning algorithm to achieve optimal network architecture. Several works have designed NNs using EAs (Huang and Du, 2008; Kaylani et al., 2009; Masutti and de Castro, 2009). EAs were developed as a biologically plausible strategy to adapt various parameters of NNs, such as weights and architectures (Angeline et al., 1994). However, encoding an NN into a chromosome depended on the maximum structure of the network, which is problem-dependent and must be defined by user. This property limited the flexibility of problem representation and the efficiency of EAs. One study (Yang and Chen, 2012) proposed an evolutionary constructive and pruning algorithm (ECPA) without predefining the maximum structure of the network, which made the evolution of the network structure more efficient. Because the NNs used in BMIs were designed in a subject-dependent manner, the automatic optimization of the NN for a specific task is a desired feature. This study adopted the ECPA (Yang and Chen, 2012) to develop an NN with an appropriate structure as a neural decoder for each subject in BMI applications.

This work proposed an evolutionary constructive and pruning neural network with error feedback (ECPNN-EF) to decode

neural activity into the forelimb movement of a rat by using only a few days of data to train the neural decoder. A lever-pressing task for the rat was designed to evaluate the effectiveness of the proposed neural decoder. The error feedback providing the difference between the decoded and actual kinematics might compensate for decreases in decoding performance when the neural recording conditions change. Thus, the ECPNN-EF might achieve stable and accurate long-term decoding performance. The rest of this paper is organized as follows. First, we describe the experimental setup and the proposed decoder. Second, we demonstrate the influence of several parameters, namely the probabilities of *crossover* and *mutation*. Furthermore, the effects of evolution progress, cluster-based pruning (CBP) and age-based survival selection (ABSS) on the performance of the proposed decoder are also shown and discussed. Finally, we describe how partially connected topology and error feedback improve the long-term decoding performance.

MATERIALS AND METHODS

Animals

Four male adult Wistar rats were aged 8 weeks old, weighed between 250 and 350 g, and were kept in the animal facility with well-controlled laboratory conditions (12: 12 light/dark cycle with light at 7 AM; 20° ± 3°C) and fed on *ad libitum*. The care and experimental manipulation of the animals were reviewed and approved by the Institutional Animal Care and Use Committee of the National Yang Ming University.

Surgery for Neural Implantation

Animals were anesthetized with 40 mg/kg Zolazepam and Tiletamine (Zoletil 50, Virbac., Corros, France) and 8 μg/kg dexmedetomidine hydrochloride (Dexdomitor®, Pfizer Inc., New York, NY, USA) through intramuscular injections. Rats were positioned in a stereotaxic frame (Stoelting Co. Ltd., Wood Dale, IL, USA) and secured with the ear bars and tooth bar. An incision was made between the ears. The skin of the scalp was pulled back to expose the surface of the skull from the bregma to the lambdoid suture. Small burr holes were drilled into the skull for the microwire electrode array implanted and for the positioning of screws (Shoukin Industry Co., Ltd., New Taipei City, Taiwan).

For each rat, an 8-channel laboratory-made stainless microwire electrode array (product # M177390, diameter of 0.002 ft., California Fine Wire Co., Grover Beach, CA, USA; the electrodes were spaced 500 μm apart) was vertically implanted into the layer V of the forelimb territory of the primary motor (M1) cortex (anterior-posterior [AP]: +2.0 mm to −1.0 mm, medial-lateral [ML]: +2.7 mm, dorsal-ventral [DV]: 1.5 mm. For determining the location of the forelimb representation of M1 for the electrode implantation, the intracortical microstimulation was applied to confirm via forelimb muscle twitches observed (Yang et al., 2016). Following a 1-week post-surgery recovery period, the animals received the water reward-related lever-pressing training.

Behavioral Training

The rats were trained to press a lever with their right forelimb to obtain a water reward. Before reward training, the rats were single-housed and deprived of water for at least 8 h. During reward training, the rats were placed in a 30 × 30 × 60 cm^3 laboratory-designed Plexiglas testing box, and a 14 × 14 × 37.5 cm^3 barrier was placed to construct an L-shaped path for the behavioral task. A lever (height of 15 cm from bottom) was set at one end of the path, and an automatic feeder with a water tube that provided water on a plate was set at the other end of the path. The rats could obtain 0.25-ml water drop as a reward on the plate after pressing the lever. Thirsty rats were trained to press a lever in order to receive water reward without any cues because they learned to make an operant response for positive reinforcement (water reward). Rats were trained to press a lever on the left side of the box then freely move along the U-shaped path to the right side of the box. This had to be completed within 3 s to receive a reward. The experimental time course included the behavioral training and data collection phases. In the behavioral training phase, implanted rats learned the lever pressing and water reward association within 3–5 d without neural recordings. To meet criteria for successful learning of the behavioral task, the rats had to complete continuous repetition of five successive trials of associated lever pressing and water reward without missing any trial between successive trials (Lin et al., 2016). Once reaching the criteria, animals entered the data collection phase. During this 12-d phase, forelimb movement trajectories were simultaneously acquired with corresponding electrophysiological recordings of neural spikes as they performed the water reward task.

Data Recording

In this study, forelimb kinematics and neuronal activity were simultaneously recorded while the animal performed the water reward-related lever pressing as shown in **Figure 1**. During the behavioral task, a blue-colored marker made of nylon was mounted on the right wrist of the rat to track forelimb trajectory. The trajectory of the rat's forelimb movement was captured by a charge-coupled device camera (DFK21F04, Imaging Source, Bremen, Germany) that provided a 640 × 480 RGB image at 30 Hz and then analyzed by a video tracking system (CinePlex, Plexon Inc., Dallas, TX, USA). When the lever was pressed, it triggered the micro-switch of the pull position to generate a transistor–transistor logic pulse to the multichannel acquisition processor (Plexon Inc., Dallas, TX, USA) which allowed the neuronal data to be accurately synchronized to the lever pressing event and then water reward was delivered through a computer-controlled solenoid valve connected to the laboratory-designed pressurized water supply.

Neuronal spiking activity of the rat was sampled at 40 kHz and analog filtered from 300 to 5,000 Hz. A spike-sorting algorithm was used to determine single-unit activity. First, an amplitude threshold with four standard deviations of filtered neuronal signals was set to identify spikes from the filtered neuronal

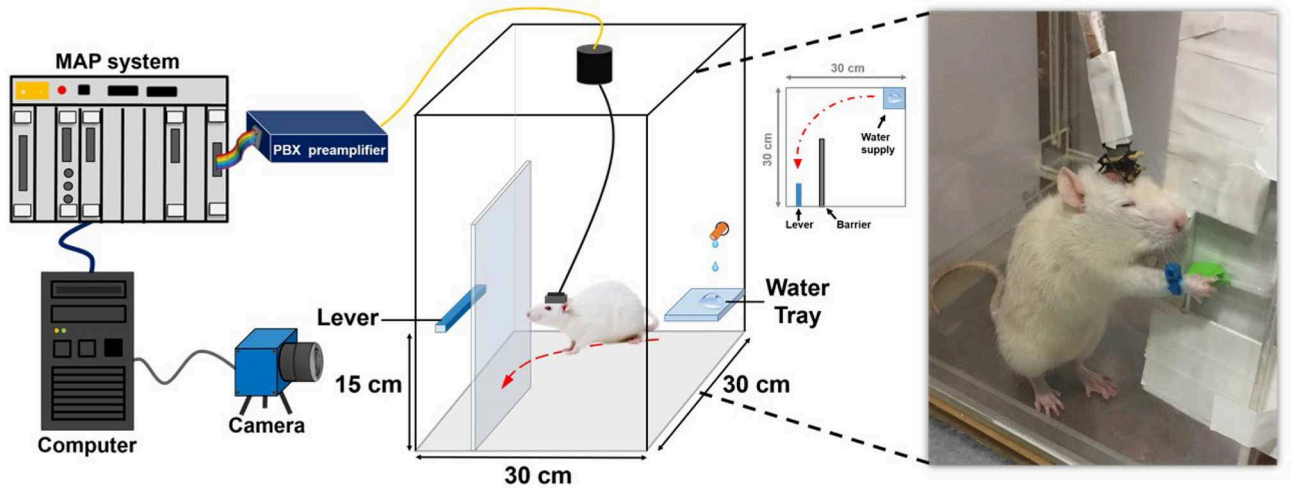

FIGURE 1 | System architecture and experimental setting of the water-reward lever-pressing task. While the rat was pressing the lever to obtain the water reward, the neural recording system recorded and preprocessed the neuronal spiking activity from the electrode array implanted in the rat's cortex. The trajectory-tracking system acquired the corresponding forelimb trajectory from the camera.

signals. Then, spikes were sorted by a trained technician through principal component analysis using a commercial spike-sorting software (Sort Client, Plexon Inc., Dallas, TX, USA).

Neural Decoder: ECPNN-EF

The firing rates of each sorted unit from M1 cortex of rat were decoded into the instantaneous velocity of the forelimb trajectory. Both horizontal and vertical velocities were estimated from the position of the blue-colored marker by a two-point digital differentiation. The firing rates of each sorted neuron was determined by counting spikes in a given time bin whose length was 33 ms and was equal to the temporal resolution of the video tracking system. **Figure 2** showed an example of the rat forelimb movement while pressing the lever and corresponding neural spike trains. A time-lag was known to exist between neuronal firing and the associated forelimb state because of their causal relationship (Paninski et al., 2004; Wu et al., 2004; Yang et al., 2016). Furthermore, the decoding accuracy was improved when the optimal time-lag is considered. Here, the water-restricted rats easily learn a lever pressing behavior within a few training sessions, allowing for recording neuronal activity during acquisition of a motor sequence as shown in **Figures 2A,B** showed some M1 neurons displayed increased activity for sequential motor behavior prior to the lever-pressing event, which presented the maximum firing rate at the third time-bin (with 99 ms lag). Therefore, we empirically choose 363 ms of spike train over 11 time-bins (8 bins before and 2 bins after the 3rd time-bin prior to the lever pressing) to predict a series of movement velocities.

The spike train was discretized in 11 time-bins for each trial, corresponding to each entire trajectory of forelimb movements during the lever reaching task. With total k neurons sorted from all channels, we defined $N(t) = \{n_i(t)\}_{i=1}^{k}$ as a set of neuronal features, where t denoted time step which was time bin in this study, $n_i(t)$ represented as spike count of sorted neuron in current bin, and i denoted index of sorted neuron from 1 to k. In this study, we used both concurrent and preceding bin as neuronal features, which is $N(t)$ and $N(t_{pre})$, to predict current velocity $\hat{v}(t)$, where t and t_{pre} represented current time bin and preceding time bin, respectively. The step of data processing was shown in **Figure 3**.

The ECPNN-EF is an RNN-based neural decoder designed using the ECPA as proposed in Yang and Chen (2012). The input–output function of the ECPNN-EF was denoted by:

$$\hat{v}(t) = f_W\left(N(t), N(t_{pre}), v_{error}\right) \tag{1}$$

where $\hat{v}(t)$ represented the predicted velocity and W represented the weights of the ECPNN-EF. The prediction error v_{error} was adopted as the error feedback which was the absolute value of difference between the actual velocity and predicted velocity, and was calculated by $v_{error} = \left|v(t_{pre}) - \hat{v}(t_{pre})\right|$ where t_{pre} denoted as preceding time bin.

The structure of ECPNN-EF was showed in **Figure 4**. Note that there was only one output neuron representing the predicted velocity in the neural decoder. The vertical and horizontal velocities were predicted in two separate neural decoders.

Mean squared error was adopted as loss function due to its wide use in regression application and was defined as follows:

$$L = \sum_{t}\left(v_t - f_W\left(N(t), N(t_{pre}), v_{error}\right)\right)^2 \tag{2}$$

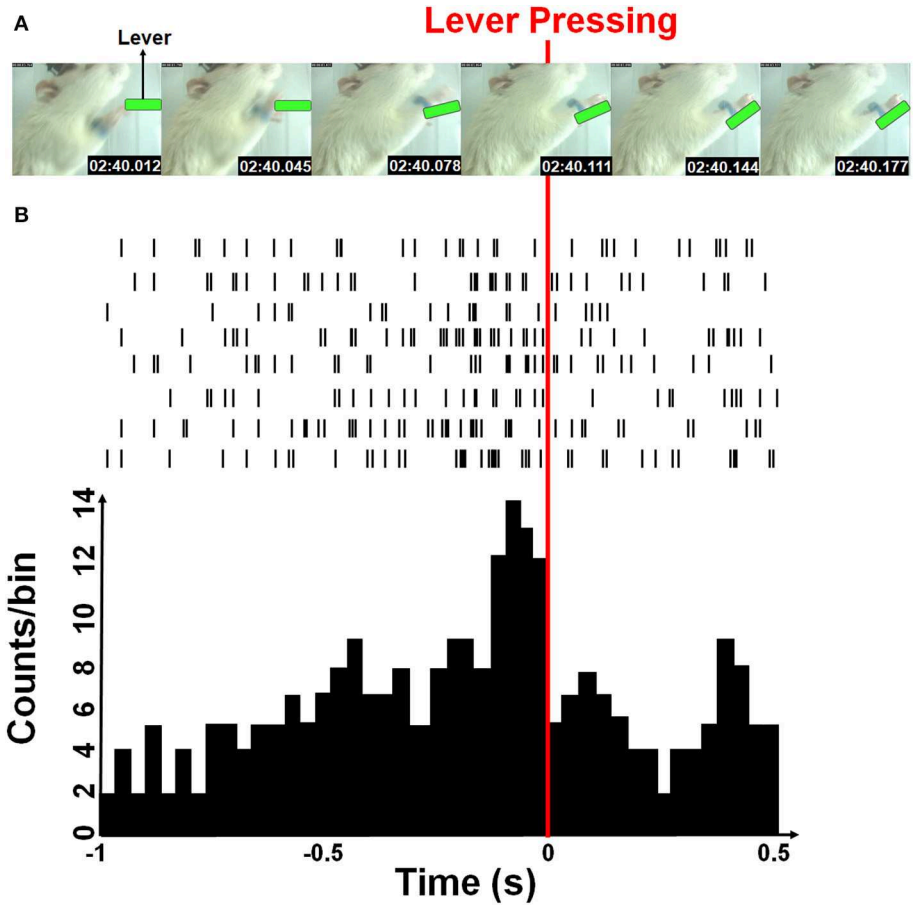

FIGURE 2 | Simultaneous forelimb movement trajectory and spike train recordings during the water-reward-related lever-pressing task. **(A)** Stop-motion animation representing forelimb movement from the video-tracked time-series data (see **Supplemental Video**). Six consecutive photographs showed a rat in the test cage successfully reaching and pressing the lever (marked with green) while the forelimb movement trajectories and neural activity were simultaneously recorded. **(B)** Neuronal activities recorded from eight neurons during one movement displayed as spike trains and the neuronal activity histogram (a bin size of 33 ms). The red line indicates the moment when the rat pressed down the lever with its right forelimb.

The optimal weights of the ECPNN-EF were obtained by minimizing the loss as follows:

$$W^* = \arg\min_W L \tag{3}$$

This study applied backpropagation through time (BPTT) to find the optimal weights of the ECPNN-EF by iteratively determining the gradient of the loss with respect to the weights as follows:

$$W \leftarrow W - \eta \nabla_W L \tag{4}$$

where η is learning rate. Details of the BPTT (Werbos, 1988) are described in the **Supplementary Note 1**. The details of designing structure of the ECPNN-EF are described in the **Supplementary Note 2**.

The ECPNN-EF adopted a hyperbolic tangent sigmoid transfer function for all hidden neurons and the output neuron. Skip connections existed between discontinuous layers, such as from the input layer to the output layer. Furthermore, the hidden layer possessed self-recurrent connections. After both the structure and weights of the ECPNN-EF had been trained, the fixed model was adopted to predict the velocity of the rat's forelimb without the additional cost of training.

The pseudo code of ECPNN-EF training algorithm appears in Algorithm 1. The initial population started with a set of initial NNs, each NN of which had a single hidden neuron. A single connection was generated from one non-error-related input neuron to the hidden neuron. A skip connection was generated from one non-error-related input neuron to the output neuron. A single connection was generated from one error-related input neuron to the hidden neuron or to the output neuron. The detail description of population initialization was in the **Supplementary Note 3**. Furthermore, a self-recurrent connection was constructed in the hidden neuron with a probability of 0.5. Here, the error-related input neuron received the prediction error, as indicated in **Figure 4**, whereas non-error-related input neurons received the instantaneous firing

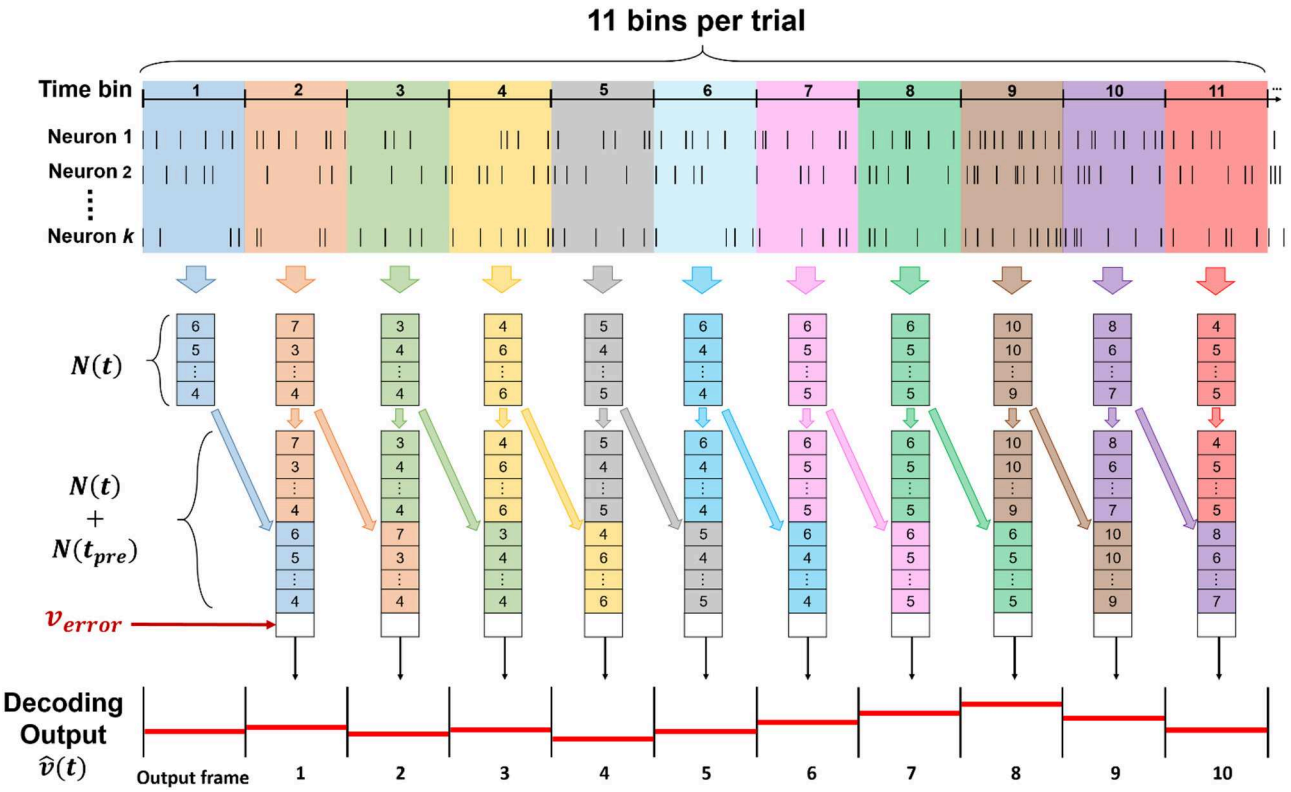

FIGURE 3 | The data structure of input for the ECPNN-EF decoder. The input of the decoder was consisted of (t), $N\left(t_{pre}\right)$ and v_{error}, whose length was $2k + 1$, including $2k$ spike counts of both concurrent and preceding bin, and an error feedback calculated by $\left|v(t_{pre}) - \hat{v}\left(t_{pre}\right)\right|$. To predict a whole forelimb movement in a trial, 11 bins were used and decoded to $\hat{v}(t)$ in the time series.

rate of each unit. This mechanism of separately generating connections of error-related input neuron and non-error-related input neurons ensures that the initial NNs can immediately process error feedback. As a result, a set of initial NNs with partially connected topology was generated.

The purpose of the *network crossover operator* was to explore the structural search space and thus improve the processing capabilities of the ECPNN-EF. The *network crossover operation* randomly selected two parent NNs through tournament selection and then combined their structures to generate an offspring NN with a *crossover probability*, p_c (see **Supplementary Note 4**). The *network mutation operator* exploited the structural search space to achieve a small perturbation of structure by randomly generating a new connection from the input to the hidden neuron. Furthermore, the *network mutation operation* randomly constructed a self-recurrent connection of a hidden neuron or a new skip connection from the output or the hidden neuron to its previous consecutive or non-consecutive layer with a *mutation probability*, p_m (see **Supplementary Note 5**).

CBP mainly pruned insignificant hidden neurons to avoid an excessively complex ECPNN-EF with poor generalization performance owing to the use of *network crossover operation*. It first clustered the hidden neurons into two groups (i.e., better and worse groups, depending on their significance in the NN) and then removed the hidden neurons in the worse group in a stochastic manner. The detailed description of CBP was in the **Supplementary Note 6**.

ABSS prevented the ECPNN-EF from achieving a fully connected structure. It selected NNs for the next generation according to age, which indicated how many generations the NN had survived. Older NNs tended to have a fully connected structure because of the use of *network mutation operation*. ABSS replaced old age NNs with initial NNs (see **Supplementary Note 3**) in a stochastic manner and thus prevented the population from achieving a fully connected structure. ABSS mainly removed fully connected networks and made the rest of the NNs survive to the next generation through a stochastic mechanism. The detailed description of ABSS was in the **Supplementary Note 7**. The evolution process terminated when a generalization loss (GL) met an early stopping criterion or the maximum number of generations was reached. The early stopping criterion motivated from Islam et al. (2009) evaluated the evolution progress using training and validation errors in order to avoid overfitting. It first defined the GL at the τth generation as:

$$GL\left(\tau\right) = \frac{E_{va}(\tau)}{E_{low}(\tau)} - 1 \tag{5}$$

where $E_{va}(\tau)$ is a validation error of the NN with the best fitness at the τth generation and $E_{low}(\tau)$ is the lowest $E_{va}(\tau)$ up to the τth generation. The difference between the average training error and the minimum training error at the τth generation of a strip k was defined as:

$$P_k(\tau) = \frac{\sum_{\omega=\tau-k+1}^{\tau} E_{tr}(\omega)}{k \times \min_{\omega=\tau-k+1}^{\tau} E_{tr}(\omega)} - 1 \quad (6)$$

where $E_{tr}(\omega)$ is the training error of the NN with the best fitness at the ωth generation and k is the strip length. k was set to 5 in this work. Note that $GL(\tau)$ and $P_k(\tau)$ were determined using the validation and training sets, respectively. $E_{va}(\tau)$ and $E_{tr}(\omega)$ were calculated by the loss function provided in **(2)**. The ECPNN-EF training algorithm terminated when $GL(\tau) > P_k(\tau)$. The optimal NN with a partially connected topology was selected as the neural decoder.

In summary, *network crossover* and *mutation* evolved NNs in a constructive manner to improve their processing ability, whereas CBP and ABSS evolved NNs in a destructive way that enhanced their generalization capabilities and reduced hardware costs (Yang and Chen, 2012). An early stopping criterion was adopted to terminate the evolution process by observing both training and validation errors to avoid overfitting during training phase, which reduced the training time and retained generalization capability (Islam et al., 2009). The ECPNN-EF was implemented and trained in MATLAB (MathWorks, Natick, MA, USA).

Data Sets and Optimizing the Structure of Neural Networks

Data collected in a recording session were divided into a training set for developing the neural decoder, a validation set for avoiding overfitting during training phase, and a testing set for evaluating the generalization ability of the neural decoder. For each rat, the experimental trials of the first 2 days were used as training and validation sets, and the remaining 10 days were used as testing set. The number of trials used for each rat was shown in **Table 1.**

The present study evaluated the prediction accuracy (decoding performance) of the proposed neural decoder using Pearson's correlation coefficient (***r***), which measured

TABLE 1 | Experimental data characteristics.

Animal no.	Number of trials for training in day 1 and day 2	Number of trials for testing per day	Number of neurons used per trial
Rat #11	70	24	8
Rat #14	80	33	12
Rat #16	140	41	8
Rat #17	95	36	8

Experimental data recorded from four rats were used in this study. The decoder of each rat was trained and tested only by its own experimental trials. The experimental data of the first 2 days and subsequent 10 days were used for training and testing, respectively. The criteria for selecting neurons into neural decoder as the input were described in the ***Supplementary Note 8****.*

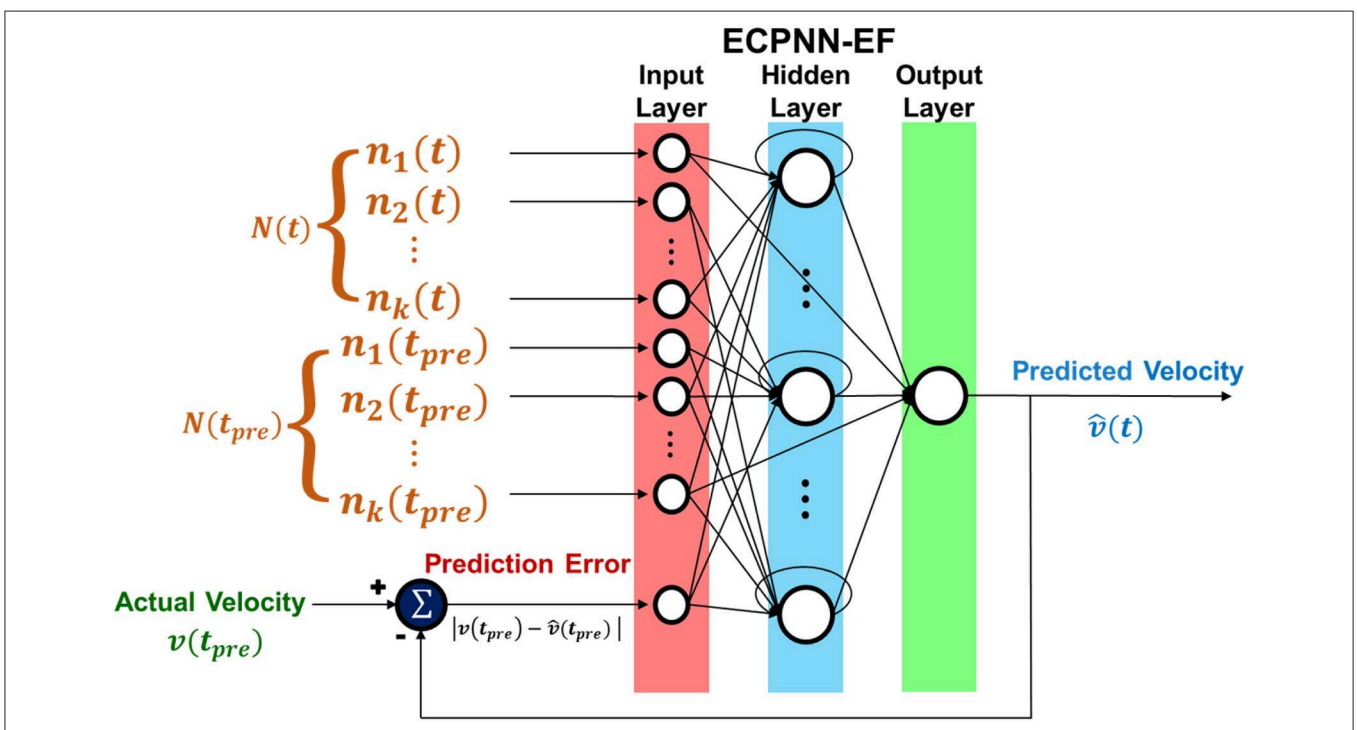

FIGURE 4 | Structure of ECPNN-EF. Network included input, hidden, and output layer. ECPNN-EF took the neuronal feature from combination of concurrent bin $N(t)$, preceding bin $N(t_{pre})$ and prediction error (error feedback) v_{error} to predict velocity $\hat{v}(t)$.

the strength of a linear relationship between the observed and predicted forelimb trajectories (Manohar et al., 2012; Shimoda et al., 2012). When evolving ECPNN-EF with good generalization ability and compact structure, a 5-fold cross validation was adopted to determine the optimal p_c, p_m and terminated generation. For each given pair of p_c and p_m, the experimental trials of the first 2 days were randomly partitioned into five equal-sized disjoint sets where four sets were used as the training set to evolve ECPNN-EF and one set was used as the validation set to evaluate the decoding performance of the evolved ECPNN-EF during training phase. Once the ECPNN-EF was evolved through the optimal p_c and p_m, the validation set also was used to determine the best terminated generation of the evolved ECPNN-EF.

To investigate the effects of CBP and ABSS on the ECPNN-EF evolution, two variants of ECPNN-EF that only adopted either CBP or ABSS were implemented. One variant of ECPNN-EF only with CBP was referred to as ECPNN-EFWC, and the other variant of ECPNN-EF only with ABSS was referred to as ECPNN-EFWA. The decoding performances of ECPNN-EF, ECPNN-EFWC, and ECPNN-EFWA were compared using the validation set in terms of $\boldsymbol{r}$, number of hidden neurons (N_h), number of connections (N_c), connection ratio (R_c), and termination generation (G_T). The R_c was defined as follows:

$$R_c = \frac{N_c}{N_f} \tag{7}$$

where N_f is the number of connections in a network with a fully connected topology. The network had fully connected topology when $R_c = 1$; however, the network had partially connected topology when $R_c < 1$.

Statistical Analysis

In this study, we investigated the decoding performance dependency on the parameters of p_c and $p_m$by employing the statistical method, two-way analysis of variance (ANOVA) followed by Tukey's *post-hoc* test and adjusted the *P*-value by multiple comparison using Bonferroni correction, on the validation set. We set p_c at 7 levels (0.6, 0.65, 0.7, 0.75, 0.8, 0.85, and 0.9). In addition, 7 levels of p_m (0.6, 0.65, 0.7, 0.75, 0.8, 0.85, and 0.9) were employed for each p_c to determine whether the algorithm found the near-optimum solution. This evaluated whether there were any significant differences in decoding performance according to the parameters used. Additionally, we analyzed the effects of CBP and ABSS on the ECPNN-EF reconfiguration, and then assessed the decoding performance comparison of ECPNN-EF, ECPNN-EFWC, and ECPNN-EFWA on the validation set by one-way ANOVA with *post-hoc* Tukey's HSD test.

In order to investigate the decoding performance and stability of ECPNN-EF as well as impact of the prediction error feedback on enhancing the prediction accuracy of ECPNN-EF without error-correction learning (ECPNN), a mixed model ANOVA with three decoders [ECPNN-EF, a fully connected RNN with error feedback (RNN-EF), and ECPNN] as fixed factors and the repeated measure of daily testing set over 10 testing days followed by Tukey's *post-hoc* test and then adjusted the *P*-value by Bonferroni multiple comparison correction. The decoding performances of the four rats were presented as means ± standard deviation (SD). The data analysis was performed in SPSS version 20.0 (SPSS Inc., Chicago, IL, USA).

RESULTS

On the Decoding Performance of Different Crossover and Mutation Probabilities

The decoding performances of the ECPNN-EF evolved under different p_c and p_m values were evaluated by the validation set as shown in **Figure 5**. The results demonstrated that the more increasing in p_c and p_m and the worse decoding accuracy ($\boldsymbol{r}$). A simple main effects analysis which examined the effects of 7 levels of p_m at the fixed level of $p_c = 0.75$ and 0.8 was provided in the **Supplementary Note 9**. The best decoding performance ($\boldsymbol{r} = 0.912 \pm 0.019$) was achieved using $p_c = 0.75$ and $p_m = 0.75$ (compared to other combinations of p_c and p_m, $P < 0.05$ analyzed by ANOVA for multiple comparisons).

Evolution Progress of ECPNN-EF

Figure 6 presented the evolution progress of the ECPNN-EF using the optimal *probabilities* of *crossover* and *mutation* ($p_c = 0.75$ and $p_m = 0.75$) obtained in **Figure 5**. The results showed that the *GL* and the difference between the average training error and minimum training error (P_k) were almost zero in the early generations. Afterward, the *GL* slightly increased but the P_k varied. Notably, the *GL* was not consistently larger than the P_k. Most *GL*s dramatically increased and were larger than the P_k after the 33th generation marked by a black vertical dashed line. This potentially indicated the overfitting problem that

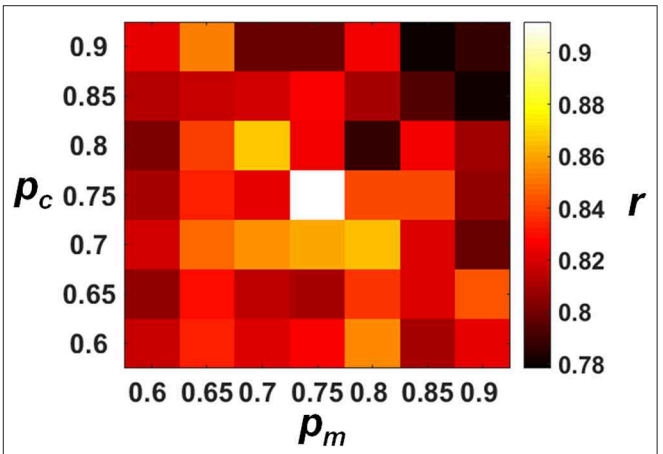

FIGURE 5 | Decoding performance of the ECPNN-EF under various p_c and p_m. We performed the *post-hoc* analysis based on the estimated marginal means of correlation coefficient ($\boldsymbol{r}$) and adjusted the *P*-value by multiple comparison using Bonferroni correction (see the **Table S2** in the **Supplementary Note 8**). We found that the highest $\boldsymbol{r}$ was observed when the p_m= 0.75 and the $p_c = 0.75$ ($\boldsymbol{r} = 0.912 \pm 0.019$) and showed significant differences in $\boldsymbol{r}$ of $p_c = 0.8$ and $p_m = 0.75$. Therefore, the near-optimum solution of the algorithm was p_c= 0.75 and $p_m = 0.75$.

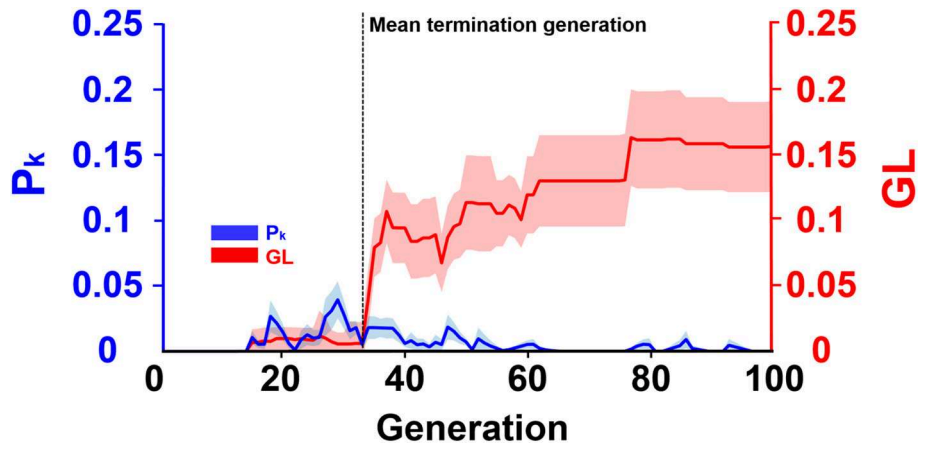

FIGURE 6 | Evolution progress of the ECPNN-EF. The shaded regions represented SD. The vertical axis on the left represented P_k (blue line). The vertical axis on the right represented *GL* (red line). Most *GL*s met the early stopping criterion in the mean terminated generation ($G_T = 33.2 \pm 1.1$) indicated by a black vertical dashed line.

might lead to worse evolutions. Therefore, the ECPNN-EF was suggested to terminate evolution in this generation according to an early stopping criterion in order to maintain stable decoding performance. The mean termination generation was 33 in this study ($G_T = 33.2 \pm 1.1$).

Effects of CBP and ABSS on Decoding Performance

Table 2 showed the decoding performance of the ECPNN-EF, ECPNN-EFWC, and ECPNN-EFWA. ECPNN-EF achieved significantly higher decoding performance ($\boldsymbol{r} = 0.912 \pm 0.019$) than did the ECPNN-EFWC ($\boldsymbol{r} = 0.602 \pm 0.083$) and ECPNN-EFWA ($\boldsymbol{r} = 0.708 \pm 0.066$) ($P < 0.05$ analyzed by one-way ANOVA with *post-hoc* Tukey's HSD test). The ECPNN-EF possessed a more compact structure ($N_h = 4.2 \pm 2.7$ and $N_c = 20.6 \pm 7.2$) than both ECPNN-EFWC ($N_h = 4.6 \pm 3.8$ and $N_c = 23.0 \pm 10.1$) and ECPNN-EFWA ($N_h = 14.4 \pm 14.4$ and $N_c = 57.9 \pm 52.1$). Moreover, the ECPNN-EFWA had a greater standard deviation than the other two methods. All three methods possessed almost the same R_c. The ECPNN-EF ($R_c = 0.12 \pm 0.02$) and ECPNN-EFWA ($R_c = 0.12 \pm 0.01$) produced slightly more sparse structures than ECPNN-EFWC ($R_c = 0.13 \pm 0.01$). All three methods terminated the evolution before 38th generation. The ECPNN-EF terminated slightly earlier ($G_T = 33.2 \pm 1.1$) than did the other two decoders.

Decoding Performance Comparison

We applied a mixed model ANOVA with three decoders (ECPNN-EF, RNN-EF, and ECPNN) as fixed factors and the repeated measure of time, then adjusted the *P*-value by multiple comparison using Bonferroni correction. The three decoders reconstructed movement trajectories similar to the actual movement trajectories (**Figure 7**). However, the ECPNN-EF decoder showed the best reconstruction and stability and was significantly better than the ECPNN and RNN-EF decoders over 10 test days.

To investigate the effectiveness of the partially connected topology of ECPNN-EF, the ECPNN-EF was compared with RNN-EF using the *post-hoc* analysis. Here, the number of hidden neurons of the RNN-EF was the same as that in the ECPNN-EF for fair comparison [the weights were adjusted by the BPTT] (Werbos, 1988). **Figure 8** statistically showed the daily $\boldsymbol{r}$ comparison between the decoders of ECPNN-EF and RNN-EF. The mean $\boldsymbol{r}$ of the decoder of RNN-EF monotonically decreased with gradually increasing in the variability of $\boldsymbol{r}$ over 10 test days. The result showed that the RNN-EF could not offer a stable long-term decoding performance. By contrast, the decoding performance of the ECPNN-EF decreased slightly in each day and achieved $\boldsymbol{r} = 0.740 \pm 0.042$ at Test Day 10. Moreover, the variation in neural decoding performance (SD) of the ECPNN-EF was smaller than that of the RNN-EF in each day. The decoding performance of the ECPNN-EF was significantly higher than that of RNN-EF ($P < 0.05$ analyzed by repeated measures analysis using mixed model ANOVA with *post-hoc* test, $N = 4$) in each day.

To investigate the effect of the error-correction learning (error feedback) in the decoder, the ECPNN-EF was compared with ECPNN using the *post-hoc* test. As depicted in **Figure 8**, the ECPNN-EF decoder performed higher and more stable accuracy of predicted trajectories in comparison with those of the ECPNN decoder over 10 test days. The mean $\boldsymbol{r}$ of the decoder of ECPNN dropped noticeably and the corresponding variability of $\boldsymbol{r}$ became huge after Test Day 5. By contrast, the ECPNN-EF's daily $\boldsymbol{r}$ slowly decreased, and the daily variability of $\boldsymbol{r}$ did not considerably change over 10 days. The ECPNN-EF's $\boldsymbol{r}$ was significantly higher than that of the ECPNN in each day ($P < 0.05$ analyzed by repeated measures analysis using mixed model ANOVA with *post-hoc* test, $N = 4$), and the corresponding variation (SD) in daily $\boldsymbol{r}$ of the ECPNN-EF was smaller than that of the ECPNN. The lowest $\boldsymbol{r}$ of the ECPNN-EF ($\boldsymbol{r} = 0.740 \pm 0.042$) and ECPNN ($\boldsymbol{r} = 0.413 \pm 0.158$) was observed at Test Day 10.

TABLE 2 | Evolutionary results of ECPNN-EF, ECPNN-EFWC, and ECPNN-EFWA.

Decoder	R	N_h	N_c	R_c	G_T
ECPNN-EF	0.912 ± 0.019*	4.2 ± 2.7	20.6 ± 7.2	0.12 ± 0.02	33.2 ± 1.1
ECPNN-EFWC	0.602 ± 0.083	4.6 ± 3.8	23.0 ± 10.1	0.13 ± 0.01	37.5 ± 7.9
ECPNN-EFWA	0.708 ± 0.066	14.4 ± 14.4*	57.9 ± 52.1*	0.12 ± 0.01	37.3 ± 3.5

*The symbol * indicated statistical significance among the three decoders ($P < 0.05$ analyzed by one-way ANOVA with post-hoc Tukey's HSD test).*

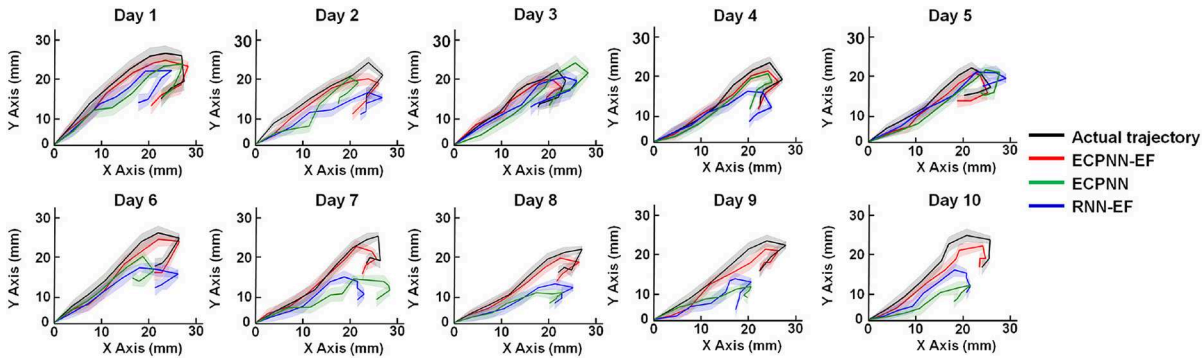

FIGURE 7 | Data visualization of average predicted trajectories of the ECPNN-EF, ECPNN, and RNN-EF. Representative daily reconstructed trajectories of the test trials in Rat #16. The average reconstructed trajectories of the ECPNN-EF (red line) were more similar to the actual ones (black line) and exhibited less variance than did those of the ECPNN (green line) and RNN-EF (blue line) over 10 test days, where shadow regions represented their corresponding SDs of the predicted trajectories.

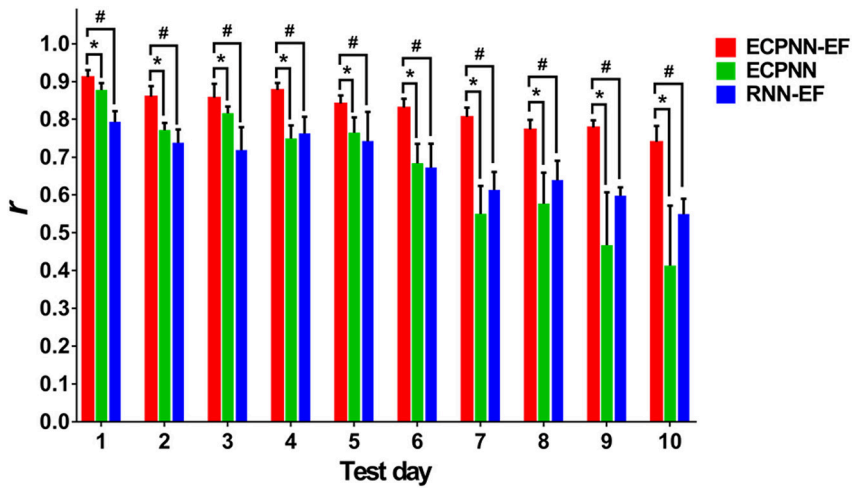

FIGURE 8 | Comparison of daily *r* of the ECPNN-EF, ECPNN, and RNN-EF. The decoding performance of ECPNN-EF at the 1st, 2nd, 3rd, 4th, 5th, 6th, 7th, 8th, 9th, and 10th. Test Day was significantly higher than those of ECPNN and RNN-EF (also see the *post-hoc* analysis of the comparison of decoding performance in the **Table S3** in the **Supplementary Note 10**), and the corresponding variation of ***r*** was smaller than that of the ECPNN and RNN-EF after Test Day 4. The symbols * and # indicate $P < 0.05$, as analyzed by the repeated measures analysis using mixed model ANOVA with Bonferroni correction for multiple testing.

DISCUSSION

Best Performance With NN Structure Determined by Near Optimal Probabilities of Crossover and Mutation

The p_c and p_m affected the evolution of the network structure and thus involved neuronal contributions to forelimb movement. Both *crossover* and *mutation operators* increased the model complexity. The *crossover* provided a chance to add hidden neurons while the *mutation* achieved a small perturbation of model structure by adding connections. Previous paper Schwartz et al. (1988) has reported that individual neuron in the motor cortex discharges with movements in its preferred direction. A high p_c led to large network structure which possessed sufficient

information processing capability but might result in overfitting. On the contrary, a low p_c led to simple network structure which might result in underfitting. A high p_m allowed the hidden neurons to have more connections from the neuronal inputs which led to fully connected topology. Increasing p_c and p_m may not consistently improve the decoding performance of the evolved neural decoder. Increasing p_c and p_m from 0.6 to 0.75 enlarged the computational complexity of the neural decoder so that relevant neuronal inputs could be accurately decoded into forelimb movement. However, frequent *crossover* or *mutation* (high p_c and p_m, respectively) in the 0.8–0.9 range may introduce redundant connections from irrelevant neurons with firing rates that did not contribute to the kinematic parameters. Conversely, a low p_m allowed the hidden neurons to have few connections, resulting in sparse topology. However, some neuronal inputs had a lower likelihood of being processed. Low p_c and p_m may reproduce a topology that is too sparse to build connections between kinematic parameters and relevant neurons, resulting in less accurate neural decoding. Our experimental results showed that $p_c = 0.75$ and $p_m = 0.75$ could achieve the best decoding performance. The evolved ECPNN-EF possessed not only sufficient hidden neurons to decode neuronal activities, but appropriate topology which selected forelimb movement related inputs to the hidden neurons.

Early Stopping to Counteract Overfitting in Evolutionary Progress of ECPNN-EF

Most evolutions of the ECPNN-EF terminated around the mean termination generation because the early stopping criterion was met. The early stopping criterion employed both training and validation errors. In the early generations, the *GL* was almost zero, which indicated that the validation error was almost the same with the lowest validation error among the recent generations. This indicates that the validation error did not increase. Although the functional mapping between neural activity and kinematic parameters varied across days due to variability in the neural recording conditions, the training set may have similar neural recording conditions as the validation set. The ECPNN-EF learned the common functional mapping of the training and validation sets in the early generations, allowing for its evolved sparse topology to gradually learn to decode common firing patterns into forelimb movements in the validation set. Furthermore, the P_k was almost zero, which indicated that the average training error was not larger than the minimum training error among the recent generations. This demonstrated that the training error gradually decreased. Both the *GL* and P_k indicated that the evolution improved the generalization ability of the ECPNN-EF in the early generations. Before the mean termination generation, the slight increase of the *GL* might indicate overfitting, but the *GL* was not always higher than the P_k. This implied that the generalization ability of the ECPNN-EF had a chance to be repaired by the evolution as illustrated in Prechelt (1998), Sussillo et al. (2016). Most *GL*s dramatically increased and were consistently higher than the P_k after the mean termination generation. This demonstrated that the validation error increased, indicating overfitting. Previous work (Kao et al., 2015) has suggested that a neural decoder with too many parameters may result in overfitting. The evolution tended to construct a more complex neural decoder with several weights, potentially contributing to overfitting in the later generations. Therefore, the evolution terminated to prevent decreased generalization ability from overfitting the training set and to save computational time.

Best Performance Based on NN With Good Generalization Ability and Compact Structure

The fact that the ECPNN-EF significantly outperformed the ECPNN-EFWC and ECPNN-EFWA in terms of $\boldsymbol{r}$ suggested that both CBP and ABSS were essential to evolve the neural decoder with generalization ability. The CBP pruned insignificant hidden neurons and led to lower N_h and N_c in ECPNN-EF and ECPNN-EFWC. This mechanism made the network more compact and prevented the network from excessively complex structure caused by the network crossover through many generations. On the other hand, the ECPNN-EFWC's R_c was expected to be considerably larger than those of ECPNN-EF and ECPNN-EFWA because the ABSS tended to select network with sparsely connected topology. However, the difference of R_c among the ECPNN-EF, ECPNN-EFWC, and ECPNN-EFWA was not significant because of the effect of early stopping. All the three approaches stopped evolution before 38 generations. The networks in the population underwent only few *crossovers* and *mutations*, and thus their network structures were less complex. Nevertheless, the poor $\boldsymbol{r}$ in the ECPNN-EFWC suggested that although early stopping led to lower R_c, the evolution without ABSS would evolve a neural decoder with poor generalization ability. ABSS selected networks without redundant connections into next generation and thus prevented the network from fully connected topology caused by the network mutation. Excessively complex neural decoders may include redundant hidden neurons that overfit the training set. This can disrupt accurate decoding of neural activity in the testing set, which may have different neural recording conditions from the training set. Furthermore, redundant weights may connect to neurons with preferred directions that are irrelevant to vertical or horizontal velocities.

The ECPNN-EF terminated and obtained near-optimum neural decoder earlier than the ECPNN-EFWC and ECPNN-EFWA. The validation error in these three models increased after their termination generation. This resulted in overfitting because their evolved structures were more complex than the near-optimum neural decoders. Evolution of the ECPNN-EF was more efficient than the ECPNN-EFWC and ECPNN-EFWA, indicating that it obtained near-optimum neural decoder faster than its reduced models. Thus, ECPNN-EF's termination generation was earlier than its reduced models. These results indicate that CBP and ABSS helped evolve a neural decoder with less complex structure and better generalization ability. Power efficiency and power management are extremely important concerns for fully implantable neural decoders in BMIs. Due to its sparse topology, ECPNN-EF offers a practical approach to computationally efficient neural decoding by reducing the

number of hidden neurons and interlayer connections, resulting in less memory usage and power consumption (Chen et al., 2015). Less power consumption results in a longer battery lifetime, which could facilitate brain implantation of neural decoders (Sarpeshkar et al., 2008).

Best Performance Based on Appropriate Connected Topology-Based Network

Several studies have shown that a partially connected NN (PCNN) achieves better performance than does a fully connected neural network (FCNN) (Elizondo and Fiesler, 1997). The ECPNN-EF, a type of PCNN, achieved significantly higher daily mean r than does the RNN-EF, which is a type of FCNN; this suggests that an FCNN might consist of a large amount of redundant connections and lead to overfitting with poor generalization when compared to a PCNN (Elizondo and Fiesler, 1997; Wong et al., 2010; Guo et al., 2012). Some information, which was irrelevant to the forelimb movement and was processed by the redundant connections, may hamper the performance of the neural decoder and increase the likelihood of NNs being stuck in local minima. Furthermore, the variation in decoding performance of the RNN-EF from Test Day 3 to Test Day 10 was larger than that for Test Day 1 and Test Day 2, whereas the variation in decoding performance of the ECPNN-EF did not change dramatically. This suggested that the redundant weights in the RNN-EF could not deal with the variation of the neural recording conditions and thus led to unstable decoding performance. The ECPNN-EF outperformed the RNN-EF due to the use of the partially connected topology. The trends observed in the present study followed the suggestion that the number of connections is not the key aspect of an NN but rather of an appropriate connected topology (Yang and Chen, 2012).

Comparing Linear Neural Decoder-Based Error-Correction Learning

Our prior work demonstrated a linear decoding model of the relationship between neural firing and kinematic parameters (Yang et al., 2016). A sliced inverse regression (SIR) with error-feedback learning (SIR-EF) was implemented based on an SIR linear neural decoder to fairly compare to the ECPNN-EF algorithm (see **Supplementary Note 11**). Because the ECPNN-EF had to process changing neural recording conditions over time, it possessed more processing capabilities than the linear model. The SIR-EF could not deal with long-term variability in neural recording conditions because of linear properties and limited computational complexity. The SIR-EF assigned weights to the slices with neurons that had a similar contribution to the lever-pressing forelimb movement. However, variations in neural recording conditions due to the tissue's reaction to neural implants or micromotion of the electrodes across days resulted in firing pattern variations (Barrese et al., 2013; Sussillo et al., 2016). Thus, the decoding performance decreased because the weights calculated using the training data over the first 2 days could not predict velocity in the subsequent testing days with different neural conditions.

NN-Based Error-Correction Learning to Improve Long-Term Decoding Stability

It has been revealed that the functional mapping between instantaneous firing rate and kinematic parameters might vary in chronic recording due to the changes of neural recording conditions (Sussillo et al., 2016). A relative increase in ECPNN's mean r at Test Day 3 and Test Day 5 might exhibit that the recording conditions probably had some commonality with those in the training phase. Therefore, the non-linear model of ECPNN, which learned the time-dependent functional mapping from the training set, could accurately decode the instantaneous firing rate into kinematic parameters. The error feedback played a subsidiary role of the neural decoding in this situation. A considerable decrease in ECPNN's mean r after Test Day 5 might indicate that the neural recording conditions were different from those in the training phase. The learned functional mapping between instantaneous firing rate and kinematic parameters was of no use for making ECPNN's long-term decoding performance stable.

In contrast, when the neural recording conditions changed after Test Day 5, ECPNN-EF′ error feedback provided immediate kinematic information and thus compensated for across-day changes in functional mapping between instantaneous firing rate and kinematic parameters. The ECPNN-EF could achieve not only more robust within-day decoding (smaller SD) but also more robust across-day decoding (smaller fluctuations in daily mean r) than those of the ECPNN. This demonstrated that employing error feedback in the ECPNN-EF improved the long-term decoding stability when only a few days of training data were available.

DATA AVAILABILITY STATEMENT

The datasets generated for this study are available on request to the corresponding author.

ETHICS STATEMENT

The animal study was reviewed and approved by the Institutional Animal Care and Use Committee of the Taipei Medical University.

AUTHOR CONTRIBUTIONS

S-HY, C-HK, and Y-YC designed the project, organized the entire research. Y-CL, H-YL, and S-HL conceived the experiments. CC, J-WH, H-LW, C-FW, and C-CK conducted the experiments. CC, S-HY, Y-CL, H-LW, K-YC, and C-FW implemented code from software designed and planned. CC, S-HL, J-WH, H-YL, and Y-HL analyzed the results. S-HY, CC, and Y-YC wrote the manuscript. All authors discussed the results and reviewed on the manuscript.

FUNDING

This work was financially supported by Ministry of Science and Technology of Taiwan under Contract numbers of

MOST 109-2636-E-006-010 (Young Scholar Fellowship Program), 108-2321-B-010-008-MY2, 108-2314-B-303-010, 108-2636-E-006-010, 107-2221-E-010-021-MY2, and 107-2221-E-010-011. We also are grateful for support from the Headquarters of University Advancement at the National Cheng Kung University, which is sponsored by the Ministry of Education, Taiwan.

SUPPLEMENTARY MATERIAL

The Supplementary Material for this article can be found online at: https://www.frontiersin.org/articles/10.3389/fncom.2020.00022/full#supplementary-material

Supplemental Video | The supplemental video showed forelimb reaching for lever pressing and simultaneous neural recording in M1.

REFERENCES

Angeline, P. J., Saunders, G. M., and Pollack, J. B. (1994). An evolutionary algorithm that constructs recurrent neural networks. *IEEE Transact. Neural Netw.* 5, 54–65. doi: 10.1109/72.265960

Barrese, J. C., Rao, N., Paroo, K., Triebwasser, C., Vargas-Irwin, C., Franquemont, L., et al. (2013). Failure mode analysis of silicon-based intracortical microelectrode arrays in non-human primates. *J. Neural Eng.* 10:066014. doi: 10.1088/1741-2560/10/6/066014

Bishop, W., Chestek, C. C., Gilja, V., Nuyujukian, P., Foster, J. D., Ryu, S. I., et al. (2014). Self-recalibrating classifiers for intracortical brain–computer interfaces. *J. Neural Eng.* 11:026001. doi: 10.1088/1741-2560/11/2/026001

Chen, Y., Yao, E., and Basu, A. (2015). A 128-channel extreme learning machine-based neural decoder for brain machine interfaces. *IEEE Transact. Biomed. Circuits Syst.* 10, 679–692. doi: 10.1109/TBCAS.2015.2483618

Chen, Y.-Y., Lai, H.-Y., Lin, S.-H., Cho, C.-W., Chao, W.-H., Liao, C.-H., et al. (2009). Design and fabrication of a polyimide-based microelectrode array: Application in neural recording and repeatable electrolytic lesion in rat brain. *J. Neurosci. Methods* 182, 6–16. doi: 10.1016/j.jneumeth.2009.05.010

Chestek, C. A., Gilja, V., Nuyujukian, P., Foster, J. D., Fan, J. M., Kaufman, M. T., et al. (2011). Long-term stability of neural prosthetic control signals from silicon cortical arrays in rhesus macaque motor cortex. *J. Neural Eng.* 8:045005. doi: 10.1088/1741-2560/8/4/045005

Collinger, J. L., Wodlinger, B., Downey, J. E., Wang, W., Tyler-Kabara, E. C., Weber, D. J., et al. (2013). High-performance neuroprosthetic control by an individual with tetraplegia. *Lancet* 381, 557–564. doi: 10.1016/S0140-6736(12)61816-9

Connor, J. T., Martin, R. D., and Atlas, L. E. (1994). Recurrent neural networks and robust time series prediction. *IEEE Transact. Neural Netw.* 5, 240–254. doi: 10.1109/72.279188

Downey, J. E., Schwed, N., Chase, S. M., Schwartz, A. B., and Collinger, J. L. (2018). Intracortical recording stability in human brain–computer interface users. *J. Neural Eng.* 15:046016. doi: 10.1088/1741-2552/aab7a0

Elizondo, D., and Fiesler, E. (1997). A survey of partially connected neural networks. *Int. J. Neural Syst.* 8, 535–558. doi: 10.1142/S0129065797000513

Fernández, E., Greger, B., House, P. A., Aranda, I., Botella, C., Albisua, J., et al. (2014). Acute human brain responses to intracortical microelectrode arrays: challenges and future prospects. *Front. Neuroeng.* 7:24. doi: 10.3389/fneng.2014.00024

Gilja, V., Nuyujukian, P., Chestek, C. A., Cunningham, J. P., Byron, M. Y., Fan, J. M., et al. (2012). A high-performance neural prosthesis enabled by control algorithm design. *Nat. Neurosci.* 15, 1752–1757. doi: 10.1038/nn.3265

Glaser, J. I., Benjamin, A. S., Chowdhury, R. H., Perich, M. G., Miller, L. E., and Kording, K. P. (2017). Machine learning for neural decoding. *arXiv*:1708.00909 [q-bio.NC].

Guo, Z., Wong, W. K., and Li, M. (2012). Sparsely connected neural network-based time series forecasting. *Inform. Sci.* 193, 54–71. doi: 10.1016/j.ins.2012.01.011

Haykin, S. (1994). *Neural Networks: A Comprehensive Foundation.* Prentice Hall PTR.

Hong, G., and Lieber, C. M. (2019). Novel electrode technologies for neural recordings. *Nat. Rev. Neurosci.* 20, 330–345. doi: 10.1038/s41583-019-0140-6

Hornik, K., Stinchcombe, M., and White, H. (1989). Multilayer feedforward networks are universal approximators. *Neural Netw.* 2, 359–366. doi: 10.1016/0893-6080(89)90020-8

Huang, D.-S., and Du, J.-X. (2008). A constructive hybrid structure optimization methodology for radial basis probabilistic neural networks. *IEEE Transact. Neural Netw.* 19, 2099–2115. doi: 10.1109/TNN.2008.2004370

Islam, M. M., Sattar, M. A., Amin, M. F., Yao, X., and Murase, K. (2009). A new adaptive merging and growing algorithm for designing artificial neural networks. *IEEE Transact. Syst. Man Cybernet.* 39, 705–722. doi: 10.1109/TSMCB.2008.2008724

Jackson, A., Mavoori, J., and Fetz, E. E. (2006). Long-term motor cortex plasticity induced by an electronic neural implant. *Nature* 444, 56–60. doi: 10.1038/nature05226

Jaeger, H., and Haas, H. (2004). Harnessing nonlinearity: predicting chaotic systems and saving energy in wireless communication. *Science* 304, 78–80. doi: 10.1126/science.1091277

Jarosiewicz, B., Masse, N. Y., Bacher, D., Cash, S. S., Eskandar, E., Friehs, G., et al. (2013). Advantages of closed-loop calibration in intracortical brain–computer interfaces for people with tetraplegia. *J. Neural Eng.* 10:046012. doi: 10.1088/1741-2560/10/4/046012

Jarosiewicz, B., Sarma, A. A., Bacher, D., Masse, N. Y., Simeral, J. D., Sorice, B., et al. (2015). Virtual typing by people with tetraplegia using a self-calibrating intracortical brain-computer interface. *Sci. Transl. Med.* 7:313ra179–313ra179. doi: 10.1126/scitranslmed.aac7328

Kao, J. C., Nuyujukian, P., Ryu, S. I., Churchland, M. M., Cunningham, J. P., and Shenoy, K. V. (2015). Single-trial dynamics of motor cortex and their applications to brain-machine interfaces. *Nat. Commun.* 6:7759. doi: 10.1038/ncomms8759

Kao, J. C., Stavisky, S. D., Sussillo, D., Nuyujukian, P., and Shenoy, K. V. (2014). Information systems opportunities in brain–machine interface decoders. *Proc. IEEE* 102, 666–682. doi: 10.1109/JPROC.2014.2307357

Kawato, M. (1990). "Feedback-error-learning neural network for supervised motor learning," in *Advanced Neural Computers* (Elsevier), 365–372. doi: 10.1016/B978-0-444-88400-8.50047-9

Kaylani, A., Georgiopoulos, M., Mollaghasemi, M., and Anagnostopoulos, G. C. (2009). AG-ART: an adaptive approach to evolving ART architectures. *Neurocomputing* 72, 2079–2092. doi: 10.1016/j.neucom.2008.09.016

Kifouche, A., Vigneron, V., Shamsollahi, M. B., and Guessoum, A. (2014). "Decoding hand trajectory from primary motor cortex ECoG using time delay neural network," in *International Conference on Engineering Applications of Neural Networks* eds V. Mladenov, C. Jayne, and L. Iliadis (Sofia: Springer), 237–247. doi: 10.1007/978-3-319-11071-4_23

Kim, S.-P., Wood, F., Fellows, M., Donoghue, J. P., and Black, M. J. (2006). "Statistical analysis of the non-stationarity of neural population codes," in *Biomedical Robotics and Biomechatronics, 2006. The First IEEE/RAS-EMBS International Conference on: IEEE* (Pisa), 811–816.

Kwok, T.-Y., and Yeung, D.-Y. (1997). Constructive algorithms for structure learning in feedforward neural networks for regression problems. *IEEE Transact. Neural Netw.* 8, 630–645. doi: 10.1109/72.572102

Lin, H.-C., Pan, H.-C., Lin, S.-H., Lo, Y.-C., Shen, E. T.-H., Liao, L.-D., et al. (2016). Central thalamic deep-brain stimulation alters striatal-thalamic connectivity in cognitive neural behavior. *Front. Neural Circuits* 9:87. doi: 10.3389/fncir.2015.00087

Løvaas, C., Seron, M. M., and Goodwin, G. C. (2008). Robust output-feedback model predictive control for systems with unstructured uncertainty. *Automatica* 44, 1933–1943. doi: 10.1016/j.automatica.2007.10.003

Mahmud, M. S., and Meesad, P. (2016). An innovative recurrent error-based neuro-fuzzy system with momentum for stock price prediction. *Soft Comput.* 20, 4173–4191. doi: 10.1007/s00500-015-1752-z

Manohar, A., Flint, R. D., Knudsen, E., and Moxon, K. A. (2012). Decoding hindlimb movement for a brain machine interface after a complete spinal transection. *PLoS ONE* 7:e52173. doi: 10.1371/journal.pone.0052173

Masutti, T. A., and de Castro, L. N. (2009). Neuro-immune approach to solve routing problems. *Neurocomputing* 72, 2189–2197. doi: 10.1016/j.neucom.2008.07.015

Michelson, N. J., Vazquez, A. L., Eles, J. R., Salatino, J. W., Purcell, E. K., Williams, J. J., et al. (2018). Multi-scale, multi-modal analysis uncovers complex relationship at the brain tissue-implant neural interface: new emphasis on the biological interface. *J. Neural Eng.* 15:033001. doi: 10.1088/1741-2552/aa9dae

Miyamoto, H., Kawato, M., Setoyama, T., and Suzuki, R. (1988). Feedback-error-learning neural network for trajectory control of a robotic manipulator. *Neural Netw.* 1, 251–265. doi: 10.1016/0893-6080(88)90030-5

Nuyujukian, P., Kao, J. C., Fan, J. M., Stavisky, S. D., Ryu, S. I., and Shenoy, K. V. (2014). Performance sustaining intracortical neural prostheses. *J. Neural Eng.* 11:066003. doi: 10.1088/1741-2560/11/6/066003

Orsborn, A. L., Moorman, H. G., Overduin, S. A., Shanechi, M. M., Dimitrov, D. F., and Carmena, J. M. (2014). Closed-loop decoder adaptation shapes neural plasticity for skillful neuroprosthetic control. *Neuron* 82, 1380–1393. doi: 10.1016/j.neuron.2014.04.048

Pais-Vieira, M., Lebedev, M., Kunicki, C., Wang, J., and Nicolelis, M. A. L. (2013). A brain-to-brain interface for real-time sharing of sensorimotor information. *Sci. Rep.* 3, 1319–1319. doi: 10.1038/srep01319

Paninski, L., Fellows, M. R., Hatsopoulos, N. G., and Donoghue, J. P. (2004). Spatiotemporal tuning of motor cortical neurons for hand position and velocity. *J. Neurophysiol.* 91, 515–532. doi: 10.1152/jn.00587.2002

Perge, J. A., Homer, M. L., Malik, W. Q., Cash, S., Eskandar, E., Friehs, G., et al. (2013). Intra-day signal instabilities affect decoding performance in an intracortical neural interface system. *J. Neural Eng.* 10:036004. doi: 10.1088/1741-2560/10/3/036004

Perge, J. A., Zhang, S., Malik, W. Q., Homer, M. L., Cash, S., Friehs, G., et al. (2014). Reliability of directional information in unsorted spikes and local field potentials recorded in human motor cortex. *J. Neural Eng.* 11:046007. doi: 10.1088/1741-2560/11/4/046007

Prechelt, L. (1998). Automatic early stopping using cross validation: quantifying the criteria. *Neural Netw.* 11, 761–767. doi: 10.1016/S0893-6080(98)00010-0

Reed, R. (1993). Pruning algorithms-a survey. *IEEE Transact. Neural Netw.* 4, 740–747. doi: 10.1109/72.248452

Roelfsema, P. R., Denys, D., and Klink, P. C. (2018). Mind reading and writing: the future of neurotechnology. *Trends Cognit. Sci.* 22, 598–610. doi: 10.1016/j.tics.2018.04.001

Salatino, J. W., Ludwig, K. A., Kozai, T. D., and Purcell, E. K. (2017). Glial responses to implanted electrodes in the brain. *Nat. Biomed. Eng.* 1:862. doi: 10.1038/s41551-017-0154-1

Sanchez, J., Principe, J., Carmena, J., Lebedev, M. A., and Nicolelis, M. (2004). "Simultaneus prediction of four kinematic variables for a brain-machine interface using a single recurrent neural network." in *Engineering in Medicine and Biology Society, 2004. IEMBS'04, 26th Annual International Conference of the IEEE* (San Francisco, CA: IEEE), 5321–5324.

Sanchez, J. C., Erdogmus, D., Nicolelis, M. A., Wessberg, J., and Principe, J. C. (2005). Interpreting spatial and temporal neural activity through a recurrent neural network brain-machine interface. *IEEE Transact. Neural Syst. Rehabil. Eng.* 13, 213–219. doi: 10.1109/TNSRE.2005.847382

Sarpeshkar, R., Wattanapanitch, W., Arfin, S. K., Rapoport, B. I., Mandal, S., Baker, M. W., et al. (2008). Low-power circuits for brain–machine interfaces. *IEEE Transact. Biomed. Circuits Syst.* 2, 173–183. doi: 10.1109/TBCAS.2008.2003198

Schwartz, A. B., Kettner, R. E., and Georgopoulos, A. P. (1988). Primate motor cortex and free arm movements to visual targets in three-dimensional space. I. Relations between single cell discharge and direction of movement. *J. Neurosci.* 8, 2913–2927. doi: 10.1523/JNEUROSCI.08-08-02913.1988

Shah, S., Haghi, B., Kellis, S., Bashford, L., Kramer, D., Lee, B., et al. (2019). "Decoding Kinematics from Human Parietal Cortex using Neural Networks," in *2019 9th International IEEE/EMBS Conference on Neural Engineering (NER): IEEE*, 1138–1141. doi: 10.1109/NER.2019.8717137

Shimoda, K., Nagasaka, Y., Chao, Z. C., and Fujii, N. (2012). Decoding continuous three-dimensional hand trajectories from epidural electrocorticographic signals in Japanese macaques. *J. Neural Eng.* 9:036015. doi: 10.1088/1741-2560/9/3/036015

Simeral, J., Kim, S.-P., Black, M., Donoghue, J., and Hochberg, L. (2011). Neural control of cursor trajectory and click by a human with tetraplegia 1000 days after implant of an intracortical microelectrode array. *J. Neural Eng.* 8:025027. doi: 10.1088/1741-2560/8/2/025027

Slutzky, M. W. (2018). Brain-machine interfaces: powerful tools for clinical treatment and neuroscientific investigations. *Neuroscientist* 25, 139–154. doi: 10.1177/1073858418775355

Sussillo, D., Nuyujukian, P., Fan, J. M., Kao, J. C., Stavisky, S. D., Ryu, S., et al. (2012). A recurrent neural network for closed-loop intracortical brain–machine interface decoders. *J. Neural Eng.* 9:026027. doi: 10.1088/1741-2560/9/2/026027

Sussillo, D., Stavisky, S. D., Kao, J. C., Ryu, S. I., and Shenoy, K. V. (2016). Making brain-machine interfaces robust to future neural variability. *Nat. Commun.* 7, 13749–13749. doi: 10.1038/ncomms13749

Tampuu, A., Matiisen, T., Ólafsdóttir, H. F., Barry, C., and Vicente, R. (2019). Efficient neural decoding of self-location with a deep recurrent network. *PLoS Comput. Biol.* 15:e1006822. doi: 10.1371/journal.pcbi.1006822

Todorov, E., and Jordan, M. I. (2002). Optimal feedback control as a theory of motor coordination. *Nat. Neurosci.* 5, 1226–1235. doi: 10.1038/nn963

Waheeb, W., Ghazali, R., and Herawan, T. (2016). Ridge polynomial neural network with error feedback for time series forecasting. *PLoS ONE* 11:e0167248. doi: 10.1371/journal.pone.0167248

Waibel, A., Hanazawa, T., Hinton, G., Shikano, K., and Lang, K. J. (1989). Phoneme recognition using time-delay neural networks. *IEEE Transact. Acoustics Speech Signal Proce.* 37, 328–339. doi: 10.1109/29.21701

Werbos, P. J. (1988). Generalization of backpropagation with application to a recurrent gas market model. *Neural Netw.* 1, 339–356. doi: 10.1016/0893-6080(88)90007-X

Willett, F. R., Young, D. R., Murphy, B. A., Memberg, W. D., Blabe, C. H., Pandarinath, C., et al. (2019). Principled BCI decoder design and parameter selection using a feedback control model. *Sci. Rep.* 9:8881. doi: 10.1038/s41598-019-44166-7

Wodlinger, B., Downey, J., Tyler-Kabara, E., Schwartz, A., Boninger, M., and Collinger, J. (2014). Ten-dimensional anthropomorphic arm control in a human brain– machine interface: difficulties, solutions, and limitations. *J. Neural Eng.* 12:016011. doi: 10.1088/1741-2560/12/1/016011

Wong, W.-K., Guo, Z., and Leung, S. (2010). Partially connected feedforward neural networks on Apollonian networks. *Physica A* 389, 5298–5307. doi: 10.1016/j.physa.2010.06.061

Wu, W., Black, M. J., Mumford, D., Gao, Y., Bienenstock, E., and Donoghue, J. P. (2004). Modeling and decoding motor cortical activity using a switching Kalman filter. *IEEE Transact. Biomed. Eng.* 51, 933–942. doi: 10.1109/TBME.2004.826666

Yang, S.-H., and Chen, Y.-P. (2012). An evolutionary constructive and pruning algorithm for artificial neural networks and its prediction applications. *Neurocomputing* 86, 140–149. doi: 10.1016/j.neucom.2012.01.024

Yang, S.-H., Chen, Y.-Y., Lin, S.-H., Liao, L.-D., Lu, H. H.-S., Wang, C.-F., et al. (2016). A sliced inverse regression (SIR) decoding the forelimb movement from neuronal spikes in the rat motor cortex. *Front. Neurosci.* 10, 556–556. doi: 10.3389/fnins.2016.00556

Zhou, F., Liu, J., Yu, Y., Tian, X., Liu, H., Hao, Y., et al. (2010). Field-programmable gate array implementation of a probabilistic neural network for motor cortical decoding in rats. *J. Neurosci. Methods* 185, 299–306. doi: 10.1016/j.jneumeth.2009.10.001

Conflict of Interest: The authors declare that the research was conducted in the absence of any commercial or financial relationships that could be construed as a potential conflict of interest.

frontiers in Neuroscience

ORIGINAL RESEARCH
published: 21 April 2020
doi: 10.3389/fnins.2020.00351

Modulation on Glutamic Pathway of Frontal-Striatum-Thalamus by rs11146020 and rs3813296 Gene Polymorphism in First-Episode Negative Schizophrenia

Suping Cai[1†], Yahui Lv[1], Kexin Huang[1], Wei Zhang[1], Qiang Wang[2], Liyu Huang[1†] and Jijun Wang[3*]*

[1] School of Life Sciences and Technology, Xidian University, Xi'an, China, [2] The First Affiliated Hospital, Xi'an Jiaotong University, Xi'an, China, [3] Shanghai Mental Health Center, Shanghai Jiao Tong University, Shanghai, China

OPEN ACCESS

Edited by:
Wei Wu,
South China University of Technology, China

Reviewed by:
Yuanchao Zhang,
University of Electronic Science and Technology of China, China
Dandan Zhang,
Shenzhen University, China

***Correspondence:**
Liyu Huang
huangly@mail.xidian.edu.cn
Jijun Wang
jijunwang27@163.com

†ORCID:
Suping Cai
orcid.org/0000-0001-8605-0874
Liyu Huang
orcid.org/0000-0001-6534-2712

Specialty section:
This article was submitted to Brain Imaging Methods, a section of the journal Frontiers in Neuroscience

Received: *03 September 2019*
Accepted: *23 March 2020*
Published: *21 April 2020*

Citation:
Cai S, Lv Y, Huang K, Zhang W, Wang Q, Huang L and Wang J (2020) Modulation on Glutamic Pathway of Frontal-Striatum-Thalamus by rs11146020 and rs3813296 Gene Polymorphism in First-Episode Negative Schizophrenia. Front. Neurosci. 14:351. doi: 10.3389/fnins.2020.00351

Objectives: The frontal-striatum-thalamus pathway is important in the glutamic neural circuit. The hypofunction of GRIN1 and GRIA2 subunits from glutamic receptors has been hypothesized as the primary process in the etiology of schizophrenia. Identified gene polymorphism involved in the pathogenesis of schizophrenia may uncover relevant mechanism pathways.

Methods: We selected two loci of rs11146020 and rs3813296 distributed in GRIN1 and GRIA2 genes and tested their main and interaction effects on causality connections and structural characteristics in the frontal-striatum-thalamus pathway in 55 Han Chinese first-episode negative schizophrenia patients.

Results: We found that: (1) rs11146020 has a significant main effect on the causality connections between the bilateral dorsolateral prefrontal cortex, and rs3813296 mainly influences those of the descending pathway from the prefrontal cortex to the striatum; (2) interaction effect of rs11146020 and rs3813296 on causality connections are located in the ascending pathway from the pallidum to the dorsolateral prefrontal cortex; and (3) the two loci have effects on the volumes of several regions of this pathway.

Conclusion: Our results suggested there is modulation on glutamic frontal-striatum-thalamus pathway by rs11146020 and rs3813296 gene polymorphism. Patients with different genotypes have different neuroimaging characteristics, which indirectly reminded clinicians those patients should receive different clinical interventions.

Keywords: single nucleotide polymorphism, magnetic resonance imaging, glutamic pathway, causality connection, schizophrenia

INTRODUCTION

Traditionally, abnormal dopamine has been considered the major underlying cause of schizophrenia (Gründer and Cumming, 2016). However, this conventional hypothesis does not readily elucidate the negative symptoms and cognitive deficits that are often observed in schizophrenia (Yang and Tsai, 2017). Glutamate, an important excitatory neurotransmitter in the

brain, is necessary for neuronal growth, maturation, and synaptic plasticity (Garthwaite and Balazs, 1978; Choi, 1988; Derkach et al., 2007; Lau and Zukin, 2007). Previous studies have demonstrated that altered glutamate signaling may provide a better explanation for the pathological basis of schizophrenia (Stahl, 2007). One hypothesis declares that aberrant functioning of glutamatergic synapses leads to an imbalance between excitation and inhibition and, ultimately, to generate changes in the neural circuitry, such as in the frontal-striatum-thalamus pathway which is an important glutamic neural circuit, that drives psychosis and the impairment of cognitive functions (Schwartz et al., 2012).

N-methyl-D-aspartate (NMDA) and α-amino-3-hydroxy-5-methylisoxazole-4-propionic acid (AMPA) are two ionotropic receptors of glutamate that have been proposed as mediators of numerous common neuropsychiatric phenotypes such as cognition deficit, psychosis, and degeneration (Nakanishi et al., 1998). NMDA receptor is crucial for neuronal communication and the formation of tetrameric complexes of its was encoded by seven homologous subunits genes (Traynelis et al., 2010; Zhu et al., 2016). Although all are good candidate genes for the pathogenesis of schizophrenia, GRIN1 gene gets special attention, which codes NMDA receptor subunit 1 (NR1). Reducing expression of NR1 in mice gives rise to behavioral anomalies which is similar to those observed in pharmacologically induced animal models of schizophrenia (Mohn et al., 1999). rs11146020 is located in the 5′ untranslated region (UTR) in the GRIN1 gene, which may influence gene expression by affecting transcription, stability of mRNA, and translation efficiency (Meijer and Thomas, 2002; Wilkie et al., 2003). Liu et al. (2019) have illustrated that single nucleotide polymorphism (SNP) of rs11146020 in the promoter region of the GRIN1 gene are associated with schizophrenia in a Chinese Han population.

α-amino-3-hydroxy-5-methylisoxazole-4-propionic acid receptor is mainly located in excitatory synapses, where it mediates the most of fast synaptic transmission and participates in synaptic plasticity (Huganir and Nicoll, 2013). There are four AMPA receptor subunits assembled into functional homo- and hetero-tetrameric receptor complexes (Keinanen et al., 1990). Four genes (GRIA1-4) encode these receptor subunits which are expressed in several brain regions, such as the nucleus accumbens, striatum and prefrontal cortex (Reimers et al., 2011). Among the four receptor subunits, the Ca^{2+} permeability of AMPA receptors is dependent on the encoding of GRIA2 gene and AMPA receptors not containing the GRIA2 subunit are Ca^{2+} impermeable, increasing neuronal vulnerability to excitotoxicity, which results in neuropsychiatric symptoms (Isaac et al., 2007). GRIA2 is expressed on pyramidal cells and GABAergic interneurons, the cellular source of the expression difference would have a substantial effect on its physiological consequences (Lake et al., 2016). Moreover, The association of genotype rs3813296 T/T in the GRIA2 gene with a low efficacy of antipsychotics against negative symptoms was demonstrated when studying the association of polymorphisms of GRIA2 encoding a number of subunits of AMPA (Gareeva, 2018).

A previous study concluded that a series of glutamic neurons that begin in the prefrontal lobe connect and project into brainstem, midbrain, and limbic system (Schwartz et al., 2012). By this means, neurons originating in the prefrontal cortex may penetrate into deeper brain areas to control over midbrain neurons that are primarily in charge of creating and projecting neurotransmitter activities that are eventually responsible for drive and affective initiation. These deeper brain areas, such as the striatum and thalamus, play an important role on creating appropriate perceptual balance versus psychosis (Marx et al., 2015).

More importantly, twin and family studies indicated that genetic factors contributed substantially to the possibility of developing schizophrenia (Ripke et al., 2014). The extant data suggested that schizophrenia involved complex interactions between multiple genes, each exerting relatively small effects on vulnerability. Several SNPs have been associated with increased risk for developing schizophrenia, although few of these findings have been replicated (Jagannath et al., 2018). If confirmed in additional studies, these genetic markers would implicate glutamatergic neurotransmitter pathways in the pathogenesis of schizophrenia (Dauvermann et al., 2017; Saini et al., 2017; Han et al., 2018).

Taken together, the modulation relationship between the SNP variants in specific genes and glutamic neural circuits remains a challenge to understand. If we obtained the association relationship between them, it could potentially help clinicians regulate intervention strategies for those patients with some genotypes. Based on this challenge, in the present study, we selected an important glutamic neural circuit, the frontal-striatum-thalamus pathway, and two SNPs in GRIN1 and GRIA2 genes to explore their effects on the causality connections and structural characteristics of this neural pathway and then investigated the correlation between the causality connection strength and clinical cognitive behavioral scores. The hypothesis is that there is a modulation on glutamic pathway of frontal-striatum-thalamus by rs11146020 and rs3813296 gene polymorphism in first-episode negative schizophrenia.

MATERIALS AND METHODS

Participant Selection

We selected fifty-five first-episode negative schizophrenic patients from the Shanghai Mental Health Center. All patients met the inclusion criteria as follows: (1) they were first-episode and had no medication history; (2) they were diagnosed as schizophrenia by senior clinical psychiatrists using a structural clinical interview from the DSM-IV-TR (patient edition); (3) they did not present severe agitation or aggression; and (4) they were 18–45 years old and right-handed.

Behavioral Measurement Scales

The patients were assessed using scales for the assessment of negative symptoms (SANS), duration of untreated psychosis (DUP), and education years (EDU). Intravenous peripheral blood of each patient was drawn for the extraction genotype. More importantly, the internationally recognized consensus version of cognitive function tests for schizophrenia were measured,

including the trail making test (TMT); brief assessment of cognition in schizophrenia-symbol coding (BACS-SC); verbal fluency (VF); continuous performance test-identical pairs (CPT-IP); Wechsler memory scale, third edition: spatial span (WMS-III SS); Hopkins verbal learning test, revised (HVLT-R); brief visuospatial memory test, revised (BVMT-R); neuropsychological assessment battery, mazes (NAB-M); and Mayer-Salovey-Caruso emotional intelligence test, managing emotions (MSCEIT-ME). All tests were confirmed by three experienced psychiatrists who underwent consistency training for approximately 1 week, and all scores were assessed objectively. For more detailed information, please see **Table 1**.

Genotyping

Peripheral blood was drawn from a participant's vein into a sterile tube containing EDTA. We stored the plasma samples at −80°C. Genomic DNA was isolated from peripheral blood leukocytes according to the manufacturer's protocol (Thermo Fisher Scientific, United States). DNA was also stored at −80°C for SNP analysis. Genotyping was performed for all SNPs by SnaPshot using a 3730xl DNA Analyzer (Thermo Fisher Scientific, United States).

Single nucleotide polymorphism rs11146020 from the GRIN1 gene and rs3813296 from the GRIA2 gene were genotyped in all patients by allele-specific polymerase chain reaction primers. The success rate of the genotyping in our study was 100%. Information from the Hardy-Weinberg equilibrium (HWE) and minor allele frequency (MAF) are shown in **Table 1**. In addition, we have uploaded the SNP data to a publicly available repository[1]. The link to the SNP data is https://www.synapse.org/#!Synapse:syn21788916/tables/.

There were two genotypes for rs11146020 among the 55 schizophrenia patients: CG (23 patients) and GG (32 patients). Analogously, there were three genotypes for rs3813296: GT (24 patients), TT (29 patients), and GG (2 patients). Because only two participants were the carriers of genotype GG, we did not select these participants. To further investigate the interaction effect of rs11146020 and rs3813296, we divided the patients into four subgroups (14 GG/GT, 17 GG/TT, 10 CG/GT, and 12 CG/TT) for follow-up analysis.

Data Acquisition

All MRI images were scanned using a 3T Siemens Magnetom Verio Syngo MR B17 scanner. Participants were informed to keep their eyes closed, not to focus their thoughts on anything and stay awake.

The parameters of functional MRI data are as follows: echo time [TE] = 30 ms, repetition time [TR] = 3 s, flip angle [FA] = 90°, slice thickness = 3.0 mm, slices = 45, field of view [FOV] = 220 mm × 220 mm, matrix size = 64 × 64, voxel size = 3 mm × 3 mm × 3 mm and 170 slices.

Structural MRI data were obtained with a high-resolution T1-weighted magnetization-prepared rapid gradient echo (MPRAGE) sequence. The parameters used are as follows: TE = 2.56 ms, TR = 2530 ms, FA = 7°, FOV = 256 mm × 256 mm, matrix = 256 × 256, slice thickness = 1 mm, inversion time = 1100 ms, and 192 coronal slices.

Data Preprocessing

T1-Weighted Data Preprocessing

We performed T1-weighted data processing with the FSL-VBM protocol with the FMRIB Software Library 4.1 (FSL[2]). More detailed processing, please see our recent study (Cai et al., 2017a). There were four steps: brain extraction; the segmentation of white matter, gray matter and cerebrospinal fluid; image registration to the standard template; and image smoothing with a Gaussian kernel with 8 mm.

We segmented white matter and gray matter and divided the images into four subgroups based on different genotypes (GG/GT, GG/TT, CG/GT, and CG/TT) for follow-up statistical analysis.

fMRI Data Preprocessing

fMRI data processing was performed using a MATLAB toolbox called DPABI (Yan et al., 2016), which evolved from REST (Song et al., 2011), and DPARSF (Chao-Gan and Yu-Feng, 2010). For more details on fMRI data processing, please see our previous study (Cai et al., 2015). There were eight steps: discarding the first ten time points, slice timing correction, correcting for head motion (exclusion criteria: exceeding 1.5 mm in any dimension of x, y, and z or 1.5° in any angular motion; two participants were removed), normalizing to individual T1-weighted anatomical images, smoothing images, removing linear trends, filtering (0.01–0.1 Hz) and regressing the covariates (A Friston-24 parameter, the global mean signal, cerebrospinal fluid signal, and white matter signal were the nuisance covariates) (Friston et al., 1996; Yan et al., 2013). We also examined if there are any differences in head motion among groups as described in the study of Power et al. (2012).

Data Processing and Statistical Analysis

Frontal-Striatum-Thalamus Pathway and Core Regions Selection

At a molecular level, glutamate neurotransmitter release and synaptic discharge circuit are mainly from the frontal lobe, and go through the striatum to the basal ganglia (Carlsson et al., 1999; Schwartz et al., 2012; **Figures 1A,B**). Based on these studies, we concluded and focused on one of the glutamic neurotransmission pathways: the frontal-striatum-thalamus pathway (**Figure 1**) and selected 10 core brain regions in this pathway: left and right dorsolateral prefrontal cortex (L/R. dLPFC), L/R. caudate, L/R. putamen, L/R. pallidum, and L/R. thalamus (Schwartz et al., 2012). We extracted these brain regions using an anatomical automatic labeling (AAL) template implemented with REST (Song et al., 2011). It should be noted that dLPFC is a functional definition, thus we used dorsolateral superior frontal gyrus to represent this region based on the AAL template. Ten brain regions were resampled to the spatial resolution of fMRI images.

[1] https://www.synapse.org/

[2] http://fsl.fmrib.ox.ac.uk/fsl

TABLE 1 | Genotypic, demographic, and clinical information of all participants.

SNP ID	Alleles	Location	Call Rate (%)	Test for HWE (*P* Value)	MAF	
GRIN1						
rs11146020	C/G	upstream 9:137138632	100	0.6142[a]	C: 0.195	
GRIA2						
rs3813296	G/T	Intron 4:157360371	100	0.1999[a]	G:0.246	
rs11146020	**GG = 31**		**CG = 22**		***F* value**	***P* value**
rs3813296	**GT = 14**	**TT = 17**	**GT = 10**	**TT = 12**		
Gender	6M/8F	8M/9F	6M/54F	7M/5F	1.14	0.79[b]
AGE	26.67 ± 6.08	23.87 ± 5.85	25.11 ± 7.41	25.11 ± 5.04	0.47	0.71[c]
EDU	12.42 ± 3.80	12.07 ± 2.81	12.78 ± 2.68	13.56 ± 2.40	0.48	0.70[c]
Head motion	0.36 ± 0.21	0.44 ± 0.24	0.29 ± 0.20	0.38 ± 0.19	0.51	0.63[c]
DUP	38.42 ± 44.01	26.47 ± 16.08	24.22 ± 18.44	36.89 ± 47.96	0.50	0.68[c]
SANS	14.75 ± 11.38	14.40 ± 13.14	14.00 ± 10.42	24.67 ± 13.30	1.69	0.18[c]
TMT	46.08 ± 18.83	31.07 ± 18.10	40.89 ± 16.10	52.56 ± 24.98	2.63	0.06[c]
BACS-SC	51.75 ± 10.06	52.33 ± 13.07	47.89 ± 14.22	47.56 ± 12.07	0.45	0.72[c]
HVLT-R	22.08 ± 5.18	24.00 ± 7.00	20.56 ± 6.15	24.00 ± 4.80	0.80	0.50[c]
WMS-III SS	14.58 ± 2.78	13.93 ± 4.51	13.11 ± 3.44	15.11 ± 3.66	0.50	0.68[c]
NAB-M	15.00 ± 7.06	14.13 ± 5.96	11.66 ± 7.90	12.22 ± 9.52	0.47	0.71[c]
BVMT-R	23.17 ± 7.25	25.27 ± 9.19	21.89 ± 8.40	20.44 ± 9.88	0.65	0.59[c]
VF	20.08 ± 6.65	18.53 ± 6.00	19.33 ± 5.98	23.56 ± 7.84	1.16	0.34[c]
MSCEIT-ME	86.92 ± 13.19	84.93 ± 15.11	81.56 ± 15.11	96.67 ± 19.98	1.58	0.21[c]
CPT-IP	2.42 ± 1.08	1.80 ± 1.01	2.33 ± 0.87	2.22 ± 0.83	1.07	0.37[c]
Head motion	0.34 ± 0.07	0.29 ± 0.06	0.37 ± 0.09	0.33 ± 0.08	0.70	0.55[c]

Data are given as mean ± standard deviation; [a]P value was obtained by hardy-weinberg equilibrium (HWE) test; [b]P value was obtained by an independence Pearson chi-square test. [c]The P and corresponding F values were obtained by a one-way analysis of variance test. MAF, minor allele frequency; EDU, education years; DUP, duration of untreated psychosis; SANS, assessment of negative symptoms; TMT, trail making test; BACS-SC, brief assessment of cognition in schizophrenia-symbol coding; HVLT-R, Hopkins verbal learning test, revised; WMS-III SS, Wechsler memory scale, third edition: spatial span; NAB-M, neuropsychological assessment battery, mazes; BVMT-R, brief visuospatial memory test, revised; VF, verbal fluency; MSCEIT-ME, Mayer-Salovey-Caruso emotional intelligence test, managing emotions; CPT-IP, continuous performance test-identical pairs.

Granger Causality Analysis

Granger causality analysis (GCA) is an approach used to explore the dynamic causal relationship between two time series (Granger, 1969). A brief introduction of the Granger procedure is provided here. For two given fMRI time series x(t) and y(t), x(t) is the Granger causing y(t) if the past information of x(t) can improve the prediction of the current value of y(t). The Granger causal relationship between the two series is often estimated by vector autoregressive (VAR) modeling. Granger causality can evaluate the direct linear influence from x(t) to y(t) ($F_{X to Y}$) and the linear direct influence from y(t) to x(t) ($F_{Y to X}$). Formula (1) is the mathematic model of GCA:

$$\begin{aligned} x(t) &= \alpha_{x,0} + \sum^{p} \alpha_{xx,i} x(t-i) \\ &+ \sum^{p} \alpha_{xy,i} y(t-i) + \sum^{q} \beta_{x,i} z_j(t) + \varepsilon_x(t) \\ y(t) &= \alpha_{y,0} + \sum^{p} \alpha_{yx,i} x(t-i) \\ &+ \sum^{p} \alpha_{yy,i} y(t-i) + \sum^{q} \beta_{y,i} z_j(t) + \varepsilon_y(t) \end{aligned} \quad (1)$$

where $z_j(t)$ represents up to q exogenous processes (six orthogonal motion estimates and physiological noise) independent of the path network (j = 1,...., q). Contributions of each lagged variable to the prediction of its respective target are denoted by α; β corresponds to the covariate effect, and prediction errors of individual models are denoted by ε. A similar method was used in one of our previous studies (Cai et al., 2017b).

We applied bivariate coefficient-based GCA to compute the causality of the 10 brain regions for each participant. The average time courses of each region were input to the GCA using REST (Song et al., 2011). Then, we obtained the path coefficients characterized by the direction and the strength of the temporal relation among the 10 brain regions.

Main and Interaction Effect Analysis of rs11146020 and rs3813296

To understand the main and interaction effects of rs11146020 and rs3813296 on the frontal-striatum-thalamus pathway, we performed multivariable general linear model (GLM) analysis with gender, EDU, and age as regressors using IBM SPSS Statistical 23. There are two main effect analyses of rs11146020 and rs3813296 and one interaction effect analysis of

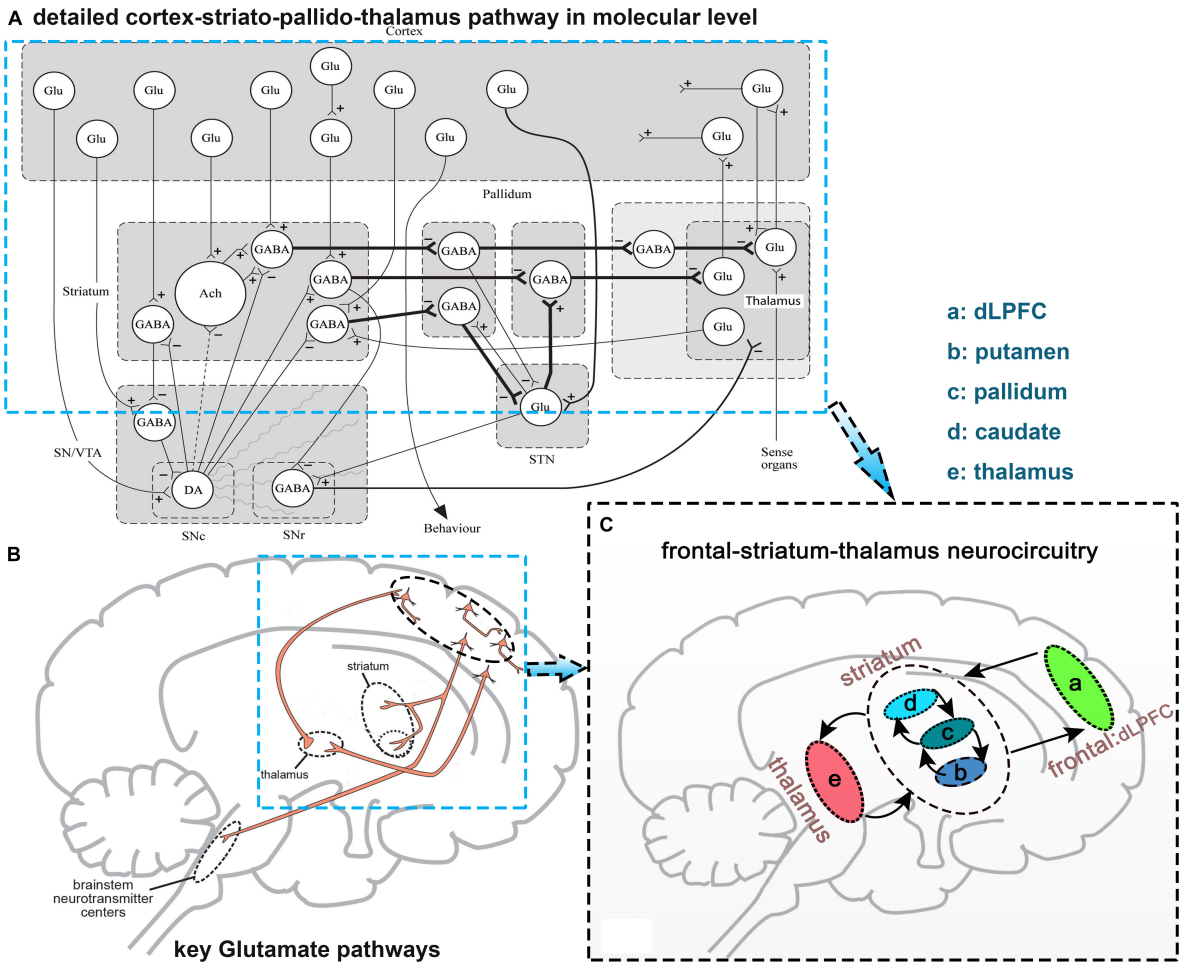

FIGURE 1 | Diagram explaining the selection of the frontal-striatum-thalamus pathway. **(A)** Detailed cortex-striato-pallido-thalamus pathway at the molecular level, this figure is from Carlsson et al. (1999); **(B)** several key glutamic pathways in synaptic release level, this figure from Schwartz et al. (2012); **(C)** selected frontal-striatum-thalamus pathway. Abbreviations: Glu, Glutamate; DA, dopamine; GABA, gamma aminobutyric acid.

rs11146020*rs3813296 in 90 (A_{10}^2) causality connections. If there are significant interactions, simple effect analysis was conducted with a script embedded into IBM SPSS Statistical 23. We applied the Mann–Whitney *U* test to test significance and false discovery rate (FDR) to correct the multiple comparisons ($P < 0.01$).

Gray and White Matter Structural Analysis

To investigate the differences between four subgroups (GG/GT, GG/TT, CG/GT, and CG/TT) in the gray and white matter structure, we applied two-sample *t*-tests to assess structural alterations in gray and white matter with gender, ages and EDU as regressors. The statistical images were corrected by FDR for multiple comparisons correction ($P < 0.01$).

Correlation Analysis Between Connection Strength and Behavioral Scores

The Spearman test for correlation was applied to investigate the correlation between connection strength, which showed significant group difference, and clinical scales, including TMT, BACS-SC, VF, CPT-IP, WMS-III SS, HVLT-R, BVMT-R, NAB-M, and MSCEIT-ME. The significance levels were set at $P < 0.01$ (two-tailed, FDR correction).

RESULTS

No Significant Subgroup Difference in Demographic Information and Clinical Scores

No significant difference were found in gender, age, gender, head motion, EDU, DUP, SANS, TMT, BACS-SC, VF, CPT-IP, WMS-III SS, HVLT-R, BVMT-R, NAB-M, and MSCEIT-ME among the four subgroups ($P > 0.05$). There is no difference in head motion among groups. All demographic information and clinical scores are shown in **Table 1**.

Main and Interaction Effects on Causality Connectivity in the Frontal-Striatum-Thalamus Pathway

Rs11146020 mainly affects the causality connectivity within the dLPFC: L. dLPFC → R. dLPFC and L. dLPFC → R. dLPFC (**Figure 2A** and **Table 2**). Rs3813296 mainly affects the causality connectivity of the descending pathway from the dorsolateral prefrontal cortex to thalamus and striatum: L. dLPFC → R. caudate and R. dLPFC → R. thalamus (**Figure 2B** and **Table 2**).

Rs11146020 and rs3813296 interactively affect the information flow of the upstream pathway from striatum to dLPFC: L. pallidum → L. dLPFC, L. pallidum → R. dLPFC, R. pallidum → R. dLPFC, and R. pallidum → R. caudate (**Figure 3A** and **Table 2**).

Main and Interaction Effects on Gray and White Matter Structures

There is no main effect of rs11146020 on gray and white matter volumes and no main effect of rs3813296 on gray matter volumes. Main effect of rs3813296 on white matter were located in left/right superior corona radiata fiber (**Figure 4B** and **Table 3**) ($P < 0.01$, FDR correction). The interaction effect of rs3813296*rs11146020 on gray and white matter volumes were located in the left/right putamen, left/right caudate, left/right thalamus (**Figure 4A** and **Table 3**) and left/right superior corona radiata fiber (**Figure 4C** and **Table 3**), respectively ($P < 0.01$, FDR correction).

Significant Correlation Between Causality Connection Strength and Behavioral Scales

We found that the strength of causality connection L. dLPFC → R. dLPFC has a significant positive correlation with DUP (**Figure 2C** and **Table 4**); the connection strengths of R. dLPFC → R. caudate and R. dLPFC → R. thalamus have significant positive correlations with BVMT-R scores (**Figures 2D,E** and **Table 4**); and the connection strength of R. dLPFC → R. thalamus has a significant positive correlation with VF test scores (**Figure 2F** and **Table 4**). More interestingly, four ascending causality connections interactively effected by rs11146020 and rs3813296 were all significant negative correlation with MSCEIT-ME scores (**Figures 3B–E** and **Table 4**).

DISCUSSION

The hypo-function of GRIN1 and GRIA2 subunits from glutamic receptors has been hypothesized as a primary process in the pathophysiology of schizophrenia. Identified gene polymorphism involved in the etiology of schizophrenia may reveal relevant mechanistic pathways. Whether the polymorphisms in the subunit genes of GRIN1 and GRIA2 receptors contribute to the risk of schizophrenia is still in question. In our study, we selected two SNPs distributed in GRIN1 and GRIA2 genes and tested their effects on the causality connections and structural characteristics of the frontal-striatum-thalamus pathway in Han Chinese schizophrenia patients. There were three major findings: (1) rs11146020 has a significant main effect on the causality connections between the left and right dLPFC and rs3813296 mainly influences the descending pathway from the prefrontal lobe to the striatum; (2) the interaction effect of rs11146020 and rs3813296 is mainly located in the ascending pathway from the bilateral pallidum to the right caudate and the bilateral dLPFC; and (3) the two SNPs have main and interaction effects on the volumes of gray and white matter in several regions of this pathway. Some causality connection strengths affected by the two SNPs have remarkable correlation with clinical cognitive performances in VF, visuospatial memory and emotion management. The detailed explanation is as follows.

Main Effect of rs11146020 on Causality Connectivity in Frontal-Striatum-Thalamus Pathway

Rs11146020 has a significant main effect on the causality connections between the left and right dLPFC. The ancestral and variant alleles of rs11146020 are G and C, respectively. There is a significant difference between homozygous GG and heterozygous GC in schizophrenia patients, indicating that genotype influences functional connections. Zhao et al. (2006) found that the C allele was expressed in a high frequency in schizophrenia patients. rs11146020 is located in the GRIN1 gene, which is a subunit of NMDAR. The gene responsible for its expression is located at 9q34 in the promoter region (Begni et al., 2003). The GRIN1 gene product plays a foundational role in many brain functions, and its involvement in the pathogenesis of schizophrenia has been widely investigated (Hung et al., 2002; Zhao et al., 2006). Moreover, GRIN1 knockout animals showed abnormal behavior characteristics which were commonly similar with patients with schizophrenia, such as impairment of working memory, reduced "self-care" (nest building) and social activity (Tatard-Leitman et al., 2015). Gray et al. (2015) reported higher expression levels of the majority of glutamatergic genes, especially GRIN1, were detected in the dLPFC. The rs11146020 genotype has a significant association with the causality connection between the left and right dLPFC, which is opportunely proved the suggestion by Zhao et al. (2006) that rs11146020 is a potential candidate to alter the risk of schizophrenia and worth further replication and functional investigation.

Interestingly, causality connection between the left and right dLPFC in schizophrenia patients with ancestral genotype GG has a significant positive correlation with DUP but was not found in GC carriers. For patients who carried the GG genotype, Increased connection strength could lead to protracted DUP in patients who carried the GG genotype. Research shows that there is a close relationship between longer DUP and poorer outcomes in first-episode psychosis (Rubio and Correll, 2017). Hence, enhanced connectivity between the left and right dLPFC is not an optimistic phenomenon, especially in patients with the GG genotype.

In terms of brain structure, we did not find a remarkable difference in the volumes of gray and white matter between

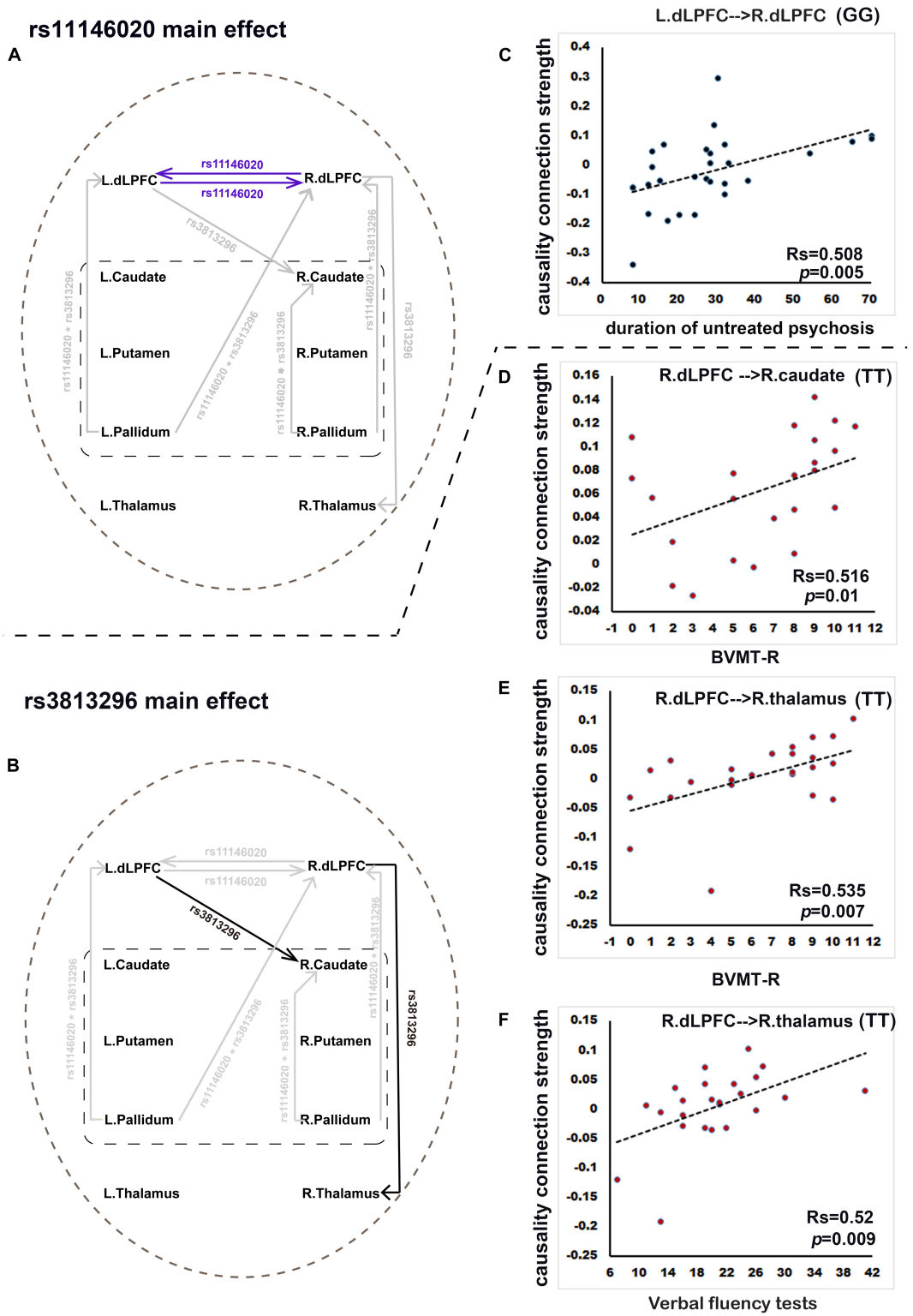

FIGURE 2 | Rs11146020 and rs3813296 main effects on causality connections and relationships with behavioral variables ($P < 0.01$, FDR correction). **(A)** rs11146020 and **(B)** rs3813296 main effects on causality connections; **(C)** causality connection strength of L. dLPFC → R. dLPFC has significant positive correlation with duration of untreated psychosis in patients with the GG genotype; **(D)** causality connection strength of R. dLPFC → R. caudate has a significant positive correlation with BVMT scores in patients with the TT genotype; causality connection strength of R. dLPFC → R. thalamus has a significant positive correlation with BVMT-R scores **(E)** and verbal fluency test scores **(F)** in patients with the TT genotype. Abbreviations: dLPFC, dorsolateral prefrontal cortex; BVMT-R, brief visuospatial memory test, revised.

TABLE 2 | Main and interaction effects of rs11146020 and rs3813296 on causality connectivity in frontal-striatum-thalamus pathway.

rs11146020 main effect on causality connectivity in frontal- striatum- thalamus pathway				
GG vs. CG				
Causality connectivity	**Connection strength**		***F*(1) value**	***P* value**
	GG	**CG**		
L.dLPFCR.dLPFC	−0.028 ± 0.022	0.047 ± 0.027	8.29	0.006
R.dLPFCL.dLPFC	0.02 ± 0.024	−0.085 ± 0.03	7.539	0.009
rs3813296 main effect on causality connectivity in frontal- striatum- thalamus pathway				
GT vs. TT				
Causality connectivity	**Connection strength**		***F*(1) value**	***P* value**
	TT	**GT**		
L.dLPFCR.Caudate	0.056 ± 0.016	0.015 ± 0.015	7.535	0.009
R.dLPFCR.Thalamus	0.008 ± 0.012	0.026 ± 0.013	9.147	0.003
rs11146020*rs3813296 inteaction effect on causality connectivity in frontal- striatum- thalamus pathway				
CG/GT vs. GG/GT				
Causality connectivity	**Connection strength**		***F*(1) value**	***P* value**
	GG/GT	**CG/GT**		
L.PallidumL.dLPFC	−0.032 ± 0.06	0.116 ± 0.071	8.691	0.0043
L.PallidumR.dLPFC	−0.078 ± 0.051	0.096 ± 0.06	9.487	0.0024
CG/TT vs. GG/GT				
Causality connectivity	**Connection strength**		***F*(1) value**	***P* value**
	GG/GT	**CG/TT**		
R.PallidumR.dLPFC	−0.08 ± 0.057	0.169 ± 0.068	9.366	0.0029
R.PallidumR.Caudate	0.036 ± 0.026	0.134 ± 0.025	8.662	0.0044

Data are given as mean ± standard deviation; P and corresponding F values were obtained from multivariable GLM analysis by applying the Mann–Whitney U test and FDR correction (P < 0.01). GLM, general linear model; FDR, false discovery rate; dLPFC, dorsolateral prefrontal cortex.

GG and GC genotypes, suggesting that the association between genotype and function was unrelated to cortex and subcortex sizes. This is possibly because the mutation from allele G to C is not enough to change brain volume.

Main Effect of rs3813296 on Causality Connectivity in the Frontal-Striatum-Thalamus Pathway

Rs3813296 mainly influences the causality connections of the descending pathway from the prefrontal lobe to the striatum, including L. dLPFC → R. caudate and R. dLPFC → R. thalamus. The connection strength of L. dLPFC → R. caudate in schizophrenia patients with the GT genotype is significantly lower than those with the TT genotype. Rs3813296 is located in the GRIA2 gene which is one subunit of the AMPA receptor (Lu et al., 2009). The Ca^{2+} permeability of AMPA receptors rely on the GRIA2 subunit and AMPA receptors without the GRIA2 subunit are Ca^{2+} impermeable, which increases the neuronal vulnerability to excitotoxicity and can result in neuropsychiatric symptoms (Isaac et al., 2007). The lower connection strength of L. dLPFC → R. caudate in patients with the GT genotype may be due to a deficit in Ca^{2+} permeability from cortex to subcortex. Based on the current result regarding to rs3813296, deficit Ca^{2+} permeability should be associated with the variation of T to G. However, this variation has significant relevance to the enhanced connection strength of R. dLPFC → R. thalamus, which could be interpreted as compensation phenomenon.

A literature study returned two studies containing rs3813296 (Crisafulli et al., 2012; Iamjan et al., 2018). Few studies are similar with our study; thus, we tried to search for supporting results from the current dataset and found that the white matter volume of the superior corona radiata in schizophrenia patients with the GT genotype is significantly larger than those with the TT genotype. Corona radiata are the most prominent projection fibers, and they are afferents that carry information to the cerebral cortex and efferent that carry information away from it (Morecraft et al., 2002). Gray matter of the striatum and white matter of the corona radiata are the main components of the basal ganglia. The difference of the white matter volume of the superior corona

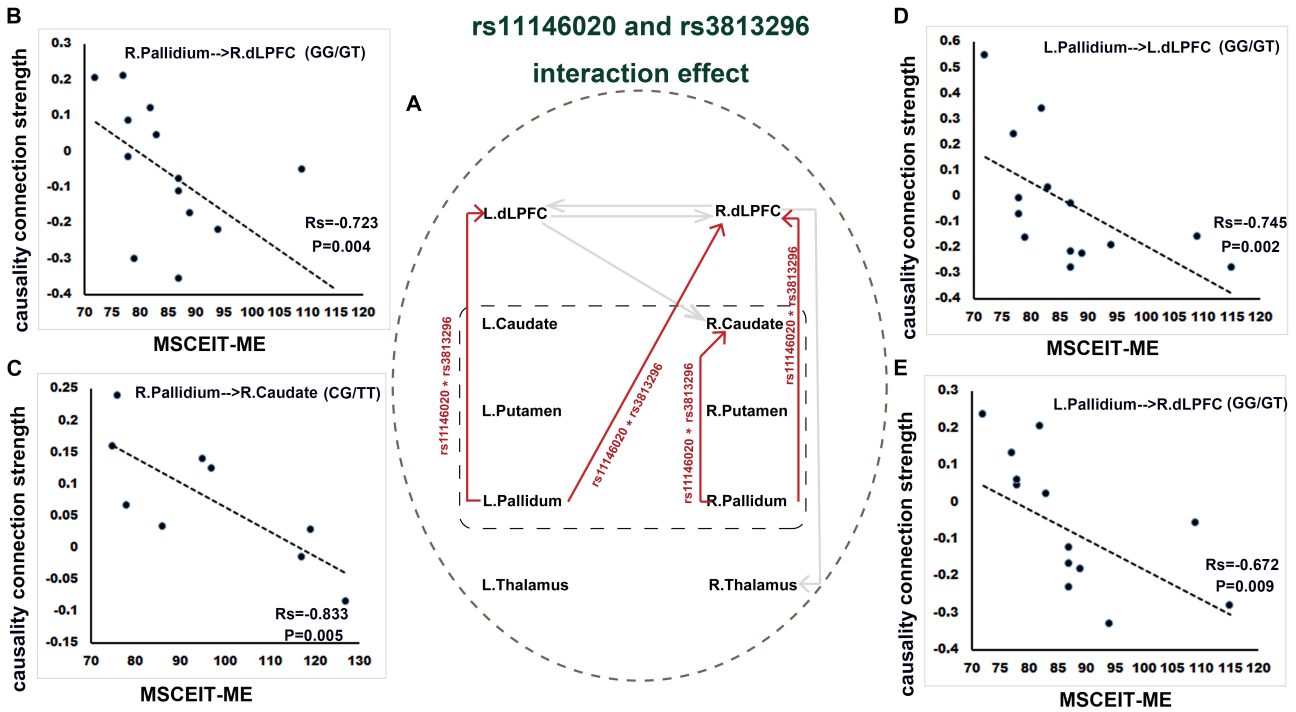

FIGURE 3 | Interaction effect of rs11146020 and rs3813296 on causality connections and relationship with behavioral variables ($P < 0.01$, FDR correction). **(A)** interaction effect of rs11146020 and rs3813296 on causality connections; causality connection strength of R. pallidum → R. dLPFC **(B)**, L. pallidum → L. dLPFC **(D)** and L. pallidum → R. dLPFC **(E)** has a significant negative correlation with MSCEIT-ME in patients with the GG/GT genotype; causality connection strength of R. pallidum → R. caudate **(C)** has a significant negative correlation with MSCEIT-ME in patients with the CG/TT genotype; Abbreviations: dLPFC, dorsolateral prefrontal cortex; MSCEIT-ME, Mayer-Salovey-Caruso emotional intelligence test (managing emotions).

radiata between GT and TT genotypes explains the lower connection strength of L. dLPFC → R. caudate in patients with the GT genotype: inflated volume of the superior corona radiata indirectly causes dispersive connection strength between the two regions.

Causality connection strengths of L. dLPFC → R. caudate and R. dLPFC → R. thalamus in patients with the TT genotype have a significant positive correlation with scores in VF and brief visuospatial memory tests. The functional anatomy of VF has been well characterized in normal participants using positron emission tomography (PET) (Spence et al., 1998). The study also demonstrated that generating words beginning with a given letter activates the dLPFC. Another study suggested that the thalamus is involved in the encoding of verbal material and that thalamic damage impairs verbal recall (Ruggeri, 2016). Benson et al. (2008) hypothesized that cognitive impairments could be related to the dysfunction of the physiological metabolic activity between the dLPFC and subcortical regions. In particular, hypoactivation of the dLPFC observed in schizophrenia patients could result in hyperactivation of subcortical structures, such as the striatum and thalamus (Groerewegen, 1991). Thus, the significant correlation suggested that VF and brief visuospatial memory tests scores have important clinical significance. As suggested in previous studies, it is also closely associated with the degeneration of the brain in schizophrenia patients (Zhang et al., 2012, 2014; Cetin-Karayumak et al., 2019). Further, recent research mentioned that words and visuospatial memory information are conveyed across aforesaid regions via the excitatory projections of glutamatergic pyramidal neurons (Hoftman et al., 2017; Nikolova et al., 2017). More importantly, the current results are especially helpful for reminding clinical researchers to pay attention to the first-episode negative schizophrenia patients with the TT genotype. These patients are vulnerable to VF and visual spatial memory. In the long run, patients with the TT genotype have different characteristic and should be treated using different clinical interventions.

Interaction Effect of rs11146020*rs3813296 on Causality Connectivity in the Frontal-Striatum-Thalamus Pathway

The interaction effects of rs11146020*rs3813296 on the causality connection are mainly located in the ascending pathway from the bilateral pallidum to the right caudate and bilateral dLPFC. After the interaction effect of the two SNPs, simple effect tests showed that modulation by rs11146020 on the causality connection of L. pallidum → R. dLPFC and L. pallidum → R. dLPFC is influenced by the GT genotype in rs3813296. Similarly, modulation by rs3813296 on the causality connection of R. pallidum → R. caudate is influenced by the GG genotype in rs11146020. Moreover, the interaction effect of the

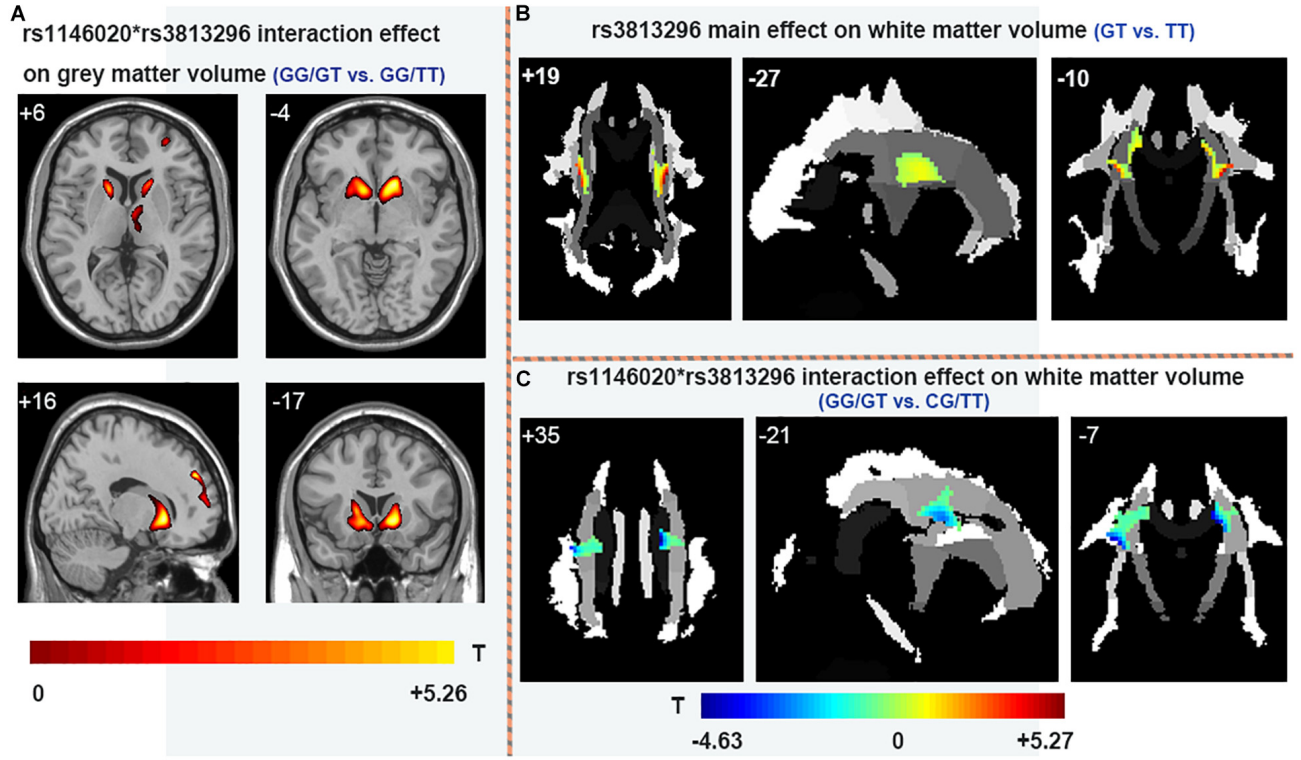

FIGURE 4 | Main and interaction effects of rs11146020 and rs3813296 on gray and white matter ($P < 0.01$, FDR correction). **(A)** rs11146020 and rs3813296 interaction effect on gray matter volume (GG/GT vs. GG/TT); **(B)** rs3813296 main effect on white matter volume (GT vs. TT); **(C)** rs11146020 and rs3813296 interaction effect on white matter volume (GG/GT vs. CG/TT).

two SNP is also on the gray and white matter volumes of several regions in this pathway, such as parts of the caudate, thalamus, putamen and fiber of the superior corona radiata. Taken together, these results imply that the effect of two SNPs on brain structure and function is greater than that of a single SNP. It is consistent with a comment provided by previous research that suggested that the risk of common diseases is potentially determined by the complex interaction between genetic factors, including SNPs (Lohmueller et al., 2003; Mechanic et al., 2008).

Moreover, four causality connections, among those mentioned, have a significant negative correlation with MSCEIT-ME scores. To understand the negative correlation between them, we investigated the literature and examined gamma aminobutyric acid (GABA) interneurons, which are purported to ultimately inhibit the generation of excessive mesolimbic dopamine activity (Stahl, 2007). Disturbances in GABA neurotransmission could represent a common pathophysiology for different domains of cortical dysfunction in schizophrenia (Hashimoto et al., 2008). For example, if the GABA interneuron was dysfunctional, it would lead to excessive suppression and produce decreasing activity. In the current study, the stronger the connectivity strength of the ascending pathway from the bilateral pallidum to the bilateral dLPFC, the stronger the inhibition projecting onto the dLPFC, leading to restrained glutamate release. Buzsáki and Draguhn (2004) demonstrated that the regulation or stabilization of GABA interneurons is critical for the coordination of cortical-mediated behaviors. The dLPFC is activated in emotion tasks and is a main region in managing emotion control (Aupperle et al., 2012). Thus, decreased release of glutamate excitatory neurotransmitter in dLPFC indirectly results in weak emotion management ability.

In addition, gray matter volumes of parts of bilateral caudate, thalamus and putamen in patients with the GG/GT genotype are larger than those with the GG/TT genotype. It was suggested that the T allele in rs3813296 was indirectly associated with inflated volume in these regions. In white matter, the volume of the superior corona radiata fiber in patients with the GG/GT genotype is lower than those with the CG/TT genotype. As mentioned above, the white matter of the corona radiata is the main joint component of the basal ganglia and striatum. Combining the two results regarding gray and white matter, we explained the opposite phenomenon (larger vs. lower) as increscent gray matter volumes (caudate, thalamus, and putamen) extruded contiguous white matter (superior corona radiata fiber) in patients with the GG/GT genotype. This interpretation is inspired by Alliey-Rodriguez et al. (2017).

Until now, we noticed that dLPFC is a key region in the frontal-striatum-thalamus pathway and has the strongest association with other regions. In particular, the causality connections of dLPFC exhibit a significant relationship with

TABLE 3 | Main and interaction effects of rs11146020 and rs3813296 on gray and white matter volumes.

rs11146020*rs3813296 inteaction effect on gray matter volumes					
GG/GT vs. GG/TT					
Brain region	**MNI**			***T* value**	***P* value**
	X	**Y**	**Z**		
L.Caudate/thalamus	−15	14	6	4.563	0.005
R. Caudate/thalamus	17	17	6	4.288	0.005
L.Putamen/caudate	−9	13	−4	4.892	0.004
R. Putamen/caudate	16	17	−4	5.184	0.002
rs3813296 main effect on white matter volumes					
GT vs. TT					
Brain region	**MNI**			***T* value**	***P* value**
	X	**Y**	**Z**		
L. Superior corona radiata	−26	−3	21	3.681	0.008
R. Superior corona radiata	26	−8	32	3.455	0.010
rs11146020*rs3813296 inteaction effect on white matter volumes					
GG/GT vs. CG/TT					
Brain region	**MNI**			***T* value**	***P* value**
	X	**Y**	**Z**		
L. Superior corona radiata	−16	−6	35	−3.47	0.009
R. Superior corona radiata	29	−10	35	−3.394	0.010

P and corresponding T values were obtained by two samples t-test (P < 0.01, FDR correction). X, Y, and Z from MNI (Montreal Neurological Institute) coordinates.

TABLE 4 | Significant correlation between causality connection strength and behavioral scales.

Causality connectivity	**Genotype**	**SNP**	**Clinical scales**	**Rs value**	***P* value**
L.dLPFC → R.dLPFC	GG	rs11146020	DUP	0.508	0.005
R.dLPFC → R.Caudate	TT	rs3813296	BVMT-R	0.516	0.01
R.dLPFC → R.Thalamus	TT	rs3813296	BVMT-R	0.535	0.007
R.dLPFC → R.Thalamus	TT	rs3813296	VF	0.52	0.009
R.Pallidum → R.dLPFC	GG/GT	GG:rs11146020 GT:rs3813296	MSCEIT-ME	−0.723	0.004
R.Pallidum → R.Caudate	CG/TT	CG:rs11146020 TT:rs3813296	MSCEIT-ME	−0.833	0.005
L.pallidum → L.dLPFC	GG/GT	GG:rs11146020 GT:rs3813296	MSCEIT-ME	−0.745	0.002
L.Pallidum → R.dLPFC	GG/GT	GG:rs11146020 GT:rs3813296	MSCEIT-ME	−0.672	0.009

Rs and P values were obtained from Spearman rank correlation test, P < 0.01, FDR correction. dLPFC, dorsolateral prefrontal cortex; DUP, duration of untreated psychosis; BVMT-R, brief visuospatial memory test, revised; VF, verbal fluency; MSCEIT-ME, Mayer-Salovey-Caruso emotional intelligence test, managing emotions.

clinical behaviors. The current results verified that dLPFC is an important region in the treatment or research of schizophrenia (Olagunju et al., 2017; Schneider et al., 2017).

Limitations

Two limitations of this study should be considered. First, there was a relatively small sample size in the four subgroups. Currently, gene and neuroimaging data are being collected, and we will replicate and verify these results using a larger sample in the near future. Additionally, the lack of knowledge about the relationships between the region-specific variation in glutamic neurotransmission and temporal patterns of GRIN1 and GRIA2 expression is a common concern to studies of neuroimaging genetics.

CONCLUSION

We investigated the main and interaction effects of rs11146020 and rs3813296 on causality connections and structural characteristics in the frontal-striatum-thalamus pathway in

Han Chinese patients with schizophrenia. Significant association was found between them, and causality connection strengths affected by two SNPs were remarkably correlated with clinical cognitive performance. Our results suggested that patients with different genotypes have different characteristics, and those patients should receive different clinical interventions.

DATA AVAILABILITY STATEMENT

The datasets generated in this study is publicly available on the SNP dataset repository: https://www.synapse.org/#!Synapse:syn21788916/tables/, with the following accession no: syn21788916.

ETHICS STATEMENT

The studies involving human participants were reviewed and approved by the Shanghai Mental Health Center Ethics Committee (Serial number: 2012-45). The participants or their legal guardian, provided their written informed consent to participate in this study.

AUTHOR CONTRIBUTIONS

SC and YL collected the data. KH and WZ analyzed the data and performed the measurements. SC wrote the manuscript. LH and JW had the major responsibility for preparing the manuscript. QW revised the manuscript.

FUNDING

This work was supported by the National Natural Science Foundation of China (grant nos. 81671778, 81801789, and 81671332); China Postdoctoral Science Foundation (grant no. 2017M623128); National Natural Science Foundation of Shaanxi Province of China (grant no. 2020JM-212); and the Fundamental Research Funds for the Central Universities (grant no. XJS201203).

REFERENCES

Alliey-Rodriguez, N., Grey, T. A., Shafee, R., Padmanabhan, J., Tandon, N., Klinger, M., et al. (2017). Common variants of NRXN1, LRP1B and RORA are associated with increased ventricular volumes in psychosis-GWAS findings from the B-SNIP deep phenotyping study. *bioRxiv*. [preprint]. doi: 10.1101/175489

Aupperle, R. L., Allard, C. B., Grimes, E. M., Simmons, A. N., Flagan, T., Behrooznia, M., et al. (2012). Dorsolateral prefrontal cortex activation during emotional anticipation and neuropsychological performance in posttraumatic stress disorder. *Arch. Gen. Psychiatry* 69, 360–371.

Begni, S., Moraschi, S., Bignotti, S., Fumagalli, F., Rillosi, L., Perez, J., et al. (2003). Association between the G1001C polymorphism in the GRIN1 gene promoter region and schizophrenia. *Biol. Psychiatry* 53, 617–619. doi: 10.1016/s0006-3223(02)01783-3

Benson, B. E., Willis, M. W., Ketter, T. A., Speer, A., Kimbrell, T. A., George, M. S., et al. (2008). Interregional cerebral metabolic associativity during a continuous performance task (Part II): differential alterations in bipolar and unipolar disorders. *Psychiatry Res. Neuroimaging* 164, 30–47. doi: 10.1016/j.pscychresns.2007.12.016

Buzsáki, G., and Draguhn, A. (2004). Neuronal oscillations in cortical networks. *Science* 304, 1926–1929. doi: 10.1126/science.1099745

Cai, S., Chong, T., Zhang, Y., Li, J., Von Deneen, K. M., Ren, J., et al. (2015). Altered functional connectivity of fusiform gyrus in subjects with amnestic mild cognitive impairment: a resting-state fMRI study. *Front. Hum. Neurosci.* 9:471. doi: 10.3389/fnhum.2015.00471

Cai, S., Jiang, Y., Wang, Y., Wu, X., Ren, J., Lee, M. S., et al. (2017a). Modulation on brain gray matter activity and white matter integrity by APOE ε4 risk gene in cognitively intact elderly: a multimodal neuroimaging study. *Behav. Brain Res.* 322, 100–109. doi: 10.1016/j.bbr.2017.01.027

Cai, S., Peng, Y., Chong, T., Zhang, Y. M., Von Deneen, K., Huang, L., et al. (2017b). Differentiated effective connectivity patterns of the executive control network in progressive MCI: a potential biomarker for predicting AD. *Curr. Alzheimer Res.* 14, 937–950.

Carlsson, A., Waters, N., and Carlsson, M. L. (1999). Neurotransmitter interactions in schizophrenia—therapeutic implications. *Biol. Psychiatry* 46, 1388–1395. doi: 10.1016/s0006-3223(99)00117-1

Cetin-Karayumak, S., Di Biase, M. A., Chunga, N., Reid, B., Somes, N., Lyall, A. E., et al. (2019). White matter abnormalities across the lifespan of schizophrenia: a harmonized multi-site diffusion MRI study. *Mol. Psychiatry*.

Chao-Gan, Y., and Yu-Feng, Z. (2010). DPARSF: a MATLAB toolbox for "pipeline" data analysis of resting-state fMRI. *Fron. Syst. Neurosci.* 4:13. doi: 10.3389/fnsys.2010.00013

Choi, D. W. (1988). Glutamate neurotoxicity and diseases of the nervous system. *Neuron* 1, 623–634. doi: 10.1016/0896-6273(88)90162-6

Crisafulli, C., Chiesa, A., De, R. D., Han, C., Lee, S. J., Park, M. H., et al. (2012). Influence of GRIA1, GRIA2 and GRIA4 polymorphisms on diagnosis and response to antipsychotic treatment in patients with schizophrenia. *Neurosci. Lett.* 506, 170–174. doi: 10.1016/j.neulet.2011.10.074

Dauvermann, M. R., Lee, G., and Dawson, N. (2017). Glutamatergic regulation of cognition and functional brain connectivity: insights from pharmacological, genetic and translational schizophrenia research. *Br. J. Pharmacol.* 174, 3136–3160. doi: 10.1111/bph.13919

Derkach, V. A., Oh, M. C., Guire, E. S., and Soderling, T. R. (2007). Regulatory mechanisms of AMPA receptors in synaptic plasticity. *Nat. Rev. Neurosci.* 8, 101. doi: 10.1038/nrn2055

Friston, K. J., Williams, S., Howard, R., Frackowiak, R. S., and Turner, R. (1996). Movement-related effects in fMRI time-series. *Magn. Reson. Med.* 35, 346–355. doi: 10.1002/mrm.1910350312

Gareeva, A. (2018). Peculiarities of the effect of antipsychotics: pharmacogenetic studies. *Hum. Physiol.* 44, 706–719. doi: 10.1134/s0362119718050031

Garthwaite, J., and Balazs, R. (1978). Supersensitivity to the cyclic GMP response to glutamate during cerebellar maturation. *Nature* 275, 328–329. doi: 10.1038/275328a0

Granger, C. W. (1969). Investigating causal relations by econometric models and cross-spectral methods. *Econometrica* 37, 424–438.

Gray, A., Hyde, T., Deep-Soboslay, A., Kleinman, J., and Sodhi, M. (2015). Sex differences in glutamate receptor gene expression in major depression and suicide. *Mol. Psychiatry* 20, 1057–1068. doi: 10.1038/mp.2015.91

Groerewegen, H. (1991). "Functional anatomy of the ventral, limbic system-innervated striatum," in *The Mesolimbic Dopaminec System: From Motivation to Action*, eds P. Willner and J. Scheel-Krüger (Hoboken, NJ: Wiley), 19–59.

Gründer, G., and Cumming, P. (2016). "The dopamine hypothesis of schizophrenia: Current status," in *The Neurobiology of Schizophrenia*, eds T. Abel and T. Nickl-Jockschat (Amsterdam: Elsevier), 109–124.

Han, S., An, Z., Luo, X., Zhang, L., Zhong, X., Du, W., et al. (2018). Association between CMYA5 gene polymorphisms and risk of schizophrenia in U ygur population and a meta-analysis. *Early Interv. Psychiatry* 12, 15–21. doi: 10.1111/eip.12276

Hashimoto, T., Bazmi, H. H., Mirnics, K., Wu, Q., Sampson, A. R., and Lewis, D. A. (2008). Conserved regional patterns of GABA-related transcript expression in the neocortex of subjects with schizophrenia. *Am. J. Psychiatry* 165, 479–489. doi: 10.1176/appi.ajp.2007.07081223

Hoftman, G. D., Dienel, S. J., Bazmi, H. H., Zhang, Y., Chen, K., and Lewis, D. A. (2017). Altered gradients of glutamate and gamma-aminobutyric acid transcripts in the cortical visuospatial working memory network in schizophrenia. *Biol. Psychiatry* 83, 670–679. doi: 10.1016/j.biopsych.2017.11.029

Huganir, R. L., and Nicoll, R. A. (2013). AMPARs and synaptic plasticity: the last 25 years. *Neuron* 80, 704–717. doi: 10.1016/j.neuron.2013.10.025

Hung, C.-C., Chen, H.-Y., and Chen, C.-H. (2002). Systematic mutation analysis of the human glutamate receptor, ionotropic, N-methyl-D-aspartate 1 gene (GRIN1) in schizophrenic patients. *Psychiatr. Genet.* 12, 225–230. doi: 10.1097/00041444-200212000-00005

Iamjan, S. A., Thanoi, S., Watiktinkorn, P., Reynolds, G. P., and Nudmamudthanoi, S. (2018). Genetic variation of GRIA3 gene is associated with vulnerability to methamphetamine dependence and its associated psychosis. *J. Psychopharmacol.* 32, 309–315. doi: 10.1177/0269881117750153

Isaac, J. T., Ashby, M. C., and Mcbain, C. J. (2007). The role of the GluR2 subunit in AMPA receptor function and synaptic plasticity. *Neuron* 54, 859–871. doi: 10.1016/j.neuron.2007.06.001

Jagannath, V., Gerstenberg, M., Correll, C. U., Walitza, S., and Grünblatt, E. (2018). A systematic meta-analysis of the association of neuregulin 1 (NRG1), D-amino acid oxidase (DAO), and DAO activator (DAOA)/G72 polymorphisms with schizophrenia. *J. Neural. Transm.* 125, 89–102. doi: 10.1007/s00702-017-1782-z

Keinanen, K., Wisden, W., Sommer, B., Werner, P., Herb, A., Verdoorn, T. A., et al. (1990). A family of AMPA-selective glutamate receptors. *Science* 249, 556–560. doi: 10.1126/science.2166337

Lake, B. B., Ai, R., Kaeser, G. E., Salathia, N. S., Yung, Y. C., Liu, R., et al. (2016). Neuronal subtypes and diversity revealed by single-nucleus RNA sequencing of the human brain. *Science* 352, 1586–1590. doi: 10.1126/science.aaf1204

Lau, C. G., and Zukin, R. S. (2007). NMDA receptor trafficking in synaptic plasticity and neuropsychiatric disorders. *Nat. Rev. Neurosci.* 8, 413–426. doi: 10.1038/nrn2153

Liu, Y.-P., Ding, M., Zhang, X.-C., Liu, Y., Xuan, J.-F., Xing, J.-X., et al. (2019). Association between polymorphisms in the GRIN1 gene 5' regulatory region and schizophrenia in a northern Han Chinese population and haplotype effects on protein expression in vitro. *BMC Med. Genet.* 20:26. doi: 10.1186/s12881-019-0757-3

Lohmueller, K. E., Pearce, C. L., Pike, M., Lander, E. S., and Hirschhorn, J. N. (2003). Meta-analysis of genetic association studies supports a contribution of common variants to susceptibility to common disease. *Nat. Genet.* 33, 177–182. doi: 10.1038/ng1071

Lu, W., Shi, Y., Jackson, A. C., Bjorgan, K., During, M. J., Sprengel, R., et al. (2009). Subunit composition of synaptic AMPA receptors revealed by a single-cell genetic approach. *Neuron* 62, 254–268. doi: 10.1016/j.neuron.2009.02.027

Marx, M. C., Billups, D., and Billups, B. (2015). Maintaining the presynaptic glutamate supply for excitatory neurotransmission. *J. Neurosci. Res.* 93, 1031–1044. doi: 10.1002/jnr.23561

Mechanic, L. E., Luke, B. T., Goodman, J. E., Chanock, S. J., and Harris, C. C. (2008). Polymorphism Interaction Analysis (PIA): a method for investigating complex gene-gene interactions. *BMC Bioinform.* 9:146. doi: 10.1186/1471-2105-9-146

Meijer, H. A., and Thomas, A. A. (2002). Control of eukaryotic protein synthesis by upstream open reading frames in the 5'-untranslated region of an mRNA. *Biochem. J.* 367, 1–11. doi: 10.1042/bj20011706

Mohn, A. R., Gainetdinov, R. R., Caron, M. G., and Koller, B. H. (1999). Mice with reduced NMDA receptor expression display behaviors related to schizophrenia. *Cell* 98, 427–436. doi: 10.1016/s0092-8674(00)81972-8

Morecraft, R. J., Herrick, J. L., Stilwell-Morecraft, K. S., Louie, J. L., Schroeder, C. M., Ottenbacher, J. G., et al. (2002). Localization of arm representation in the corona radiata and internal capsule in the non-human primate. *Brain* 125, 176–198. doi: 10.1093/brain/awf011

Nakanishi, S., Nakajima, Y., Masu, M., Ueda, Y., Nakahara, K., Watanabe, D., et al. (1998). Glutamate receptors: brain function and signal transduction1. *Brain Res. Rev.* 26, 230–235. doi: 10.1016/s0165-0173(97)00033-7

Nikolova, S., Stark, S. M., and Cel, S. (2017). 3T hippocampal glutamate-glutamine complex reflects verbal memory decline in aging. *Neurobiol. Aging* 54, 103–111. doi: 10.1016/j.neurobiolaging.2017.01.026

Olagunju, A., Clark, S., and Baune, B. (2017). Transcranial magnetic stimulation of the dorsolateral prefrontal cortex: a review of methods and utility in psychiatry. *Biol. Psychiatry* 81:S132.

Power, J. D., Barnes, K. A., Snyder, A. Z., Schlaggar, B. L., and Petersen, S. E. (2012). Spurious but systematic correlations in functional connectivity MRI networks arise from subject motion. *Neuroimage* 59, 2142–2154. doi: 10.1016/j.neuroimage.2011.10.018

Reimers, J. M., Milovanovic, M., and Wolf, M. E. (2011). Quantitative analysis of AMPA receptor subunit composition in addiction-related brain regions. *Brain Res.* 1367, 223. doi: 10.1016/j.brainres.2010.10.016

Ripke, S., Neale, B. M., Corvin, A., Walters, J. T., Farh, K.-H., Holmans, P. A., et al. (2014). Biological insights from 108 schizophrenia-associated genetic loci. *Nature* 511, 421–427. doi: 10.1038/nature13595

Rubio, J. M., and Correll, C. U. (2017). Duration and relevance of untreated psychiatric disorders, 2: nonpsychotic psychiatric disorders and substance use disorders. *J. Clin. Psychiatry* 78, 464–465. doi: 10.4088/jcp.17ac11544

Ruggeri, M. (2016). Left dorsomedial thalamic damage impairs verbal recall more than recognition: a case report. *Cogn. Behav. Neurol.* 29, 158–165. doi: 10.1097/wnn.0000000000000103

Saini, S. M., Mancuso, S., Mostaid, M. S., Liu, C., Pantelis, C., Everall, I., et al. (2017). Meta-analysis supports GWAS-implicated link between GRM3 and schizophrenia risk. *Transl. Psychiatry* 7:e1196. doi: 10.1038/tp.2017.172

Schneider, M., Walter, H., Moessnang, C., Schã¤Fer, A., Erk, S., Mohnke, S., et al. (2017). Altered DLPFC-Hippocampus connectivity during working memory: independent replication and disorder specificity of a putative genetic risk phenotype for schizophrenia. *Schizophr. Bull.* 43, 1114–1122. doi: 10.1093/schbul/sbx001

Schwartz, T. L., Sachdeva, S., and Stahl, S. M. (2012). Glutamate neurocircuitry: theoretical underpinnings in schizophrenia. *Front. Pharmacol.* 3:195. doi: 10.3389/fphar.2012.00195

Song, X.-W., Dong, Z.-Y., Long, X.-Y., Li, S.-F., Zuo, X.-N., Zhu, C.-Z., et al. (2011). REST: a toolkit for resting-state functional magnetic resonance imaging data processing. *PLoS One* 6:e25031. doi: 10.1371/journal.pone.0025031

Spence, S. A., Hirsch, S. R., Brooks, D. J., and Grasby, P. M. (1998). Prefrontal cortex activity in people with schizophrenia and control subjects: evidence from positron emission tomography for remission of 'hypofrontality'with recovery from acute schizophrenia. *Br. J. Psychiatry* 172, 316–323. doi: 10.1192/bjp.172.4.316

Stahl, S. M. (2007). Beyond the dopamine hypothesis to the NMDA glutamate receptor hypofunction hypothesis of schizophrenia. *CNS Spectr.* 12, 265–268. doi: 10.1017/s1092852900021015

Tatard-Leitman, V. M., Jutzeler, C. R., Suh, J., Saunders, J. A., Billingslea, E. N., Morita, S., et al. (2015). Pyramidal cell selective ablation of N-methyl-D-aspartate receptor 1 causes increase in cellular and network excitability. *Biol. Psychiatry* 77, 556–568. doi: 10.1016/j.biopsych.2014.06.026

Traynelis, S. F., Wollmuth, L. P., Mcbain, C. J., Menniti, F. S., Vance, K. M., Ogden, K. K., et al. (2010). Glutamate receptor ion channels: structure, regulation, and function. *Pharmacol. Rev.* 62, 405–496.

Wilkie, G. S., Dickson, K. S., and Gray, N. K. (2003). Regulation of mRNA translation by 5'-and 3'-UTR-binding factors. *Trends Biochem. Sci.* 28, 182–188. doi: 10.1016/s0968-0004(03)00051-3

Yan, C. G., Cheung, B., Kelly, C., Colcombe, S., Craddock, R. C., Di Martino, A., et al. (2013). A comprehensive assessment of regional variation in the impact of head micromovements on functional connectomics. *Neuroimage* 76, 183–201. doi: 10.1016/j.neuroimage.2013.03.004

Yan, C.-G., Wang, X.-D., Zuo, X.-N., and Zang, Y.-F. (2016). DPABI: data processing & analysis for (Resting-State) brain imaging. *Neuroinformatics* 14, 339–351. doi: 10.1007/s12021-016-9299-4

Yang, A. C., and Tsai, S.-J. (2017). New targets for schizophrenia treatment beyond the dopamine hypothesis. *Int. J. Mol. Sci.* 18:1689. doi: 10.3390/ijms18081689

Zhang, Y., Lin, L., Lin, C. P., Zhou, Y., Chou, K. H., Lo, C. Y., et al. (2012). Abnormal topological organization of structural brain networks in schizophrenia. *Schizophr. Res.* 141, 109–118. doi: 10.1016/j.schres.2012.08.021

Zhang, Y., Su, T. P., Liu, B., Zhou, Y., Chou, K. H., Lo, C. Y., et al. (2014). Disrupted thalamo-cortical connectivity in schizophrenia: a morphometric correlation analysis. *Schizophr. Res.* 153, 129–135. doi: 10.1016/j.schres.2014.01.023

Zhao, X., Li, H., Shi, Y., Tang, R., Chen, W., Liu, J., et al. (2006). Significant association between the genetic variations in the 5' end of the N-methyl-D-aspartate receptor subunit gene GRIN1 and schizophrenia. *Biol. Psychiatry* 59, 747–753. doi: 10.1016/j.biopsych.2005.10.023

Zhu, S., Stein, R. A., Yoshioka, C., Lee, C.-H., Goehring, A., Mchaourab, H. S., et al. (2016). Mechanism of NMDA receptor inhibition and activation. *Cell* 165, 704–714. doi: 10.1016/j.cell.2016.03.028

Conflict of Interest: The authors declare that the research was conducted in the absence of any commercial or financial relationships that could be construed as a potential conflict of interest.

frontiers in Human Neuroscience

ORIGINAL RESEARCH
published: 21 April 2020
doi: 10.3389/fnhum.2020.00103

Cross-Dataset Variability Problem in EEG Decoding With Deep Learning

Lichao Xu[1†], *Minpeng Xu*[1,2†], *Yufeng Ke*[1], *Xingwei An*[1], *Shuang Liu*[1] *and Dong Ming*[1,2*]

[1] *Academy of Medical Engineering and Translational Medicine, Tianjin University, Tianjin, China,* [2] *Department of Biomedical Engineering, College of Precision Instruments and Optoelectronics Engineering, Tianjin University, Tianjin, China*

Cross-subject variability problems hinder practical usages of Brain-Computer Interfaces. Recently, deep learning has been introduced into the BCI community due to its better generalization and feature representation abilities. However, most studies currently only have validated deep learning models for single datasets, and the generalization ability for other datasets still needs to be further verified. In this paper, we validated deep learning models for eight MI datasets and demonstrated that the cross-dataset variability problem weakened the generalization ability of models. To alleviate the impact of cross-dataset variability, we proposed an online pre-alignment strategy for aligning the EEG distributions of different subjects before training and inference processes. The results of this study show that deep learning models with online pre-alignment strategies could significantly improve the generalization ability across datasets without any additional calibration data.

Keywords: brain-computer interface, cross-subject variability, cross-dataset variability, deep learning, transfer learning, EEG

OPEN ACCESS

Edited by:
Junhua Li,
University of Essex, United Kingdom

Reviewed by:
Ren Xu,
Guger Technologies, Austria
Dongrui Wu,
Huazhong University of Science and Technology, China
Sung Chan Jun,
Gwangju Institute of Science and Technology, South Korea

***Correspondence:**
Dong Ming
richardming@tju.edu.cn

[†] *These authors have contributed equally to this work*

Specialty section:
This article was submitted to Brain-Computer Interfaces, a section of the journal Frontiers in Human Neuroscience

Received: *09 December 2019*
Accepted: *05 March 2020*
Published: *21 April 2020*

Citation:
Xu L, Xu M, Ke Y, An X, Liu S and Ming D (2020) Cross-Dataset Variability Problem in EEG Decoding With Deep Learning. Front. Hum. Neurosci. 14:103. doi: 10.3389/fnhum.2020.00103

1. INTRODUCTION

Brain-Computer Interfaces (BCIs) enable humans to directly control machines via brain signals without any physical intervention (Wolpaw et al., 2002). A typical BCI system consists of three parts: paradigms, neuroimaging techniques, and decoding algorithms. Paradigms are mental tasks that invoke brain activities while the corresponding brain signals are recorded by neuroimaging techniques. Researchers prefer electroencephalography (EEG) among various neuroimaging techniques because of its non-invasive, high temporal resolution, and low-cost characteristics. Decoding algorithms further translate measured brain signals into commands to control computerized devices.

Decoding algorithms are crucial to achieving an efficient and robust BCI system. Over the past 20 years, many effective BCI decoding algorithms have been proposed due to advances in machine learning. Most decoding algorithms extract discriminant features with well-designed spatial filters for improving within-subject classification accuracy. Common Spatial Pattern (CSP) and its variants (Ramoser et al., 2000; Grosse-Wentrup and Buss, 2008; Kai Keng Ang et al., 2008; Lotte and Guan, 2011; Samek et al., 2012) are still most commonly used algorithms for motor imagery (MI) paradigm. For the steady-state visually evoked potential (SSVEP) paradigm, Canonical Correlation Analysis (CCA) (Lin et al., 2007) and Task-related Component Analysis (TRCA) (Nakanishi et al., 2018) are able to improve the speed of SSVEP-based BCI spellers. xDAWN (Rivet et al., 2009) and DCPM (Xu et al., 2018) algorithms are also perform well on P300-based BCI applications. Recently, algorithms based on Riemannian geometry have been introduced into the BCI community, and they provide a unified signal processing framework for decoding brain signals (Barachant et al., 2010; Congedo et al., 2013, 2017a; Lotte et al., 2018). However, most

algorithms are unable to reuse pre-trained models across subjects or different sessions of the same subject. These two problems in BCI are referred to as cross-subject and cross-session variability problems. To reduce high variability in individual EEG data, a calibration stage is required to collect training data at the beginning of each session, which is inconvenient for both patients and healthy subjects.

A natural idea for decoding brain signals is to use deep learning models instead of handcrafted feature extraction methods. Manual feature extraction reduces the possibility of utilizing information across subjects. Deep learning utilizes all information in data to train a robust classifier, which often outperforms other machine learning models in classification tasks. Some deep learning models [e.g., Shallow ConvNet (Schirrmeister et al., 2017), EEGNet (Lawhern et al., 2018)] can achieve better performance than traditional methods in within-subject classification task.

Deep learning is also able to ameliorate cross-session and cross-subject variability problems with its robust feature extraction architecture. However, deep learning models used in BCI suffer the lack of data problem. It is hard to collect a sufficient amount of high-quality training data for a specific BCI task. The lack of data problems makes deep learning models easily overfit. Some data augmentation methods may alleviate the overfitting problem for within-subject classification tasks (Wang et al., 2018; Dai et al., 2020). For cross-subject classification tasks, an easier way is to train the model directly on the entire dataset regardless of subject-specific information (Schirrmeister et al., 2017; Lawhern et al., 2018). In practice, however, we found that a pre-trained model from one public dataset may fail to predict new data from another public dataset even if the model performs well on its training dataset. The model is highly specialized in its training dataset structure that a minor change to the test data may make the model invalid. A similar phenomenon was reported in Jayaram and Barachant (2018), where the authors found that the performance of classical supervised BCI algorithms depends on the specific dataset. A public dataset is usually acquired under the same condition in the same lab. Can an algorithm that performs well on one dataset work on another dataset under different conditions? Currently, most studies have only validated the use of deep learning models for a specific dataset, and the generalization ability for other datasets still needs to be further verified. The cross-dataset variability problem in deep learning was proved in our cross-dataset experiment.

In this work, we studied the cross-dataset variability problem of deep learning models. We validated deep learning models across multiple datasets and observed that the optimal model trained for one dataset performs significantly worse on other datasets. The results indicate that deep learning models for BCIs are unable to generalize well outside the training dataset. To alleviate the impact of cross-dataset variability, we introduced an online pre-alignment strategy before the training and validation processes. The results demonstrate that deep learning models with online pre-alignment strategy have better generalization ability across EEG datasets.

2. MATERIALS AND METHODS

2.1. Datasets

Eight MI datasets were used in our experiments (Schalk et al., 2004; Leeb et al., 2007; Tangermann et al., 2012; Yi et al., 2014; Zhou et al., 2016; Cho et al., 2017). All datasets are publicly available and details of them are listed in **Table 1**. CNBCIC2019004 and CBCIC2019004 datasets were downloaded from the 3rd China Brain-computer Interface Competition website. The rest of datasets were downloaded using the MOABB package (Jayaram and Barachant, 2018).

Three channels (C3, CZ, C4) were used in this work. These channels are located on sensorimotor area and exist in all datasets. Only the left-hand and right-hand MI classes were included in our experiments. Each trial was 3 s in length and downsampled to 100 Hz such that the size of a trial was 3×300. All trials were filtered with a 4-order Butterworth bandpass filter of 3–40 Hz. Zero-phase forward and reverse filtering was implemented using filter_data() function in MNE (Gramfort et al., 2013).

For evaluating performance of models, trials were randomly split into training, validation, and test sets. The training set was 80% of the available data. The remaining 20% data were equally partitioned and referred to as validation and test sets. This splitting process was repeated 10 times on each subject, producing 10 different folds.

2.2. Notation

In this section, we give the notation and assumptions used throughout the paper. An overview of the notation is listed in **Table 2**. We assume that the EEG data of each channel is zero mean. This assumption is reasonable in the real world which also widely adopted in many BCI algorithms (Ramoser et al., 2000; Grosse-Wentrup and Buss, 2008). All algorithms below are described with the two-class classification problem in MI paradigm.

2.3. Traditional Decoding Methods

2.3.1. CSP

The goal of CSP is to find a projection matrix $W = [w_1, w_2, \cdots, w_L]$, that leads to new time series $\hat{E} = W^T E$, which maximizes the discriminance between classes. The CSP algorithm solves the following optimization problem

$$w^* = \underset{w_i \in \mathbb{R}^{N_c}, i \in \{1,2,\cdots,L\}}{\operatorname{argmax}} \frac{w_i^T \bar{C}^1 w_i}{w_i^T \bar{C}^2 w_i} \tag{1}$$

with $\bar{C}^1, \bar{C}^2$ are average normalized covariance matrices of each class obtained from

$$\bar{C}^k = \sum_{i=1}^{N_t^k} \frac{E_i^k E_i^{k\,T}}{\operatorname{tr}(E_i^k E_i^{k\,T})} \tag{2}$$

where N_t^k is the number of trials of class k, $k \in \{1, 2\}$ and $\operatorname{tr}(\cdot)$ denotes the trace operator. Solutions to (1) are given by eigenvectors of the generalized eigenvalue problem

$$\bar{C}^1 w_i = \lambda_i \bar{C}^2 w_i \tag{3}$$

TABLE 1 | Details of datasets.

Dataset	Classes	Subjects	Trials per class	Trial duration (s)	Channels	Sampling rate (Hz)
BNCI2014001	Left/right/feet/tongue	9	144	4	22	250
BNCI2014004	Left/right	9	360	4.5	3	250
PhysionetMI	Left/right/hands/feet	109	20–30	3	64	250
Cho2017	Left/right	52	100	3	64	512
Weibo2014	Left/right/hands/feet	10	80	4	60	200
Zhou2016	Left/right/feet	4	160	5	14	250
CBCIC2019001	Left/right	18	60	4	59	1000
CBCIC2019004	Left/right	6	40	4	59	250

TABLE 2 | Symbols and notations.

Symbol	Description
N_t	Number of trials
N_c	Number of channels
N_s	Number of samples
E_i	EEG data matrix of a single trial, $E_i \in \mathbb{R}^{N_c \times N_s}$
C_i	Covariance of E_i, $C_i \in \mathbb{R}^{N_c \times N_c}$
W	Spatial filter matrix, $W \in \mathbb{R}^{N_c \times L}, L \leq N_c$
w_i	A spatial filter vector, $w_i \in \mathbb{R}^{N_c}, W = [w_1, w_2, \cdots, w_L]$

where eigenvalues are sorted in descending order. CSP selects eigenvectors with the $L/2$ largest/smallest eigenvalues to form projection matrix W, which is also named spatial filters. The feature vector $f_i \in \mathbb{R}^L$ of E_i is given by

$$f_i = \log\left(\frac{\text{var}(W^T E_i)}{\sum \text{var}(W^T E_i)}\right) \tag{4}$$

where var(·) denotes the variance operator on each row of $\hat{E}_i$ and log(·) denotes the logarithm operator of elements. CSP is usually followed by a linear or non-linear classifier to classify test data.

2.3.2. FBCSP

The Filter Bank Common Spatial Pattern (FBCSP) (Kai Keng Ang et al., 2008) extends the CSP algorithm to EEG data with multiple frequency bands. The goal of FBCSP is to address the problem of manually selecting the subject-specific frequency band for the CSP algorithm. The key step in FBCSP is feature selection, which selects a subset of features that leads to the smallest classification error. FBCSP estimates the importance of each feature vector with mutual information and selects the L most important w to form the projection matrix W used in (4).

2.3.3. MDRM

The Minimum Distance to Riemannian Mean (MDRM) (Barachant et al., 2011) is an algorithm based on Riemannian Geometry. Riemannian Geometry considers matrix C_i as a point in a Riemannian manifold. MDRM computes the Riemannian center of each class and compares Riemannian distances from test points to centers. The Riemannian distance of two covariance matrices C_1, C_2 is given by

$$\delta_{\text{R}}(C_1, C_2) = \|\text{Log}(C_1^{-1} C_2)\|_F = \left[\sum_{i=1}^{N_c} \log^2(\lambda_i)\right]^{1/2} \tag{5}$$

where Log(·) is the logarithm operator of a matrix, and λ_i is the i-th eigenvalue of matrix $C_1^{-1} C_2$. The Riemannian center $\bar{C}_R^k$ of each class is defined as follows

$$\bar{C}_R^k = \underset{\bar{C}_R^k}{\text{argmin}} \sum_{i=1}^{N_t^k} \delta_{\text{R}}(\bar{C}_R^k, C_i^k) \tag{6}$$

with $k \in \{1, 2\}$. Although there is no closed form solution to (6) when $N_t^k > 2$, the problem can be solved with iterative algorithms (Moakher, 2005; Pennec et al., 2006; Congedo et al., 2017b). With Riemannian centers, a new test covariance C_{test} is classified as follows:

$$\underset{k \in \{1,2\}}{\text{argmin}}\, \delta_{\text{R}}(\bar{C}_R^k, C_{test}) \tag{7}$$

2.4. Deep Learning Models

2.4.1. ShallowNet

ShallowNet (Schirrmeister et al., 2017) imitates FBCSP's design in the deep learning structure. The architecture of ShallowNet is listed in **Table 3**. The first convolution layer is designed to convolve in a temporal direction, which is analogous to bandpass filtering. The second convolution layer is designed to convolve in a spatial direction, which is analogous to spatial filters in CSP. Shallow ConvNet uses a squaring activation function and average pooling layer to imitate feature mapping in (5). Instead of mutual information selection in FBCSP, ShallowNet uses a fully connected layer to combine all features and predict probabilities of classes.

2.4.2. EEGNet

EEGNet is a CNN-based model proposed by Lawhern et al. (2018). The architecture of EEGNet is listed in **Table 4**. EEGNet is designed for general EEG recognition tasks. EEGNet retains temporal and spatial convolution layers in Shallow ConvNet. Instead of simple convolution in ShallowNet, EEGNet introduces

TABLE 3 | ShallowNet architecture.

Layer	Input size	Output size	Kernels	Kernel size	Stride	Padding
Conv2d	1 × 3 × 300	10 × 3 × 300	10	(1, 21)	(1, 1)	(0, 10)
BatchNorm2d	10 × 3 × 300	10 × 3 × 300				
Conv2d	10 × 3 × 300	15 × 1 × 300	15	(3, 1)	(1, 1)	(0, 0)
BatchNorm2d	15 × 1 × 300	15 × 1 × 300				
Pow2	15 × 1 × 300	15 × 1 × 300				
AvgPool2d	15 × 1 × 300	15 × 1 × 17		(1, 55)	(1, 15)	(0, 0)
Log	15 × 1 × 17	15 × 1 × 17				
Dropout	15 × 1 × 17	15 × 1 × 17				
Linear	255	2				

TABLE 4 | EEGNet architecture.

Layer	Input size	Output size	Kernels	Kernel size	Stride	Padding
Conv2d	1 × 3 × 300	8 × 3 × 300	8	(1, 31)	(1, 1)	(0, 15)
BatchNorm2d	8 × 3 × 300	8 × 3 × 300				
Depthwise Conv2d	8 × 3 × 300	16 × 1 × 300	16	(3, 1)	(1, 1)	(0, 0)
BatchNorm2d	16 × 1 × 300	16 × 1 × 300				
Elu	16 × 1 × 300	16 × 1 × 300				
AvgPool2d	16 × 1 × 300	16 × 1 × 75		(1, 4)	(1, 4)	(0, 0)
Dropout	16 × 1 × 75	16 × 1 × 75				
Seperable Conv2d	16 × 1 × 75	16 × 1 × 75	16	(1, 15)	(1, 1)	(0, 7)
BatchNorm2d	16 × 1 × 75	16 × 1 × 75				
Elu	16 × 1 × 75	16 × 1 × 75				
AvgPool2d	16 × 1 × 75	16 × 1 × 9		(1, 8)	(1, 8)	(0, 0)
Dropout	16 × 1 × 9	16 × 1 × 9				
Linear	144	2				

depthwise separable convolution (Chollet, 2017) to reduce the number of training parameters. EEGNet also replaces squaring activation with ELU activation.

2.5. Online Pre-alignment Strategy

Recently, many Transfer Learning approaches have been introduced into BCIs to reduce cross-subject variability (Zanini et al., 2018; Rodrigues et al., 2019; Yair et al., 2019). An approach named Riemannian Procrustes Analysis (RPA) was proposed by Rodrigues et al. (2019). RPA takes three steps to match data distributions of source domain and target domain: re-centering, stretching, and rotation. The re-centering step aligns the Riemannian center of covariance matrices to identity matrix. The stretching step modulates dispersions of two domains to the same level. The rotation step further rotates matrices from target domain to match that of source domain with predetermined markers. The re-centering step has also been mentioned in Reuderink et al. (2011) and Zanini et al. (2018) as follows

$$\hat{C}_i = M^{-1/2} C_i M^{-1/2} \tag{8}$$

where M is the Riemannian center of training covariances and $\hat{C}_i$ is the aligned covariance matrix. In this work, we applied re-centering step before the training and validation processes, and this is named the pre-alignment strategy (PS). Instead of direct operation on covariances, we transformed E_{i+1} to aligned time series $\hat{E}_{i+1}$ by

$$\hat{E}_i = \frac{1}{N_s} M^{-1/2} E_i \tag{9}$$

The above transformation has also been mentioned in He and Wu (2020), where the authors used Euclidean mean covariance instead of Riemannian mean covariance M here. Although PS is an unsupervised method, they still require enough calibration data of each subject to compute the expected Riemannian center M. We implemented an online pre-alignment strategy (OPS) on continuous EEG data for each subject. Assuming that M_i is the Riemannian mean of previous available covariances, E_{i+1} is the EEG data of the next trial, and C_{i+1} is the covariance of E_{i+1}. A

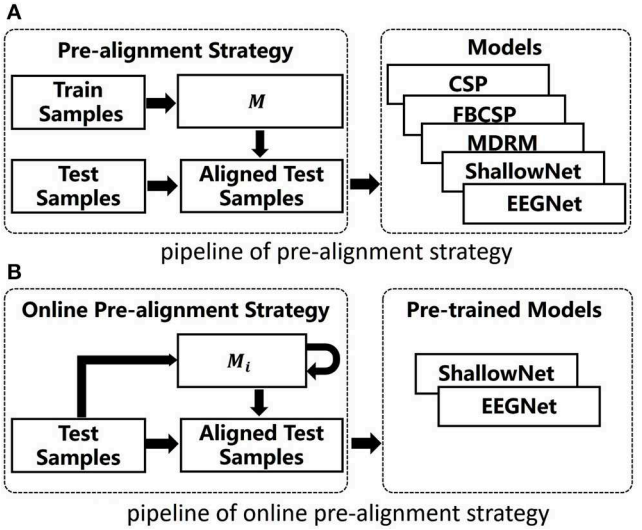

FIGURE 1 | Pipelines of our methods. **(A)** The pipeline of pre-alignment strategy. **(B)** The pipeline of online pre-alignment strategy.

recursive Riemannian mean update rule is given as follows

$$\begin{aligned} M_{i+1} &= \text{geodesic}\left(M_i, C_{i+1}, \frac{1}{i+1}\right) \\ &= M_i^{1/2}\left(M_i^{-1/2} C_{i+1} M_i^{-1/2}\right)^{\frac{1}{i+1}} M_i^{1/2} \end{aligned} \tag{10}$$

where $M_1 = C_1$. This recursive algorithm was proposed by Ho et al. (2013), which asymptotically converges in probability to the Riemannian mean expectation. OPS is efficient in practice since it avoids the calibration stage and repeatedly recalculating the Riemannian mean of the previous data. **Figure 1** shows the pipelines of our methods. The aligned time series are given by

$$\hat{E}_{i+1} = \frac{1}{N_s} M_{i+1}^{-1/2} E_{i+1} \tag{11}$$

2.6. Experiments

Within-subject, cross-subject, and cross-dataset experiments were carried out in this work. In the within-subject experiment, we compared the subject-specific performance of both traditional methods and deep learning models. In the cross-subject experiment, the unsupervised transfer ability of two deep learning models was verified in a single dataset. In the cross-dataset experiment, we further validated deep learning models on different datasets with/without online re-centering transformation. The Wilcoxon signed rank test was used to compare the performance of different methods.

In the within-subject experiment, a Linear Discriminant Analysis classifier was used for CSP and FBCSP feature extraction methods. In CSP method, the number of selected spatial filters was set to two. The filter bank of FBCSP is 4–9, 8–15, and 15–30 Hz. The number of selected spatial filters in FBCSP was set to four. Both traditional algorithms and deep learning models were trained on the training and validation sets for each subject. In the cross-subject experiment, leave-one-subject-out cross-validation was carried out on each dataset. One subject was chosen as a test subject, and deep learning models were trained on the rest of subjects in the same dataset. In cross-dataset experiment, deep learning models were trained on all subjects of one dataset while the rest of datasets were both test datasets.

Architectures of Shallow ConvNet and EEGNet in experiments are listed in **Tables 3**, **4**, respectively. Parameters of models were mainly from original papers (Schirrmeister et al., 2017; Lawhern et al., 2018) but were adjusted to fit our input size and sampling rate of data. The dropout probability was set to 0.5. The optimizer was Adam with learning rate set to 0.001. The batch size was 16 in within-subject experiment due to the limited number of available trials. In cross-subject and cross-dataset experiments, the batch size was 128. Instead of early stopping used in Schirrmeister et al. (2017), we trained for 120 epochs and selected the best model on validation set. Both models were implemented in PyTorch framework (Paszke et al., 2017).

3. RESULTS

3.1. Within-Subject Classification Results

Within-subject classification accuracies of both traditional methods and deep learning models on eight datasets are listed in **Table 5**. Each method was tested under two conditions (with PS and without PS). Both methods achieved accuracies beyond the random level. The boldface in **Table 5** shows that the accuracy of method with PS is higher than that without PS. The Wilcoxon signed rank test showed that the performance of EEGNet with PS was significantly better than that of EEGNet without PS (ShallowNet: $p = 0.06$; EEGNet: $p = 0.008$). No significant improvement was observed between traditional methods with PS and that without PS. In PhysionetMI and CBCIC2019004 datasets, the accuracies of deep learning models were lower than that of traditional methods.

Figure 2 shows results of the Wilcoxon signed rank test on each pair of methods. The dark square indicates that the performance of row method is significantly better than that of column method ($p < 0.05$). Under without PS condition, FBCSP and ShallowNet were significantly better than CSP and MDRM. Under with PS condition, all methods were significantly better than CSP. FBCSP, ShallowNet and EEGNet were significantly better than MDRM, whereas no significant differences were observed between deep learning models and FBCSP.

3.2. Cross-Subject Classification Results

Figures 3, **4** show results of cross-subject classification on eight datasets for ShallowNet and EEGNet, respectively. The performance of deep learning models without OPS in cross-subject classification was significantly higher than the random level (ShallowNet: $p = 0.008$; EEGNet: $p = 0.008$). ShallowNet with OPS was significantly better than that without OPS (ShallowNet: $p = 0.046$; EEGNet: $p = 0.062$). Specifically, for CNBCI2019004 dataset, ShallowNet with OPS increased the accuracy by 19.8% and EEGNet with OPS increased the

TABLE 5 | Within-subject Classification accuracies averaged on 10-folds.

	CSP		FBCSP		MDRM		ShallowNet		EEGNet***	
	w/o PS	w/ PS	w/o PS	w/ PS	w/o PS	w/ PS	w/o PS	w/ PS	w/o PS	w/ PS
BNCI2014001	0.68	0.66	0.70	**0.72**	0.68	0.68	0.76	**0.77**	0.78	**0.79**
BNCI2014004	0.70	0.69	0.74	**0.75**	0.69	0.69	0.79	0.79	0.79	**0.80**
PhysionetMI	0.56	0.56	0.59	**0.61**	0.57	0.57	0.53	**0.56**	0.51	**0.56**
Cho2017	0.57	0.57	0.60	0.59	0.58	0.58	0.68	0.68	0.65	**0.66**
Weibo2014	0.66	0.65	0.68	**0.69**	0.68	0.65	0.75	**0.76**	0.71	**0.74**
Zhou2016	0.81	**0.82**	0.89	0.88	0.80	**0.82**	0.83	**0.87**	0.84	**0.88**
CBCIC2019001	0.57	0.55	0.60	0.60	0.59	0.57	0.66	0.66	0.71	0.71
CBCIC2019004	0.69	0.69	0.74	0.73	0.70	0.70	0.65	0.65	0.62	**0.65**
Mean	0.65	0.65	0.69	**0.70**	0.66	0.66	0.71	**0.72**	0.70	**0.72**

Stars correspond to $^{***}p < 0.01$. *The boldface shows that the accuracy of method with pre-alignment strategy (w/ PS) is higher than that without pre-alignment strategy (w/o PS).*

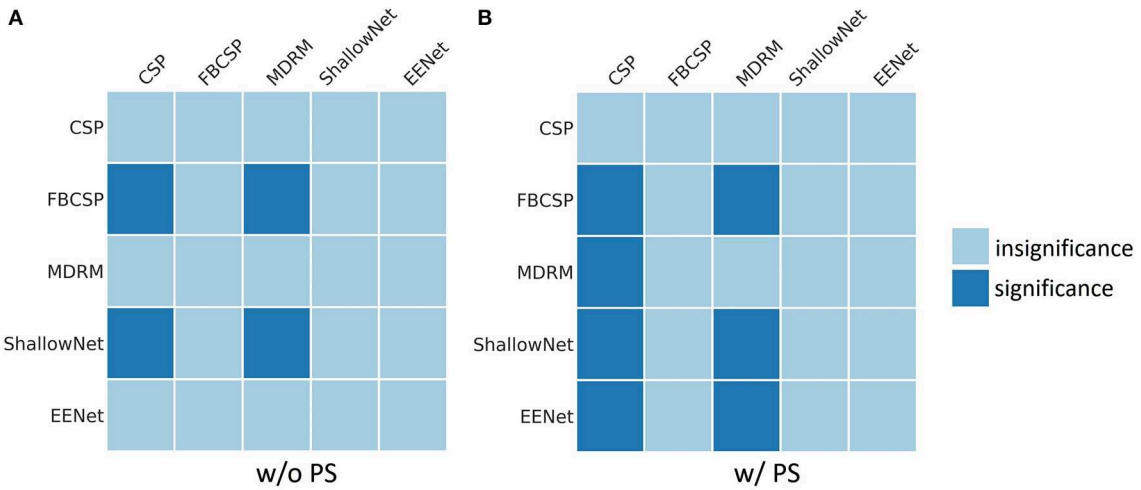

FIGURE 2 | Results of the Wilcoxon signed rank tests on pairs of methods. The dark square shows that the performance of row method is significantly better than that of column method ($p < 0.05$). **(A)** Results of methods without pre-alignment strategy (w/o PS). **(B)** Results of methods with pre-alignment strategy (w/ PS).

accuracy by 14.3%. But for Cho2017 dataset, accuracies of models with OPS both suffered a little decrease (ShallowNet: 4%, EEGNet: 8%).

3.3. Cross-Dataset Classification Results

Figures 5, **6** show results of cross-dataset classification for ShallowNet and EEGNet, respectively. The row label is the name of training dataset and the column label is the name of test dataset. The main diagonal element of each heatmap, where the training dataset is also the test dataset, is the cross-subject classification accuracy of the current dataset indicated in **Figures 3**, **4**.

Figure 5A shows that most cross-dataset accuracies of ShallowNet without OPS were near the random level, although their within-dataset accuracies (elements of the main diagonal) were not. **Figure 5B** shows that cross-dataset accuracies with OPS were significantly more improved than that without OPS in all datasets ($p < 0.05$). **Figure 5C** shows the difference between **Figure 5A** and **Figure 5B**. **Figure 6** shows similar results of EEGNet to that in **Figure 5**.

4. DISCUSSION

To compare traditional methods and deep learning models, we first validated three traditional methods and two deep learning models in within-subject experiment. The results of within-subject experiment are listed in **Table 5** and **Figure 2**. The performance of FBCSP was significantly better than that of CSP and MDRM while no significant differences were observed between deep learning models and FBCSP.

However, traditional methods are more robust in small sample learning. The performance of deep learning models is limited by the amount of data available. We observed that deep learning models were unable to achieve the same performance as traditional models in PhysionetMI and CBCIC2019004 datasets, which have relatively small number of trials per subject (PhysionetMI: 44; CBCIC2019004: 80). We also observed

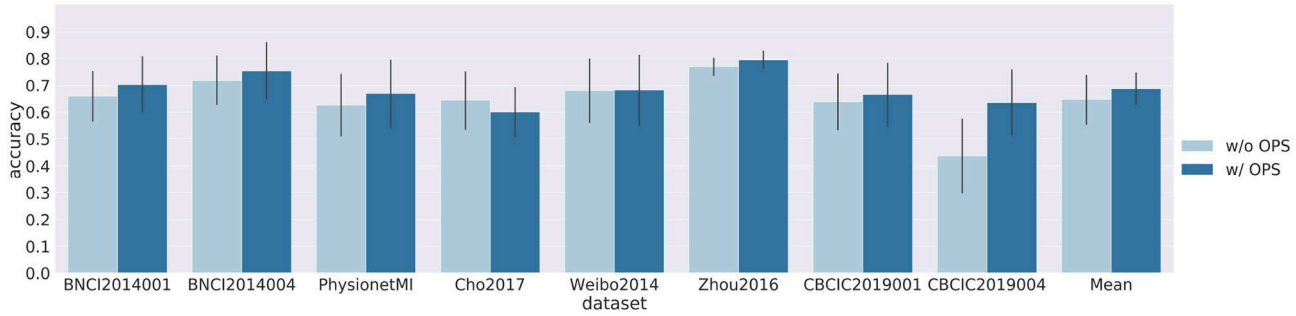

FIGURE 3 | Results of cross-subject classification on eight datasets for ShallowNet with online pre-alignment strategy (w/ OPS) and without online pre-alignment strategy (w/o OPS). Leave-one-subject-out validation was implemented on each dataset, and the validation for each subject was repeated 10 times.

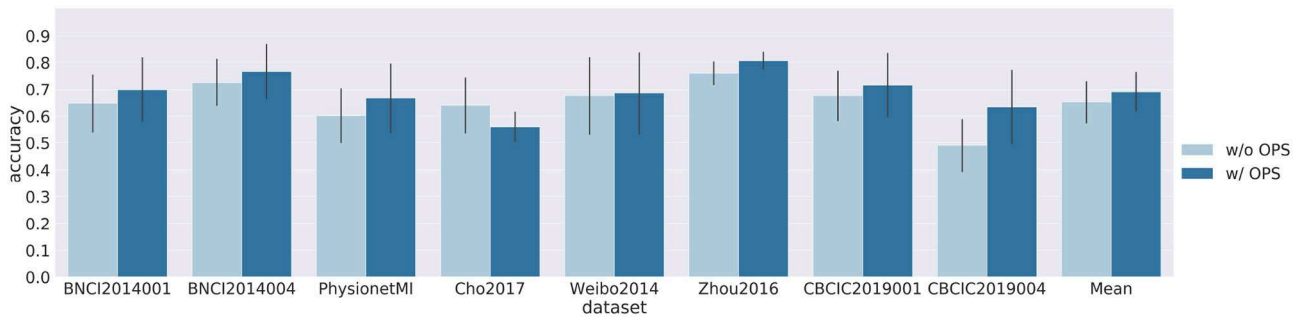

FIGURE 4 | Results of cross-subject classification on eight datasets for EEGNet with online pre-alignment strategy (w/ OPS) and without online pre-alignment strategy (w/o OPS). Leave-one-subject-out validation was implemented on each dataset, and the validation for each subject was repeated 10 times.

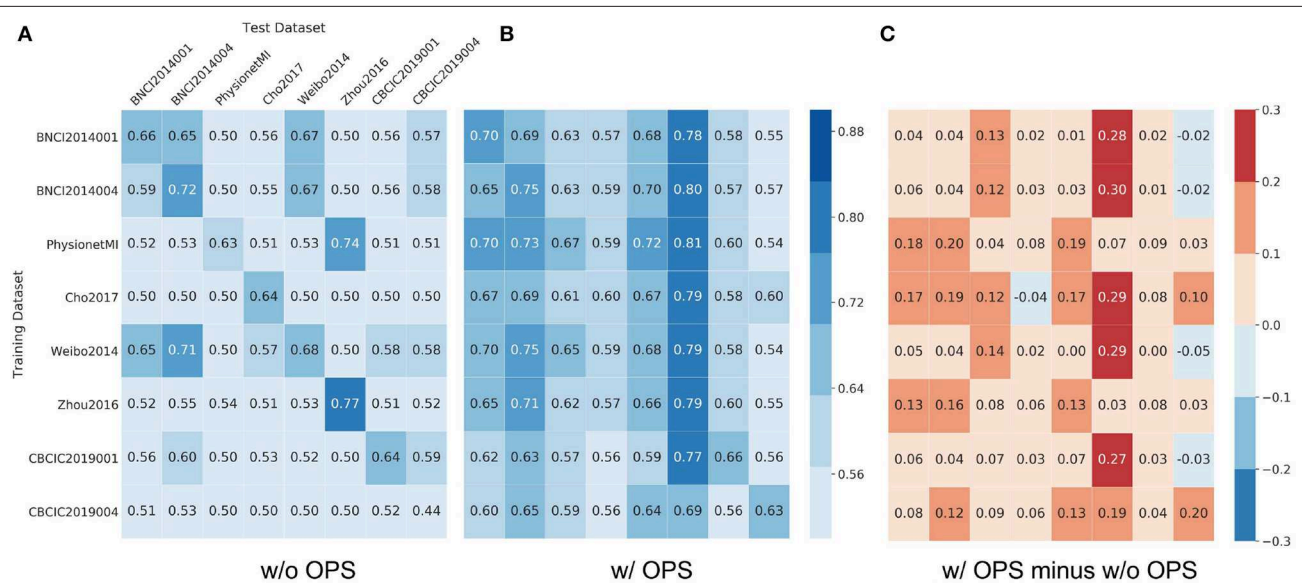

FIGURE 5 | Results of cross-dataset classification for ShallowNet. The model was trained using the row dataset and validated on column datasets. In **(A)** Results of ShallowNet without online pre-alignment strategy (w/o OPS) and **(B)** Results of ShallowNet with online pre-alignment strategy (w/ OPS), the number in each square is the validation accuracy and the element of main diagonal is the cross-subject accuracy in each dataset showed in **Figure 3**. **(C)** The difference between **(B)** and **(A)**.

that pre-alignment strategy could significantly improve the performance of deep learning models while no significant improvement was found in traditional methods. The analysis of within-subject experiment indicates that deep learning models can achieve the same performance as traditional methods in subject-specific classification tasks with enough training data.

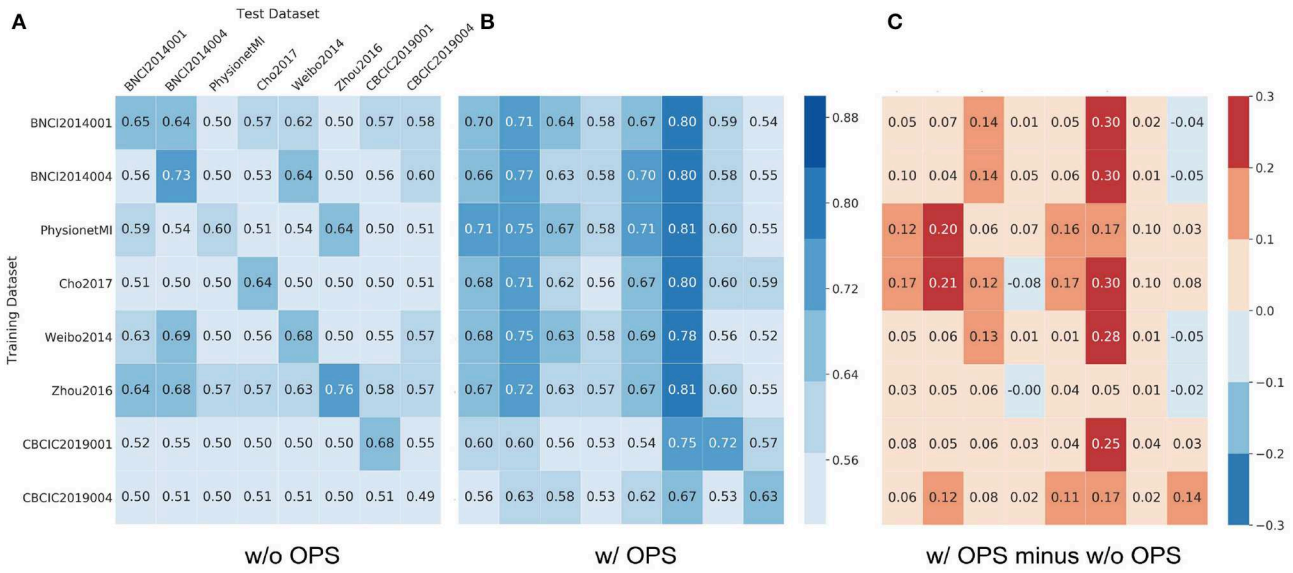

FIGURE 6 | Results of cross-dataset classification for EEGNet. The model was trained using the row dataset and validated on column datasets. In **(A)** Results of EEGNet without online pre-alignment strategy (w/o OPS) and **(B)** Results of EEGNet with online pre-alignment strategy (w/ OPS), the number in each square is the validation accuracy and the element of main diagonal is the cross-subject accuracy in each dataset showed in **Figure 4**. **(C)** The difference between **(B)** and **(A)**.

Our second analysis considered the feasibility of using deep learning models to solve cross-subject variability problems. Leave-one-subject-out cross-validation was carried out on each dataset. The results of the cross-subject experiment are shown in **Figures 3**, **4**. The performance of deep learning models without OPS was significantly higher than the random level. The results indicate that deep learning models are able to transfer a pre-trained classifier to a new subject without additional subject-specific calibration data. We also tested deep learning models with OPS on eight datasets. Deep learning models with OPS were significantly better than those without OPS. The OPS aligns the data of each subject to the similar distribution, which makes deep learning models much easier to learn common patterns across subjects. We also noticed that Cho2017 dataset suffers performance lost in both deep models with OPS. This may due to different motor imagery instructions. The authors in Cho et al. (2017) asked subjects to imagine four sequential finger movements instead of the clench of fist in other datasets. Imagining finger movement, which is still an open problem, is much harder to decode than imagining fist clenching. Besides, we only used Cz, C3, and C4 channels to decode fist clenching imagery, which are not sufficient to decode finger movements. Using more channels around central area may improve the performance of Cho2017 since they can cover much larger motorsensory area.

Although deep learning models seem feasible in solving the cross-subject variability problem as depicted in **Figures 3**, **4**, we note that deep learning models fail to generalize well in practice. Our third analysis explored the generalization ability of deep learning models on large datasets in the cross-dataset experiment. The results indicate that the cross-dataset variability problem reduces the generalization ability of deep learning models. In our second analysis, two models indeed have the ability to classify trials of a new subject without any calibration data in the same dataset. However, the pre-trained model in one dataset is unable to achieve the same performance on other datasets, which suggests that the model is highly specialized in its training dataset structure. Similar phenomenon was reported in paper (Jayaram and Barachant, 2018), where authors validated the use of traditional methods of different datasets in within-subject classification experiment. They found that the significance between algorithms depends on the specific dataset and results of a single dataset need to be tested on more datasets.

The reason for cross-dataset variability is still under exploring, but it may be caused by model overfitting problem. In cross-dataset classification scenario, a BCI dataset contains two kinds of variability: physiological variability and environmental variability. Physiological variability is responsible for the cross-subject variability while environmental variability is responsible for the environmental changes. Each dataset has its own specific configurations, including the amplifier, the electrode cap, the sampling rate, and the bandpass filtering settings. Moreover, data of subjects in the same dataset are acquired in the same laboratory environment. Deep learning models are usually trained on the data of all subjects of the same dataset. Since the distribution of environmental variability is more stable than that of physiological variability in the same dataset, deep learning models can easily overfit on the environmental variability. When the pre-trained model is validated on other datasets, which have

different distributions of environmental variability, the model loses its generalization ability since the model is not robust to environmental changes.

One way to alleviate cross-dataset variability is to add more subjects from different datasets into the training set. However, cleaning data is hard due to different settings of public datasets. Instead of adding more subjects, we use an online pre-alignment strategy to reduce physiological variability of each subject without any calibration data. OPS significantly improves the generalization ability of deep learning models. Zhou2016 is the dataset with the most significant improvement. All models trained on other datasets can achieve more than 70% accuracy except for CBCIC2019004. The result is reasonable since Zhou2016 is a biased dataset in which all subjects are experienced subjects. We found that the classification accuracies for some datasets are even higher than their within-subject classification accuracies (comparing to FBCSP without PS). For example, for PhysionetMI, nearly all models trained on other datasets (except CBCIC2019001 and CBCIC2019004) can achieve more than 60% accuracy, which is higher than its within-subject accuracy (59%). This finding may suggest that deep learning models can extract more stable feature representation than traditional methods. We also found that different datasets have different impacts on deep learning model training process. The improvement of CNBCIC2019004 on other test datasets is limited compared to other training datasets. This may be due to one drawback of deep learning models. CBCIC2019004, which only has 480 trials totally, does not have enough data for training comparing to other datasets. In summary, we recommend two tips that may be helpful for deep learning based BCI research:

(1) Use OPS as a preprocessing step.
(2) Collect enough training data.

5. CONCLUSION

In this paper, we have validated deep learning models across eight MI datasets. The analysis shows that the cross-dataset variability would reduce the performance of deep learning models, suggesting the need of validating models on different datasets for future cross-subject studies. We also proposed the online pre-alignment strategy to improve generalization ability of deep learning models. The results demonstrate that deep learning models with OPS could achieve high performance for cross-subject classification without the calibration stage.

DATA AVAILABILITY STATEMENT

The datasets for this study, CBCIC2019001 and CBCIC2019004 can be found in the DataFountain website [https://www.datafountain.cn/competitions/342]. The remaining datasets for this study can be downloaded with MOABB package [https://github.com/NeuroTechX/moabb]. The source code for this study is available on request to the corresponding author.

AUTHOR CONTRIBUTIONS

All authors contributed to manuscript revision, and they read and approved the submitted version.

FUNDING

This work was supported by the National Key Research and Development Program of China (No. 2017YFB1300302), the National Natural Science Foundation of China (No. 61976152, 81630051), the Tianjin Key Technology R&D Program (No. 17ZXRGGX00020), and the Young Elite Scientist Sponsorship Program by CAST (No. 2018QNRC001).

REFERENCES

Ang, K. K., Chin, Z. Y., Zhang, H., and Guan, C. (2008). Filter bak common spatial pattern (FBCSP) in brain-computer interface? in *2008 IEEE International Joint Conference on Neural Networks* (Hong Kong: IEEE World Congress on Computational Intelligence), 2390–2397. doi: 10.1109/IJCNN.2008.4634130

Barachant, A., Bonnet, S., Congedo, M., and Jutten, C. (2010). Riemannian geometry applied to BCI classification? in *Latent Variable Analysis and Signal Separation*, eds V. Vigneron, V. Zarzoso, E. Moreau, R. Gribonval, and E. Vincent (Berlin, Heidelberg: Springer), 629–636. doi: 10.1007/978-3-642-15995-4_78

Barachant, A., Bonnet, S., Congedo, M., and Jutten, C. (2011). Multiclass brain-computer interface classification by Riemannian geometry. *IEEE Trans. Biomed. Eng.* 59, 920–928. doi: 10.1109/TBME.2011.2172210

Cho, H., Ahn, M., Ahn, S., Kwon, M., and Jun, S. C. (2017). EEG datasets for motor imagery brain-computer interface. *GigaScience* 6, 1–8. doi: 10.1093/gigascience/gix034

Chollet, F. (2017). Xception: deep learning with depthwise separable convolutions, in *Proceedings of the IEEE Conference on Computer Vision and Pattern Recognition* (Honolulu, HI), 1251–1258. doi: 10.1109/CVPR.2017.195

Congedo, M., Barachant, A., and Andreev, A. (2013). A new generation of brain-computer interface based on Riemannian geometry. *arXiv preprint arXiv:1310.8115*.

Congedo, M., Barachant, A., and Bhatia, R. (2017a). Riemannian geometry for EEG-based brain-computer interfaces; a primer and a review. *Brain Comput Interfaces* 4, 155–174. doi: 10.1080/2326263X.2017.1297192

Congedo, M., Barachant, A., and Koopaei, E. K. (2017b). Fixed point algorithms for estimating power means of positive definite matrices. *IEEE Trans. Signal Process.* 65, 2211–2220. doi: 10.1109/TSP.2017.2649483

Dai, G., Zhou, J., Huang, J., and Wang, N. (2020). HS-CNN: a CNN with hybrid convolution scale for EEG motor imagery classification. *J. Neural Eng.* 17:016025. doi: 10.1088/1741-2552/ab405f

Gramfort, A., Luessi, M., Larson, E., Engemann, D. A., Strohmeier, D., Brodbeck, C., et al. (2013). MEG and EEG data analysis with MNE-python. *Front. Neurosci.* 7:267. doi: 10.3389/fnins.2013.00267

Grosse-Wentrup, M., and Buss, M. (2008). Multiclass common spatial patterns and information theoretic feature extraction. *IEEE Trans. Biomed. Eng.* 55, 1991–2000. doi: 10.1109/TBME.2008.921154

He, H., and Wu, D. (2020). Transfer learning for brain-computer interfaces: a Euclidean space data alignment approach. *IEEE Trans. Biomed. Eng.* 67, 399–410. doi: 10.1109/TBME.2019.2913914

Ho, J., Cheng, G., Salehian, H., and Vemuri, B. (2013). Recursive Karcher expectation estimators and geometric law of large numbers, in *Artificial Intelligence and Statistics* (Scottsdale, AZ), 325–332.

Jayaram, V., and Barachant, A. (2018). MOABB: trustworthy algorithm benchmarking for BCIs. *J. Neural Eng.* 15:066011. doi: 10.1088/1741-2552/aadea0

Lawhern, V. J., Solon, A. J., Waytowich, N. R., Gordon, S. M., Hung, C. P., and Lance, B. J. (2018). EEGNet: a compact convolutional neural network for EEG-based brain-computer interfaces. *J. Neural Eng.* 15:056013. doi: 10.1088/1741-2552/aace8c

Leeb, R., Lee, F., Keinrath, C., Scherer, R., Bischof, H., and Pfurtscheller, G. (2007). Brain-computer communication: Motivation, aim, and impact of exploring a virtual apartment. *IEEE Trans. Neural Syst. Rehabil. Eng.* 15, 473–482. doi: 10.1109/TNSRE.2007.906956

Lin, Z., Zhang, C., Wu, W., and Gao, X. (2007). Frequency recognition based on canonical correlation analysis for SSVEP-based BCIs. *IEEE Trans. Biomed. Eng.* 54, 1172–1176. doi: 10.1109/TBME.2006.889197

Lotte, F., Bougrain, L., Cichocki, A., Clerc, M., Congedo, M., Rakotomamonjy, A., et al. (2018). A review of classification algorithms for EEG-based brain-computer interfaces: a 10 year update. *J. Neural Eng.* 15:031005. doi: 10.1088/1741-2552/aab2f2

Lotte, F., and Guan, C. (2011). Regularizing common spatial patterns to improve BCI designs: unified theory and new algorithms. *IEEE Trans. Biomed. Eng.* 58, 355–362. doi: 10.1109/TBME.2010.2082539

Moakher, M. (2005). A differential geometric approach to the geometric mean of symmetric positive-definite matrices. *SIAM J. Matrix Anal. Appl.* 26, 735–747. doi: 10.1137/S0895479803436937

Nakanishi, M., Wang, Y., Chen, X., Wang, Y., Gao, X., and Jung, T. (2018). Enhancing detection of ssveps for a high-speed brain speller using task-related component analysis. *IEEE Trans. Biomed. Eng.* 65, 104–112. doi: 10.1109/TBME.2017.2694818

Paszke, A., Gross, S., Massa, F., Lerer, A., Bradbury, J., Chanan, G., et al. (2019). "PyTorch: an imperative style, high-performance deep learning library," in *Advances in Neural Information Processing Systems 32*, eds H. Wallach, H. Larochelle, A. Beygelzimer, F. d Alché-Buc, E. Fox, and R. Garnett (Curran Associates, Inc.), 8024–8035. Available online at: http://papers.neurips.cc/paper/9015-pytorch-an-imperative-style-high-performance-deep-learning-library.pdf

Pennec, X., Fillard, P., and Ayache, N. (2006). A Riemannian framework for tensor computing. *Int. J. Comput. Vis.* 66, 41–66. doi: 10.1007/s11263-005-3222-z

Ramoser, H., Muller-Gerking, J., and Pfurtscheller, G. (2000). Optimal spatial filtering of single trial EEG during imagined hand movement. *IEEE Trans. Rehabil. Eng.* 8, 441–446. doi: 10.1109/86.895946

Reuderink, B., Farquhar, J., Poel, M., and Nijholt, A. (2011). A subject-independent brain-computer interface based on smoothed, second-order baselining, in *2011 Annual International Conference of the IEEE Engineering in Medicine and Biology Society* (Boston, MA), 4600–4604. doi: 10.1109/IEMBS.2011.6091139

Rivet, B., Souloumiac, A., Attina, V., and Gibert, G. (2009). xdawn algorithm to enhance evoked potentials: application to brain-computer interface. *IEEE Trans. Biomed. Eng.* 56, 2035–2043. doi: 10.1109/TBME.2009.2012869

Rodrigues, P. L. C., Jutten, C., and Congedo, M. (2019). Riemannian procrustes analysis: Transfer learning for brain-computer interfaces. *IEEE Trans. Biomed. Eng.* 66, 2390–2401. doi: 10.1109/TBME.2018.2889705

Samek, W., Vidaurre, C., Muller, K.-R., and Kawanabe, M. (2012). Stationary common spatial patterns for brain-computer interfacing. *J. Neural Eng.* 9:026013. doi: 10.1088/1741-2560/9/2/026013

Schalk, G., McFarland, D. J., Hinterberger, T., Birbaumer, N., and Wolpaw, J. R. (2004). BCI2000: a general-purpose brain-computer interface (BCI) system. *IEEE Trans. Biomed. Eng.* 51, 1034–1043. doi: 10.1109/TBME.2004.827072

Schirrmeister, R. T., Springenberg, J. T., Fiederer, L. D. J., Glasstetter, M., Eggensperger, K., Tangermann, M., et al. (2017). Deep learning with convolutional neural networks for EEG decoding and visualization. *Hum. Brain Mapp.* 38, 5391–5420. doi: 10.1002/hbm.23730

Tangermann, M., Muller, K.-R., Aertsen, A., Birbaumer, N., Braun, C., Brunner, C., et al. (2012). Review of the BCI competition IV. *Front. Neurosci.* 6:55. doi: 10.3389/fnins.2012.00055

Wang, F., Zhong, S.-h., Peng, J., Jiang, J., and Liu, Y. (2018). "Data augmentation for EEG-based emotion recognition with deep convolutional neural networks," in *MultiMedia Modeling*, eds K. Schoeffmann, T. H. Chalidabhongse, C. W. Ngo, S. Aramvith, N. E. O'Connor, Y.-S. Ho, M. Gabbouj, and A. Elgammal (Cham: Springer International Publishing), 82–93. doi: 10.1007/978-3-319-73600-6_8

Wolpaw, J. R., Birbaumer, N., McFarland, D. J., Pfurtscheller, G., and Vaughan, T. M. (2002). Brain-computer interfaces for communication and control. *Clin. Neurophysiol.* 113, 767–791. doi: 10.1016/S1388-2457(02)00057-3

Xu, M., Xiao, X., Wang, Y., Qi, H., Jung, T., and Ming, D. (2018). A brain-computer interface based on miniature-event-related potentials induced by very small lateral visual stimuli. *IEEE Trans. Biomed. Eng.* 65, 1166–1175. doi: 10.1109/TBME.2018.2799661

Yair, O., Ben-Chen, M., and Talmon, R. (2019). Parallel transport on the cone manifold of spd matrices for domain adaptation. *IEEE Trans. Signal Process.* 67, 1797–1811. doi: 10.1109/TSP.2019.2894801

Yi, W., Qiu, S., Wang, K., Qi, H., Zhang, L., Zhou, P., et al. (2014). Evaluation of EEG oscillatory patterns and cognitive process during simple and compound limb motor imagery. *PLoS ONE* 9:e114853. doi: 10.1371/journal.pone.0114853

Zanini, P., Congedo, M., Jutten, C., Said, S., and Berthoumieu, Y. (2018). Transfer learning: a Riemannian geometry framework with applications to brain-computer interfaces. *IEEE Trans. Biomed. Eng.* 65, 1107–1116. doi: 10.1109/TBME.2017.2742541

Zhou, B., Wu, X., Lv, Z., Zhang, L., and Guo, X. (2016). A fully automated trial selection method for optimization of motor imagery based brain-computer interface. *PLoS ONE* 11:e0162657. doi: 10.1371/journal.pone.0162657

Conflict of Interest: The authors declare that the research was conducted in the absence of any commercial or financial relationships that could be construed as a potential conflict of interest.

frontiers in Human Neuroscience

ORIGINAL RESEARCH
published: 09 June 2020
doi: 10.3389/fnhum.2020.00173

Independent Low-Rank Matrix Analysis-Based Automatic Artifact Reduction Technique Applied to Three BCI Paradigms

Suguru Kanoga[1]*, *Takayuki Hoshino*[1,2] and *Hideki Asoh*[1]

[1] Artificial Intelligence Research Center, Department of Information Technology and Human Factors, National Institute of Advanced Industrial Science and Technology (AIST), Tokyo, Japan, [2] Graduate School of Media and Governance, Keio University, Kanagawa, Japan

Electroencephalogram (EEG)-based brain-computer interfaces (BCIs) can potentially enable people to non-invasively and directly communicate with others using brain activities. Artifacts generated from body activities (e.g., eyeblinks and teeth clenches) often contaminate EEGs and make EEG-based classification/identification hard. Although independent component analysis (ICA) is the gold-standard technique for attenuating the effects of such contamination, the estimated independent components are still mixed with artifactual and neuronal information because ICA relies only on the independence assumption. The same problem occurs when using independent vector analysis (IVA), an extended ICA method. To solve this problem, we designed an independent low-rank matrix analysis (ILRMA)-based automatic artifact reduction technique that clearly models sources from observations under the independence assumption and a low-rank nature in the frequency domain. For automatic artifact reduction, we combined the signal separation technique with an independent component classifier for EEGs named ICLabel. To assess the comparative efficiency of the proposed method, the discriminabilities of artifact-reduced EEGs using ICA, IVA, and ILRMA were determined using an open-access EEG dataset named OpenBMI, which contains EEG data obtained through three BCI paradigms [motor-imagery (MI), event-related potential (ERP), and steady-state visual evoked potential (SSVEP)]. BCI performances were obtained using these three paradigms after applying artifact reduction techniques, and the results suggested that our proposed method has the potential to achieve higher discriminability than ICA and IVA for BCIs. In addition, artifact reduction using the ILRMA approach clearly improved (by over 70%) the averaged BCI performances using artifact-reduced data sufficiently for most needs of the BCI community. The extension of ICA families to supervised separation that leaves the discriminative ability would further improve the usability of BCIs for real-life environments in which artifacts frequently contaminate EEGs.

Keywords: electroencephalogram, brain–computer interface, independent component analysis, artifact reduction, independent low-rank matrix analysis

OPEN ACCESS

Edited by:
Tzyy-Ping Jung,
University of California, San Diego,
United States

Reviewed by:
Erwei Yin,
China Astronaut Research and Training Center, China
Dong Ming,
Tianjin University, China

***Correspondence:**
Suguru Kanoga
s.kanouga@aist.go.jp

Specialty section:
This article was submitted to Brain-Computer Interfaces, a section of the journal Frontiers in Human Neuroscience

Received: *25 February 2020*
Accepted: *20 April 2020*
Published: *09 June 2020*

Citation:
Kanoga S, Hoshino T and Asoh H (2020) Independent Low-Rank Matrix Analysis-Based Automatic Artifact Reduction Technique Applied to Three BCI Paradigms. Front. Hum. Neurosci. 14:173. doi: 10.3389/fnhum.2020.00173

1. INTRODUCTION

An electroencephalogram (EEG)-based brain–computer interface (BCI) is a well-established technology that enables communicating with others without performing actual body movements by finding specific brain activity patterns from EEGs and converting these into predefined commands (Wolpaw et al., 2002). Several paradigms are used for eliciting robust time-independent or -dependent potentials in EEGs, such as motor imagery (MI) (Pfurtscheller and Da Silva, 1999), event-related potential (ERP) (Squires et al., 1976), and steady-state visual evoked potential (SSVEP) (Regan, 1966). Along with these paradigms, developments in machine-learning-based classifiers/identifiers have contributed to improvements in finding specific (elicited) patterns. These paradigms, in combination with signal processing modules and emerging technologies (e.g., wearable sensing, mobile computing, and virtual/augmented reality), have attracted increasing attention in many domains, such as medicine and robotics for real-world applications (Wang et al., 2018; Ogino et al., 2019; Vourvopoulos et al., 2019).

Artifact potentials must be reduced in all EEGs in order to realize robust real-world BCI applications because strong artifact contamination effects can easily reduce BCI performances (Kanoga et al., 2019b). During EEG measurements in real environments, biological artifacts like muscular and ocular ones cannot be avoided because it is difficult for people to voluntarily control the number of their artifact-generating activities. For example, healthy adult males blink ∼20 times per minute (i.e., once every ∼3 s) to maintain the moisture of their eyes (Karson, 1983). Most BCI paradigms provide visual stimuli or cues for eliciting specific neuronal patterns, and the abovementioned artifacts could contaminate the resulting EEGs. Further, muscular and ocular artifacts will contaminate all EEGs as long as the scalp has some conductivity. These unavoidable artifacts have high-amplitude electrical potentials and overlapping frequency characteristics compared to EEGs (Halliday et al., 1998; Hagemann and Naumann, 2001); thus, contamination by such artifacts makes EEG-based classification/identification hard. These contamination effects can be attenuated by increasing the distance from the source (Kanoga et al., 2016).

For denoising the contamination effects in EEG analysis, the well-known and powerful blind source separation (BSS) technique based on independent component analysis (ICA) has been widely used for the last 20 years (Jung et al., 2000). Usually, artifact reduction involves three steps: (1) training a demixing matrix, (2) identifying the types of separated independent components (ICs), and (3) remixing EEGs by using only neuronal ICs and an inverse demixing matrix. To improve both the computational cost and the accuracy of training a demixing matrix, many ICA algorithms, such as fast ICA (Hyvärinen and Oja, 1997), second-order blind interference (SOBI) (Belouchrani et al., 1997), and information maximization (infomax) ICA (Bell and Sejnowski, 1995), have been proposed. The SOBI and infomax ICA algorithms are used most commonly for EEG signal processing (Choi et al., 2005; Urigüen and Garcia-Zapirain, 2015). For example, EEGLAB, an enormous interactive toolbox for EEG analysis, implements the infomax ICA algorithm (Delorme and Makeig, 2004). Recently, ICLabel (Pion-Tonachini et al., 2019), an automatic IC classifier, has been integrated into the EEGLAB toolbox for online streaming EEG data. Overall, an ICA-based approach remains the gold-standard for artifact reduction.

While real-world EEG-based BCI applications are being developed steadily, ICA-based source estimation still poses some problems. ICA algorithms comprehensively minimize the reconstruction error with a linear combination for an entire sequence of trials. However, this approach overestimates sources for representing the latent waveform of an observation; thus, the estimation leads to oversubtraction or spectral distortion of the EEG power (Wallstrom et al., 2004; Castellanos and Makarov, 2006). Proposing a more rigorous representation of estimated sources than ICA is a major challenge in EEG signal processing for constructing effective classifiers/identifiers.

To represent meaningful waveforms from an observation, we focused on the recurrent properties of an artifactual waveform over trials. Biological artifacts are based on a person's organ structure. An organ system reproducibly and unconsciously activates a non-cerebral source (e.g., eyeball) in the same manner and generates similar electrical potentials (e.g., electrooculogram signals); therefore, person-specific artifacts share a few basic functions for representing the waveforms and can be considered low-rank matrices comprising multiple short time segments. This study represents and removes such waveforms using an independent low-rank matrix analysis (ILRMA) that finds a low-rank non-negative matrix based on statistical independence (Kitamura et al., 2016). To improve its usability for EEG analysis, we used ICLabel for artifact reduction. We investigated the discriminabilities of artifact-reduced EEGs obtained by different methods by using OpenBMI, an open-access EEG dataset that contains EEG data, through the three abovementioned BCI paradigms (MI, ERP, and SSVEP). The BCI performances with these three paradigms after applying artifact reduction techniques were obtained. The results suggest that the proposed method can potentially achieve higher discriminability than ICA for BCIs.

2. ARTIFACT REDUCTION TECHNIQUES

2.1. Mixing and Demixing of EEGs

A typical approach to artifact reduction in EEG observations is based on the following assumption: P-channel EEG observations are overdetermined/determined and linear combinations of unknown cerebral Q sources including artifactual and neuronal ones and white noises. Neuronal cells have limited propagation because the cortical connectivity is highly weighted toward short ($< 500\ \mu$m) connections (Budd and Kisvárday, 2001). Thus, the electrical potentials of neuronal activities spread through a contiguous cortical region with a high attenuation penalty in proportion with the distance from the sources (Arieli et al., 1996; Onton and Makeig, 2006). By matching the underlying dynamics of the generation and propagation of EEG potentials,

the aforementioned assumption can be represented as

$$\boldsymbol{x}(n) = \boldsymbol{A}\boldsymbol{s}(n) + \boldsymbol{d}(n), \tag{1}$$

where $\boldsymbol{x}(n) = [x_1(n), x_2(n), \ldots, x_P(n)]^{\mathrm{T}}$ is the EEG observation at the nth sampling point ($1 \leq n \leq N$), $\boldsymbol{s}(n) = [s_1(n), s_2(n), \ldots, s_Q(n)]^{\mathrm{T}}$ is the unknown source, $\boldsymbol{A}$ is the $P \times Q$ full-rank unknown mixing matrix, and $\boldsymbol{d}(n) = [d_1(n), d_2(n), \ldots, d_P(n)]^{\mathrm{T}}$ is the additive zero-mean noise ($^{\mathrm{T}}$ indicates the transpose).

Here, we have only an artifact-(un)contaminated EEG observation matrix $\boldsymbol{X} = [\boldsymbol{x}(1), \ldots, \boldsymbol{x}(N)] \in \mathbb{R}^{P \times N}$. Because source estimation through the inverse process is evidently intractable, four additional assumptions are made (James and Hesse, 2004; Vigario and Oja, 2008): (1) the noise is spatially uncorrelated with the observed data ($\mathbb{E}[\boldsymbol{A}\boldsymbol{s}(n)\boldsymbol{d}(n)] = \boldsymbol{0}$, where $\mathbb{E}[\cdot]$ is the expectation operator); (2) the noise is temporally uncorrelated ($\mathbb{E}[\boldsymbol{d}(n)\boldsymbol{d}(n+\tau)] = \boldsymbol{0}$, where τ is the lag time ($\forall \tau > 0$)); (3) the number of sources is equal to or lower than the number of observations ($P \geq Q$); and (4) the mixing matrix $\boldsymbol{A}$ does not change over time. Under these assumptions, we can simultaneously estimate both the source matrix $\hat{\boldsymbol{S}} = [\hat{\boldsymbol{s}}(1), \ldots, \hat{\boldsymbol{s}}(N)] \in \mathbb{R}^{Q \times N}$ and the demixing matrix $\boldsymbol{W}(= \boldsymbol{A}^{-1}) \in \mathbb{R}^{Q \times P}$ to blindly separate the observations into artifactual/neuronal sources:

$$\hat{\boldsymbol{s}}(n) = \boldsymbol{W}\boldsymbol{x}(n). \tag{2}$$

The linear mixing and demixing of EEGs shown in **Figure 1** accounts for the comprehensive demixing matrix $\boldsymbol{W}(= \boldsymbol{W}_1\boldsymbol{W}_2)$ because signal separation algorithms sometimes first decorrelate the data by $\boldsymbol{W}_1$ and then demix them by $\boldsymbol{W}_2$, which is originally learned from the algorithm. In this study, we decorrelated the data before applying a matrix factorization technique; thus, the following representation of $\boldsymbol{W}$ has the same meaning as $\boldsymbol{W}_2$ in **Figure 1**.

In practice, artifact reduction requires three stages of processing: (1) decomposing the input matrix; (2) identifying whether the decomposed component is artifactual or neuronal; and (3) reconstructing the artifact-reduced signals using only neuronal components. In this case, we assumed that the EEG observations are labeled signals; the dimensionality of the sources and observations is the same (the value of P and Q is 20, 32, or 10 for MI, ERP, or SSVEP paradigm. The value depends on the number of selected channels in the BCI paradigm. More detailed information is described in sections 3.1, 3.2, and 3.3). In addition, we decomposed datasets using three BSS methods for ICA families: ICA, independent vector analysis (IVA), and ILRMA. Then, the decomposed components were automatically identified using the ICLabel function in the EEGLAB toolbox proposed by Pion-Tonachini et al. (2019). Based on the labels, artifact-reduced signals were linearly reconstructed.

Although ICA algorithms handle time-series data, IVA and ILRMA algorithms approximate a bin-wise instantaneous mixture model in a short-time Fourier transform (STFT) domain. An EEG time series is transformed into a sequence of complex-valued signals by using STFT with a 50% overlapped 1-s Hamming window. Thus, the observations and sources in each time-frequency slot are described as $\boldsymbol{x}_{ij} = [x_{ij1}, x_{ij2}, \ldots, x_{ijP}]^{\mathrm{T}} \in \mathbb{C}^P$ and $\hat{\boldsymbol{s}}_{ij} = [\hat{s}_{ij1}, \hat{s}_{ij2}, \ldots, \hat{s}_{ijQ}]^{\mathrm{T}} \in \mathbb{C}^Q$, where a couple of (i, j) defines the ith frequency bin and jth time frame over STFT ($1 \leq i \leq I$ and $1 \leq j \leq J$). IVA and ILRMA algorithms assume the following mixing system:

$$\boldsymbol{x}_{ij} = \boldsymbol{A}_i \, \boldsymbol{s}_{ij}, \tag{3}$$

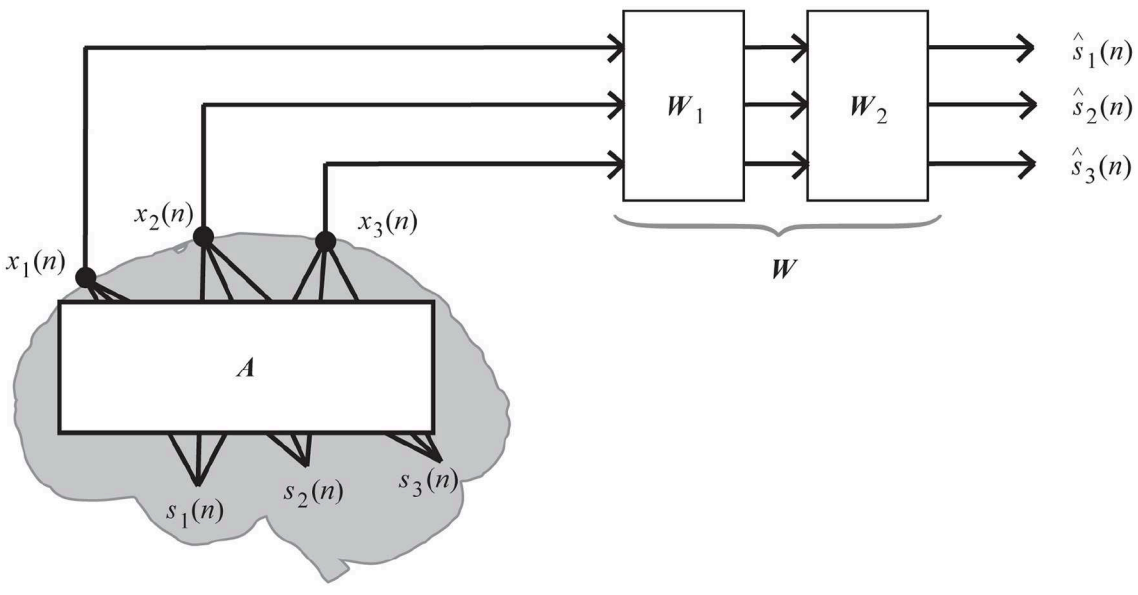

FIGURE 1 | Linear mixing and demixing of EEGs (Kanoga and Mitsukura, 2017).

where $\boldsymbol{A}_i = [\boldsymbol{a}_{i1}, \boldsymbol{a}_{i2}, \ldots, \boldsymbol{a}_{iQ}]^{\mathrm{H}} \in \mathbb{C}^{P\times Q}$ is a frequency-wise mixing matrix ($\boldsymbol{a}_{iq}$ is the steering vector for the qth source, and $^{\mathrm{H}}$ indicates the Hermitian transpose). In this paper, we set the value of time length to 1 s because some frequency-domain artifact reduction techniques translate EEG data into STFT domain based on 1-s windows (Kanoga and Mitsukura, 2014; Mohammadpour and Rahmani, 2017) and ILRMA showed its high separation accuracy for 1-s time length data (Kitamura et al., 2017). This mixing system is the rank-1 spatial model (Duong et al., 2010); thus, the relationships between observations and sources can be represented:

$$\hat{\boldsymbol{s}}_{ij} \approx \boldsymbol{y}_{ij} = \boldsymbol{W}_i\, \boldsymbol{x}_{ij}, \tag{4}$$

where $\boldsymbol{y}_{ij} = [y_{ij1}, y_{ij2}, \ldots, y_{ijQ}]^{\mathrm{T}} \in \mathbb{C}^{Q}$ is the STFT of the estimated signals and $\boldsymbol{W}_i = [\boldsymbol{w}_{i1}, \boldsymbol{w}_{i2}, \ldots, \boldsymbol{w}_{iQ}]^{\mathrm{H}} = \boldsymbol{A}_i{}^{-1} \in \mathbb{C}^{Q\times P}$ is the demixing matrix. Note that the demixing matrices for IVA, ILRMA, and ICA have different dimensionalities because of the differences in the domain used (IVA and ILRMA: $\boldsymbol{W} \in \mathbb{R}^{Q\times P\times I}$, ICA: $\boldsymbol{W} \in \mathbb{R}^{Q\times P}$).

2.2. Matrix Factorization Techniques

2.2.1. Independent Component Analysis

ICA is the most famous classical method for separating multichannel EEG observations $\boldsymbol{x}(n)$ into statistically independent sources $\hat{\boldsymbol{s}}(n)$ based on an estimated demixing matrix $\boldsymbol{W}$ (Jung et al., 2000; Delorme et al., 2007). The sources can be said to be statistically independent when the following relationship holds:

$$p(\hat{\boldsymbol{s}}) = \prod_{q=1}^{Q} p(\hat{\boldsymbol{s}}_q), \tag{5}$$

where $p(\hat{\boldsymbol{s}})$ and $p(\hat{\boldsymbol{s}}_q)$ are the joint and the marginal probability distribution of the sources, respectively. Thus, ICA algorithms optimize the demixing matrix $\boldsymbol{W}$ by minimizing the dependence between these distributions. This study applied the extended infomax ICA algorithm implemented by Lee et al. (1999) using the `runica` function in EEGLAB to the observations. In this algorithm, the dependence in the distributions is represented as the mutual information (Kullback–Leibler distribution) between the estimated sources and observations $\mathcal{I}(\hat{\boldsymbol{s}}; \boldsymbol{x})$:

$$\mathcal{I}(\hat{\boldsymbol{s}}; \boldsymbol{x}) = \mathcal{H}(\hat{\boldsymbol{s}}) - \sum_{q=1}^{Q} \mathcal{H}(\hat{\boldsymbol{s}}_q), \tag{6}$$

where

$$\mathcal{H}(\hat{\boldsymbol{s}}) = -\int p(\hat{\boldsymbol{s}}) \log p(\hat{\boldsymbol{s}}) d\hat{\boldsymbol{s}}, \tag{7}$$

$$\mathcal{H}(\hat{\boldsymbol{s}}_q) = -\int p(\hat{\boldsymbol{s}}_q) \log p(\hat{\boldsymbol{s}}_q) d\hat{\boldsymbol{s}}_q. \tag{8}$$

By applying the relationship $p(\boldsymbol{x}) = p(\hat{\boldsymbol{s}})/|\det \boldsymbol{W}|$ to Equation (7), Equation (6) can be rewritten as a cost function for optimizing the demixing matrix:

$$\mathcal{I}(\boldsymbol{W}) = \text{const.} - \sum_{q=1}^{Q} \mathcal{H}(\hat{\boldsymbol{s}}_q) - \log|\det \boldsymbol{W}|. \tag{9}$$

The entropy of given observations $\mathcal{H}(\boldsymbol{x})$ is a constant. In addition, a gradient update rule based on the natural gradient (Amari, 1998) with learning rate η is used to solve the optimization problem:

$$\boldsymbol{W} \leftarrow \boldsymbol{W} + \eta \Delta \boldsymbol{W}, \tag{10}$$

where

$$\Delta \boldsymbol{W} = (\boldsymbol{I} - \mathbb{E}[\varphi(\hat{\boldsymbol{s}})\hat{\boldsymbol{s}}^T])\boldsymbol{W}. \tag{11}$$

In every iteration, the distribution of the estimated source for the score function $\varphi(\hat{\boldsymbol{s}}_q)$ is chosen from the super-Gaussian or sub-Gaussian based on the sign of the fourth cumulant of each source $c_4 = M_4 - 3M_2^2$, where M_k is the kth moment ($M_k = \mathbb{E}[\hat{\boldsymbol{s}}_q^k]$).

$$\varphi(\hat{\boldsymbol{s}}_q) = -(\hat{\boldsymbol{s}}_q + \mathrm{sgn}(c_4)\tanh(\hat{\boldsymbol{s}}_q)). \tag{12}$$

In a real environment, the expectation operator $\mathbb{E}[\cdot]$ is the expected value of the empirical distribution (the sample average of the variable).

2.2.2. Independent Vector Analysis

IVA is an extension of the ICA algorithm to multivariate components (vectorized signals) (Hiroe, 2006; Kim et al., 2006b). Like ICA algorithms, IVA defines the dependence between joint probability distributions and marginal probability products using the Kullback–Leibler divergence; however, it introduces a vector density model that has a variance dependency within a source vector. This study applied the natural-gradient-based IVA algorithm implemented by Kim et al. (2006b) based on the `ivabss` function from an open-access toolbox available on Github (https://github.com/teradepth/iva).

Two conditions are assumed: (1) elements of a source vector are mutually independent of those of other source vectors; and (2) within a source vector, the elements are highly dependent on each other. Based on these assumptions, the cost function for multivariate random variables to separate the components from the observations can be written as

$$\mathcal{I}(\boldsymbol{W}) = \text{const.} - \sum_{q=1}^{Q} \mathcal{H}(\hat{\boldsymbol{s}}_q) - \sum_{i=1}^{I} \log|\det \boldsymbol{W}_i|. \tag{13}$$

The cost function preserves the inherent dependency within each source vector, though it removes the dependency between different source vectors.

By differentiating the object function with respect to the coefficients of demixing matrices $\boldsymbol{W}_i$ and using the natural gradient, we can derive a gradient update rule as

$$\Delta \boldsymbol{W}_i \leftarrow \boldsymbol{W}_i + \eta \Delta \boldsymbol{W}_i, \tag{14}$$

where

$$\Delta \boldsymbol{W}_i = (\boldsymbol{I} - \mathbb{E}[\varphi_i(\hat{\boldsymbol{s}}_1, \ldots, \hat{\boldsymbol{s}}_I)\hat{\boldsymbol{s}}_i^{\star})]\boldsymbol{W}_i, \tag{15}$$

where $\boldsymbol{a}^{\star}$ denotes the complex conjugate of $\boldsymbol{a}$. Among a number of possible function forms, one of the simplest and most effective score functions is given as follows:

$$\varphi_i(\hat{\boldsymbol{s}}_1, \ldots, \hat{\boldsymbol{s}}_I) = \frac{\hat{\boldsymbol{s}}_i}{\sqrt{\sum_{i=1}^{I} |\hat{\boldsymbol{s}}_i|^2}} \tag{16}$$

To define an optimal form of the function $p(\hat{\boldsymbol{s}}_q)$, which has dependency within a source vector, IVA algorithms introduce a vector density model as a scale mixture of a Gaussian distribution with a fixed mean and a variable variance (Kim et al., 2006a):

$$p(\hat{\boldsymbol{s}}_q) = \prod_{i=1}^{I} p(\hat{\boldsymbol{s}}_{iq}) = \alpha \prod_{i=1}^{I} \exp\left(-\sqrt{(\hat{\boldsymbol{s}}_{iq} - \mu_{iq})^{\dagger} {\Sigma_{iq}}^{-1} (\hat{\boldsymbol{s}}_{iq} - \mu_{iq})}\right) \tag{17}$$

where α is a normalization term, μ_{iq} and Σ_{iq} are respectively the mean vector and covariance matrix of the qth source signal in the ith frequency bin, and $\boldsymbol{a}^{\dagger}$ is the conjugate transpose of $\boldsymbol{a}$.

2.2.3. Independent Low-Rank Matrix Analysis

The ILRMA method unifies IVA and non-negative matrix factorization (Lee and Seung, 1999; Sawada et al., 2013) by considering the determined situation ($P = Q$) and a linear time-invariant mixing system (Kitamura et al., 2016). This study applied the ILRMA algorithm implemented by Kitamura et al. (2016) using the `ILRMA` function from an open-access toolbox available on Github (https://github.com/d-kitamura/ILRMA). The algorithm estimates both the demixing matrix $\boldsymbol{W}_i$ and the STFT of the estimated signals $\boldsymbol{y}_{ij}$ by approximately decomposing $|y_{ijq}|^2$ into the non-negative elements t_{ik} and v_{kj} of the basis matrix $\boldsymbol{T}_q \in \mathbb{R}^{I \times K}$ and the activation matrix $\boldsymbol{V}_q \in \mathbb{R}^{K \times J}$ with a latent variable z_{qk} of the partitioning function $\boldsymbol{Z}$, which indicates whether or not the kth basis ($1 \leq k \leq K$) belongs to the qth source. For the decomposition, the ILRMA algorithm has the following cost function:

$$\mathcal{I}(\boldsymbol{W}) = \sum_{ij}\left\{\sum_{q} \log \sum_{k} z_{qk} t_{ik} v_{kj} + \sum_{q} \frac{|y_{ijq}|^2}{\sum_k z_{qk} t_{ik} v_{kj}} - 2\log|\det \boldsymbol{W}_i|\right\}, \tag{18}$$

where $y_{ijq} = {\boldsymbol{w}_{iq}}^{\mathrm{H}} \boldsymbol{x}_{ij}$. The cost function finds a low-rank time-frequency structure for sources using the first and second terms in Equation (18) and maximizes the statistical independence between sources using the second and third terms in Equation (18).

In this algorithm, the demixing matrix $\boldsymbol{W}_i$ can be efficiently updated through iterative projection based on the auxiliary function technique (Ono, 2011):

$$V_{iq} = \frac{1}{J} \sum_{j} \frac{1}{r_{ijq}} \boldsymbol{x}_{ij} \boldsymbol{x}_{ij}^{\mathrm{H}}, \tag{19}$$

$$\boldsymbol{w}_{iq} \leftarrow (\boldsymbol{W}_i V_{iq})^{-1} \boldsymbol{e}_q, \tag{20}$$

$$\boldsymbol{w}_{iq} \leftarrow \boldsymbol{w}_{iq} (\boldsymbol{w}_{iq}^{H} V_{iq} \boldsymbol{w}_{iq})^{-\frac{1}{2}}, \tag{21}$$

where r_{ijq} is the estimated variance of each source under the complex Gaussian distribution and $\boldsymbol{e}_q$, a unit vector in which the qth element is equal to unity. These update rules have been reported to be faster and more stable than conventional update rules (e.g., natural gradient). After the update, the separated signal $\boldsymbol{y}_{ij}$ is also updated:

$$y_{ijq} \leftarrow \boldsymbol{w}_{iq}^{\mathrm{H}} \boldsymbol{x}_{ij}. \tag{22}$$

In addition, the basis matrix $\boldsymbol{T}_q$, activation matrix $\boldsymbol{V}_q$, and partitioning function $\boldsymbol{Z}$ can be updated by the majorization-minimization algorithm (Hunter and Lange, 2000):

$$z_{qk} \leftarrow z_{qk} \sqrt{\frac{\sum_{ij} |y_{ijq}|^2 t_{ik} v_{kj} (\sum_{k'} z_{qk'} t_{ik'} v_{k'j})^{-2}}{\sum_{ij} t_{ik} v_{kj} (\sum_{k'} z_{qk'} t_{ik'} v_{k'j})^{-1}}}, \tag{23}$$

$$t_{ik} \leftarrow t_{ik} \sqrt{\frac{\sum_{jq} |y_{ijq}|^2 z_{qk} v_{kj} (\sum_{k'} z_{qk'} t_{ik'} v_{k'j})^{-2}}{\sum_{jq} z_{qk} v_{kj} (\sum_{k'} z_{qk'} t_{ik'} v_{k'j})^{-1}}}, \tag{24}$$

$$v_{kj} \leftarrow v_{kj} \sqrt{\frac{\sum_{iq} |y_{ijq}|^2 z_{qk} t_{ik} (\sum_{k'} z_{qk'} t_{ik'} v_{k'j})^{-2}}{\sum_{iq} z_{qk} t_{ik} (\sum_{k'} z_{qk'} t_{ik'} v_{k'j})^{-1}}}. \tag{25}$$

Finally, the estimated source model is represented as

$$r_{ijq} = \sum_{k} z_{qk} t_{ik} v_{kj}. \tag{26}$$

Note that the demixing matrix $\boldsymbol{W}_i$ and the estimated variance r_{ijq} are normalized at each iteration to avoid the risk of diverging as follows:

$$\lambda_q = \sqrt{\frac{1}{IJ} \sum_{ij} |y_{ijq}|^2}, \tag{27}$$

$$\boldsymbol{w}_{iq} \leftarrow \boldsymbol{w}_{iq} \lambda_q^{-1}, \tag{28}$$

$$y_{ijq} \leftarrow y_{ijq} \lambda_q^{-1}, \tag{29}$$

$$r_{ijq} \leftarrow r_{ijq} \lambda_q^{-2}. \tag{30}$$

The number of bases for all sources K and number of iterations were set to $J/10$ and 200, respectively.

2.3. Component Identification

For identifying the estimated ICs obtained from ICA, IVA, and ILRMA, we used the ICLabel (https://github.com/sccn/ICLabel) classifier proposed by Pion-Tonachini et al. (2019) (freely available as a package in EEGLAB; Delorme and Makeig, 2004; Delorme et al., 2011). This classifier uses three artificial neural networks (ANNs) (specifically, two "Classifier" networks and one "Generator" network): (1) a convolutional neural network (CNN) optimized by an unweighted cross-entropy loss, (2) a

CNN optimized by a weighted cross-entropy loss and neuronal IC classification errors, and (3) a semi-supervised learning generative adversarial network (SSGAN) (Odena, 2016; Salimans et al., 2016). The ICLabel classifier inputs, architectures, and training paradigms are described in detail in Appendices B and E in Pion-Tonachini et al. (2019). By using these three ANNs and the three IC features, the ICLabel classifier classified unlabeled EEG ICs into seven categories: (1) brain, (2) muscle, (3) eye, (4) heart, (5) line noise, (6) channel noise, and (7) others. In this study, because of the property of the epoch identification method described in section 4, we removed ICs whose labels were "muscle" or "eye." Currently, the ICLabel classifier has been trained using 6352 EEG recordings in storage drives collected over the past 15 years at Swartz Center for Computational Neuroscience (SCCN) at UC San Diego.

To accurately identify IC labels using the ICLabel classifier, three discriminable features were calculated from each IC: (1) 32×32 pixel scalp topography using the `topoplot` function in EEGLAB, (2) median power spectral densities (PSDs) from 1 to 50 Hz using a variation of the Welch method (Welch, 1967), and (3) the autocorrelation function. The scalp topographies and PSDs were scaled such that each had a maximum absolute value of 0.99. Further, the autocorrelation vectors were normalized such that the zero-lag value was 0.99. Note that the estimated mixing matrix ($\boldsymbol{W}^{-1}$), channel locations in 3D space, and channel labels were required to generate the scalp topographies. We collected information about the channel locations in 3D space from the `sample_locs` folder in EEGLAB toolbox. In addition, the estimated demixing matrix has a 3D structure except for ICA; thus, the corresponding frequency band (e.g., 8–30 Hz) was extracted from whole frequency bins, and the summation was computed to transform the matrix into a 2D structure. Furthermore, the matrix was scaled by the number of extracted frequency bins.

2.4. Signal Reconstruction

By performing the identification process using ICLabel, labels are obtained for the estimated ICs. If the label is "eye" or "muscle," all components of the artifactual IC are set to zeros. Based on the modified sources, artifact-reduced EEG signals in EEG observations were reconstructed using the inverse linear demixing process in ICA. While applying IVA and ILRMA, the sources were translated into frequency components. Thus, all frequency components of the artifactual ICs were set to zeros and translated into time-series data by the inverse STFT. Then, the artifact-reduced EEG signals were reconstructed, and the inverse ICA linear demixing process was performed.

3. MATERIALS AND BASELINE METHODS

To assess the discriminability of artifact-reduced EEGs by ICA, IVA, and ILRMA, we downloaded an open-access EEG dataset published by Lee et al. (2019) from the webpage http://gigadb.org/dataset/view/id/100542/File_page. The EEG data were recorded using 62 electrodes according to the International 10-20 system using BrainAmp (Brain Products; Munich, Germany) with a sampling rate of 1,000 Hz. In the analysis procedures, we commonly downsampled all EEG data to 100 Hz. The reference and ground channels were nasion and AFz, respectively. The impedance of the EEG electrodes was maintained below 10 kΩ. Participants were instructed to comfortably sit in a chair with armrests ∼60 cm in front of a 21-inch LCD monitor (refresh rate: 60 Hz; resolution: $1,600 \times 1,200$). In addition, they were asked to relax their muscles and minimize their eye and muscle movements during the BCI paradigms. Before beginning the experiments, five kinds of 10-s artifact-contaminated EEG data were measured: (1) eye blinking, (2) repetitive horizontal eye movements, (3) repetitive vertical eye movements, (4) teeth clenching, and (5) flexing both arms.

The dataset has the following three properties: (1) a large number of subjects (54 healthy participants; 29 males and 25 females; age: 24–35 years), (2) multiple sessions (two sessions on different days), and (3) multiple paradigms (a binary-class MI, a 36-symbol ERP, and a four-target-frequency SSVEP). Each session consisted of training and testing phases. All BCI paradigms were developed based on the OpenBMI toolbox (Lee et al., 2016) and Psychtoolbox (Brainard, 1997). We used this dataset because (1) EEGs in the three BCI paradigms were collected from the same participants, (2) each paradigm was conducted for 2 days, and (3) baseline analysis methods based on Matlab functions in the OpenBMI toolbox (https://github.com/PatternRecognition/OpenBMI) are available. A single dataset having all these properties is very important for fairly comparing algorithms to reveal general performances with intra- and inter-subject/paradigm variabilities in BCI research. To verify the change in the discrimination accuracy with artifact-reduced EEGs, the baseline analysis methods, including feature extraction and classification algorithms for each paradigm described in Lee et al. (2019), were used. Each paradigm and processing stream are described in detail in the following subsections.

3.1. MI Paradigm and Processing

The MI paradigm was designed based on a well-established protocol (Pfurtscheller and Neuper, 2001): a training/testing phase had 100 trials with 50 right and 50 left hand motion imagery tasks resulting in binary classification. Each trial lasted 13 ± 1.5 s. In the first 3 s, a black fixation cross appeared at the center of the monitor. After the preparation time, the participant imagined a right or left grasping motion for 4 s depending on whether a right arrow or left arrow was displayed, respectively, and then remained in the resting state for 6 ± 1.5 s.

In the MI paradigm, 20 electrodes in the motor cortex region (FC-5/3/1/2/4/6, C-5/3/1/z/2/4/6, and CP-5/3/1/z/2/4/6) were selected. The EEG data of the selected channels were band-pass filtered between 8 and 30 Hz through a fifth order Butterworth filter and further segmented into 2.5-s epochs, which are data segments of 1.0 to 3.5 s after the cue onsets (Pfurtscheller and Neuper, 2001; Fazli et al., 2009). We applied the filter bank common spatial pattern (FBCSP) to the epochs, which has been widely used in MI-based BCIs to maximize the discrimination of the binary class (Ang et al., 2008). A subset of the top and bottom two rows from the projection matrix was used for calculating log-variance features. Based on the features, linear discriminant analysis (LDA) classifiers were constructed and used.

3.2. ERP Paradigm and Processing

The ERP paradigm was designed based on a typical row-column speller system with random-set presentation (Yeom et al., 2014) and face stimuli (Kaufmann et al., 2011). The six rows and six columns were configured with 36 symbols (alphabets A to Z, numerals 1 to 9, and underscore "_"). Each trial sequence lasted 19.5 s. In the first 4.5 s, a target character was highlighted for attracting the participant's attention. After the preparation time, all rows and columns were flashed one by one (12 stimulus flashes) for 13 s and then remained in the resting state for 2 s. The stimulus-time interval was set to 80 ms and the interstimulus interval (ISI) to 135 ms. The highlighted target character was estimated based on data of five sequences (i.e., 60 flashes). In the training phase, participants were asked to copy the 33 characters including spaces in "NEURAL_NETWORKS_AND_DEEP_LEARNING" by gazing at the target character on the monitor, resulting in 1980 trials and binary classification (target or non-target character). In the testing phase, participants tried to copy the 36 characters including spaces in "PATTERN_RECOGNITION_MACHINE_LEARNING," resulting in 2,160 trials.

In the ERP paradigm, 32 electrodes (Fp-1/2, F-7/3/z/4/8, FC-5/1/2/6, T-7/8, C-3/z/4, TP-9/10, CP-5/1/2/6, P-7/3/z/4/8, PO-9/10, and O-1/z/2) were selected. The EEG data of the selected channels were band-pass filtered between 0.5 and 40 Hz through a fifth order Butterworth filter and then baseline-corrected by subtracting the average amplitudes of the prestimulus within an interval of 200 ms with respect to the stimulus onset. In addition, 0.8-s epochs after the onset were extracted for analysis. From the epochs, the mean amplitudes (MAs) over eight non-overlapping samples were calculated as the 320-dimensional subject-dependent spatio-temporal features (10 dimensions, 32 channels). Based on the features, LDA classifiers were constructed and used.

3.3. SSVEP Paradigm and Processing

The SSVEP paradigm was designed based on general requirements for SSVEP-based BCIs that run over four specific commands (Parini et al., 2009). Four flickers at 5.45, 6.67, 8.57, and 12 Hz were displayed at four positions (down, right, left, and up) on a monitor. Each target frequency was presented 25 times for both the training and the testing phases, resulting in four target identification problems. Each trial lasted 10 s. In the first 4 s, the participant gazed in the box where the target was highlighted (not flickering) in a different color, and the target flicker was then presented for 4 s with an ISI of 6 s to induce the target SSVEP.

In the SSVEP paradigm, 10 electrodes in the occipital region (P-7/3/z/4/8, PO-9/10, and O-1/z/2) were selected. The EEG data of the selected channels were segmented into 2-s epochs with respect to the stimulus onset. We applied multichannel canonical correlation analysis (CCA) (Lin et al., 2006) for identifying the target frequency index by calculating the correlation values between the input data and the prepared sinusoidal templates of the corresponding frequencies (5.45, 6.67, 8.57, and 12 Hz). Although this identification process does not need training data owing to the use of an unsupervised classifier, only data from the testing phase were used for evaluating the BCI performance.

4. ASSESSMENTS

In this study, we assumed that artifact-reduced epochs are correctly classified if the artifact reduction technique effectively reduced artifactual effects from artifact-contaminated epochs. However, we do not know how many epochs of the aforementioned paradigms were contaminated by artifacts because the open-access EEG dataset does not provide such information. Empirically, it is difficult to completely avoid the generation of biological artifacts during EEG paradigms. Thus, we expected that some epochs were contaminated by some artifacts during each BCI paradigm. To identify the type of epoch (not artifact-contaminated or artifact-contaminated), we applied the detection of events in continuous time (DETECT) epoch identification method proposed by Lawhern et al. (2013); this method requires training data with clean and artifactual label information to make a multiclass SVM model (https://github.com/VisLab/detect). Usually, training data has a short time length (e.g., less than 5 s). Thus, in this study, 10 1-s no artifact-contaminated EEG data detected based on a manual inspection and extracted from the training phase of each BCI paradigm as "clean" epochs and five types of 10-s EEG data contaminated by artifacts, such as eye blinking, horizontal/vertical eye movements, teeth clenching, and flexing both arms, were prepared as "artifactual" epochs because these are well-known to generate ocular/muscular artifacts during EEG measurements. For training an SVM model, each 10-s-length artifactual data was separated into 10 1-s-length data without overlapping. Based on the 60 1-s epochs (10 1-s epochs $\times$ 6 classes), a 6-class SVM model was constructed. Note that segmented epochs of the BCI paradigms have different time length (i.e., MI: 2.5, ERP: 0.8, and SSVEP: 2.0 s). To apply DETECT based on a processing strategy for 1-s-length data, we extracted first 1-s data from the "clean" epochs if the target BCI paradigm was MI or SSVEP. For the epochs of the ERP paradigm, 0.2-s data before the stimulus onsets were concatenated to the "clean" epochs. Then, autoregressive features were extracted from the epochs to construct a multiclass SVM classifier of each BCI paradigm. The classifier and hard thresholding for the estimated artifactual class (certainty value obtained using the DETECT toolbox was over 0.5 or not) finally identified each epoch as being clean or artifact contaminated. **Table 1** lists the identification results. In all paradigms, data recorded in session 2 (day 2) had less artifactual data than data recorded in session 1 (day 1). In the MI and ERP paradigms, the number of artifactual data recorded in day 2 was significantly lower than data recorded in day 1 ($p = 0.001, 0.009$ for MI and ERP paradigms in t-test). However, in the SSVEP paradigm, the number in day 2 was not significantly lower ($p = 0.172$ in t-test). Note that we identify the epoch is neuronal unless a certainty value of all classes exceeded the hard threshold; thus, the thresholding process found an explicit artifactual class over 6 class labels. If the certainty values distributed throughout all classes and no one did not exceed the threshold, this modest

TABLE 1 | Number of artifact-contaminated epochs in training and testing phases of each BCI paradigm and subject.

Subject	MI				ERP				SSVEP			
	Session 1		Session 2		Session 1		Session 2		Session 1		Session 2	
	Train	Test	Train	Test	Train	Test	Train	Test	Train	Test	Train	Test
s1	6	2	8	6	149	330 (36)	80	215 (33)	3	2	0	1
s2	2	0	0	1	95	5 (5)	38	115 (25)	0	0	0	0
s3	1	0	7	10	158	62 (20)	17	14 (9)	14	10	1	2
s4	0	0	0	0	32	34 (14)	7	10 (4)	9	18	0	0
s5	4	4	7	5	0	0 (0)	395	282 (25)	19	11	14	8
s6	4	2	4	3	159	113 (24)	171	146 (29)	25	26	5	6
s7	21	30	6	8	75	200 (25)	52	21 (10)	8	7	4	4
s8	2	0	4	1	427	325 (32)	35	87 (22)	3	2	9	5
s9	0	0	9	2	43	73 (24)	145	99 (25)	1	9	0	1
s10	0	2	0	0	94	15 (6)	61	78 (20)	0	0	2	4
s11	5	4	0	0	50	56 (15)	16	47 (17)	0	0	0	0
s12	0	16	2	6	75	94 (22)	98	185 (31)	0	1	1	7
s13	1	0	1	1	131	212 (29)	139	103 (26)	6	3	3	1
s14	1	0	2	1	18	35 (11)	234	190 (32)	4	6	13	22
s15	3	20	0	1	25	19 (11)	48	7 (5)	1	1	3	16
s16	0	2	13	10	492	322 (33)	113	92 (19)	0	0	8	9
s17	27	36	4	6	232	187 (30)	263	267 (34)	1	1	15	21
s18	1	11	13	9	166	404 (31)	92	122 (29)	3	2	2	4
s19	1	8	2	7	159	300 (33)	36	169 (30)	7	15	2	3
s20	0	7	1	1	236	240 (34)	112	323 (35)	2	2	1	2
s21	31	30	0	0	69	84 (29)	268	129 (26)	15	9	3	5
s22	2	8	2	0	131	128 (32)	11	48 (18)	9	2	0	1
s23	0	0	9	0	141	194 (29)	160	227 (26)	0	36	1	1
s24	0	1	8	4	65	106 (27)	87	158 (31)	2	1	1	5
s25	3	11	6	2	184	122 (24)	14	59 (15)	2	2	8	4
s26	0	1	0	0	447	552 (36)	196	265 (32)	20	22	7	6
s27	3	12	1	1	172	312 (34)	150	346 (32)	1	5	11	14
s28	2	6	0	0	93	63 (21)	37	52 (19)	6	4	2	1
s29	8	20	2	4	32	159 (25)	101	27 (9)	3	4	3	3
s30	3	9	4	0	141	171 (34)	38	30 (14)	0	1	0	0
s31	7	3	0	1	33	82 (23)	25	60 (29)	0	0	1	0
s32	33	67	0	2	122	339 (33)	80	32 (13)	13	34	19	21
s33	0	1	4	0	119	52 (17)	107	59 (15)	0	2	1	2
s34	32	18	8	19	254	181 (33)	142	441 (35)	13	21	18	16
s35	7	2	0	3	35	41 (13)	135	82 (22)	1	0	11	18
s36	3	2	6	17	178	189 (34)	110	159 (32)	3	4	0	4
s37	5	15	0	1	353	557 (36)	2	2 (1)	6	4	0	2
s38	11	8	0	0	194	119 (29)	53	29 (10)	17	11	11	11
s39	21	32	2	0	111	55 (22)	0	37 (11)	1	3	2	6
s40	1	2	1	0	145	206 (33)	11	56 (16)	31	26	3	7
s41	0	2	4	9	107	101 (28)	137	265 (31)	5	6	2	2
s42	0	0	9	10	121	191 (31)	35	62 (19)	10	15	10	2
s43	0	0	9	7	148	290 (35)	11	13 (7)	2	13	0	0
s44	3	7	3	13	293	392 (35)	32	76 (25)	10	7	7	0
s45	27	13	0	0	160	270 (34)	19	52 (19)	1	4	1	0
s46	0	1	6	11	226	307 (35)	52	175 (34)	1	4	2	4
s47	3	5	2	1	261	438 (36)	159	319 (36)	7	6	1	5
s48	6	1	0	2	25	52 (18)	41	35 (13)	2	5	20	12

(Continued)

TABLE 1 | Continued

Subject	MI				ERP				SSVEP			
	Session 1		Session 2		Session 1		Session 2		Session 1		Session 2	
	Train	Test	Train	Test	Train	Test	Train	Test	Train	Test	Train	Test
s49	3	10	6	8	104	54 (15)	54	22 (7)	14	8	1	1
s50	23	48	4	9	48	229 (24)	2	0 (0)	0	0	5	6
s51	9	9	3	1	354	170 (31)	136	173 (29)	0	3	3	1
s52	0	0	2	1	20	74 (23)	57	139 (31)	3	8	0	2
s53	2	2	0	2	370	176 (30)	16	25 (8)	3	3	1	4
s54	3	14	1	0	149	107 (18)	66	51 (17)	7	6	7	4
Mean	6.11	9.33	3.43	3.81	152	178 (25.8)	87.0	116 (21.1)	5.82	7.31	4.54	5.30
Std	9.27	13.2	3.54	4.63	115	136 (8.99)	79.6	104 (10.1)	6.97	8.55	5.39	5.86

The total number of epochs in training and testing phases of the MI and SSVEP BCI paradigms is 100, respectively. The total number of epochs in training or testing phases of the ERP paradigm is 1,980 or 2,160. Numbers in parentheses indicate that the number of target 36 characters including spaces in "PATTERN_RECOGNITION_MACHINE_LEARNING" have been affected by artifact-contaminated epochs. When the number is 36, all copying processes contained the effect of artifacts.

identification method can not find artifact-contaminated epochs. In **Table 1**, there was an outlier: subject 5 in the session 1 of ERP paradigm had no artifact-contaminated epoch. This phenomenon might be caused by the above-mentioned reason.

Through the epoch identification process, artifact-contaminated epochs in both the training and the testing phases were detected. In the training phase, we also assumed that artifact-reduced epochs contribute to the construction of an effective classifier if the artifact reduction technique effectively reduced artifactual effects from the artifact-contaminated epochs. Therefore, the demixing matrix $\boldsymbol{W}$ was first trained by using all epochs in the training phase, and artifactual ICs were then removed from the artifact-contaminated epochs using the artifact reduction process described in sections 2.2, 2.3, and 2.4. After artifact reduction, the clean and artifact-reduced epochs in the training phase were applied to the baseline analysis methods described in section 3. For performance evaluation, the artifact-contaminated epochs in the testing phase were used to compute the classification accuracy of the artifact-reduced epochs:

$$Acc = \frac{N_{\text{correct}}}{N_{\text{total}}} \times 100\%, \tag{31}$$

where N_{correct} is the number of correct predictions, and N_{total} is the total number of artifact-contaminated epochs in the testing phase, as listed in **Table 1**, when the BCI paradigm was MI or SSVEP. Note that ERP data requires an averaging process for finding obvious feature waveforms (e.g., N200 and P300), and the averaged waveform relates to the classification performance. In other words, we cannot calculate the classification accuracy for each artifact-contaminated epoch in the paradigm. The numbers in parentheses in **Table 1** indicate the number of characters affected by artifacts (N_{total}), which is directly related to the assessment results. **Figure 2** shows the block diagram of the assessment procedure used in this study.

A three-way repeated measures analysis of variances (ANOVAs) was applied to the classification accuracy to explore the effect of the two sessions, three BCI paradigms, and three artifact reduction methods. In addition, artifact-reduced signals obtained using ICA, IVA, and ILRMA and that were reconstructed from muscular or ocular artifact-contaminated signals were visualized to qualitatively investigate the artifact reduction performances.

5. RESULTS

5.1. BCI Performance Before/After Applying Artifact Reduction Technique

Table 2 lists the classification accuracies for all subjects, sessions, paradigms, and artifact reduction methods. In addition, **Figure 3** shows the averaged classification accuracies over all subjects. A three-way repeated measures ANOVA using the classification accuracies of all subjects showed the significant main effects of the BCI paradigms [$F_{(2,829)} = 113.09$, $p < 0.001$] and artifact reduction methods [$F_{(2,829)} = 3.05$, $p = 0.048$]; however, it did not show any significant main effect of the sessions [$F_{(1,829)} = 1.29$, $p = 0.256$]. There were no interaction effects among them. *post-hoc* analysis using Tukey test revealed that the ICA and ILRMA results had a significant difference ($p = 0.039$).

The classification accuracies obtained using ILRMA in all cases were always equal to or higher than the higher accuracy of using ICA or IVA (see **Table 2**). In particular, ILRMA improved the discriminability of artifact-reduced data for 31 subjects in session 1 and 24 subjects in session 2. When there was a difference in the artifact reduction performance, we highlighted the superior results in bold in the table. The averaged accuracy of using ILRMA in all BCI paradigms was also equal to or higher than that of using ICA and IVA (**Figure 3**). Interestingly, in some cases, artifact-contaminated data showed higher BCI performance than ICA and IVA. However, ILRMA always showed equal or higher performance compared to artifact-contaminated situations. For these results, ILRMA salvaged effective components for solving the classification problem from artifact-contaminated signals in the MI and SSVEP paradigms.

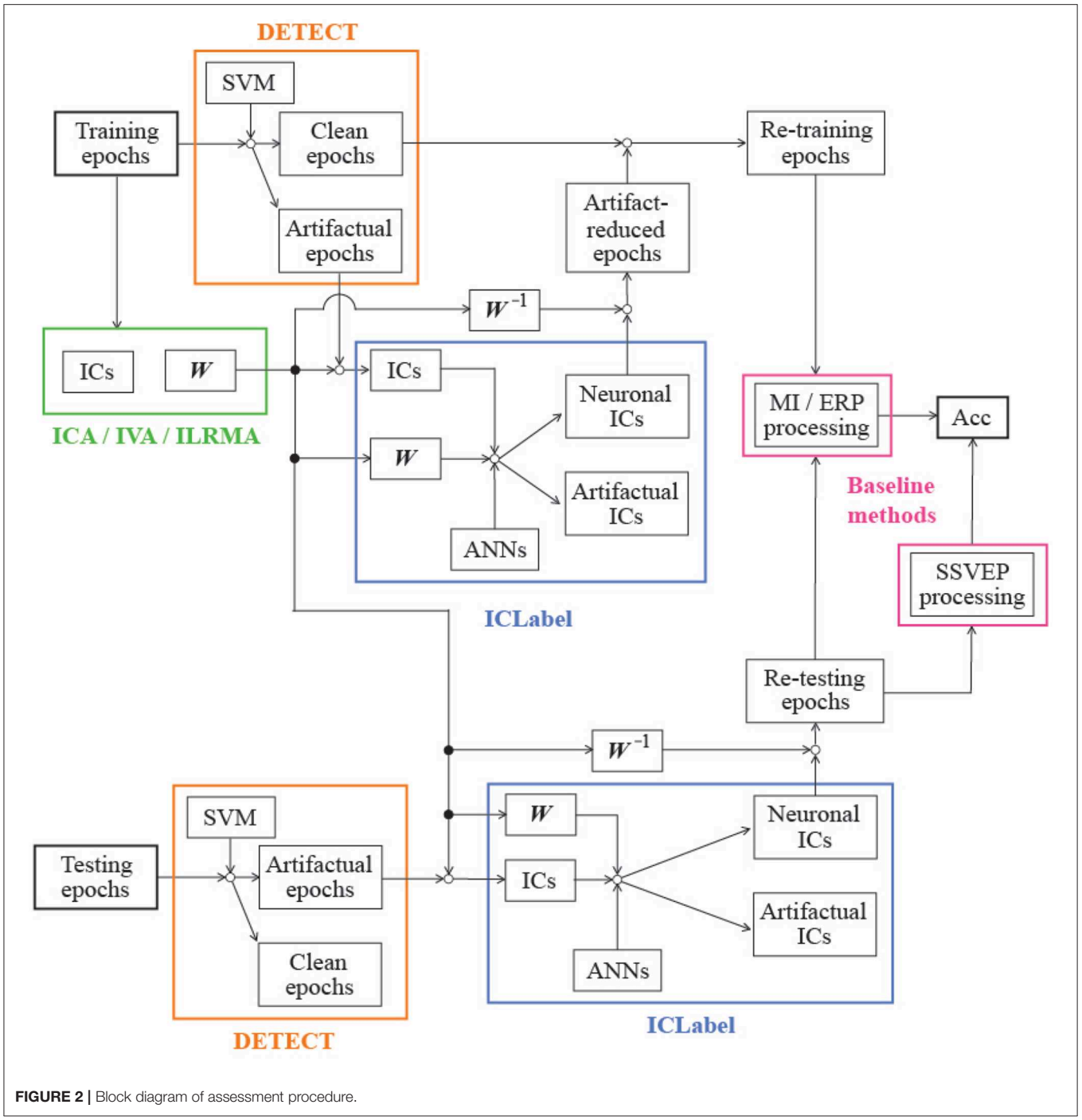

FIGURE 2 | Block diagram of assessment procedure.

Conversely, in the ERP paradigm, ICA was sufficient to remove the artifactual components and achieved almost 100% accuracy.

5.2. Representation of Original and Artifact-Reduced Signals

Figures 4, **5** show artifact-contaminated EEG epochs and artifact-reduced EEG epochs obtained using ICA, IVA, and ILRMA in the MI, ERP, and SSVEP paradigms. They were qualitatively indicated that ILRMA could better remove artifact effects compared to ICA and IVA. In addition, the task-independent components were removed by ILRMA to leave characteristic features in each paradigm (e.g., event-related desynchronization caused by motor imagery and evoked potential by steady-state visual stimulus) instead of the attenuating power of all frequency components. This resulted in improvements in these BCI performances.

TABLE 2 | Classification accuracies for all subjects, sessions, paradigms, and artifact reduction methods.

Subject	ICA						IVA						ILRMA					
	MI		ERP		SSVEP		MI		ERP		SSVEP		MI		ERP		SSVEP	
	Se1	Se2	Se1	Se2	Se1	Se2	Se1	Se2	Se1	Se2	Se1	Se2	Se1	Se2	Se1	Se2	Se1	Se2
s1	0	33.3	55.6	**90.9**	**100**	100	0	16.7	**61.1**	81.8	50.0	100	0	**66.7**	**61.1**	**90.9**	**100**	100
s2	–	0	100	100	–	–	–	**100**	100	100	–	–	–	**100**	100	100	–	–
s3	–	100	100	100	80.0	50.0	–	100	100	100	**90.0**	**100**	–	100	100	100	**90.0**	**100**
s4	–	–	85.7	100	100	–	–	–	85.7	100	100	–	–	–	85.7	100	100	–
s5	100	80.0	–	56.0	**90.9**	100	100	80.0	–	56.0	72.7	100	100	80.0	–	56.0	**90.9**	100
s6	100	66.7	100	100	92.3	100	100	66.7	100	100	92.3	100	100	66.7	100	100	**96.2**	100
s7	**50.0**	62.5	100	100	85.7	100	46.7	62.5	100	100	85.7	100	**50.0**	62.5	100	100	85.7	100
s8	–	100	81.3	**100**	50.0	**40.0**	–	100	**87.5**	95.5	50.0	20.0	–	100	**87.5**	**100**	50.0	**40.0**
s9	–	100	100	100	55.6	0	–	100	100	100	55.6	0	–	100	100	100	55.6	0
s10	0	–	100	100	–	100	**50.0**	–	100	100	–	100	**50.0**	–	100	100	–	100
s11	75.0	–	100	100	–	–	**100**	–	100	100	–	–	**100**	–	100	100	–	–
s12	37.5	50.0	100	96.8	0	100	43.8	50.0	100	96.8	0	100	**50.0**	50.0	100	96.8	**100**	100
s13	–	0	100	100	100	0	–	0	100	100	100	0	–	0	100	100	100	0
s14	–	0	100	96.9	83.3	81.8	–	0	100	96.9	83.3	81.8	–	0	100	96.9	83.3	**90.9**
s15	70.0	0	100	100	100	87.5	70.0	0	100	100	100	87.5	70.0	0	100	100	100	**93.8**
s16	0	70.0	100	100	–	100	**100**	**90.0**	100	100	–	100	**100**	**90.0**	100	100	–	100
s17	86.1	**50.0**	**93.3**	91.2	0	81.0	86.1	33.3	90.0	91.2	**100**	81.0	86.1	**50.0**	**93.3**	**94.1**	**100**	**85.7**
s18	**81.8**	88.9	100	100	100	100	72.7	88.9	100	100	100	100	**81.8**	88.9	100	100	100	100
s19	100	71.4	100	100	73.3	100	100	**85.7**	100	100	73.3	100	100	**85.7**	100	100	**80.0**	100
s20	**71.4**	0	100	100	100	100	57.1	0	100	100	100	100	**71.4**	0	100	100	100	100
s21	86.7	–	100	100	**100**	100	93.3	–	100	100	88.9	100	**96.7**	–	100	100	**100**	100
s22	75.0	–	93.8	88.9	100	0	**87.5**	–	93.8	88.9	100	0	**87.5**	–	93.8	88.9	100	0
s23	–	–	**86.2**	69.2	47.2	0	–	–	72.4	**73.1**	52.8	0	–	–	**86.2**	**73.1**	**55.6**	0
s24	0	25.0	100	90.3	0	80.0	0	**75.0**	100	**93.6**	0	80.0	0	**75.0**	100	**93.6**	**100**	80.0
s25	27.3	**50.0**	100	93.3	100	75.0	**45.5**	0	100	93.3	100	**100**	**45.5**	**50.0**	100	93.3	100	**100**
s26	100	–	**83.3**	87.5	90.9	100	100	–	80.6	87.5	90.9	100	100	–	**83.3**	**90.6**	90.9	100
s27	41.7	0	100	100	100	85.7	50.0	0	100	100	100	92.9	**58.3**	**100**	100	100	100	**100**
s28	83.3	–	100	94.7	100	100	**100**	–	100	94.7	100	100	**100**	–	100	94.7	100	100
s29	65.0	50.0	88.0	100	75.0	100	85.0	75.0	**96.0**	100	75.0	100	**100**	**100**	**96.0**	100	75.0	100
s30	55.6	–	82.4	92.9	100	–	55.6	–	82.4	92.9	100	–	55.6	–	**85.3**	92.9	100	–
s31	100	0	100	100	–	–	100	0	100	100	–	–	100	0	100	100	–	–
s32	43.3	100	100	100	88.2	95.2	44.8	100	100	100	**91.2**	95.2	**52.2**	100	100	100	**91.2**	95.2
s33	100	–	100	93.3	100	0	100	–	100	93.3	100	0	100	–	100	93.3	100	0
s34	55.6	42.1	87.8	91.4	76.2	81.3	55.6	**47.4**	**90.9**	**97.1**	76.2	81.3	55.6	**47.4**	**90.9**	**97.1**	**90.5**	81.3
s35	**50.0**	66.7	100	95.5	–	83.3	0	66.7	100	95.5	–	83.3	**50.0**	66.7	100	95.5	–	83.3
s36	50.0	94.1	100	87.5	100	100	50.0	94.1	100	87.5	100	100	50.0	94.1	100	87.5	100	100
s37	86.7	100	69.4	100	100	100	**100**	100	72.2	100	100	100	**100**	100	**75.0**	100	100	100
s38	**75.0**	–	96.6	100	100	72.7	62.5	–	96.6	100	100	72.7	**75.0**	–	96.6	100	100	72.7
s39	62.5	–	86.4	100	100	**83.3**	62.5	–	86.4	100	100	50.0	62.5	–	86.4	100	100	**83.3**
s40	0	–	97.0	100	**57.7**	85.7	0	–	90.9	100	46.2	85.7	0	–	97.0	100	**57.7**	85.7
s41	50.0	66.7	100	100	**83.3**	100	50.0	66.7	100	100	66.7	100	50.0	66.7	100	100	**83.3**	100
s42	–	80.0	100	94.7	66.7	100	–	80.0	100	94.7	**73.3**	100	–	80.0	100	94.7	**73.3**	100
s43	–	85.7	100	100	100	–	–	85.7	100	100	100	–	–	85.7	100	100	100	–
s44	100	100	100	100	0	–	100	100	100	100	**100**	–	100	100	100	100	**100**	–
s45	76.9	–	91.2	94.7	100	–	**92.3**	–	91.2	94.7	100	–	**92.3**	–	91.2	94.7	100	–
s46	100	63.6	100	94.1	100	100	100	63.6	100	94.1	100	100	100	63.6	100	94.1	100	100
s47	80.0	100	100	**100**	33.3	80.0	80.0	100	100	97.2	33.3	80.0	80.0	100	100	**100**	33.3	80.0
s48	100	0	100	100	100	100	100	0	100	100	100	100	100	0	100	100	100	100

(Continued)

TABLE 2 | Continued

Subject	ICA						IVA						ILRMA					
	MI		ERP		SSVEP		MI		ERP		SSVEP		MI		ERP		SSVEP	
	Se1	Se2	Se1	Se2	Se1	Se2	Se1	Se2	Se1	Se2	Se1	Se2	Se1	Se2	Se1	Se2	Se1	Se2
s49	50.0	50.0	100	100	100	100	60.0	50.0	100	100	87.5	100	**70.0**	50.0	100	100	100	100
s50	60.4	55.6	87.5	–	–	83.3	62.5	44.4	87.5	–	–	83.3	**68.8**	**66.7**	**91.7**	–	–	83.3
s51	44.4	0	87.1	89.7	66.7	100	44.4	**100**	**90.3**	89.7	66.7	100	44.4	**100**	**90.3**	89.7	66.7	100
s52	–	100	100	100	75.0	100	–	100	100	100	**100**	100	–	100	100	100	**100**	100
s53	0	100	96.7	100	100	100	0	100	96.7	100	100	75.0	0	100	96.7	100	100	100
s54	57.1	–	100	100	83.3	100	42.9	–	100	100	**100**	100	57.1	–	100	100	**100**	100
Mean	61.6	59.4	95.3	96.0	82.0	81.4	66.3	62.1	95.3	96.0	83.0	81.5	**70.0**	**67.3**	**96.0**	**96.4**	**90.4**	**83.8**
SE	4.91	5.98	1.22	1.08	4.01	4.66	4.93	6.09	1.17	1.06	3.70	4.78	4.65	5.80	1.04	1.03	2.40	4.65

Hyphens indicate that no artifact-contaminated epochs existed in the testing phase on the session. Bold values indicate that the accuracies over the three artifact reduction methods have different values and the results were higher than the other ones.

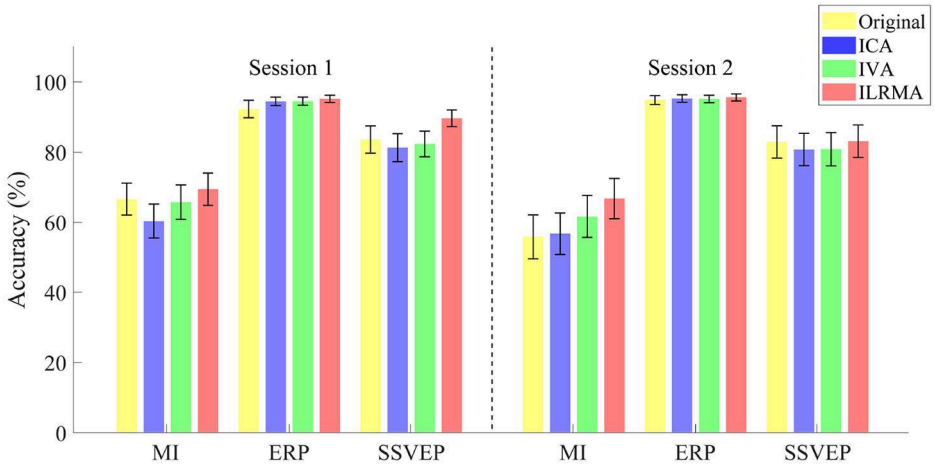

FIGURE 3 | Averaged classification accuracies over all subjects for sessions, paradigms, and artifact reduction methods. Original indicates the results of using all data without artifact reduction method.

6. DISCUSSION

6.1. Automatic Processing Architecture

ICA-based artifact reduction techniques have been widely used in the field of EEG signal processing because of their powerful signal separation accuracy, simplicity (low computational cost), and ease of use (Delorme et al., 2007; Dimigen, 2019; Jiang et al., 2019). The techniques for limiting ocular and muscular artifacts (Chen et al., 2019; Tian et al., 2020) other than the ICA family are useful if they are integrated in a cascade-type processing module, which can automatically identify the type of artifact contained in the EEG observation. A simple filtering (linear combination) approach such as ICA, which multiplies the demixing matrix $\boldsymbol{W}$ as a filter, is faster and user-friendly. IVA and ILRMA use this property and can sufficiently cope with online processing as long as they can learn the demixing matrix. In addition, these algorithms can benefit from the ICLabel classifier (Pion-Tonachini et al., 2019) for IC identification to realize an automatic artifact reduction method. Thus, the ILRMA-based artifact reduction technique (1) has higher accuracy than ICA, (2) has low computational cost (equivalent to ICA) in an online process, (3) is a changeable module for the ICA decomposition function, and (4) can simultaneously remove multiple types of artifacts. Note that the ICLabel classifier is expected to be updated frequently in the future. Although the EEGLAB toolbox keeps track of updates in the `run_ICL` function, the label assignment results may change depending on the updates. In this study, we selected the "default" version for IC identification.

6.2. Efficacy of Artifact Reduction for BCIs

Researchers who propose original artifact reduction techniques for BCIs should describe not only the signal quality but also the discriminative performance of the extracted components to demonstrate their efficacy in BCIs. The performances of proposed artifact reduction techniques in most previous studies were evaluated and ranked based on a metric (e.g., signal-to-noise

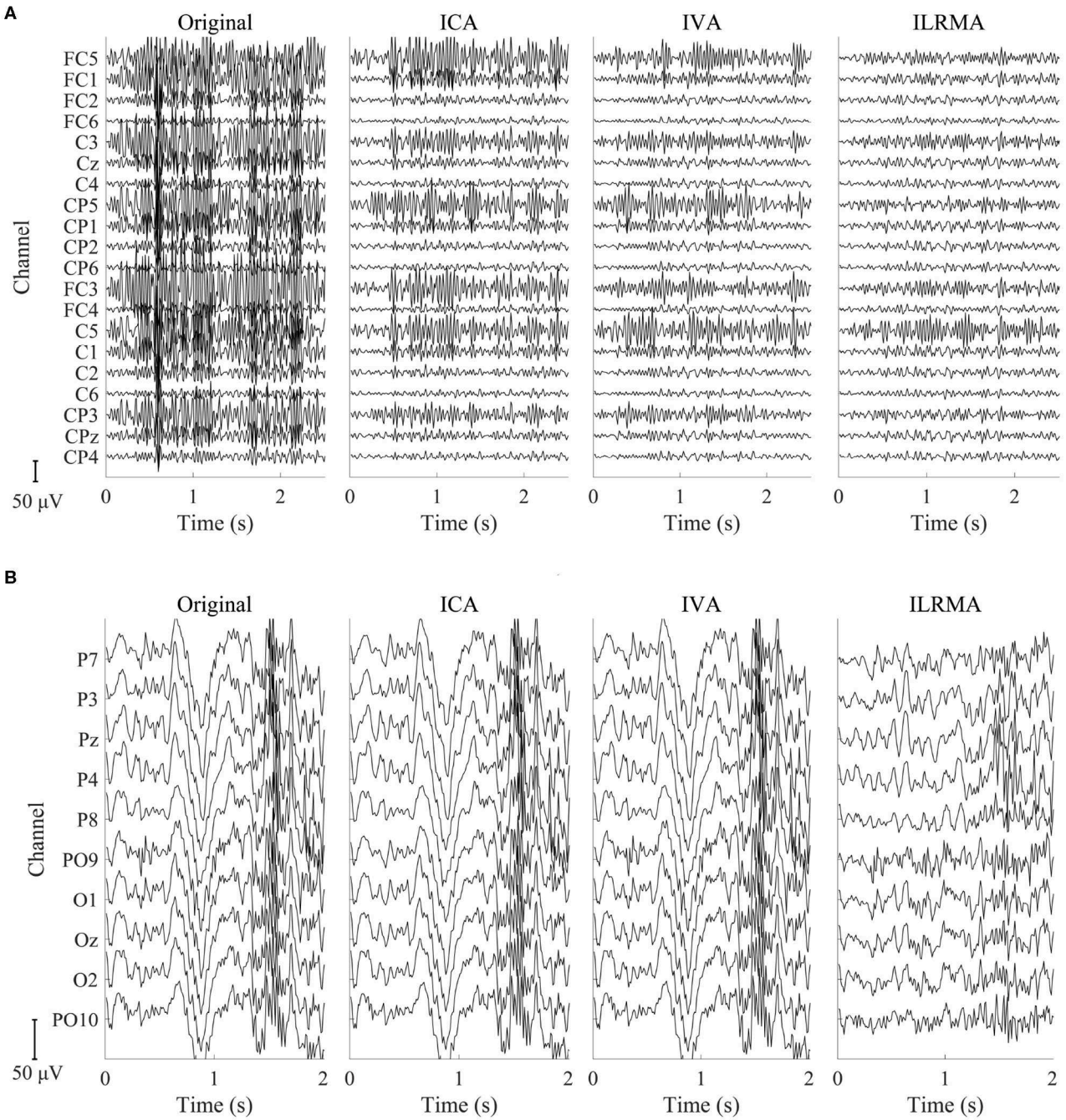

FIGURE 4 | Artifact-contaminated EEG epoch and artifact-reduced EEG epochs estimated by ICA, IVA, and ILRMA in the **(A)** MI paradigm and **(B)** SSVEP paradigm.

ratio and correlation) that indicates how the signal quality of the estimated neuronal sources was preserved (Islam et al., 2016). We do not know the original (true) neuronal sources of EEG observations; thus, synthetic data whose pseudo-neuronal/pseudo-artifactual sources and mixing process are known were usually used to calculate the metric (Chen et al., 2019; Mucarquer et al., 2019). After the quantified evaluation of signal quality in the estimated sources through the proposed artifact reduction technique, the separation ability for real data is qualitatively shown (Blum et al., 2019; Kanoga et al., 2019a). However, the evaluation of the discriminative performance of the remaining sources (extracted components) is not a major/standard quantitative one in this field. To implement an artifact reduction technique into the BCI framework, it is more

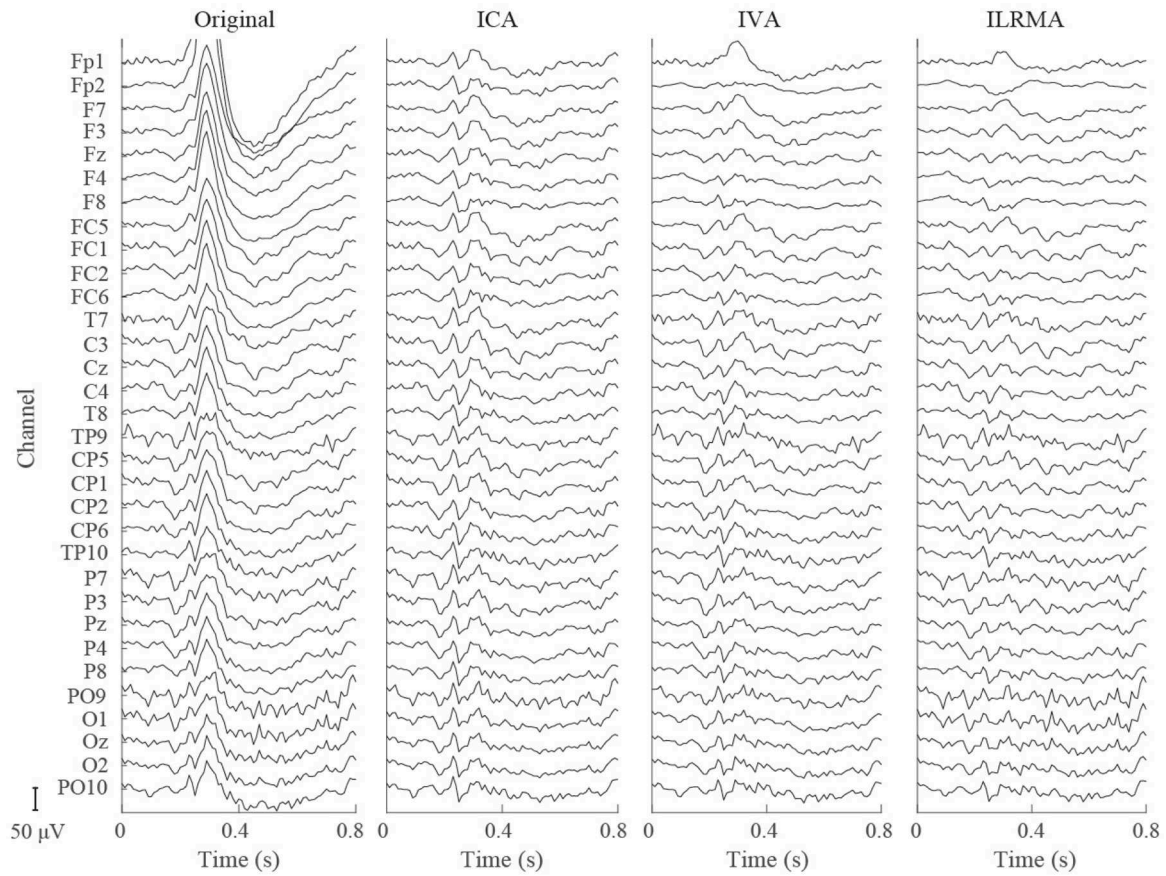

FIGURE 5 | Artifact-contaminated EEG epoch and artifact-reduced EEG epochs estimated by ICA, IVA, and ILRMA in the ERP paradigm.

important to know which aspect of the technique is the most crucial to the classification/identification performance. In this study, we demonstrated improved MI- and SSVEP-based BCI performances using our proposed technique, which represents common and recurrent properties of artifactual waveforms into trials over all classes in low-rank bases and automatically removes them. Except for session 2 in the MI-based BCI performance, our proposed method showed over 70% averaged accuracies (**Table 2**), which is required for satisfactory BCI control (Sellers et al., 2006). When we consider the time latency during an MI period and change the starting time point of MI features from fixed to flexible by using time window selection algorithm such as correlation-based time window selection (Feng et al., 2018), the average performance of the MI-based BCI might be improved. Furthermore, using other kind of feature extraction method such as sparse FBCSP (Zhang et al., 2015) is one of good solution to improve the MI-based BCI performance because the method automatically chose the filter bands with superior accuracies compared with FBCSP. In the case of the ERP-based BCI, ICA was already effective enough. Therefore, the superiority of ILRMA could not be confirmed; however, its performance is equivalent to that of ICA. Although this paper did not present the quantitative signal quality of the estimated neuronal sources because we did not prepare synthetic data to avoid the artificial bias of neuronal characteristics (all EEG observations have unclear individual differences such as amplitudes and latencies, so we could not easily predict the features and generate pseudo/synthetic data), the classification/identification results obtained with three well-known BCI paradigms should be helpful information for practitioners and implementers.

6.3. Limitations

The results obtained using the DETECT toolbox were treated as the grand truth. However, the muscular label reflected the characteristics of "clenching" and "flexing both arms." Other types of muscular artifacts, such as "changing head direction," may not be extracted as artifactual epochs. In addition, the "100% accuracy" was sometimes calculated using only one testing epoch although other accuracies were calculated using more epochs (e.g., 20). The comparison of artifact reduction techniques was fair because the number of artifact-contaminated epochs was the same over the factor. However, the comparisons of BCI paradigms and multiday effects were not fair: each factor has different numbers of artifact-contaminated epochs. Evaluating the techniques as fairly as possible by using the DETECT

toolbox is very difficult. For solving this problem, an artifact-contaminated EEG dataset with multiple types of intensity-manipulated artifacts is required in this research field to enable rapid developments in artifact reduction techniques for BCIs.

6.4. Future Works

Further improvement of ILRMA-based artifact reduction techniques is expected through the introduction of an identification algorithm for decomposed frequency components and a soft-threshold-like wavelet-enhanced ICA (Castellanos and Makarov, 2006). Despite the fact that ILRMA decomposes the STFT of the original signals up to each frequency bin, our automatic processing architecture reconstructs artifact-reduced signals by replacing artifactual source(s) with zeros (replacing entire frequency bins with zeros) to adapt the ICLabel classifier, which needs time-series ICs. In other words, a lot of neural information is lost in the reduction step. Signal reconstruction should be made more sophisticated by considering the effective frequency band adjusted to the BCI paradigm.

Moreover, we need further investigations of artifact reduction methods in practical situations such as using wearable devices that have small number of channels (in an extreme case, the number of channels is only one) for EEG measurements. In such situation, the performance of artifact reduction techniques will change and might be decreased. Recent studies attempt to propose a generic artifact removal algorithm (Chen et al., 2019). Unlike the time-domain algorithm, frequency-domain methods (i.e., IVA and ILRMA) can separate single-channel data if the differences in data-driven spectral basis functions can be learned well (Kanoga and Mitsukura, 2014; Kanoga et al., 2019a). Thus, we will investigate our proposed algorithm in practical situations and extend it as a generic and user-friendly algorithm for reducing artifacts from EEG data.

The ICA family, including IVA and ILRMA, represents EEG observations through linear combinations of sources based on a time-invariant demixing matrix; the trained demixing matrix may sometimes cause instability through inter-/intrasubject variabilities. By integrating with a transfer learning algorithm (Pan and Yang, 2009; Tan et al., 2018), relearning from the general filter (demixing matrix) to the user-specific filter according to the data while performing online processing could potentially reduce the variability and provide more convenient and practical BCIs.

DATA AVAILABILITY STATEMENT

Publicly available datasets were analyzed in this study. This data can be found here: http://gigadb.org/dataset/view/id/100542/File_page/1.

AUTHOR CONTRIBUTIONS

SK obtained the initial idea for this study. All authors contributed to the planning and design of the study. SK and TH analyzed the data and interpreted the results. SK compiled the first draft of the article. All authors participated in revisions to finalize the draft of the manuscript.

FUNDING

This research was supported in part by the New Energy and Industrial Technology Development Organization (NEDO), Japan.

REFERENCES

Amari, S.-I. (1998). Natural gradient works efficiently in learning. *Neural Comput.* 10, 251–276. doi: 10.1162/089976698300017746

Ang, K. K., Chin, Z. Y., Zhang, H., and Guan, C. (2008). "Filter bank common spatial pattern (FBCSP) in brain-computer interface," in *2008 IEEE International Joint Conference on Neural Networks (IEEE World Congress on Computational Intelligence)* (Hong Kong: IEEE), 2390–2397.

Arieli, A., Sterkin, A., Grinvald, A., and Aertsen, A. (1996). Dynamics of ongoing activity: Explanation of the large variability in evoked cortical responses. *Science* 273, 1868–1871. doi: 10.1126/science.273.5283.1868

Bell, A. J., and Sejnowski, T. J. (1995). An information-maximization approach to blind separation and blind deconvolution. *Neural Comput.* 7, 1129–1159. doi: 10.1162/neco.1995.7.6.1129

Belouchrani, A., Abed-Meraim, K., Cardoso, J.-F., and Moulines, E. (1997). A blind source separation technique using second-order statistics. *IEEE Trans. Signal Process.* 45, 434–444. doi: 10.1109/78.554307

Blum, S., Jacobsen, N., Bleichner, M. G., and Debener, S. (2019). A Riemannian modification of artifact subspace reconstruction for EEG artifact handling. *Front. Hum. Neurosci.* 13:141. doi: 10.3389/fnhum.2019.00141

Brainard, D. H. (1997). The psychophysics toolbox. *Spatial Vis.* 10, 433–436. doi: 10.1163/156856897X00357

Budd, J. M., and Kisvárday, Z. F. (2001). Local lateral connectivity of inhibitory clutch cells in layer 4 of cat visual cortex (area 17). *Exp. Brain Res.* 140, 245–250. doi: 10.1007/s002210100817

Castellanos, N. P., and Makarov, V. A. (2006). Recovering EEG brain signals: artifact suppression with wavelet enhanced independent component analysis. *J. Neurosci. Methods* 158, 300–312. doi: 10.1016/j.jneumeth.2006.05.033

Chen, X., Liu, Q., Tao, W., Li, L., Lee, S., Liua, A., et al. (2019). ReMAE: a user-friendly toolbox for removing muscle artifacts from EEG. *IEEE Trans. Instrum. Meas.* 69, 2105–2119. doi: 10.1109/TIM.2019.2920186

Choi, S., Cichocki, A., Park, H.-M., and Lee, S.-Y. (2005). Blind source separation and independent component analysis: a review. *Neural Inform. Process. Lett. Rev.* 6, 1–57.

Delorme, A., and Makeig, S. (2004). EEGLAB: An open source toolbox for analysis of single-trial EEG dynamics including independent component analysis. *J. Neurosci. Methods* 134, 9–21. doi: 10.1016/j.jneumeth.2003.10.009

Delorme, A., Mullen, T., Kothe, C., Acar, Z. A., Bigdely-Shamlo, N., Vankov, A., et al. (2011). EEGLAB, SIFT, NFT, BCILAB, and ERICA: New tools for advanced EEG processing. *Comput. Intell. Neurosci.* 2011:10. doi: 10.1155/2011/130714

Delorme, A., Sejnowski, T., and Makeig, S. (2007). Enhanced detection of artifacts in EEG data using higher-order statistics and independent component analysis. *Neuroimage* 34, 1443–1449. doi: 10.1016/j.neuroimage.2006.11.004

Dimigen, O. (2019). Optimizing the ICA-based removal of ocular EEG artifacts from free viewing experiments. *Neuroimage* 207:116117. doi: 10.1016/j.neuroimage.2019.116117

Duong, N. Q., Vincent, E., and Gribonval, R. (2010). Under-determined reverberant audio source separation using a full-rank spatial covariance model. *IEEE Trans. Audio Speech Lang. Process.* 18, 1830–1840. doi: 10.1109/TASL.2010.2050716

Fazli, S., Popescu, F., Danóczy, M., Blankertz, B., Müller, K.-R., and Grozea, C. (2009). Subject-independent mental state classification in single trials. *Neural Netw*. 22, 1305–1312. doi: 10.1016/j.neunet.2009.06.003

Feng, J., Yin, E., Jin, J., Saab, R., Daly, I., Wang, X., et al. (2018). Towards correlation-based time window selection method for motor imagery BCIs. *Neural Netw*. 102, 87–95. doi: 10.1016/j.neunet.2018.02.011

Hagemann, D., and Naumann, E. (2001). The effects of ocular artifacts on (lateralized) broadband power in the EEG. *Clin. Neurophysiol*. 112, 215–231. doi: 10.1016/S1388-2457(00)00541-1

Halliday, D. M., Conway, B. A., Farmer, S. F., and Rosenberg, J. R. (1998). Using electroencephalography to study functional coupling between cortical activity and electromyograms during voluntary contractions in humans. *Neurosci. Lett*. 241, 5–8. doi: 10.1016/S0304-3940(97)00964-6

Hiroe, A. (2006). "Solution of permutation problem in frequency domain ICA, using multivariate probability density functions," in *International Conference on Independent Component Analysis and Signal Separation* (Charleston: Springer), 601–608. doi: 10.1007/11679363_75

Hunter, D. R., and Lange, K. (2000). Quantile regression via an mm algorithm. *J. Comput. Graph. Stat*. 9, 60–77. doi: 10.1080/10618600.2000.10474866

Hyvärinen, A., and Oja, E. (1997). A fast fixed-point algorithm for independent component analysis. *Neural Comput*. 9, 1483–1492. doi: 10.1162/neco.1997.9.7.1483

Islam, M. K., Rastegarnia, A., and Yang, Z. (2016). Methods for artifact detection and removal from scalp EEG: a review. *Neurophysiol. Clin*. 46, 287–305. doi: 10.1016/j.neucli.2016.07.002

James, C. J., and Hesse, C. W. (2004). Independent component analysis for biomedical signals. *Physiol. Meas*. 26:R15. doi: 10.1088/0967-3334/26/1/R02

Jiang, X., Bian, G.-B., and Tian, Z. (2019). Removal of artifacts from EEG signals: a review. *Sensors* 19:987. doi: 10.3390/s19050987

Jung, T.-P., Makeig, S., Humphries, C., Lee, T.-W., McKeown, M. J., Iragui, V., et al. (2000). Removing electroencephalographic artifacts by blind source separation. *Psychophysiology* 37, 163–178. doi: 10.1111/1469-8986.3720163

Kanoga, S., Kanemura, A., and Asoh, H. (2019a). Multi-scale dictionary learning for ocular artifact reduction from single-channel electroencephalograms. *Neurocomputing* 347, 240–250. doi: 10.1016/j.neucom.2019.02.060

Kanoga, S., and Mitsukura, Y. (2014). Eye-blink artifact reduction using 2-step nonnegative matrix factorization for single-channel electroencephalographic signals. *J. Signal Process*. 18, 251–257. doi: 10.2299/jsp.18.251

Kanoga, S., and Mitsukura, Y. (2017). "Review of artifact rejection methods for electroencephalographic systems," in *Electroencephalography* 69, 69–89. doi: 10.5772/68023

Kanoga, S., Nakanishi, M., and Mitsukura, Y. (2016). Assessing the effects of voluntary and involuntary eyeblinks in independent components of electroencephalogram. *Neurocomputing* 193, 20–32. doi: 10.1016/j.neucom.2016.01.057

Kanoga, S., Nakanishi, M., Murai, A., Tada, M., and Kanemura, A. (2019b). Robustness analysis of decoding SSVEPs in humans with head movements using a moving visual flicker. *J. Neural Eng*. 17:016009. doi: 10.1088/1741-2552/ab5760

Karson, C. N. (1983). Spontaneous eye-blink rates and dopaminergic systems. *Brain* 106, 643–653. doi: 10.1093/brain/106.3.643

Kaufmann, T., Schulz, S., Grünzinger, C., and Kübler, A. (2011). Flashing characters with famous faces improves ERP-based brain-computer interface performance. *J. Neural Eng*. 8:056016. doi: 10.1088/1741-2560/8/5/056016

Kim, T., Attias, H. T., Lee, S.-Y., and Lee, T.-W. (2006a). Blind source separation exploiting higher-order frequency dependencies. *IEEE Trans. Audio Speech Lang. Process*. 15, 70–79. doi: 10.1109/TASL.2006.872618

Kim, T., Lee, I., and Lee, T.-W. (2006b). "Independent vector analysis: definition and algorithms," in *2006 Fortieth Asilomar Conference on Signals, Systems and Computers* (Pacific Grove, CA: IEEE), 1393–1396. doi: 10.1109/ACSSC.2006.354986

Kitamura, D., Ono, N., and Saruwatari, H. (2017). "Experimental analysis of optimal window length for independent low-rank matrix analysis," in *2017 25th European Signal Processing Conference (EUSIPCO)* (Kos: IEEE), 1170–1174. doi: 10.23919/EUSIPCO.2017.8081392

Kitamura, D., Ono, N., Sawada, H., Kameoka, H., and Saruwatari, H. (2016). Determined blind source separation unifying independent vector analysis and nonnegative matrix factorization. *IEEE/ACM Trans. Audio Speech Lang. Process*. 24, 1622–1637. doi: 10.1109/TASLP.2016.2577880

Lawhern, V., Hairston, W. D., and Robbins, K. (2013). Detect: A MATLAB toolbox for event detection and identification in time series, with applications to artifact detection in EEG signals. *PLoS ONE* 8:e62944. doi: 10.1371/journal.pone.0062944

Lee, D. D., and Seung, H. S. (1999). Learning the parts of objects by non-negative matrix factorization. *Nature* 401:788. doi: 10.1038/44565

Lee, M.-H., Fazli, S., Kim, K.-T., and Lee, S.-W. (2016). "Development of an open source platform for brain-machine interface: OpenBMI," in *2016 4th International Winter Conference on Brain-Computer Interface (BCI)* (Yongpyong: IEEE), 1–2. doi: 10.1109/IWW-BCI.2016.7457440

Lee, M.-H., Kwon, O.-Y., Kim, Y.-J., Kim, H.-K., Lee, Y.-E., Williamson, J., et al. (2019). EEG dataset and OpenBMI toolbox for three BCI paradigms: an investigation into BCI illiteracy. *GigaScience* 8:giz002. doi: 10.1093/gigascience/giz002

Lee, T.-W., Girolami, M., and Sejnowski, T. J. (1999). Independent component analysis using an extended infomax algorithm for mixed subgaussian and supergaussian sources. *Neural Comput*. 11, 417–441. doi: 10.1162/089976699300016719

Lin, Z., Zhang, C., Wu, W., and Gao, X. (2006). Frequency recognition based on canonical correlation analysis for SSVEP-based BCIs. *IEEE Trans. Biomed. Eng*. 53, 2610–2614. doi: 10.1109/TBME.2006.886577

Mohammadpour, M., and Rahmani, V. (2017). "A hidden Markov model-based approach to removing EEG artifact," in *2017 5th Iranian Joint Congress on Fuzzy and Intelligent Systems (CFIS)* (Qazvin: IEEE), 46–49. doi: 10.1109/CFIS.2017.8003655

Mucarquer, J. A., Prado, P., Escobar, M.-J., El-Deredy, W., and Zañartu, M. (2019). Improving EEG muscle artifact removal with an EMG array. *IEEE Trans. Instrum. Meas*. 69, 815–824. doi: 10.1109/TIM.2019.2906967

Odena, A. (2016). Semi-supervised learning with generative adversarial networks. *arXiv preprint arXiv:1606.01583*.

Ogino, M., Kanoga, S., Muto, M., and Mitsukura, Y. (2019). Analysis of prefrontal single-channel EEG data for portable auditory ERP-based brain-computer interfaces. *Front. Hum. Neurosci*. 13:250. doi: 10.3389/fnhum.2019.00250

Ono, N. (2011). "Stable and fast update rules for independent vector analysis based on auxiliary function technique," in *2011 IEEE Workshop on Applications of Signal Processing to Audio and Acoustics (WASPAA)* (New Paltz, NY: IEEE), 189–192. doi: 10.1109/ASPAA.2011.6082320

Onton, J., and Makeig, S. (2006). Information-based modeling of event-related brain dynamics. *Prog. Brain Res*. 159, 99–120. doi: 10.1016/S0079-6123(06)59007-7

Pan, S. J., and Yang, Q. (2009). A survey on transfer learning. *IEEE Trans. Knowl. Data Eng*. 22, 1345–1359. doi: 10.1109/TKDE.2009.191

Parini, S., Maggi, L., Turconi, A. C., and Andreoni, G. (2009). A robust and self-paced BCI system based on a four class SSVEP paradigm: algorithms and protocols for a high-transfer-rate direct brain communication. *Comput. Intell. Neurosci*. 2009:864564. doi: 10.1155/2009/864564

Pfurtscheller, G., and Da Silva, F. L. (1999). Event-related EEG/MEG synchronization and desynchronization: basic principles. *Clin. Neurophysiol*. 110, 1842–1857. doi: 10.1016/S1388-2457(99)00141-8

Pfurtscheller, G., and Neuper, C. (2001). Motor imagery and direct brain-computer communication. *Proc. IEEE* 89, 1123–1134. doi: 10.1109/5.939829

Pion-Tonachini, L., Kreutz-Delgado, K., and Makeig, S. (2019). ICLabel: an automated electroencephalographic independent component classifier, dataset, and website. *Neuroimage* 198, 181–197. doi: 10.1016/j.neuroimage.2019.05.026

Regan, D. (1966). Some characteristics of average steady-state and transient responses evoked by modulated light. *Electroencephalogr. Clin. Neurophysiol*. 20, 238–248. doi: 10.1016/0013-4694(66)90088-5

Salimans, T., Goodfellow, I., Zaremba, W., Cheung, V., Radford, A., and Chen, X. (2016). "Improved techniques for training GANs," in *Advances in Neural Information Processing Systems* (Barcelona), 2234–2242.

Sawada, H., Kameoka, H., Araki, S., and Ueda, N. (2013). Multichannel extensions of non-negative matrix factorization with complex-valued data. *IEEE Trans. Audio Speech Lang. Process*. 21, 971–982. doi: 10.1109/TASL.2013.2239990

Sellers, E. W., Krusienski, D. J., McFarland, D. J., Vaughan, T. M., and Wolpaw, J. R. (2006). A P300 event-related potential brain-computer interface (BCI): the

effects of matrix size and inter stimulus interval on performance. *Biol. Psychol.* 73, 242–252. doi: 10.1016/j.biopsycho.2006.04.007

Squires, K. C., Wickens, C., Squires, N. K., and Donchin, E. (1976). The effect of stimulus sequence on the waveform of the cortical event-related potential. *Science* 193, 1142–1146. doi: 10.1126/science.959831

Tan, C., Sun, F., Kong, T., Zhang, W., Yang, C., and Liu, C. (2018). "A survey on deep transfer learning," in *International Conference on Artificial Neural Networks* (Rhodes: Springer), 270–279. doi: 10.1007/978-3-030-01424-7_27

Tian, Z., Ling, B. W.-K., Zhou, X., Lam, R. W.-K., and Teo, K.-L. (2020). Suppressing the spikes in electroencephalogram via an iterative joint singular spectrum analysis and low-rank decomposition approach. *Sensors* 20:341. doi: 10.3390/s20020341

Urigüen, J. A., and Garcia-Zapirain, B. (2015). EEG artifact removal—state-of-the-art and guidelines. *J. Neural Eng.* 12:031001. doi: 10.1088/1741-2560/12/3/031001

Vigario, R., and Oja, E. (2008). BSS and ICA in neuroinformatics: from current practices to open challenges. *IEEE Rev. Biomed. Eng.* 1, 50–61. doi: 10.1109/RBME.2008.2008244

Vourvopoulos, A. T., Jorge, C., Abreu, R., Figueiredo, P., Fernandes, J.-C., and Bermúdez i Badia, S. (2019). Efficacy and brain imaging correlates of an immersive motor imagery BCI-driven VR system for upper limb motor rehabilitation: a clinical case report. *Front. Hum. Neurosci.* 13:244. doi: 10.3389/fnhum.2019.00244

Wallstrom, G. L., Kass, R. E., Miller, A., Cohn, J. F., and Fox, N. A. (2004). Automatic correction of ocular artifacts in the EEG: a comparison of regression-based and component-based methods. *Int. J. Psychophysiol.* 53, 105–119. doi: 10.1016/j.ijpsycho.2004.03.007

Wang, M., Li, R., Zhang, R., Li, G., and Zhang, D. (2018). A wearable SSVEP-based BCI system for quadcopter control using head-mounted device. *IEEE Access* 6, 26789–26798. doi: 10.1109/ACCESS.2018.2825378

Welch, P. (1967). The use of fast Fourier transform for the estimation of power spectra: a method based on time averaging over short, modified periodograms. *IEEE Trans. Audio Electroacoust.* 15, 70–73. doi: 10.1109/TAU.1967.1161901

Wolpaw, J. R., Birbaumer, N., McFarland, D. J., Pfurtscheller, G., and Vaughan, T. M. (2002). Brain-computer interfaces for communication and control. *Clin. Neurophysiol.* 113, 767–791. doi: 10.1016/S1388-2457(02)00057-3

Yeom, S.-K., Fazli, S., Müller, K.-R., and Lee, S.-W. (2014). An efficient ERP-based brain-computer interface using random set presentation and face familiarity. *PLoS ONE* 9:e111157. doi: 10.1371/journal.pone.0111157

Zhang, Y., Zhou, G., Jin, J., Wang, X., and Cichocki, A. (2015). Optimizing spatial patterns with sparse filter bands for motor-imagery based brain-computer interface. *J. Neurosci. Methods* 255, 85–91. doi: 10.1016/j.jneumeth.2015.08.004

Conflict of Interest: The authors declare that the research was conducted in the absence of any commercial or financial relationships that could be construed as a potential conflict of interest.

frontiers in Human Neuroscience

ORIGINAL RESEARCH
published: 06 August 2020
doi: 10.3389/fnhum.2020.00321

Predicting Motor Imagery Performance From Resting-State EEG Using Dynamic Causal Modeling

Minji Lee[1†], Jae-Geun Yoon[1†] and Seong-Whan Lee[2]*

[1] Department of Brain and Cognitive Engineering, Korea University, Seoul, South Korea, [2] Department of Artificial Intelligence, Korea University, Seoul, South Korea

Motor imagery-based brain–computer interfaces (MI-BCIs) send commands to a computer using the brain activity registered when a subject imagines—but does not perform—a given movement. However, inconsistent MI-BCI performance occurs in variations of brain signals across subjects and experiments; this is considered to be a significant problem in practical BCI. Moreover, some subjects exhibit a phenomenon referred to as "BCI-inefficiency," in which they are unable to generate brain signals for BCI control. These subjects have significant difficulties in using BCI. The primary goal of this study is to identify the connections of the resting-state network that affect MI performance and predict MI performance using these connections. We used a public database of MI, which includes the results of psychological questionnaires and pre-experimental resting-state taken over two sessions on different days. A dynamic causal model was used to calculate the coupling strengths between brain regions with directionality. Specifically, we investigated the motor network in resting-state, including the dorsolateral prefrontal cortex, which performs motor planning. As a result, we observed a significant difference in the connectivity strength from the supplementary motor area to the right dorsolateral prefrontal cortex between the low- and high-MI performance groups. This coupling, measured in the resting-state, is significantly stronger in the high-MI performance group than the low-MI performance group. The connection strength is positively correlated with MI-BCI performance (Session 1: $r = 0.54$; Session 2: $r = 0.42$). We also predicted MI performance using linear regression based on this connection (*r-squared* = 0.31). The proposed predictors, based on dynamic causal modeling, can develop new strategies for improving BCI performance. These findings can further our understanding of BCI-inefficiency and help BCI users to lower costs and save time.

Keywords: motor imagery, brain-computer interface, dynamic causal modeling, effective connectivity, electroencephalography

OPEN ACCESS

Edited by:
Yu Zhang,
Stanford University, United States

Reviewed by:
Yongtian He,
University of Houston, United States
Sangtae Ahn,
Kyungpook National University, South Korea
Fabien Lotte,
Institut National de Recherche en Informatique et en Automatique (INRIA), France

***Correspondence:**
Seong-Whan Lee
sw.lee@korea.ac.kr

[†]These authors have contributed equally to this work

Specialty section:
This article was submitted to Brain-Computer Interfaces, a section of the journal Frontiers in Human Neuroscience

Received: *14 February 2020*
Accepted: *20 July 2020*
Published: *06 August 2020*

Citation:
Lee M, Yoon J-G and Lee S-W (2020) Predicting Motor Imagery Performance From Resting-State EEG Using Dynamic Causal Modeling. Front. Hum. Neurosci. 14:321. doi: 10.3389/fnhum.2020.00321

INTRODUCTION

Motor imagery-based brain–computer interface (MI-BCI) systems allow users to control computer applications by imagining a movement, without physically performing the muscle activity (Wolpaw et al., 2002). For example, robot arms (Edelman et al., 2019), wheelchairs (Kim et al., 2016), and exoskeletons (Jeong et al., 2020) can be controlled by the user's brain activity. Thus, these systems

have the potential for application in medical fields related to disabled people and motor function rehabilitation. Many researchers have recently sought to expand its application to able-bodied people (Van Gerven et al., 2009; Lee et al., 2016). Generally, MI-BCIs use electroencephalography (EEG) to measure the voluntary modulation of brain rhythms. One of the most representative features is event-related desynchronization/synchronization (ERD/ERS), which reflects a decrease or an increase of oscillatory activity pertaining to events, respectively (Neuper et al., 2006). These changes in brain signals are used as the fundamental characteristics of MI, which measure the power decrease or increase at specific frequencies and in certain brain regions. Many methods have been proposed to improve the performance of MI-BCIs; however, considerable issues must be addressed before MI-BCIs can be practically implemented in real scenarios. The most prominent issue is the inconsistent MI performance that results from the variations in brain signals between different subjects and experiments (Lotte et al., 2007; Lee et al., 2019a). Previous studies have reported that subject performances fluctuate and 15–30% of subjects cannot generate voluntary brain rhythms (Guger et al., 2003; Ahn and Jun, 2015; Sannelli et al., 2019)—a phenomenon known as "BCI-illiteracy" or "BCI-inefficiency" (Sannelli et al., 2019). Therefore, understanding this phenomenon and performance variations is considered an important issue in MI-BCI (Lotte and Jeunet, 2018). In addition, BCI-illiteracy is a methodologically improper concept because it depends on faulty assumptions that BCI users have functional or physiological characteristics that interfere with their skilled BCI performance. Consequently, this term is an inappropriate concept to describe the difficulties that users face when operating a BCI system (Thompson, 2019). In this sense, we use an alternative term, BCI-inefficiency.

Many studies have been performed to find pre-experimental predictors of MI-BCI performance, to save resources and time (Blankertz et al., 2009; Sannelli et al., 2019). Most of these studies can be categorized into either (i) assessing a subject's condition through psychological questionnaires or (ii) assessing their brain activity by taking EEG measurements directly before the MI experiment. Among the psychological predictors, fatigue is directly related to BCI performance. The feature was extracted using dimension reduction and linear discriminant analysis (LDA) classifier was trained. This BCI performance was compared by quantifying into two groups according to the self-reported rating about fatigue. As a result, BCI performance was significantly high when self-reported fatigue was low during BCI game. Because low fatigue showed effortless control of BCI (Myrden and Chau, 2015). In addition, physical fatigue recorded by physiological changes affected self-reported MI ability. In specific, MI ability was significantly decreased after intermittent exercise (Ferreira et al., 2020). One study surveyed the questionnaire associated with kinesthetic imagery before the MI experiment. Common spatial pattern (CSP) and Fisher LDA were used in a conventional way. Consequently, users' self-prediction responses to a questionnaire have been reported to correlate with their MI-BCI performance (r = 0.64) (Ahn et al., 2018). However, some psychological factors such as fatigue are subjective and therefore are not suitable for describing BCI-inefficiency. In addition, given the length of each training session, limitations still exist in that mental state is unlikely to be consistent overall.

Objective psychological factors such as spatial and visuo-motor coordination abilities also were related to BCI performance. The BCI performance measured from CSP and shrinkage LDA and personality and cognitive profile using psychometric questionnaires were compared. The mental rotation test, which measures spatial ability, showed significantly correlated with BCI performance (r = 0.69). However, neurophysiological patterns such as alpha and beta power did not relate to BCI performance (Jeunet et al., 2015, 2016). Similarly, MI performance was calculated using CSP and LDA, and motor skills (r = 0.42) and concentration level (r = 0.50) were explored as sensorimotor rhythm (SMR) predictors (Hammer et al., 2012). This study focused on pattern recognition rather than human learning for BCI control. So, the next study explored these two psychological factors in the neurofeedback training session. As a result, SMR could only be modulated well by visuo-motor coordination ability, which represents motor skills (*r-squared* = 0.082) in the neurofeedback training session (Hammer et al., 2014). Another study had reported the relationship with age and the average amount of upper limb movement for modulating alpha power associated with BCI. These two factors were positively correlated with the strength of alpha power with 94% confidence using the multiple linear regression (Randolph et al., 2010). The reliable and reproducible predictors of BCI performance contribute to a better understanding of the BCI control. However, these predictors may be less practical because they cannot evaluate and train potential BCI users in a locked-in state, in whose muscular movement is impossible and BCI control is really necessary.

The SMR has been proposed as a neurophysiological indicator (Blankertz et al., 2010), and it is calculated from the mu rhythms (about 9–14 Hz) measured over sensorimotor areas in the C3 and C4 channels in resting-state EEG. These rhythms have shown a significant correlation with MI performance trained using CSP and LDA (r = 0.53). Furthermore, higher theta and lower alpha powers were observed in the BCI-inefficiency compared with the BCI-efficient subjects. As a result, this study demonstrated a positive correlation between MI performance using CSP and Fisher LDA and the alpha-theta ratio predictor (r = 0.59) (Ahn et al., 2013). Some studies have indicated a relationship between BCI-inefficiency and power spectral density at different frequencies. In particular, gamma oscillations used to infer a subject's intention have a causal influence on a subject's BCI capacities. Consequently, BCI performance using spectral power and support vector machine was significantly correlated with predicted BCI accuracy using gamma power (r = 0.10) (Grosse-Wentrup et al., 2011). However, these studies predicted MI performance for a single session only. Given the variability of brain signals across different conditions within the same subject, it is necessary to investigate the effects of applying these predictors across various sessions. In addition to the SMR, other EEG features have been proposed to predict MI-BCI performance. Spectral entropy in the C3 channel of eye closed resting-state EEG has been found to correlate with SMR-BCI

performance using CSP and LDA in both sessions (Session 1: r = 0.61; Session 2: r = 0.70) (Zhang et al., 2015a). This predictor can apply for both intra- and inter-session conditions. However, it has not been proven to be applicable to patients such as stroke. In another approach, inter-region connectivity was investigated, not simply the brain activity in a particular region. One study used coherence and phase lag index as the functional connectivity measure. Based on these two measures, network properties were calculated. In the eye closed resting-state, many network properties were directly related to BCI performance. Specifically, mean functional connectivity, node degrees, edge strengths, clustering coefficient, local efficiency, and global efficiency were positively correlated with BCI classification accuracy, whereas the characteristic path length was negatively correlated with BCI classification accuracy. As a primary result, a positive correlation with MI performance using CSP and LDA was observed using a coherence-based clustering coefficient across two sessions (Session 1: r = 0.29; Session 2: r = 0.42). MI performance was predicted using coherence (except outliers) in Session 2 [root mean square error (RMSE) = 12.2%] (Zhang et al., 2015b). These studies applied the predictor to two sessions and demonstrated that it had a significant correlation with MI performance. However, the relationship was not sufficiently close for the predictor to be employed as an MI-BCI performance indicator in real life applications. Furthermore, these studies have used only one classifier when calculating MI-BCI performance, even though the performance variation depends on both classifier and session. Therefore, a large public database should be used to find possible predictors across a variety of classifiers and sessions, to verify the utility of this MI predictor.

Brain connectivity describes the exchange of information between brain regions (Zhang et al., 2017). The functional connectivity is observable evidence that can be determined as a measure of statistical dependencies. This measure of functional connectivity between the two regions is the same, and it does not indicate directionality (Friston, 2011). However, effective connectivity explains how one region of the brain affects other regions (Lee et al., 2019b). Therefore, it is useful to observe interregional changes in brain networks when investigating certain phenomena. Effective connectivity can be described using a set of common measures that plot directionality between brain regions. For example, there are the following measures: Granger causality, partial directed coherence, and the direct transfer function (Sakkalis, 2011). Above all, dynamic causal modeling (DCM) reflects inferences about the couplings between brain regions/sources and is based on a Bayesian approach (Kiebel et al., 2008). As a consequence, in contrast to functional connectivity and some causal model, DCM needs a defined *a priori* knowledge and hypothesis-driven models (Kasess et al., 2010). This Bayesian approach directly assesses the posterior probability distribution of the estimated model parameters, given measured EEG data and a specific priori model at the single-subject level. For group-level analysis of model parameters, this approach based on fixed-effects analysis as the inference method has the advantage that the precisions of the subject-specific multivariate parameter estimates are considered (Chen et al., 2008; Kasess et al., 2010; Bönstrup et al., 2016). This approach compares various hypothesis-based models and helps to select an optimal specific model. Furthermore, volume conduction—a problem for the conventional measurement methods—can be avoided by including the source reconstruction to assess directionality between brain regions (Lee et al., 2019b).

Many studies have used DCM to investigate the connections between brain regions during MI. In a DCM study using functional magnetic resonance imaging (fMRI), a forward connection was found between the supplementary motor area (SMA) and the primary motor cortex (M1). In particular, the SMA exhibited a strong suppressive influence on M1 during MI (Kasess et al., 2008). In addition, by using a combined fMRI and EEG approach, the coupling between SMA and M1 was shown to contain significant information for MI (Bönstrup et al., 2016). The SMA is considered to be the main active region in MI generation and is involved in the preparation of movements (Kuhtz-Buschbeck et al., 2003). Recent studies have shown that effective connectivity is similar under motor execution (ME) and MI tasks through DCM; furthermore, these networks have been reported to include the dorsolateral prefrontal cortex (DLPFC) and premotor cortex (PMC) in addition to the SMA and M1 (Kim et al., 2018). These brain regions are necessary to generate the rich MI sources used to control BCIs (Hochberg et al., 2006; Aflalo et al., 2015). The PMC exhibits overlapping between active and peripheral regions during ME and MI, and it is employed in language production, movement observation, and action recognition (Lotze and Halsband, 2006). The DLPFC is closely connected with the cortical control of movement and may be linked with the SMA (Middleton and Strick, 1994). In this regard, certain brain regions—though not directly related to the motor cortex—can be associated with MI.

In this study, we investigate the correlations between MI-BCI performance and the subject's resting-state network before the BCI experiment takes place. DCM was used to explore the effective connectivity between two regions with directionality. In particular, we considered the DLPFC in addition to the conventional sensorimotor areas as the DCM region of interest (ROI). We assessed the subjects' psychological questionnaires and band powers (from their resting-state EEG) before the MI experiment, for comparison with previous studies. We hypothesized that the coupling strength in the motor network constructed using DCM would be correlated with the MI-BCI performance. Finally, using linear regression, we predicted the MI-BCI performance with the proposed coupling strength. These findings could help build an understanding of the MI mechanism and improve overall MI-BCI performances by investigating the characteristics of poorly performing subjects.

MATERIALS AND METHODS

EEG Dataset

We used a public EEG dataset from GigaDB (Lee et al., 2019a). These data contain EEG signals measured during MI experiments focusing on left and right hand grasping motions. The subjects' psychological and physical conditions were surveyed using

questionnaires and 1 min eye-open resting-state EEG data were recorded before the MI experiments. The experiments were conducted over two sessions, which took place on different days. The data comprised 54 healthy subjects (24.8 ± 3.8 years; 25 females). Among the subjects, 38 were naive BCI users and the remainder had previous experience. EEG signals were recorded using 62 Ag/AgCl electrodes.

MI-BCI Performance and Group Categorization

The EEG signals were processed using the OpenBMI toolbox (Lee et al., 2019a); the data were band-pass filtered between 8 and 30 Hz—the frequency band relevant to motor movements. A 5th order Butterworth filter was used for all band-pass filter analyses; next, the continuous EEG signals were segmented from 1 to 3.5 sec (measured from stimulus onset) (Pfurtscheller and Neuper, 2001). Moreover, 20 channels were selected in the motor cortex region (FC1, FC2, FC3, FC4, FC5, FC6, Cz, C1, C2, C3, C4, C5, C6, CPz, CP1, CP2, CP3, CP4, CP5, and CP6).

We used several popular methods to calculate MI performance (Lee et al., 2019a). We extracted four features, as follows: (i) CSP (Ramoser et al., 2000)—a spatial pattern that maximizes the discrimination of the binary classes; (ii) common spatio-spectral pattern (CSSP) (Lemm et al., 2005)—a pattern using spectral information based on CSP; (iii) filter bank common spatial pattern (FBCSP) (Ang et al., 2012)—a pattern using optimal spatio-spectral filters based on a filter bank composed of several frequency bands; and (iv) Bayesian spatio-spectral filter optimization (BSSFO) (Suk and Lee, 2012)—a pattern using subject-dependent frequency bands within the Bayesian framework. For the classifier, LDA was used to decode the left or right hand imagery. Each experimental task comprised a training phase and a testing phase. To validate the MI performance, ten-fold cross-validation was used for all data (training + testing data) (CSP-cv). In summary, we achieved the MI-BCI performance with CSP-cv, CSP, CSSP, FBCSP, and BSSFO.

To compare the MI performance against the resting-state EEG, we divided them into two performance groups: high (good MI performance group) and low (poor MI performance group). The median performance in each five performance according to classifiers was used to separate the subjects into high- or low-MI performance groups (Zhang et al., 2016).

Relationship With MI-BCI Performance

Questionnaire Scores

We took seven response fields from the pre-experimental questionnaire: comfort, motivation, concentration, eye fatigue, drowsiness, physical condition, and mental condition. These items were graded on a Likert scale from 1 to 5. For "comfort," 1 signified relaxation, and 5 signified anxiety. Under "motivation," 1 indicated excitement, and 5 indicated boredom. In the "concentration," "eye fatigue," "drowsiness," "physical condition," and "mental condition," 1 and 5 indicated very good and very bad or tired in intensity level, respectively.

Band Power of Resting-State EEG

We calculated the average power of the EEG signals, to decompose them into functionally distinct frequency bands. We further divided them into five regions: frontal (Fp1-2, AF3-4, AF7-8, AFz, F3-4, F7-8, and Fz), sensorimotor (FC1-6, C1-6, Cz, CP1-6, and CPz), temporal (FT9-10, T7-8, and TP7-10), parietal (P1-4, P7-8, PO3-4, and POz), and occipital (O1-2, Oz, and PO9-10) regions (**Supplementary Figure S1**). At the sensor level, EEG signals were averaged according to five different cortical regions. The band powers were also measured for the delta (1–4 Hz), theta (4–8 Hz), alpha (8–15 Hz), beta (15–25 Hz), and gamma (25–40 Hz) bands (Ahn et al., 2013).

Dynamic Causal Modeling of Resting-State EEG

Pre-processing

The continuous EEG signals were pre-processed using the EEGLAB toolbox (Delorme and Makeig, 2004) based on MATLAB. Data from 56 channels across the scalp surface (using the international 10–10 system) were obtained to implement DCM (Lee et al., 2017). The resting-state EEG was band-pass filtered in the 4–45 Hz (Van de Steen et al., 2019). The delta band in the 1–4 Hz range was excluded because, unlike other frequency bands, it can be contaminated relatively easily by artifacts such as eyeball movement and blinking (Ahn et al., 2013). The continuous 1 min EEG data were segmented from 1 sec without overlap (Van de Steen et al., 2019). Then, the eye-blink correction was manually performed using infomax, which is one of the most widely used independent component analysis algorithm to minimize the artifacts. Finally, the epoched data were average-referenced.

3D source reconstruction

We used the statistical parametric mapping (SPM) toolbox in MATLAB (Litvak et al., 2011). In the 3D channel location information, EEG channel locations were transformed to match the template head. This head model was assigned to all subjects using 3D coordinate values. The boundary element method (BEM) was used for building a head model (forward model, mapping source signals to sensor signals). Each source was also modeled by a single equivalent current dipole (ECD) (Kiebel et al., 2006) for reconstructing sources (inverse model, mapping sensor signals to the source signals). To estimate the cortical sources, the inversion index was set to 1 to trace different types of forward models and inverse solutions. Mesh resolution can be maintained at normal (approximately 4,000 vertices per hemisphere).

DCM specification

M1, SMA, and PMC are well known to be linked to MI (Kasess et al., 2008; Begliomini et al., 2015; Bönstrup et al., 2016). Recently, the role of DLPFC in MI has been revealed (Kim et al., 2018). Therefore, we selected the seven ROIs: SMA, left/right M1, left/right PMC, and left/right DLPFC. We also employed the Montreal Neurological Institute (MNI) coordinates for both side regions, based on the source locations reported in previous work (Kim et al., 2018). **Table 1** lists

TABLE 1 | Montreal Neurological Institute (MNI) coordinates for location information.

ROI	MNI coordinates		
	x	*y*	*z*
SMA	0	−4	65
Left M1	−38	−26	53
Right M1	38	−26	53
Left PMC	−48	−15	50
Right PMC	48	−15	50
Left DLPFC	−42	40	25
Right DLPFC	42	40	25

ROI, region of interest; SMA, supplementary motor area; M1, primary motor cortex; PMC, premotor cortex; DLPFC, dorsolateral prefrontal cortex.

the MNI coordinates for seven ROIs. The prefrontal-dependent regions were reported to have no physiologically specific interactions with the M1 (Luppino et al., 1993; Rizzolatti and Luppino, 2001). Therefore, we excluded the connection between DLPFC and M1 and finally organized the eight DCM models (**Figure 1**). In addition, for the resting-state, we did not select an input from the neural model because no external input exists.

Dynamic causal modeling uses a neural mass model to explain the source activity of EEG signals (David and Friston, 2003). The model imitates the source activity by using three neural sublayers assigned to the three cortical layers, namely the granular sublayer, the supra-granular sublayer, and the infra-granular sublayer. This model has hierarchical features; forward connections start in the infra-granular layer and end in the granular layer and backward connections link agranular layers (Garrido et al., 2007). All cortico-cortical connections are excitatory, so the DCM can be identified in neuronal state equation by average synaptic dynamics in each sublayer.

$$\dot{x} = f(x,\ u,\ \theta) \tag{1}$$

where $\dot{x}$ indicates the evolution of neuronal state x parameterized by θ of the state and input u.

$$y = L(\theta)\, x_0 + \varepsilon \tag{2}$$

where x_0 is output of specific states and $L(\theta)$ indicates the local field indicating the location and orientation of sources (i.e., spatial forward model). In specific, θ includes the parameters for forward and backward connections (coupling strength). The ε refers to observation error. Finally, EEG signals y connects the neuronal states to observed EEG channel data (Kiebel et al., 2006).

Bayesian model selection (BMS)

Bayesian model selection (BMS) is an effective method of deciding the most likely set of competitive hypotheses for the models that generated the observed data (Stephan et al., 2009). We applied BMS averaging with fixed-effects analysis to determine the most likely model given the data.

The inversion of a particular DCM, m, coincides with an approximation of the posterior probability on the several models.

$$p(\theta|y, m) \propto p\left(y|\theta, m\right) p(\theta|m) \tag{3}$$

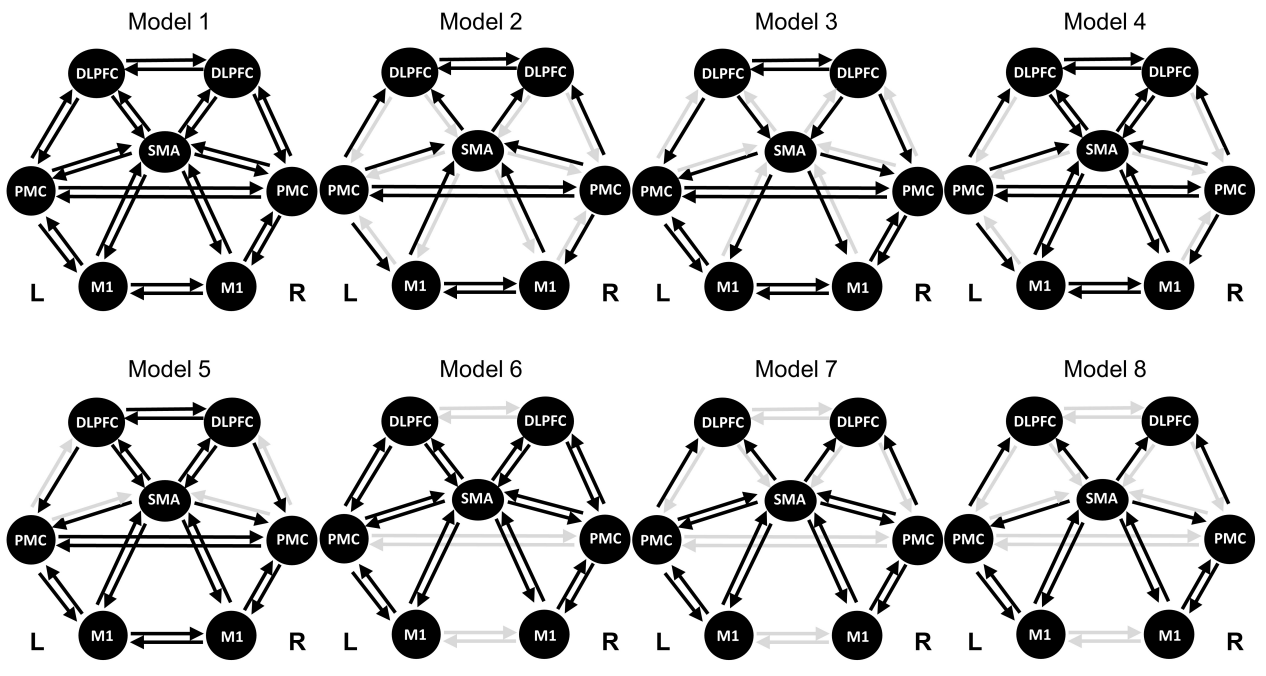

FIGURE 1 | Model specifications of effective connectivity based on the dynamic causal model. The regions of interest (ROIs) consist of the SMA, left/right PMC, left/right M1, and left/right DLPFC. The resting-state has no external stimulus, thus no input is specified. The selected connection for each model is indicated by a black arrow. SMA, supplementary motor area; PMC, premotor cortex; M1, primary motor cortex; DLPFC, dorsolateral prefrontal cortex.

TABLE 2 | Statistical results for the differences in MI performance.

Classifier	Session			Group			Session × Group		
	dof	*F*	*p*-value	dof	*F*	*p*-value	dof	*F*	*p*-value
CSP_cv	1	0.40	0.527	1	2.28	0.133	1	0.09	0.768
CSP	1	0.16	0.690	1	1.87	0.174	1	0.71	0.401
CSSP	1	0.16	0.692	1	0.81	0.369	1	0.04	0.835
FBCSP	1	0.16	0.694	1	1.51	0.221	1	0.02	0.899
BSSFO	1	0.20	0.658	1	0.29	0.592	1	0.24	0.626

The session factor indicates Session 1 and Session 2, whereas the group factor indicates high-MI performance group and low-MI performance group. The session × group represents the interaction between session and group factors. dof, degree of freedom; CSP_cv, common spatial pattern with cross-validation; CSP, common spatial pattern; CSSP, common spatio-spectral pattern; FBCSP, filter bank common spatial pattern; BSSFO, Bayesian spatio-spectral filter optimization.

This approximation uses the Bayes factor based on Expectation-Maximization algorithm. This aims to minimize the free energy $F = -\ln p(y|m)$ as the negative marginal log-likelihood. Then, the variational Bayes factor is used as an approximation and the log-evidence is used for model comparison. Finally, the best model is the highest log-evidence $\ln p(y|m)$ (Garrido et al., 2007). In our study, eight DCM models were estimated and one was selected using BMS.

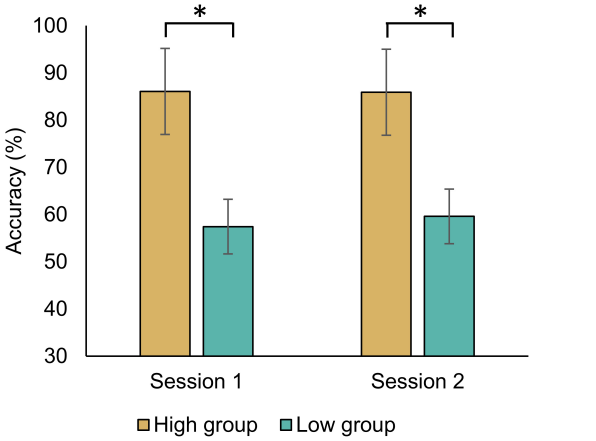

FIGURE 2 | Averaged MI classification performance based on CSP-cv for both sessions. The group was divided based on the median of MI classification accuracy across all subjects. The *p*-values below 0.05 are highlighted by an asterisk.

Statistical Analysis

We first performed the one-way analysis of variance (ANOVA) to investigate the differences in MI performance using CSP-cv, CSP, CSSP, FBCSP, and BSSFO. Next, the correlation was used to verify that the MI performance between the two sessions was similar. To investigate the differences in resting-state EEG between the high- and low-MI performance groups, we performed the two-way ANOVA (session × group). In all ANOVA, the two-sample *t*-test was used with Bonferroni correction for multiple comparisons as *post hoc* analysis. Pearson's correlation was also used to examine the relationship between MI performance and resting-state EEG. Similarly, Bonferroni correction was applied to correlation analysis for multiple comparisons. For the questionnaire and band power, we used only the MI performance measured by CSP-cv for a fair comparison with previous studies (Ahn et al., 2013, 2018; Zhang et al., 2015b). We also predicted the MI performance based on significantly selected coupling strength, by applying linear regression to the MI-BCI performance in the resting-state. The 10-fold cross-validation was used to prevent overfitting (Lever et al., 2016). Then,

TABLE 3 | Statistical results for the differences in questionnaire scores according to MI performance using CSP-cv.

Questionnaire	Session			Group			Session × Group		
	dof	*F*	*p*-value	dof	*F*	*p*-value	dof	*F*	*p*-value
Comfort	1	0.01	0.963	1	2.28	0.134	1	0.89	0.348
Motivation	1	0.01	0.922	1	0.16	0.692	1	0.01	0.906
Concentration	1	0.08	0.782	1	1.03	0.312	1	0.62	0.434
Eye fatigue	1	0.36	0.552	1	0.08	0.784	1	0.27	0.607
Drowsiness	1	0.04	0.838	1	0.50	0.481	1	0.20	0.655
Physical condition	1	0.28	0.597	1	2.80	0.097	1	2.40	0.124
Mental condition	1	0.64	0.423	1	0.49	0.486	1	0.26	0.608

The questionnaires consisted of seven questionnaires and were taken for each session before the MI experiment took place. The session factor indicates Session 1 and Session 2, whereas the group factor indicates high-MI performance group and low-MI performance group. The session × group represents the interaction between session and group factors. dof, degree of freedom.

TABLE 4 | Statistical results for correlation in questionnaire scores according to MI performance using CSP-cv.

Questionnaire	Session 1		Session 2	
	r-value	*p*-value	*r*-value	*p*-value
Comfort	0.043	0.758	−0.147	0.295
Motivation	0.042	0.764	−0.002	0.990
Concentration	−0.020	0.888	−0.154	0.271
Eye fatigue	0.089	0.520	0.020	0.886
Drowsiness	−0.133	0.379	−0.076	0.588
Physical condition	−0.096	0.490	−0.197	0.158
Mental condition	−0.144	0.300	−0.039	0.784

The questionnaires consisted of seven questions and were taken for each session before the MI experiment took place.

we evaluated the predicted MI-BCI performance compared with the actual MI-BCI performance based on CSP-cv, CSP, CSSP, FBCSP, and BSSFO, using the *r*-squared and RMSE, where *r*-squared is a statistical value of how close the data are to the fitted regression line, and RMSE is a measure of the difference between the actual and the predicted MI-BCI performance (Varatharajan et al., 2018).

RESULTS

Differences in MI Performance

Using CSP-cv, CSP, CSSP, FBCSP, and BSSFO, we observed a significantly positive correlation of the two-class MI performances between two sessions on different days (CSP-cv: $r = 0.986$, $p < 0.001$; CSP: $r = 0.988$, $p < 0.001$; CSSP: $r = 0.993$, $p < 0.001$; FBCSP: $r = 0.993$, $p < 0.001$; BSSFO: $r = 0.993$, $p < 0.001$). We also investigated the differences in MI-BCI performances using five methods within each session. No significant differences in MI performances using five methods with Bonferroni correction were observed in both sessions [Session 1: $F_{(4,265)} = 0.22$, $p = 0.929$; Session 2: $F_{(4,265)} = 0.33$, $p = 0.859$].

We divided the high- and low-MI groups in each classifier. There was no significant difference in MI performance with Bonferroni correction according to session and group using

TABLE 5 | Statistical results for the differences in band power according to MI performance using CSP-cv.

Region	Frequency	Session			Group			Session × Group		
		dof	*F*	*p*-value	*dof*	*F*	*p*-value	*dof*	*F*	*p*-value
Frontal	Delta	1	3.24	0.074	1	4.27	**0.041**	1	0.85	0.357
	Theta	1	0.20	0.655	1	0.96	0.338	1	0.24	0.624
	Alpha	1	0.45	0.505	1	0.01	0.942	1	0.77	0.383
	Beta	1	0.06	0.814	1	0.75	0.389	1	0.46	0.497
	Gamma	1	0.69	0.406	1	0.05	0.825	1	0.66	0.418
Sensorimotor	Delta	1	1.08	0.301	1	2.20	0.141	1	0.01	0.950
	Theta	1	0.36	0.552	1	2.12	0.148	1	0.09	0.762
	Alpha	1	0.01	0.919	1	2.64	0.107	1	0.01	0.965
	Beta	1	0.30	0.583	1	5.58	**0.020**	1	0.39	0.533
	Gamma	1	1.09	0.299	1	1.39	0.241	1	0.01	0.996
Temporal	Delta	1	0.45	0.504	1	1.15	0.286	1	0.13	0.715
	Theta	1	0.19	0.661	1	1.74	0.189	1	0.13	0.719
	Alpha	1	0.01	0.963	1	0.52	0.472	1	0.11	0.745
	Beta	1	0.05	0.822	1	0.88	0.349	1	1.80	0.182
	Gamma	1	0.32	0.573	1	0.44	0.506	1	1.38	0.243
Parietal	Delta	1	0.95	0.330	1	0.77	0.381	1	0.06	0.813
	Theta	1	0.64	0.426	1	0.36	0.551	1	0.07	0.790
	Alpha	1	0.01	0.912	1	0.03	0.856	1	0.04	0.835
	Beta	1	0.03	0.863	1	2.72	0.102	1	0.34	0.563
	Gamma	1	0.13	0.717	1	0.72	0.399	1	0.53	0.467
Occipital	Delta	1	0.76	0.386	1	0.28	0.596	1	0.14	0.705
	Theta	1	0.26	0.608	1	0.04	0.837	1	0.06	0.805
	Alpha	1	0.04	0.847	1	0.77	0.383	1	0.02	0.877
	Beta	1	0.08	0.777	1	0.01	0.969	1	0.80	0.373
	Gamma	1	0.01	0.996	1	0.01	0.911	1	0.51	0.476

The brain region was divided into five sub-regions, and the frequency was also divided into five bands as follows: delta (1–4 Hz), theta (4–8 Hz), alpha (8–15 Hz), beta (15–25 Hz), and gamma (25–40 Hz) bands. The session factor indicates Session 1 and Session 2, whereas the group factor indicates high-MI performance group and low-MI performance group. The session × group represents the interaction between session and group factors. The p-values below 0.05 are highlighted in bold. dof, degree of freedom.

five methods (**Table 2**). Nevertheless, we compared the MI performance of each group because the classification accuracy in high-MI group was all higher than that in the low-MI group by dividing each group based on the median of the performance of all subjects. For MI-BCI performances based on the CSP-cv, five subjects were displaced from a low-MI group to a high-MI group; moreover, two subjects were displaced from a high-MI group to a low-MI group between Sessions 1 and 2. The significant differences in MI performance observed between the high- and low-MI groups were explored using CSP-cv [Session 1: $t_{(52)} = 14.125$, $p < 0.001$; Session 2: $t_{(52)} = 12.115$, $p < 0.001$] (**Figure 2**). As expected, the MI classification accuracy for the higher group was greater than that for the lower group during both sessions. **Supplementary Figure S2** shows the MI performances in high- and low-MI groups for CSP, CSSP, FBCSP, and BSSFO. Similar to CSP-cv, there were significant differences observed in MI performance across the other four classifiers [CSP – Session 1: $t_{(52)} = 16.323$, $p < 0.001$, Session 2: $t_{(52)} = 13.094$, $p < 0.001$; CSSP – Session 1: $t_{(52)} = 17.833$, $p < 0.001$, Session 2: $t_{(52)} = 15.341$, $p < 0.001$; FBCSP – Session 1: $t_{(52)} = 19.320$, $p < 0.001$, Session 2: $t_{(52)} = 15.509$, $p < 0.001$; BSSFO – Session 1: $t_{(52)} = 19.777$, $p < 0.001$, Session 2: $t_{(52)} = 18.961$, $p < 0.001$]. In addition, 7, 5, 6, and 7 subjects changed from the low- to high-MI group between Sessions 1 and 2 under CSP, CSSP, FBCSP, and BSSFO, respectively; conversely, 3, 4, 6, and 5 subjects changed from the high- to low-MI group on different days under CSP, CSSP, FBCSP, and BSSFO, respectively. To summarize, the MI classification accuracy for the low-MI group tended to not exceed 60%, whereas the high-MI group showed an average classification accuracy greater than 80%.

Relationship With Questionnaire Score

We investigated differences in questionnaire score between the high- and low-MI groups based on CSP-cv (**Table 3**). There were no significant differences observed in any score according to session and group with Bonferroni correction. In addition, we calculated the correlation with MI-BCI performance (**Table 4**). Similarly, no significant correlation with MI-BCI performance with Bonferroni correction was found in either session.

Relationship With Band Power

Table 5 summarizes the statistical differences in band power between the high- and low-MI groups according to session and group. As a result, the beta power in the sensorimotor region showed a significant difference between the high- and low-MI groups in Session 1 with Bonferroni correction [$t_{(52)} = 2.67$, $p = 0.009$]. However, no significant power differences in other frequency bands were found between the two groups in either session. In addition, an only positive correlation was observed between theta power in the parietal region and MI-BCI performance based on CSP-cv (**Table 6**).

Relationship With Coupling Strength Based on DCM

For Session 1, Model 4 was chosen through BMS and the connectivity strengths of 20 connections were calculated. For Session 2, Model 2 was determined as a suitable model; this model included 16 connections.

TABLE 6 | Statistical results for band power correlations according to MI performance using CSP-cv.

Region	Frequency	Session 1		Session 2	
		r-value	*p*-value	*r*-value	*p*-value
Frontal	Delta	0.130	0.350	0.219	0.111
	Theta	0.075	0.589	0.225	0.102
	Alpha	0.032	0.817	0.231	0.093
	Beta	0.014	0.920	0.233	0.089
	Gamma	−0.018	0.896	0.221	0.109
Sensorimotor	Delta	−0.022	0.876	0.089	0.523
	Theta	0.067	0.633	0.093	0.503
	Alpha	0.048	0.732	0.077	0.580
	Beta	−0.039	0.781	0.078	0.575
	Gamma	−0.050	0.719	0.033	0.813
Temporal	Delta	−0.108	0.438	0.147	0.289
	Theta	0.224	0.104	0.246	0.073
	Alpha	0.064	0.645	0.136	0.325
	Beta	0.057	0.680	0.068	0.625
	Gamma	−0.004	0.980	−0.022	0.874
Parietal	Delta	0.130	0.349	0.180	0.193
	Theta	0.272	**0.047***	0.106	0.446
	Alpha	0.132	0.341	−0.029	0.837
	Beta	0.147	0.289	0.134	0.335
	Gamma	0.070	0.613	−0.038	0.786
Occipital	Delta	0.192	0.165	0.106	0.445
	Theta	0.137	0.323	0.025	0.855
	Alpha	0.097	0.486	−0.046	0.742
	Beta	0.047	0.737	0.057	0.680
	Gamma	0.035	0.800	0.031	0.827

*The brain region was divided into five sub-regions, and the frequency was also divided into five bands as follows: delta (1–4 Hz), theta (4–8 Hz), alpha (8–15 Hz), beta (15–25 Hz), and gamma (25–40 Hz) bands. The p-values below 0.05 are highlighted in bold. * with no correction.*

Difference Between High- and Low-MI Performance Groups

Table 7 lists the differences across 20 connections between high- and low-MI performance groups for MI-BCI performance, based on CSP-cv. **Figure 3** shows the significant connectivity strength between the two groups in each session, based on CSP-cv. In particular, the coupling strength from the SMA to the right DLPFC in the high-MI group was significantly higher than in the low-MI group in both sessions [Session 1: $t_{(52)} = 2.71$, $p = 0.008$ with Bonferroni correction; Session 2: $t_{(52)} = 4.31$, $p < 0.001$ with Bonferroni correction]. Additionally, in Session 1, a higher coupling strength from left DLPFC to SMA was observed in the high-MI group [$t_{(52)} = 2.76$, $p = 0.008$ with Bonferroni correction], whereas a lower coupling strength from right M1 to left M1 was observed in the high-MI group compared with the low-MI group [$t_{(52)} = -2.78$, $p = 0.009$ with Bonferroni correction]. In addition, the differences in coupling strength between high- and low-MI groups based on CSP (**Supplementary Table S1**), CSSP (**Supplementary Table S2**),

TABLE 7 | The statistical differences in effective connectivity between high- and low-MI performance groups based on CSP-cv.

ROI		Session			Group			Session × Group		
From	**To**	**dof**	***F***	***p*-value**	**dof**	***F***	***p*-value**	**dof**	***F***	***p*-value**
lM1	SMA	1	1.58	0.211	1	0.48	0.489	1	0.52	0.474
rM1	SMA	1	0.78	0.380	1	0.39	0.534	1	0.01	0.942
lPMC	SMA	1	1.72	0.192	1	1.42	0.236	1	0.10	0.747
rPMC	SMA	1	0.98	0.324	1	0.62	0.434	1	0.01	0.991
lDLPFC	SMA	0	0	NaN	1	7.62	**0.008**	0	0	NaN
rDLPFC	SMA	0	0	NaN	1	0.45	0.506	0	0	NaN
SMA	lM1	0	0	NaN	1	0.56	0.455	0	0	NaN
rM1	lM1	1	3.43	0.067	1	4.79	**0.030**	1	1.38	0.242
lPMC	lM1	1	1.34	0.250	1	2.65	0.106	1	0.69	0.409
SMA	rM1	0	0	NaN	1	0.04	0.842	0	0	NaN
lM1	rM1	1	0.88	0.350	1	0.03	0.861	1	0.01	0.973
rPMC	rM1	1	0.99	0.322	1	1.06	0.306	1	0.01	0.941
rPMC	lPMC	1	3.53	0.062	1	0.36	0.547	1	0.14	0.709
lPMC	rPMC	1	0.42	0.517	1	0.23	0.634	1	0.64	0.423
SMA	lDLPFC	1	0.51	0.477	1	0.02	0.898	1	0.37	0.542
lPMC	lDLPFC	1	0.14	0.704	1	2.33	0.130	1	2.47	0.119
rDLPFC	lDLPFC	1	0.35	0.552	1	0.08	0.780	1	0.06	0.813
SMA	rDLPFC	1	0.74	0.391	1	25.01	**<0.001**	1	1.66	0.200
rPMC	rDLPFC	1	0.13	0.714	1	0.29	0.593	1	0.99	0.323
lDLPFC	rDLPFC	1	1.59	0.210	1	0.21	0.648	1	0.01	0.974

In Session 1, Model 4 is selected and there are 20 connections. In Session 2, Model 2 is selected and there are 16 connections. Therefore, four connections in Session 2 are excluded ('NaN'). The session factor indicates Session 1 and Session 2, whereas the group factor indicates high-MI performance group and low-MI performance group. The session × group represents the interaction between session and group factors. The p-values below 0.05 are highlighted in bold. ROI, region of interest; dof, degree of freedom; l/rM1, left/right primary motor cortex; l/rPMC, left/right pre-motor cortex; l/rDLPFC, left/right dorsolateral prefrontal cortex; SMA, supplementary motor area.

FBCSP (**Supplementary Table S3**), and BSSFO (**Supplementary Table S4**) are listed. As with CSP-cv, the coupling strength from the SMA to the right DLPFC in the high-MI group was higher than in the low-MI group in two sessions based on four classifiers in both Session 1 [CSP: $t_{(52)} = 3.26$, $p = 0.001$ with Bonferroni correction; CSSP: $t_{(52)} = 3.96$, $p < 0.001$ with Bonferroni correction; FBCSP: $t_{(52)} = 2.93$, $p = 0.005$ with Bonferroni correction; BSSFO: $t_{(52)} = 2.76$, $p = 0.008$ with Bonferroni correction] and Session 2 [CSP: $t_{(52)} = 2.90$, $p = 0.005$ with Bonferroni correction; CSSP: $t_{(52)} = 2.91$, $p = 0.005$; FBCSP: $t_{(52)} = 2.76$, $p = 0.008$ with Bonferroni correction; BSSFO: $t_{(52)} = 2.46$, $p = 0.017$ with Bonferroni correction]. Similarly, differences in coupling strength from left DLPFC to SMA between two MI groups were observed in Session 1 based on four methods [CSP: $t_{(52)} = 3.40$, $p = 0.001$ with Bonferroni correction; CSSP: $t_{(52)} = 2.64$, $p = 0.010$ with Bonferroni correction; FBCSP: $t_{(52)} = 3.12$, $p = 0.002$ with Bonferroni correction; BSSFO: $t_{(52)} = 3.07$, $p = 0.003$ with Bonferroni correction]. However, there was significant difference in coupling strength from right M1 to left M1 in Session 1 using four classifiers, and in Session 2, strength from left PMC and left DLPFC showed the significant differences between two groups only in CSP [$t_{(52)} = -2.55$, $p = 0.013$ with Bonferroni correction].

Correlation With MI Performance

To verify the reliability of the proposed predictors, we investigated their correlations with MI-BCI performance. **Table 8** lists the correlations between 20 connections in a resting-state EEG and MI-BCI performance, based on CSP-cv. Positive correlation in connectivity strength from the SMA to right DLPFC with Bonferroni correction was observed in both sessions. In Session 1, strength from the left DLPFC to SMA was positively correlated with the MI-BCI performance. Furthermore, the strength from the left PMC to left DLPFC was negatively correlated with MI performance in Session 2. However, there was no correlation with the directionality from right M1 to left M1 that had significant differences between the two MI groups in Session 1. Similar results to those obtained under CSP-cv were obtained when assessing MI performance with CSP, CSSP, FBCSP, and BSSFO (**Supplementary Table S5**). In particular, the coupling strength from the SMA to right DLPFC was significant in both sessions, for all classifiers. Thus, we depicted the correlation between coupling from SMA to right DLPFC and MI-BCI performance through five methods (**Figure 4**). In both sessions, this coupling strength was significantly correlated. In Session 1, strength from left DLPFC to SMA was correlated with MI-BCI performance using five methods (**Supplementary Figure S3**).

Prediction of MI Performance Using Coupling Strength

We predicted MI-BCI performance using the coupling strength from SMA to right DLPFC in resting-state EEG. **Table 9**

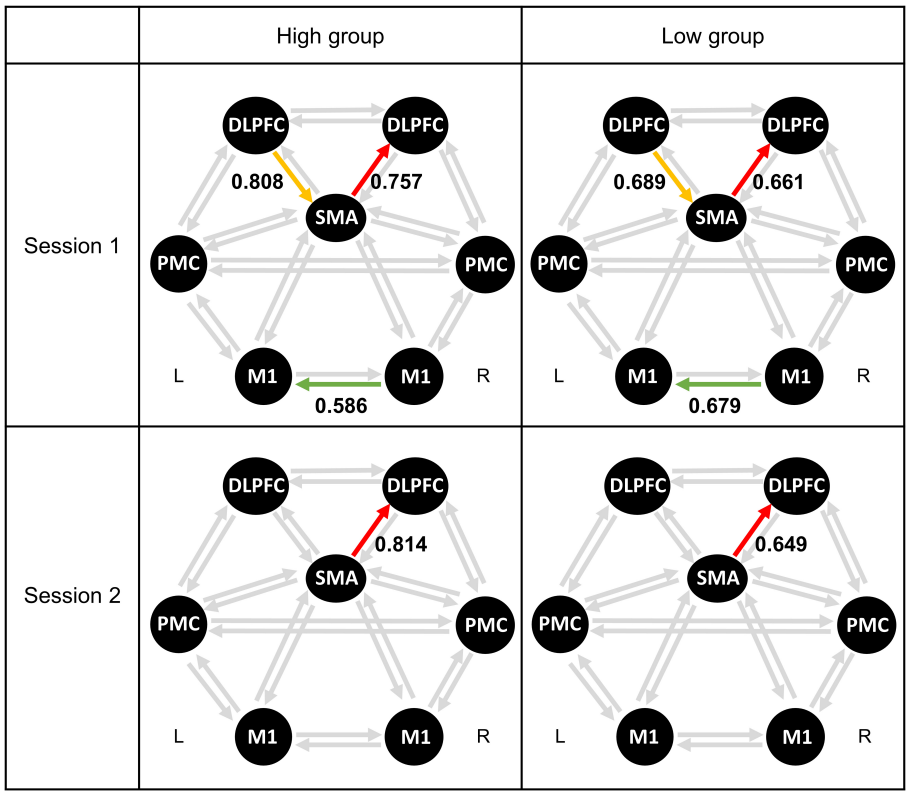

FIGURE 3 | Averaged connectivity strength in resting-state EEG between high- and low-MI performance groups based on CSP-cv. Each colored arrow represents a connection with a significant difference between the high- and low-MI performance groups. SMA, supplementary motor area; PMC, premotor cortex; M1, primary motor cortex; DLPFC, dorsolateral prefrontal cortex.

shows the *r*-squared and RMSE values between the predicted and the actual MI classification accuracies, based on CSP-cv, CSP, CSSP, FBCSP, and BSSFO. The predicted performance had the highest *r*-squared with actual MI performance, based on CSP and FBCSP in Sessions 1 and 2, respectively (Session 1: *r*-squared = 0.31; Session 2: *r*-squared = 0.17). The lowest RMSE for actual MI performance was found under CSP-cv in both sessions (Session 1: RMSE = 13.79%; Session 2: RMSE = 14.55%).

DISCUSSION

In this study, we investigated coupling strength as a new correlate with MI-BCI performance, using the DCM of the resting-state EEG. The MI-BCI performance was predicted by measuring this coupling between brain regions. A connection from the SMA to right DLPFC in the high-MI group was observed to be significantly higher than in the low-MI group. Moreover, this connection showed a significantly positive correlation with MI performance in both sessions under five classifiers.

The MI involves a variety of brain regions and successfully performs the information exchange for the integration of relevant regions. Specifically, a resting-state network with an efficient exchange of information facilitates MI-BCI performance (Zhang et al., 2015b). Interestingly, our results show that the MI-BCI performance can be predicted using the coupling strength from the SMA to right DLPFC in resting-state EEG; during MI, the SMA and DLPFC exhibited observable activations (Mizuguchi et al., 2013). The SMA plays a central role in the preparation of behavior, and it acts as a high-level motor control prohibiting the execution of MI responses (Nachev et al., 2008; Kim et al., 2018). These findings have already been proved using the DCM (Kasess et al., 2008). The DLPFC has been reported to be involved in the early phases of motor training (Pascual-Leone et al., 1996). The frontal region is also affected by cognitive events, and it is responsible for motor planning and programming (Kim et al., 2018). In particular, the right DLPFC plays a crucial role in cognitive controls such as motor attention or inhibition (Mizuguchi et al., 2013). In fact, it is already reported that right DLPFC in the resting-state as a core region is correlated with MI-BCI performance (Zhang et al., 2016). During MI, coupling from SMA to DLPFC has been reported to play a critical role in the motor control needed to move a finger (Kim et al., 2018). As a result of fMRI, DLPFC was not connected to M1, but to SMA during MI (Mizuguchi et al., 2013). The SMA is causally connected into the DLPFC and this relates to higher-order cognitive motor processes such as motor control and preparation (O'Shea and Moran, 2017). Therefore, the coupling strength from the

SMA to right DLPFC, which is already determined in the resting-state, affects brain activity during MI; it influences MI-BCI performance.

We observed changes in MI-BCI performance across different sessions with various classifiers. This was motivated by the variations observed in EEG (Lotte et al., 2007). We also confirmed that different coupling strengths correlated with MI-BCI performance (depending on the session or classifier), except for the connections from the SMA to right DLPFC. Although we did not observe a significant correlation with MI-BCI performance across both sessions, coupling strength from the left DLPFC to SMA, or from the left PMC to left DLPFC, may also be important. Because there is no actual movement taking place during MI, secondary motor areas such as the PMC and SMA are more relevant to MI than M1 (Park et al., 2015b). We found relations across several motor areas; however, none were observed for M1. Even in stroke patients, the activity of the SMA affects MI performance more than M1 (Park et al., 2015a).

The crucial relationship with MI-BCI performance was not found using band power and questionnaires. Some studies have reported that SMR such as mu rhythms in the resting-state is related to MI performance (Blankertz et al., 2010; Kwon et al., 2020). In fact, this argument seems plausible because alpha and beta power are decreased during the MI and used as typical features of the MI paradigm. However, other studies did not observe the significant correlation between spectral power and MI-BCI performance (Jeunet et al., 2015). Interestingly, even though it turns out to be an obvious consistent relationship between the MI-BCI performance and SMR, no significant correlation has been revealed. This is probably due to differences in experimental protocols. Previous studies presented SMR as a reliable predictor were instructed to imagine moving the hand itself. However, in other studies, the rotation of hand can be imagined. In other words, it is a different protocol. In our study, the subject imagines grasping their hands. Therefore, the resting-state SMR is clearly associated with brain changes during the MI, but their role as an MI-BCI predictor may vary depending on the experimental protocol. We also used the mu power based on a shorter baseline period, whereas the mu rhythm predictor in another study was computed as the maximum difference between the power spectral density and the estimated noise floor over the Laplace-filtered sensorimotor channels (Blankertz et al., 2010). In this regard, different ways of extracting mu rhythm are likely to have had these different observations. In addition, the brain activity—such as band power during resting-state—simply indicates the state of certain brain regions, but it cannot indicate the interregional relationships (Lee et al., 2017); these connections, in addition to the sensorimotor cortex associated with the motor network, seem significant (Sharma et al., 2006). In fact, resting-state connectivity is correlated with motor task performance (Gregory et al., 2014). Previous studies have investigated several networks enacting MI (Lorey et al., 2011). It appears that brain connectivity is more relevant to MI performance than the brain activity of certain regions. Furthermore, the questionnaires were too subjective because each subject had different criteria for predicting MI-BCI performance.

TABLE 8 | Correlations between connectivity strength and MI performance based on CSP-cv.

ROI		Session 1		Session 2	
From	**To**	***r*-value**	***p*-value**	***r*-value**	***p*-value**
lM1	SMA	0.054	0.698	0.018	0.898
rM1	SMA	−0.084	0.546	0.034	0.805
lPMC	SMA	−0.193	0.163	−0.177	0.200
rPMC	SMA	−0.076	0.584	−0.069	0.618
lDLPFC	SMA	0.381	**0.005***	NaN	NaN
rDLPFC	SMA	−0.037	0.791	NaN	NaN
SMA	lM1	−0.117	0.398	NaN	NaN
rM1	lM1	−0.217	0.115	−0.082	0.554
lPMC	lM1	−0.173	0.212	−0.104	0.453
SMA	rM1	0.010	0.940	NaN	NaN
lM1	rM1	−0.055	0.694	−0.052	0.708
rPMC	rM1	0.091	0.513	0.058	0.675
rPMC	lPMC	0.175	0.206	−0.030	0.831
lPMC	rPMC	0.073	0.599	0.076	0.586
SMA	lDLPFC	0.010	0.943	−0.071	0.610
lPMC	lDLPFC	−0.061	0.659	−0.331	**0.014***
rDLPFC	lDLPFC	0.117	0.398	−0.211	0.125
SMA	rDLPFC	0.536	**<0.001****	0.419	**0.002****
rPMC	rDLPFC	−0.020	0.883	0.154	0.266
lDLPFC	rDLPFC	0.036	0.795	−0.017	0.906

*In Session 1, Model 4 is selected and there are 20 connections. In Session 2, Model 2 is selected and there are 16 connections. Therefore, four connections in Session 2 are excluded ('NaN'). The p-values below 0.05 are highlighted in bold. ROI, region of interest; l/rM1, left/right primary motor cortex; l/rPMC, left/right pre-motor cortex; l/rDLPFC, left/right dorsolateral prefrontal cortex; SMA, supplementary motor area. * with no correction and **<Bonferroni correction.*

By applying our results to the BCI-inefficiency problem, it can be seen that a possible reason for BCI-inefficiency is that subjects have a less active motor network in the motor preparation regions related to cognitive processes in the resting-state (Ahn et al., 2013). Therefore, improvement of MI performance requires a new approach to activate the motor network. Performing upper extremity exercises is a good way to activate a motor network during the resting-state (Ma et al., 2011). In stroke patients, upper extremity rehabilitation has been shown to activate the resting-state effective connectivity of the motor network (Andrew James et al., 2009). This implies that MI-BCI performance can be improved by enhancing the connectivity strengths associated with motor planning, such as the coupling strength from the SMA to right DLPFC. Therefore, if subjects had been asked about their exercise habits in the pre-experimental questionnaire, the responses may have shown some correlation with MI performance. As another approach, the resting-state motor network can be improved by the direct stimulation of the brain, through transcranial direct current stimulation or transcranial magnetic stimulation (Fischer et al., 2017).

This study had a few limitations. First, we did not check whether ME performance was predictable using our proposed coupling strength. ME and MI share a common mechanism and motor circuit-related motor network (Lee et al., 2016;

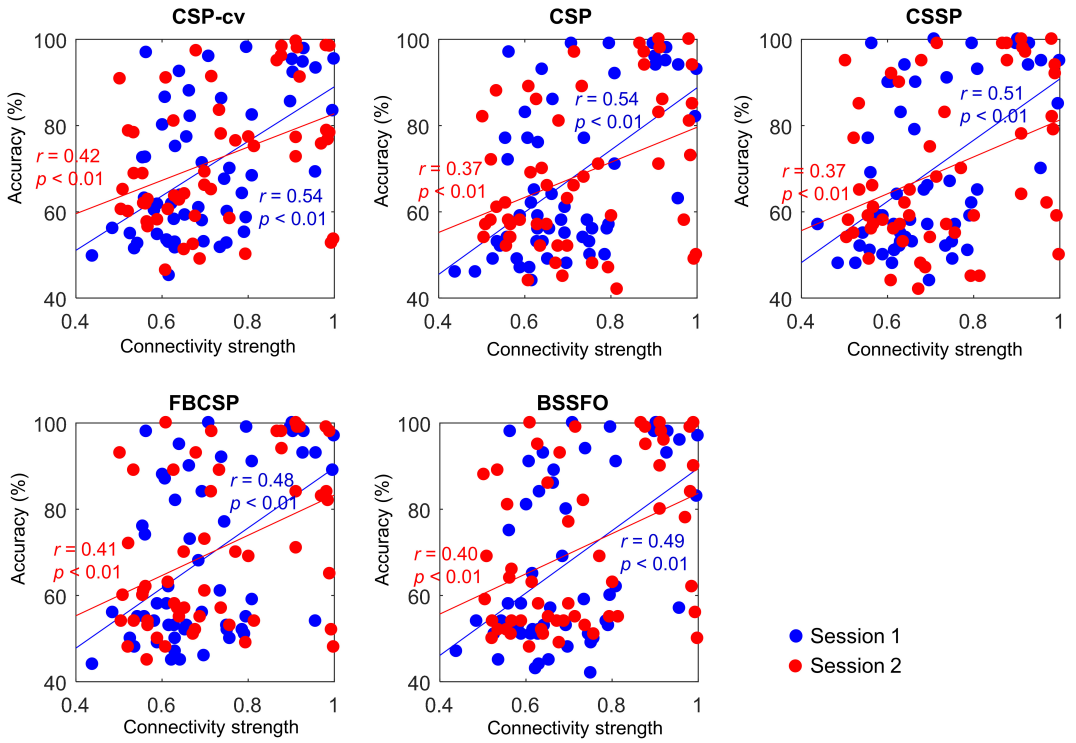

FIGURE 4 | Correlation between connectivity strength from SMA to right DLPFC and MI-BCI performance. Each colored dot represents an individual connectivity strength from SMA to right DLPFC and MI performance. Blue and red indicate Session 1 and Session 2, respectively. SMA, supplementary motor area; DLPFC, dorsolateral prefrontal cortex; CSP-cv, common spatial pattern with cross-validation; CSP, common spatial pattern; CSSP, common spatio-spectral pattern; FBCSP, filter bank common spatial pattern; BSSFO, Bayesian spatio-spectral filter optimization.

TABLE 9 | Relationship between actual MI performance and predicted MI performance using connectivity strength from SMA to right DLPFC.

Classifier	Session 1		Session 2	
	r-squared	RMSE (%)	*r*-squared	RMSE (%)
CSP_cv	0.28	13.79	0.11	14.55
CSP	0.31	15.78	0.10	16.73
CSSP	0.25	16.46	0.14	17.21
FBCSP	0.20	17.97	0.17	17.05
BSSFO	0.21	18.04	0.11	17.63

CSP_cv, common spatial pattern with cross-validation; CSP, common spatial pattern; CSSP, common spatio-spectral pattern; FBCSP, filter bank common spatial pattern; BSSFO, Bayesian spatio-spectral filter optimization.

Daeglau et al., 2020). In this regard, it would have been more effective to examine the relationship with ME performance, to enable the wider use of the predictor in the future. Second, we used all brain regions when finding predictors through the DCM. However, measuring the entire brain is impractical. Therefore, based on our results, we need to use only a small number of EEG channels to predict MI-BCI performance in the future. Third, we used only grasping imagery, and brain activity is known to vary depending on the type of action. For example, the SMA activity depends on whether it executes a large movement (e.g., wrist movements of hand rotation) or a small movement (e.g., finger movements in hand grasping) (Park et al., 2015b). Therefore, it is necessary to apply them accordingly to different actions. Last, computation time is very important in real applications. The model and specific ROIs are already selected, so we can measure the proposed strength in sec. Nevertheless, we did not directly compare the existing paper with the computation time. Therefore, in the future, it is necessary to compare the computing time for this practicality.

CONCLUSION

We proposed an MI-BCI predictor from the resting-state EEG using DCM. Our study is valuable in two ways. The first is its investigation of the effective connectivity (with directionality) related to MI performance; it facilitates a more analytical understanding of why the performance is lower in low-MI groups. Our results suggest that for subjects with "BCI-inefficiency," appropriate alternatives can be implemented to improve MI-BCI performance. Second, we show the possibility of predicting MI performance using predictors measured before the time-consuming MI-BCI experiment takes place. Therefore, our predictor can be used to sort out BCI-inefficiency before subjects perform a task in the real application. This can help prevent

the unnecessary waste of time and resources when implementing MI-BCI in practice.

DATA AVAILABILITY STATEMENT

The datasets generated for this study are available on request to the corresponding author.

ETHICS STATEMENT

The studies involving human participants were reviewed and approved by Korea University Institutional Review Board (1040548-KUIRB-16-159-A-2). The patients/participants provided their written informed consent to participate in this study.

AUTHOR CONTRIBUTIONS

ML, J-GY, and S-WL designed the experiments. ML and J-GY analyzed the data and drafted the manuscript. ML and S-WL critically revised the manuscript and contributed important intellectual comments. All authors contributed to the article and approved the submitted version.

FUNDING

This work was partly supported by an Institute for Information & Communications Technology Planning & Evaluation (IITP) grant, funded by the Korea government (No. 2017-0-00451; Development of BCI based Brain and Cognitive Computing Technology for Recognizing User's Intentions using Deep Learning) and an Institute for Information & Communications Technology Planning & Evaluation (IITP) grant, funded by the Korea government (MSIT) (No. 2019-0-00079; Department of Artificial Intelligence, Korea University).

SUPPLEMENTARY MATERIAL

The Supplementary Material for this article can be found online at: https://www.frontiersin.org/articles/10.3389/fnhum.2020.00321/full#supplementary-material

REFERENCES

Aflalo, T., Kellis, S., Klaes, C., Lee, B., Shi, Y., Pejsa, K., et al. (2015). Decoding motor imagery from the posterior parietal cortex of a tetraplegic human. *Science* 348, 906–910. doi: 10.1126/science.aaa5417

Ahn, M., Cho, H., Ahn, S., and Jun, S. C. (2013). High theta and low alpha powers may be indicative of BCI-illiteracy in motor imagery. *PLoS One* 8:e80886. doi: 10.1371/journal.pone.0080886

Ahn, M., Cho, H., Ahn, S., and Jun, S. C. (2018). User's self-prediction of performance in motor imagery brain–computer Interface. *Front. Hum. Neurosci.* 12:59. doi: 10.3389/fnhum.2018.00059

Ahn, M., and Jun, S. C. (2015). Performance variation in motor imagery brain–computer interface: a brief review. *J. Neurosci. Methods* 243, 103–110. doi: 10.1016/j.jneumeth.2015.01.033

Andrew James, G., Lu, Z.-L., VanMeter, J. W., Sathian, K., Hu, X. P., and Butler, A. J. (2009). Changes in resting state effective connectivity in the motor network following rehabilitation of upper extremity poststroke paresis. *Top. Stroke Rehabil.* 16, 270–281. doi: 10.1310/tsr1604-270

Ang, K. K., Chin, Z. Y., Wang, C., Guan, C., and Zhang, H. (2012). Filter bank common spatial pattern algorithm on BCI competition IV datasets 2a and 2b. *Front. Neurosci.* 6:39. doi: 10.3389/fnins.2012.00039

Begliomini, C., Sartori, L., Miotto, D., Stramare, R., Motta, R., and Castiello, U. (2015). Exploring manual asymmetries during grasping: a dynamic causal modeling approach. *Front. Psychol.* 6:167. doi: 10.3389/fpsyg.2015.00167

Blankertz, B., Sanelli, C., Halder, S., Hammer, E., Kübler, A., Müller, K.-R., et al. (2009). Predicting BCI performance to study BCI illiteracy. *BMC Neurosci.* 10:84. doi: 10.1186/1471-2202-10-S1-P84

Blankertz, B., Sannelli, C., Halder, S., Hammer, E. M., Kübler, A., Müller, K.-R., et al. (2010). Neurophysiological predictor of SMR-based BCI performance. *Neuroimage* 51, 1303–1309. doi: 10.1016/j.neuroimage.2010.03.022

Bönstrup, M., Schulz, R., Feldheim, J., Hummel, F. C., and Gerloff, C. (2016). Dynamic causal modelling of EEG and fMRI to characterize network architectures in a simple motor task. *Neuroimage* 124, 498–508. doi: 10.1016/j.neuroimage.2015.08.052

Chen, C., Kiebel, S. J., and Friston, K. J. (2008). Dynamic causal modelling of induced responses. *Neuroimage* 41, 1293–1312. doi: 10.1016/j.neuroimage.2008.03.026

Daeglau, M., Zich, C., Emkes, R., Welzel, J., Debener, S., and Kranczioch, C. (2020). Investigating priming effects of physical practice on motor imagery-induced event-related desynchronization. *Front. Psychol.* 11:57. doi: 10.3389/fpsyg.2020.00057

David, O., and Friston, K. J. (2003). A neural mass model for MEG/EEG: coupling and neuronal dynamics. *Neuroimage* 20, 1743–1755. doi: 10.1016/j.neuroimage.2003.07.015

Delorme, A., and Makeig, S. (2004). EEGLAB: an open source toolbox for analysis of single-trial EEG dynamics including independent component analysis. *J. Neurosci. Methods* 134, 9–21. doi: 10.1016/j.jneumeth.2003.10.009

Edelman, B. J., Meng, J., Suma, D., Zurn, C., Nagarajan, E., Baxter, B. S., et al. (2019). Noninvasive neuroimaging enhances continuous neural tracking for robotic device control. *Sci. Robot.* 4:eaaw6844. doi: 10.1126/scirobotics.aaw6844

Ferreira, D. K. T., Guillot, A., Clémençon, M., Debarnot, U., and Di Rienzo, F. (2020). Effect of physical fatigue elicited by continuous and intermittent exercise on motor imagery ability. *Res. Q. Exerc. Sport* doi: 10.1080/02701367.2019.1691709 [Epub ahead of print],

Fischer, D. B., Fried, P. J., Ruffini, G., Ripolles, O., Salvador, R., Banus, J., et al. (2017). Multifocal tDCS targeting the resting state motor network increases cortical excitability beyond traditional tDCS targeting unilateral motor cortex. *Neuroimage* 157, 34–44. doi: 10.1016/j.neuroimage.2017.05.060

Friston, K. J. (2011). Functional and effective connectivity: a review. *Brain Connec.* 1, 13–36. doi: 10.1089/brain.2011.0008

Garrido, M. I., Kilner, J. M., Kiebel, S. J., Stephan, K. E., and Friston, K. J. (2007). Dynamic causal modelling of evoked potentials: a reproducibility study. *Neuroimage* 36, 571–580. doi: 10.1016/j.neuroimage.2007.03.014

Gregory, M. D., Agam, Y., Selvadurai, C., Nagy, A., Vangel, M., Tucker, M., et al. (2014). Resting state connectivity immediately following learning correlates with subsequent sleep-dependent enhancement of motor task performance. *Neuroimage* 102, 666–673. doi: 10.1016/j.neuroimage.2014.08.044

Grosse-Wentrup, M., Schölkopf, B., and Hill, J. (2011). Causal influence of gamma oscillations on the sensorimotor rhythm. *Neuroimage* 56, 837–842. doi: 10.1016/j.neuroimage.2010.04.265

Guger, C., Edlinger, G., Harkam, W., Niedermayer, I., and Pfurtscheller, G. (2003). How many people are able to operate an EEG-based brain-computer interface (BCI)? *IEEE Trans. Neural Syst. Rehabil. Eng.* 11, 145–147. doi: 10.1109/tnsre.2003.814481

Hammer, E. M., Halder, S., Blankertz, B., Sannelli, C., Dickhaus, T., Kleih, S., et al. (2012). Psychological predictors of SMR-BCI performance. *Biol. Psychol.* 89, 80–86. doi: 10.1016/j.biopsycho.2011.09.006

Hammer, E. M., Kaufmann, T., Kleih, S. C., Blankertz, B., and Kübler, A. (2014). Visuo-motor coordination ability predicts performance with brain-computer interfaces controlled by modulation of sensorimotor rhythms (SMR). *Front. Hum. Neurosci.* 8:574. doi: 10.3389/fnhum.2014.00574

Hochberg, L. R., Serruya, M. D., Friehs, G. M., Mukand, J. A., Saleh, M., Caplan, A. H., et al. (2006). Neuronal ensemble control of prosthetic devices by a human with tetraplegia. *Nature* 442, 164–171. doi: 10.1038/nature04970

Jeong, J., Kwak, N., Guan, C., and Lee, S. (2020). Decoding movement-related cortical potentials based on subject-dependent and section-wise spectral filtering. *IEEE Trans. Neural Syst. Rehabil. Eng.* 28, 687–698. doi: 10.1109/tnsre.2020.2966826

Jeunet, C., N'Kaoua, B., and Lotte, F. (2016). "Advances in user-training for mental-imagery-based BCI control: psychological and cognitive factors and their neural correlates," in *Progress in Brain Research*, eds S. Waxman, D. G. Stein, D. Swaab, and H. Fields (Amsterdam: Elsevier), 3–35. doi: 10.1016/bs.pbr.2016.04.002

Jeunet, C., N'Kaoua, B., Subramanian, S., Hachet, M., and Lotte, F. (2015). Predicting mental imagery-based BCI performance from personality, cognitive profile and neurophysiological patterns. *PLoS One* 10:e0143962. doi: 10.1371/journal.pone.0143962

Kasess, C. H., Stephan, K. E., Weissenbacher, A., Pezawas, L., Moser, E., and Windischberger, C. (2010). Multi-subject analyses with dynamic causal modeling. *Neuroimage* 49, 3065–3074. doi: 10.1016/j.neuroimage.2009.11.037

Kasess, C. H., Windischberger, C., Cunnington, R., Lanzenberger, R., Pezawas, L., and Moser, E. (2008). The suppressive influence of SMA on M1 in motor imagery revealed by fMRI and dynamic causal modeling. *Neuroimage* 40, 828–837. doi: 10.1016/j.neuroimage.2007.11.040

Kiebel, S. J., David, O., and Friston, K. J. (2006). Dynamic causal modelling of evoked responses in EEG/MEG with lead field parameterization. *Neuroimage* 30, 1273–1284. doi: 10.1016/j.neuroimage.2005.12.055

Kiebel, S. J., Garrido, M. I., Moran, R. J., and Friston, K. J. (2008). Dynamic causal modelling for EEG and MEG. *Cogn. Neurodynamics* 2:121. doi: 10.1007/s11571-008-9038-0

Kim, K.-T., Suk, H.-I., and Lee, S.-W. (2016). Commanding a brain-controlled wheelchair using steady-state somatosensory evoked potentials. *IEEE Trans. Neural Syst. Rehabil. Eng.* 26, 654–665. doi: 10.1109/tnsre.2016.2597854

Kim, Y. K., Park, E., Lee, A., Im, C.-H., and Kim, Y.-H. (2018). Changes in network connectivity during motor imagery and execution. *PLoS One* 13:e0190715. doi: 10.1371/journal.pone.0190715

Kuhtz-Buschbeck, J., Mahnkopf, C., Holzknecht, C., Siebner, H., Ulmer, S., and Jansen, O. (2003). Effector-independent representations of simple and complex imagined finger movements: a combined fMRI and TMS study. *Eur. J. Neurosci.* 18, 3375–3387. doi: 10.1111/j.1460-9568.2003.03066.x

Kwon, M., Cho, H., Won, K., Ahn, M., and Jun, S. C. (2020). Use of both eyes-open and eyes-closed resting states may yield a more robust predictor of motor imagery BCI performance. *Electronics* 9:690. doi: 10.3390/electronics9040690

Lee, M., Baird, B., Gosseries, O., Nieminen, J. O., Boly, M., Postle, B. R., et al. (2019b). Connectivity differences between consciousness and unconsciousness in non-rapid eye movement sleep: a TMS–EEG study. *Sci. Rep.* 9:5175.

Lee, M., Park, C.-H., Im, C.-H., Kim, J.-H., Kwon, G.-H., Kim, L., et al. (2016). Motor imagery learning across a sequence of trials in stroke patients. *Restor. Neurol. Neurosci.* 34, 635–645. doi: 10.3233/rnn-150534

Lee, M., Sanders, R. D., Yeom, S.-K., Won, D.-O., Seo, K.-S., Kim, H. J., et al. (2017). Network properties in transitions of consciousness during propofol-induced sedation. *Sci. Rep.* 7:16791.

Lee, M.-H., Kwon, O.-Y., Kim, Y.-J., Kim, H.-K., Lee, Y.-E., Williamson, J., et al. (2019a). EEG dataset and OpenBMI toolbox for three BCI paradigms: an investigation into BCI illiteracy. *GigaScience* 8:giz002.

Lemm, S., Blankertz, B., Curio, G., and Muller, K.-R. (2005). Spatio-spectral filters for improving the classification of single trial EEG. *IEEE Trans. Biomed. Eng.* 52, 1541–1548. doi: 10.1109/tbme.2005.851521

Lever, J., Krzywinski, M., and Altman, N. (2016). Model selection and overfitting. *Nat. Methods* 13, 703–704. doi: 10.1038/nmeth.3968

Litvak, V., Mattout, J., Kiebel, S., Phillips, C., Henson, R., Kilner, J., et al. (2011). EEG and MEG data analysis in SPM8. *Comput. Intell. Neurosci.* 2011:852961.

Lorey, B., Pilgramm, S., Bischoff, M., Stark, R., Vaitl, D., Kindermann, S., et al. (2011). Activation of the parieto-premotor network is associated with vivid motor imagery—a parametric fMRI study. *PLoS One* 6:e20368. doi: 10.1371/journal.pone.0020368

Lotte, F., Congedo, M., Lécuyer, A., Lamarche, F., and Arnaldi, B. (2007). A review of classification algorithms for EEG-based brain-computer interfaces. *J. Neural Eng.* 4, R1–R13.

Lotte, F., and Jeunet, C. (2018). Defining and quantifying users' mental imagery-based BCI skills: a first step. *J. Neural Eng.* 15:046030. doi: 10.1088/1741-2552/aac577

Lotze, M., and Halsband, U. (2006). Motor imagery. *J. Physiol.* 99, 386–395.

Luppino, G., Matelli, M., Camarda, R., and Rizzolatti, G. (1993). Corticocortical connections of area F3 (SMA−proper) and area F6 (pre−SMA) in the macaque monkey. *J. Comp. Neurol.* 338, 114–140. doi: 10.1002/cne.903380109

Ma, L., Narayana, S., Robin, D. A., Fox, P. T., and Xiong, J. (2011). Changes occur in resting state network of motor system during 4 weeks of motor skill learning. *Neuroimage* 58, 226–233. doi: 10.1016/j.neuroimage.2011.06.014

Middleton, F. A., and Strick, P. L. (1994). Anatomical evidence for cerebellar and basal ganglia involvement in higher cognitive function. *Science* 266, 458–461. doi: 10.1126/science.7939688

Mizuguchi, N., Nakata, H., Hayashi, T., Sakamoto, M., Muraoka, T., Uchida, Y., et al. (2013). Brain activity during motor imagery of an action with an object: a functional magnetic resonance imaging study. *Neurosci. Res.* 76, 150–155. doi: 10.1016/j.neures.2013.03.012

Myrden, A., and Chau, T. (2015). Effects of user mental state on EEG-BCI performance. *Front. Hum. Neurosci.* 9:308. doi: 10.3389/fnhum.2015.00308

Nachev, P., Kennard, C., and Husain, M. (2008). Functional role of the supplementary and pre-supplementary motor areas. *Nat. Rev. Neurosci.* 9, 856–869. doi: 10.1038/nrn2478

Neuper, C., Wörtz, M., and Pfurtscheller, G. (2006). ERD/ERS patterns reflecting sensorimotor activation and deactivation. *Prog. Brain Res.* 159, 211–222. doi: 10.1016/s0079-6123(06)59014-4

O'Shea, H., and Moran, A. (2017). Does motor simulation theory explain the cognitive mechanisms underlying motor imagery? A critical review. *Front. Hum. Neurosci.* 11:72. doi: 10.3389/fnhum.2017.00072

Park, C.-H., Chang, W. H., Lee, M., Kwon, G. H., Kim, L., Kim, S. T., et al. (2015a). Predicting the performance of motor imagery in stroke patients: multivariate pattern analysis of functional MRI data. *Neurorehabil. Neural Repair* 29, 247–254. doi: 10.1177/1545968314543308

Park, C.-H., Chang, W. H., Lee, M., Kwon, G. H., Kim, L., Kim, S. T., et al. (2015b). Which motor cortical region best predicts imagined movement? *Neuroimage* 113, 101–110. doi: 10.1016/j.neuroimage.2015.03.033

Pascual-Leone, A., Wassermann, E. M., Grafman, J., and Hallett, M. (1996). The role of the dorsolateral prefrontal cortex in implicit procedural learning. *Exp. Brain Res.* 107, 479–485.

Pfurtscheller, G., and Neuper, C. (2001). Motor imagery and direct brain-computer communication. *Proc. IEEE* 89, 1123–1134. doi: 10.1109/5.939829

Ramoser, H., Muller-Gerking, J., and Pfurtscheller, G. (2000). Optimal spatial filtering of single trial EEG during imagined hand movement. *IEEE Trans. Rehabil. Eng.* 8, 441–446. doi: 10.1109/86.895946

Randolph, A. B., Jackson, M. M., and Karmakar, S. (2010). Individual characteristics and their effect on predicting mu rhythm modulation. *Int. J. Hum. Comput. Interact.* 27, 24–37. doi: 10.1080/10447318.2011.535750

Rizzolatti, G., and Luppino, G. (2001). The cortical motor system. *Neuron* 31, 889–901. doi: 10.1016/s0896-6273(01)00423-8

Sakkalis, V. (2011). Review of advanced techniques for the estimation of brain connectivity measured with EEG/MEG. *Comput. Biol. Med.* 41, 1110–1117. doi: 10.1016/j.compbiomed.2011.06.020

Sannelli, C., Vidaurre, C., Müller, K.-R., and Blankertz, B. (2019). A large scale screening study with a SMR-based BCI: categorization of BCI users and differences in their SMR activity. *PLoS One* 14:e0207351. doi: 10.1371/journal.pone.0207351

Sharma, N., Pomeroy, V. M., and Baron, J.-C. (2006). Motor imagery: a backdoor to the motor system after stroke? *Stroke* 37, 1941–1952. doi: 10.1161/01.str.0000226902.43357.fc

Stephan, K. E., Penny, W. D., Daunizeau, J., Moran, R. J., and Friston, K. J. (2009). Bayesian model selection for group studies. *Neuroimage* 46, 1004–1017.

Suk, H.-I., and Lee, S.-W. (2012). A novel Bayesian framework for discriminative feature extraction in brain-computer interfaces. *IEEE Trans. Pattern Anal. Mach. Intell.* 35, 286–299. doi: 10.1109/tpami.2012.69

Thompson, M. C. (2019). Critiquing the concept of BCI illiteracy. *Sci. Eng. Ethics* 25, 1217–1233. doi: 10.1007/s11948-018-0061-1

Van de Steen, F., Almgren, H., Razi, A., Friston, K., and Marinazzo, D. (2019). Dynamic causal modelling of fluctuating connectivity in resting-state EEG. *Neuroimage* 189, 476–484. doi: 10.1016/j.neuroimage.2019.01.055

Van Gerven, M., Farquhar, J., Schaefer, R., Vlek, R., Geuze, J., Nijholt, A., et al. (2009). The brain–computer interface cycle. *J. Neural Eng.* 6:041001.

Varatharajan, R., Manogaran, G., and Priyan, M. K. (2018). A big data classification approach using LDA with an enhanced SVM method for ECG signals in cloud computing. *Multimed. Tools Appl.* 77, 10195–10215. doi: 10.1007/s11042-017-5318-1

Wolpaw, J. R., Birbaumer, N., McFarland, D. J., Pfurtscheller, G., and Vaughan, T. M. (2002). Brain-computer interfaces for communication and control. *Clin. Neurophysiol.* 113, 767–791.

Zhang, R., Xu, P., Chen, R., Li, F., Guo, L., Li, P., et al. (2015a). Predicting inter-session performance of SMR-based brain–computer interface using the spectral entropy of resting-state EEG. *Brain Topogr.* 28, 680–690. doi: 10.1007/s10548-015-0429-3

Zhang, R., Yao, D., Valdés-Sosa, P. A., Li, F., Li, P., Zhang, T., et al. (2015b). Efficient resting-state EEG network facilitates motor imagery performance. *J. Neural Eng.* 12:066024. doi: 10.1088/1741-2560/12/6/066024

Zhang, T., Liu, T., Li, F., Li, M., Liu, D., Zhang, R., et al. (2016). Structural and functional correlates of motor imagery BCI performance: insights from the patterns of fronto-parietal attention network. *Neuroimage* 134, 475–485. doi: 10.1016/j.neuroimage.2016.04.030

Zhang, Y., Zhang, H., Chen, X., Lee, S.-W., and Shen, D. (2017). Hybrid high-order functional connectivity networks using resting-state functional MRI for mild cognitive impairment diagnosis. *Sci. Rep.* 7:6530.

Conflict of Interest: The authors declare that the research was conducted in the absence of any commercial or financial relationships that could be construed as a potential conflict of interest.

frontiers in Human Neuroscience

ORIGINAL RESEARCH
published: 21 August 2020
doi: 10.3389/fnhum.2020.00326

Changes in Empathy in Patients With Chronic Low Back Pain: A Structural–Functional Magnetic Resonance Imaging Study

Junqin Ma[1], *Xianglong Wang*[1], *Qing Qiu*[2], *Hongrui Zhan*[1,3] *and Wen Wu*[1]*

[1]*Department of Rehabilitation, Zhujiang Hospital, Southern Medical University, Guangzhou, China,* [2]*Department of Radiology, Zhujiang Hospital, Southern Medical University, Guangzhou, China,* [3]*Department of Physical Medicine and Rehabilitation, The Fifth Affiliated Hospital of Sun Yat-sen University, Zhuhai, China*

Objective: Many pieces of research have focused on pain within individuals, but little attention has been paid to whether pain can change an individual's empathic ability and affect social relationships. The purpose of this study is to explore how chronic low back pain changes empathy.

Methods: Twenty-four chronic low back pain patients and 22 healthy controls were recruited. We set up an experimental pain-exposed model for each healthy subject. All subjects received a painful-empathic magnetic resonance scan. After the scan, all subjects rated the pain intensity and multiple empathy-related indicators. The clinical assessment scale was the 20-item Basic Empathy Scale in Adults.

Result: The chronic low back pain patients reported lower scores on the total scores of BES-A, the subscale scores of emotional disconnection and cognitive empathy, and the discomfort rating. The fMRI results in the chronic low back pain patients showed that there were multiple abnormal brain pathways centered on the anterior insula. The DTI results in the chronic low back pain patients showed that there were reduced fractional anisotropy values in the corpus callosum, bilateral anterior thalamic radiation (ATR), right posterior thalamic radiation (PTR), right superior longitudinal fasciculus (SLF), and left anterior corona radiate (ACR).

Conclusion: Our study found that patients with chronic low back pain have impaired empathy ability. The abnormal functional connectivity of multiple brain networks, multiple damaged white matter tracts, and the lower behavioral scores in chronic low back pain patients supported our findings.

Keywords: empathy, chronic low back pain, functional magnetic resonance imaging, diffusion tensor imaging, brain networks

OPEN ACCESS

Edited by:
Wei Wu,
South China University of Technology, China

Reviewed by:
Claudia Altamura,
Campus Bio-Medico University, Italy
Jiu Chen,
Nanjing Medical University, China

***Correspondence:**
Wen Wu
wuwen66@163.com

Specialty section:
This article was submitted to Brain Imaging and Stimulation, a section of the journal Frontiers in Human Neuroscience

Received: *03 April 2020*
Accepted: *22 July 2020*
Published: *21 August 2020*

Citation:
Ma J, Wang X, Qiu Q, Zhan H and Wu W (2020) Changes in Empathy in Patients With Chronic Low Back Pain: A Structural–Functional Magnetic Resonance Imaging Study. Front. Hum. Neurosci. 14:326. doi: 10.3389/fnhum.2020.00326

Abbreviations: fMRI, functional magnetic resonance imaging; DTI, diffusion tensor imaging; FA, fractional anisotropy; BES-A, Basic Empathy Scale in Adults; cLBP, chronic low back pain; VAS, visual analogue scale; TBSS, Tract-Based Spatial Statistics; AI, anterior insula; FC, functional connectivity; CC, corpus callosum; ATR, anterior thalamic radiation; PTR, posterior thalamic radiation; SLF, superior longitudinal fasciculus; ACR, anterior corona radiata; DLPFC, dorsolateral prefrontal cortex; SPL, superior parietal lobule; PHP, parahippocampal gyrus; gCC, genu of corpus callosum; sCC, splenium of corpus callosum.

INTRODUCTION

Imagine that your hand was accidentally scratched. This experience can lead to nociceptive pain, which originates in the peripheral nociceptors. This stimulus eventually leads to cerebral cortex, causing changes in brain network activity. Now imagine that you saw someone else's hand accidentally being scratched. This experience typically produces empathy for pain, a phenomenon that, despite differences in origin, has the same characteristics of nociceptive pain and changes in brain network activity.

Briefly speaking, empathy can be generated by directly observing or imagining the emotions of the target. The occurrence of empathy can lead individuals to altruistic and prosocial behaviors towards the plight of others, and this ability to perceive the distress of others also keeps individuals alert to dangerous stimuli (Xiang et al., 2018). Therefore, empathy is of great significance for maintaining social relations and maintaining interactions with others. However, in the eyes of ordinary people, the ability to empathize with others is so common that it seems to be innate in everyone. Many pieces of research have focused on pain, distress, and disability within individuals (Goubert et al., 2005), but little attention has been paid to whether diseases can change an individual's empathic ability and affect social relationships.

The importance of empathy is also evident in pain medicine. Chronic pain is notorious for harming individuals in many ways. It not only physically tortures patients, but it also stigmatizes them (Cohen et al., 2011). When there is no objective evidence of bodily injury, the subjective pain feeling expressed by patients is often misunderstood as a mental disorder (Cohen et al., 2011). Therefore, the stigmatization has led to the collapse of interpersonal trust between chronic pain patients and others, which is not conducive to social harmony due to the large group of chronic pain patients. Furthermore, on the psychological level, chronic pain can lead to pain catastrophizing and mood disorders such as anxiety and depression. These problems further isolate patients with chronic pain and inhibit the development of prosocial behaviors. Therefore, it is urgent to study the relationship between chronic pain and empathy. A pioneering study by Singer et al. (2004) found that there is a partial overlap between empathy for pain and original pain-activated brain regions. Multiple pain-related brain regions in patients with chronic pain were found to have decreased gray matter volume, altered functional connectivity, and cortical thickness (Hubbard et al., 2014; Seminowicz and Moayedi, 2017). These evidences drive us to link the change of empathy ability to chronic pain.

Previous studies on empathy were mostly behavioral and neuroimaging studies on normal people (Lamm et al., 2011). A few studies have focused on changes in empathy (Roche and Harmon, 2017). Our knowledge is very limited about how empathy has changed in patients with chronic pain. Therefore, the purpose of this study is to explore how chronic pain changes empathy (i.e., what changes have taken place in the empathy ability of patients with chronic pain).

The implicit measures, such as functional magnetic resonance imaging (fMRI), may be a good method to explore empathy. Previous studies have explored the neural brain network mechanism of empathy in healthy adults through fMRI technology and have gotten some excellent results (Engen and Singer, 2013). However, the absence of structural image studies, such as diffusion tensor imaging (DTI), makes the evidence chain of these studies relatively weak, which is one of the limitations of these studies.

Based on the above description, after designating the chronic low back pain (cLBP) group (experimental group) and experimental pain group (EP group), fMRI and DTI technology will be jointly used in this study to explore the brain structural abnormalities and the functional brain changes during empathy state in patients with chronic pain. Diffusion tensor imaging is a magnetic resonance technique that reflects the random diffusion of water molecules in the brain. The Basic Empathy Scale in Adults (BES-A) will be used to quantify the empathy ability of all subjects (Carré et al., 2013). BES-A is usually divided into three subscales, namely, emotional contagion, emotional disconnection, and cognitive empathy. These three components represent three dimensions of empathy. The picture-based paradigm will be used to induce the subjects' empathy state.

EXPERIMENTAL PROCEDURES

Recruitment of Subjects

To reduce confounding factors, we limit the patients included to those with cLBP. We recruited 25 cLBP patients and 25 healthy controls from Zhujiang Hospital of Southern Medical University. For the patients, inclusion criteria were as follows: (1) clinically diagnosed as cLBP (Kreiner et al., 2020); (2) the results assessed by the self-rating anxiety scale (SAS) and self-rating depression scale (SDS) are normal; (3) no fMRI contraindication; (4) did not receive psychological induction training; (5) no cerebral lesions; and (6) no mental or neurological disease. For the controls, inclusion criteria were the same as the patients except for the diagnosis of cLBP, and the demographic characteristics of all subjects (age, gender, and education) were collected.

This experiment was approved by the ethics committee of Zhujiang Hospital of Southern Medical University (Ministry of Health of the PRC, 2018). All subjects signed informed consent. We explained the detailed instructions, experimental procedures, possible risks and discomforts of the study to all volunteers, and answered their questions in detail.

Procedures

Preparation of the Pain Model

To match the patient's pain status, we set up an experimental pain-exposed model for each healthy subject. The process was as follows: With subjects in a lateral decubitus position, an indwelling needle attached to a 2-ml syringe containing 2 ml of sterile hypertonic (3%) saline was inserted into the lower back muscles, 2 cm to the right of the 4th lumbar vertebra. The time that was taken for the pain caused by the needle puncture to subside ranged from 10 to 30 s in all subjects. After the pain resolved, subjects turned from the lateral decubitus to the supine position, and the hypertonic saline was injected into

the lower back muscles of the subjects through the indwelling needle at a speed of 0.15 ml/min, maintaining pain until all scans were completed.

Scanning Materials Preparation

The best bottom-up input to produce emotional resonance may be to observe the facial expression of the target directly (Goubert et al., 2005). Besides, many previous studies used photos of limbs with noxious stimuli as empathic stimuli (Gu and Han, 2007; Gu et al., 2010). Consequently, photographs related to pain with both facial expressions and body language may be better experimental stimulus materials for empathy. Before the experiment, we collected photographs that met the above features from various online picture websites. We then put more than 100 questionnaires into society to screen out photos that can cause public empathy. The photos screening paradigm through questionnaire survey was based on a previous pioneering study (Jackson et al., 2005). We finally screened 24 photos as experimental stimulus materials (see **Supplementary Figure S1, Table S4** for photo screening). The scanning process was fully explained to each subject and they were instructed to focus on the content of the stimululs materials rather than other things during the scanning process.

Scanning Process

Brain scanning consisted of three sessions. First, the T1 sequence was performed. Second, the brain functional sequence was performed and the duration of this session was 6 min. In this session, the stimulus materials were displayed in two consecutive rounds for each participant, and each photo was presented for 7.5 s. Third, each subject underwent a DTI sequence scan lasting 8 min.

Postscan Tests

Immediately after the scan, each subject was asked to rate their current pain intensity, discomfort ratings ("How uncomfortable were you when you saw these photos?"), and the intensity of pain suffered by the individual in each photo ("How painful do you think the person in the photo is?"). The assessment of pain intensity of oneself and others can be used to measure the cognitive-evaluative dimension of subjects. The evaluation of the degree of discomfort after receiving stimulation can be used to measure the emotional dimension of empathy (Rutgen et al., 2015). The visual analogue scale (VAS) ranging from 0 to 10 was used to quantify these types of evaluations, for which 0 was painless or no discomfort, and 10 was the maximum intensity of pain or discomfort. The subjects also completed the 20-item BES-A. Each item had a score ranging from 1 to 5, for which one was completely inconsistent, and five was completely consistent. The 20 items were equally divided into three subscales: emotional contagion, emotional disconnection, and cognitive empathy, so that the empathy capacity of subjects could be quantified from different dimensions.

Data Acquisition and Processing

Data Acquisition

All image data were collected by a Philips 3.0 T Achieva magnetic resonance imager in Zhujiang Hospital, Southern Medical University, and scanned in a standard radio-frequency head coil. T1 data were acquired with a T1-weighted rapid spin echo sequence: repetition time (TR)/echo time (TE) = 25/3 ms; flip angle = 90°; field of view (FOV) = 220 mm × 220 mm; matrix size = 256 × 256; 0.859 mm × 0.859 mm in-plane resolution; slice thickness = 5 mm; 24 slices; slice gap = 0.7 mm. Functional MRI data were acquired using a T2*-weighted, single-shot, gradient-recalled echo planar imaging (EPI) sequence, TR/TE = 2,000/35 ms; field of view (FOV) = 230 mm × 230 mm; matrix size = 64 × 64; flip angle = 90°; 3.4 mm × 3.4 mm in-plane resolution; slice thickness = 5 mm; 24 slices; slice gap = 0.7 mm; number of signals averaged (NSA) = 1. DTI data were acquired using a single-shot EPI sequence: TR/TE = 12,500/112 ms; FOV = 256 mm × 256 mm; matrix = 128 × 128; 2 mm × 2 mm in-plane resolution; number of slices = 75; slice thickness of 2 mm and no gap. There were 33 images acquired for each scan: 32 diffusion-weighted images (b = 1,000 s/mm^2) and 1 non-diffusion-weighted image (b = 0 s/mm^2).

DTI Data Preprocessing

The Pipeline for Analyzing braiN Diffusion imAges toolbox (PANDA[1]) was used to preprocess the DTI data (Cui et al., 2013). PANDA is a toolbox designed for pipeline processing of diffusion MRI images implemented in MATLAB. Pre-processing included DICOM data conversion, skull removal (the threshold was 0.25), correction of eddy current distortion, and head motion. A voxel-wise tensor matrix map and fractional anisotropy results were obtained for each subject after producing diffusion metrics.

Tract-Based Spatial Statistics

Tract-Based Spatial Statistics (TBSS; Smith et al., 2006) were employed to evaluate voxel-based whole-brain white matter measures and the values of fractional anisotropy (FA, one of the important measures of water molecule diffusion, which characterizes the anisotropy of water molecule diffusion and can reflect the integrity of the myelin sheath and axon membrane). The TBSS analysis was carried out using the FMRIB software library (FSL 4.1.4[2]). Briefly, all FA images were nonlinearly registered to the FMRIB58_FA template space. The mean FA image and the white matter tract skeleton (FA threshold was 0.2 to exclude non-WM voxels) were then created. Each subject's aligned FA image was then projected onto this skeleton. Finally, the Johns Hopkins University ICBM-DTI-81 White-Matter atlas[3] provided in the FSL toolbox was overlaid on the white matter skeleton, and the FA values of 50 WM regions of interest (ROIs) defined in this standard space were extracted.

fMRI Data Preprocessing

The fMRI image data were pre-processed with the Data Processing Assistant for Resting-State fMRI (DPARSF[4]) on the MatlabR2014a platform. Pre-processing included DICOM data conversion, removing the first 10 time points, correcting slice-timing, realignment, nuisance regressors, spatial normalization, smoothing, linear de-trending, and filtering. The first 10 volumes

[1]http://www.nitrc.org/projects/panda
[2]http://www.fmrib.ox.ac.uk/fsl
[3]http://cmrm.med.jhmi.edu/
[4]http://rfmri.org/DPARSF

of each scan were discarded to eliminate the instability of the machine magnetic field and the maladjustment of the subject. The motion time courses were used to select subjects' head movements of <2 mm in translation and 2° in rotation, which were used for further analysis. The nuisances including white matter signals, cerebrospinal fluid signals, and global signal were removed. The images of each subject were registered to the standard plane echo imaging template and resampled at a resolution of 3 mm × 3 mm × 3 mm. The normalized functional images were smoothed spatially using a 6-mm full width at half maximum (FWHM) Gaussian kernel. Finally, linear de-trending was used to reduce the effects of very low-frequency drift and filtering was used to retain the low-frequency band (0.01–0.08 Hz).

Location of ROI in Functional Image

As the core brain region of pain empathy, the anterior insula (AI) plays an important role in the emotion-cognitive empathy network. Therefore, locating the ROI in the AI is an important means to explore the joint nodes of the brain network of empathy for pain. In our study, the specific ROI coordinate of AI ($x = -32$, $y = 25$, $z = 9$) was based on our DTI data analysis (for detailed information, see **Supplementary Materials**), and a spherical ROI with a radius of 3 mm centered on the MNI coordinate was generated.

Functional Connectivity Analysis

We used the functional connectivity (FC) function in the rest toolkit[5] to perform a functional connectivity analysis of the time series of the ROI and the time series of each voxel within the brain. Then, the Pearson correlation coefficients between the time series of brain voxels were obtained, and the Fisher's r-to-z transform was used to convert the correlation coefficients into Z-scores to obey the normal distribution. ROI-to-whole-brain FC analysis was performed on the patients and healthy controls, based on Gaussian random field theory (GRF) correction (voxel-level $p < 0.001$, cluster-level $p < 0.05$), and the minimum voxel threshold was set to 20. Finally, each subject's brain Z-score image was acquired (**Figure 2**).

Based on the results of voxel-wise analysis, each brain region with abnormal functional connectivity to ROI in patients with cLBP was included in the ROI–ROI analysis. These brain regions were set to spherical ROIs with a radius of 3 mm centered on the MNI coordinate point, and the time series of each ROI (including the initial ROI) was extracted and incorporated into the ROI-Wise analysis module in the rest toolkit. We then calculated the correlation coefficient based on time series between the ROIs, and generated an $n \times n$ FC matrix (n is the number of ROI). Finally, the statistical analysis of the inter-group FC matrix was carried out.

Statistical Analysis

The SPSS22.0 (SPSS, Chicago, IL, USA) software package was used to conduct statistical analysis on the demographic characteristics, BES-A scores, and behavior data of subjects in both groups. Two independent sample t-tests were used for comparing the data between groups. Non-parametric tests were used for data that were not normally distributed. Pearson correlation analysis was used to calculate the correlation between the FC correlation coefficient with the behavioral results (Spearman correlation analysis for data that did not obey the normal distribution). Chi-square test was used for comparing the dichotomous variables between groups. All statistical assessments were two-tailed, and the significance threshold was $p < 0.05$. The results satisfying normal distribution were expressed as means ± standard deviations; otherwise, they were expressed as median (InterQuartile Range). The effect of age on behavioral data is shown in the **Supplementary Tables S1, S2**.

The FMRIB software library was used for statistical analysis of DTI data, the significance threshold for intergroup differences was $p < 0.05$ [family-wise error (FWE) corrected for multiple comparisons performed by permutation test with threshold-free cluster enhancement (TFCE)], and the number of permutations was set to 5,000. The rest toolkit was used for statistical analysis of fMRI data, and the significance threshold for intergroup differences was also $p < 0.05$. The resulting images were shown by the rest toolkit, and the FC correlation coefficient between the brain areas was shown by Circlize (Gu et al., 2014). Age was entered into the statistical analysis as a confound regressor in both fMRI data and DTI data.

RESULTS

Demographic and Behavioral Data

One patient and three healthy controls were excluded due to poor image quality. There were no significant differences between the groups in education, gender, self-report pain intensity, and others' pain intensity distribution. The age ($p < 0.001$) and the discomfort rating ($p = 0.014$) distribution between the groups were significantly different (**Table 1**). For the BES-A scale, there were no significant differences between the groups in the subscale scores of emotional contagion. The total scores ($p = 0.005$), the subscale scores of emotional disconnection ($p = 0.017$), and cognitive empathy ($p = 0.015$) between the groups were significantly different (**Table 1**).

Correlation Analysis

In the cLBP group, the functional connectivity between the AI and right parahippocampal gyrus (PHP) showed a significant correlation with the discomfort ratings ($p < 0.001$, $r = 0.6456$), the functional connectivity between the AI and left dorsolateral prefrontal cortex (DLPFC) showed a significant correlation with the cognitive empathy scores ($p = 0.0063$, $r = 0.5416$), the functional connectivity between the left superior parietal lobule (SPL) and right precuneus showed a significant correlation with the emotional disconnection scores ($p = 0.0251$, $r = 0.4561$), but no correlation was found between the SPL-DLPFC functional connectivity and the emotional disconnection scores (**Figure 3**). No correlation was found between the BES-A scores and the FA values (**Supplementary Table S3**).

[5]http://www.restfmri.net/forum/rest

TABLE 1 | Demographic and clinical characteristics and behavioral scores of the participants.

	Patients (n = 24)	Controls (n = 22)	Test statistics	P-value
Demographic features				
Age, years	39.17 ± 8.36	24.91 ± 2.96	7.567	<0.001
Education, years	13.17 ± 1.63	13.23 ± 1.72	−0.123	0.903
Sex ratio, male	9 (37.5%)	8 (36.4%)	0.006*	0.937
Clinical features				
Duration of pain, months				
3–6 months	4 (16.7%)	NA	NA	NA
7–12 months	2 (8.3%)	NA	NA	NA
>12 months	18 (75%)	NA	NA	NA
Pain symptom severity				
Pain intensity, by VAS	5 (2.5)	5 (3)	−1.414**	0.157
Empathy rating				
Discomfort, by VAS	7 (3.5)	5 (2.5)	−2.425**	0.014
Other pain, by VAS	8.5 (1.75)	7.85 (2.58)	−1.078**	0.281
BES-A scores				
Emotional contagion	19.71 ± 4.51	21.55 ± 3.13	−1.592	0.119
Cognitive empathy	30.04 ± 6.58	33.95 ± 3.18	−2.530	0.015
Emotional disconnection	20.79 ± 5.55	23.95 ± 2.65	−2.500	0.017
Total	70.54 ± 13.17	79.45 ± 5.75	−3.017	0.005

***Non-parametric tests. *Chi-square test. The results satisfying normal distribution were expressed as means ± standard deviations; otherwise, they were expressed as median (interquartile range). NA, not applicable; VAS, visual analogue scale (ranging from 0 to 10). Other pain = "How painful do you think the person in the photo is?" Discomfort = "How uncomfortable were you when you saw these photos?".*

TABLE 2 | The fractional anisotropy values of the participants.

Regions	Patients	Controls	t-value	P-value
ATR.L	0.37 ± 0.03	0.39 ± 0.02	−2.897	0.006
ATR.R	0.36 ± 0.03	0.37 ± 0.01	−2.485	0.018
gCC	0.56 ± 0.03	0.59 ± 0.02	−3.921	<0.001
bCC	0.54 ± 0.04	0.58 ± 0.03	−3.977	<0.001
sCC	0.62 ± 0.03	0.65 ± 0.02	−3.621	0.001
PTR.R	0.51 ± 0.04	0.53 ± 0.02	−2.515	0.016
SLF.R	0.43 ± 0.03	0.45 ± 0.02	−2.536	0.015
ACR.L	0.36 ± 0.04	0.39 ± 0.02	−3.040	0.004

All the data satisfying normal distribution. ATR, anterior thalamic radiation; gCC, genu of corpus callosum; bCC, body of corpus callosum; sCC, splenium of corpus callosum; PTR, posterior thalamic radiation; SLF, superior longitudinal fasciculus; ACR, anterior corona radiata.

fMRI and DTI Results

The cLBP group showed significantly reduced FA values in the corpus callosum (CC), bilateral anterior thalamic radiation (ATR), right posterior thalamic radiation (PTR), right superior longitudinal fasciculus (SLF), and left anterior corona radiata (ACR; **Table 2** and **Figure 1**).

Compared with the EP group, the cLBP group showed increased AI functional connectivity to the left DLPFC, left fusiform gyrus, left SPL, right precuneus, left postcentral gyrus, right PHP, and bilateral cerebellum. The left caudate demonstrated a noticeably decreased connectivity to the AI. The left SPL showed increased functional connectivity to the left fusiform gyrus, left DLPFC, and right precuneus. The left fusiform gyrus showed increased functional connectivity to the left DLPFC. The left caudate showed increased functional connectivity to the right parahippocampal gyrus (**Table 3**, **Figure 2**).

DISCUSSION

The empathy for pain has long been a focus of social psychology research. With the progress of research methods and technologies, the study of empathy for pain has developed into a multi-disciplinary and dynamic field, attracting great interest from disciplines such as cognitive psychology, and emotional and cognitive neuroscience. However, as a complex physiological and psychological experience involving multiple dimensions, the exploration of the neurogenesis and development mechanisms of empathy for pain is still in its infancy. At present, there is still a lack of research on whether the progress of some diseases will affect a patients' ability for pain empathy and then foster social prejudice. In our study, the protocol was specially designed for neuroimaging the change of pain empathy in patients with chronic lower back pain. The behavior measure results showed that there was a significant difference in self-experienced negative emotions (as defined by "discomfort" rating) between the two groups, which is considered to be one of the most specific assessment methods of affective sharing (Singer and Lamm, 2009). For the evaluation results of the BES-A scale, cLBP not only showed a weaker capacity for cognitive empathy but also scored lower on emotional disconnection. The heterogeneity of these behavioral measurement results may provide us with the possibility to combine them with neural measurements for further discussion.

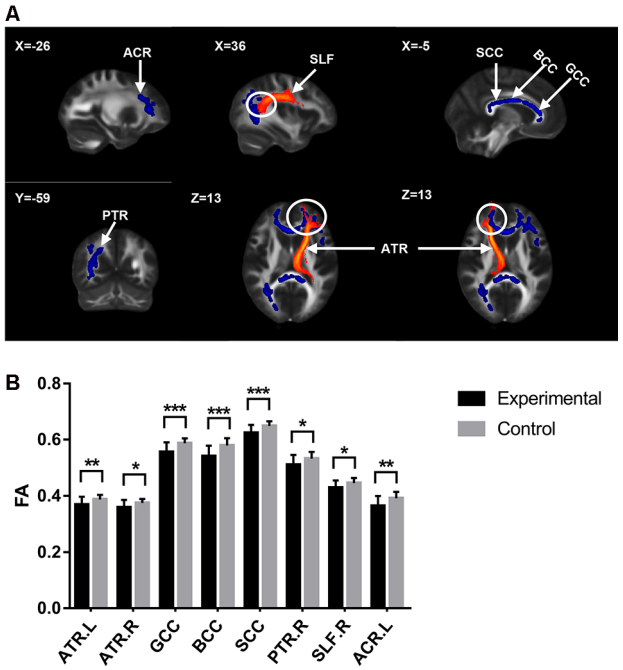

FIGURE 1 | Diffusion tensor imaging (DTI) results with significant difference between groups. **(A)** White matter tracts with significant fractional anisotropy (FA) values change between groups. The upper left number represents the MNI coordinate slice position. Warm tone (red) represents white matter tracts reference system, while cold tone (blue) represents white matter tracts with significant FA values changes between groups. **(B)** The comparison of FA values of white matter tracts with significant differences between groups. Experimental = patients. Control = healty control. $^{*}p < 0.05$; $^{**}p < 0.01$; $^{***}p < 0.001$.

Broadly speaking, empathy is generally composed of cognitive empathy and emotional empathy. Cognitive empathy includes the abilities associated with "mentalizing," such as "perspective-taking," "self-other distinction," and "working memory." Emotional empathy, on the other hand, involves responding emotionally to the emotional states of others. This so-called "affective sharing," which involves activation of the "empathy" brain network regarding a certain emotion that underpins the first-hand experience of that emotion (Lamm et al., 2019). As the core brain area of the empathy network, neuroimaging studies have found that the AI plays a key role in the integration of pain, negative emotion processing, affective sharing, sensory coding, and cognitive control (Shackman et al., 2011; Decety et al., 2012). Therefore, AI is activated in both emotional empathy and cognitive empathy, which requires in-depth analysis.

In the field of cognitive empathy, "mentalizing" is an aggregation of various cognitive functions. When cognitive empathy is activated, the activity of several brain areas related to cognitive function enables the brain to analyze the incoming empathy information based on prior knowledge and previous experience, infer the other's intentions and thoughts, and read the mental state of others without confusing the external information with the own experience, thus producing the top-down empathy regulation effect (Goubert et al., 2005). In our study, cLBP had lower scores of cognitive empathy subscale in BES-A, indicating that cLBP cognitive empathy ability was impaired. However, the term "cognition" is too broad, so it needs to be refined at the neuroscience level. Our results showed that the cLBP's FC correlation coefficient between the caudate and AI decreased, while that of the AI and DLPFC increased. The cLBP's FC correlation coefficient between the AI and DLPFC showed a significant correlation with the cognitive empathy scores. Research has found that the caudate is connected to the prefrontal lobe through multiple parallel circuits. One of them, the dorsolateral loop, which connects the DLPFC and caudate, is considered to be closely related to executive function (Kemp et al., 2013). As a high-level cognitive ability, executive function is regarded as the control mechanism of the brain and covers the process of planning, decision-making, judgment, self-regulation, and inhibition. It is essential for goal-oriented behavior and for responding to new events (Chung et al., 2013). Therefore, in this study, we believe that the impairment of cognitive empathy ability in cLBP is related to the low connectivity of the executive function loop. Furthermore, the above discussion seems to be supported by the structural MRI results. The DTI results showed decreased FA values of ACR and genu of corpus callosum (gCC) in cLBP. The damages of ACR and gCC have also been reported in various pain diseases studies (DeSouza et al., 2014; Chong and Schwedt, 2015). As white matter tracts radiate to a wide area of the prefrontal lobe, the decrease of FA values of the

TABLE 3 | The brain regions with significant functional connectivity strength between groups.

Regions	R/L	BA	Cluster size	MNI			*z* values
			voxels	*x*	*y*	*z*	
Cerebellum posterior lobe	L		42	−21	−75	−42	4.3892
Cerebellum anterior lobe	R		87	6	−69	−15	4.5225
PHP	R	35	21	24	−18	−27	4.7116
Fusiform gyrus	L	37	38	−33	−54	−12	4.1623
Caudate	L	22	37	−18	24	9	−4.2419
Precuneus	R	39	274	9	−63	18	5.1913
DLPFC	L	4/6	100	−48	6	54	5.0656
SPL	L	7	27	−33	−54	63	4.8991
Postcentral gyrus	L	1/2/3	23	−45	−27	66	4.9983

The minimum voxel threshold was set to 20, based on Gaussian random field theory (GRF) correction (voxel-level $p < 0.001$, cluster-level $p < 0.05$). BA, Brodmann areas; MNI, Montreal Neurological Institute; PHP, parahippocampal gyrus; DLPFC, dorsolateral prefrontal cortex; SPL, superior parietal lobule.

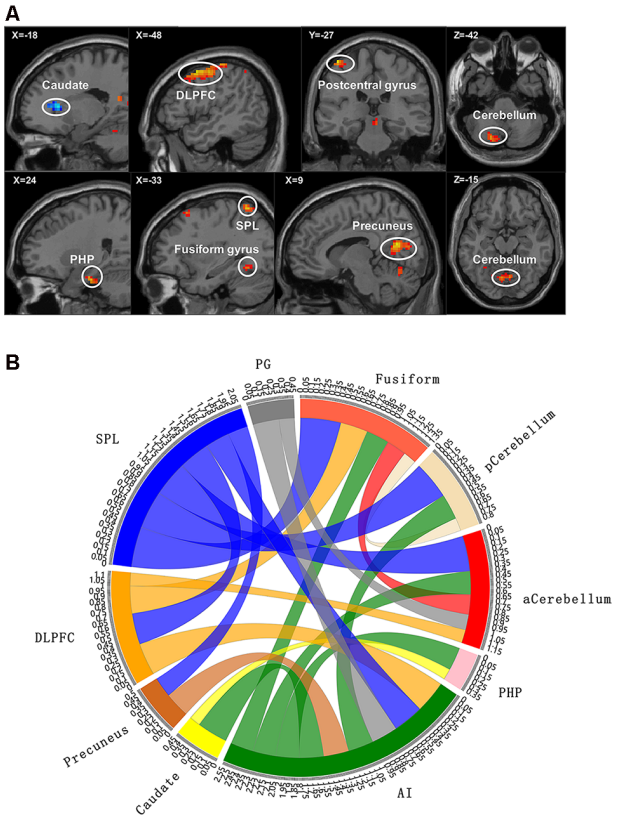

FIGURE 2 | Functional magnetic resonance imaging (fMRI) results with significant difference between groups. **(A)** The brain map of voxel-wise functional connectivity analysis results. The upper left number represents the MNI coordinate slice position. Warm tone (red) represents brain regions with increased functional connectivity strength between groups, while cold tone (blue) represents brain regions with decreased functional connectivity strength between groups. **(B)** Circlize map of functional connectivity between groups from ROI–ROI analysis. The parameters represent the strength of the functional connectivity. PG, postcentral gyrus; aCerebellum, anterior cerebellum; pCerebellum, posterior cerebellum. The parameters represent the functional connectivity (FC) correlation coefficient. Different colors represent different brain regions. For example, yellow represents caudate, and yellow curve represents the FC between caudate and parahippocampal gyrus (PHP).

ACR and gCC is related to abnormal myelination, axon loss, and inflammation. This means that the functional connection and information transmission between the prefrontal lobe and other brain areas are damaged, which affects the top-down regulation of empathy.

The current study also found that the cLBP had lower scores of emotional disconnection subscale in BES-A. Emotional disconnection is considered to be self-protection regulation mechanism. When witnessing others being hurt, emotional disconnection enables individuals to correctly distinguish the boundaries between themselves and others and to protect individuals against injury and emotional impact (Carré et al., 2013). However, excessive self-protection and resistance to the influence of the external environment will breed indifference. Individuals can easily immerse themselves in their own world and gradually lose the ability to turn their attention outward, which eventually breeds emotional diseases (Hugdahl et al., 2015). In this study, our results showed a circuit with decreased functional connection, which is associated with emotional disconnection, namely, SPL–precuneus–AI–caudate. The cLBP's FC correlation coefficient between the SPL and precuneus showed a significant correlation with the emotional disconnection scores. The main function of the precuneus is related to "perspective-taking" (Lamm et al., 2011), which allows subjects to generate empathy not only through direct observation but also through imaging other people's emotions. Furthermore, the precuneus is also involved in the identification and processing of emotional valences in others (Pires et al., 2018). Therefore, we can make an inference in the current study: when patients with cLBP are watching photos, the precuneus with abnormal activities transfers the wrong evaluation information to the executive network, thus affecting the ability to empathize. In addition, the SPL and DLPFC are considered part of the attention network (Corbetta and Shulman, 2002; Fritz et al., 2016). The abnormal functional connection state of SPL and DLPFC caused incorrect attention resources allocation. Although no correlation was found between the SPL-DLPFC functional connectivity and the emotional disconnection scores, there was still a tendency towards statistical significance (r = 0.39, p = 0.0586). As a result, we can still assume that the cLBP reduced the resource distribution of external attention and allocated more attention resources to self-regulation, which is one of the reasons for the decreased scores of emotional disconnection in cLBP. For structural MRI analysis, the DTI results showed a decreased FA value of the right SLF in cLBP. Research has found that the white matter tract of SLF underlying the temporoparietal cortex and the right temporoparietal junction are considered to be a component of the ventral attention network, a right-lateralized supervisory system (Kucyi et al., 2012). Consequently, the damage of the SLF tracts may affect the distribution of attention resources and then affect the discrimination of self and other emotional states.

A study has proposed that the discomfort ratings of watching photos may be the most appropriate index to evaluate the ability of affective sharing (Singer and Lamm, 2009). In our study, higher discomfort ratings of cLBP represent an abnormal increase in cLBP's ability to share others' emotions. The cLBP's FC correlation coefficient between the AI and PHP showed a significant correlation with the discomfort ratings. The fMRI results showed that the FC correlation coefficient between the fusiform gyrus and AI and that between the AI and PHP were both increased in cLBP. The fusiform gyrus is considered to be an important brain area for facial recognition, and damage to the fusiform gyrus usually results in long-term facial recognition problems (Ghuman et al., 2014). Thus, the fusiform gyrus is the primary activation area of the whole empathy process. The increased functional connectivity between the fusiform gyrus and other brain regions indicated that cLBP enhances the recognition of the face, i.e., increases the bottom-up input. Research has found that the main function of PHP is to extract emotional memory (de Greck et al., 2013). Other studies have found that an individual's prior experience of pain makes them more likely to develop an empathic response (Goubert et al., 2005), which we

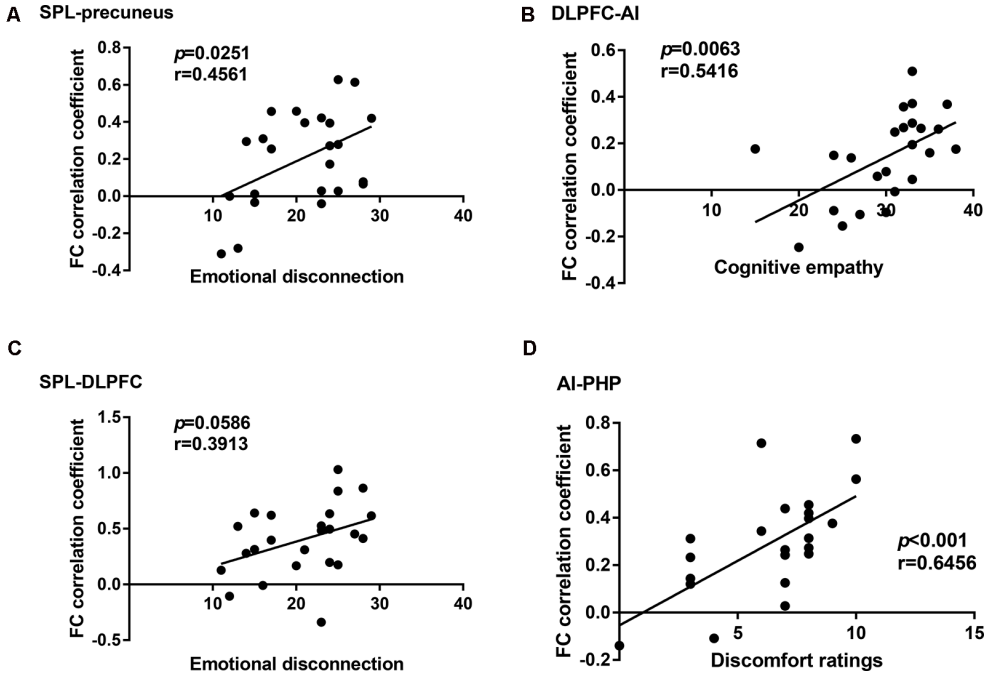

FIGURE 3 | Correlation analysis between the functional connectivity and the behavioral results in the chronic low back pain (cLBP) group. **(A)** Correlation analysis between the subscale scores of emotional disconnection and the functional connectivity coefficient of superior parietal lobule (SPL)-precuneus. **(B)** Correlation analysis between the subscale scores of cognitive empathy and the functional connectivity coefficient of dorsolateral prefrontal cortex-anterior insula (DLPFC-AI). **(C)** Correlation analysis between the subscale scores of emotional disconnection and the functional connectivity coefficient of SPL-DLPFC. **(D)** Correlation analysis between the subscale scores of discomfort ratings and the functional connectivity coefficient of AI-PHP.

consider may be related to deep pain memories. Therefore, in this experiment, we infer that the increase of bottom-up input and the enhancement of pain emotional memory extraction made cLBP more willing to report unpleasant experiences. For structural MRI analysis, the DTI results showed a decreased FA value of ATR and splenium of corpus callosum (sCC) in cLBP. Some studies have found that the ATR is related to the memory and emotional response of autonomic arousal (Huang et al., 2016), while the sCC is closely related to the processing of somatosensory and external input information (Lieberman et al., 2014). The decrease of FA values of these two white matter tracts seems to contradict the fMRI results.

However, a large number of studies have reported that the FA value of the white matter tracts related to somatosensory in patients with chronic pain is decreased (DeSouza et al., 2014; Chong and Schwedt, 2015; Leung et al., 2018), but many patients with chronic pain have symptoms such as hyperalgesia and catastrophizing. Thus, it is worth noting that although the abnormality of the white matter tracts represents the abnormality of related functions, it is not necessarily the decrease. In this study, the damage of the ATR and SCC tracts seems to be consistent with the abnormally enhanced affective sharing ability of cLBP.

LIMITATIONS

Although the results of this study demonstrate the impaired empathy ability of cLBP patients, we still need to pay attention to some shortcomings in this study. First, the sample size was small. The sample size of each group in this study is about 23 cases, which may decrease generalizability. It is necessary to increase the sample size in future experiments. Second, the covariate effect of the age gap on behavior data did not reach statistical significance. However, the significant difference in age distribution between the groups should be avoided in future studies. Third, voxel-based morphometry is useful for studying the damage of chronic pain to the volume of cerebral gray matter, and it could be employed in future experiments. Fourth, selecting multiple ROIs in the same brain area can detect the changes of functional connectivity more thoroughly. Therefore, multiple ROIs and even symmetrical ROIs in brain regions of interest need to be considered in future studies.

CONCLUSION

In conclusion, we found that patients with cLBP have impaired empathy ability, which involves cognitive empathy and emotional empathy. We found that the impairment of cognitive empathy is mainly related to the impairment of attention network in patients with cLBP, while the damage of emotional empathy is related to the pain emotional memory. The lower behavioral scores, the abnormal functional connectivity of multiple brain networks, the correlation between behavioral scores and functional connectivity of brain regions, and multiple damaged white matter tracts in chronic pain patients supported our findings. These findings enrich the neural theory of the

change of empathy in patients with cLBP. Moreover, we hope that these findings will call attention to the impairment of prosocial behavior in patients with chronic pain.

DATA AVAILABILITY STATEMENT

The raw data supporting the conclusions of this article will be made available by the authors, without undue reservation.

ETHICS STATEMENT

The studies involving human participants were reviewed and approved by the ethics committee of Zhujiang Hospital of Southern Medical University. The patients/participants provided their written informed consent to participate in this study.

AUTHOR CONTRIBUTIONS

All authors had full access to all the data in the study and take responsibility for the integrity of the data and the accuracy of the data analysis. JM and WW: conceptualization, methodology and writing—review and editing. JM and XW: investigation. JM: formal analysis, data curation and writing—original draft. JM, XW, QQ, and HZ: resources. WW: supervision and funding acquisition.

FUNDING

This work was supported by the National Natural Science Foundation of China (NNSFC; contract grant number: 81473769), the National Natural Science Foundation of China (NNSFC; contract grant number: 81772430), and the Clinical Research Foundation of Southern Medical University, China (contract grant number: LC2016PY037).

ACKNOWLEDGMENTS

We thank all subjects for assistance in the scanning.

SUPPLEMENTARY MATERIAL

The Supplementary Material for this article can be found online at: https://www.frontiersin.org/articles/10.3389/fnhum.2020.00326/full#supplementary-material.

REFERENCES

Carré, A., Stefaniak, N., D'Ambrosio, F., Bensalah, L., and Besche-Richard, C. (2013). The Basic Empathy Scale in adults (BES-A): factor structure of a revised form. *Psychol. Assess.* 25, 679–691. doi: 10.1037/a0032297

Chong, C., and Schwedt, T. (2015). Migraine affects white-matter tract integrity: a diffusion-tensor imaging study. *Cephalalgia* 35, 1162–1171. doi: 10.1177/0333102415573513

Chung, C., Pollock, A., Campbell, T., Durward, B., and Hagen, S. (2013). Cognitive rehabilitation for executive dysfunction in adults with stroke or other adult non-progressive acquired brain damage. *Cochrane Database Syst. Rev.* 4:CD008391. doi: 10.1002/14651858.cd008391.pub2

Cohen, M., Quintner, J., Buchanan, D., Nielsen, M., and Guy, L. (2011). Stigmatization of patients with chronic pain: the extinction of empathy. *Pain Med.* 12, 1637–1643. doi: 10.1111/j.1526-4637.2011.01264.x

Corbetta, M., and Shulman, G. (2002). Control of goal-directed and stimulus-driven attention in the brain. *Nat. Rev. Neurosci.* 3, 201–215. doi: 10.1038/nrn755

Cui, Z., Zhong, S., Xu, P., He, Y., and Gong, G. (2013). PANDA: a pipeline toolbox for analyzing brain diffusion images. *Front. Hum. Neurosci.* 7:42. doi: 10.3389/fnhum.2013.00042

de Greck, M., Bolter, A. F., Lehmann, L., Ulrich, C., Stockum, E., Enzi, B., et al. (2013). Changes in brain activity of somatoform disorder patients during emotional empathy after multimodal psychodynamic psychotherapy. *Front. Hum. Neurosci.* 7:410. doi: 10.3389/fnhum.2013.00410

Decety, J., Norman, G., Berntson, G., and Cacioppo, J. (2012). A neurobehavioral evolutionary perspective on the mechanisms underlying empathy. *Prog. Neurobiol.* 98, 38–48. doi: 10.1016/j.pneurobio.2012.05.001

DeSouza, D., Hodaie, M., and Davis, K. (2014). Abnormal trigeminal nerve microstructure and brain white matter in idiopathic trigeminal neuralgia. *Pain* 155, 37–44. doi: 10.1016/j.pain.2013.08.029

Engen, H. G., and Singer, T. (2013). Empathy circuits. *Curr. Opin. Neurobiol.* 23, 275–282. doi: 10.1016/j.conb.2012.11.003

Fritz, H., McAuley, J., Wittfeld, K., Hegenscheid, K., Schmidt, C., Langner, S., et al. (2016). Chronic back pain is associated with decreased prefrontal and anterior insular gray matter: results from a population-based cohort study. *J. Pain* 17, 111–118. doi: 10.1016/j.jpain.2015.10.003

Ghuman, A., Brunet, N., Li, Y., Konecky, R., Pyles, J., Walls, S., et al. (2014). Dynamic encoding of face information in the human fusiform gyrus. *Nat. Commun.* 5:5672. doi: 10.1038/ncomms6672

Goubert, L., Craig, K. D., Vervoort, T., Morley, S., Sullivan, M. J., de C Williams, A. C., et al. (2005). Facing others in pain: the effects of empathy. *Pain* 118, 285–288. doi: 10.1016/j.pain.2005.10.025

Gu, Z., Gu, L., Eils, R., Schlesner, M., and Brors, B. (2014). circlize implements and enhances circular visualization in R. *Bioinformatics* 30, 2811–2812. doi: 10.1093/bioinformatics/btu393

Gu, X., and Han, S. (2007). Attention and reality constraints on the neural processes of empathy for pain. *NeuroImage* 36, 256–267. doi: 10.1016/j.neuroimage.2007.02.025

Gu, X., Liu, X., Guise, K., Naidich, T., Hof, P., and Fan, J. (2010). Functional dissociation of the frontoinsular and anterior cingulate cortices in empathy for pain. *J. Neurosci.* 30, 3739–3744. doi: 10.1523/JNEUROSCI.4844-09.2010

Huang, L., Kutch, J., Ellingson, B., Martucci, K., Harris, R., Clauw, D., et al. (2016). Brain white matter changes associated with urological chronic pelvic pain syndrome: multisite neuroimaging from a MAPP case-control study. *Pain* 157, 2782–2791. doi: 10.1097/j.pain.0000000000000703

Hubbard, C. S., Khan, S. A., Keaser, M. L., Mathur, V. A., Goyal, M., and Seminowicz, D. A. (2014). Altered brain structure and function correlate with disease severity and pain catastrophizing in migraine patients. *eNeuro* 1:e20.14. doi: 10.1523/eneuro.0006-14.2014

Hugdahl, K., Raichle, M., Mitra, A., and Specht, K. (2015). On the existence of a generalized non-specific task-dependent network. *Front. Hum. Neurosci.* 9:430. doi: 10.3389/fnhum.2015.00430

Jackson, P., Meltzoff, A., and Decety, J. (2005). How do we perceive the pain of others? A window into the neural processes involved in empathy. *NeuroImage* 24, 771–779. doi: 10.1016/j.neuroimage.2004.09.006

Kemp, J., Berthel, M., Dufour, A., Després, O., Henry, A., Namer, I., et al. (2013). Caudate nucleus and social cognition: neuropsychological and SPECT evidence from a patient with focal caudate lesion. *Cortex* 49, 559–571. doi: 10.1016/j.cortex.2012.01.004

Kreiner, D. S., Matz, P., Bono, C. M., Cho, C. H., and Yahiro, A. (2020). Guideline summary review: an evidence-based clinical guideline for the diagnosis and treatment of low back pain. *Spine J.* 20, 998–1024. doi: 10.1016/j.spinee.2020.04.006

Kucyi, A., Moayedi, M., Weissman-Fogel, I., Hodaie, M., and Davis, K. (2012). Hemispheric asymmetry in white matter connectivity of the temporoparietal junction with the insula and prefrontal cortex. *PLoS One* 7:e35589. doi: 10.1371/journal.pone.0035589

Lamm, C., Decety, J., and Singer, T. (2011). Meta-analytic evidence for common and distinct neural networks associated with directly experienced pain and empathy for pain. *NeuroImage* 54, 2492–2502. doi: 10.1016/j.neuroimage.2010.10.014

Lamm, C., Rutgen, M., and Wagner, I. C. (2019). Imaging empathy and prosocial emotions. *Neurosci. Lett.* 693, 49–53. doi: 10.1016/j.neulet.2017.06.054

Leung, A., Yang, E., Lim, M., Metzger-Smith, V., Theilmann, R., Song, D., et al. (2018). Pain-related white matter tract abnormalities in mild traumatic brain injury patients with persistent headache. *Mol. Pain* 14:1744806918810297. doi: 10.1177/1744806918810297

Lieberman, G., Shpaner, M., Watts, R., Andrews, T., Filippi, C., Davis, M., et al. (2014). White matter involvement in chronic musculoskeletal pain. *J. Pain* 15, 1110–1119. doi: 10.1016/j.jpain.2014.08.002

Ministry of Health of the PRC (2018). Detailed rules for the implementation of regulations on the administration of medical institutions. Available online at: http://www.nhc.gov.cn/fzs/s3576/201808/7a922e4803fa452f99d43a25ec0a3d77.shtml

Pires, F. B. C., Lacerda, S. S., Balardin, J. B., Portes, B., Tobo, P. R., Barrichello, C. R. C., et al. (2018). Self-compassion is associated with less stress and depression and greater attention and brain response to affective stimuli in women managers. *BMC Womens Health* 18:195. doi: 10.1186/s12905-018-0685-y

Roche, J., and Harmon, D. (2017). Exploring the facets of empathy and pain in clinical practice: a review. *Pain Pract.* 17, 1089–1096. doi: 10.1111/papr.12563

Rutgen, M., Seidel, E. M., Silani, G., Riecansky, I., Hummer, A., Windischberger, C., et al. (2015). Placebo analgesia and its opioidergic regulation suggest that empathy for pain is grounded in self pain. *Proc. Natl. Acad. Sci. U S A* 112, E5638–E5646. doi: 10.1073/pnas.1511269112

Seminowicz, D. A., and Moayedi, M. (2017). The dorsolateral prefrontal cortex in acute and chronic pain. *J. Pain* 18, 1027–1035. doi: 10.1016/j.jpain.2017.03.008

Shackman, A. J., Salomons, T. V., Slagter, H. A., Fox, A. S., Winter, J. J., and Davidson, R. J. (2011). The integration of negative affect, pain and cognitive control in the cingulate cortex. *Nat. Rev. Neurosci.* 12, 154–167. doi: 10.1038/nrn2994

Singer, T., and Lamm, C. (2009). The social neuroscience of empathy. *Ann. N Y Acad. Sci.* 1156, 81–96. doi: 10.1111/j.1749-6632.2009.04418.x016

Singer, T., Seymour, B., O'Doherty, J., Kaube, H., Dolan, R. J., and Frith, C. D. (2004). Empathy for pain involves the affective but not sensory components of pain. *Science* 303, 1157–1162. doi: 10.1126/science.1093535

Smith, S., Jenkinson, M., Johansen-Berg, H., Rueckert, D., Nichols, T., Mackay, C., et al. (2006). Tract-based spatial statistics: voxelwise analysis of multi-subject diffusion data. *NeuroImage* 31, 1487–1505. doi: 10.1016/j.neuroimage.2006.02.024

Xiang, Y., Wang, Y., Gao, S., Zhang, X., and Cui, R. (2018). Neural mechanisms with respect to different paradigms and relevant regulatory factors in empathy for pain. *Front. Neurosci.* 12:507. doi: 10.3389/fnins.2018.00507

Conflict of Interest: The authors declare that the research was conducted in the absence of any commercial or financial relationships that could be construed as a potential conflict of interest.

frontiers in Neuroscience

METHODS
published: 09 September 2020
doi: 10.3389/fnins.2020.00717

Inter- and Intra-subject Template-Based Multivariate Synchronization Index Using an Adaptive Threshold for SSVEP-Based BCIs

Haoran Wang[1], Yaoru Sun[1], Yunxia Li[2]*, Shiyi Chen[1] and Wei Zhou[3]*

[1] Department of Computer Science and Technolgy, College of Electronic and Information Engineering, Tongji University, Shanghai, China, [2] Department of Neurology, Shanghai Tongji Hospital, School of Medicine, Tongji University, Shanghai, China, [3] Department of Information and Communication Engineering, Tongji University, Shanghai, China

OPEN ACCESS

Edited by:
Yu Zhang,
Stanford University, United States

Reviewed by:
Yunyong Punsawad,
Silpakorn University, Thailand
Toshihisa Tanaka,
Tokyo University of Agriculture and Technology, Japan

***Correspondence:**
Yaoru Sun
yaoru@tongji.edu.cn
Yunxia Li
doctorliyunxia@163.com

Specialty section:
This article was submitted to Brain Imaging Methods, a section of the journal Frontiers in Neuroscience

Received: *15 December 2019*
Accepted: *15 June 2020*
Published: *09 September 2020*

Citation:
Wang H, Sun Y, Li Y, Chen S and Zhou W (2020) Inter- and Intra-subject Template-Based Multivariate Synchronization Index Using an Adaptive Threshold for SSVEP-Based BCIs. Front. Neurosci. 14:717. doi: 10.3389/fnins.2020.00717

The steady-state visually evoked potential (SSVEP) has been widely used in brain-computer interfaces (BCIs). Many studies have proved that the Multivariate synchronization index (MSI) is an efficient method for recognizing the frequency components in SSVEP-based BCIs. Despite its success, the recognition accuracy has not been satisfactory because the simplified pre-constructed sine-cosine waves lack abundant features from the real electroencephalogram (EEG) data. Recent advances in addressing this issue have achieved a significant improvement in recognition accuracy by using individual calibration data. In this study, a new extension based on inter- and intra-subject template signals is introduced to improve the performance of the standard MSI method. Through template transfer, inter-subject similarity and variability are employed to enhance the robustness of SSVEP recognition. Additionally, most existed methods for SSVEP recognition utilize a fixed time window (TW) to perform frequency domain analysis, which limits the information transfer rate (ITR) of BCIs. For addressing this problem, a novel adaptive threshold strategy is integrated into the extension of MSI, which uses a dynamic window to extract the temporal features of SSVEPs and recognizes the stimulus frequency based on a pre-set threshold. The pre-set threshold contributes to obtaining an appropriate and shorter signal length for frequency recognition and filtering ignored-invalid trials. The proposed method is evaluated on a 12-class SSVEP dataset recorded from 10 subjects, and the result shows that this achieves higher recognition accuracy and information transfer rate when compared with the CCA, MSI, Multi-set CCA, and Individual Template-based CCA. This paper demonstrates that the proposed method is a promising approach for developing high-speed BCIs.

Keywords: brain-computer interface (BCI), steady-state visually evoked potentials (SSVEP), inter- and intra-subject template-based multivariate synchronization index, transfer learning, adaptive threshold

1. INTRODUCTION

The Brain-Computer Interfaces (BCIs) provide humans with a direct communication and control channel between human brains and external devices by utilizing brain signals produced along the cerebral cortex within the brain to directly control external devices without the aid of muscular movements (Dornhege et al., 2007; Faller et al., 2010). People with disabilities, such as limb loss, spinal cord injury, and amyotrophic lateral sclerosis, can draw support from BCIs to assist with the activities involved in daily life. Further research is being conducted on developing the EEG-Based Brain-Computer Interfaces due to its non-invasive nature, high temporal resolution, ease of acquisition, and beneficial cost-effectiveness (Nicolas-Alonso and Gomez-Gil, 2012; Al-Hudhud, 2016).

In recent years, several specific brain activity patterns, including Slow Cortical Potentials (SCPs), P300 evoked potentials, Steady-State Visually Evoked Potentials (SSVEPs), Event-Related Desynchronization (ERD), and Synchronization (ERS), have been investigated extensively, as these have served as the source of stimulation signals for BCI control (Zhang et al., 2014b). Among these, the SSVEP paradigm has become a promising option in BCI applications due to its high signal-to-noise ratio (SNR), high information transfer rate (ITR), reliability, and design flexibility (Bin et al., 2009; Zhu et al., 2010; Bakardjian et al., 2011). The SSVEP-BCIs rely on oscillatory responses occurring in the occipital and the occipito-parietal cortex that are elicited from a stimulus flickering at a specific frequency (Vu et al., 2016; Georgiadis et al., 2018). While people focus attention on a visual stimulation at a fixed frequency, such as flashing lights or flickering icons on a computer screen, the SSVEP signals can be observed at the same fundamental frequency as the stimulation and also at higher harmonics of the driving stimulus (Muller-Putz and Pfurtscheller, 2007; Bakardjian et al., 2010; Zhang Z. et al., 2018). Hence, the SSVEP signals are the inherent response of the brain, and the SSVEP-based BCI systems required minimal to no training (Bin et al., 2009).

In the past few decades, many studies have revealed that the SSVEP pattern is effective for BCI control, and various SSVEP-based brain-computer interface (BCI) systems have been proposed by numerous laboratories and research groups (Poryzala and Materka, 2014). It has been verified that four driving rates in an evoked potential interface system are distinguishable (Skidmore and Hill, 1991). In the study, the stimulation frequency was set at 35.050, 23.367, 17.525, and 14.020 Hz, and it was found that the responses corresponding to the stimulation frequencies were generated during the analysis. The SSVEP-based BCI system with high transfer rates was also used to help operators input phone numbers (Cheng et al., 2002) in which four buttons flickering at different frequencies represented the four directions. The operators could move the cursor in different directions to the target position by gazing at these buttons. Finally, eight of the 13 subjects completed the task where subjects were asked to select the correct number on the telephone keypad to input phone numbers with the help of the SSVEP-based BCI system. In another work, a new dual-frequency-SSVEP for BCI systems was developed that could increase the number of selections through different combinations of four frequencies, i.e., 16.4, 17.5, 19.1, and 20.2 Hz (Shyu et al., 2010). The result indicated that this dual-frequency approach was effective for an SSVEP BCI system.

Previous studies for SSVEP recognition focused on the amplitude and spatial distribution of SSVEP responses (Zhang et al., 2013a; Norcia et al., 2015). However, these traditional methods using single-channel EEG data [e.g., Power spectral density analysis (PSDA)] are sensitive to noise and require a long period of recognition time to improve the accuracy of the results. Moreover, these SSVEP recognition techniques cannot detect and identify harmonic stimulation frequencies (Zhang et al., 2011, 2015). Therefore, many advanced multichannel approaches have been developed to enhance the recognition performance of SSVEPs. For frequency recognition, the Canonical Correlation Analysis (CCA) algorithm was first introduced to find the correlation between the multichannel EEG data and reference signals consisting of sin-cosine waves at each of the target frequencies (Lin et al., 2006). Recent work has already validated that the CCA method could achieve better recognition performance than the traditional power spectral density analysis (Zhang et al., 2014c). Until now, there have been many methods proposed to improve recognition accuracy further by optimizing the pre-constructed sine-cosine reference signals, such as Multiway Canonical Correlation Analysis (MCCA) (Zhang et al., 2011), L1-regularized Multiway Canonical Correlation (L1-MCCA) (Zhang et al., 2013b), and Multi-set Canonical Correlation Analysis (Multi-set CCA) (Zhang et al., 2014c)—all proposed as multiway extensions of standard CCA. Although the sine-cosine reference signals usually perform well for specific frequency components recognition, the simplified single or multiple frequency signals are incapable of exactly representing the complex neural responses, which are collaboratively created by several neural populations in the visual cortex rather than a single signal source. Recently, researchers constructed a laminar microcircuits model consisting of two visual areas (V1 and V2) to imitate the dynamics of neuronal population response in the visual cortex, which revealed the modulation mechanism of the SSVEP, confirming the hypothesis (Zhou et al., 2013; Yang et al., 2019). Beside this, the new spatial filtering method, known as Minimum Energy Combination (MEC), found a linear combination of multichannel signals, which reduces the number of channels, to minimize the noise energy (Friman et al., 2007; Nan et al., 2011). Nakanishi et al. used multiple spatial filters to remove the EEG background artifacts, enhance discriminability and SNR of the signals (Nakanishi et al., 2017). Zhang et al. introduced the Correlated Component Analysis (CORCA) to find linear combinations of electrodes across subjects and maximize correlation between them (Zhang et al., 2018a,b). Recently, the Multivariate Synchronization Index (MSI) (Zhang et al., 2014b) has attracted attention as a novel feature extraction method, which calculates the synchronization index between the multichannel EEG data and the pre-constructed reference signals, showing better recognition performance than both CCA and MEC.

Although previous studies have demonstrated that the MSI method is an efficient method for frequency component recognition, the temporal features of the EEG signals have not been explored yet. The analysis of Global Field Power highlighted time periods results in the most robust performance (Jrad and Congedo, 2012), showing the importance of time domain analysis for recognizing the specific frequency in SSVEPs. Recent research has also confirmed that considering temporal information of EEG signals can improve the performance of the algorithm, such as the temporal local structure of the signals (Wang and Zheng, 2008), the time-delayed copy (Lemm et al., 2005), and certain temporal features (Jrad and Congedo, 2012). To address this issue, Zhang et al. proposed a temporally local MSI (TMSI) method, which explicitly considers the time-local information of the EEG signal, further improving the accuracy of the recognition algorithm for SSVEP-Based BCIs (Zhang et al., 2016). The time delay embedding method has also been employed to extend MSI (known as EMSI), further enhancing the performance of SSVEP, which combined the first-order time-delayed version of EEG data during the calculation of the synchronous index (Zhang et al., 2017). Zhang combined adaptive TWL selection strategy with the MSI method, which is superior to fixed TWL in SSVEP recognition (Zhang et al., 2014a).

In the present study, the reference signals of sine-cosine waves are replaced with inter-subject and intra-subject template signals. The intra-subject template signals, also termed as the individual template signals, are obtained by averaging multichannel EEG data of the individual training dataset and provided more abundant subject-specific and inter-trial information for correlation analysis. It has been shown that the CCA based on the individual template signals significantly outperforms the standard CCA (Bin et al., 2011; Nan et al., 2011). Additionally, the inter-subject template signals are obtained by averaging the partial trials selected from other subjects. Recent studies have demonstrated inter-subject similarity in neural responses occurs because subjects are instructed to perform a specific task over time (Saha and Baumert, 2019). Yuan et al. presented transfer template-based canonical correlation analysis (tt-CCA) to enhance the detection of SSVEPs by exploiting inter-subject information (Yuan et al., 2015). Several studies attempted to apply session-to-session and inter-subject transfer to simplify the training procedure (Nakanishi et al., 2016; Waytowich et al., 2016). This paper proposes an efficient way for transfer learning to improve SSVEP-based BCIs performance. After this, an expanding time window over time is used to extract temporal features of SSVEP, and the stimulus frequency is recognized based on the pre-set threshold. Dynamic window recognition algorithms are often integrated into other algorithms to adaptively control the recognition time while maintaining a high accuracy, which significantly improves the information transfer rate (ITR), and adaptability of systems to different individuals (Zhang et al., 2014a; Cao et al., 2015; Yang et al., 2018). In the method presented in this paper, the pre-set threshold obtained from the training dataset of individual subjects makes the algorithm shutdown at the appropriate data length and filters the potentially invalid trial resulted from attention lapses (Russell et al., 2016) or the reaction times of subjects considered to be too long. It has been reported that attention lapses may lead to an increase of reaction times and the number of incorrect responses because irrelevant information cannot be effectively suppressed, shifting attention to irrelevant visual stimuli (Ko et al., 2017; Wang et al., 2018). The novel extension of multivariate synchronization index method is verified with an SSVEP dataset involving 10 healthy subjects and compared to the CCA, standard MSI, Multi-set CCA, and Individual Template-based CCA. The results in this paper show that the proposed method significantly enhances the individual recognition performance of SSVEP frequency, resulting in an improvement in overall accuracy and the information transfer rate.

2. METHODS

2.1. The Standard Multivariate Synchronization Index

The MSI method aims to estimate the synchronization between the multichannel EEG data and the reference signals for frequency detection. Let $X \in \mathbb{R}^{N_1 \times M}$ denote the multivariate EEG signals and $Y \in \mathbb{R}^{N_2 \times M}$ denote the reference signal, which is constructed as follows:

$$Y = \begin{pmatrix} \sin(2\pi f_i t) \\ \cos(2\pi f_i t) \\ \vdots \\ \sin(2\pi N_h f_i t) \\ \cos(2\pi N_h f_i t) \end{pmatrix}, t = \frac{1}{Fs}, \frac{2}{Fs}, \ldots, \frac{M}{Fs} \tag{1}$$

where N_h denotes the number of harmonics, Fs is the sampling rate. N_1 and N_2 are the number of channels, respectively, and M is the number of samples. X and Y are normalized to have zero mean and unit variance without loss of generality. The covariance matrix of concatenation of X and Y can subsequently be calculated as

$$C = \begin{pmatrix} C_{11} & C_{12} \\ C_{21} & C_{22} \end{pmatrix} \tag{2}$$

where

$$C_{11} = \frac{1}{M} X X^T \tag{3}$$

$$C_{22} = \frac{1}{M} Y Y^T \tag{4}$$

$$C_{12} = \frac{1}{M} X Y^T = C_{21}^T \tag{5}$$

Because both the autocorrelation and cross-correlation of matrix C, which is calculated from the concatenation of X and Y, could influence the synchronization computing, a linear transformation is employed:

$$U = \begin{pmatrix} C_{11}^{-\frac{1}{2}} & 0 \\ 0 & C_{22}^{-\frac{1}{2}} \end{pmatrix} \tag{6}$$

Then, the transformed correlation matrix can be described as follows:

$$R = UCU^T \tag{7}$$

Assume $\lambda_1, \lambda_2, \ldots, \lambda_P$ are the eigenvalues of matrix R. Then, the normalized eigenvalues are represented by

$$\lambda_i' = \frac{\lambda_i}{\sum_{i=1}^{P} \lambda_i} = \frac{\lambda_i}{tr(R)} \tag{8}$$

where $P = N_1 + N_2$. Finally, the synchronization index between two multivariate signals can be calculated using the following formula:

$$S = 1 + \frac{\sum_{i=1}^{P} \lambda_i' \log(\lambda_i')}{\log(P)} \tag{9}$$

Based on the formula (9), the synchronization index of each frequency $f_i (i = 1, \ldots, K)$ used in SSVEP-based BCI can be calculated. The target frequency f_t can now be computed by the formula.

$$f_t = \max_{f_i} S_i, i = 1, \ldots, K \tag{10}$$

2.2. Inter- and Intra-subject Template-Based Multivariate Synchronization Index (IIST-MSI)

We propose a variant version of multivariate synchronization index based on transferred inter- and intra-subject template signals. Considering $\chi_{i,h} \in \mathbb{R}^{N_c \times N_t}$, which is the h-th trial from the individual training set corresponding to the stimulus frequency f_i, an individual template signal $Y_i \in \mathbb{R}^{N_c \times N_t}$ is obtained by averaging training trials as

$$Y_i = \frac{1}{N_n} \sum_{h=1}^{N_n} \chi_{i,h} \tag{11}$$

where N_c, N_t, and N_n are the numbers of channels, samples, and trials, respectively. For structuring the transferred inter-subject templates, the core issue is how to pick up credible trials. We propose a threshold policy for supervised adaptation of trials. Assume $\chi_{p,i,h} \in \mathbb{R}^{N_c \times N_t}$ is the h-th trial recorded from the subject p corresponding to the stimulus frequency f_i. The confidence of this trial is defined as

$$C_{p,i,h} = \frac{S_{p,i,h}}{\frac{1}{K} \sum_{k=1}^{K} S_{p,k,h}} \tag{12}$$

where K is the number of stimulus frequencies, $S_{p,i,h}$ is the multivariate synchronization index between EEG signals and the sine-cosine reference signals at the labeled stimulus frequency f_i, and $S_{p,k,h}$ is the multivariate synchronization index between EEG signals and the sine-cosine reference signals at the stimulus frequency f_k. Only high-confidence trials are selected for transfer learning, and the threshold function for confidence is formulated as

$$f(C_{p,i,h}) = \begin{cases} 1, & C_{p,i,h} > 1 + \ln(\frac{N_t}{F_s}), \\ -1, & otherwise. \end{cases} \tag{13}$$

where Fs is the sampling rate. Suppose $A_{p,i}$ is a set composed of high-confidence trials belonging to subject p, and the initial set is the empty set ($A_{p,i} = \emptyset$). The trial selection procedure establishes an iterator to loop over all trials corresponding to the stimulus frequency f_i and pick up high-confidence trials:

$$A_{p,i} \leftarrow \begin{cases} A_{p,i} \cup \{\chi_{p,i,h}\}, & f(C_{p,i,h}) > 0, \\ A_{p,i}, & otherwise. \end{cases} \tag{14}$$

If P is the set of ideal subjects used for templates, the inter-subject template is obtained by averaging high-confidence trials across subjects:

$$Y_i^* = \frac{1}{|P|} \sum_{p \in P} \frac{1}{|A_{p,i}|} \sum_{\chi_{p,i,h} \in A_{p,i}} \chi_{p,i,h} \tag{15}$$

Then, the sine-cosine reference signals of the standard MSI can be replaced by the inter- and intra-subject template signals. The multivariate synchronization index S_i^* and S_i between the inter- and intra-subject template signals and the test trial can be calculated with the formula (2–9), respectively. Finally, a sum-of-squares γ_i based the multivariate synchronization index represents the final detection score for the stimulus frequency f_i:

$$\gamma_i = (S_i)^2 + (S_i^*)^2 \tag{16}$$

The target frequency f_t can be recognized by the formula:

$$f_t = \max_{f_i} \gamma_i, i = 1, \ldots, K \tag{17}$$

2.3. Dynamic Window-Based Adaptive Threshold (AT) Strategy

In order to exploit the temporal features of EEG signal, a dynamic window approach is incorporated into the IIST-MSI method. In a trial where the EEG data is continuously received, the inter- and intra-subject template-based multivariate synchronization index of a small initial time window (ITW) corresponding to each stimulus frequency can be first computed. The probability ratio $r_{1,i}$ of the stimulus frequency f_i can be then defined as

$$r_{1,i} = \frac{\sqrt{\gamma_{1,i}}}{\frac{1}{K} \sum_{k=1}^{K} \sqrt{\gamma_{1,k}}} \tag{18}$$

where K is the number of stimulus frequencies. The probability ratio reflects the confidence of each stimulus frequency. When the probability ratio of each stimulus frequency is less than the

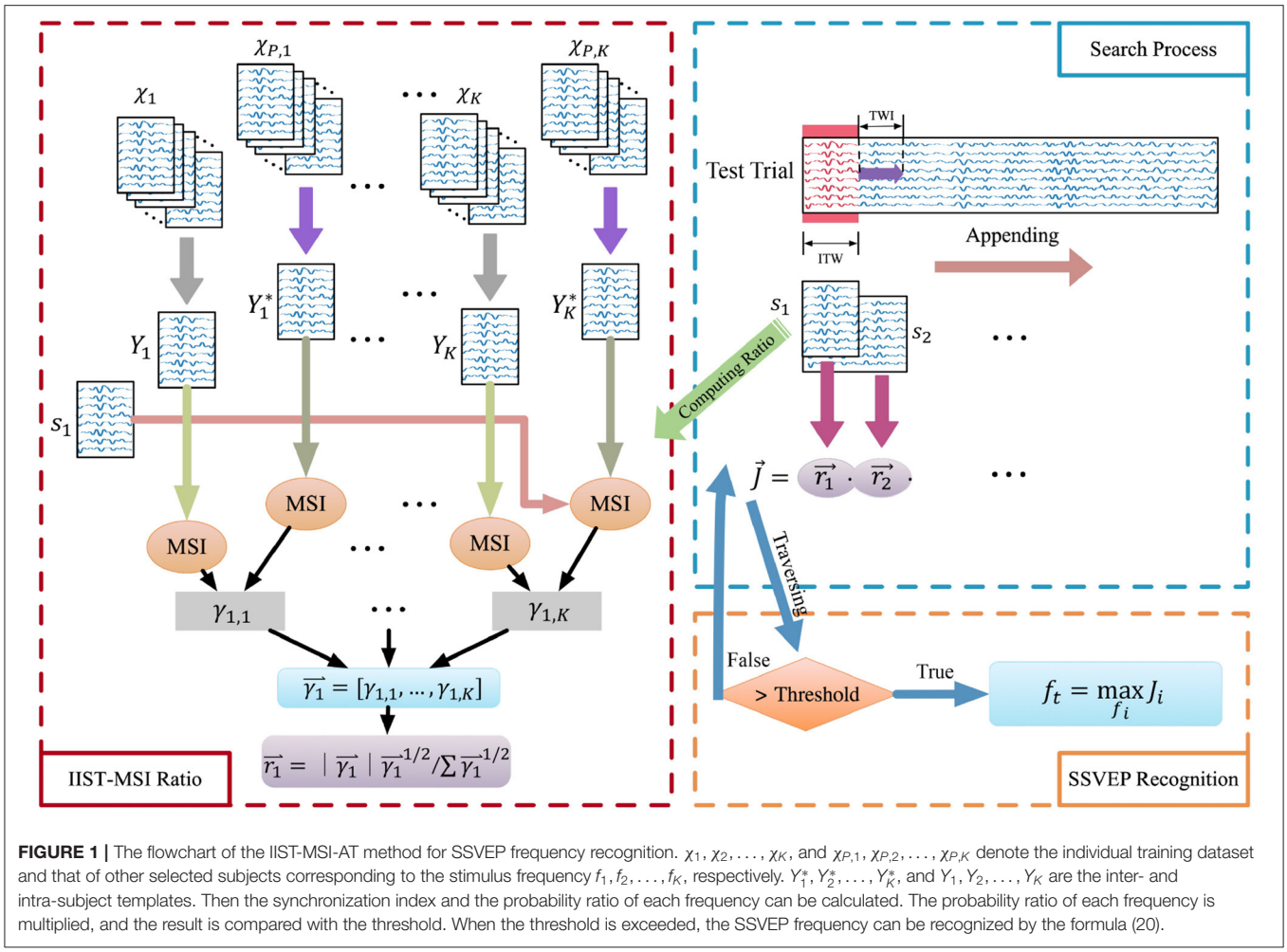

FIGURE 1 | The flowchart of the IIST-MSI-AT method for SSVEP frequency recognition. $\chi_1, \chi_2, \ldots, \chi_K$, and $\chi_{P,1}, \chi_{P,2}, \ldots, \chi_{P,K}$ denote the individual training dataset and that of other selected subjects corresponding to the stimulus frequency $f_1, f_2, \ldots, f_K$, respectively. $Y_1^*, Y_2^*, \ldots, Y_K^*$, and $Y_1, Y_2, \ldots, Y_K$ are the inter- and intra-subject templates. Then the synchronization index and the probability ratio of each frequency can be calculated. The probability ratio of each frequency is multiplied, and the result is compared with the threshold. When the threshold is exceeded, the SSVEP frequency can be recognized by the formula (20).

pre-set threshold, it indicates that the current data length is not enough to make a reasonable decision, so the algorithm requires more data. A time window increment (TWI) is appended to the last data segment, and the algorithm recalculates the probability ratio of this new data segment corresponding to each stimulus frequency. A joint probability of the new data segment and the last data segment can then be computed. After m subsequences, the joint probability J_i of the stimulus frequency f_i is calculated as:

$$J_i \leftarrow J_i \times r_{m,i} \tag{19}$$

where the initial value is set as $J_i \leftarrow r_{1,i}$. The threshold T_c serves as the cut-off condition for this method. To paraphrase, if $max\{J_1, \ldots, J_K\} < T_c$, the iterative process is continued. When all EEG signals are depleted, and $max\{J_1, \ldots, J_K\}$ still is less than T_c, the trial is regarded as an invalid trial. Once the method reaches the threshold T_c, the target stimulus frequency f_t can be computed as follows:

$$f_t = \max_{f_i} J_i, i = 1, \ldots, K \tag{20}$$

where K is the number of stimulus frequencies used in SSVEP-based BCI. **Figure 1** illustrates the frequency recognition method.

2.4. Contrast Method

For validating effectiveness for frequency recognition in SSVEPs, the classification performance of the proposed method is compared with various algorithms, including Canonical Correlation Analysis (CCA), the standard Multivariate Synchronization Index (MSI), Multi-set CCA, and Individual Template-based CCA.

2.4.1. Canonical Correlation Analysis

Canonical Correlation Analysis (CCA) is a multivariable statistical technique used to reveal the underlying correlation between two multidimensional variables (Hardoon et al., 2004). Given two sets of random variables $X \in \mathbb{R}^{N_1 \times M}$, $Y \in \mathbb{R}^{N_2 \times M}$. Their linear combinations can be define as $\widetilde{\boldsymbol{x}} = \boldsymbol{w}^{\mathrm{T}} X$ and $\widetilde{\boldsymbol{y}} = \boldsymbol{v}^{\mathrm{T}} X$, respectively. The CCA method is aimed at finding a pair of vectors $\boldsymbol{w} \in \mathbb{R}^{N_1 \times 1}$ and $\boldsymbol{v} \in \mathbb{R}^{N_2 \times 1}$, such that the correlation between $\widetilde{\boldsymbol{x}}$ and $\widetilde{\boldsymbol{y}}$ is maximized. In other words, the following

optimization problem is solved:

$$\rho = \max_{\boldsymbol{w},\boldsymbol{v}} \frac{\mathbb{E}\left[\widetilde{\boldsymbol{x}}\widetilde{\boldsymbol{y}}\right]}{\sqrt{\mathbb{E}\left[\widetilde{\boldsymbol{x}}^2\right]\mathbb{E}\left[\widetilde{\boldsymbol{y}}^2\right]}} = \frac{\boldsymbol{w}^{\mathrm{T}}XY^{\mathrm{T}}\boldsymbol{v}}{\boldsymbol{w}^{\mathrm{T}}XX^{\mathrm{T}}\boldsymbol{w}\boldsymbol{v}^{\mathrm{T}}YY^{\mathrm{T}}\boldsymbol{v}} \tag{21}$$

The maximum canonical correlation between the canonical variates $\widetilde{\boldsymbol{x}}$ and $\widetilde{\boldsymbol{y}}$ is the maximum of ρ. Assume X represents a multichannel EEG data, and Y is the reference signal constructed according to the formula (1). The maximum canonical correlation of each frequency $f_i (i = 1, \ldots, K)$ can thus be calculated. Then, the target frequency f_t can be recognized by the formula.

$$f_t = \max_{f_i} \rho_i, i = 1, \ldots, K \tag{22}$$

2.4.2. Multi-Set Canonical Correlation Analysis

Multi-set canonical correlation analysis (Multi-set CCA) is developed as an extension of CCA to analyze linear relationships between multiple sets of features. In order to improve the classification accuracy of SSVEPs, The Multi-set CCA method is implemented to optimize the reference signal, and the pre-constructed sine-cosine waves, by learning from the joint spatial filtering of training sets of EEG signals (Zhang et al., 2014c).

Assume the h-th training trial of EEG signals corresponding to the stimulus frequency f_i is $\chi_{i,h} \in \mathbb{R}^{N_c \times N_s}$, and the spatial filters used to extract common features of training sets are $\boldsymbol{w_1}, \ldots, \boldsymbol{w_n}$. To maximize the sum of the pairwise correlation between multiple sets of training data, the optimization problem of Multi-set CCA is presented as follows:

$$\begin{aligned} \tilde{\boldsymbol{w}}_{i,1}, \ldots, \tilde{\boldsymbol{w}}_{i,n} &= \underset{\boldsymbol{w_1},\ldots,\boldsymbol{w_n}}{\arg\max} \sum_{h_1 \neq h_2}^{n} \boldsymbol{w}_{h_1}^T \chi_{i,h_1} \chi_{i,h_2}^T \boldsymbol{w}_{h_2} \\ \text{subject to} \quad & \frac{1}{n} \sum_{h_1=1}^{n} \boldsymbol{w}_{h_1}^T \chi_{i,h_1} \chi_{i,h_1}^T \boldsymbol{w}_{h_1} = 1 \end{aligned} \tag{23}$$

The objective function can then be transformed into the following generalized eigenvalue problem with the Lagrange multipliers:

$$(\boldsymbol{R}_i - \boldsymbol{S}_i)\boldsymbol{w} = \rho \boldsymbol{S}_i \boldsymbol{w} \tag{24}$$

where

$$\boldsymbol{R}_i = \begin{bmatrix} \chi_{i,1}\chi_{i,1}^T & \cdots & \chi_{i,1}\chi_{i,n}^T \\ \vdots & \ddots & \vdots \\ \chi_{i,n}\chi_{i,1}^T & \cdots & \chi_{i,n}\chi_{i,n}^T \end{bmatrix},$$

$$\boldsymbol{S}_i = \begin{bmatrix} \chi_{i,1}\chi_{i,1}^T & \cdots & 0 \\ \vdots & \ddots & \vdots \\ 0 & \cdots & \chi_{i,n}\chi_{i,n}^T \end{bmatrix},$$

$$\boldsymbol{w} = \begin{bmatrix} \boldsymbol{w}_1 \\ \vdots \\ \boldsymbol{w}_n \end{bmatrix}$$

After obtaining the multiple linear transforms $\boldsymbol{w_1}, \ldots, \boldsymbol{w_n}$ and utilizing the joint spatial filtering $\tilde{\boldsymbol{z}}_{i,h} = \tilde{\boldsymbol{w}}_{i,h}^T \chi_{i,h}$, the optimized reference signal is constructed as

$$\boldsymbol{Z}_n = [\tilde{\boldsymbol{z}}_{i,1}^T, \tilde{\boldsymbol{z}}_{i,2}^T, \ldots, \tilde{\boldsymbol{z}}_{i,n}^T]^T \tag{25}$$

Next, the maximum canonical correlation between the test data and the optimized reference signal can be calculated using CCA, and the target stimulus frequency f_t can be recognized with the formula (22).

2.4.3. Individual Template Based CCA

To explore temporal features of EEG signals, the Individual Template-based CCA (IT-CCA) approach was proposed for SSVEP detection (Bin et al., 2011). For each stimulus frequency f_i, the individual template signal $Y_i \in \mathbb{R}^{N_c \times N_t}$ is obtained by averaging training trials using the formula (11). The CCA process can then be used to calculate the maximum canonical correlation between the test data and the individual template signal, and the target stimulus frequency f_t can be recognized with the formula (22).

2.5. Experiment and Data

To validate our proposed method, a 12-class joint frequency-phase modulated SSVEP dataset from Nakanishi et al. (2015) is used, which contains ten healthy subjects (nine males and one female, the average age being 28 years old), each having 15 trials corresponding to all 12 stimulus frequencies. In their experiment, the 12-target stimuli were presented on an LCD screen with a 60 Hz refresh rate. These stimuli were placed in a 4×3 matrix regarded as a virtual keypad, as shown in **Figure 2A**, and tagged with different frequencies ranging from 9.25 to 14.75 Hz and phases ranging from 0 to 1.5π, as shown in **Figure 2B**.

When conducting this experiment, the subjects were seated on a comfortable chair within a dim room, with their eyes 60 cm away from the LCD screen. The visual stimuli were presented by the stimulus program in random order. At the beginning of a trial, a red square emerged at the position of the target stimulus for 1 s, which indicated that the subjects should shift their gaze to the target. Afterward, all stimuli started to flicker simultaneously and the subjects were required to stare at the visual stimuli for 4 s. At the same time, EEG signals were recorded with eight electrodes placed over the occipital area with reference to the CMS electrode close to Cz. In this experiment, each subject completed 15 trials corresponding to all 12 targets.

Considering that visual stimulation emerged at the 15th millisecond, the data epochs were extracted from 0.15 to 4.15 s. Each epoch was band-pass filtered from 6 to 80 Hz with an infinite impulse response (IIR) filter and was then used as the input for recognition algorithms.

To determine ideal subjects used for templates, we selected subjects in descending order of the MSI accuracy. For adaptive threshold strategy, the initial time window ITW and the time

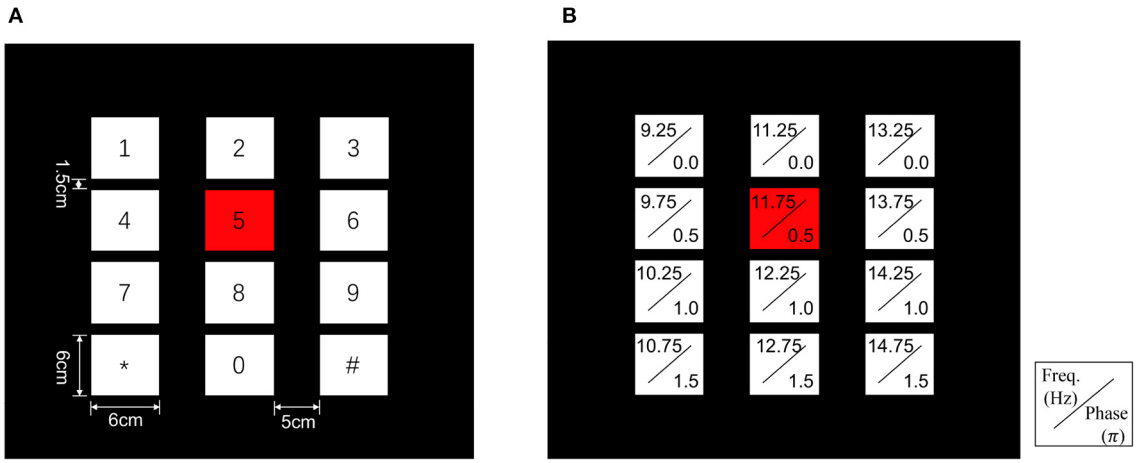

FIGURE 2 | Stimulus design of the 12-target BCI system. **(A)** The user interface of the virtual keypad. **(B)** Frequency and phase values for each target.

window increment TWI were set to 0.5 *s*. The threshold T_c took values from a range ($d \leq 1s$: ranging from 1 to 2 with an interval of 0.05; $1s < d \leq 2s$: ranging from 1 to 4 with an interval of 0.1; $2s < d \leq 3s$: ranging from 3 to 8 with an interval of 0.2; and $3s < d \leq 4s$: ranging from 3 to 16 with an interval of 0.4). The number of harmonics pre-defined for reference signals was 3 uniquely. During the process of performing parameter optimization, the combination of parameters would be discarded once the proportion of invalid trials was more than 20%. In the end, an optimum set of parameters was obtained by tuning the parameters to reach maximum recognition accuracy on the training dataset, and the optimal parameters were then applied to frequency recognition of the test dataset.

2.6. Evaluation Methods

The classification accuracy is estimated using three-fold cross-validation to evaluate the proposed method. The sample dataset is divided into the training set for choosing the optimal parameter (i.e., the threshold T_c) and test set for estimating the performance of the model for frequency recognition. The accuracy is defined as the percentage of valid trials classified correctly. Thus, the classification accuracy is calculated as follows:

$$acc = \frac{1}{3}\sum_{i=1}^{3}\frac{P_i}{N_i} \times 100\% \tag{26}$$

where P_i is the number of valid trials correctly classified and N_i is the number of valid trials from the i-th fold.

In addition to the classification accuracy, the information transfer rate (ITR) is adopted to evaluate the communication capacity of the BCI system (Wolpaw et al., 2002):

$$B = \log N + P\log P + (1-P)\log\frac{1-P}{N-1} \tag{27}$$

$$ITR = B \times 60/T \tag{28}$$

where P denotes the classification accuracy, N is the number of possible selections, and T is the average time required to select a command. Here, the ITR is calculated using different values of T (Target gazing time: 0.5 to 4.0 s with an interval of 0.5 s; Gaze shifting time: 1 s).

3. RESULTS

Since the number of subjects used for transfer $|P|$ plays an important role in the IIST-MSI method, we explore the effects of varying $|P|$ on the recognition performance firstly. As a special case, the individual template-based MSI (IT-MSI) is the same as the IIST-MSI with $|P| = 0$. **Figure 3** shows the averaged accuracy and ITR obtained by the IIST-MSI with the $|P|$ varying from 0 to 6 and TWs from 0.5 to 4 s. When TW is <1 s, the method only using the individual template performs better than that using the combined inter- and intra-subject templates. When TW is more than 2 s, the result is the contrary. For $|P| = 4$, the IIST-MSI achieved the best recognition performance. In the following analysis, the performance of the IIST-MSI with fixed $|P| = 4$ is compared with that of other methods.

Figure 4 depicts the averaged SSVEP recognition accuracy of ten subjects derived by CCA, MSI, Multi-set CCA, IT-CCA, IT-MSI and IIST-MSI with different data epochs lengths, ranging from 0.5 to 4 s, which shows that the recognition accuracy of subject 2 and 7 is significantly improved by the IIST-MSI. The one-way repeated-measure ANOVA results show that there is a statistically significant difference in the accuracy between these methods under the data length ranging from 0.5 to 3 s [$d = 0.5$ s: $F_{(5, 45)} = 29.402$, $p < 0.001$; $d = 1s$: $F_{(5, 45)} = 52.036$, $p < 0.001$; $d = 1.5s$: $F_{(5, 45)} = 11.894$, $p < 0.001$; $d = 2s$: $F_{(5, 45)} = 5.269$, $p < 0.01$; $d = 2.5s$: $F_{(5, 45)} = 3.395$, $p < 0.05$; $d = 3s$: $F_{(5, 45)} = 2.592$, $p < 0.05$; $d = 3.5s$: $F_{(5, 45)} = 1.819$, $0.1 < p$; and $d = 4s$: $F_{(5, 45)} = 1.396$, $0.1 < p$]. For a more intuitive comparison of these methods, **Figures 5A,B** depict the averaged accuracy and the ITR across all subjects with different data lengths from 0.5

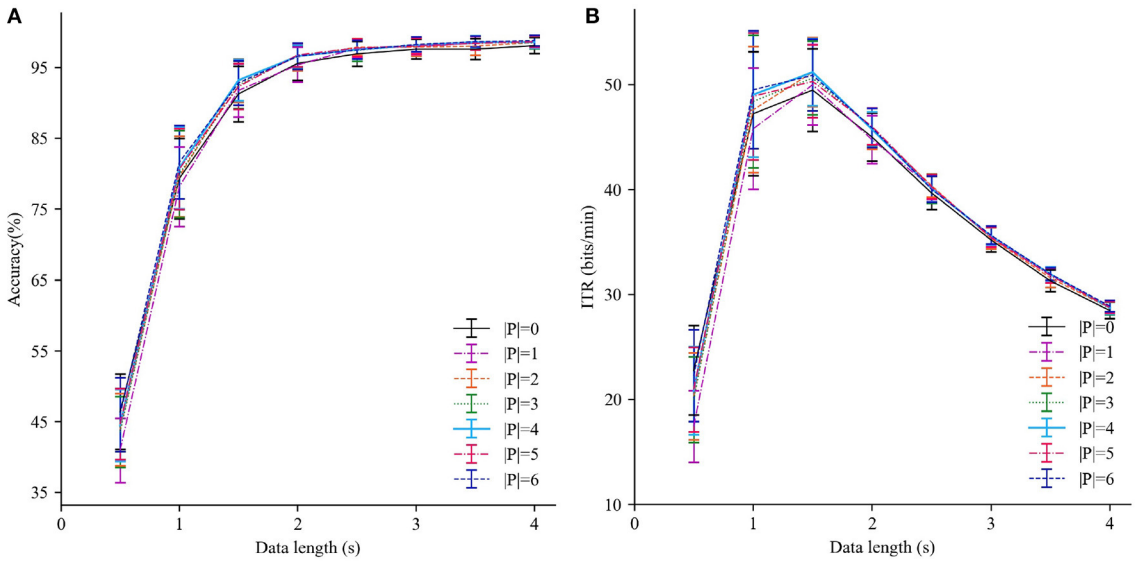

FIGURE 3 | Performance comparison of IIST-MSI with various |*P*|. **(A)** The averaged accuracy and **(B)** ITR across all subjects with different data lengths from 0.5 to 4 s. Error bars show standard errors.

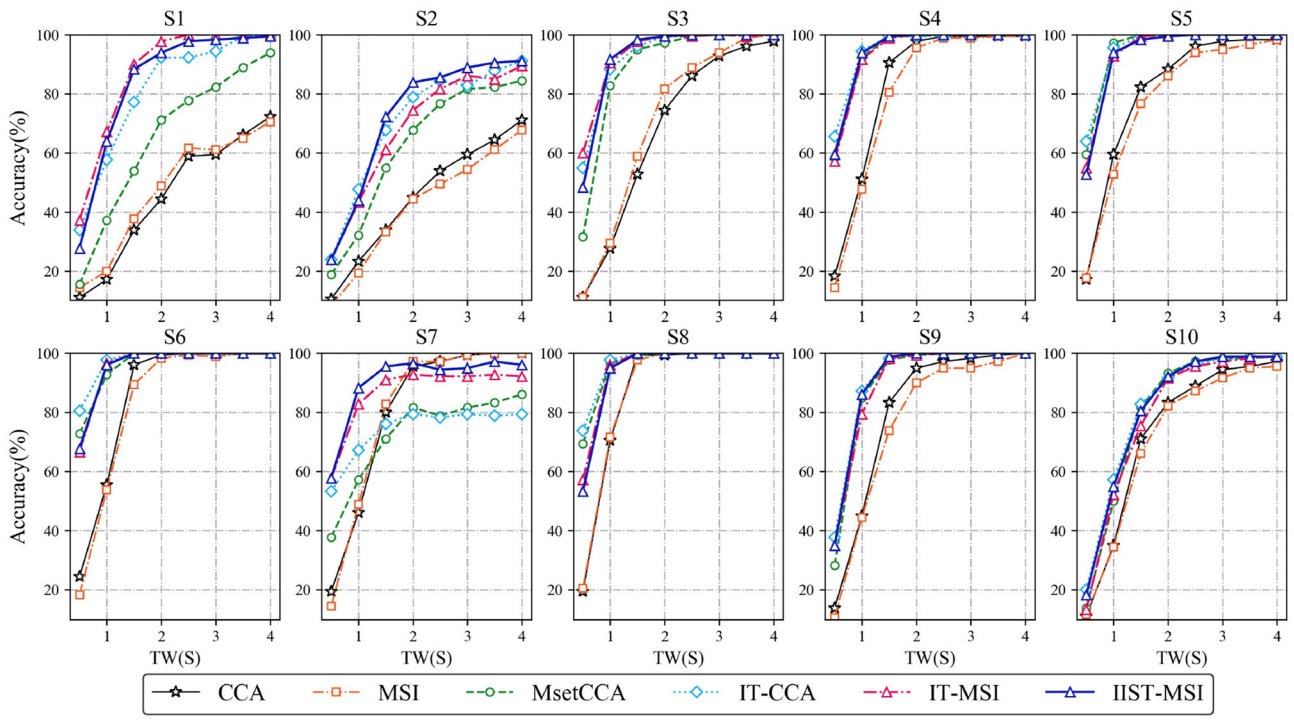

FIGURE 4 | Averaged SSVEP recognition accuracies of 10 subjects derived by CCA, MSI, Multi-set CCA, IT-CCA, IT-MSI, and IIST-MSI, with different length of data epochs from 0.5 to 4 s.

to 4 s. In terms of the mean classification accuracies of all ten subjects, from 1 to 4 s, the IIST-MSI method achieves a higher accuracy than the other methods.

To investigate the superiority of adaptive threshold strategy, the IIST-MSI using adaptive threshold (IIST-MSI-AT) is compared with the basic IIST-MSI. **Figure 6** depicts the mean detection accuracy and ITR for the basic and the combined version of IIST-MSI method. The paired-sample *t*-test shows there are no statistical differences in the accuracy between them, but there are significant differences in the ITR from 1.5 to 4 s.

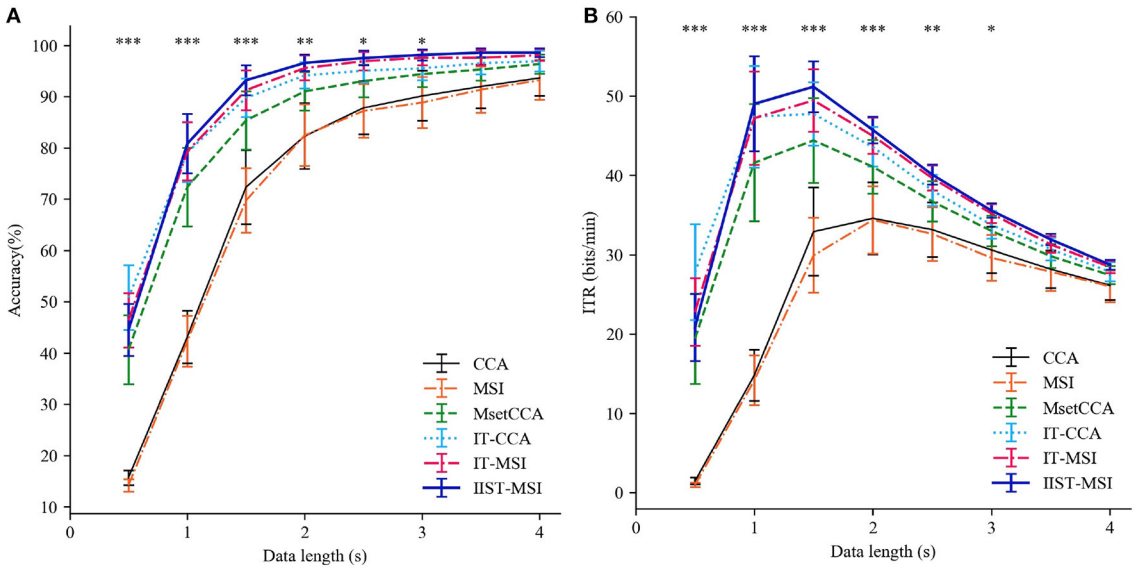

FIGURE 5 | Performance comparison between IIST-MSI and other methods. **(A)** The averaged accuracy and **(B)** ITR across all subjects with different data lengths from 0.5 to 4 s. Error bars show standard errors. The asterisk indicates the statistically significant differences (*$p < 0.05$; **$p < 0.01$; ***$p < 0.001$).

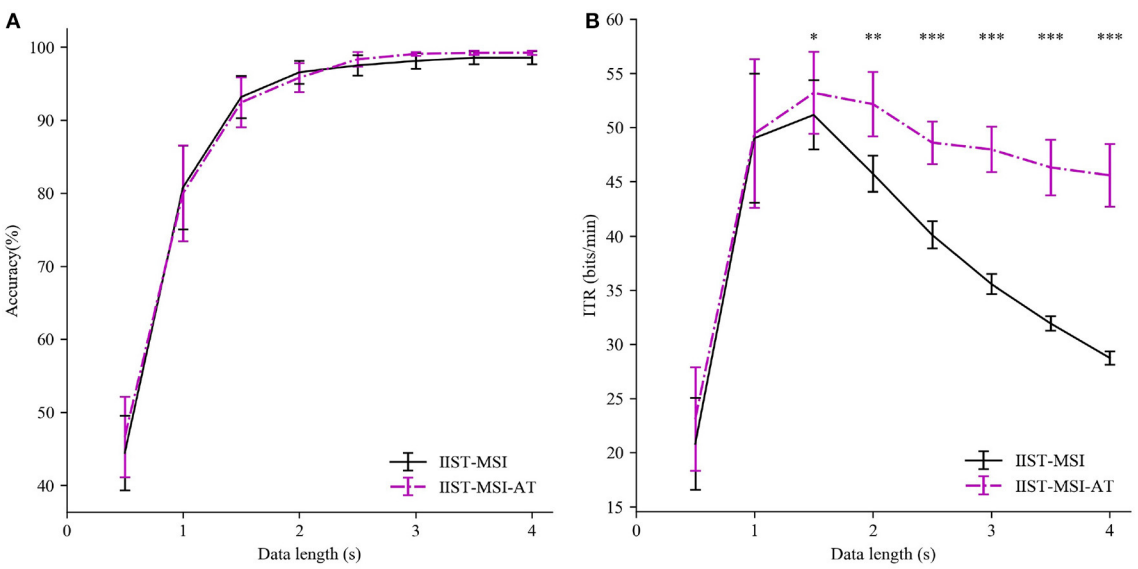

FIGURE 6 | Performance comparison between IIST-MSI and IIST-MSI-AT. **(A)** The averaged accuracy and **(B)** ITR across all subjects with different data lengths from 0.5 to 4 s. Error bars show standard errors. The asterisk indicates the statistically significant differences (paired *t*-tests, *$p < 0.05$; **$p < 0.01$; ***$p < 0.001$).

The experimental result coincides with the expectation that the dynamic window algorithm can adaptively determine the shorter time window, while maintaining high accuracy. Hence the IIST-MSI-AT method significantly outperformed the other methods in terms of ITR. The highest ITR obtained by the IIST-MSI-AT method is 53.08 ± 3.65 bits/min.

Table 1 presents the recognition accuracy and ITR obtained by CCA, MSI, Multi-set CCA, IT-CCA, and IIST-MSI-AT for each subject with a 4 s data length. Here, the accuracy of CCA, MSI, Multi-set CCA, and IT-CCA are the average values computed over 180 trials for each subject. The accuracy of IIST-MSI-AT is described as the average accuracy of the test set in a three-fold cross-validation as formulated in the equation (26). For the epoch length of 4 s, the IIST-MSI-AT method gets the highest accuracy (99.23 ± 0.29%),which achieves an increase of 5.62% compared to CCA (93.61 ± 3.48%), 6.06% compared to MSI (93.17 ± 3.82%), 2.90% compared to Multi-set CCA (96.33 ± 1.84%), and 2.34% compared to IT-CCA (96.89 ± 2.02%). These results demonstrate that the proposed method is a promising way to

TABLE 1 | Classification accuracy (%) and ITR (bits/min) of CCA, MSI, Multi-set CCA, IT-CCA, and IIST-MSI-AT for each subject with 4*s* data length.

Subject	CCA		MSI		Multi-set CCA		IT-CCA		IIST-MSI-AT	
	Accuracy	ITR	Accuracy	ITR	Accuracy	ITR	Accuracy	ITR	Accuracy	ITR
S1	72.22	14.74	70.55	14.07	93.89	25.30	99.44	29.25	98.83	35.12
S2	71.11	14.29	67.78	13.00	84.44	20.16	91.11	23.66	99.32	33.38
S3	97.78	27.90	100.00	29.82	100.00	29.82	100.00	29.82	100.00	52.99
S4	99.44	29.25	99.44	29.25	100.00	29.82	100.00	29.82	100.00	53.04
S5	98.33	28.32	98.33	28.32	100.00	29.82	100.00	29.82	98.89	43.77
S6	100.00	29.82	100.00	29.82	100.00	29.82	100.00	29.82	100.00	57.53
S7	100.00	29.82	100.00	29.82	86.11	20.99	79.44	17.81	97.19	38.43
S8	100.00	29.82	100.00	29.82	100.00	29.82	100.00	29.82	100.00	55.91
S9	100.00	29.82	100.00	29.82	100.00	29.82	100.00	29.82	100.00	51.51
S10	97.22	27.5	95.56	26.36	98.89	28.77	98.89	28.77	98.11	34.17
Mean ± STD	93.61 ± 3.48	26.13 ± 1.85	93.17 ± 3.82	26.01 ± 2.00	96.33 ± 1.84	27.41±1.16	96.89 ± 2.02	27.84 ± 1.2	99.23 ± 0.29	45.58 ± 2.89

develop more high-performance SSVEP-based brain-computer interface systems.

4. DISCUSSION

The most recent state-of-the-art methods for SSVEP recognition use the individual calibration data as the template of correlation analysis and significantly improve the detection performance (Nakanishi et al., 2015). The individual templates can accumulate the frequency components while maintaining the phase information and, conversely, reduce the effect of the background EEG artifacts. Furthermore, it contributes to improving the individual adaptability of methods, as the individual templates can learn spontaneous EEG signals from calibration data. However, the training data collection process may be time-consuming. The visual fatigue and attention lapses make the training data not perfect enough for every subject. For addressing this problem, inter-subject transfer learning is exploited to provide inter-subject similarity and variability for enhancing target recognition in SSVEP-based BCIs. For each subject, the frequency components of SSVEPs induced by a specific target frequency are similar, but the visual latencies in the visual system are various. According to the superposition principle, the averaged inter-subject transferred templates can contain the same frequency and little phase differences (Yuan et al., 2015). Based on this, this study replaces the commonly used sine-cosine reference signals with the inter- and intra-subject templates for improving adaptability and robustness of the MSI method. Indeed, the experimental results show that the detection accuracy of a few individuals is obviously improved.

On the other hand, this paper employs a dynamic time window to explore the temporal features of SSVEP signals neglected by the standard MSI method and a pre-set threshold to determine when to stop the algorithm, which can balance the recognition accuracy and data length. Hence, the proposed method can significantly improve the information transmission rate, which is critical to the development of high-speed BCIs. Considering the limited reliability of short data, the threshold not only acts as the stopping condition but assists in filtering these invalid trials to avoid wrong commands. Accordingly, the method will improve the effectiveness of the dry-electrode based BCI system with a low signal-to-noise ratio by filtering invalid trials, which can avoid mistakes and ensure the stability of BCI.

5. CONCLUSION

In this paper, we introduce a novel method based on the inter- and intra-subject template and adaptive threshold strategy to enhance the detection of SSVEPs for high-speed BCIs. The experimental results on ten subjects indicate that our approach obtains higher recognition accuracy and ITR than the CCA, MSI, Multi-set CCA, and Individual Template-based CCA. The results remind us that the inter-subject template transfer and the threshold search based on other methods could further improve the performance of BCIs, which will be investigated in our future work.

DATA AVAILABILITY STATEMENT

Publicly available datasets were analyzed in this study. This data can be found here: https://github.com/mnakanishi/12JFPM_SSVEP.

AUTHOR CONTRIBUTIONS

HW contributed conception and realization of algorithm. SC organized the database. WZ performed the statistical analysis. All authors contributed to manuscript revision, read, and approved the submitted version.

FUNDING

This work was supported by the Grants from the National Key R &D Program of China (2018YFC1314700), the National Natural Science Foundation of China (91748122, 81671307), and the Priority of Shanghai Key Discipline of Medicine (2017ZZ02020).

REFERENCES

Al-Hudhud, G. (2016). Smart brain interaction systems for office access and control in smart city context. *Smart Cities Technol.* 101, 101–119. doi: 10.5772/65902

Bakardjian, H., Tanaka, T., and Cichocki, A. (2010). Optimization of ssvep brain responses with application to eight-command brain-computer interface. *Neurosci. Lett.* 469, 34–38. doi: 10.1016/j.neulet.2009.11.039

Bakardjian, H., Tanaka, T., and Cichocki, A. (2011). Emotional faces boost up steady-state visual responsesforbrain-computer interface. *Neuroreport* 22, 121–125. doi: 10.1097/WNR.0b013e32834308b0

Bin, G., Gao, X., Wang, Y., Li, Y., Hong, B., and Gao, S. (2011). A high-speed BCI based on code modulation VEP. *J. Neural Eng.* 8:025015. doi: 10.1088/1741-2560/8/2/025015

Bin, G., Gao, X., Yan, Z., Hong, B., and Gao, S. (2009). An online multi-channel SSVEP-based brain-computer interface using a canonical correlation analysis method. *J. Neural Eng.* 6:046002. doi: 10.1088/1741-2560/6/4/046002

Cao, L., Ju, Z., Li, J., Jian, R., and Jiang, C. (2015). Sequence detection analysis based on canonical correlation for steady-state visual evoked potential brain computer interfaces. *J. Neurosci. Methods* 253, 10–17. doi: 10.1016/j.jneumeth.2015.05.014

Cheng, M., Gao, X., Gao, S., and Xu, D. (2002). Design and implementation of a brain-computer interface with high transfer rates. *IEEE Trans. Biomed. Eng.* 49, 1181–1186. doi: 10.1109/TBME.2002.803536

Dornhege, G., Millan, J. d. R., Hinterberger, T., McFarland, D. J., and Müller, K.-R. (2007). *Toward Brain-Computer Interfacing*. MIT Press. doi: 10.7551/mitpress/7493.001.0001

Faller, J., Müller-Putz, G., Schmalstieg, D., and Pfurtscheller, G. (2010). An application framework for controlling an avatar in a desktop-based virtual environment via a software SSVEP brain-computer interface. *Presence* 19, 25–34. doi: 10.1162/pres.19.1.25

Friman, O., Volosyak, I., and Graser, A. (2007). Multiple channel detection of steady-state visual evoked potentials for brain-computer interfaces. *IEEE Trans. Biomed. Eng.* 54, 742–750. doi: 10.1109/TBME.2006.889160

Georgiadis, K., Laskaris, N., Nikolopoulos, S., and Kompatsiaris, I. (2018). Discriminative codewaves: a symbolic dynamics approach to SSVEP recognition for asynchronous BCI. *J. Neural Eng.* 15:026008. doi: 10.1088/1741-2552/aa904c

Hardoon, D. R., Szedmak, S., and Shawe-Taylor, J. (2004). Canonical correlation analysis: an overview with application to learning methods. *Neural Comput.* 16, 2639–2664. doi: 10.1162/0899766042321814

Jrad, N., and Congedo, M. (2012). Identification of spatial and temporal features of EEG. *Neurocomputing* 90, 66–71. doi: 10.1016/j.neucom.2012.02.032

Ko, L.-W., Komarov, O., Hairston, W. D., Jung, T.-P., and Lin, C.-T. (2017). Sustained attention in real classroom settings: an EEG study. *Front. Hum. Neurosci.* 11:388. doi: 10.3389/fnhum.2017.00388

Lemm, S., Blankertz, B., Curio, G., and Muller, K.-R. (2005). Spatio-spectral filters for improving the classification of single trial EEG. *IEEE Trans. Biomed. Eng.* 52, 1541–1548. doi: 10.1109/TBME.2005.851521

Lin, Z., Zhang, C., Wu, W., and Gao, X. (2006). Frequency recognition based on canonical correlation analysis for SSVEP-based BCIs. *IEEE Trans. Biomed. Eng.* 53, 2610–2614. doi: 10.1109/TBME.2006.886577

Muller-Putz, G. R., and Pfurtscheller, G. (2007). Control of an electrical prosthesis with an SSVEP-based BCI. *IEEE Trans. Biomed. Eng.* 55, 361–364. doi: 10.1109/TBME.2007.897815

Nakanishi, M., Wang, Y., Chen, X., Wang, Y.-T., Gao, X., and Jung, T.-P. (2017). Enhancing detection of SSVEPs for a high-speed brain speller using task-related component analysis. *IEEE Trans. Biomed. Eng.* 65, 104–112. doi: 10.1109/TBME.2017.2694818

Nakanishi, M., Wang, Y., and Jung, T.-P. (2016). "Session-to-session transfer in detecting steady-state visual evoked potentials with individual training data," in *International Conference on Augmented Cognition* (Toronto, ON: Springer), 253–260. doi: 10.1007/978-3-319-39955-3_24

Nakanishi, M., Wang, Y., Wang, Y.-T., and Jung, T.-P. (2015). A comparison study of canonical correlation analysis based methods for detecting steady-state visual evoked potentials. *PLoS ONE* 10:e0140703. doi: 10.1371/journal.pone.0140703

Nan, W., Wong, C. M., Wang, B., Wan, F., Mak, P. U., Mak, P. I., et al. (2011). "A comparison of minimum energy combination and canonical correlation analysis for SSVEP detection," in *2011 5th International IEEE/EMBS Conference on Neural Engineering* (Cancun), 469–472. doi: 10.1109/NER.2011.5910588

Nicolas-Alonso, L. F., and Gomez-Gil, J. (2012). Brain computer interfaces, a review. *Sensors* 12, 1211–1279. doi: 10.3390/s120201211

Norcia, A. M., Appelbaum, L. G., Ales, J. M., Cottereau, B. R., and Rossion, B. (2015). The steady-state visual evoked potential in vision research: a review. *J. Vis.* 15:4. doi: 10.1167/15.6.4

Poryzala, P., and Materka, A. (2014). Cluster analysis of CCA coefficients for robust detection of the asynchronous SSVEPs in brain-computer interfaces. *Biomed. Signal Process. Control* 10, 201–208. doi: 10.1016/j.bspc.2013.11.003

Russell, B. A., Russo, J. C., Warfield, I. P., and Casebeer, W. D. (2016). "Monitoring attention with embedded frequency markers for simulation environments," in *International Conference on Augmented Cognition* (Toronto, ON: Springer), 394–403. doi: 10.1007/978-3-319-39955-3_37

Saha, S., and Baumert, M. (2019). Intra-and inter-subject variability in EEG-based sensorimotor brain computer interface: a review. *Front. Comput. Neurosci.* 13:87. doi: 10.3389/fncom.2019.00087

Shyu, K.-K., Lee, P.-L., Liu, Y.-J., and Sie, J.-J. (2010). Dual-frequency steady-state visual evoked potential for brain computer interface. *Neurosci. Lett.* 483, 28–31. doi: 10.1016/j.neulet.2010.07.043

Skidmore, T., and Hill, H. (1991). "The evoked potential human-computer interface," in *Proceedings of the Annual International Conference of the IEEE Engineering in Medicine and Biology Society, Vol. 13* (Orlando, FL), 407–408.

Vu, H., Koo, B., and Choi, S. (2016). "Frequency detection for SSVEP-based BCI using deep canonical correlation analysis," in *2016 IEEE International Conference on Systems, Man, and Cybernetics (SMC)* (Budapest), 001983–001987.

Wang, H., and Zheng, W. (2008). Local temporal common spatial patterns for robust single-trial EEG classification. *IEEE Trans. Neural Syst. Rehabil. Eng.* 16, 131–139. doi: 10.1109/TNSRE.2007.914468

Wang, Y.-K., Jung, T.-P., and Lin, C.-T. (2018). Theta and alpha oscillations in attentional interaction during distracted driving. *Front. Behav. Neurosci.* 12:3. doi: 10.3389/fnbeh.2018.00003

Waytowich, N. R., Faller, J., Garcia, J. O., Vettel, J. M., and Sajda, P. (2016). "Unsupervised adaptive transfer learning for steady-state visual evoked potential brain-computer interfaces," in *2016 IEEE International Conference on Systems, Man, and Cybernetics (SMC)* (Budapest), 004135–004140. doi: 10.1109/SMC.2016.7844880

Wolpaw, J. R., Birbaumer, N., McFarland, D. J., Pfurtscheller, G., and Vaughan, T. M. (2002). Brain-computer interfaces for communication and control. *Clin. Neurophysiol.* 113, 767–791. doi: 10.1016/S1388-2457(02)00057-3

Yang, C., Han, X., Wang, Y., Saab, R., Gao, S., and Gao, X. (2018). A dynamic window recognition algorithm for SSVEP-based brain-computer interfaces using a spatio-temporal equalizer. *Int. J. Neural Syst.* 28:1850028. doi: 10.1142/S0129065718500284

Yang, Z., Guo, D., Zhang, Y., Wu, S., and Yao, D. (2019). Visual evoked response modulation occurs in a complementary manner under dynamic circuit framework. *IEEE Trans. Neural Syst. Rehabil. Eng.* 27, 2005–2014. doi: 10.1109/TNSRE.2019.2940712

Yuan, P., Chen, X., Wang, Y., Gao, X., and Gao, S. (2015). Enhancing performances of SSVEP-based brain-computer interfaces via exploiting inter-subject information. *J. Neural Eng.* 12:046006. doi: 10.1088/1741-2560/12/4/046006

Zhang, Y., Guo, D., Li, F., Yin, E., Zhang, Y., Li, P., et al. (2018a). Correlated component analysis for enhancing the performance of SSVEP-based brain-computer interface. *IEEE Trans. Neural Syst. Rehabil. Eng.* 26, 948–956. doi: 10.1109/TNSRE.2018.2826541

Zhang, Y., Guo, D., Xu, P., Zhang, Y., and Yao, D. (2016). Robust frequency recognition for SSVEP-based BCI with temporally local multivariate synchronization index. *Cogn. Neurodyn.* 10, 505–511. doi: 10.1007/s11571-016-9398-9

Zhang, Y., Guo, D., Yao, D., and Xu, P. (2017). The extension of multivariate synchronization index method for SSVEP-based BCI. *Neurocomputing* 269, 226–231. doi: 10.1016/j.neucom.2017.03.082

Zhang, Y., Ma, H., Jin, J., and Wang, X. (2014a). "Adaptive strategy for time window length in SSVEP-based brain-computer interface," in *2014 international Conference on Mechatronics and Control (ICMC)* (Jinzhou), 140–143. doi: 10.1109/ICMC.2014.7231535

Zhang, Y., Xu, P., Cheng, K., and Yao, D. (2014b). Multivariate synchronization index for frequency recognition of SSVEP-based brain-computer interface. *J. Neurosci. Methods* 221, 32–40. doi: 10.1016/j.jneumeth.2013.07.018

Zhang, Y., Xu, P., Huang, Y., Cheng, K., and Yao, D. (2013a). SSVEP response is related to functional brain network topology entrained by the flickering stimulus. *PLoS ONE* 8:e72654. doi: 10.1371/journal.pone.0072654

Zhang, Y., Yin, E., Li, F., Zhang, Y., Tanaka, T., Zhao, Q., et al. (2018b). Two-stage frequency recognition method based on correlated component analysis for SSVEP-based BCI. *IEEE Trans. Neural Syst. Rehabil. Eng.* 26, 1314–1323. doi: 10.1109/TNSRE.2018.2848222

Zhang, Y., Zhou, G., Jin, J., Wang, M., Wang, X., and Cichocki, A. (2013b). L1-regularized multiway canonical correlation analysis for SSVEP-based BCI. *IEEE Trans. Neural Syst. Rehabil. Eng.* 21, 887–896. doi: 10.1109/TNSRE.2013.2279680

Zhang, Y., Zhou, G., Jin, J., Wang, X., and Cichocki, A. (2014c). Frequency recognition in SSVEP-based BCI using multiset canonical correlation analysis. *Int. J. Neural Syst.* 24:1450013. doi: 10.1142/S0129065714500130

Zhang, Y., Zhou, G., Jin, J., Wang, X., and Cichocki, A. (2015). SSVEP recognition using common feature analysis in brain-computer interface. *J. Neurosci. Methods* 244, 8–15. doi: 10.1016/j.jneumeth.2014.03.012

Zhang, Y., Zhou, G., Zhao, Q., Onishi, A., Jin, J., Wang, X., and Cichocki, A. (2011). "Multiway canonical correlation analysis for frequency components recognition in SSVEP-based BCIs," in *International Conference on Neural Information Processing* (Shanghai: Springer), 287–295. doi: 10.1007/978-3-642-24955-6_35

Zhang, Z., Wang, C., Ang, K. K., Wai, A. A. P., and Nanyang, C. G. (2018). "Spectrum and phase adaptive CCA for SSVEP-based brain computer interface," in *2018 40th Annual International Conference of the IEEE Engineering in Medicine and Biology Society (EMBC)*, 311–314. doi: 10.1109/EMBC.2018.8512267

Zhou, D., Rangan, A. V., McLaughlin, D. W., and Cai, D. (2013). Spatiotemporal dynamics of neuronal population response in the primary visual cortex. *Proc. Natl. Acad. Sci. U.S.A.* 110, 9517–9522. doi: 10.1073/pnas.1308167110

Zhu, D., Bieger, J., Molina, G. G., and Aarts, R. M. (2010). A survey of stimulation methods used in SSVEP-based BCIs. *Comput. Intell. Neurosci.* 2010:702357. doi: 10.1155/2010/702357

Conflict of Interest: The authors declare that the research was conducted in the absence of any commercial or financial relationships that could be construed as a potential conflict of interest.

frontiers in Human Neuroscience

ORIGINAL RESEARCH
published: 23 September 2020
doi: 10.3389/fnhum.2020.00284

Machine Learning Approaches for MDD Detection and Emotion Decoding Using EEG Signals

Lijuan Duan[1,2,3†], *Huifeng Duan*[1,2,3†], *Yuanhua Qiao*[4†], *Sha Sha*[5,6*], *Shunai Qi*[1,2,3], *Xiaolong Zhang*[5,6], *Juan Huang*[5,6], *Xiaohan Huang*[5,6] *and Changming Wang*[6,7,8*]

[1] Faculty of Information Technology, Beijing University of Technology, Beijing, China, [2] Beijing Key Laboratory of Trusted Computing, Beijing, China, [3] National Engineering Laboratory for Critical Technologies of Information Security Classified Protection, Beijing, China, [4] College of Applied Sciences, Beijing University of Technology, Beijing, China, [5] Beijing Anding Hospital, Capital Medical University, Beijing, China, [6] Advanced Innovation Center for Human Brain Protection, Capital Medical University, Beijing, China, [7] Brain-inspired Intelligence and Clinical Translational Research Center, Xuanwu Hospital, Capitap Medical University, Beijing, China, [8] Department of Neurosurgery, Xuanwu Hospital, Capitap Medical University, Beijing, China

OPEN ACCESS

Edited by:
Chun-Shu Wei,
National Chiao Tung University, Taiwan

Reviewed by:
Reza Abiri,
University of California, San Francisco, United States
Yu-Kai Wang,
University of Technology Sydney, Australia

***Correspondence:**
Sha Sha
sarahbon@163.com
Changming Wang
superwcm@163.com

[†]*These authors have contributed equally to this work*

Specialty section:
This article was submitted to Brain-Computer Interfaces, a section of the journal Frontiers in Human Neuroscience

Received: *15 December 2019*
Accepted: *24 June 2020*
Published: *23 September 2020*

Citation:
Duan L, Duan H, Qiao Y, Sha S, Qi S, Zhang X, Huang J, Huang X and Wang C (2020) Machine Learning Approaches for MDD Detection and Emotion Decoding Using EEG Signals. Front. Hum. Neurosci. 14:284. doi: 10.3389/fnhum.2020.00284

Emotional decoding and automatic identification of major depressive disorder (MDD) are helpful for the timely diagnosis of the disease. Electroencephalography (EEG) is sensitive to changes in the functional state of the human brain, showing its potential to help doctors diagnose MDD. In this paper, an approach for identifying MDD by fusing interhemispheric asymmetry and cross-correlation with EEG signals is proposed and tested on 32 subjects [16 patients with MDD and 16 healthy controls (HCs)]. First, the structural features and connectivity features of the θ-, α-, and β-frequency bands are extracted on the preprocessed and segmented EEG signals. Second, the structural feature matrix of the θ-, α-, and β-frequency bands are added to and subtracted from the connectivity feature matrix to obtain mixed features. Finally, the structural features, connectivity features, and the mixed features are fed to three classifiers to select suitable features for the classification, and it is found that our mode achieves the best classification results using the mixed features. The results are also compared with those from some state-of-the-art methods, and we achieved an accuracy of 94.13%, a sensitivity of 95.74%, a specificity of 93.52%, and an F1-score (f1) of 95.62% on the data from Beijing Anding Hospital, Capital Medical University. The study could be generalized to develop a system that may be helpful in clinical purposes.

Keywords: EEG, major depressive disorder (MDD), interhemispheric asymmetry, cross correlation, feature

INTRODUCTION

Major depressive disorder (MDD) is a major mental disorder and is characterized by loss of interest, poor concentration, and even suicidal thoughts (Acharya et al., 2018).

It has been reported that more than 264 million people worldwide suffer from depression, which heavily impacts quality of life (World Health Organization, 2020). An accurate diagnosis of MDD is of great importance for early intervention and effective treatment. Traditional diagnosis of MDD mainly depends on subjective evaluation of symptom intensity using interview sessions and psychiatric scales. These methods are useful but time consuming and sometimes may lead to misdiagnoses due to human and environmental factors. Thus, it is crucial to develop objective approaches to help clinicians diagnose MDD more effectively.

Electroencephalography (EEG) is a noninvasive technique with high temporal resolution; this technique is sensitive to changes in the functional state of the human brain (Schmidt et al., 2013). Resting-state EEG (rsEEG) reveals brain network activity and can be applied to neurological evaluations (Tóth et al., 2014). EEG signals can be viewed as a group of multivariate time series, and extracting features is essential to tracking changes in EEG signals (Ting et al., 2008). Studies of depression have found that depressed patients show significant obstacles in interpreting fear, anger, happiness, surprise, and sadness (Filomena et al., 2016). Depressed patients are different from healthy subjects in the decoding of negative emotions. In a study, it was found that electroconvulsive therapy (ECT) could modulate the functional connectivity of the left angular gyrus in patients with depression (Wei et al., 2018). From the performance and treatment of depression, it can be concluded that there may be differences in brain structure between patients with depression and healthy subjects. Various studies indicate that interhemispheric frontal EEG α asymmetry is considered a key marker of structural alteration of the human brain in MDD (Allen et al., 2004; Allen and Reznik, 2015; Cantisani et al., 2015; Mumtaz et al., 2017a). Except for the α frequency band, activity in other bands and brain regions may also be associated with a disordered brain state caused by MDD, and EEG signals confounded with noises also influence the identification of specific signals. It has also been investigated whether brain connectivity is altered in MDD patients (Iseger et al., 2017). Therefore, connectivity should be taken into consideration in the recognition of special EEG signals. In real EEG data classification tasks, extracting reliable EEG features is sometimes challenging, and EEG signals in depression have both structural (Michalopoulos and Bourbakis, 2015) and connectivity features. Therefore, we propose a mixture of structural features and connectivity features for MDD classification; that is, we extract features from different viewpoints and combine them together for MDD classification.

In recent years, as the main type of artificial intelligence, deep learning (DL) has been widely used for the classification and prediction of patterns in EEG signals. DL methods can extract many abstract features from a large set of training data without human supervision. In this paper, we utilize the K-nearest neighbor (KNN) (Dasarathy, 1997), support vector machine (SVM) (Cortes, 1995) and convolutional neural network (CNN) algorithms to verify the effectiveness of the extracted features for the classification of EEG signals for patients with MDD and healthy controls (HCs).

In the literature, various features have been extracted from EEG signals and have shown the importance of MDD diagnosis. Mantri et al. (2015) reported a classification accuracy of 84% based on the power spectrum, involving 13 patients with depression and 12 HCs. In 2017, Mumtaz et al. (2017b) extracted features using wavelet transform to achieve an accuracy of 87.5%. Acharya et al. (2018) attained a high accuracy of 94% from the left hemisphere and 96% from the right hemisphere. Despite all of these research findings, the clinical applications of structural features and connectivity features remain largely unclear.

In this paper, two types of features, including the interhemispheric asymmetry value and cross-correlation value, are extracted from segmented EEG epochs, and the extracted structural and connectivity changes are combined using addition and subtraction rules for the classification. Several classifiers are introduced to verify the effectiveness of the extracted features and achieve emotion decoding.

The paper is organized as follows: in section materials and methods, the dataset is described, preprocessing is performed, and the main framework of the proposed approach is given. In section results, the experimental results are given; the conclusion and discussion are presented in section discussion and section conclusion, respectively.

TABLE 1 | Demographic and clinical information.

Factors	MDD	HC
Age (years)	31.0 ± 1.0	26.1 ± 5.4
Sex (male/female)	7/9	7/9
Education (years)	12.5 ± 1.0	13.0 ± 2.6
HAMD	19.3 ± 8.9	-

MATERIALS AND METHODS

Participants and Criteria

In this study, experimental data were acquired from 32 subjects (16 patients with MDD and 16 HCs) recruited from Beijing Anding Hospital, Capital Medical University. The experiment was approved by the Ethics Committee of Beijing Anding Hospital, Capital Medical University. All the participants signed consent forms for participation and were fully informed of the experimental and data acquisition procedures. The inclusion and exclusion criteria are based on the symptoms of depression as mentioned in the section in the Diagnostic and Statistical Manual of Mental Disorders (DSM-IV) on depression (Hu, 2003). MDD participants with psychotic symptoms, pregnant patients, people with alcoholism and patients with epilepsy were excluded. The HCs were screened for possible mental or physical illness and were found to be disease free.

Independent samples *t*-test was used to measure the difference in demographic and neuropsychological assessments between the MDD and HC groups; the analysis was performed in SPSS 20.0 (IBM SPSS, Inc., Armonk, NY, USA). The significance level was set to $p < 0.05$. The results are shown in **Table 1**. In the descriptive analysis of the demographics, the two groups are matched in age, sex, and education level.

Recording and Preprocessing of EEG Signals

The rsEEG signal recordings were performed in Beijing Anding Hospital, Capital Medical University. During the EEG recording period, all the subjects sat in a comfortable armchair, were relaxed and stayed awake for about 3 min in a quiet, dim room, with room temperature maintained at 23 ± 2°C. The EEG headset used to collect the data is shown in **Figure 1**.

The 3-min rsEEG data were recorded from 64-channel brain products with the averaged mastoids (M1 and M2) as

FIGURE 1 | The EEG headset used to collect the data.

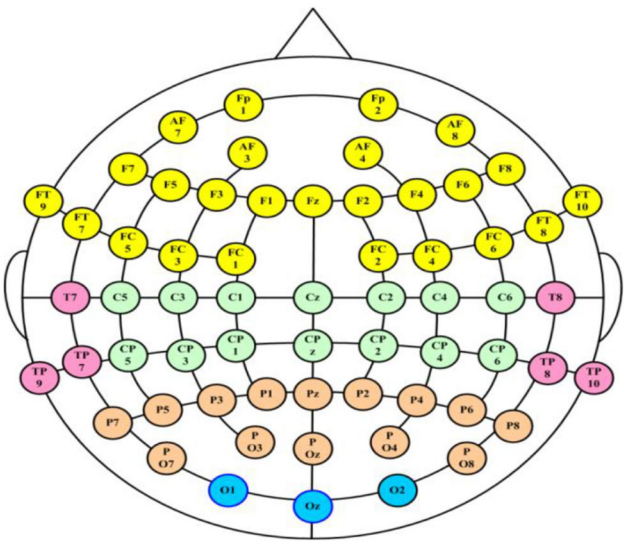

FIGURE 2 | The distribution of the electrodes in the acquisition system.

the reference electrodes. The channel location is shown in **Figure 2**. The EEG data were collected with electrode impedances below 10 kΩ.

Framework

The MDD EEG analysis framework is shown in **Figure 3**, and it mainly contains four parts: (1) EEG signal preprocessing and segmentation; (2) feature extraction; (3) construction of the feature matrix; and (4) classification.

EEG Signal Preprocessing and Segmentation

To comprehensively analyze the changes in patients with MDD, 28 pairs of electrodes from five brain regions (the frontal region, temporal region, central region, parietal region and occipital region) and three frequency bands [the θ-frequency band (4–8 Hz), the α-frequency band (8–13 Hz), and the β-frequency band (13–40 Hz)] were used to conduct experiments to explore the changes in interhemispheric asymmetry in MDD patients.

In this study, the recorded EEG data have a high temporal sensitivity and are extremely susceptible to external interference during collection. For example, eye blinks, movements and muscular activates (e.g., the heart beats) could cause EEG artifacts, and the EEG data with these artifacts may not truly represent the underlying brain activities. Hence, removing artifacts is an essential preprocessing step for further data analysis. We used a finite impulse response (FIR) filter to filter out unnecessary signals, and frequencies of 0.5–47 Hz remained for the analysis. Then, the independent component analysis (ICA) algorithm in EEGLAB was applied to remove ocular artifacts from the raw EEG data (Delorme and Makeig, 2004).

EEG signals are time-varying and nonstationary signals. There are different frequency components at different times and in different states. As machine learning techniques require a large number of training sets, we divided each channel in the EEG data into small, non-overlapping segments with durations of 1s, 2s, and 3s. Thus, we have a large number of samples to avoid underfitting. The sample information is given in **Table 2**. The average EEG recording time for all subjects is 3 min; however, this time was not the same for all the patients, so the number of epochs in the MDD and HC groups are slightly different. Three different frequency bands of EEG data, θ (4–8 Hz), α (8–13 Hz), and β (13–40 Hz), are extracted from the segmented EEG signals using a fast Fourier transform (FFT), and the number of FFT points is set to 1,024. Welch's method is applied to calculate the power spectrum of EEG bands. Welch's method consists of splitting the time series signal into epochs, computing a modified periodogram for each epoch, and then averaging the power spectrum density estimates (Alkan and Kiymik, 2007).

Feature Extraction

Two EEG features, namely, the interhemispheric asymmetry and cross-correlation, are extracted. Then, the two features are combined in two ways.

Interhemispheric asymmetry

The interhemispheric asymmetry is computed by the power value of the electrode in the left and right brain regions. The interhemispheric EEG asymmetry is shown in **Equation (1)**:

$$P = ln(P_2) - ln(P_1) \tag{1}$$

P denotes the interhemispheric asymmetry value. P_2 is the power value of one electrode in the left brain region, P_1 is the power value of the electrode in the right brain region, $\ln(P_2)$ indicates the absolute power of the left brain region, and $\ln(P_1)$ is the absolute power of the right brain region.

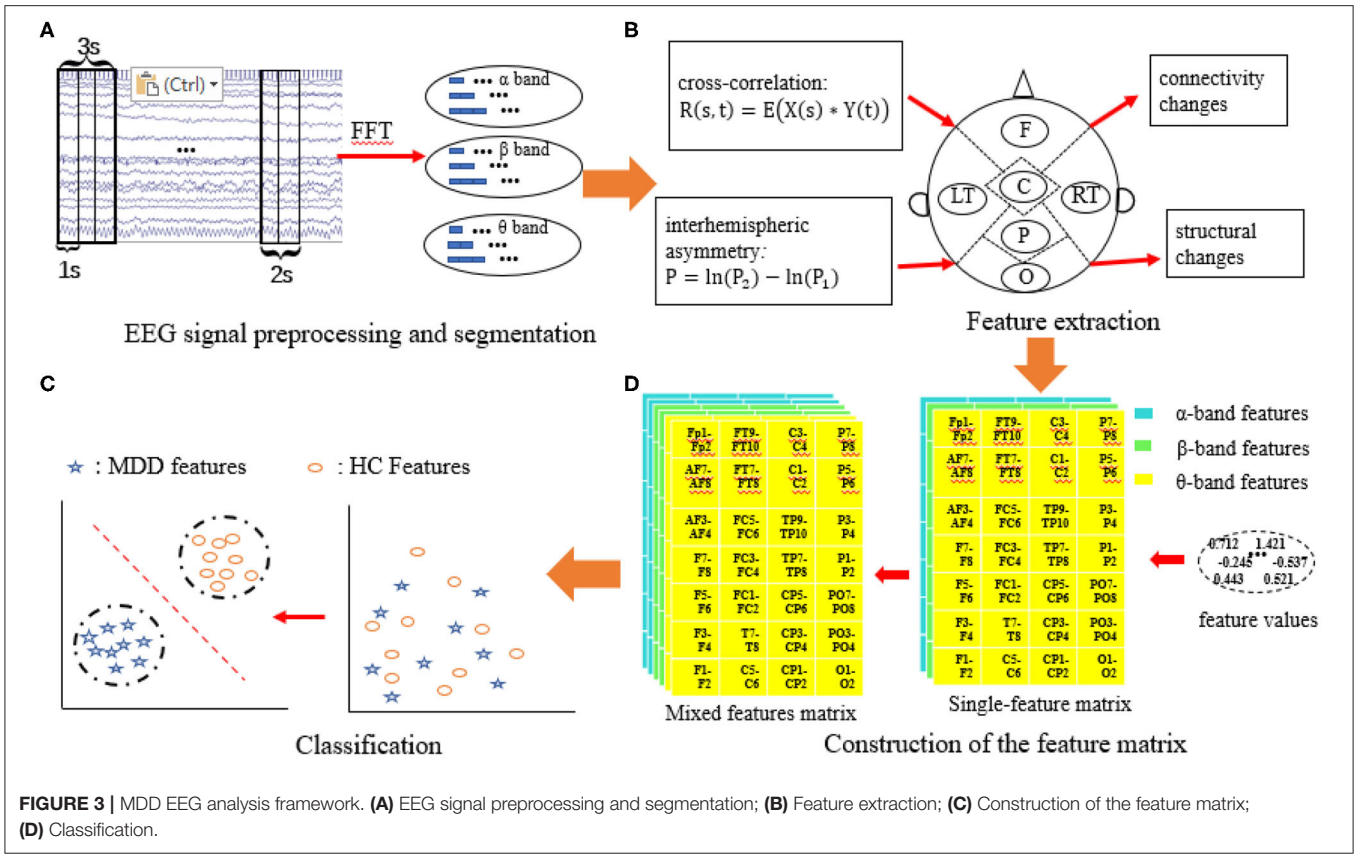

FIGURE 3 | MDD EEG analysis framework. **(A)** EEG signal preprocessing and segmentation; **(B)** Feature extraction; **(C)** Construction of the feature matrix; **(D)** Classification.

TABLE 2 | Basic information on the samples.

Time window size (s)	1		2		3	
Sample label	**MDD**	**HC**	**MDD**	**HC**	**MDD**	**HC**
Number of samples	20,143	16,708	10,068	8,349	5,031	4,172

Cross-correlation

The formula for calculating the correlation coefficient of the two symmetric electrodes X(s) and Y(t) is:

$$R(s,t) = E(X(s) * Y(t)) \tag{2}$$

where * indicates the convolution of the two sequences. The correlation coefficient is normalized by:

$$\mathrm{R} = \frac{\hat{\mathrm{R}} - \min(\mathrm{R})}{\max(\mathrm{R}) - \min(\mathrm{R})} \tag{3}$$

The range of R is from 0 to 1. The larger the value of the correlation is, the greater the correlation between the two electrodes.

Feature mixing

The features are extracted and constructed into data matrices. To avoid information loss for a single feature and to improve the classification accuracy, the EEG features are combined. Two ways of combining features are attempted to provide a better presentation of human brain state changes in MDD. To remedy the information deficiency of single features, the two single features (the feature matrix) are added together using formula (4). To reduce the amount of redundant information, the two types of features are combined using formula (5).

$$MIX1 = \frac{k_1}{k_1 + k_2} * F_1 + \frac{k_2}{k_1 + k_2} * F_2 \tag{4}$$

$$MIX2 = \frac{k_1}{k_1 + k_2} * F_1 - \frac{k_2}{k_1 + k_2} * F_2 \tag{5}$$

where k_1 and k_2 are the ingredient coefficients of the two features and their range is from 0 to 1; both k_1 and k_2 are set to 0.5. F_1 denotes the interhemispheric asymmetry matrix, and F_2 denotes the cross-correlation matrix. MIX1 is an index indicating the integrated brain state of interhemispheric asymmetry and cross-correlation. MIX2 is an index indicating the difference in the brain state of interhemispheric asymmetry and cross-correlation.

Construction of the Feature Matrix

Three feature matrices are constructed to feed into the classifiers: two are single-feature matrices, and the third is the mixed-feature matrix.

The single-feature matrix contains three layers: the first layer is α interhemispheric asymmetry (or cross-correlation),

the second layer is β interhemispheric asymmetry (or cross-correlation) and the last layer is θ interhemispheric asymmetry (or cross-correlation).

The mixed-feature matrix contains six layers: the first two layers are the MIX1 and MIX2 feature matrices in the α band, the middle two layers are the MIX1 and MIX2 feature matrices in the β band, and the last two layers are the MIX1 and MIX2 feature matrices in the θ-frequency band. Thus, the size of the single-feature input matrix is $7 \times 4 \times 3$, while the size of the mixed-feature input matrix is $7 \times 4 \times 6$. The structure of the single-feature matrix and mixed feature matrix are shown in **Figure 4**.

Classification

Classifier

Selecting a suitable classifier is important for MDD identification, and the KNN, SVM, and CNN algorithms are used to verify the effectiveness of the extracted features.

The KNN algorithm, which was proposed by Dasarathy (Dasarathy, 1997) in 1991, is a basic machine learning method used for classification and regression. It is adept at handling noise and large datasets. It performs classifications by a majority voting of the neighbors, with the case being assigned to the class most common among its K-nearest neighbors measured by a distance function. The algorithm involves three main factors: a training set, distance or similarity measure, and the size parameter K. Several distance metrics are utilized to define the distance or similarity in the KNN technique. To avoid the matching problem between objects, the Euclidean distance is used. The KNN algorithm has been widely used in EEG signal detection fields, such as epilepsy (Acharya et al., 2012), anxiety disorder (Wang et al., 2013), and depression (Rowley and Kanade, 1998). In this study, K is set to 7 to ensure a better classification accuracy.

The SVM algorithm, which was proposed by Cortes and Vapnik (Cortes, 1995) in 1995, is a supervised machine learning method used in classification and regression. The SVM algorithm can discriminate non-linearly separable data by mapping them to higher dimension space by using a kernel function to make the data more separable. We chose a poly kernel function; the degree of the polynomial is set to 3, gamma is set to 2, and the maximum number of iterations is set to 30,000.

CNN is a kind of feedforward neural network with a deep structure and convolutional computations, and it is one of the representation algorithms of deep learning. The CNN used in this study mainly contains three layers: a convolutional layer, a pooling layer and a fully connected layer. The structure of the CNN is shown in **Figure 5**. As shown in the figure, in the convolutional layer, two $2 \times 2 \times 3$ convolution kernels are selected. The outputs of the convolutional layers are two $7 \times 4 \times 2$ feature maps, and they are the input of the pooling layer. We chose max pooling, and the step size is set to 1. After reshaping, the output matrix is resized $1 \times 1 \times 56$, and it is input into the fully connected layer. To overcome overfitting in the fully connected layer, the dropout method is applied to each layer, and 50% of the training results are retained.

Evaluation of the classification performance

To evaluate the performance of different classifiers with different EEG features, the following statistical measures are utilized.

(1) Accuracy: The accuracy is defined as the percentage of correctly classified EEG segments of MDD patients and HCs, and it is defined mathematically in formula (6). False positives (FP) and false negatives (FN) are misclassifications of MDD and HC, respectively.

$$Accuracy = \frac{TP + TN}{TP + FN + TN + FP} \tag{6}$$

where TP indicates the number of true positives, TN indicates the number of true negatives, FN indicates the number of false negatives and FP indicates the number of false positive.

(2) Sensitivity: The sensitivity is evaluated by the accuracy rate of the positive samples, and it is defined as the accuracy rate of the MDD EEG epochs and is given by formula (7).

$$Sensitivity = \frac{TP}{TP + FN} \tag{7}$$

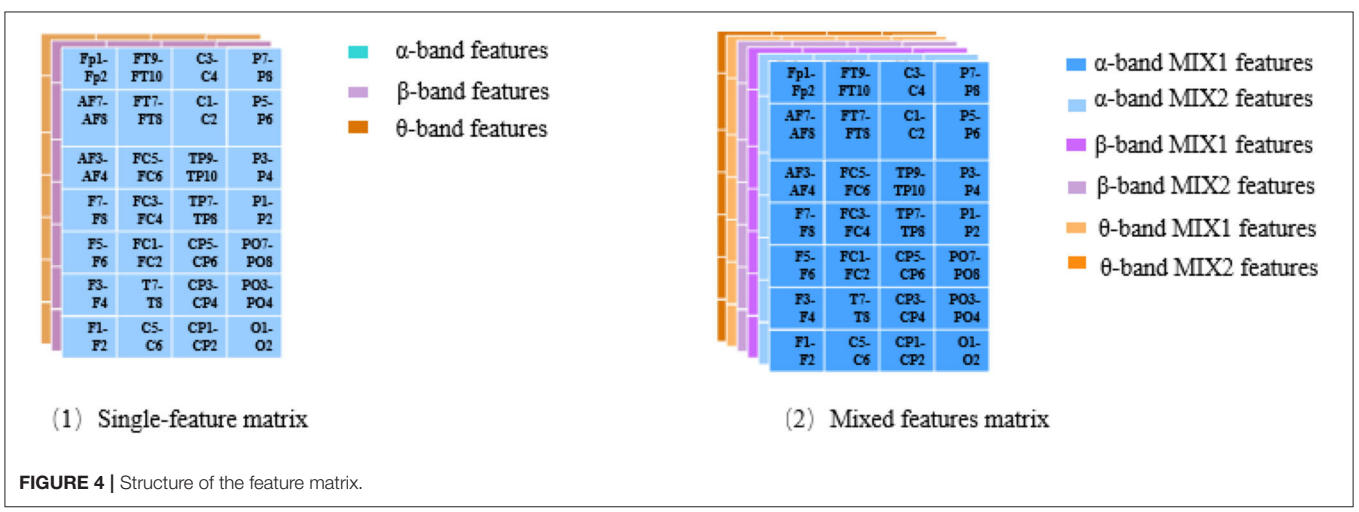

FIGURE 4 | Structure of the feature matrix.

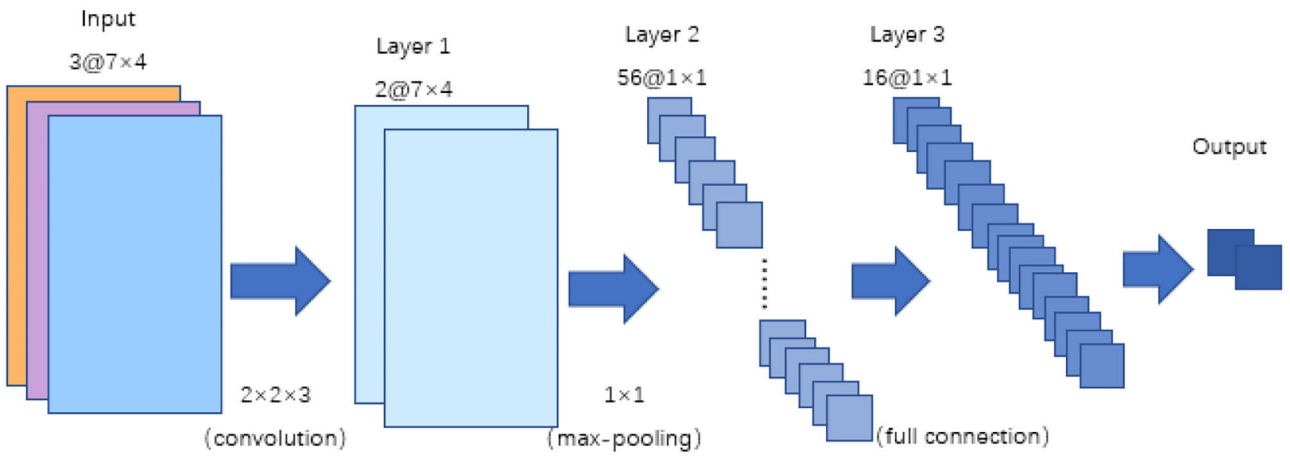

FIGURE 5 | Structure of the CNN.

(3) Specificity: The specificity is defined as the accuracy rate of the negative samples. It is defined as the accuracy rate of the HC EEG epochs and is given by formula (8).

$$Specificity = \frac{TN}{TN + FP} \tag{8}$$

(4) F1-score: The F1-score is regarded as the weighted average of the model precision and recall. It is defined by formula (9); its maximum value is 1, and its minimum value is 0.

$$F1 - score = \frac{2 * TP}{2 * TP + FP + FN} \tag{9}$$

RESULTS

To assess the ability of the proposed framework to detect and classify MDD EEG signals, several experiments are conducted, which mainly contain statistical analysis and classification. The statistical analysis was performed by one-factor analysis of variance (ANOVA) using SPSS 22.0. The classification is implemented in PyCharm (version 2017.3.4, Community Edition).

Statistical Analysis Results

ANOVA was used to examine significant differences between the two groups (patients MDD and HCs). The significance level was set to $p < 0.05$. Single features (asymmetry, cross-correlation) and mixed features (MIX1 and MIX2) in the different frequency bands (α band, β band, and θ band) are all analyzed. In terms of EEG segmentation, a segmentation of 2s is demonstrated and analyzed in detail in this study.

Statistical Analysis of the Interhemispheric Asymmetry

The results of the statistical analysis of the interhemispheric asymmetry in all the frequency bands of the MDD and HC groups are shown in **Figure 6A**. A positive value for the interhemispheric asymmetry indicates that the power value of the left brain is greater than that of the right brain. Similarly, a negative value for the interhemispheric asymmetry indicates that the power value of the left brain is less than that of the right brain.

As shown in **Figure 6A**, in the α-frequency band, the interhemispheric asymmetry in patients with MDD at C5-C6 is significantly higher than that of the HCs. In the β-frequency band, the significant electrode pairs for the interhemispheric asymmetry are from the whole brain except the parietal region, and the values for the patients MDD are significantly larger than those of the HCs. The significant electrode pairs of the interhemispheric asymmetry are from the frontal, central and occipital regions. From **Figure 6A**, it is easy to see that the values for the patients with MDD are significantly larger than those of the HCs, which indicates that the difference between the interhemispheric power in patients with MDD is larger than that in HCs. The importance of EEG alpha interhemispheric asymmetry in the diagnosis of depression is evident from various studies. For example, hypo-activation of the left frontal has been observed during MDD (Kemp et al., 2010).

Statistical Analysis of the Cross-Correlation

The results of the statistical analysis of the cross-correlation in patients with MDD and HCs are shown in **Figure 6B**. The significant electrode pairs in the α-frequency band came from the whole brain except for the occipital region, and the cross-correlation in the patients with MDD was significantly larger than that in the HCs, which means that compared with the HCs, EEG connectivity in patients with MDD in the α-frequency band was enhanced. There was no significant difference in patients with MDD and HCs in terms of the cross-correlation in the θ-frequency band. The significant electrode pairs of cross-correlation in the β-frequency band came from the parietal and central regions, and the cross-correlation values for the patients with MDD were significantly larger than those of the HCs. From the results of the statistical analysis of the cross-correlation, it is easy to see that patients with MDD have more brain connectivity

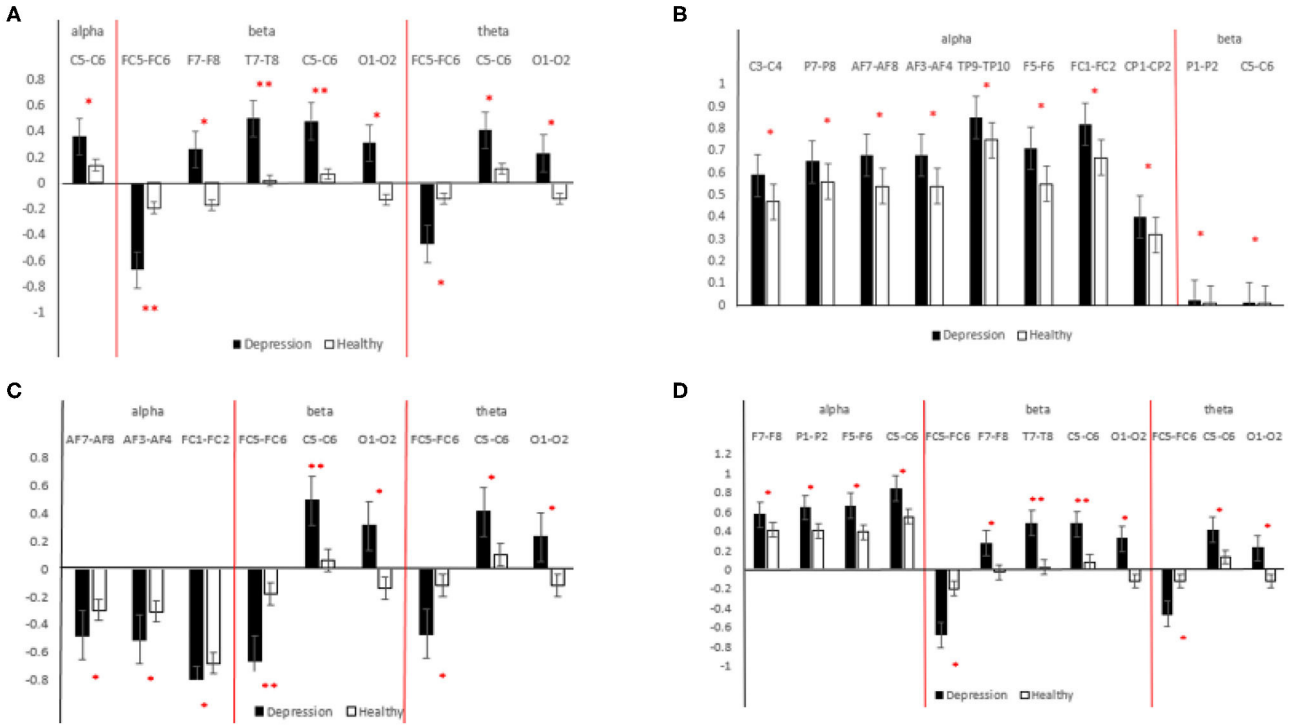

FIGURE 6 | Statistical analysis results for different features [**(A)** interhemispheric asymmetry; **(B)** cross-correlation; **(C)** MIX1; **(D)** MIX2]. The black bar indicates the MDD group, and the white bar indicates the HCs. **indicates $0.001 < p < 0.01$, *indicates $0.01 < p < 0.05$.

than HCs. EEG signals in depression have connectivity features. Knott et al. (2001) reported that significant group differences in inter-hemispheric coherence pervaded all four frequency bands.

Statistical Analysis of MIX1

The results of the statistical analysis of MIX1 in all the frequency bands of the patients with MDD and the HCs are shown in **Figure 6C**. As shown in this figure, for significant electrode pairs in all the frequency bands, the value of MIX1 in the patients with MDD is larger than that in the HCs. MIX1 indicates the integrated brain state of interhemispheric asymmetry and cross-correlation. In the α-frequency band, the significant electrode pairs are all from the frontal region. In the β-frequency band, the significant electrode pairs are from the frontal, central and occipital regions. For brain regions such as central, temporal, frontal and parietal, the depressed individual showed greater anterior EEG activity. In a study, greater left frontal activity is associated with fewer depressive symptoms (Deslandes et al., 2008).

Statistical Analysis of MIX2

The results of the statistical analysis of MIX2 in all the frequency bands of the patients with MDD and the HCs are shown in **Figure 6D**. MIX2 is an index indicating the differential brain state of the interhemispheric asymmetry and cross-correlation. As shown in **Figure 6D**, for significant electrode pairs in all the frequency bands, the value of MIX2 in the patients with MDD is larger than that of the HCs. The significant electrode pairs in the α-frequency band are from the frontal, central and parietal regions. The significant electrode pairs in the β- and θ-frequency bands are from the frontal, central and occipital regions. In addition to α-frequency band, activity in other bands such as θ-frequency band has shown relevance such as a decreased frontal theta activity has also been reported (Saletu et al., 2010).

Classification Results

A 10-fold cross-validation scheme is performed to prevent overfitting. All the feature matrices are randomly divided into 10 groups, nine of which are used for training, and the other group is used for verification. To ensure the stability of the classification model, each experiment is performed 10 times, and the averaged value is considered the result. At the same time, we set the shuffle parameter in this method to shuffle the data before splitting into batches. In this way, we reduce the error rate. The interhemispheric asymmetry, cross-correlation, and mixed features of the 1s, 2s, and 3s segments of the α-, β-, and θ-frequency bands in the MDD and HC groups were analyzed. The classification results are given in **Table 3**. In **Table 3**, the standard error of the classification results is around 0.001.

Table 3 presents the classification results in terms of the accuracy, sensitivity, specificity and the F1-score (f1) for the 1s, 2s, and 3s EEG epochs for each of the classifiers. **Table 3** shows that the F2 (cross-correlation) and F1 (asymmetry) are more suitable for MDD detection than the mixed features. Each classification index for F1 is ∼85%, while each classification

TABLE 3 | Classification results of the EEG signals from all classifiers.

Classifiers	Feature	1s				2s				3s			
		Acc (%)	Sen (%)	Spe (%)	f1 (%)	Acc (%)	Sen (%)	Spe (%)	f1 (%)	Acc (%)	Sen (%)	Spe (%)	f1 (%)
KNN	F1	79.10	86.58	70.07	81.89	81.76	88.19	74.04	84.08	80.74	87.76	72.29	83.27
	F2	62.38	71.29	51.64	67.43	59.98	68.81	49.38	65.25	81.74	83.01	80.10	82.70
	MF	79.50	87.29	70.13	82.30	83.15	88.97	76.14	85.22	82.43	88.51	75.10	84.61
SVM	F1	83.78	85.88	81.52	85.36	84.13	86.24	81.60	85.59	82.83	85.53	79.62	84.46
	F2	76.31	78.55	73.62	78.36	80.91	83.15	78.26	82.62	84.27	83.49	84.97	83.21
	MF	87.95	89.24	86.38	89.00	88.22	89.69	86.44	89.26	86.15	88.28	83.60	87.43
CNN	F1	91.10	91.45	89.42	91.62	92.70	93.72	91.27	93.52	92.11	93.62	92.23	91.64
	F2	93.14	92.41	94.17	93.61	93.07	93.25	92.24	94.45	93.31	94.43	93.27	92.87
	MF	94.10	93.61	91.69	93.82	**94.13**	**95.74**	**93.52**	**95.62**	93.58	94.74	93.72	94.81

F1 indicates asymmetry, F2 indicates cross-correlation and MF indicates mixed features. Acc indicates accuracy; Sen indicates the sensitivity; Spe indicates the specificity; f1 indicates the F1-score. Bold values indicates the best performance.

index for F2 is ∼70%. The results show the consistency in the performance of all the classifiers. The classification results of the KNN, SVM, and CNN models based on the mixed features are better than those of the single features.

Among all the classifiers, the CNN achieved the best performance with the mixed features for the 2s time window (accuracy = 94.13%, sensitivity = 95.74%, specificity = 93.52%, and f1 = 95.62%). For the SVM, the best classification results were achieved with the mixed features in the 2s time window (accuracy = 88.22%, sensitivity = 89.69%, specificity = 86.44%, and f1 = 89.26%). For the KNN, the best performance was achieved with the mixed features in the 2s time window (accuracy = 83.15%, sensitivity = 88.97%, specificity = 76.14%, and f1 = 89.26%). Compared with the segmentation results for the 1s and 3s EEG epochs, and the segmentations of the 2s time window achieve better classification results.

DISCUSSION

We attempted to discover the useful features reflecting the intrinsic changes in brain activity in depressed patients to construct an automatic system for MDD detection. Two types of feature matrices were computed for MDD detection, and three classifiers were introduced to classify the EEG data from patients with MDD and HCs. First, the feature matrix for interhemispheric asymmetry was fed to three classifiers, and we obtained the best classification accuracy of 92.70% using the CNN algorithm. Second, the feature matrix for electrode connectivity was fed to the three classifiers, and we achieved the best accuracy result of 93.31% using the CNN algorithm. Finally, the two types of features were added and subtracted to form mixed features for the classification, and the accuracy was greatly improved for the three classifiers. Therefore, we concluded that the feature-combining strategy is effective. Statistical analysis and automatic classification based on the extracted and mixed features were performed. The statistical analysis explored the difference in the patients with MDD and the HCs at the group level, while the classification method studied the EEG of patients' MDD in another way.

In this study, greater left frontal activity was associated with fewer depressive symptoms. In addition, EEG interhemispheric asymmetry was concluded to be a risk marker for MDD because the study participants with depressive symptoms showed less relative frontal activity than the HCs.

We also compared the detection results with those from other investigations; this comparison is given in **Table 4**, which shows that we achieved the best accuracy of 94.13% using the mixed features. In 2017, the accuracy was 91.67% using kernel eigen-filter-bank common spatial patterns (Knott et al., 2001). Compared with the accuracy of 60–80% involving 48 depressed patients and 26 HCs based on the Lep-Ziv complexity (Deslandes et al., 2008), our system was considerably improved. Of course, the comparisons may be improper as we used different datasets, but our analysis at least implies the importance of our feature extraction and mixing strategy. We will collect more subject EEGs for future investigations, as 32 subjects are not enough to validate the effectiveness of the developed system. Other nonlinear EEG features related to the human brain, such as fractal dimension and entropy, should be analyzed and introduced into the feature combination for MDD detection.

CONCLUSION

In this study, we propose a feature extraction and mixing method to try to discover the correlated characteristics describing intrinsic changes in depressed patients, and the feature extraction and classifiers are integrated to construct a system for the discrimination of MDD. Both interhemispheric asymmetry and cross-correlation were extracted to analyze the structural and connective changes in the EEG signals of MDD patients. The two features were combined in two ways to comprehensively interpret the brain state of MDD. Both features were helpful for MDD detection. The classification accuracy based on interhemispheric asymmetry was ∼85% for the three classifiers, while the

TABLE 4 | Summary of previous works on EEG signal analysis for depression.

Paper format	Year	Sample size	Feature(s) used	Analysis method	Accuracy
Mantri et al. (2015)	2015	13 MDD and 12 HC	Power spectrum, FFT	ANN	84%
Akdemir (2015)	2015	53 MDD and 43 HC	EEG band power	DT	80%
Liao et al. (2017)	2017	12 MDD and 12 HC	Kernel eigen-filter-bank common spatial patterns	SVM	91.67%
Mumtaz et al. (2017b)	2017	34 MDD and 30 HC	Wavelet transform	LR	87.5%
Acharya et al. (2018)	2018	33 MDD and 30 HC	Left and right hemispheres	CNN	93.5% and 96%
Fan et al. (2005)	2019	48 HCC and 26 HC	Lep-Ziv complexity BP	ANN	60-80%
Our Study		16 MDD and 16 HC	Asymmetry, cross-correlation, mixed features	CNN	94.13%

classification accuracy based on cross-correlation was ∼70% using the three classifiers. The classification results using the mixed features were greatly improved compared with using the single features. We also found that the mixed features with a 2s time window using a CNN perform the best.

The proposed depressed patient detection system is promising for exploring the pathogenesis, early diagnosis, and intervention treatment of MDD. In future research, we will try to investigate more useful information for MDD detection and emotion decoding.

DATA AVAILABILITY STATEMENT

The datasets generated for this study are available on request to the corresponding author.

ETHICS STATEMENT

The studies involving human participants were reviewed and approved by Ethics Committee of Beijing Anding Hospital, Capital Medical University. The patients/participants provided their written informed consent to participate in this study. Written informed consent was obtained from the individual(s).

AUTHOR CONTRIBUTIONS

HD and LD designed this study and revised and guided the experiment. HD and SQ wrote this manuscript and participated in the whole experiment process. XZ and YQ managed the whole experiment and analyzed the data. LD, SS and CW participated all the experiments. YQ, JH, XH and CW helped for the sampling process. All authors read and approved the final manuscript.

FUNDING

This research was sponsored in part by the National Natural Science Foundation of China (Nos. 61672070 and 61572004), the Key Project of Beijing Municipal Education Commission (No. KZ201910005008), the Beijing Municipal Natural Science Foundation (Nos. 4202025 and 4182005), the Beijing Municipal Administration of Hospitals Clinical Medicine Development of Special Funding Support (No. ZYLX201607), the Beijing Municipal Administration of Hospitals' Ascent Plan (No. DFL20151801), the Beijing Municipal Science & Tech Commission (No. Z171100000117004), and the Clinical Technology Innovation Program of Beijing Municipal Administration of Hospitals (No. XMLX201805).

REFERENCES

Acharya, U. R., Molinari, F., Vinitha Sree, S., Chatttopadhyay, S., Ng, K. H., and Suri, J. S. (2012). Automated diagnosis of epileptic eeg using entropies. *Biomed. Signal Process. Control* 7, 401–408. doi: 10.1016/j.bspc,.2011.07.007

Acharya, U. R., Oh, S. L., Hagiwara, Y., Tan, J. H., Adeli, H., and Subha, D. P. (2018). Automated EEG-based screening of depression using deep convolutional neural network. *Comp. Methods Progr. Biomed.* 161, 103–113. doi: 10.1016/j.cmpb.2018.04.012

Akdemir, A. S, and Kara, S. (2015). Nonlinear analysis of eegs of patients with major depression during different emotional states. *Comp. Biol. Med.* 67, 49–60. doi: 10.1016/j.compbiomed.2015.09.019

Alkan, A., and Kiymik, M. K. (2007). Comparison of ar and welch methods in epileptic seizure detection. *J. Med. Syst.* 30, 413–419. doi: 10.1007/s,109166-005-90011-0

Allen, J. J. B., and Reznik, S. J. (2015). Frontal eeg asymmetry as a promising marker of depression vulnerability: summary and methodological considerations. *Curr. Opin. Psychol.* 4, 93–97. doi: 10.1016/j.copsyc.2014.12.017

Allen, J. J. B., Urry, H. L., Hitt, S. K., and Coan, J. A. (2004). The stability of resting frontal electroencephalographic asymmetry in depression. *Psychophysiology* 41, 269–280. doi: 10.1111/j.14699-8986.2003.00149.x

Cantisani, A., Koenig, T., Horn, H., Muller, T. J., Strik, W., and Walther, S. (2015). Psychomotor retardation is linked to frontal alpha asymmetry in major depression. *J. Affective Disord.* 188, 167–172. doi: 10.1016/j.jad.2015.08.018

Cortes, C. V. V. (1995). Support-vector networks. *Machine Learning* 20, 273–297. doi: 10.1007/BF0F0994018

Dasarathy, B. V. (1997). Nearest neighbor (nn) norms: Nn pattern classification tech-niques. *Los Alamitos IEEE Computer Society Press* 13, 21–27. doi: 10.1109/TIT.1967.1053964

Delorme, A., and Makeig, S. (2004). Eeglab: an open source toolbox for analysis of single-trial eeg dynamics including independent component analysis. *J. Neurosci. Methods* 134, 9–21. doi: 10.1016/j.jneumeth.2003.10.009

Deslandes, A. C., de Moraes, H., Pompeu, F. A., and Ribeiro, P. (2008). Electroencephalographic frontal asymmetry and depressive symptoms in the elderly. *Biol. Psychol.* 79, 317–322. doi: 10.1016/j.biopsycho.2008.07.008

Fan, F. Y., Li, Y. J., Qiu, Y. H., and Zhu, Y. S. (2005). "Use of ann and complexity measures in cognitive eeg dis-crimination," in *27th Annual International Conference of the Engineering in Medicine and Biology Society*. Shanghai:IEEE. doi: 10.1109/IEMBS.2005.1615504

Filomena, S., Alda, T., Laurence, L. S., Alessandro, V., and Anna, E. (2016). How major depressive disorder affects the ability to decode multimodal dynamic emotional stimuli. *Front. ICT* 3:16. doi: 10.3389/fict.2016.00016

Hu, R. J. (2003). Diagnostic and statistical manual of mental disorders (dsm-iv). *Encyclopedia Neurol. Sci.* 25, 4–8. doi: 10.1016/B0B0-12-2268700-9/010700-4

Iseger, T. A., Korgaonkar, M. S., Kenemans, J. L., Grieve, S. M., Baeken, C., Fitzgerald, P. B., et al. (2017). Eeg connectivity between the subgenual anterior cingulate and prefrontal cortices in response to antidepressant medication. *Eur. Neuropsychopharmacol.* 27, 301–312. doi: 10.1016/j.euroneuro.2017.02.002

Kemp, K., Griffiths, K., Felmingham, S., and Shankman, W. (2010). Disorder specificity despite comorbidity: resting EEG alpha asymmetry in major depressive disorder and post-traumatic stress disorder. *Biol. Psychol.* 85, 350–354. doi: 10.1016/j.biopsycho.2010.08.001

Knott, V., Mahoney, C., Kennedy, S., and Evans, K. (2001). EEG power, frequency, asymmetry and coherence in male depression. *Psychiatry Res.* 106.2:140. doi: 10.1016/S.09255-4927(00)000800-9

Liao, S. C., Wu, C-T., Huang, H-C., Cheng, W-T., and Liu, Y-H. (2017). Major depression detection from eeg signals using kernel eigen-filter-bank common spatial patterns. *Sensors* 17:1385. doi: 10.3390/s1s7061385

Mantri, S., Patil, D., Agrawal, P., and Wadhai, V. (2015). Non invasive eeg signal processing framework for real time depression analysis. *Sai Intelligent Systems Conference*. IEEE. 518–521. doi: 10.1109/IntelliSys.2015.7361188

Michalopoulos, K., Bourbakis, N. (2015). Combining EEG microstates with fMRI structural features for modeling brain activity. *Int. J. Neural Syst.* 2015:1550041. doi: 10.1142/S0S129065715500410

Mumtaz, W., Xia, L., Azhar Ali, S. S., Mohd Yasin, M. A., Hussain, M., Saeed Malik, A. (2017a). Electroencephalogram (eeg)-based computer-aided technique to diagnose major depressive disorder (mdd). *Biomed. Signal Process. Control* 31, 108–115. doi: 10.1016/j.bspc.2016.07.006

Mumtaz, W., Xia, L., Mohd Yasin, M. A., Azhar Ali, S. S., and Malik, A. S. (2017b). A wavelet-based technique to predict treatment outcome for major depressive disorder. *PLoS ONE* 12:0171409. doi: 10.1371/journal.pone.0171409

Rowley, H. A., and Kanade, S. B. T. (1998). Neural networkbased face detection. *IEEE Trans. Pattern Anal. Machine Intellgence* 20, 23–38. doi: 10.1109/34.655647

Saletu, B., Anderer, P., and Saletu-Zyhlarz, G. (2010). EEG topography and tomography (LORETA) in diagnosis and pharmacotherapy of depression. *Clin. EEG Neurosci.* 41, 203–210. doi: 10.1177/155005941004100407

Schmidt, M. T., Kanda, P. A. M., Basile, L. F. H., Frederico, D. S. L. H., Regina, B., Demario, J. L. C., et al. (2013). Index of alpha/theta ratio of the electroencephalogram: a new marker for alzheimer's disease. *Front. Aging Neurosci.* 5:60. doi: 10.3389/fnagi.2013.00060

Ting, W., Guozheng, Y., Banghua, Y., and Hong, S. (2008). Eeg feature extraction based on wavelet packet decomposition for brain computer interface. *Measurement* 41, 618–625. doi: 10.1016/j.measurement.2007.07.007

Tóth, B., Bálint, B., Boha, R., Kardos, Z., Hidasi, Z., Gaál, Z. A., et al. (2014). Eeg network connectivity changes in mild cognitive impairment—preliminary results. *Int. J. Psychophysiol.* 92, 1–7. doi: 10.1016/j.ijpsycho.2014.02.001

Wang, J-S., Lin, C. W., and Yang, Y.-T.C. (2013). A k-nearest-neighbor classifer with heart rate variability feature-based transformation algorithm for driving stress recognition. *Neuro-computing* 116, 136–143. doi: 10.1016/j.neucom.2011.10.047

Wei, Q., Bai, T. J., Chen, Y., Ji, G. J., Hu, X. P., Xie, W., et al. (2018). The changes of functional connectivity strength in electroconvulsive therapy. *Front. Neurosci.*12:661. doi: 10.3389/fnins.2018.00661

World Health Organization (2020). *Depression*. Available online at: http://www.who.int/mediacentre/factsheets/fs369/en/ (accessed December 10, 2019).

Conflict of Interest: The authors declare that the research was conducted in the absence of any commercial or financial relationships that could be construed as a potential conflict of interest.

frontiers in Neuroscience

ORIGINAL RESEARCH
published: 14 October 2020
doi: 10.3389/fnins.2020.567797

Cross-Subject Commonality of Emotion Representations in Dorsal Motion-Sensitive Areas

Yin Liang[1]* *and Baolin Liu*[2]*

[1] Faculty of Information Technology, College of Computer Science and Technology, Beijing Artificial Intelligence Institute, Beijing University of Technology, Beijing, China, [2] School of Computer and Communication Engineering, University of Science and Technology Beijing, Beijing, China

Emotion perception is a crucial question in cognitive neuroscience and the underlying neural substrates have been the subject of intense study. One of our previous studies demonstrated that motion-sensitive areas are involved in the perception of facial expressions. However, it remains unclear whether emotions perceived from whole-person stimuli can be decoded from the motion-sensitive areas. In addition, if emotions are represented in the motion-sensitive areas, we may further ask whether the representations of emotions in the motion-sensitive areas can be shared across individual subjects. To address these questions, this study collected neural images while participants viewed emotions (joy, anger, and fear) from videos of whole-person expressions (contained both face and body parts) in a block-design functional magnetic resonance imaging (fMRI) experiment. Multivariate pattern analysis (MVPA) was conducted to explore the emotion decoding performance in individual-defined dorsal motion-sensitive regions of interest (ROIs). Results revealed that emotions could be successfully decoded from motion-sensitive ROIs with statistically significant classification accuracies for three emotions as well as positive versus negative emotions. Moreover, results from the cross-subject classification analysis showed that a person's emotion representation could be robustly predicted by others' emotion representations in motion-sensitive areas. Together, these results reveal that emotions are represented in dorsal motion-sensitive areas and that the representation of emotions is consistent across subjects. Our findings provide new evidence of the involvement of motion-sensitive areas in the emotion decoding, and further suggest that there exists a common emotion code in the motion-sensitive areas across individual subjects.

Keywords: functional magnetic resonance imaging, emotion perception, multivariate pattern analysis, motion-sensitive areas, cross-subject decoding

OPEN ACCESS

Edited by:
Yu Zhang,
Stanford University, United States

Reviewed by:
Kaundinya S. Gopinath,
Emory University, United States
Zhuo Fang,
University of Ottawa, Canada

***Correspondence:**
Yin Liang
yinliang@bjut.edu.cn
Baolin Liu
liubaolin@tsinghua.edu.cn

Specialty section:
This article was submitted to Brain Imaging Methods, a section of the journal Frontiers in Neuroscience

Received: *30 May 2020*
Accepted: *22 September 2020*
Published: *14 October 2020*

Citation:
Liang Y and Liu B (2020) Cross-Subject Commonality of Emotion Representations in Dorsal Motion-Sensitive Areas. Front. Neurosci. 14:567797. doi: 10.3389/fnins.2020.567797

INTRODUCTION

The ability to understand emotions is a crucial social skill in humans. It has been proposed that body language plays an important role in conveying emotions (Calbi et al., 2017). Body language refers to the non-verbal signals in which physical behaviors, including facial expressions, body posture, gestures, eye movement, touch and the use of space, are used to express our true

feelings and emotions. According to experts, these non-verbal signals make up a huge part of our daily communication. Humans can easily recognize others' emotions from their whole-person expressions and perceive them in a categorical manner. Since the human brain can readily decode emotions, considerable functional magnetic resonance imaging (fMRI) studies have investigated the potential neural substrates and mechanisms underlying the perception of emotions.

Neuroimaging studies on emotion perception have used emotional faces or non-face bodies as stimuli and identified specific areas showing preferential activation patterns, respectively known as face-selective and body-selective areas. Classical face-selective areas mainly contain the fusiform face area (FFA), occipital face area (OFA), and superior temporal sulcus (STS), which are together considered the "core system" in Haxby's model (Haxby et al., 2000; Kanwisher and Yovel, 2006; Gobbini and Haxby, 2007; Pitcher, 2014; Henriksson et al., 2015). Emotional bodies are found to be represented in the extrastriate body area (EBA) and fusiform body area (FBA), and some similarities have been revealed between the processing of emotional bodies and faces (Minnebusch and Daum, 2009; de Gelder et al., 2010; Kret et al., 2011; Downing and Peelen, 2016). In addition, the STS, which acts as a crucial node for social information processing, has been found to be involved in the processing of emotions in both faces and bodies (Candidi et al., 2011; Zhu et al., 2013). Previous fMRI studies mainly assessed the perception of emotions using either isolated faces or non-face bodies as visual stimuli. However, behavioral studies have indicated that human brain prefers whole-person expressions which contain both the face and body parts, similar to that which we commonly perceive in real scenes, and encoding whole-person expressions in a holistic rather than part-based manner (Soria Bauser and Suchan, 2015). Therefore, it is essential to explore the neural representation of whole-person expressions individually rather than in an integrated manner based on the isolated emotional faces and bodies (Zhang et al., 2012; Soria Bauser and Suchan, 2015). Moreover, most previous studies used static emotional images as stimuli, but, considering that the emotions we mostly encounter in a natural context are dynamic, recent studies have proposed that dynamic stimuli are more ecologically valid than their static counterparts (Johnston et al., 2013; Yang et al., 2018). Thus, using dynamic emotional stimuli may be more appropriate to investigate the authentic mechanisms used to recognize emotions in daily life.

Compared to univariate analyses that estimate emotion-evoked responses, a multivariate pattern analysis (MVPA), as demonstrated by recent fMRI studies, can take advantage of distributed activation patterns in fMRI data, thus providing a more effective method to infer the functional roles of cortical regions in emotion perception (Mahmoudi et al., 2012). A growing number of studies have used ROI-based MVPA to explore emotion decoding performances in specific brain areas (Said et al., 2010; Harry et al., 2013; Wegrzyn et al., 2015). In addition, studies with dynamic stimuli have found that dorsal motion-sensitive areas within human motion complex (hMT) + /V5 and STS exhibited significant responses to facial expressions (Furl et al., 2013, 2015). A macaque study identified motion-sensitive areas in the STS, which may be homologous to human STS, and found that facial expressions could be successfully decoded from motion-sensitive areas (Furl et al., 2012). Moreover, one of our recent studies has also identified the successful decoding of dynamic facial expressions in motion-sensitive areas (Liang et al., 2017). These findings suggest that motion-sensitive areas may transmit measurable quantities of expression information and may play an important role in emotion perception. However, these studies only used facial expressions as stimuli, and the full role of motion-sensitive areas in the decoding of whole-person expressions therefore remains unclear. Since we commonly perceive emotions from whole-person expressions in our daily lives, exploring the decoding performance of whole-person expressions in motion-sensitive areas may be meaningful in revealing the potential mechanisms by which the human brain efficiently recognizes emotions from body movements. Furthermore, if emotions are represented in the motion-sensitive areas, we may further ask whether emotion codes in the motion-sensitive areas can be shared across individual subjects. This would shed light on whether an individual's subjective emotion representation in motion-sensitive areas corresponds to those observed in others, which would be helpful in assessing the commonality and variability of emotion coding.

In this study, we conducted a regions of interest (ROI) MVPA to assess the potential role of dorsal motion-sensitive areas in emotion decoding. We performed a block-design fMRI experiment and collected neural images while participants viewed emotional videos expressed by whole-person expressions (joy, anger, and fear). Dynamic emotion stimuli were used in this study to enhance ecological validity and to assess the authentic mechanisms of emotion recognition in daily life. A separate localizer was used to identify individual-defined motion-sensitive ROIs. We first examined whether emotions could be decoded based on the activation patterns from motion-sensitive ROIs, after which we examined whether there exists a common representation of emotions in motion-sensitive areas across individuals.

MATERIALS AND METHODS

Participants

A total of 24 healthy, righted-handed college students participated in the experiment (12 males, ranging from 19–25-years-old). All subjects had normal or corrected-to-normal vision, with no history of neurological disorders, and signed informed written consent forms before the experiment. Experimental procedures were explained to them before the scanning. The threshold for head motion was framewise displacement (FD) < 0.5 mm (Power et al., 2012). Four subjects were discarded due to excessive head motion, and the final fMRI analysis was focused on the data of 20 subjects (10 males, mean age 21.8 ± 1.83 years old). This experiment was approved by the local Ethics Committee of Yantai Affiliated Hospital of Binzhou

Medical University. A separate group of subjects (n = 18, 8 females, mean age: 22.2 years old) participated in a preliminary behavioral experiment for the stimulus validation.

Experimental Procedures

The fMRI experiment was based on a block design, with four "main experiment" runs for the emotion perception task and one "localizer" run for the ROI identification. A separate localizer was used in our study to ensure that the data used for the ROI definition was independent of the data used for the classification in the main experiment analysis (Axelrod and Yovel, 2012, 2015; Furl et al., 2013; Harry et al., 2013).

Figure 1A shows the process of the main experiment. Each run began with a 10 s fixation cross followed by 18 stimulus blocks presented in a pseudo-random order (Axelrod and Yovel, 2012; Furl et al., 2013, 2015). Successive stimulus blocks were separated by 10 s intervals of a fixation cross. For the first three runs, three emotions (joy, anger, and fear) expressed by three stimulus types (facial, non-face bodily, and whole-person stimuli) were presented in different blocks, while for the fourth run, only three emotions expressed by the whole-person stimuli were presented. In each block, eight video clips of different examples per emotion category were displayed (each for 2000 ms), with an interstimulus interval (ISI) of 500 ms. At the end of each block, there was a 2 s button task instructing participants to indicate the emotion category they had seen by pressing a button. The emotion stimuli were taken from the geneva multimodal emotion portrayals (GEMEP) corpus (Banziger et al., 2012). Videos of eight individuals (four males and four females) displaying three emotions (joy, anger, and fear) were selected as whole-person emotion stimuli (Cao et al., 2018; Yang et al., 2018). Facial and bodily emotion stimuli were generated from the whole-person videos by cutting out and obscuring the irrelevant part with Gaussian blur masks using Adobe Premiere Pro CC (Kret et al., 2011). All video clips were cropped to 2,000 ms (25 frames/s) to retain the transition from a neutral expression to the emotion apex, and were converted into grayscale using MATLAB (Furl et al., 2012, 2013, 2015; Kaiser et al., 2014; Soria Bauser and Suchan, 2015). The resulting videos were resized to 720 × 576 pixels and presented on the center of the screen. All generated emotion stimuli were validated by another group of participants before scanning, confirming the validity of the stimuli in representing all expressions. **Figure 1B** shows the examples of whole-person emotion stimuli in the main experiment.

In the functional localizer run, participants viewed video clips or static images of four categories: faces, non-face bodies, whole-persons and objects. Each category appeared two times in a pseudo-random order, resulting in 16 blocks in total (4 categories × video/image × 2 repetitions). Each block contained 8 stimuli (7 novel and 1 repeated), and each was presented for 1,400ms, separated by an ISI of 100 ms. Participants performed a "one-back" task during the localizer run, that is, to press a button when they observed two identical stimuli appearing in consecutive trials.

The stimuli were presented using E-Prime 2.0 Professional (Psychology Software Tools, Pittsburgh, PA, United States) and the behavioral results were collected using the response pad in the scanner. After scanning, participants were required to complete a questionnaire recording whether participants performed the experiment according to the instructions, their feelings during the fMRI experiment, and any difficulties they encountered.

Data Acquisition

Imaging data were acquired from Yantai Affiliated Hospital of Binzhou Medical University, using a 3.0-T SIEMENS MRI scanner with an eight-channel head coil. Acquisition parameters of task-related functional images and anatomical images were as follows: T2*-weighted functional images were collected using a gradient echo-planar imaging (EPI) sequence, with repetition time (TR) = 2,000 ms, echo time (TE) = 30 ms, voxel size = 3.1 mm × 3.1 mm × 4.0 mm, matrix size = 64 × 64, slices = 33, slices thickness = 4 mm, slice gap = 0.6 mm (Yang et al., 2018). T1-weighted anatomical images were acquired using a three-dimensional magnetization-prepared rapid-acquisition gradient echo (3D MPRAGE) sequence, with TR = 1,900 ms, TE = 2.52 ms, time of inversion (TI) = 1100 ms, voxel size = 1 mm × 1 mm × 1 mm, matrix size = 256 × 256. Participants viewed the emotion stimuli through the high-resolution stereo 3D glasses of the VisuaStim Digital MRI Compatible fMRI system. Foam pads and earplugs were used during scanning to reduce head motion and scanner noise.

Preprocessing

Statistical parametric mapping 8 (SPM8) software[1] was used to preprocess the functional and structural images. For each functional run, the first five volumes were discarded to minimize the magnetic saturation effect. Slice-timing and head motion correction were performed for the remaining functional images. The threshold for head motion was FD < 0.5 mm (Power et al., 2012). Next, the structural images were co-registered to the mean functional image after motion correction, and were then unified segmented into gray matter, white matter (WM) and cerebrospinal fluid (CSF). The functional data were spatially normalized to the standard Montreal Neurological Institute (MNI) space using normalization parameters estimated from the unified segmentation, after which the voxel size was re-sampled into 3 mm × 3 mm × 3 mm. Subsequently, the normalized functional images of the localizer run were spatially smoothed with a 6-mm full-width at half-maximum Gaussian kernel to improve the signal-to-noise ratio.

Localization of Dorsal Motion-Sensitive Regions of Interest (ROIs)

Individual ROIs were defined using the localizer run data in which participants viewed static and dynamic faces, non-face bodies, whole persons and objects. At the first-level (within-subject) analysis, a general linear model (GLM) was constructed for each subject to estimate the task effect for each condition: dynamic face, static face, dynamic body, static body, dynamic whole-person, static whole-person, dynamic object and static

[1] http://www.fil.ion.ucl.ac.uk/spm/software/spm8/

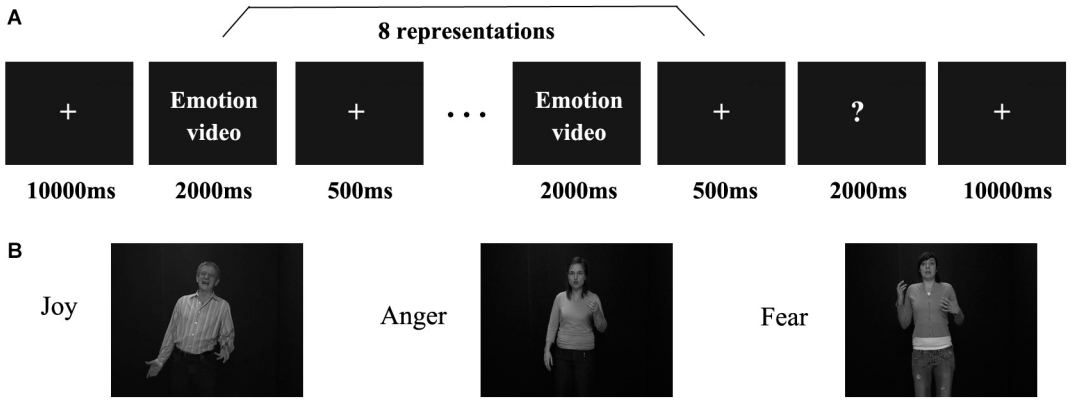

FIGURE 1 | Paradigm representation of the main experiment and example emotional stimuli. **(A)** Schematic representation of the paradigm used. A cross was presented for 10 s before each block, after which eight emotional stimuli appeared. Subsequently, participants completed a button task to indicate their identification of the emotion category they had seen in the previous block. **(B)** All emotional stimuli were taken from the geneva multimodal emotion portrayals (GEMEP) database. Videos of whole individuals displaying three emotions (joy, anger, and fear) were used in the experiment.

object. Each regressor was modeled by a boxcar function (representing the onsets and the durations of the stimulus blocks) convolved with a canonical hemodynamic response function (HRF). Several confounding nuisances were regressed out along with their temporal derivatives, including the realignment parameters from head motion correction and the physiological noise from WM and CSF were regressed using the CompCor (Behzadi et al., 2007; Whitfield-Gabrieli and Nieto-Castanon, 2012; Woo et al., 2014; Power et al., 2015; Xu et al., 2017; Geng et al., 2018). The low-frequency drifts of the time series were removed with a 1/128 Hz high-pass filter. The dorsal motion-sensitive ROIs were then identified by contrasting the average response to dynamic versus static conditions. The aim of using this contrast was to identify the motion-sensitive areas which are relatively domain-general, as both person and person parts, as well as those focused on non-person objects. We were especially interested in whether emotions perceived from whole-person expressions could be decoded from the relatively domain-general motion-sensitive areas, which are not specialized for representing only facial or bodily attributes. Thus, we chose to use a contrast which was expected to elicit motion areas to be domain general. Previous studies have showed that combined different types of stimuli together would be expected to localize motion-sensitive responses subsuming areas to be relatively domain-general (Furl et al., 2012, 2013, 2015; Liang et al., 2017). Therefore, to maximize the available data and to identify relatively domain-general motion-sensitive areas, we chose to average the results for ROI definition. We identified bilateral areas within human hMT + /V5 for all twenty subjects and bilateral STS areas for eighteen subjects, with two subjects only demonstrating a unilateral STS area in the left or right hemisphere. The ROIs were generated with a liberal threshold ($p < 0.05$; Skerry and Saxe, 2014; Miao et al., 2018; Yang et al., 2018). Individual subjects' motion-sensitive ROIs were defined as 9 mm spheres surrounding the peak coordinates. Subsequent emotion classification analyses were carried out based on these individually defined ROIs using the data from the main experiment runs. **Table 1** summarizes the average MNI coordinates (mean ± standard deviation SD) for each ROI, and **Figure 2** shows the statistical maps of the significant clusters in the ROI definition of a representative subject (uncorrected $p < 0.05$ with a cluster size > 20 voxels).

TABLE 1 | Localization of motion-sensitive regions of interest (ROIs) used in the decoding analysis of main experiment data.

Functional ROIs	Hemisphere	Number of Subjects	MNI Coordinates		
			x	*Y*	*z*
STS	L	19	−55 ± 10	−42 ± 5	14 ± 5
	R	19	57 ± 8	−39 ± 8	13 ± 6
hMT + /V5	L	20	−53 ± 5	−67 ± 5	6 ± 6
	R	20	53 ± 6	−64 ± 7	3 ± 5

Number of subjects in whom the ROIs were localized and the average Montreal Neurological Institute (MNI) coordinates (mean ± standard deviation SD) are reported. STS, superior temporal sulcus.

Within-Subject and Cross-Subject Emotion Classifications

Emotion classification analyses were conducted on the unsmoothed data from the main experiment (Harry et al., 2013; Yang et al., 2018) using a MVPA. We carried out MVPA classifications within ROIs that were functionally localized based on individual subject localizer runs. Similar procedures as those in previous MVPA studies were used in this study. For each participant, raw intensity values for all voxels within an ROI were extracted and normalized using the *z*-score function. The MVPA classification was carried out based on the multi-voxel activation patterns. Feature selection was performed using an ANOVA, which yielded a *p*-value for each voxel to tell the probability that a given voxel's activity varied significantly between emotion conditions. Feature selection was executed only on the training set to avoid peeking, and the threshold for ANOVA was $p < 0.05$. Next, the data were classified using a linear support vector

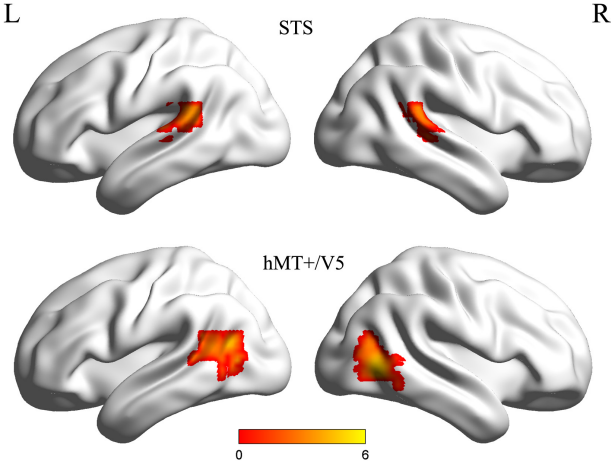

FIGURE 2 | Statistical maps of the significant clusters of superior temporal sulcus (STS) and hMT + /V5 of a representative subject (uncorrected $p < 0.05$ with a cluster size > 20 voxels). Individual subjects' motion-sensitive regions of interest (ROIs) were defined as 9 mm spheres surrounding the peak coordinates.

machine (SVM) that was implemented in LIBSVM[2] (Chang and Lin, 2011; Skerry and Saxe, 2014). The activation patterns for each condition were used to train and test the SVM classifier to perform classification over emotions. **Figure 3** represents the framework of our emotion classification analyses. We conducted two types of classifications in this section to assess the potential role of motion-sensitive ROIs in emotion decoding: first, a classical within-subject emotion classification was carried out as implemented in previous MVPA studies (classifier was trained and tested within the same subject data); next, a cross-subject emotion classification was conducted (classifier was trained iteratively on all subjects but one and tested on the remaining one) to assess whether there is any commonality to emotional representations in motion-sensitive areas across individual subjects. The cross-subject classification was performed using a leave-one-subject-out cross-validation (LOOCV) scheme (Chikazoe et al., 2014). In each fold of LOOCV, we trained the classifier in all but one subject and the remaining one was used as the test set. The cross-validation procedure was repeated until each subject was used as the test set, and the classification performance was averaged over all folds. The cross-subject classification was used to further investigate whether emotion codes in the motion-sensitive areas can be shared across subjects.

We ran both three-way (joy vs. anger vs. fear) and two-way (joy versus anger/fear, which could be considered as positive vs. negative) emotion classifications. The three-way classification was implemented similarly as previous MVPA studies (Wang et al., 2016; Liang et al., 2017), using a one-against-one voting strategy. That is, we obtained classifiers for each pair of emotions and these pairwise classifiers were then added to yield the linear ensemble classifier for each emotion. Classifying positive versus negative emotions is essential since these results basically demonstrate coarse-grained emotion codes which can clearly distinguish positive-to-negative valences in bipolar representations, all the while taking into account the fact that some regions may not classify specific emotions in a fine-grained way, but may be able to distinguish positive and negative valence emotion representations (Kim et al., 2017). Data were partitioned into multiple cross-validation folds and the classification accuracies were averaged across folds to yield a single classification accuracy in each ROI. For the within-subject emotion classification, a cross-validation was performed across blocks, while for the cross-subject emotion classification, the cross-validation folds were based on subjects (testing each participant's activation pattern by a classifier that was trained by all other participants). For the classification of positive versus negative emotions, half of the data from anger and fear conditions were randomly dropped for each cross-validation, equating the base rates and therefore generating a chance level of 0.5 (Kim et al., 2017; Cao et al., 2018). To evaluate the emotion decoding performance, the significance of the classification results was established as a group level one-sample *t*-test above chance level (with a chance of 0.33 for the classification of three emotions, and a chance of 0.5 for the classification of positive versus negative emotions; Wurm and Lingnau, 2015; Cao et al., 2018), and were subsequently corrected for multiple comparisons by false discovery rate (FDR) and Bonferroni corrections according to the number of ROIs.

[2]http://www.csie.ntu.edu.tw/~cjlin/libsvm/

RESULTS

Behavioral Results

Behavioral results of the emotion classification accuracies and the reaction times for each emotion (joy, anger, and fear) are summarized in **Table 2**. These results confirmed the validity of the emotion stimuli used in our experiment as all emotions were well recognized with a high level of accuracy. Paired *t*-tests for the classification accuracies and reaction times were performed among the three emotions. Results showed that the classification accuracy for joy was significantly higher than that for anger and fear and that there was no significant difference between the accuracies for anger and fear [joy vs. anger: $t_{(19)} = 1.831$, $p = 0.041$; joy vs. fear: $t_{(19)} = 2.333$, $p = 0.015$; anger vs. fear: $t_{(19)} = 1.286$, $p = 0.107$; one-tailed]. For the reaction times, participants showed a significantly quicker response to joy than to anger or fear, and the response time for anger was shorter than that for fear [joy vs. anger: $t_{(19)} = -3.514$, $p = 0.001$; joy vs. fear: $t_{(19)} = -6.180$, $p < 0.001$; anger vs. fear: $t_{(19)} = -3.161$, $p = 0.003$; one-tailed].

Within-Subject and Cross-Subject Emotion Decoding Results

In this section, we conducted MVPA emotion classifications based on the individually defined ROIs. Two types of classification analyses were performed to assess the potential role of the motion-sensitive ROIs in emotion decoding. The first one was a classical within-subject emotion classification which was implemented in a similar way as previous MVPA

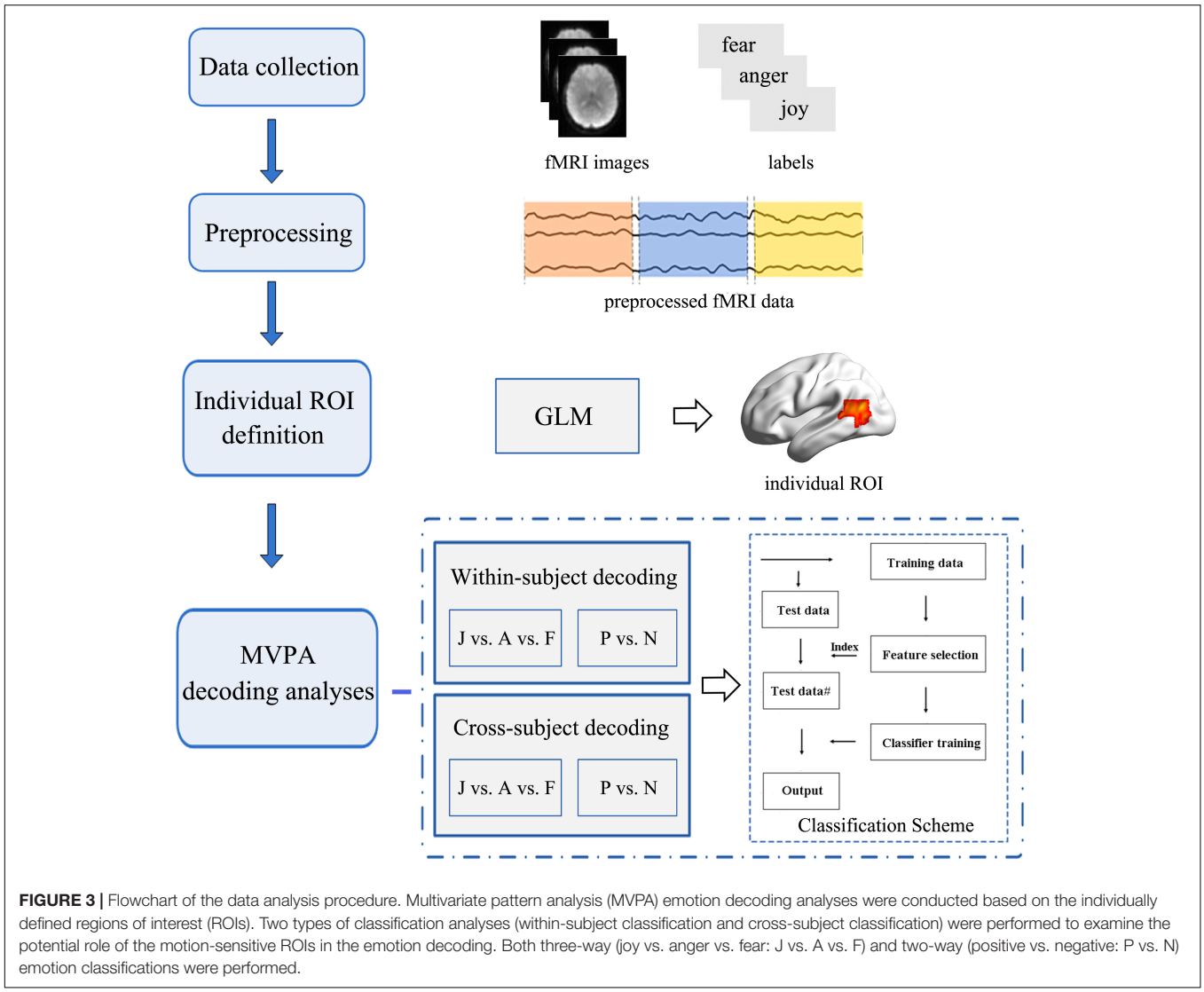

FIGURE 3 | Flowchart of the data analysis procedure. Multivariate pattern analysis (MVPA) emotion decoding analyses were conducted based on the individually defined regions of interest (ROIs). Two types of classification analyses (within-subject classification and cross-subject classification) were performed to examine the potential role of the motion-sensitive ROIs in the emotion decoding. Both three-way (joy vs. anger vs. fear: J vs. A vs. F) and two-way (positive vs. negative: P vs. N) emotion classifications were performed.

TABLE 2 | Behavioral results (mean % and standard deviations SD).

	Classification Accuracy (%)		Reaction Time (ms)	
	Mean	**SD**	**Mean**	**SD**
Joy	100	0	675.25	155.35
Anger	98.75	3.05	767.05	224.22
Fear	97.08	5.59	836.10	210.54

studies (Axelrod and Yovel, 2012, 2015; Wurm and Lingnau, 2015; Liang et al., 2017). In addition, we conducted a cross-subject emotion classification to assess whether there is any commonality in emotion representations in motion-sensitive areas across individual subjects. Both three-way (joy vs. anger vs. fear) and two-way (joy versus anger/fear, which could be considered as positive vs. negative) emotion classifications were performed. Feature selection was conducted using ANOVA which was executed only on the training data, with a threshold of $p < 0.05$. SVM classifier was trained and tested with cross-validation scheme to perform classification analysis over emotion categories. The classification accuracies for each ROI and subject were entered into one-tailed one-sample *t*-tests against the chance levels (Wurm and Lingnau, 2015), and the statistical results were corrected for multiple comparisons by FDR and Bonferroni corrections according to the number of ROIs. **Figures 4, 5** separately show the results for within-subject and cross-subject emotion classifications and the statistical significances for multiple comparisons correction results are indicated by asterisks.

Results for the within-subject emotion decoding analysis are shown in **Figure 4**, which illustrates the average percent signal change for each emotion (**Figure 4A**) and the classification accuracies for three emotions (**Figure 4B**) and for positive versus negative emotions (**Figure 4C**) in all ROIs. We found that the classification accuracies for three emotions and for positive versus negative emotions were significantly higher than chance in all ROIs [For three emotions classification: left STS: $t_{(18)} = 4.692$,

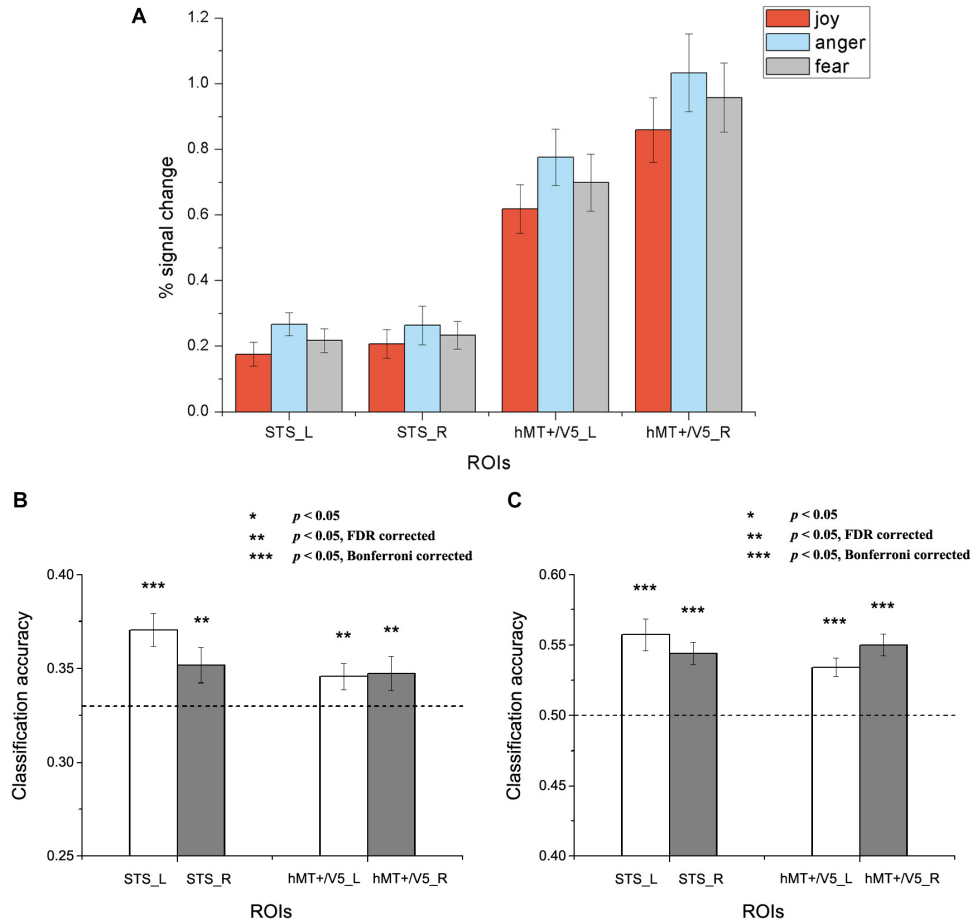

FIGURE 4 | Results of the within-subject emotion decoding analysis. **(A)** Average percent signal change for each emotion, **(B)** Classification accuracies for three emotions, and **(C)** Classification accuracies for positive versus negative emotions. The dashed line indicates chance level, and all error bars represent the standard error of the mean (SEM). Asterisks indicate statistical significance with a one-sample *t*-test, $p < 0.05$ [** $p < 0.05$ false discovery rate (FDR) corrected; *** $p < 0.05$ Bonferroni corrected].

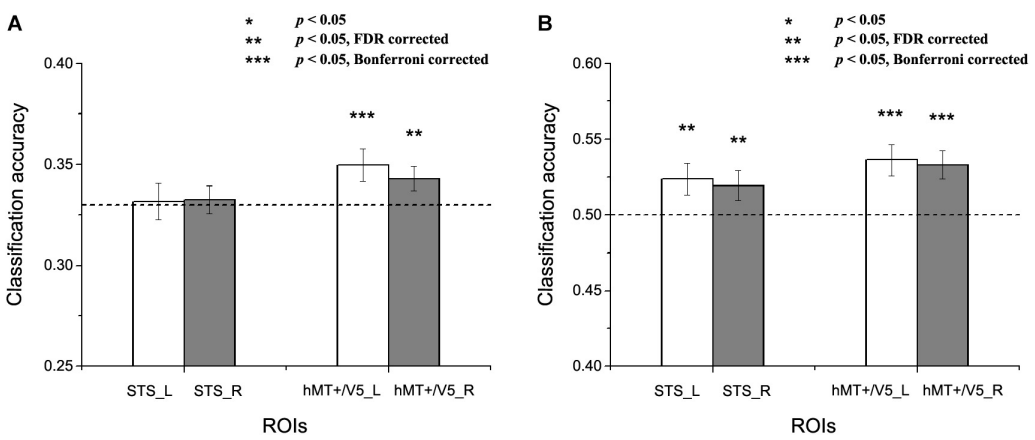

FIGURE 5 | Results of the cross-subject emotion decoding analysis. **(A)** Classification accuracies for three emotions, and **(B)** Classification accuracies for positive versus negative emotions. The dashed line indicates chance level, and all error bars reflect the SEM. Asterisks indicate statistical significance with a one-sample *t*-test, $p < 0.05$ [** $p < 0.05$ false discovery rate (FDR) corrected; *** $p < 0.05$ Bonferroni corrected].

$p < 0.001$; right STS: $t_{(18)} = 2.336$, $p = 0.016$; left hMT + /V5: $t_{(19)} = 2.294$, $p = 0.018$; right hMT + /V5: $t_{(19)} = 1.950$, $p = 0.033$. For positive versus negative emotions classification: left STS: $t_{(18)} = 5.149$, $p < 0.001$; right STS: $t_{(18)} = 5.478$, $p < 0.001$; left hMT + /V5: $t_{(19)} = 5.202$, $p < 0.001$; right hMT + /V5: $t_{(19)} = 6.548$, $p < 0.001$).

We next assessed whether a person's emotion representations in the motion-sensitive areas could be predicted by others' emotion representations. **Figure 5** shows the results for the cross-subject emotion classifications in all motion-sensitive ROIs (**Figure 5A** shows the classification results for three emotions and 5B shows the classification results for positive versus negative emotions). When classifying emotions from the classifiers trained by the activation patterns of other subjects, we found that classification accuracies were significantly higher than chance in hMT + /V5 both for the three emotions and for the positive versus negative emotions [classification of three emotions: left hMT + /V5: $t_{(19)} = 2.483$, $p = 0.01$; right hMT + /V5: $t_{(19)} = 2.116$, $p = 0.024$; classification of positive vs. negative emotions: left hMT + /V5: $t_{(19)} = 3.510$, $p = 0.001$; right hMT + /V5: $t_{(19)} = 3.523$, $p = 0.001$]. In the STS, although the classification accuracies for the three emotions did not achieve significance [left STS: $t_{(18)} = 0.174$, $p = 0.432$; right STS: $t_{(18)} = 0.351$, $p = 0.365$], we did find successful cross-subject positive-to-negative emotion decoding [left STS: $t_{(18)} = 2.199$, $p = 0.021$; right STS: $t_{(18)} = 1.995$, $p = 0.031$].

DISCUSSION

In this study, we performed a block-design fMRI experiment and collected neural data while participants viewed emotions (joy, anger, and fear) from videos representing whole-person expressions. Both within-subject and cross-subject MVPA emotion classification analyses were performed to examine the decoding performance of individual-defined motion-sensitive ROIs. We ran both three-way (joy vs. anger vs. fear) and two-way (positive vs. negative) emotion classifications. Our results showed that emotions could be successfully decoded based on the activation patterns in dorsal motion-sensitive areas. Moreover, results from the cross-subject classification analysis showed that motion-sensitive areas supported the classification of individual emotion representation across subjects.

Emotions Perceived From Whole-Person Expressions Are Represented in Dorsal Motion-Sensitive Areas

We obtained significant classification results for both the classification of the three emotions and the positive versus negative emotions, indicating that emotions perceived from whole-person expressions are represented in the motion-sensitive areas.

Previous studies on facial expressions with dynamic stimuli have revealed a certain degree of sensitivity in dorsal temporal areas, showing that motion-sensitive areas within hMT + /V5 and STS exhibited strong responses to dynamic facial emotions (Foley et al., 2011; Furl et al., 2013, 2015). Considering that the results of the average response from the univariate analysis alone are insufficient to reveal the potential role of a specific brain area underlying decoding (Axelrod and Yovel, 2012; Mahmoudi et al., 2012), recent fMRI studies used ROI-based MVPA to examine the decoding performance of motion-sensitive areas. Furl et al. (2012) used macaque STS as a model system and revealed the successful decoding of facial emotions in motion-sensitive areas. Similar results were obtained in one of our recent studies (Liang et al., 2017). These studies suggest that motion-sensitive areas may transmit measurable quantities of expression information and may be involved in the processing of emotional information. In this study, we defined individual motion-sensitive ROIs and found that emotions perceived from whole-person expressions could be successfully decoded from motion-sensitive areas. Our results are consistent with previous findings, and provide new evidence that emotions perceived from whole-person expressions are represented in the motion-sensitive areas. It should be noted that our results revealed the emotion decoding performance of the relatively domain-general motion-sensitive areas, as the localization contrast we used contained both person and person parts, as well as non-person objects, which was expected to reflect all responses to visual motion (Furl et al., 2012, 2015). Therefore, our results suggest that motion sensitive voxels which respond to various motions, not only specific to facial or bodily attributes, may make a significant contribution to emotion decoding.

Taken together, our findings provide new evidence that emotions are represented in dorsal motion-sensitive areas, pointing to the role of dorsal motion-sensitive areas as key regions in the processing of emotional information in daily communication.

Commonality of Emotion Representations in Motion-Sensitive Areas Across Individuals

Furthermore, we assessed whether an individual's emotion representation in the motion-sensitive areas corresponds to that observed in others by conducting a cross-subject emotion classification analysis (classifier was trained iteratively on all subjects but one and tested on the remaining one). This may provide evidence of whether an individual's subjective emotion representation in the motion-sensitive areas corresponds to that observed in others, which may be helpful in evaluating the commonality and variability in emotion coding (Haxby et al., 2011; Raizada and Connolly, 2012; Chikazoe et al., 2014). We obtained statistically significant results for both the cross-subject classification of three emotions and positive versus negative emotions in the hMT + /V5, indicating that the hMT + /V5 code may reflect experienced emotions in the same way across participants. In addition, although much less significant emotion classification results were identified for the three emotions, we revealed the successful cross-subject classification of positive versus negative emotions in the STS. This reveals that population codes in the STS were less able to decode a specific emotion in a fine-grained way, but demonstrated that the similarity in emotion representations among people may allow for the robust distinction of coarsely defined positive-to-negative

emotional valences in the context of bipolar representations (Kim et al., 2017). Our results also suggest that subjective emotion representations are more similarly structured across individual subjects in the hMT + /V5 than in the STS, since hMT + /V5 supported the cross-subject classification of both fine-grained three emotions and coarse-grained positive-to-negative emotions, while the STS only supported the coarse-grained classification in a significant way.

Overall, our study indicates that the representation of emotions in motion-sensitive areas may be similar across participants. This may provide evidence that even in the most subjective perception of an individual's emotion experience, its internal emotion coding can be predicted on the basis of the patterns observed in others in the motion-sensitive areas. This finding is important, since such cross-subject commonality may allow for the common scaling of the valence of emotional experiences across participants. In summary, we show that a person's emotional representations in motion-sensitive areas may be predicted by others' emotional representations, suggesting that there exists a common emotion code in the motion-sensitive areas across individuals.

In the present study, different types of emotional stimuli (facial, bodily, and whole-person expressions) were contained in the main experiment. Future studies with whole-person stimuli separately may further improve the implementation of the classification scheme and lead to better understanding of the whole-person expressions decoding. In addition, compared with ROI-based analyses, whole-brain group-level analyses would provide more informative results. Future studies combine both whole-brain activation-based and FC-based analyses would further enrich our findings about the neural substrates and the mechanisms for the quick and effortless recognition of whole-person emotions.

CONCLUSION

Our results showed that emotions perceived from whole-person expressions can be robustly decoded in dorsal motion-sensitive areas. Moreover, successful cross-subject emotion decoding suggests that the emotion representations in motion-sensitive areas could be shared across participants. This study extends previous MVPA studies to the emotion perception of whole-person expressions, which are more frequently perceived in daily life, and may further our understanding of the potential neural substrates underlying the efficient recognition of emotions from body language. Our findings provide new evidence that emotions are represented in dorsal motion-sensitive areas, underscoring the important role of the motion-sensitive areas in the emotion perception. Our study also suggests that emotion representations in motion-sensitive areas are similar across individuals.

DATA AVAILABILITY STATEMENT

The raw data supporting the conclusions of this article will be made available by the authors, without undue reservation.

ETHICS STATEMENT

The studies involving human participants were reviewed and approved by local Ethics Committee of Yantai Affiliated Hospital of Binzhou Medical University. The patients/participants provided their written informed consent to participate in this study.

AUTHOR CONTRIBUTIONS

YL and BL designed the study. YL performed the experiments, analyzed results, and wrote the manuscript. Both authors have approved the final manuscript.

FUNDING

This work was supported by the Beijing Natural Science Foundation (No. 4204089), National Natural Science Foundation of China (Nos. 61906006 and U1736219), China Postdoctoral Science Foundation funded project (No. 2018M641135), Beijing Postdoctoral Research Foundation (No. zz2019-74), Beijing Chaoyang District Postdoctoral Research Foundation (zz2019-02), National Key Research and Development Program of China (No. 2018YFB0204304), and Fundamental Research Funds for the Central Universities of China (No. FRF-MP-19-007).

ACKNOWLEDGMENTS

We would like to thank the Medical Imaging Research Institute of Binzhou Medical University, Yantai Affiliated Hospital of Binzhou Medical University, as well as the volunteers for the assistance in the data acquisition. We also thank Prof. Irene Rotondi (Campus Biotech, University of Geneva, Switzerland) for supplying the GEMEP Corpus.

REFERENCES

Axelrod, V., and Yovel, G. (2012). Hierarchical processing of face viewpoint in human visual cortex. *J. Neurosci.* 32, 2442–2452. doi: 10.1523/jneurosci.4770-11.2012

Axelrod, V., and Yovel, G. (2015). Successful decoding of famous faces in the fusiform face area. *PLoS One* 10:e0117126. doi: 10.1371/journal.pone.0117126

Banziger, T., Mortillaro, M., and Scherer, K. R. (2012). Introducing the Geneva Multimodal expression corpus for experimental research on emotion perception. *Emotion* 12, 1161–1179. doi: 10.1037/a0025827

Behzadi, Y., Restom, K., Liau, J., and Liu, T. T. (2007). A component based noise correction method (CompCor) for BOLD and perfusion based fMRI. *Neuroimage* 37, 90–101. doi: 10.1016/j.neuroimage.2007.04.042

Calbi, M., Angelini, M., Gallese, V., and Umiltà, M. A. (2017). "Embodied Body Language": an electrical neuroimaging study with emotional faces and bodies. *Sci. Rep*. 7:6875.

Candidi, M., Stienen, B. M., Aglioti, S. M., and De Gelder, B. (2011). Event-related repetitive transcranial magnetic stimulation of posterior superior temporal sulcus improves the detection of threatening postural changes in human bodies. *J. Neurosci.* 31, 17547–17554. doi: 10.1523/jneurosci.0697-11.2011

Cao, L. J., Xu, J. H., Yang, X. L., Li, X. L., and Liu, B. L. (2018). Abstract representations of emotions perceived from the face, body, and whole-person expressions in the left postcentral gyrus. *Front. Hum. Neurosci.* 12:419. doi: 10.3389/fnhum.2018.00419

Chang, C., and Lin, C. (2011). LIBSVM: a library for support vector machines. *ACM Trans. Intellig. Syst. Tech.* 2, 1–27. doi: 10.1145/1961189.1961199

Chikazoe, J., Lee, D., Kriegeskorte, N., and Anderson, A. (2014). Population coding of affect across stimuli, modalities and individuals. *Nat. Neurosci.* 17, 1114–1122. doi: 10.1038/nn.3749

de Gelder, B., Van Den Stock, J., Meeren, H. K., Sinke, C. B., Kret, M. E., and Tamietto, M. (2010). Standing up for the body. Recent progress in uncovering the networks involved in the perception of bodies and bodily expressions. *Neurosci. Biobehav. Rev.* 34, 513–527. doi: 10.1016/j.neubiorev.2009.10.008

Downing, P. E., and Peelen, M. V. (2016). Body selectivity in occipitotemporal cortex: causal evidence. *Neuropsychologia* 83, 138–148. doi: 10.1016/j.neuropsychologia.2015.05.033

Foley, E., Rippon, G., Thai, N., Longe, O., and Senior, C. (2011). Dynamic facial expressions evoke distinct activation in the face perception network: a connectivity analysis sudy. *J. Cogn. Neurosci.* 24, 507–520. doi: 10.1162/jocn_a_00120

Furl, N., Hadj-Bouziane, F., Liu, N., Averbeck, B. B., and Ungerleider, L. G. (2012). Dynamic and static facial expressions decoded from motion-sensitive areas in the macaque monkey. *J. Neurosci.* 32, 15952–15962. doi: 10.1523/jneurosci.1992-12.2012

Furl, N., Henson, R. N., Friston, K. J., and Calder, A. J. (2013). Top-down control of visual responses to fear by the amygdala. *J. Neurosci.* 33, 17435–17443. doi: 10.1523/jneurosci.2992-13.2013

Furl, N., Henson, R. N., Friston, K. J., and Calder, A. J. (2015). Network interactions explain sensitivity to dynamic faces in the superior temporal sulcus. *Cereb. Cortex* 25, 2876–2882. doi: 10.1093/cercor/bhu083

Geng, X., Xu, J., Liu, B., and Shi, Y. (2018). Multivariate classification of major depressive disorder using the effective connectivity and functional connectivity. *Front. Neurosci.* 12:38. doi: 10.3389/fnins.2018.00038

Gobbini, M. I., and Haxby, J. V. (2007). Neural systems for recognition of familiar faces. *Neuropsychologia* 45, 32–41. doi: 10.1016/j.neuropsychologia.2006.04.015

Harry, B., Williams, M. A., Davis, C., and Kim, J. (2013). Emotional expressions evoke a differential response in the fusiform face area. *Front. Hum. Neurosci.* 7:692. doi: 10.3389/fnhum.2013.00692

Haxby, J. V., Guntupalli, J. S., Connolly, A. C., Halchenko, Y. O., Conroy, B. R., Gobbini, M. I., et al. (2011). A common, high-dimensional model of the representational space in human ventral temporal cortex. *Neuron* 72, 404–416. doi: 10.1016/j.neuron.2011.08.026

Haxby, J. V., Hoffman, E. A., and Gobbini, M. I. (2000). The distributed human neural system for face perception. *Trends Cogn. Sci.* 4, 223–233. doi: 10.1016/s1364-6613(00)01482-0

Henriksson, L., Mur, M., and Kriegeskorte, N. (2015). Faciotopy-A face-feature map with face-like topology in the human occipital face area. *Cortex* 72, 156–167. doi: 10.1016/j.cortex.2015.06.030

Johnston, P., Mayes, A., Hughes, M., and Young, A. W. (2013). Brain networks subserving the evaluation of static and dynamic facial expressions. *Cortex* 49, 2462–2472. doi: 10.1016/j.cortex.2013.01.002

Kaiser, D., Strnad, L., Seidl, K. N., Kastner, S., and Peelen, M. V. (2014). Whole person-evoked fMRI activity patterns in human fusiform gyrus are accurately modeled by a linear combination of face- and body-evoked activity patterns. *J. Neurophysiol.* 111, 82–90. doi: 10.1152/jn.00371.2013

Kanwisher, N., and Yovel, G. (2006). The fusiform face area: a cortical region specialized for the perception of faces. *Philos. Trans. R. Soc. Lond. B Biol. Sci.* 361, 2109–2128.

Kim, J., Shinkareva, S., and Wedell, D. (2017). Representations of modality-general valence for videos and music derived from fMRI data. *Neuroimage* 148, 42–54. doi: 10.1016/j.neuroimage.2017.01.002

Kret, M. E., Pichon, S., Grezes, J., and De Gelder, B. (2011). Similarities and differences in perceiving threat from dynamic faces and bodies. An fMRI study. *Neuroimage* 54, 1755–1762. doi: 10.1016/j.neuroimage.2010.08.012

Liang, Y., Liu, B. L., Xu, J. H., Zhang, G. Y., Li, X. L., Wang, P. Y., et al. (2017). Decoding facial expressions based on face-selective and motion-sensitive areas. *Hum. Brain Mapp.* 38, 3113–3125. doi: 10.1002/hbm.23578

Mahmoudi, A., Takerkart, S., Regragui, F., Boussaoud, D., and Brovelli, A. (2012). Multivoxel pattern analysis for fMRI data: a review. *Comput. Math Methods Med.* 2012:961257.

Miao, Q. M., Zhang, G. Y., Yan, W. R., and Liu, B. L. (2018). Investigating the brain neural mechanism when signature objects were masked during a scene categorization task using functional MRI. *Neuroscience* 388, 248–262. doi: 10.1016/j.neuroscience.2018.07.030

Minnebusch, D. A., and Daum, I. (2009). Neuropsychological mechanisms of visual face and body perception. *Neurosci. Biobehav. Rev.* 33, 1133–1144. doi: 10.1016/j.neubiorev.2009.05.008

Pitcher, D. (2014). Facial expression recognition takes longer in the posterior superior temporal sulcus than in the occipital face area. *J. Neurosci.* 34, 9173–9177. doi: 10.1523/jneurosci.5038-13.2014

Power, J. D., Barnes, K. A., Snyder, A. Z., Schlaggar, B. L., and Petersen, S. E. (2012). Spurious but systematic correlations in functional connectivity MRI networks arise from subject motion. *Neuroimage* 59, 2142–2154. doi: 10.1016/j.neuroimage.2011.10.018

Power, J. D., Schlaggar, B. L., and Petersen, S. E. (2015). Recent progress and outstanding issues in motion correction in resting state fMRI. *Neuroimage* 105, 536–551. doi: 10.1016/j.neuroimage.2014.10.044

Raizada, R. D., and Connolly, A. C. (2012). What makes different people's representations alike: neural similarity space solves the problem of across-subject fMRI decoding. *J. Cogn. Neurosci.* 24, 868–877. doi: 10.1162/jocn_a_00189

Said, C. P., Moore, C. D., Engell, A. D., Todorov, A., and Haxby, J. V. (2010). Distributed representations of dynamic facial expressions in the superior temporal sulcus. *J. Vis.* 10, 71–76.

Skerry, A., and Saxe, R. (2014). A common neural code for perceived and inferred emotion. *J. Neurosci.* 34, 15997–16008. doi: 10.1523/jneurosci.1676-14.2014

Soria Bauser, D., and Suchan, B. (2015). Is the whole the sum of its parts? Configural processing of headless bodies in the right fusiform gyrus. *Behav. Brain Res* 281, 102–110. doi: 10.1016/j.bbr.2014.12.015

Wang, X. S., Fang, Y. X., Cui, Z. X., Xu, Y. W., He, Y., Guo, Q. H., et al. (2016). Representing object categories by connections: evidence from a mutivariate connectivity pattern classification approach. *Hum. Brain Mapp.* 37, 3685–3697. doi: 10.1002/hbm.23268

Wegrzyn, M., Riehle, M., Labudda, K., Woermann, F., Baumgartner, F., Pollmann, S., et al. (2015). Investigating the brain basis of facial expression perception using multi-voxel pattern analysis. *Cortex* 69, 131–140. doi: 10.1016/j.cortex.2015.05.003

Whitfield-Gabrieli, S., and Nieto-Castanon, A. (2012). Conn: a functional connectivity toolbox for correlated and anticorrelated brain networks. *Brain Connect* 2, 125–141. doi: 10.1089/brain.2012.0073

Woo, C. W., Koban, L., Kross, E., Lindquist, M. A., Banich, M. T., Ruzic, L., et al. (2014). Separate neural representations for physical pain and social rejection. *Nat. Commun.* 5:5380.

Wurm, M., and Lingnau, A. (2015). Decoding actions at different levels of abstraction. *J. Neurosci.* 35, 7727–7735. doi: 10.1523/jneurosci.0188-15.2015

Xu, J., Yin, X., Ge, H., Han, Y., Pang, Z., Liu, B., et al. (2017). Heritability of the effective connectivity in the resting-state default mode network. *Cereb. Cortex* 27, 5626–5634. doi: 10.1093/cercor/bhw332

Yang, X. L., Xu, J. H., Cao, L. J., Li, X. L., Wang, P. Y., Wang, B., et al. (2018). Linear representation of emotions in whole persons by combining facial and

bodily expressions in the extrastriate body area. *Front. Hum. Neurosci.* 11:653. doi: 10.3389/fnhum.2017.00653

Zhang, J., Li, X., Song, Y., and Liu, J. (2012). The fusiform face area is engaged in holistic, not parts-based, representation of faces. *PLoS One* 7:e40390. doi: 10.1371/journal.pone.0040390

Zhu, Q., Nelissen, K., Van Den Stock, J., De Winter, F. L., Pauwels, K., De Gelder, B., et al. (2013). Dissimilar processing of emotional facial expressions in human and monkey temporal cortex. *Neuroimage* 66, 402–411. doi: 10.1016/j.neuroimage.2012.10.083

Conflict of Interest: The authors declare that the research was conducted in the absence of any commercial or financial relationships that could be construed as a potential conflict of interest.

frontiers in Human Neuroscience

METHODS
published: 30 October 2020
doi: 10.3389/fnhum.2020.576241

Inter- and Intra-individual Variability in Brain Oscillations During Sports Motor Imagery

Selina C. Wriessnegger[1,2], Gernot R. Müller-Putz[1,2], Clemens Brunner[3] and Andreea I. Sburlea[1]*

[1] Institute of Neural Engineering, Graz University of Technology, Graz, Austria, [2] BioTechMed-Graz, Graz, Austria, [3] Institute of Psychology, University of Graz, Graz, Austria

The aim of this work was to re-evaluate electrophysiological data from a previous study on motor imagery (MI) with a special focus on observed inter- and intra-individual differences. More concretely, we investigated event-related desynchronization/synchronization patterns during sports MI (playing tennis) compared with simple MI (squeezing a ball) and discovered high variability across participants. Thirty healthy volunteers were divided in two groups; the experimental group (EG) performed a physical exercise between two imagery sessions, and the control group (CG) watched a landscape movie without physical activity. We computed inter-individual differences by assessing the dissimilarities among subjects for each group, condition, time period, and frequency band. In the alpha band, we observe some clustering in the ranking of the subjects, therefore showing smaller distances than others. Moreover, in our statistical evaluation, we observed a consistency in ranking across time periods both for the EG and for the CG. For the latter, we also observed similar rankings across conditions. On the contrary, in the beta band, the ranking of the subjects was more similar for the EG across conditions and time periods than for the subjects of the CG. With this study, we would like to draw attention to variability measures instead of primarily focusing on the identification of common patterns across participants, which often do not reflect the whole neurophysiological reality.

Keywords: EEG, ERD/S, motor imagery, variability, inter-individual differences

OPEN ACCESS

Edited by:
Masaki Nakanishi, University of California, San Diego, United States

Reviewed by:
Mitsuaki Takemi, The University of Tokyo, Japan
Pavel Bobrov, Institute of Higher Nervous Activity and Neurophysiology (RAS), Russia

****Correspondence:***
Selina C. Wriessnegger
s.wriessnegger@tugraz.at

Specialty section:
This article was submitted to Brain Imaging and Stimulation, a section of the journal Frontiers in Human Neuroscience

Received: *25 June 2020*
Accepted: *24 September 2020*
Published: *30 October 2020*

Citation:
Wriessnegger SC, Müller-Putz GR, Brunner C and Sburlea AI (2020) Inter- and Intra-individual Variability in Brain Oscillations During Sports Motor Imagery. Front. Hum. Neurosci. 14:576241. doi: 10.3389/fnhum.2020.576241

INTRODUCTION

Motor imagery (MI) is defined as an internal representation of simple or complex movements in absence of any physical action or any kind of peripheral muscular activity (Jeannerod, 1994; Annett, 1995; Jeannerod and Decety, 1995; Porro et al., 1996). It is well-known that MI improves motor learning comparable with real physical exercises which results in neural and structural changes in the brain (Grèzes and Decety, 2001; Miller et al., 2010; Sharma and Baron, 2013). Furthermore, MI is a common task in brain–computer interface (BCI) research because users often cannot perform an overt motor execution task due to some degree of motor disability (Neuper et al., 2006; Pfurtscheller and Neuper, 2006; Pfurtscheller et al., 2006; Leeb et al., 2007a; Höhne et al., 2014). With the so-called motor-imagery-based BCI, users send mental commands by performing

MI tasks, e.g., movement imagination or attempts (Pfurtscheller and Neuper, 2001; Neuper and Pfurtscheller, 2010; Lotte et al., 2013). Even though improved signal processing and classification algorithms are available, a tremendous inter- and intra-subject variability has been observed in terms of performance (Allison and Neuper, 2010; Wolpaw and Wolpaw, 2012; Kübler et al., 2013). Thus, it is indisputable that one of the major aspects contributing to MI–BCI control performance is the individual characteristic and consequently neural pattern of the BCI user (Kübler et al., 2013; Ahn and Jun, 2015).

In the past years, researchers identified different factors like cognitive, attentional, or personal skills which influence BCI performance (Leeb et al., 2007a,b; Blankertz et al., 2010; González-Franco et al., 2011; Kübler et al., 2011; Halder et al., 2013; Kleih and Kübler, 2013; Lotte et al., 2013; Höhne et al., 2014; Schreuder, 2014). The observed large inter-individual variability motivated researchers to investigate important predictors related to a user's personality and cognitive profile. Jeunet et al. (2016) suggested the following three categories of MI–BCI performance predictors: (1) users' relationship with the technology, (2) attention, and (3) spatial abilities. The attention-related predictors seem to be particularly relevant. There is large inter-individual variability in the efficiency of neural activity in the attention network accounting for the inter-individual variations in attentional abilities important for BCI control (Petersen and Posner, 2012). Moreover, several other researchers have identified attention-related brain patterns which are important to BCI performance.

For example, Grosse-Wentrup and Schölkopf (2012) found that the variation in gamma power highly correlates with BCI performance, hence being able to predict successful or unsuccessful classification (Grosse-Wentrup et al., 2011; Grosse-Wentrup, 2012; Grosse-Wentrup and Schölkopf, 2012; Schumacher et al., 2015). Others found that the extent of activation of the dorsolateral prefrontal cortex (associated with the executive attention system; Posner and Petersen, 1990) differs between high and low BCI performers (Halder et al., 2011). Finally, Bamdadian et al. (2014) found that frontal theta, occipital alpha, and midline beta power could be other predictors for BCI performance.

Besides attention, there are several other factors that contribute to a high variability in BCI users. For example, Kübler et al. (2011) suggested a model of BCI control that contains four categories: "Individual characteristics," "Characteristics of the BCI," "Feedback and Instruction," and "Application." Summarizing this classification, it can be distinguished between two fundamental aspects. One aspect is the user's part and the other one the system's part. It has been shown that within the same BCI system, some subjects cannot perform successfully (Allison and Neuper, 2010; Blankertz et al., 2010). These results indicate the importance to understand why some individuals perform differently in the same system. Other researchers like Saha and Baumert (2019) reported that neurophysiological processes during MI often vary over time and across subjects (Meyer et al., 2013; Saha et al., 2017). Because the motor learning process differs across individuals and consequently cortical activity varies among subjects during MI, its utility for BCI applications is largely restricted. Hence, it is very important to more closely investigate inter- and intra-subject variability during MI to find further predictors of inter-individual differences that can improve future MI-based BCI systems.

In a former study, we investigated MI of playing tennis, resulting in different mu rhythm patterns of activation on the basis of individual expertise for the specific task. For instance, experienced tennis players showed a more focal event-related desynchronization (ERD) pattern over sensorimotor regions surrounded by ERS with respect to non-experts (Wriessnegger et al., 2018). Surprisingly, our data clearly show high inter- and intra-individual differences in event-related desynchronization/synchronization (ERD/S) patterns in all tasks and groups reflected in the time–frequency visualization of ERD/S patterns in the alpha band for the same tasks. For example, while one person showed increased ERD during MI of tennis, another one showed increased ERS for the same task. Consequently, an overall analysis of the grand average activity during tennis MI was quite problematic. Such high inter- and intra-subject variability of mu rhythms during MI tasks was also reported by other studies (Doppelmayr et al., 1998; Pineda, 2005; Pfurtscheller and Neuper, 2006; Pfurtscheller et al., 2006; Halme and Parkkonen, 2018; Corsi et al., 2019). For example, Daeglau et al. (2020) attributed the inter-individual differences in MI induced ERD to the experimental setup they used. Concretely, they assumed that task and experimental setup can affect the interplay of motor execution and MI for each individual differently. Others discussed inter-subject variability in the alpha frequency in relation with age and genetic factors, supported by twin studies (Smit et al., 2012; Bodenmann et al., 2009). But also, task demands and cognitive factors like working memory performance influence the alpha peak frequency (Klimesch, 1999). In addition, intra-subject variability in alpha peak frequency has been observed reflecting different alpha networks being activated dependent on task demands (Klimesch, 1999). Following this, alpha frequency can be interpreted as "trait" variable on the one side and "state" variable on the other side. While the former might explain differences in overall cognitive performance among subjects, the latter could explain the observed intra-subject variability. Moreover, this variability might reflect any fluctuations in real-time performance.

These results and the high inter-individual differences in ERD/S patterns elicited in our previous study (Wriessnegger et al., 2018) motivated us to investigate more closely the variability among and between subjects of this dataset. The individual activation patterns during MI are largely neglected in most of the studies which primarily focused on the identification of common patterns across participants.

MATERIALS AND METHODS

Participants

Thirty healthy right-handed students participated in the study. All reported normal or corrected to normal vision and none of them had a history of psychiatric or neurological disorders.

Participants were matched with regard to sex and age, and they were randomly assigned to the control group (CG) ($N = 15$; mean age: 24.9; range: 20–30 years; 7 women and 8 men) or to the experimental group (EG) ($N = 15$; mean age: 24.8; range: 20–28 years; 7 women and 8 men). The participants were all naive regarding MI, 70% of them regularly perform different kinds of sports and only five play tennis. The original study was approved by the local ethics committee (Medical University of Graz) and is in accordance with the ethical standards of the Declaration of Helsinki. After detailed written and oral instruction participants gave informed written consent to participate in the study. They received financial compensation (€7.50/hour) for their participation.

Experimental Design

The experimental procedure encompassed a pre-measurement, the execution or relaxing intervention, and a post-measurement. During the pre-measurement, participants from both groups performed the MI task according to the written instructions while simultaneously their EEG was recorded. Whenever the letter "T" appeared on the screen in front of them, participants had to imagine playing tennis for 6 s repetitively. The concrete instruction was to imagine a repetitive right forehand movement of returning balls from a first-person perspective. If the letter "H" appeared on the computer screen, the task was to imagine squeezing a ball for 6 s with the right hand. Participants had to imagine each type of MI 15 times per run in pseudo-randomized order. The whole experiment consisted of four runs with 60 trials of squeezing a ball and other 60 trials of playing tennis.

During the intervention phase, participants from the EG played virtual tennis via motion control (Kinect) and squeezed a real ball for 5 min each. In this phase, no EEG was recorded. The described execution interventions were performed in randomized order within the EG. In the control group (CG), participants performed no physical exercise, instead they watched a landscape movie for 10 min.

In the last session, after the intervention phase, participants of the EG and the CG performed the same MI (playing tennis and squeezing a ball) tasks like in the first session while their EEG was recorded. A trial consisted of a fixation cross (4 s), the imagery phase (6 s), and a pause (4 s), which leads to a total trail time of 14 s. In one run, 30 trials (15 per MI task) in total are performed, with four runs in the pre-recording and 4 runs in the post-recording phase. Each participant performed eight runs with 240 trials in total. For a more detailed description of the experimental setup, please see Wriessnegger et al. (2018).

EEG Preprocessing and ERD/ERS Analysis

The raw EEG data, taken from the original study (Wriessnegger et al., 2018), was down-sampled to 250 Hz and re-referenced to channel Cz. We manually inspected the continuous EEG signals and marked segments containing artifacts, which we discarded in all subsequent analyses. Next, we used non-causal FIR bandpass filters to extract time signals in the bands 8–13 Hz (alpha band) and 16–24 Hz (beta band). We considered segments from −3.5 to 3.5 s relative to each cue for our ERD/ERS calculation, where the baseline and activation intervals ranged from −3.5 to 0.5 s and 0.5 to 3.5 s, respectively. Finally, we averaged groups of channels into the following six regions of interest (ROIs) (**Figure 1**): prefrontal left (F5a, F3a, F1a, FC5b, FC3b, FC1d, and FC1c), prefrontal right (F2a, F4a, F6a, FC2c, FC2d, FC4b, and FC6b), central left (FC5a, FC3a, FC1b, FC1a, C5a, C3, C1b,C1a, CP5a, CP3a, CP1b, and CP1a), central right (FC2a, FC2b, FC4a, FC6a, C2a, C2b, C4, C6a, CP2a, CP2b, CP4a, and CP6a), parietal left (CP5b, CP3b, CP1d, CP1c, P5a, P3a, and P1a), and parietal right (CP2c, CP2d, CP4b, CP6b, P2a, P4a, and P6a). We computed time/frequency ERD/S maps similar to the procedure used to calculate ERD/S values.

Calculating Intra- and Inter-individual Differences

For every subject from the two groups (experimental and control), each condition (hand and tennis), time period (pre- and post-intervention), and frequency band (alpha and beta), we averaged the time–frequency patterns during the task (0.5 to 3.5 s) of single channels within each of the six ROIs. Then, we computed the ERD/S patterns and investigated their distribution among subjects during pre- and post-intervention time periods.

Next, we concatenated the average ERD/S values of the six ROIs for alpha and for beta frequency bands for all the subjects, and assessed the dissimilarity between these patterns by means of a pairwise distance computed as 1 - *rho*, where *rho* is the Spearman correlation. We ranked and scaled the distances between 0 and 1, and computed the distance matrix between pairs of conditions. We computed inter-individual differences by assessing the dissimilarities among subjects for each group, condition, time period, and frequency band (**Figures 4A,B**).

To visualize the distances between different subjects in several conditions, we used multidimensional scaling (MDS) (Kruskal and Wish, 1978). MDS is a general dimensionality reduction method that projects entities in a low-dimensional space, such that their distances reflect their similarities. Specifically, similar entries will be located closer to one another, while dissimilar ones will be farther apart. For MDS visualization as a 2D plot that reflects the distribution of the subjects in terms of their ranking, we performed non-metric MDS for two dimensions with the squared stress criterion.

Next, we investigated the variability of these pairwise distances among subjects in each of the two groups (experimental and control) among conditions, time periods, and frequency bands using Kendall's tau b and reporting their associated *p*-values. We corrected for multiple comparisons using the Bonferroni–Holm correction.

RESULTS

Subject-Specific ERD/S Patterns

Figure 2 shows subject-specific ERD/S values averaged over the channels of each ROI. In every subplot, the vertical black line separates the values for alpha and beta frequency bands, whereas the horizontal black line separates the two groups of subjects: experimental and control groups. Finally, the top row shows all

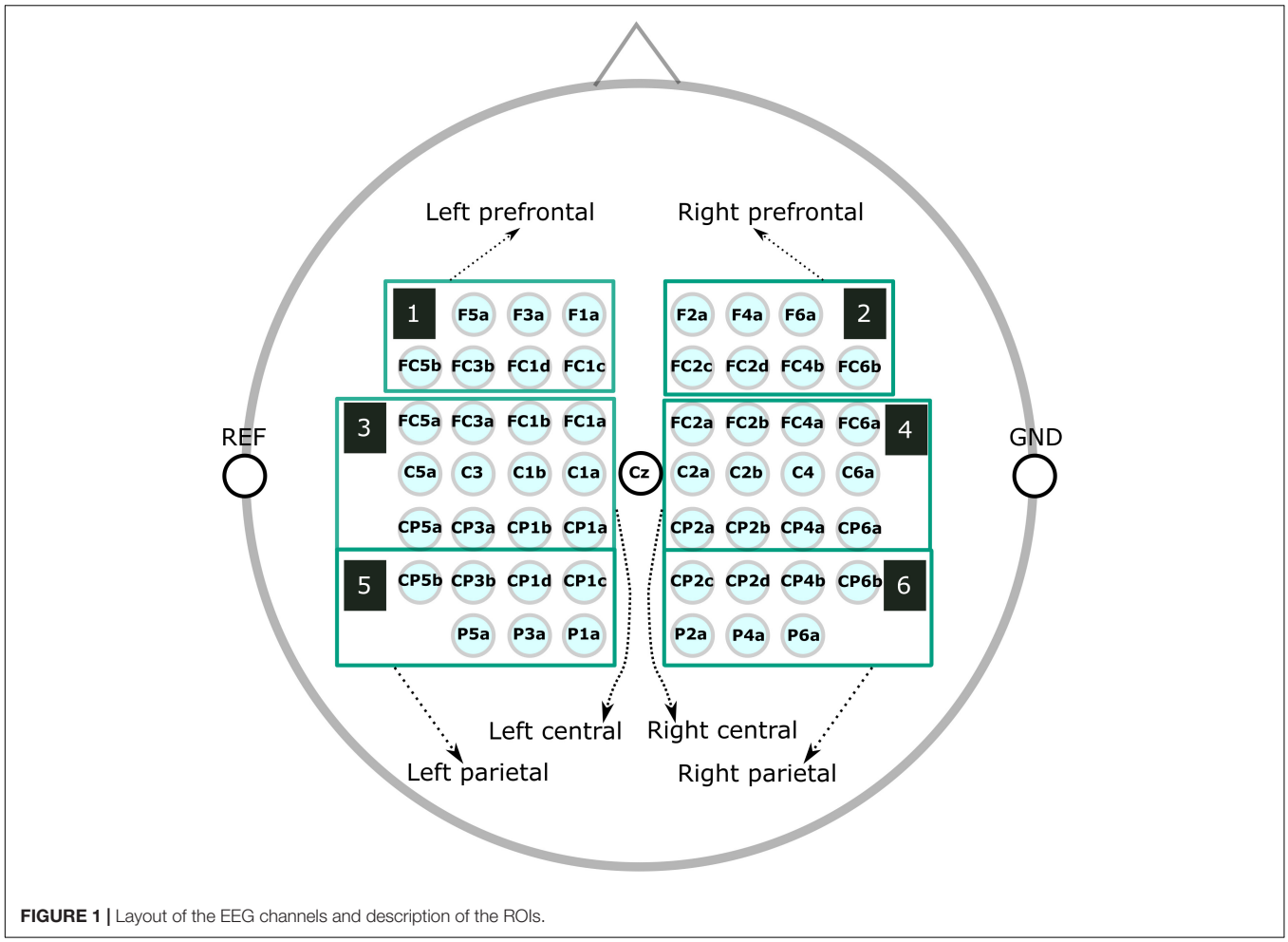

FIGURE 1 | Layout of the EEG channels and description of the ROIs.

these patterns for the hand condition: on the left side during the pre-intervention time period and on the right side during the post-intervention time period. Similarly, the bottom row shows these patterns for the tennis condition.

We can observe that for some subjects, the within-subject ERD/S values remain similar throughout the conditions and time points. However, across subjects, these values are very different. For example, subject EG3 shows a strong negative ERD/S value at the level of ROI3 and ROI5 in both hand and tennis pre-conditions for both alpha and beta frequencies. These values slightly increase but remain negative for all the conditions and frequencies in the post-intervention period. However, as another example, subject EG14 presents positive ERD/S values in all conditions. Similar observations can be found in the control group (e.g., CG3 and CG12). We also found that the ERD/S values for the beta frequency show less variability among subjects for either group compared with the alpha frequency band.

In **Figures 3A,B**, we use boxplots to visualize summary statistics at the group level, based on ERD/S values for each condition (hand and tennis), respectively, for alpha and beta frequency bands and for all six ROIs. For both conditions, the distribution of ERD/S values shows larger variability in the alpha band than in the beta band throughout the ROIs. We can also observe that in the EG, some subjects contribute as outliers to the larger variability observed in the alpha band in the pre-intervention period (large positive ERD/S values in the top left subplot in **Figures 3A,B**).

Moreover, the median values among ROIs for the hand condition are more negative for the EGs than for the control group in the pre-intervention period in the alpha band. For the tennis conditions, the medians of the ROIs are similar between groups and between time periods.

Distance Matrices and Variability Results

Inter-individual differences are illustrated in terms of distance measures between subject-specific ERD/S patterns for the alpha band in **Figure 4A** and for the beta band in **Figure 4B**, for the factors group (EG/CG), time period (pre/post), and condition (hand/tennis). The distances are calculated between pairs of subjects considering as a pattern the ERD/S during the task period of all the channels, without averaging them. In **Figure 4A**, we observe some clustering in the ranking of the subjects, therefore showing smaller distances than others. Moreover, we observed a consistency in ranking across time periods both for the EG and for the control group. For the latter, we also observed similar rankings across conditions. For example, subjects 6, 8,

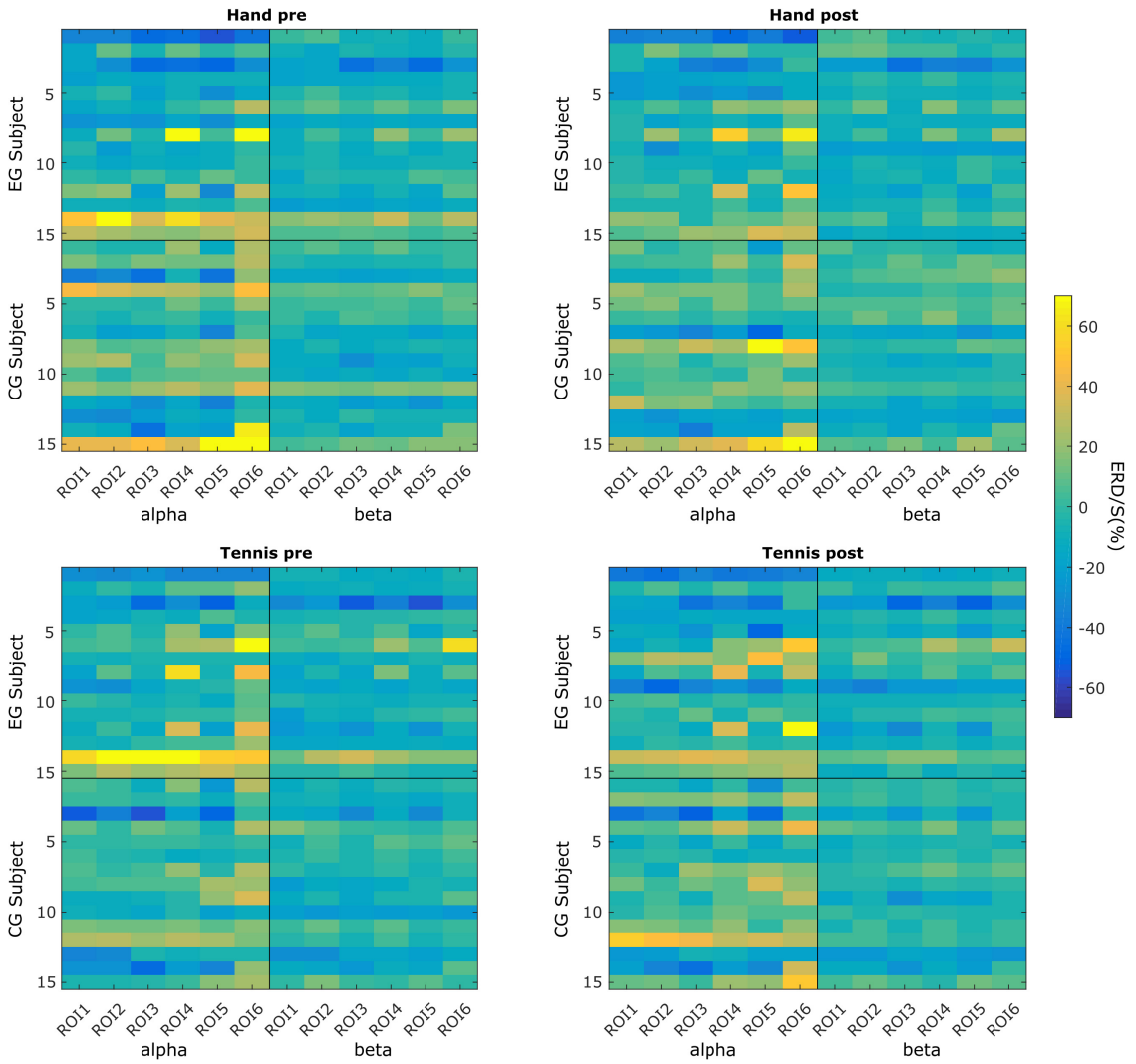

FIGURE 2 | Subject-specific ERD/S magnitudes in each of the six ROIs in the hand and tennis conditions (top and bottom panels), during the pre- and post-intervention time periods (left and right panels) within the alpha and beta frequency bands.

9, and 10 from the EG show a strong similarity, therefore small distances among each other across conditions; whereas subjects 4, 8, 9, and 12 from the control group are consistently different independent of the condition or time period, by showing large distances among each other.

In the beta band, the ranking of the subjects was more similar for the EG across conditions and time periods than for the subjects of the control group. For example, subjects 3, 8, 9, 12, and 13 were very similar in ranking across conditions and time periods. We have not observed such a consistency in the control group.

For an intuitive visualization of the relationship between the ERD/S magnitudes of different subjects, we used MDS. In **Figures 5A,B**, we show their relation for each of the two frequency bands, respectively. With red dots we show the subjects from the EG and with blue the subjects from the control group. The closer the two dots are to one another, the more similar the magnitude of the ERD/S for the two subjects. For example, in **Figure 5A**, in the EG hand pre-condition, subject 1 is similar to subjects 3 and 5 but very different to subject 2 or 13. In each figure, we visualize separately the structure of the rankings of the subjects for different conditions and time periods. We observe that some subjects remain consistent in their ranking with respect to others across conditions and time periods. For example, in the EG, subjects 8, 12, and 13 maintain their similarity across conditions and time periods. Another example is subject 6 from the control group which shows a larger dissimilarity to the other subjects from the same group independent of the condition or time period.

In **Figure 5B** for the beta band, we also observed that some subjects cluster together, for example, for the EG, subjects 12 and 13 are close in their rankings both across conditions and time periods, and also across frequency bands, as we have seen in

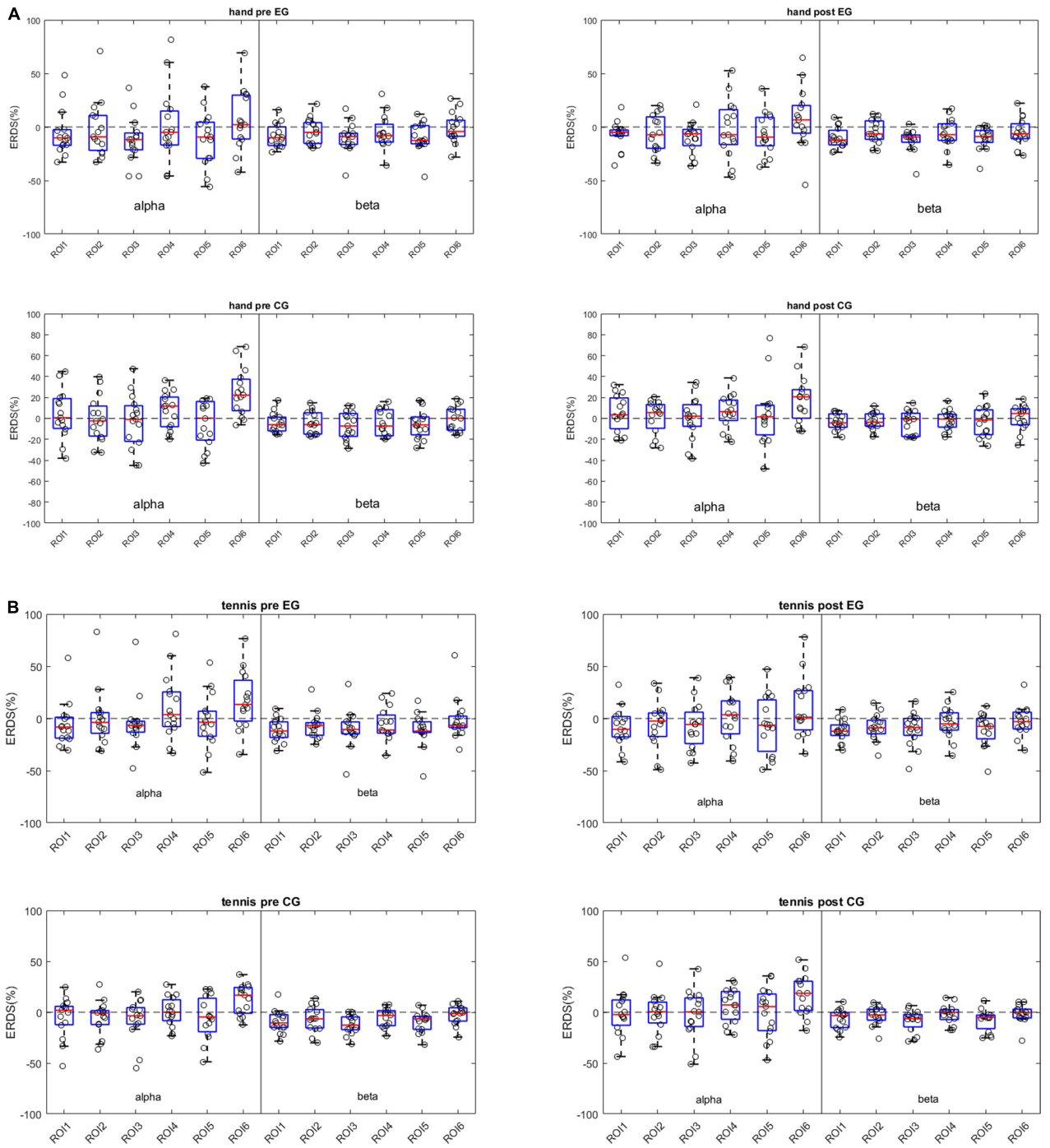

FIGURE 3 | (A) Distribution of ERD/S patterns across frequency bands and ROIs for the hand condition. Each dot represents a subject-specific average ERD/S in the time period of the task (0.5 to 3.5 s w.r.t. the task cue) for a particular frequency band and ROI. The subplots on the left column show the ERD/S distribution for the pre-intervention period for the experimental group (top) and for the control group (bottom). The right column shows the post-intervention ERD/S distribution. **(B)** Distribution of ERD/S patterns across frequency bands and ROIs for the tennis condition. Each dot represents a subject-specific average ERD/S in the time period of the task (0.5 to 3.5 s w.r.t. the task cue) for a particular frequency band and ROI. The subplots on the left column show the ERDS distribution for the pre-intervention period for the experimental group (top) and for the control group (bottom). The right column shows the post-intervention ERD/S distribution.

Figure 5A. For the control group, we observed a different ranking of the subjects between conditions and time periods compared with the consistency in ranking found in the alpha band.

Figure 6 shows the degree of similarity between the pairs of conditions and time points in which we evaluated the rankings of the subjects. We chose Kendall's Tau-b correlation coefficient

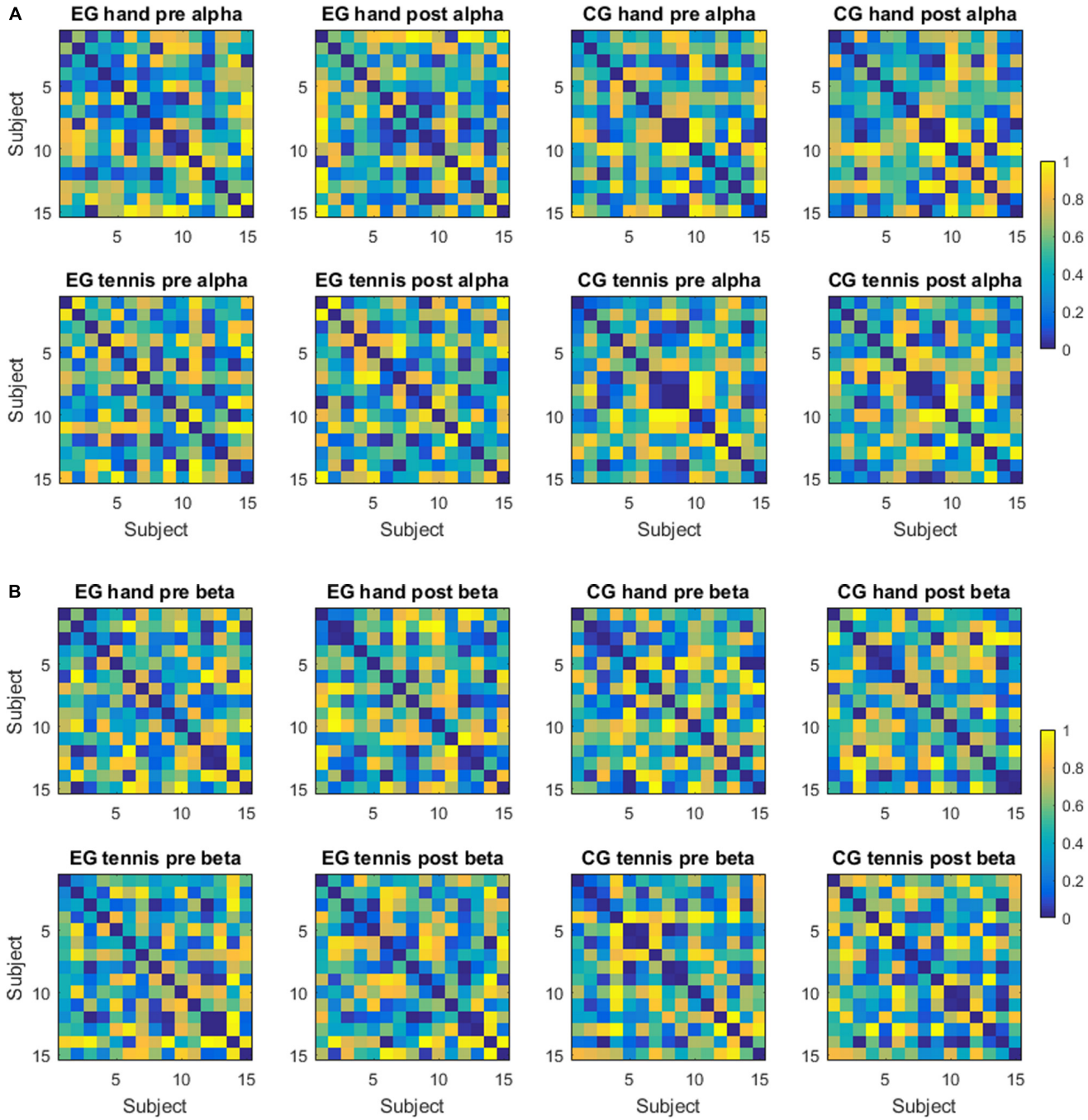

FIGURE 4 | (A) Distance matrices—alpha frequency band. Each matrix displays the distance between subject-specific ERDS patterns in the alpha frequency band for a group (experimental or control), a condition (hand or tennis motor imagery), and a time period (pre- or post-intervention). The distance is computed as 1 - rho, where rho is the Spearman correlation. **(B)** Distance matrices—beta frequency band. Each matrix displays the distance between subject-specific ERDS patterns in the beta frequency band for a group (experimental or control), a condition (hand or tennis motor imagery) and a time period (pre- or post-intervention). The distance is computed as 1 - rho, where rho is the Spearman correlation.

to adjust for ties in the ranking, and we also report the associated p-values corrected for multiple comparisons using the Bonferroni–Holm correction. We found that the ranking of the magnitude of the ERD/S patterns for the subjects in the EG hand pre-beta was correlated with the one in the EG hand pre-alpha ($\tau_b = 0.23$, $p = 0.03$), which indicates that the ranking of the subject is maintained across frequency bands for the hand condition in the pre-intervention time period. We also found stronger correlations between the EG tennis post-alpha and EG hand post-alpha ($\tau_b = 0.34$, $p = 0.0001$)

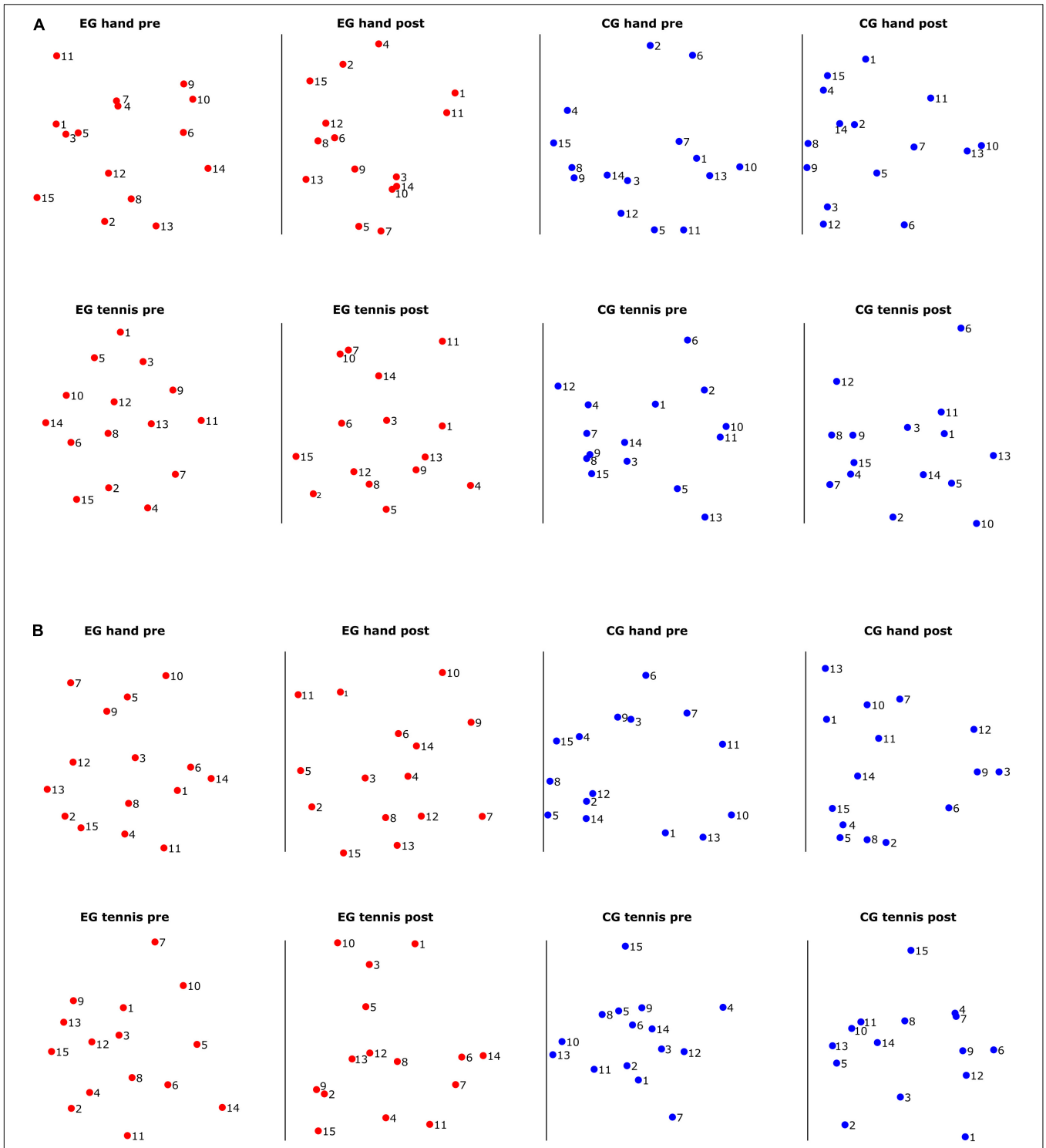

FIGURE 5 | (A) Multidimensional scaling (MDS) scatter plots showing the relation among the subject-specific ERD/S patterns in the alpha frequency band for subjects in the experimental group (red dots) and subjects in the control group (blue dots). **(B)** Multidimensional scaling scatter plots showing the relation among the subject-specific ERD/S patterns in the beta frequency band for subjects in the experimental group (red dots) and subjects in the control group (blue dots).

as well as EG tennis pre-alpha ($\tau_b = 0.35$, $p = 0.00009$), which suggest consistency in ranking in the alpha band across conditions ($\tau_b = 0.32$, $p = 0.0005$) and time periods. For the beta band, we observed a stronger correlation across both conditions: $\tau_b = 0.38$, $p = 0.000007$ for tennis pre-hand pre, and time periods: $\tau_b = 0.32$, $p = 0.0006$ for hand pre–hand post and $\tau_b = 0.38$,

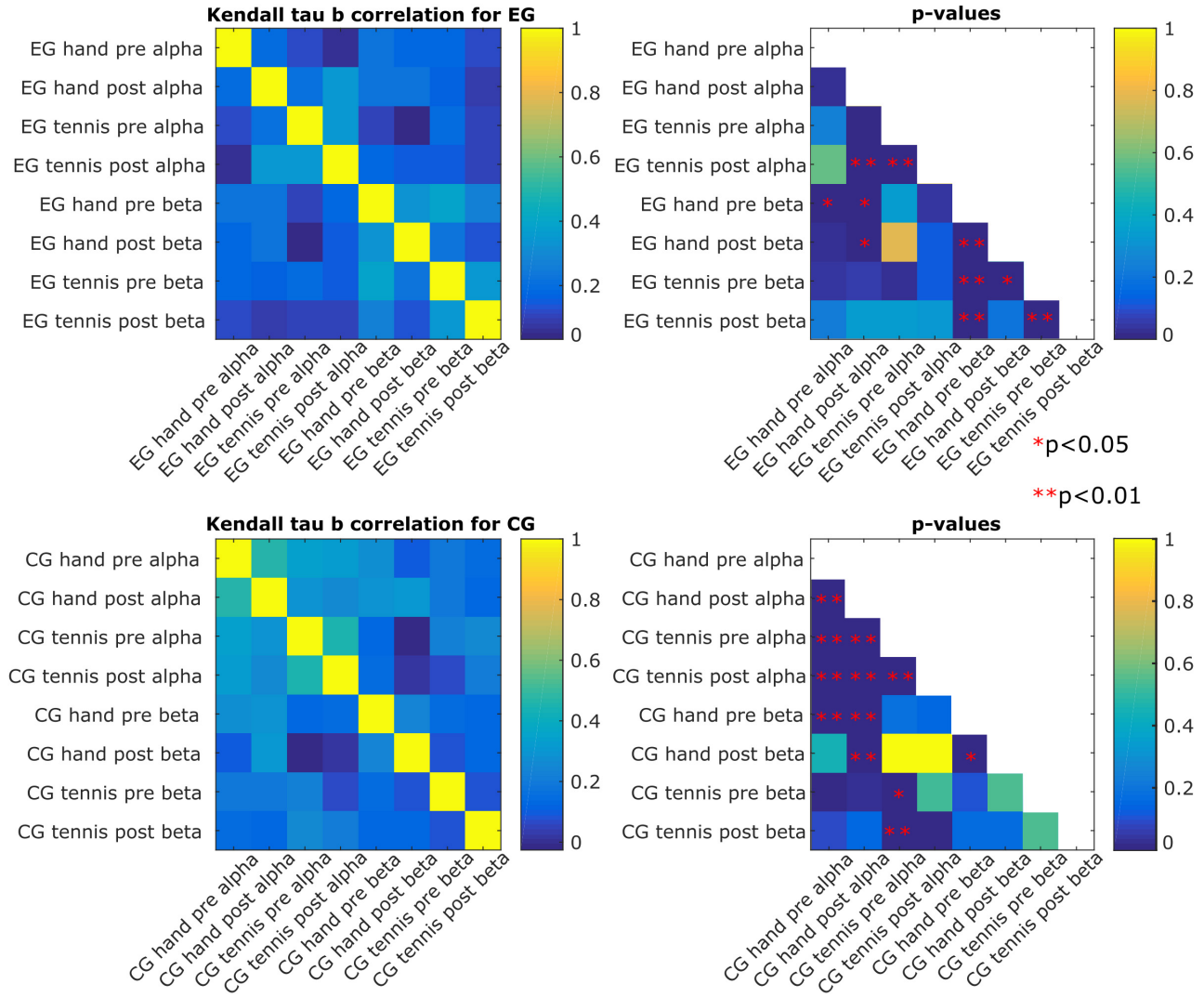

FIGURE 6 | Kendall's Tau-b correlation among the eight conditions for each of the two groups of subjects (experimental and control) and their associated *p*-values. A significant *p*-value leads to the rejection of the null hypothesis that the correlation would be 0 (i.e., independent conditions), and it indicates that the pair of conditions shares a similar distribution.

$p = 0.000007$ for tennis pre-tennis post than in the alpha band for the subjects in the EG.

For the subjects in the control group, we found a stronger consistency in ranking in the alpha band than in the beta band, especially across time periods ($\tau_b = 0.47$, $p = 9.2^*e{-}11$ for the hand pre alpha to hand post-alpha and $\tau_b = 0.45$, $p = 9.6^*e{-}10$ for the tennis pre alpha to tennis post-alpha). The consistency across conditions was also significant: $\tau_b = 0.33$, $p = 0.0005$ for tennis pre alpha to hand pre alpha and $\tau_b = 0.25$, $p = 0.006$ for tennis post-alpha to hand post-alpha. In the beta band, the only significant correlation was between hand post and the hand pre ($\tau_b = 0.23$, $p = 0.02$). The other significant correlations were found across frequency bands but for the same condition or time period ($\tau_b = 0.27$, $p = 0.002$ for hand pre beta to hand pre alpha, $\tau_b = 0.29$, $p = 0.0005$ for hand pre beta to hand post-alpha, and $\tau_b = 0.3$, $p = 0.0004$ for hand post-beta to hand post-alpha). For the tennis condition, the significant correlations were $\tau_b = 0.22$, $p = 0.047$ for pre beta to pre alpha and $\tau_b = 0.25$, $p = 0.009$ for post-beta to pre alpha.

DISCUSSION

The aim of this work was to re-evaluate data from a previous study focusing on intra- and inter-individual differences in the observed brain patterns of the individuals. More concretely, we investigated ERD/S patterns during sports motor imagery and discovered high variability among the subjects. By taking into account the ERD/S patterns at the level of all the six ROIs, we assessed the dissimilarity between these patterns by means of distances. The subject-specific ERD/S values for each ROI (**Figure 2**) shows that some subjects elicit similar ERD/S values

throughout the conditions and time points. However, we found very different ERD/S values among subjects in the EG. For example, subject EG3 shows a strong negative ERD/S value at the level of ROI3 and ROI5 in both hand and tennis pre conditions for both alpha and beta frequencies. These values slightly increase but remain negative for all the conditions and frequencies in the post-intervention period. Contrarily, another subject (EG14) presents positive ERD/S values over all conditions. Similar observations have been found in the control group, for example, subject CG3 compared with subject CG12. Moreover, we observed that the ERD/S values for the beta frequency show less variability within and among the subjects for either group compared with the alpha frequency band which was also observed in the study by Haegens et al. (2014). This variability was further assessed in the ERD/S values at the group level. For both conditions, hand and tennis, the distribution of ERD/S values shows larger variability in the alpha band than in the beta band throughout the ROIs (**Figures 3A,B**). Moreover, we observed that in the EG, some subjects show large positive ERD/S values in the alpha band in the pre-intervention period indicating a strong variability among this sample of participants. Especially for MI of tennis, the ERD/S patterns before the intervention phase show a high distribution across frequency bands and ROIs (**Figure 3B**). Based on these results, it is somehow speculative to attribute any activity changes particularly to the intervention. Beside some outliers, the variability in the beta band is quite low for all conditions and groups.

The results of inter-individual differences in terms of distance measures between subject-specific ERD/S patterns show again more differences for the alpha compared with the beta band. In the alpha band (**Figure 4A**), we observed some clustering in the ranking of the subjects, therefore showing smaller distances than others. Furthermore, a consistency in ranking across time periods both for the EG and for the control group exists. For the control group, we also observed similar rankings across conditions. In the beta band (**Figure 4B**), the ranking of the subjects was more similar for the EG across conditions and time periods than for the subjects of the control group. Moreover, the range of the variability was larger for the alpha band than for the beta band. In other words, when assessing the distance between a pair of subjects in terms of the ERD/S values in the alpha band, we can find subjects that show strong (dis)similarities with others, whereas in the beta band the magnitude of these (dis)similarities is more contained. A better visualization of the relationship between the ERD/S magnitudes of different subjects is illustrated in the MDS plots (**Figures 5A,B**). In the alpha band, we observe that some subjects remain consistent in their ranking with respect to others across conditions and time periods. For example, in the EG subjects 8, 12, and 13 maintain their similarity across conditions and time periods. For the beta band, we also observed that some subjects cluster together, for example, for the EG, subjects 12 and 13 are close in their rankings both across conditions and time periods, and also across frequency bands, as we have seen in **Figure 5A**. For the control group, we observed a different ranking of the subjects between conditions and time periods compared with the consistency in ranking found in the alpha band (**Figure 6**).

Haegens et al. (2014) reported similar findings of inter-subject variability in posterior alpha peak frequency by means of magnetoencephalography. They investigated how alpha peak frequency differed across cognitive conditions and ROIs within and between subjects with an N-back paradigm. Compared with beta peak frequencies, the alpha peak frequency in posterior regions increases with increasing cognitive demands and engagement. Furthermore, they showed that it is also valid across a wider frequency range than the commonly used 8–12 Hz band. This should be taken into account when comparing power values between different conditions. Moreover, they claimed that using a fixed alpha band might bias results against certain subjects and conditions. Even though many researchers observed that individual differences in brain oscillations predict certain cognitive performance (Klimesch et al., 1990a; Park et al., 2014; Jiang et al., 2015), further research considering individual oscillatory (dis)similarity is essential for a better understanding of its correlation. The variability in alpha power plays also an important role in studies investigating the resting state, especially in fMRI experiments (Laufs et al., 2003; Moosmann et al., 2003; Gonçalves et al., 2006). For example, Gonçalves et al. (2006) performed a simultaneous recording of EEG-fMRI to identify blood oxygenation level–dependent changes associated with spontaneous variations of the alpha rhythm, which is an indicator of the brain resting state (Goldman et al., 2002). Their analysis was focused on inter-subject variability associated with the resting state. Results suggest that the resting state varies over subjects and, sometimes, even within one subject. Following this, they suggested that the inter-subject variability of the resting state should be addressed when comparing fMRI results from different subjects. Although there is evidence that brain network structure differs between persons (Chu et al., 2012; Cox et al., 2018), the contribution of different frequency bands and oscillatory activity is still unknown and needs further fine-grained characterization.

Another study revealed anatomical structure of the premotor-parietal network to be an effective factor contributing to inter-individual differences in brain activation (Kasahara et al., 2015). They found that MI related patterns are associated with development of non-primary somatosensory and motor areas. In their study, they found that gray matter volume in motor-related cortical areas like the supplementary motor area (SMA) and the dorsal premotor cortex (PMd) correlated with BCI success rate. These areas are well-known as the substrates of motor imagery and planning (Hanakawa et al., 2003, 2008). Participants with greater gray matter volume in the SMA, SSA, and pre-PMd are more likely to show the desired brain activity during motor imagery to increase BCI performance. Advancing our understanding of BCI performance in relation to its neuroanatomical correlates may lead to better customization of BCIs based on individual brain structure.

Finally, the outcome of this variability analysis brings us to the following suggestions for future studies: especially in the application of motor imagery paradigms for EEG-based BCI systems, a user-centered measurement design might be beneficial. Beside the investigation of subject-specific motor-related oscillations (ERD or ERS), demographic and individual

features of the participants might be relevant. For example, like we observed in our study (Wriessnegger et al., 2018), participants which are used to playing tennis frequently show different ERD/S patterns in the alpha band compared with participants being less sportive. Previous studies already reported different factors influencing BCI performance (Blankertz et al., 2010; Kübler et al., 2011; Jeunet et al., 2016); nevertheless, attention should also be paid to special sports, skills, or habits that the participant might have. Moreover, a pre-investigation of the subject-specific patterns during a certain training or intervention might be important for every future study focusing on neural correlates of motor imagery, especially when comparing experts and novices in a special cognitive task or sports performance. Generally, more attention should be paid to the composition of the sample of participants and a standard analysis of variability should always be included in the usual mean value analysis. In any case, the calculation of average parameters alone might lead to an over- or underestimation of the suspected neuronal activation patterns during motor imagery performances.

Because ERD measures are conventionally analyzed within fixed frequency bands, inter-individual differences like those we have observed in our study often occur. This means that an inter-individual difference of about 1–2 Hz is quite a common case (Klimesch, 1997). These inter-individual differences in the alpha band are primarily due to differences in memory performance (Klimesch et al., 1990b, 1993). By calculating ERD in the alpha band (Pfurtscheller and Aranibar, 1977) significant parts of alpha power will fall outside of a fixed frequency window and elicited large inter-individual variability.

To solve this problem, one can adjust the frequency bands to the individual alpha frequency (IAF) for each participant and calculate the bandwidth for the alpha frequency as a percentage of IAF (Doppelmayr et al., 1998; Goljahani et al., 2012; Grandy et al., 2013).

CONCLUSION

Many authors often reported observing high inter- and intra-individual differences in brain activity among subjects but without paying much attention to it. This fact and the observation of great variability in the data of our previous study led us to perform additional (dis)similarities analysis. By calculating different distribution measurements of distances, we confirmed a high variability among participants during motor imagery primarily in the alpha frequency band. More concretely, when assessing the distance between a pair of subjects in terms of the ERD/S values in the alpha band, some subjects show strong (dis)similarities with others, whereas in the beta band the magnitude of these (dis)similarities is more contained. Moreover, we can observe that for some subjects, the within-subject ERD/S values remain similar throughout the conditions and time points; however, among subjects these values are very different. Although we identified a high variability among subjects during MI, the extent to which these inter-individual differences are a reliable indicator of the heterogeneity of a group needs to be further assessed in a longitudinal study involving further participants. In conclusion, we believe that metrics of intra- and inter-individual differences should be more frequently reported in BCI studies. These metrics could inform the development of generic BCI systems that target the adaptation among multiple users and sessions.

DATA AVAILABILITY STATEMENT

The data analyzed in this study is subject to restrictions. Requests to access these datasets should be directed to the corresponding author: s.wriessnegger@tugraz.at.

ETHICS STATEMENT

The studies involving human participants were reviewed and approved by Medical University Graz. The patients/participants provided their written informed consent to participate in this study.

AUTHOR CONTRIBUTIONS

SW conducted the study, analyzed the original data, and wrote the text of the article. CB supervised the study, performed some data analysis, and proofread the article. GM-P provided the facilities for conducting the study and proofread the article. AS performed the data analysis and wrote some text of the article. All authors read and approved the final article.

FUNDING

This work was supported by ERC Consolidator Grant 681231 "Feel Your Reach."

REFERENCES

Ahn, M., and Jun, S. C. (2015). Performance variation in motor imagery brain–computer interface: a brief review. *J. Neurosci. Methods* 243, 103–110. doi: 10.1016/j.jneumeth.2015.01.033

Allison, B. Z., and Neuper, C. (2010). "Could anyone use a BCI?," in *Brain-Computer Interfaces*, eds D. Tan and A. Nijholt (London: Springer), 35–54. doi: 10.1007/978-1-84996-272-8_3

Annett, J. (1995). Motor imagery: perception or action? *Neuropsychologia* 33, 1395–1417.

Bamdadian, A., Guan, C., Ang, K. K., and Xu, J. (2014). The predictive role of pre-cue EEG rhythms on MI-based BCI classification performance. *J. Neurosci. Methods* 235, 138–144. doi: 10.1016/j.jneumeth.2014.06.011

Blankertz, B., Sannelli, C., Halder, S., Hammer, E. M., Kübler, A., Müller, K.-R., et al. (2010). Neurophysiological predictor of SMR-based BCI performance. *NeuroImage* 51, 1303–1309. doi: 10.1016/j.neuroimage.2010.03.022

Bodenmann, S., Rusterholz, T., Dürr, R., Stoll, C., Bachmann, V., Geissler, E., et al. (2009). The functional Val158Met polymorphism of *COMT* predicts interindividual differences in brain α oscillations in young men. *J. Neurosci.* 29, 10855–10862. doi: 10.1523/JNEUROSCI.1427-09.2009

Chu, C. J., Kramer, M. A., Pathmanathan, J., Bianchi, M. T., Westover, M. B., Wizon, L., et al. (2012). Emergence of stable functional networks in long-term human electroencephalography. *J. Neurosci.* 32, 2703–2713.

Corsi, M. C., Chavez, M., Schwartz, D., Hugueville, L., Khambhati, A. N., Bassett, D. S., et al. (2019). Integrating EEG and MEG signals to improve motor imagery classification in brain–computer interface. *Int. J. Neural Syst.* 29:1850014. doi: 10.1142/S0129065718500144

Cox, R., Schapiro, A. C., and Stickgold, R. (2018). Variability and stability of large-scale cortical oscillation patterns. *Netw. Neurosci.* 2, 481–512.

Daeglau, M., Wallhoff, F., Debener, S., Condro, I. S., Kranczioch, C., and Zich, C. (2020). Challenge accepted? Individual performance gains for motor imagery practice with humanoid robotic EEG neurofeedback. *Sensors* 20:1620. doi: 10.3390/s20061620

Doppelmayr, M., Klimesch, W., Pachinger, T., and Ripper, B. (1998). Individual differences in brain dynamics: important implications for the calculation of event-related band power. *Biol. Cybernet.* 79, 49–57.

Goldman, R. I., Stern, J. M., Engel, J. Jr, and Cohen, M. S. (2002). Simultaneous EEG and fMRI of the alpha rhythm. *Neuroreport* 13, 2487–2492. doi: 10.1097/01.wnr.0000047685.08940.d0

Goljahani, A., D'Avanzo, C., Schiff, S., Amodio, P., Bisiacchi, P., and Sparacino, G. (2012). A novel method for the determination of the EEG individual alpha frequency. *Neuroimage* 60, 774–786. doi: 10.1016/j.neuroimage.2011.12.001

Gonçalves, S. I., De Munck, J. C., Pouwels, P. J., Schoonhoven, R., Kuijer, J. P., Maurits, N. M., et al. (2006). Correlating the alpha rhythm to BOLD using simultaneous EEG/fMRI: inter-subject variability. *Neuroimage* 30, 203–213. doi: 10.1016/j.neuroimage.2005.09.062

González-Franco, M., Yuan, P., Zhang, D., Hong, B., and Gao, S. (2011). "Motor imagery based brain-computer interface: a study of the effect of positive and negative feedback," in *Proceedings of the Annual International Conference of the IEEE Engineering in Medicine and Biology Society, Boston, MA*, (Piscataway, NJ: IEEE), 6323–6326.

Grandy, T. H., Werkle-Bergner, M., Chicherio, C., Schmiedek, F., Lövén, M., and Lindenberger, U. (2013). Peak individual alpha frequency qualifies as a stable neurophysiological trait marker in healthy younger and older adults. *Psychophysiology* 50, 570–582. doi: 10.1111/psyp.12043

Grèzes, J., and Decety, J. (2001). Functional anatomy of execution, mental simulation, observation, and verb generation of actions: a meta-analysis. *Hum. Brain Map.* 12, 1–19.

Grosse-Wentrup, M. (2012). Modulating attentional states by EEG-based neurofeedback. *Biomed. Eng.* 57. Available online at: https://doi.org/10.1515/bmt-2012-4526 (accessed 30 August, 2012),

Grosse-Wentrup, M., and Schölkopf, B. (2012). High gamma-power predicts performance in sensorimotor-rhythm brain–computer interfaces. *J. Neural Eng.* 9:046001. doi: 10.1088/1741-2560/9/4/046001

Grosse-Wentrup, M., Schölkopf, B., and Hill, J. (2011). Causal influence of gamma oscillations on the sensorimotor rhythm. *NeuroImage* 56, 837–842. doi: 10.1016/j.neuroimage.2010.04.265

Haegens, S., Cousijn, H., Wallis, G., Harrison, P. J., and Nobre, A. C. (2014). Inter- and intra-individual variability in alpha peak frequency. *Neuroimage* 92, 46–55. doi: 10.1016/j.neuroimage.2014.01.049

Halder, S., Agorastos, D., Veit, R., Hammer, E. M., Lee, S., Varkuti, B., et al. (2011). Neural mechanisms of brain–computer interface control. *Neuroimage* 55, 1779–1790. doi: 10.1016/j.neuroimage.2011.01.021

Halder, S., Ruf, C. A., Furdea, A., Pasqualotto, E., De Massari, D., van der Heiden, L., et al. (2013). Prediction of P300 BCI aptitude in severe motor impairment. *PLoS One* 8:e76148. doi: 10.1371/journal.pone.0076148

Halme, H. L., and Parkkonen, L. (2018). Across-subject offline decoding of motor imagery from MEG and EEG. *Sci. Rep.* 8:10087. doi: 10.1038/s41598-018-28295-z

Hanakawa, T., Dimyan, M. A., and Hallett, M. (2008). Motor planning, imagery, and execution in the distributed motor network: a time-course study with functional MRI. *Cereb. Cortex* 18, 2775–2788. doi: 10.1093/cercor/bhn036

Hanakawa, T., Immisch, I., Toma, K., Dimyan, M. A., Van Gelderen, P., and Hallett, M. (2003). Functional properties of brain areas associated with motor execution and imagery. *J. Neurophysiol.* 89, 989–1002. doi: 10.1152/jn.00132.2002

Höhne, J., Holz, E., Staiger-Sälzer, P., Müller, K.-R., Kübler, A., and Tangermann, M. (2014). Motor imagery for severely motor-impaired patients: evidence for brain-computer interfacing as superior control solution. *PLoS One* 9:e104854. doi: 10.1371/journal.pone.0104854

Jeannerod, M. (1994). The representing brain: neural correlates of motor intention and imagery. *Behav. Brain Sci.* 17, 187–202. doi: 10.1017/s0140525x00034026

Jeannerod, M., and Decety, J. (1995). Mental motor imagery: a window into the representational stages of action. *Curr. Opin. Neurobiol.* 5, 727–732.

Jeunet, C., Jahanpour, E., and Lotte, F. (2016). Why standard brain-computer interface (BCI) training protocols should be changed: an experimental study. *J. Neural Eng.* 13:036024. doi: 10.1088/1741-2560/13/3/036024

Jiang, H., van Gerven, M. A. J., and Jensen, O. (2015). Modality-specific alpha modulations facilitate long-term memory encoding in the presence of distracters. *J. Cogn. Neurosci.* 27, 583–592.

Kasahara, K., DaSalla, C. S., Honda, M., and Hanakawa, T. (2015). Neuroanatomical correlates of brain–computer interface performance. *Neuroimage* 110, 95–100. doi: 10.1016/j.neuroimage.2015.01.055

Kleih, S. C., and Kübler, A. (2013). Empathy, motivation, and P300 BCI performance. *Front. Hum. Neurosci.* 7:642. doi: 10.3389/fnhum.2013.00642

Klimesch, W. (1997). EEG-alpha rhythms and memory processes. *Int. J. Psychophysiol.* 26, 319–340. doi: 10.1016/s0167-8760(97)00773-3

Klimesch, W. (1999). EEG alpha and theta oscillations reflect cognitive and memory performance: a review and analysis. *Brain Res. Rev.* 29, 169–195. doi: 10.1016/s0165-0173(98)00056-3

Klimesch, W., Schimke, H., Ladurner, G., and Pfurtscheller, G. (1990b). Alpha frequency and memory performance. *J. Psychophysiol.* 4, 381–390.

Klimesch, W., Schimke, H. A. N. N. E. S., and Pfurtscheller, G. (1993). Alpha frequency, cognitive load and memory performance. *Brain Topogr.* 5, 241–251. doi: 10.1007/BF01128991

Klimesch, W., Pfurtscheller, G., Mohl, W., and Schimke, H. (1990a). Event-related desynchronization, ERD-mapping and hemispheric differences for words and numbers. *Int. J. Psychophysiol.* 8, 297–308.

Kruskal, J., and Wish, M. (1978). *Multidimensional Scaling. Sage University Paper Series on Quantitative Applications in the Social Sciences, No. 07-011*. Newbury Park, CA: Sage Publications.

Kübler, A., Blankertz, B., Müller, K.-R., and Neuper, C. (2011). "A model of BCI-control," in *Proceedings of the 5th International Brain–Computer Interface Workshop Train Course September 22–24 2011*, eds G. R. Müller-Putz, R. Scherer, M. Billinger, A. Kreilinger, V. Kaiser, and C. Neuper (Graz: Graz University of Technology), 100–103.

Kübler, A., Holz, E., and Kaufmann, T. (2013). "Bringing BCI controlled devices to end-users: a user centered approach and evaluation," in *Converging Clinical and Engineering Research on Neurorehabilitation*, eds J. Pons, D. Torricelli, and M. Pajaro (Berlin: Springer), 1271–1274. doi: 10.1007/978-3-642-34546-3_212

Laufs, H., Kleinschmidt, A., Beyerle, A., Eger, E., Salek-Haddadi, A., Preibisch, C., et al. (2003). EEG-correlated fMRI of human alpha activity. *Neuroimage* 19, 1463–1476. doi: 10.1016/s1053-8119(03)00286-6

Leeb, R., Friedman, D., Müller-Putz, G. R., Scherer, R., Slater, M., and Pfurtscheller, G. (2007a). Self-paced (asynchronous) BCI control of a wheelchair in virtual environments: a case study with a tetraplegic. *Comput. Intell. Neurosci.* 2007:79642.

Leeb, R., Lee, F., Keinrath, C., Scherer, R., Bischof, H., and Pfurtscheller, G. (2007b). Brain-computer communication: motivation, aim, and impact of exploring a virtual apartment. *IEEE Trans. Neural Syst. Rehabil. Eng.* 15, 473–482.

Lotte, F., Larrue, F., and Mühl, C. (2013). Flaws in current human training protocols for spontaneous brain-computer interfaces: lessons learned from instructional design. *Front. Hum. Neurosci.* 7:568. doi: 10.3389/fnhum.2013.00568

Meyer, M. C., van Oort, E. S. B., and Barth, M. (2013). Electrophysiological correlation patterns of resting state networks in single subjects: a combined EEG-fMRI study. *Brain Topogr.* 26, 98–109.

Miller, K. J., Schalk, G., Fetz, E. E., den Nijs, M., Ojemann, J. G., and Rao, R. P. N. (2010). Cortical activity during motor execution, motor imagery, and imagery-based online feedback. *Proc. Natl. Acad. Sci. U.S.A.* 107, 4430–4435.

Moosmann, M., Ritter, P., Krastel, I., Brink, A., Thees, S., Blankenburg, F., et al. (2003). Correlates of alpha rhythm in functional magnetic resonance imaging and near infrared spectroscopy. *Neuroimage* 20, 145–158. doi: 10.1016/s1053-8119(03)00344-6

Neuper, C., Müller-Putz, G. R., Scherer, R., and Pfurtscheller, G. (2006). Motor imagery and EEG-based control of spelling devices and neuroprostheses. *Prog. Brain Res.* 159, 393–409.

Neuper, C., and Pfurtscheller, G. (2010). "Electroencephalographic characteristics during motor imagery," in *The Neurophysiological Foundations of Mental and Motor Imagery*, 65–81.

Park, J., Lee, H., Kim, T., Park, G. Y., Lee, E. M., Baek, S., et al. (2014). Role of low- and high-frequency oscillations in the human hippocampus for encoding environmental novelty during a spatial navigation task. *Hippocampus* 24, 1341–1352. doi: 10.1002/hipo.22315

Petersen, S. E., and Posner, M. I. (2012). The attention system of the human brain: 20 years after. *Annu. Rev. Neurosci.* 35, 73–89. doi: 10.1146/annurev-neuro-062111-150525

Pfurtscheller, G., and Aranibar, A. (1977). Event-related cortical desynchronization detected by power measurements of scalp EEG. *Electroencephalogr. Clin. Neurophysiol.* 42, 817–826. doi: 10.1016/0013-4694(77)90235-8

Pfurtscheller, G., Leeb, R., Keinrath, C., Friedman, D., Neuper, C., Guger, C., et al. (2006). Walking from thought. *Brain Res.* 1071, 145–152.

Pfurtscheller, G., and Neuper, C. (2001). Motor imagery and direct brain-computer communication. *Proc. IEEE* 89, 1123–1134. doi: 10.1109/5.939829

Pfurtscheller, G., and Neuper, C. (2006). Future prospects of ERD/ERS in the context of brain–computer interface (BCI) developments. *Prog. Brain Res.* 159, 433–437. doi: 10.1016/s0079-6123(06)59028-4

Pineda, J. A. (2005). The functional significance of mu rhythms: translating "seeing" and "hearing" into "doing.". *Brain Res. Brain Res. Rev.* 50, 57–68.

Porro, C. A., Francescato, M. P., Cettolo, V., Diamond, M. E., Baraldi, P., Zuiani, C., et al. (1996). Primary motor and sensory cortex activation during motor performance and motor imagery: a functional magnetic resonance imaging study. *J. Neurosci.* 16, 7688–7698.

Posner, M. I., and Petersen, S. E. (1990). The attention system of the human brain. *Annu. Rev. Neurosci.* 13, 25–42. doi: 10.1146/annurev.ne.13.030190.000325

Saha, S., Ahmed, K. I., Mostafa, R., Khandoker, A. H., and Hadjileontiadis, L. (2017). Enhanced inter-subject brain computer interface with associative sensorimotor oscillations. *Healthc. Technol. Lett.* 4, 39–43. doi: 10.1049/htl.2016.0073

Saha, S., and Baumert, M. (2019). Intra- and inter-subject variability in EEG-based sensorimotor brain computer interface: a review. *Front. Comput. Neurosci.* 13:87. doi: 10.3389/fncom.2019.00087

Schreuder, M. (2014). *Towards Efficient Auditory BCI Through Optimized Paradigms and Methods*. Berlin: epubli.

Schumacher, J., Jeunet, C., and Lotte, F. (2015). "Towards explanatory feedback for user training in brain-computer interfaces," in *Proceedings of the 2015 IEEE International Conference on Systems, Man, and Cybernetics, Kowloon*. doi: 10.1109/smc.2015.550

Sharma, N., and Baron, J.-C. (2013). Does motor imagery share neural networks with executed movement: a multivariate fMRI analysis. *Front. Hum. Neurosci.* 7:564. doi: 10.3389/fnhum.2013.00564

Smit, D. J., Boomsma, D. I., Schnack, H. G., Pol, H. E. H., and de Geus, E. J. (2012). Individual differences in EEG spectral power reflect genetic variance in gray and white matter volumes. *Twin Res. Hum. Genet.* 15, 384–392. doi: 10.1017/thg.2012.6

Wolpaw, J., and Wolpaw, E. W. (2012). *Brain–Computer Interfaces Principles and Practice*. Oxford: Oxford University Press. doi: 10.1093/acprof:oso/9780195388855.001.0001

Wriessnegger, S. C., Brunner, C., and Müller-Putz, G. R. (2018). Frequency specific cortical dynamics during motor imagery are influenced by prior physical activity. *Front. Psychol.* 9:1976. doi: 10.3389/fpsyg.2018.01976

Conflict of Interest: The authors declare that the research was conducted in the absence of any commercial or financial relationships that could be construed as a potential conflict of interest.

frontiers in Neuroscience

ORIGINAL RESEARCH
published: 27 November 2020
doi: 10.3389/fnins.2020.585509

Repeatability of Neural and Autonomic Responses to Acute Psychosocial Stress

Adam M. Goodman[1], Michael David Diggs[1], Neha Balachandran[1], Pranav S. Kakulamarri[1], Robert A. Oster[2], Jane B. Allendorfer[1] and Jerzy P. Szaflarski[1]*

[1] Department of Neurology, University of Alabama at Birmingham (UAB) Epilepsy Center, University of Alabama at Birmingham, Birmingham, AL, United States, [2] Department of Medicine, University of Alabama at Birmingham (UAB), Birmingham, AL, United States

OPEN ACCESS

Edited by:
Yu Zhang,
Lehigh University, United States

Reviewed by:
Betty Jo Salmeron,
National Institute on Drug Abuse (NIDA), United States
Suril Gohel,
Rutgers Biomedical and Health Sciences, United States

***Correspondence:**
Adam M. Goodman
agoodman@uabmc.edu;
amgood@uab.edu

Specialty section:
This article was submitted to Brain Imaging Methods, a section of the journal Frontiers in Neuroscience

Received: *20 July 2020*
Accepted: *05 November 2020*
Published: *27 November 2020*

Citation:
Goodman AM, Diggs MD, Balachandran N, Kakulamarri PS, Oster RA, Allendorfer JB and Szaflarski JP (2020) Repeatability of Neural and Autonomic Responses to Acute Psychosocial Stress. Front. Neurosci. 14:585509. doi: 10.3389/fnins.2020.585509

FMRI Montreal Imaging Stress Tasks (MIST) have been shown to activate endocrine and autonomic stress responses that are mediated by a prefrontal cortex (PFC)-hippocampus-amygdala circuit. However, the stability of the neurobehavioral responses over time and the ability to monitor response to clinical interventions has yet to be validated. The objective of this study was to compare the fMRI and physiologic responses to acute psychosocial stress in healthy volunteers during initial and follow-up visits approximately 13 weeks later, simulating a typical duration of clinical intervention. We hypothesized that responses to stress would remain highly conserved across the 2 visits in the absence of an intervention. 15 healthy volunteers completed a variant of control math task (CMT) and stress math task (SMT) conditions based on MIST. Neural responses were modeled using an event-related design with estimates for math performance and auditory feedback for each task condition. For each visit, measures of stress reactivity included differential fMRI and heart rate (SMT-CMT), as well as salivary alpha-amylase before and after scanning sessions. The results revealed that differential fMRI, as well as increased heart rate and salivary alpha-amylase from before and after scanning remained similar between visits. Intraclass correlation coefficient (ICC) values revealed areas of reliable task-dependent BOLD fMRI signal response across visits for peaks of clusters for the main effect of condition (SMT vs CMT) within dorsal anterior cingulate cortex (ACC), insula, and hippocampus regions during math performance and within subgenual ACC, posterior cingulate cortex, dorsolateral PFC regions during auditory feedback. Given that the neurobehavioral response to acute stress remained highly conserved across visits in the absence of an intervention, this study confirms the utility for MIST for assessing longitudinal changes in controlled trials that can identify underlying neurobiological mechanisms involved in mediating the efficacy of stress-reduction interventions.

Keywords: stress, functional magnetic resonance imaging, intraclass correlation, repeatability, psychophysiology

INTRODUCTION

The endocrine and autonomic responses to acute stress are part of the allostatic process that serves to maintain homeostasis in response to a threat (Ulrich-Lai and Herman, 2009; Karatsoreos and McEwen, 2011). Although this process can be adaptive, dysregulation of the stress response has been implicated in the pathophysiology of a wide range of disorders (McEwen and Gianaros, 2011). Psychosocial stress arising from the threat of social evaluation plays a prominent role in adverse health effects (Dickerson and Kemeny, 2004). Experimental functional magnetic resonance imaging (fMRI) tasks that employ the use of a mild social evaluative stressor have proven a useful tool in the human studies of the neurobehavioral response to stress. In particular, the well-established fMRI Montreal Imaging Stress Task [MIST; (Dedovic et al., 2005)] is used for assessing the neural correlates of psychosocial stress reactivity. Prior studies utilizing MIST have demonstrated that a prefrontal cortex (PFC)-hippocampus-amygdala circuit mediates endocrine and autonomic stress responses (i.e., Pruessner et al., 2008; Dedovic et al., 2009a; Khalili-Mahani et al., 2010; Allendorfer et al., 2014; Wheelock et al., 2016, 2018; Goodman et al., 2019). Despite these contributions to our understanding of the neurobiology of stress, the utility of MIST for assessing longitudinal within-subject changes in reactivity to a common stressor has yet to be validated. Understanding the effects of repeated testing with MIST has important bearing on the prospective utility of this task. In particular, there is potential utility for MIST to assess changes in the neural processing of stressful information arising from clinical interventions, such as cognitive-behavioral therapy (CBT) or mindfulness meditation training (McDermott et al., 2018). Accordingly, demonstrating the validity of MIST to examine the neurobiological benefits of clinical stress-reduction techniques first requires an assessment of the neurobehavioral stress response for potential sensitization (increased) or habituation (decreased) effects that may result from repeated exposure to the task. This new knowledge of the test-retest reliability of MIST will provide valuable insight into the utility of this task for assessing the neurobiological mechanisms underlying stress-reduction techniques.

In MIST, the exposure of participants to varying levels of stressful math tasks allows comparisons between hormonal, autonomic, and neural stress reactivity. However, the effects of repeated assessments of stress-induction create difficulty in disentangling the effect of an intervention. For example, changes in elicited behavior can result simply from repeated exposure to an emotionally evocative stimulus (i.e., non-associative learning). Specifically, increased (sensitization) or decreased (habituation) elicited responses after repeated exposure to a stimulus are mediated by changes in synaptic plasticity (Kandel, 1976). In humans, both sensitization and habituation learning appears to involve changes in activation within PFC-hippocampus-amygdala regions (Breiter et al., 1996; Fischer et al., 2003; Strauss et al., 2005). Accordingly, an assessment of potential sensitization or habituation effects for repeated exposure to MIST is essential to differentiating clinical and learning related changes in neurobehavioral stress response. Examining these potential learning effects across longitudinal MIST assessments in the absence of a clinical intervention will provide novel evidence regarding the utility of MIST for assessing the neurobiological mechanisms underlying stress-reduction techniques. Thus, the objective of the current study was to compare the neural (fMRI) and autonomic (cardiac, alpha-amylase) responses to acute psychosocial stress in healthy volunteers during an initial (V1) and second MRI visit (V2) approximately 13 weeks later, simulating a typical interval before and after a clinical intervention [e.g., 12 weeks of CBT treatment (LaFrance et al., 2014; Espay et al., 2019)]. Although we expected to observe some evidence of non-associative emotional learning, we hypothesized that neural and autonomic responses to stress would remain highly conserved across the 2 visits in the absence of an intervention.

Abbreviations: 3dLME, linear mixed effects analysis in AFNI; 3dICC, intraclass correlation analysis in AFNI; Abs, absolute value; ACC, anterior cingulate cortex; AFNI, analysis of functional neuroimages; ANOVA, analysis of variance; BOLD, blood oxygen-level dependent; BPM, beats per minute; CBT, cognitive behavioral therapy; CMT, control math task; dACC, dorsal anterior cingulate; dlPFC, dorsolateral prefrontal cortex; dmPFC, dorsomedial prefrontal cortex; fMRI, functional magnetic resonance imaging; HPA, hypothalamic-pituitary-adrenal; HR, heart rate; HC, hippocampal complex (hippocampus and parahippocampal gyrus); ICC, intraclass correlation coefficient; MIST, montreal imaging stress tasks; mm, millimeters; MNI, montreal neurological institute; MTL, medial temporal lobe; Neg, negative feedback; PCC, posterior cingulate cortex; PFC, prefrontal cortex; POMS, profile of mood states; Pos, positive feedback; PSS, perceived stress scale; RT, reaction time; SAM, sympatho-adrenomedullary; SMT, stress math task; TMD, Total Mood Disturbance; TOST, Two-one sided tests; V1, Visit 1; V2, Visit 2; vlPFC, ventrolateral Prefrontal Cortex; vmPFC, ventromedial Prefrontal Cortex.

MATERIALS AND METHODS

Participants

Fifteen volunteers (male $n = 9$) with no self-reported history of neurological or psychiatric disorders were recruited from the University of Alabama at Birmingham and completed both study visits. All participants provided written informed consent based on procedures approved by the University of Alabama at Birmingham Institutional Review Board (IRB). The informed consent document provided as much details about the study as possible without revealing the true nature of the study (e.g., "During this scan you will be asked to answer some math questions... About 13 weeks later, you will be asked to return for another visit that includes the questionnaires you completed previously and another MRI."). Following completion of participation in the study, as per IRB requirement, participants were debriefed with a full explanation of the rationale for the study design and methods used for the study and received $100 for their participation.

Psychological Measures

Prior to fMRI, all participants completed the 10-item version of the Perceived Stress Scale [PSS-10; (Cohen et al., 1983)] to assess perceived life stress. The PSS-10 is a self-report measure consisting of 10 questions related to stress perception during the month prior to the experimental session scored on a zero (never) to four (very often) Likert scale. PSS-10 scores were computed

as a sum, ranging from 0 (little or no stress) to 40 (extreme or high stress), that reflected the degree to which participants found situations or life experiences stressful. Additionally, participants completed the Profile of Mood States [POMS, (McNair, 1992)] to assess affective mood state. The POMS is a self-report measure consisting of 65 questions related to how closely different adjectives described their mood during the week prior to the experimental session. Participants rated each of the 65 adjectives on a zero (Not at All) to four (Extremely) Likert scale. These adjectives provided scores for 6 different mood state subscales: Anger, Confusion, Depression, Fatigue, Anxiety/Tension, and Vigor. POMS scores were calculated by subtracting the Vigor score from the sum of all the other mood scale scores to measure overall mood state (i.e., Total Mood Disturbance; TMD). Possible scores for TMD range between −32 and 200 and reflect the degree to which participants rate their mood disturbance. To assess whether perceived stress or mood states varied between visits, paired samples t-test compared PSS-10 and TMD scores between V1 and V2 assessments.

Stress Tasks for fMRI

Prior to MRI, participants were familiarized with the MIST task that they later completed during MRI scanning (Balachandran et al., In press). All instructions were scripted to promote uniform administration of the practice and experimental tasks. Participants completed a volume control task during a multi-echo reference scan designed to calibrate audio volume for the remainder of the study. Next, during BOLD Echo-Planar imaging (EPI), participants performed control math (CMT) and stress math tasks (SMT) that were adapted to include pre-recorded evaluative auditory feedback, regardless of performance in the tasks (Allendorfer et al., 2014, 2019; Goodman et al., 2019). Participants selected the correct answer to the math problem via pressing either the "1," "2," or "3" button on an MR-compatible button box (Current Designs; Philadelphia, PA, United States). Each of the math task scans contained series of unique math trials, each lasting 5 s in duration. At eight separate fixed points during each of the CMT and SMT scans, unique pre-recorded auditory feedback messages were presented for between 6 and 10 s durations between math trials. For example, participants heard statements such as "You're doing great, so keep it up" during the CMT and "You will have to do much better in the remaining questions" during the SMT, regardless of their performance in either task. Additionally, auditory recordings of tones (1 s) were presented at eight separate fixed points in which subjects were simultaneously asked to press "1" or "2" on the button box (5 s) to ensure participants were attentive to the task. During the CMT, participants completed 34 different subtraction problems separated by 1.5 s inter-trial intervals. Between the CMT and SMT scans, participants received instructions designed to mildly increase participant's stress to performing the SMT, compared to the CMT. Specifically, participants were told that "researchers" would be evaluating their performance and they had a variable response window between 1 and 5 s in order for their answer to count. Additionally, participants were given an additional answer choice (3-item multiple choice alternatives) to each math problem and the total number of subtraction problems was increased to 63 trials during the SMT. All other aspects of the SMT were identical to the CMT, including the relative difficulty of subtraction problems. Participant's accuracy and reaction time during both math and tone trials were recorded and two separate 2 × 2 repeated measures analysis of variance (ANOVA) compared the main effects of Task (CMT vs SMT) and Visit (V1 vs V2), as well as any potential interactions between these factors during math trials. Accuracy and reaction time during math performance and tone events were assessed as a manipulation check to confirm that task performance varied between CMT and SMT as designed.

As in all prior studies, the order of CMT followed by the SMT was identical for all subjects and was not counterbalanced (Allendorfer et al., 2014, 2019; Goodman et al., 2016, 2019; Wheelock et al., 2018; Orem et al., 2019). As demonstrated repeatedly in the stress literature, the acute stress response takes up to 90 min to recover to baseline levels (Kirschbaum et al., 1993; Kudielka et al., 2004; Dedovic et al., 2005; Gaab et al., 2005). If implemented, counterbalancing the order of stress and control scans would be expected to lead to significant variability in brain activity during the control condition simply due to counterbalancing scan order. This design was optimal for detecting individual differences in fMRI signal between SMT and CMT conditions as a function of repeated exposure to the task and scanning.

Physiological Measures

Heart rate (HR) was recorded with data sampled at 50 Hz from attachment of a photoplethysmograph to the index finger of the left hand. Average beats per minute (BPM) for CMT and SMT conditions for each subject were calculated as two individual mean values based on the entire duration of each task using QRSTool software. One participant was excluded from the heart rate analysis due to equipment failure. Thus, 14 participants were included in heart rate analyses. In order to assess whether cardiac reactivity was greater during the SMT than the CMT, and whether this difference varied as a function of visit, a 2 × 2 repeated measures ANOVA and Bonferroni corrected post-hoc analyses compared the main effects of Task (CMT, SMT) and Visit (V1, V2) on HR, as well as any potential interactions between these factors. An important goal of the current study was to assess potential stress reactivity during both V1 and V2, independently. As in previous work (Allendorfer et al., 2014, 2019; Goodman et al., 2018, 2019; Orem et al., 2019), a preplanned contrasts of SMT and CMT (SMT – CMT) served as an index of increased BPM during stressful compared to control math conditions. In order to assess whether HR was greater during SMT compared to CMT during both visits, a *priori* planned contrasts compared HR for Task (CMT, SMT) at each level of Visit (V1, V2). Given the relatively modest sample size ($n = 14$) for participants that were included in the heart rate analyses, follow-up non-parametric tests (i.e., Wilcoxon signed-rank test) further assessed any significant repeated measures effects identified by the initial parametric 2 × 2 ANOVA and post-hoc tests. To provide a more comprehensive comparison of cardiac responses to acute psychosocial stress across longitudinal assessments, we further evaluated the absence of a meaningful effect of Visit

(V1 vs V2), on cardiac stress responses (SMT – CMT) using an equivalence test [i.e., two-one sided test, TOST (Lakens, 2017)]. The implemented TOST procedure was based on the paired-samples *t*-test, but instead tests the null hypothesis that repeated measures are significantly different by assessing whether a result is within an upper and lower 90% confidence interval equivalence bound. First, the obtained effect size (Cohen's d_z) was determined based on the mean difference, SD, n, and correlation between Visit (V1, V2). Then, the estimated distribution of the observed Cohen's d_z was compared to the bounds of the smallest hypothetical effect size of interest (i.e., Cohen's $d_z = \pm 0.3$). Lastly, we tested for a large hypothetical effect size of interest (i.e., Cohen's $d_z = \pm 0.9$) to provide a broad estimate of effect sizes that would demonstrate evidence of equivalence, based on the data obtained in our sample.

Cortisol, the hormonal end-result of hypothalamic-pituitary-adrenal cortex (HPA-axis) release, aids in homeostasis and can be used to assess the endocrine response to stress in humans (Jankord and Herman, 2008; Gossett et al., 2018). However, salivary alpha−amylase is closely correlated to HPA-axis activity and has recently emerged as a beneficial alternative due to complications in cortisol measures, including time-lag of effects and anticipatory stress, (Granger et al., 2007; Gossett et al., 2018). Thus, salivary alpha-amylase was assessed at three unique time points throughout each experimental session to evaluate the sympatho-adrenomedullary (SAM) autonomic responses as an additional measure of stress reactivity. At each time point, participants provided 1-ml of saliva via passive drool into plastic tubes. Two samples were collected after consenting during pre-scan assessments at 60 and 30 min prior to entering the MRI environment. One additional sample was collected, immediately at 30 min following completion of MRI scanning. The 3 salivary samples from each participant (−60 min, −30 min, +30 min) were stored on ice until being transferred to a −20 degree Celsius freezer following the experimental session. The natural diurnal pattern in humans is characterized by a pronounced drop in the first hour after waking and gradual increase until the afternoon or evening. Based on this report, we followed recommended guidelines for salivary alpha-amylase assessments to account for potential effects related to the time of day (Nater et al., 2007). Alpha-amylase (U/ml) levels were assessed using standard assay kits in duplicate and averaged at the UAB metabolism core using a standard kit (Salimetrics, LLC) to index SAM responses (Petrakova et al., 2015). One participant did not provide usable saliva and was excluded, resulting in a total of 14 participants that were included in the final alpha-amylase analysis. A 2 × 3 repeated measures ANOVA and Bonferroni-corrected post-hoc analyses assessed the main effects of Time-points (−60 min, −30 min, +30 min) and Visit (V1, V2) on alpha-amylase concentrations, as well as any potential interactions between time point and visit. In order to assess whether alpha-amylase concentrations were greater after MIST compared to before MRI scanning during both visits, a *priori* planned contrasts compared alpha-amylase concentrations for Time-points (−60 min, −30 min, +30 min) at each level of Visit (V1, V2). Given the relatively modest sample size ($n = 14$) for participants that were included in the salivary alpha-amylase analyses, follow-up non-parametric tests (e.g., Wilcoxon signed-rank test) further assessed any significant increases identified by the initial parametric 2 × 3 ANOVA and post-hoc tests. Equivalence of Visit (V1 vs V2) on any significant increases alpha-amylase within both Visits 1 and 2 were also evaluated using the TOST procedure.

Magnetic Resonance Imaging Acquisition and Analysis

Head-first supine MRI scans were completed on a 3T Siemens Prisma scanner (Siemens Medical Solutions USA Inc., Malvern, PA, United States) at the Civitan International Neuroimaging Laboratory at the University of Alabama at Birmingham. Participants were fitted with an MR-compatible button box (right hand) and viewed a mirror affixed to the head coil that reflected a video monitor (BOLDscreen 32, Cambridge Research Systems ltd., Kent, United Kingdom) in the Siemens scanner. The duration of scanning sessions lasted approximately 60 min. All MRI sessions were scheduled to begin during afternoon hours between 1,300 and 1,700 h.

High resolution T1-weighted anatomical scans were collected in the sagittal plane via magnetization-prepared rapid acquisition with gradient echo (MPRAGE) sequence (TR = 2,400 ms, TE 2.22 ms, TI = 1,000 ms, flip angle = 8°, FOV = 24.0 cm × 25.6 cm × 16.7 cm, matrix = 256 × 256, slice thickness = 0.8 mm)]. The task scans began approximately 45 min from the start of scanning sessions. During task scans, blood-oxygen-level-dependent (BOLD) fMRI signal was measured with a multiband gradient-echo echoplanar pulse sequence (TR = 1,000 ms, TE = 35.8 ms, flip angle = 60°, FOV = 26.0 cm × 26.0 cm × 15.0 cm, matrix = 260 × 260 slice thickness = 2.5 mm, multiband acceleration factor = 6).

Analysis of all MRI data was completed using Analysis of Functional Neuroimaging [AFNI; (Cox, 1996)]. FMRI time-series data were slice-time corrected, corrected for head motion, spatially smoothed with a 4 mm full-width-at-half-maximum Gaussian filter, and co-registered with the structural image (see **Supplementary Material** for pre-processing scripts). Additional motion correction was performed by censoring images with simultaneous signal change that surpassed 3% of the total number of voxels. Head motion was calculated for each participant visit by averaging the absolute values for displacement (mm) in the superior, left, and posterior directions across all volumes of CMT and SMT scans (i.e., mean absolute head motion) using motion estimates derived during registration of the fMRI time-series (*align_epi_anat.py, 3dvolreg*). Noise occurring outside of the brain was removed using binary masking. Anatomical and functional data were normalized to the MNI 152 ICBM template and resampled to a 1 mm^3 isotropic resolution. FMRI signal time series from both math tasks were concatenated and then modeled with a gamma variate hemodynamic response function using individual reference waveforms for task events including math trials, audio feedback, and tones for the CMT and SMT (*3dDeconvolve*). The six parameters of participants' head motion were modeled as regressors of no interest. No other nuisance regression was performed during first-level modeling. Thus,

there were 12 total regressors included in first-level modeling, including task relevant and nuisance factors that occurred in the time series. Percent signal change (% signal) was used as an index of the amplitude of the fMRI signal response to task events. Although responses to tone events were included in first-level modeling, these data were not submitted for further analysis in the current study.

Two separate linear mixed-effects analyses (*3dLME*) assessed the neural response to stressful math trials and negative auditory feedback. The first 3dLME analysis identified voxels with a main effect of condition (CMT, SMT), a main effect of visit (V1, V2), or voxels with significant interactions for these variables during math trials. The second *3dLME* analysis identified voxels with a main effect of condition (Positive Feedback, Negative Feedback), a main effect of visit (V1, V2), or voxels with significant interactions for these variables during auditory feedback. A gray matter mask restricted the analysis to the combined regions of interest (ROIs), including the bilateral anterior cingulate, posterior cingulate, insula, dlPFC, dmPFC, vmPFC, vlPFC, amygdala, and hippocampal complex (i.e., hippocampus and parahippocampal gyrus), generated using the standard Harvard-Oxford atlas[1] (see **Supplementary Figure 1** for depiction of the combined ROI mask). ROIs were based on *a priori* hypotheses derived from prior MIST literature (Pruessner et al., 2008; Allendorfer et al., 2014, 2019; Goodman et al., 2016, 2019; Wheelock et al., 2016). A cluster volume extent threshold was determined by the results of a Monte Carlo simulation (*3dClustSim*) in order to reduce risks of family-wise error (FWE) for the combined ROI mask. Smoothness was averaged across subjects based on spherical autocorrelation function parameters (*-acf* option in *3dFWHMx*) derived from residual volumes from the first level analysis (Cox et al., 2017). The results of this simulation yielded a critical cluster extent volume threshold of 88 mm^3 using a corrected significant threshold $p < 0.05$ and uncorrected voxelwise significance threshold of $p < 0.001$ corresponding to AFNI's cluster-forming options for nearest neighbor 3 (NN3) with two-sided criteria.

Two separate follow-up analyses were implemented to test the repeatability of task-dependent BOLD fMRI that remained consistent across visits for (1) math performance and (2) audio feedback. First, two separate cluster masks were derived from the surviving clusters identified by *3dLMEs* for the main effect of Condition. To quantify the reliability of the measurements within-subjects, a voxel-wise intraclass correlation (ICC) analysis was performed (Shrout and Fleiss, 1979) using two separate voxel-wise ICC analyses [*3dICC* (Chen et al., 2018)]. ICC values can range between 0 (low consistency) to 1 (high consistency), with ≥0.40 indicating reliable BOLD signal measures across fMRI data acquisition (Cicchetti, 1994; Szaflarski et al., 2011; McDermott et al., 2018). In the current study, two separate *3dICC* analyses with a mixed-model specification [i.e., ICC(3,1)] compared 1st-level coefficients from (1) math performance and (2) auditory feedback events across fixed factors of condition (CMT, SMT) and visit (V1, V2), and the random factor of subjects (n = 15). Resulting ICC values were identified for each cluster peak voxel. For descriptive purposes, signal extractions were performed (*3dROIstat*) on representative cluster peaks and mean BOLD signal (% change) across Condition and Visit were plotted to visualize consistency and directional differences in activation for cluster peak regions for any main effects or interactions identified by the two main *3dLME* analyses. Signal extractions were not submitted to additional statistical comparisons because these comparisons were identified as statistically significant by the two main omnibus *3dLME* tests. Accordingly, the purpose of these extractions was to interpret the direction for any significant main effects of Condition, as well as depict potential consistency for the mean estimates of these effects across Visit.

In order to provide further information on the utility of the MIST in assessing treatment mechanisms for future studies, we also calculated estimates of minimum treatment effects that would be needed to overcome the expected neural response variability between visits. More specifically, we estimated variability between visits by first calculating the standard deviation of the differences between visits obtained from results in the current study. The minimum Cohen's *d* effect size is defined as the expected difference in mean stress response (SMT – CMT; Neg – Pos) between visits (V2-V1) divided by the standard deviation of the difference in means, given our obtained sample size (n = 15), 80% power to reject the null, and a two-tailed $\alpha = 0.05$ threshold. Using the obtained mean difference for any region that met our reliability threshold (i.e., ICC ≥ 0.4), we calculated the minimum mean difference (V2-V1) that is needed to detect a statistically significant effect assuming our obtained sample size, 80% power to reject the null, and a two-tailed $\alpha = 0.05$ threshold for a paired t-test of the mean difference in stress response between Visits. All power calculations were performed using nQuery Advisor + nTerim (ver. 3.0).

Data Availability

Unthresholded statistical maps of the results from this manuscript have been made publically available at https://neurovault.org/collections/RPKVOUQF/.

RESULTS

Participants

Demographic variables are summarized in **Table 1**. Years of age were normally distributed (M = 32.00, SD = 9.03). The durations between V1 and V2 were approximately 13 weeks (M = 12.98 weeks, SD = 1.34). Two participants chose not to respond to the years of education question. Years of education for the remaining 13 participants were normally distributed (M = 16.06, SD = 2.03). Additionally, 11 participants identified as "White or European," while 3 volunteers identified as "Black or African" and 1 identified as other categories (i.e., "American Indian/Alaska Native/Black").

Psychological Measures

Participants psychological measures collected at V1 and V2 are summarized in **Table 1**. PSS-10 scores during were normally distributed during V1 (M = 14.33, SD = 6.44) and V2 (M = 14.00,

[1] http://fsl.fmrib.ox.ac.uk/fsl/

TABLE 1 | Demographics, Psychological, Control Math Task, and Stress Math Task, by Visit.

Demographics	Overall	Psychological and task measures	Visit 1 vs Visit 2		
			Visit 1	Visit 2	Mean diff
Sample size	*n* = 15	Initial saliva time-point (h:m)	13:51 (1:21)	13:12 (0:59)	0:38
Age	32.00 (9.03)	*Psychological assessments*			
Sex (male)	*n* = 9	PSS-10	14.33 (6.44)	14.00 (7.99)	0.33
Duration between visits (weeks)	12.98 (1.34)	POMS (TMD)	24.60 (31.65)	26.73 (38.20)	−2.13
		Head motion			
Years of education	16.46 (2.03)	Mean absolute motion (mm)	0.29 (0.20)	0.28 (0.19)	0.01
		Control math task			
Race		Math accuracy (% correct)	97.3 (3.2)	97.3 (3.9)	0.0
White or European	*n* = 11	Response time (ms)	2037.6 (496.1)	1825.0 (358.4)	212.6*
Black or African	*n* = 3	Tone accuracy (% correct)	100.0 (0.0)	100.0 (0.0)	0.0
Other	*n* = 1	Response time (ms)	756.0 (145.8)	780.7 (238.7)	−24.7
		Heart rate (BPM)	60.4 (6.4)	63.6 (8.0)	−3.2
		Stress math task			
		Math accuracy (% correct)	61.3 (13.3)	68.3 (13.7)	−7.0*
		Response time (ms)	2878.9 (255.7)	2938.3 (446.2)	59.4
		Tone accuracy (% correct)	98.4 (4.2)	98.4 (4.2)	0.0
		Response time (ms)	704.4 (151.5)	726.3 (209.8)	−21.9
		Heart rate (BPM)	68.9 (16.5)	66.3 (7.9)	2.6

*Data for participants reported as mean (SD) except for Sample Size, Sex, and Race which are reported as counts (n). Statistical comparisons were tested using paired samples t-tests (t) and 2 × 2 repeated measures ANOVA, with Bonferonni corrected post hocs. Results of these comparisons, including the mean difference are presented in the adjacent columns to right of the descriptive means and S.D.s for visit 1 vs. visit 2. * indicates any effect or interaction of Visit from the analysis that reached statistical significance (α = 0.05, two-tailed). h, hours; m, minutes; yrs, years; ms, milliseconds; mm, millimeters; PSS, Perceived Stress Scale; POMS, Profile of Mood States; TMD, total mood disturbance.*

SD = 7.99). Likewise, POMS TMD scores were normally distributed during V1 ($M = 24.60$, $SD = 31.65$) and V2 ($M = 26.73$, $SD = 38.20$). Paired samples *t*-tests revealed that participants PSS-10 $t(14) = 0.28$, $p = 0.78$) and POMS TMD $t(14) = -0.39$, $p = 0.70$) scores did not differ between V1 and V2 assessments.

Head Motion

Mean absolute head motion (mm) as a function of Visit is reported in **Table 1**. Paired samples t-tests revealed that participant's mean absolute head motion did not differ between V1 and V2 assessments [$t(14) = -0.10$, $p = 0.93$].

Stress Task Measures

Participant's accuracy and reaction time during math and tone trials as a function of Task and Visit are summarized in **Table 1**. The 2 × 2 repeated measures ANOVAs revealed a significant interaction between Task (CMT, SMT) and Visit (V1, V2) for math accuracy [$F(1,14) = 7.20$, $p < 0.05$]. Bonferroni-corrected *post hoc* tests revealed this interaction was driven by a difference in V1 and V2 accuracy for SMT (*mean diff* = −7.0, $p < 0.05$), but not CMT (*mean diff* = 0.0, $p = 1.0$). Furthermore, the *post hoc* tests revealed significant differences in CMT and SMT accuracy for V1 (*mean diff* = 36.0, $p < 0.001$) and V2 (*mean diff* = 29.0, $p < 0.001$). The analysis on math response time yielded a significant interaction between Task and Visit [$F(1,14) = 5.94$, $p < 0.05$]. Bonferroni-corrected *post hoc* tests revealed this interaction was driven by a difference in V1 and V2 reaction time for CMT (*mean diff* = 212.58 ms, $p < 0.05$), but not SMT (*mean diff* = −59.44 ms, $p = 0.51$). The analysis failed to yield a significant interaction between Task and Visit for tone response time [$F(1,14) = 0.00$, $p = 0.95$]. Any interactions or main effects involving Visit could not be determined for tone accuracy due to identical mean and standard deviation for Task across Visit (see **Table 1**). The analysis also revealed significant main effects for Task on math accuracy [$F(1,14) = 109.35$, $p < 0.001$], and math response time [$F(1,14) = 103.06$, $p < 0.001$], but not on tone accuracy [$F(1,14) = 2.15$, $p = 0.16$] or tone response time [$F(1,40) = 3.71$, $p = 0.08$]. Likewise, the analysis revealed a significant main effect for Visit on math accuracy [$F(1,14) = 7.36$, $p < 0.05$], but not on math response time [$F(1,14) = 1.75$, $p = 0.21$], or tone response time [$F(1,14) = 0.56$, $p = 0.47$].

Physiological Measures

Figure 1 shows participant's mean cardiac and salivary alpha-amylase stress reactivity assessments across the MRI visits. Mean BPM results for CMT and SMT across V1 and V2 are summarized in **Table 1**. The 2 × 2 repeated measures ANOVA that assessed Task (CMT, SMT) and Visit (V1, V2) on HR (BPM) failed to yield a significant interaction of Task and Visit, $F(1,13) = 2.60$, $p = 0.13$, or main effect of Visit, $F(1,13) = 0.02$, $p = 0.90$. This analysis did, however, reveal greater BPM during SMT compared to CMT (*mean diff* = 5.58 BPM), regardless of visit [$F(1,13) = 10.44$, $p < 0.01$]. Planned contrasts revealed greater BPM during SMT compared to CMT during both V1 (*mean diff* = 8.46 BPM, $p < 0.05$) and V2 (*mean diff* = 2.71 BPM, $p < 0.05$). Follow-up Wilcoxon signed-rank tests also revealed greater BPM during

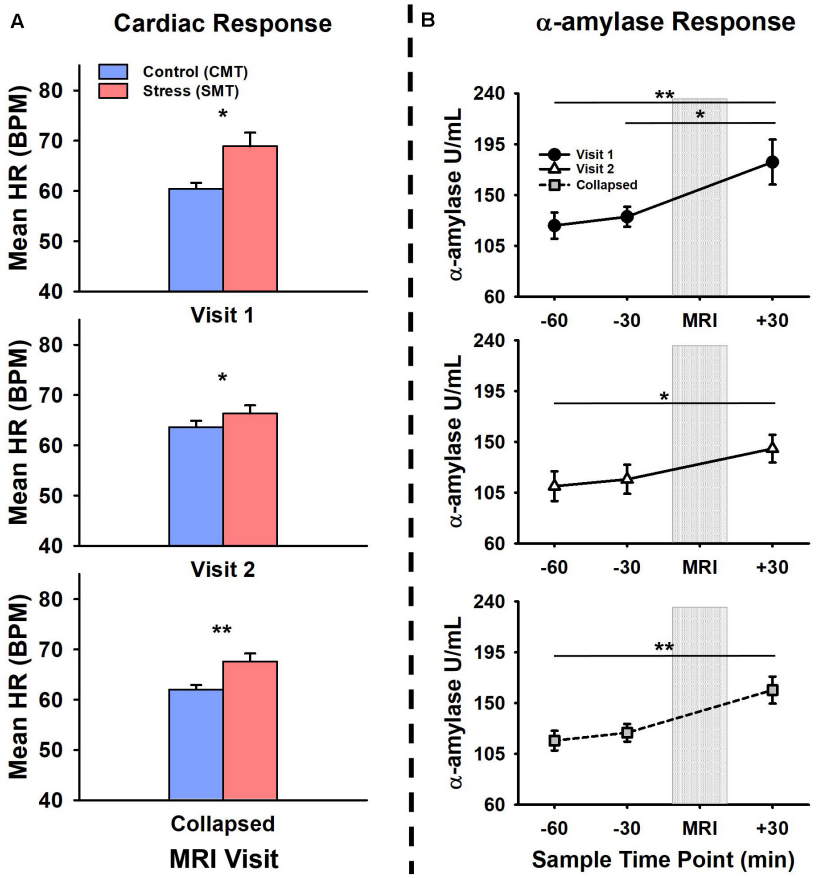

FIGURE 1 | Comparisons of visit 1 (V1), visit 2 (V2), and collapsed (visit 1 and 2 combined) assessments of **(A)** cardiac and **(B)** alpha-amylase (α-amylase; right) stress responses during V1 (top panel), V2 (middle panel), and collapsed across (bottom panel) MRI scanning visits. Heart rate (HR), measured in beats per minute (BPM) was increased during stressful math compared to control math, during V1, V2, and collapsed across visit (a). Salivary α-amylase (U/ml) was increased following stressful math at +30 min post-MRI compared to –60 min and –30 min pre-MRI collapsed across MRI scanning visits. Salivary α-amylase was increased at +30 min compared to –60 min and –30 min during V1, and at +30 min compared to –60 min during V2. Error bars reflect SEM after adjusting for between-subjects variance (Loftus and Masson, 1994). Asterisks indicate significant main effects of condition (SMT vs CMT) on mean HR and time point (–60 min vs +30 min; –30 min vs +30 min) on salivary α-amylase revealed by ANOVA, Bonferonni-corrected *post-hoc*, and planned contrast analyses, $^{*}p < 0.05$; $^{**}p < 0.01$.

SMT compared to CMT during both V1 ($z = 3.17$, $p < 0.01$) and V2 ($z = 2.97$, $p < 0.01$). The TOST procedure indicated that the observed effect size ($dz = -0.37$) was not significantly within the equivalent bounds of dz = ±0.3, (or in raw scores: ±4.48, $t(13) = -0.25$, $p = 0.60$. However, when the anticipated effect of Visit was increased to a much larger effect size of $dz = \pm 0.9$, (or in raw scores: ± 13.44), the effect of visit was significantly within the equivalent bounds $t(13) = 1.88$, $p < 0.05$.

The initial salivary sample time-point (−60 min) for all participants (see **Table 1**) did not differ between visits $t(13) = 1.38$, $p = 0.19$. The 2 × 3 repeated measures ANOVA that assessed Time-points (−60 min, −30 min, +30 min) and Visit (V1, V2), on salivary alpha-amylase (U/mL) failed to yield a significant interaction of Task and Visit, $F(2,26) = 1.17$, $p = 0.33$, or main effect of Visit, $F(1,13) = 1.37$, $p = 0.26$. This analysis did, however, reveal increased salivary alpha-amylase across Time-points (−60 min, −30 min, +30 min), [$F(2,26) = 9.03$, $p < 0.01$]. Bonferroni-corrected *post hoc* tests revealed this significant main effect was driven by increased alpha-amylase measures at +30 min compared to −60 min (*mean diff* = 55.29 U/mL, $p < 0.01$). The remaining Bonferroni-corrected *post-hoc* comparisons failed to reach significance (*mean diffs* < 33.43 U/mL, *ps* > 0.05). Planned contrasts revealed increased alpha-amylase measures at +30 min compared to −60 min (*mean diff* = 70.66 U/mL, $p < 0.05$) and −30 min (*mean diff* = 60.51 U/mL, $p < 0.01$) during V1, and at +30 min compared to −60 min (*mean diff* = 41.91 U/mL, $p < 0.05$) during V2. All remaining planned contrasts failed to reach significance (*mean diffs* < 35.55 U/mL, all *ps* > 0.23). Non-parametric follow-up tests also revealed increased alpha-amylase measures at +30 min compared to −60 min ($z = 2.73$, $p < 0.01$) and −30 min ($z = 2.61$, $p < 0.05$) during V1, and at +30 min compared to −60 min ($z = 2.10$, $p < 0.05$) during V2. Based on the failure to detect a significant interaction between the factors of Task and Visit, but significantly increased alpha-amylase between −60 min and +30 across both Visits 1 and 2, we further evaluated potential time of day effects and equivalence for alpha-amylase stress responses (−60 min > +30 min). There was no effect of time

of day on alpha-amylase stress responses (−60 min > +30 min) for Visit 1 ($r = 0.21$, $p = 0.47$) or Visit 2 ($r = -0.03$, $p = 0.92$). The results of the TOST procedure indicated that the observed effect of Visit ($dz = -0.24$) was not significantly within the equivalent bounds of $dz = \pm 0.3$, (or in raw scores: ±36.5), $t(13) = 0.24$, $p = 0.41$. However, when the anticipated effect of Visit was increased to a much larger effect size of $dz = \pm 0.9$, (or in raw scores: ±109.56), the effect of visit was significantly within the equivalent bounds $t(13) = 2.48$, $p < 0.05$.

Magnetic Resonance Imaging Results

Figure 2 (*top panel*) shows significant clusters identified by the two main *3dLME* analyses that tested for a main effect of Condition (CMT, SMT), a main effect of Visit (V1, V2), or clusters with significant interactions for these factors during math performance events (**Figure 2a**) and for a main effect of Condition (Positive Feedback, Negative Feedback), a main effect of Visit (V1, V2), or clusters with significant interactions for these factors during auditory feedback events (**Figure 2b**). Results of the voxel-wise ICC analysis exceeding the pre-determined reliability threshold [ICC ≥ 0.40 (Cicchetti, 1994; Szaflarski et al., 2011; McDermott et al., 2018) are reported in **Figure 2** (*bottom panel*) for math performance (**Figure 2c**) and auditory feedback (**Figure 2d**). **Table 2** reports the regions showing changes in neural response to math performance events during the SMT compared to the CMT that correspond to **Figure 2a** and the ICC values at peak voxel coordinates that correspond to **Figure 2c**. Clusters of activation that differed across Condition during math

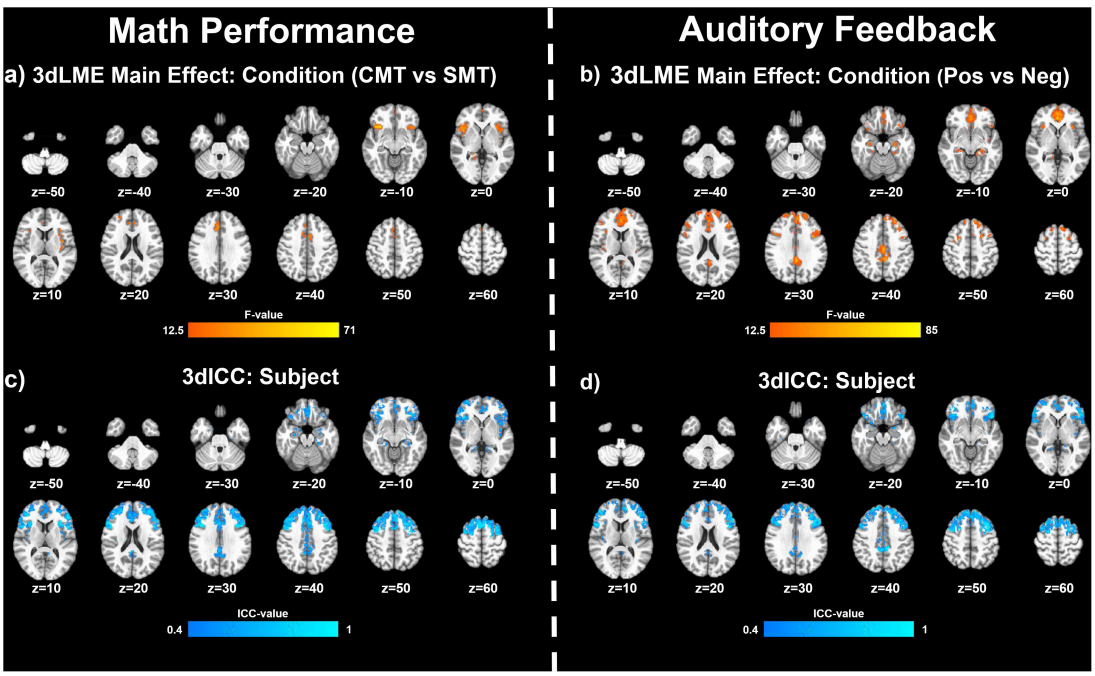

FIGURE 2 | Effects of MIST condition: Clusters (NN3) of significant activation for **(a)** the main effect of Condition (stress math task [SMT] vs control math task [CMT]) and **(b)** for the main effect of Condition (Negative Feedback [Neg] vs Positive Feedback [Pos]) that survived the volume-corrected threshold (uncorrected voxel-wise $p < 0.001$, corrected to $\alpha = 0.05$). Voxel-wise intraclass correlation (ICC) values (≥0.4) for the subject factor during **(c)** math performance and during **(d)** auditory feedback resulting from 3dLME analyses.

TABLE 2 | Regions showing effect of condition (CMT vs. SMT) during math performance.

Cluster #	Region	Hemisphere	Vol (mm^3)	MNI (x, y, z)	*F*-statistic	ICC	V2-V1 diff (obtained)	Min V2-V1 (abs)
Main effect of condition								
1	Anterior Insula	R	5335	31, 22, −8	70.92	0.56	−0.09 (0.22)	0.17
2	Dorsal Anterior Cingulate Cortex	R/L	5011	3, 29, 33	53.15	0.63	0.04 (0.37)	0.29
3	Anterior Insula	L	4482	−41, 17, −4	64.64	0.47	−0.1 (0.29)	0.23
4	Ventromedial Prefrontal Cortex	R/L	385	−1, 58, 1	27.35	0.22	–	–
5	Dorsolateral Prefrontal Cortex	R	300	28, 51, 22	33.88	0.66	−0.1 (0.19)	0.15
6	Hippocampus	R	212	19, −40, 1	28.74	0.47	−0.01 (0.28)	0.22

Cluster #, location, hemisphere, volumes, coordinates from Montreal Neurological Institute (MNI) standard space, F-statistic, and Intraclass correlation (ICC) values, difference in BOLD % signal change (SMT-CMT) reported as mean (SD) for V2 - V1, and estimates of a minimum significant treatment effect (absolute value) for the peak voxel of significant clusters. All clusters for the main effect of condition were significant at voxel-wise threshold of $p < 0.001$, corrected to cluster volume threshold of $p < 0.05$ (3dclustsim in AFNI).

performance trial events were identified with peak voxels located within the dorsal ACC (dACC), PFC, insula, and hippocampus. All clusters for the main effect of Visit and interaction of Task and Visit failed to reach volume-corrected thresholds for math performance trial events. **Table 3** reports the regions showing changes in neural response to auditory feedback events during negative feedback compared to positive feedback that correspond to **Figure 2b** and the ICC values at peak voxel coordinates that correspond to **Figure 2d**. Clusters of activation that differed across Condition during auditory feedback trial events were identified with peak voxels located within the subgenual ACC, PFC, PCC, hippocampus, and insula regions. All clusters for the main effect of visit and the interaction of Task and Visit failed to reach volume-corrected thresholds. Resultant statistical maps for the main effects and interactions effects within the combined ROI masks without voxelwise or volume-corrected thresholding are presented for Math Performance (**Supplementary Figure 2**) and Auditory Feedback (**Supplementary Figure 3**) in the **Supplementary Material**.

The results of the follow-up analysis revealed areas of reliable task-dependent BOLD signal response across visits within peak voxels of several clusters for the main effect of condition (SMT vs CMT) identified by the initial *3dLMEs*. **Figure 3** illustrates the consistency of directional differences for mean BOLD change (% signal) of between Condition (SMT vs CMT; Negative Feedback vs Positive Feedback) in an example subset of cluster peaks in regions with ICC values $\geq$0.4.

For n = 15, 80% power to reject the null, and a two-tailed α = 0.05 threshold for the paired t-test of the mean difference between Visit (H_θ: V2-V1 = 0), the minimum effect size to detect a significant difference in stress responses (SMT – CMT; Neg – Pos) for all regions is a Cohen's d = 0.778 (i.e., a moderate-to-large effect size). Estimates of the sufficient minimum treatment effects detectable by repeated assessments based on the obtained standard deviations of the difference for regions with ICC values $\geq$0.4 during Math Performance (**Table 2**) and Auditory Feedback (**Table 3**) are reported as the absolute value of the minimum mean difference (V2-V1). The minimum mean difference that is needed to detect a statistically significant difference was always greater than the mean differences observed for these regions.

DISCUSSION

The primary objective of this study was to compare the neural (fMRI) and autonomic (cardiac, alpha-amylase) responses to acute psychosocial stress in healthy volunteers during two

TABLE 3 | Regions showing effect of condition (Positive vs Negative) during audio feedback.

Cluster #	Region	Hemisphere	Vol (mm^3)	MNI (x, y, z)	*F*-statistic	ICC	V2-V1 diff (obtained)	Min V2-V1 (abs)
Main effect of condition								
1	Subgenual Anterior Cingulate Cortex	R/L	32355	−1, 37, −5	77.41	0.45	0.03 (0.71)	0.55
2	Posterior Cingulate Cortex	R/L	9148	−9, −43, 38	84.65	0.72	−0.05 (0.51)	0.39
3	Dorsolateral Prefrontal Cortex	R	3423	44, 11, 28	60.08	0.65	−0.29 (0.46)	0.36
4	Dorsolateral Prefrontal Cortex	L	3128	−37, 8, 31	59.88	0.63	−0.25 (0.53)	0.41
5	Posterior Hippocampus	L	1815	−15, −37, −9	42.99	0.27	–	–
6	Dorsolateral Prefrontal Cortex	R	1516	17, 61, 29	47.62	0.43	−0.13 (0.65)	0.50
7	Dorsolateral Prefrontal Cortex	L	1190	−41, 14, 47	65.76	0.77	−0.21 (0.32)	0.25
8	Dorsolateral Prefrontal Cortex	L	987	−26, 7, 52	43.42	0.67	−0.15 (0.24)	0.18
9	Dorsolateral Prefrontal Cortex	R	941	30, 5, 54	39.57	0.50	−0.14 (0.31)	0.25
10	Ventrolateral Prefrontal Cortex	L	881	−43, 24, −12	36.92	0.68	0.04 (0.74)	0.58
11	Anterior Insula	R	728	34, 23, 3	42.09	0.26	–	–
12	Anterior Insula	L	720	−30, 21, 2	47.94	0.56	−0.06 (0.4)	0.31
13	Dorsomedial Prefrontal Cortex	R	664	13, 36, 54	28.58	0.60	−0.1 (0.26)	0.21
14	Ventrolateral Prefrontal Cortex	R	623	36, 30, −16	29.55	0.38	–	–
15	Anterior Hippocampus	R	574	28, −20, −16	39.58	0.15	–	–
16	Posterior Parahippocampal Gyrus	R	514	21, −32, −16	29.41	0.05	–	–
17	Ventrolateral Prefrontal Cortex	L	224	−34, 61, −12	27.34	0.00	–	–
18	Posterior Insula	R	210	34, −22, 13	33.31	0.49	−0.17 (0.38)	0.29
19	Dorsomedial Prefrontal Cortex	L	186	−7, 13, 54	24.78	0.65	−0.09 (0.3)	0.23
20	Dorsolateral Prefrontal Cortex	L	165	−46, 8, 28	33.05	0.64	−0.4 (0.53)	0.41
21	Posterior Insula	L	145	−34, −25, 18	26.61	0.57	−0.24 (0.43)	0.34
22	Posterior Cingulate Cortex	R	121	8, −47, −2	27.72	0.55	−0.42 (0.64)	0.50
23	Posterior Insula	R	113	39, −9, 9	23.72	0.23	–	–
24	Posterior Insula	L	101	−39, −7, −13	21.89	0.41	−0.16 (0.37)	0.29

Cluster #, location, hemisphere, volumes, coordinates from Montreal Neurological Institute (MNI) standard space, F-statistic, and Intraclass correlation (ICC) values, difference in BOLD % signal change (SMT-CMT) reported as mean (SD) for V2 - V1, and estimates of a minimum significant treatment effect (absolute value) for the peak voxel of significant clusters. All clusters for the main effect of condition were significant at voxel-wise threshold of p < 0.001, corrected to cluster volume threshold of p < 0.05 (3dclustsim in AFNI).

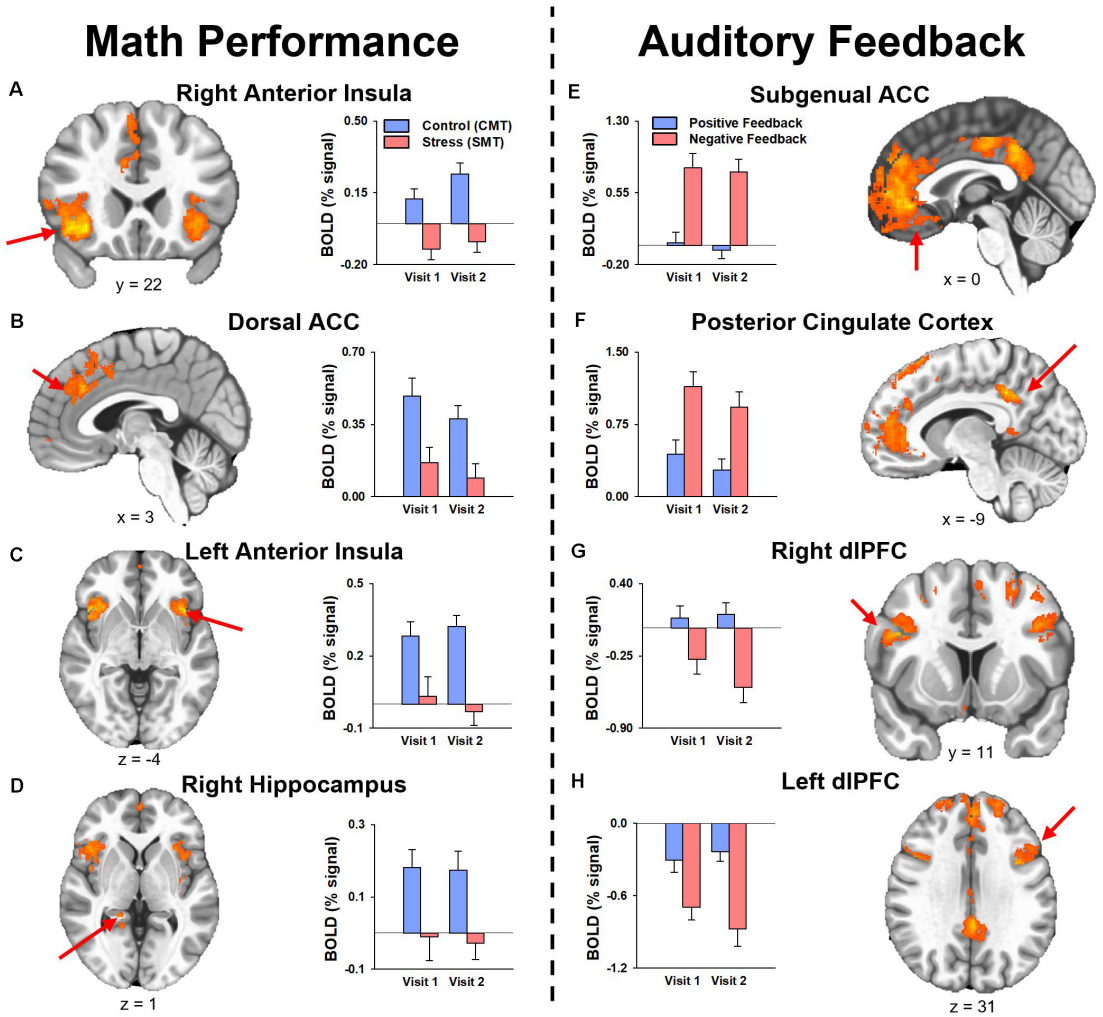

FIGURE 3 | Mean fMRI BOLD percent signal change (% signal) for cluster peaks identified by the analysis for the main effect of Condition with reliable activation across visits (i.e., ICC was ≥0.40, see **Tables 2**, **3**) during **(A–D)** math performance (*left panel*) and **(E–H)** auditory feedback (*right panel*). Mean estimates of effects demonstrated consistency of directional differences in activation for cluster peak regions identified by the two main 3dLME analyses. ACC, anterior cingulate cortex; dACC, dorsal anterior cingulate cortex; dlPFC, dorsolateral prefrontal cortex; PCC, posterior cingulate cortex.

visits separated by approximately 13 weeks simulating a typical clinical intervention duration. Although some evidence of non-associative emotional learning (i.e., sensitization and/or habituation) was predicted, we hypothesized that neural and autonomic responses to stress would remain highly conserved across the two visits in the absence of an intervention. The results indicated that responses to acute psychosocial stress during MIST remained largely consistent between V1 and V2. Further, repeatability analysis demonstrated reliable task-dependent BOLD signal responses across visits. The current study provides evidence that the neural mechanisms underlying autonomic stress responses, as well as these peripheral stress responses themselves, fail to demonstrate evidence of sensitization or habituation as a function of repeated testing with MIST when applied at approximately 13 weeks apart. Given that we observed reliability of task-dependent BOLD signal activation across visits in the absence of an intervention, these finding support the utility of longitudinal assessments of the neurobehavioral response to acute psychosocial stress to assess mechanisms of stress-targeted treatment in randomized controlled trials.

Stress Task Responses

Accuracy and reaction time comparisons during CMT and SMT conditions are utilized as a manipulation check to validate that task conditions elicited the experimenter-intended psychosocial stress in the task (e.g., Wheelock et al., 2016; Goodman et al., 2019). In the current study, decreased accuracy and increased reaction time (RT) for math trials during the SMT compared to the CMT confirms that task performance varied between MIST conditions as designed. Specifically, decreases in accuracy and increases in reaction time for the SMT compared to CMT did not differ between visits. Alternatively, reaction time was decreased in the CMT and accuracy was increased in the SMT during V2 compared to V1, suggesting that there is a small

but significant benefit in task as a function of repeated testing. Given that participants improved in response time during the CMT and providing correct answers during the SMT condition after the initial visit, these results suggests that improvements in reaction time accuracy may reflect repeated testing effects and may not serve as a valid assessment of improvements to stress management. However, it remains unclear whether similar changes in CMT response time or SMT accuracy might occur with a stress-targeted intervention in between assessments. Because we utilized increased task difficulty in the task as part of our experimental manipulation to increase psychosocial stress, there is room for interpretation that differences in accuracy and reaction time during the CMT and SMT tasks include the effects of increased difficulty as well as stress. Difficulty plays an important and interwoven role in this method assessment of the stress response and should be considered in light of future study questions. We propose that any benefits of CMT response time or SMT accuracy that may arise before and after interventions should also be compared to benefits within a control group that does not receive the intervention. Further, it is advised that the emphasis on accuracy and reaction time be placed on validation of the increased difficulty between CMT and SMT tasks, rather than to index any benefit of potential treatment effects.

Physiological Responses

In addition to math performance measures, participant autonomic responses to MIST are commonly used to validate and index stress reactivity to the task (Allendorfer et al., 2014, 2019; Wheelock et al., 2016; Elbau et al., 2018; Goodman et al., 2018, 2019; Gossett et al., 2018; Orem et al., 2019). In the present study, we sought to assess whether these measures indicated stress reactivity and whether this reactivity varied across repeated MRI visits. Our results indicated that autonomic stress reactivity was both evident and did not differ across the repeated MRI visits. More specifically, the cardiac response to acute psychosocial stress increased during the SMT compared to the CMT, regardless of visit. Likewise, alpha-amylase demonstrated increase in autonomic arousal 30 min post-scanning when compared to the initial sample, 60 min prior to scanning. Although parametric and non-parametric tests demonstrated that these responses did not differ across repeated MRI visits, follow-up equivalence tests failed to demonstrate that these cardiac and alpha-amylase responses to stress were identical across both visits. This failed equivalence result however rests on assumptions of a small-to-modest treatment effect size (i.e., $d_z = \pm 0.3$) and sample size (i.e., $n < 15$) for these comparisons. We take these findings to suggest that detection of an absent treatment effect via changes in cardiac reactivity and alpha amylase may require relatively larger individual group sample sizes (e.g., $n > 15$) and interventions with moderate-to-strong treatment effect sizes (e.g., $d_z = \pm 0.9$). Likewise, future studies of treatment effects on the physiological responses during these MRI tasks should be contextualized by comparing changes in stress reactivity between a treatment and control group(s) (see "Limitations" section). Regardless of the initial or repeated visit, cardiac and alpha-amylase reactivity appear to be both reliable and robust indices of autonomic arousal in response to acute psychosocial stress. These results suggest a need for future controlled trials to focus on cardiac and alpha-amylase reactivity to index changes in biobehavioral responses to stress.

Neural Substrates

Comparisons of fMRI activation between SMT and CMT are often utilized to assess the neural function that underlies biobehavioral responses to acute psychosocial stress during MIST (Pruessner et al., 2008; Dedovic et al., 2009b; Khalili-Mahani et al., 2010; Goodman et al., 2016, 2019; Wheelock et al., 2016; Allendorfer et al., 2019; Orem et al., 2019). Further, comparisons of task-dependent BOLD signal responses between SMT and CMT allow for assessment of unique components of stress reactivity and processing. For example, comparing BOLD signal responses during CMT and SMT conditions related to arithmetic performance may assess inhibitory neural mechanisms related to performance demands, while comparing positive and negative auditory feedback assesses the neural response to extrinsic verbal negative evaluations (Goodman et al., 2019). Thus, the current study aimed to assess whether BOLD signal responses to math performance and auditory feedback differed across repeated MRI visits.

The results indicated that responses to math performance within the dACC, PFC, insula, and hippocampus did not differ across scans and demonstrated a fair to strong (ICC range = 0.47–0.66) degree of repeatability for dACC, dlPFC, insula, and hippocampus activation peaks across visits. Decreased hippocampal activation related to math performance during SMT compared to CMT has been consistently linked to HPA-axis stress reactivity reported in prior MIST literature (Pruessner et al., 2008; Dedovic et al., 2009b; Khalili-Mahani et al., 2010; Goodman et al., 2019). Alternatively, activation of the sympatho-adrenomedullary (SAM) system provokes rapid increases in autonomic activity [e.g., cardiac (Ulrich-Lai and Herman, 2009) and alpha-amylase (Granger et al., 2007)] in response to stress. Activity within PFC and amygdala regions during stressful math vary with cardiac, sweat gland, and self-reported stress (Wheelock et al., 2016; Orem et al., 2019). Further, dACC activity corresponding to bilateral insular activity is also commonly referred to as the *salience network* (Seeley et al., 2007; Uddin, 2015) and has been implicated in emotion regulation studies of reappraisal for negative information (Ochsner et al., 2002; Phan et al., 2005; McRae et al., 2008; Buhle et al., 2014). Thus, the robust and reliable responses to stressful math within the dACC and insular regions observed in the present study implicates this neural network as regions of interest in future studies to assess the neural mechanisms underlying reappraisal-focused CBT interventions.

During auditory feedback, the results indicated that activation within subgenual ACC, PFC, PCC, hippocampus, and insula regions did not differ across scans and demonstrated a fair to strong (ICC range = 0.46–0.71) degree of repeatability for subgenual ACC, PCC, and dlPFC activation peaks across visits. Prior literature that assessed neural function related to auditory feedback during SMT compared to CMT has previously reported differential activation within ACC and PCC regions (Allendorfer et al., 2014; Goodman et al., 2019). Further, ventromedial PFC

activity corresponding to PCC activity is also commonly referred to as the *self-referencing network,* and has been implicated in mood disorder studies of self-reflection (Johnson et al., 2002; Whitfield-Gabrieli et al., 2011). Thus, the robust and reliable responses to stressful feedback within subgenual ACC and PCC regions observed in the current study implicates these areas as regions of interest in future studies of the neural mechanisms underlying self-referencing CBT interventions.

Limitations

Interpretation of the results of the current study should be considered in light of several limitations. First, the study sample was relatively small. However, the chief objective of current study was to assess repeated measures, and the current sample was sufficient to demonstrate reliability estimates in excess of our *a priori* determination for repeatability (ICC $\geq$ 0.40). **Further, stress responses are known to vary by sex** (Lee et al., 2014). Thus, a significant limitation **of** the current study was that the achieved sample size was not sufficient to assess whether acute stress reactivity was equally repeatable on all measures examined for both sexes. Additionally, the number of subjects with missing SAM reactivity assessments may affect the power to detect significant differences across visits. Although we reported no evidence for the presence of variance in autonomic measures across visits, future studies are encouraged to compare any clinical intervention against a control group for biobehavioral comparisons. Based on the findings from equivalence tests on the biobehavioral measures, relatively low sample-sizes may potentially obscure small treatment effects that differ between such an intervention and control group. Yet, we are unaware of any prior studies utilizing a comparable repeated neuroimaging stress task assessments that would provide a source for anticipated magnitude of such treatment effects. Thus, a lack of estimated treatment effect sizes should be considered a current limitation in our understanding of autonomic response variability across repeated neuroimaging stress task assessments. However, the primary focus of the current report was to validate and assess the repeatability of neural responses to repeated assessment of psychosocial stress reactivity. Related to this point, neural responses revealed no main effects of visit or interactions of condition and visit for math performance or auditory feedback. Therefore, the critical assessment of differential activation of SMT and CMT did not appear to differ across visit. Lastly, the current report did not include a clinical population studied for test-retest reliability without intervention. Our conclusions on the reliability of these neurobehavioral responses are limited to healthy individuals. As a preliminary investigation, however, the current study achieves stated goal of assessing repeated testing effects. Future controlled trial studies can provide further validation of MIST repeatability by showing changes as a function of intervention in clinical populations.

Conclusion

Given that acute stress responses remained highly conserved across visits, these findings lend support for the utility of MIST to be used to elicit neural and autonomic stress reactivity between repeated, longitudinal assessments. Demonstrating the ability of this task to elicit stress reactivity across longitudinal visits suggests this method, when implemented in a randomized control trial design, may be used to assess changes in neural and autonomic stress responses that underlie the efficacy of therapeutic interventions. In several key brain regions, peak activations of neural responses to stress were reliable between longitudinal assessments approximately 13 weeks apart in the absence of an experimenter intervention. Longitudinal assessments that utilize MIST before and after stress-reduction clinical interventions may provide new knowledge regarding changes in the neural mechanisms of emotion regulation underlying the efficacy of these interventions in clinical populations.

DATA AVAILABILITY STATEMENT

The datasets presented in this study can be found in online repositories. The names of the repository/repositories and accession number(s) can be found below: https://neurovault.org/collections/RPKVOUQF.

ETHICS STATEMENT

The studies involving human participants were reviewed and approved by the University of Alabama at Birmingham Institutional Review Board (IRB). The patients/participants provided their written informed consent to participate in this study.

AUTHOR CONTRIBUTIONS

AMG prepared the manuscript and performed statistical analysis of the data. MDD, JBA, and AMG recruited participants and administered data collection protocols. AMG, MDD, NB, and PSK analyzed and prepared the data for group-level statistics. AMG performed group-level statistics. RAO performed estimate of treatment-effects analysis. AMG, JBA, and JPS designed the study and protocols. All authors contributed to revisions of initial versions of the manuscript.

FUNDING

This study was supported by funds from the Charles Shor Foundation for Epilepsy Research, UAB Epilepsy Center, and the UAB Department of Radiology. The data were presented, in part, at the Organization for Human Brain Mapping 2019 annual meeting in Rome, IT. The UAB Center for Clinical and Translational Science: grant number UL1TR003096.

SUPPLEMENTARY MATERIAL

The Supplementary Material for this article can be found online at: https://www.frontiersin.org/articles/10.3389/fnins.2020.585509/full#supplementary-material

REFERENCES

Allendorfer, J. B., Heyse, H., Mendoza, L., Nelson, E. B., Eliassen, J. C., Storrs, J. M., et al. (2014). Physiologic and cortical response to acute psychosocial stress in left temporal lobe epilepsy - a pilot cross-sectional fMRI study. *Epilepsy Behav.* 36, 115–123. doi: 10.1016/j.yebeh.2014.05.003

Allendorfer, J. B., Nenert, R., Hernando, K. A., DeWolfe, J. L., Pati, S., Thomas, A. E., et al. (2019). FMRI response to acute psychological stress differentiates patients with psychogenic non-epileptic seizures from healthy controls - A biochemical and neuroimaging biomarker study. *Neuroimage Clin* 24:101967. doi: 10.1016/j.nicl.2019.101967

Balachandran, N., Goodman, A. M., Martin, A. N., Tocco, K., Vogel, V., LaFrance, J. W. C., et al. (in press). Relationship between neural responses to stress and mental health symptoms in psychogenic nonepileptic seizures after traumatic brain injury. *Epilepsia*. doi: 10.1111/epi.16758

Breiter, H. C., Etcoff, N. L., Whalen, P. J., Kennedy, W. A., Rauch, S. L., Buckner, R. L., et al. (1996). Response and habituation of the human amygdala during visual processing of facial expression. *Neuron* 17, 875–887. doi: 10.1016/s0896-6273(00)80219-6

Buhle, J. T., Silvers, J. A., Wager, T. D., Lopez, R., Onyemekwu, C., Kober, H., et al. (2014). Cognitive reappraisal of emotion: a meta-analysis of human neuroimaging studies. *Cereb. Cortex* 24, 2981–2990. doi: 10.1093/cercor/bht154

Chen, G., Taylor, P. A., Haller, S. P., Kircanski, K., Stoddard, J., Pine, D. S., et al. (2018). Intraclass correlation: Improved modeling approaches and applications for neuroimaging. *Hum. Brain Mapp.* 39, 1187–1206. doi: 10.1002/hbm.23909

Cicchetti, D. V. (1994). Guidelines, criteria, and rules of thumb for evaluating normed and standardized assessment instruments in psychology. *Psychol. Assess.* 6:284. doi: 10.1037/1040-3590.6.4.284

Cohen, S., Kamarck, T., and Mermelstein, R. (1983). A global measure of perceived stress. *J. Health Soc. Behav.* 24, 385–396. doi: 10.2307/2136404

Cox, R. W. (1996). AFNI: software for analysis and visualization of functional magnetic resonance neuroimages. *Comput. Biomed. Res.* 29, 162–173. doi: 10.1006/cbmr.1996.0014

Cox, R. W., Chen, G., Glen, D. R., Reynolds, R. C., and Taylor, P. A. (2017). FMRI clustering in AFNI: false-positive rates redux. *Brain Connect.* 7, 152–171. doi: 10.1089/brain.2016.0475

Dedovic, K., Duchesne, A., Andrews, J., Engert, V., and Pruessner, J. C. (2009a). The brain and the stress axis: the neural correlates of cortisol regulation in response to stress. *Neuroimage* 47, 864–871. doi: 10.1016/j.neuroimage.2009.05.074

Dedovic, K., Renwick, R., Mahani, J. K., Engert, V., Lupien, S. J., and Pruessner, J. C. (2005). The montreal imaging stress task: using functional imaging to investigate the effects of perceiving and processing psychosocial stress in the human brain. *J. Psychiatry Neurosci.* 30, 319–325.

Dedovic, K., Rexroth, M., Wolff, E., Duchesne, A., Scherling, C., Beaudry, T., et al. (2009b). Neural correlates of processing stressful information: an event-related fMRI study. *Brain Res.* 1293, 49–60. doi: 10.1016/j.brainres.2009.06.044

Dickerson, S. S., and Kemeny, M. E. (2004). Acute stressors and cortisol responses: a theoretical integration and synthesis of laboratory research. *Psychol. Bull.* 130, 355–391. doi: 10.1037/0033-2909.130.3.355

Elbau, I. G., Brucklmeier, B., Uhr, M., Arloth, J., Czamara, D., Spoormaker, V. I., et al. (2018). The brain's hemodynamic response function rapidly changes under acute psychosocial stress in association with genetic and endocrine stress response markers. *Proc. Natl. Acad. Sci. U.S.A.* 115, E10206–E10215. doi: 10.1073/pnas.1804340115

Espay, A. J., Ries, S., Maloney, T., Vannest, J., Neefus, E., Dwivedi, A. K., et al. (2019). Clinical and neural responses to cognitive behavioral therapy for functional tremor. *Neurology* 93, e1787–e1798. doi: 10.1212/WNL.0000000000008442

Fischer, H., Wright, C. I., Whalen, P. J., McInerney, S. C., Shin, L. M., and Rauch, S. L. (2003). Brain habituation during repeated exposure to fearful and neutral faces: a functional MRI study. *Brain Res. Bull.* 59, 387–392. doi: 10.1016/s0361-9230(02)00940-1

Gaab, J., Rohleder, N., Nater, U. M., and Ehlert, U. (2005). Psychological determinants of the cortisol stress response: the role of anticipatory cognitive appraisal. *Psychoneuroendocrinology* 30, 599–610. doi: 10.1016/j.psyneuen.2005.02.001

Goodman, A. M., Allendorfer, J. B., Heyse, H., Szaflarski, B. A., Eliassen, J. C., Nelson, E. B., et al. (2019). Neural response to stress and perceived stress differ in patients with left temporal lobe epilepsy. *Hum. Brain Mapp.* 40, 3415–3430. doi: 10.1002/hbm.24606

Goodman, A. M., Harnett, N. G., Wheelock, M. D., Hurst, D. R., Orem, T. R., Gossett, E. W., et al. (2018). Anticipatory prefrontal cortex activity underlies stress-induced changes in Pavlovian fear conditioning. *Neuroimage* 174, 237–247. doi: 10.1016/j.neuroimage.2018.03.030

Goodman, A. M., Wheelock, M. D., Harnett, N. G., Mrug, S., Granger, D. A., and Knight, D. C. (2016). The hippocampal response to psychosocial stress varies with salivary uric acid level. *Neuroscience* 339, 396–401. doi: 10.1016/j.neuroscience.2016.10.002

Gossett, E. W., Wheelock, M. D., Goodman, A. M., Orem, T. R., Harnett, N. G., Wood, K. H., et al. (2018). Anticipatory stress associated with functional magnetic resonance imaging: implications for psychosocial stress research. *Int. J. Psychophysiol.* 125, 35–41. doi: 10.1016/j.ijpsycho.2018.02.005

Granger, D. A., Kivlighan, K. T., el-Sheikh, M., Gordis, E. B., and Stroud, L. R. (2007). Salivary alpha-amylase in biobehavioral research: recent developments and applications. *Ann. N. Y. Acad. Sci.* 1098, 122–144. doi: 10.1196/annals.1384.008

Jankord, R., and Herman, J. P. (2008). Limbic regulation of hypothalamo-pituitary-adrenocortical function during acute and chronic stress. *Ann. N. Y. Acad. Sci.* 1148, 64–73. doi: 10.1196/annals.1410.012

Johnson, S. C., Baxter, L. C., Wilder, L. S., Pipe, J. G., Heiserman, J. E., and Prigatano, G. P. (2002). Neural correlates of self-reflection. *Brain* 125(Pt 8), 1808–1814. doi: 10.1093/brain/awf181

Kandel, E. R. (1976). *Cellular Basis of Behavior*. San Fransico: Freeman and Co.

Karatsoreos, I. N., and McEwen, B. S. (2011). Psychobiological allostasis: resistance, resilience and vulnerability. *Trends Cogn. Sci.* 15, 576–584. doi: 10.1016/j.tics.2011.10.005

Khalili-Mahani, N., Dedovic, K., Engert, V., Pruessner, M., and Pruessner, J. C. (2010). Hippocampal activation during a cognitive task is associated with subsequent neuroendocrine and cognitive responses to psychological stress. *Hippocampus* 20, 323–334. doi: 10.1002/hipo.20623

Kirschbaum, C., Pirke, K. M., and Hellhammer, D. H. (1993). The 'Trier Social Stress Test'–a tool for investigating psychobiological stress responses in a laboratory setting. *Neuropsychobiology* 28, 76–81. doi: 10.1159/000119004

Kudielka, B. M., Schommer, N. C., Hellhammer, D. H., and Kirschbaum, C. (2004). Acute HPA axis responses, heart rate, and mood changes to psychosocial stress (TSST) in humans at different times of day. *Psychoneuroendocrinology* 29, 983–992. doi: 10.1016/j.psyneuen.2003.08.009

LaFrance, W. C. Jr., Baird, G. L., Barry, J. J., Blum, A. S., Frank Webb, A., Keitner, G. I., et al. (2014). Multicenter pilot treatment trial for psychogenic nonepileptic seizures: a randomized clinical trial. *JAMA Psychiatry* 71, 997–1005. doi: 10.1001/jamapsychiatry.2014.817

Lakens, D. (2017). Equivalence tests: a practical primer for t Tests, correlations, and meta-analyses. *Soc. Psychol. Personal Sci.* 8, 355–362. doi: 10.1177/1948550617697177

Lee, M. R., Cacic, K., Demers, C. H., Haroon, M., Heishman, S., Hommer, D. W., et al. (2014). Gender differences in neural-behavioral response to self-observation during a novel fMRI social stress task. *Neuropsychologia* 53, 257–263. doi: 10.1016/j.neuropsychologia.2013.11.022

Loftus, G. R., and Masson, M. E. J. (1994). Using confidence intervals in within-subject. *Psychonomic Bulletin & Review*. 1, 476–490.

McDermott, T. J., Kirlic, N., and Aupperle, R. L. (2018). Roadmap for optimizing the clinical utility of emotional stress paradigms in human neuroimaging research. *Neurobiol. Stress* 8, 134–146. doi: 10.1016/j.ynstr.2018.05.001

McEwen, B. S., and Gianaros, P. J. (2011). Stress- and allostasis-induced brain plasticity. *Annu. Rev. Med.* 62, 431–445. doi: 10.1146/annurev-med-052209-100430

McNair, D. M. (1992). *Profile of Mood States*. Princeton, NJ: Educational and Industrial Testing Service.

McRae, K., Ochsner, K. N., Mauss, I. B., Gabrieli, J. J. D., and Gross, J. J. (2008). Gender differences in emotion regulation: an fMRI study of cognitive reappraisal. *Group Process Intergroup Relat.* 11, 143–162. doi: 10.1177/1368430207088035

Nater, U. M., Rohleder, N., Schlotz, W., Ehlert, U., and Kirschbaum, C. (2007). Determinants of the diurnal course of salivary alpha-amylase. *Psychoneuroendocrinology* 32, 392–401. doi: 10.1016/j.psyneuen.2007.02.007

Ochsner, K. N., Bunge, S. A., Gross, J. J., and Gabrieli, J. D. (2002). Rethinking feelings: an FMRI study of the cognitive regulation of emotion. *J. Cogn. Neurosci.* 14, 1215–1229. doi: 10.1162/089892902760807212

Orem, T. R., Wheelock, M. D., Goodman, A. M., Harnett, N. G., Wood, K. H., Gossett, E. W., et al. (2019). Amygdala and prefrontal cortex activity varies with individual differences in the emotional response to psychosocial stress. *Behav. Neurosci.* 133, 203–211. doi: 10.1037/bne0000305

Petrakova, L., Doering, B. K., Vits, S., Engler, H., Rief, W., Schedlowski, M., et al. (2015). Psychosocial stress increases salivary alpha-amylase activity independently from plasma noradrenaline levels. *PLoS One* 10:e0134561. doi: 10.1371/journal.pone.0134561

Phan, K. L., Fitzgerald, D. A., Nathan, P. J., Moore, G. J., Uhde, T. W., and Tancer, M. E. (2005). Neural substrates for voluntary suppression of negative affect: a functional magnetic resonance imaging study. *Biol. Psychiatry* 57, 210–219. doi: 10.1016/j.biopsych.2004.10.030

Pruessner, J. C., Dedovic, K., Khalili-Mahani, N., Engert, V., Pruessner, M., Buss, C., et al. (2008). Deactivation of the limbic system during acute psychosocial stress: evidence from positron emission tomography and functional magnetic resonance imaging studies. *Biol. Psychiatry* 63, 234–240. doi: 10.1016/j.biopsych.2007.04.041

Seeley, W. W., Menon, V., Schatzberg, A. F., Keller, J., Glover, G. H., Kenna, H., et al. (2007). Dissociable intrinsic connectivity networks for salience processing and executive control. *J. Neurosci.* 27, 2349–2356. doi: 10.1523/JNEUROSCI.5587-06.2007

Shrout, P. E., and Fleiss, J. L. (1979). Intraclass correlations: uses in assessing rater reliability. *Psychol. Bull.* 86, 420–428. doi: 10.1037/0033-2909.86.2.420

Strauss, M. M., Makris, N., Aharon, I., Vangel, M. G., Goodman, J., Kennedy, D. N., et al. (2005). fMRI of sensitization to angry faces. *Neuroimage* 26, 389–413. doi: 10.1016/j.neuroimage.2005.01.053

Szaflarski, J. P., Eaton, K., Ball, A. L., Banks, C., Vannest, J., Allendorfer, J. B., et al. (2011). Poststroke aphasia recovery assessed with functional magnetic resonance imaging and a picture identification task. *J. Stroke Cerebrovasc. Dis.* 20, 336–345. doi: 10.1016/j.jstrokecerebrovasdis.2010.02.003

Uddin, L. Q. (2015). Salience processing and insular cortical function and dysfunction. *Nat. Rev. Neurosci.* 16, 55–61. doi: 10.1038/nrn3857

Ulrich-Lai, Y. M., and Herman, J. P. (2009). Neural regulation of endocrine and autonomic stress responses. *Nat. Rev. Neurosci.* 10, 397–409. doi: 10.1038/nrn2647

Wheelock, M. D., Harnett, N. G., Wood, K. H., Orem, T. R., Granger, D. A., Mrug, S., et al. (2016). Prefrontal cortex activity is associated with biobehavioral components of the stress response. *Front. Hum. Neurosci.* 10:583. doi: 10.3389/fnhum.2016.00583

Wheelock, M. D., Rangaprakash, D., Harnett, N. G., Wood, K. H., Orem, T. R., Mrug, S., et al. (2018). Psychosocial stress reactivity is associated with decreased whole-brain network efficiency and increased amygdala centrality. *Behav. Neurosci.* 132, 561–572. doi: 10.1037/bne0000276

Whitfield-Gabrieli, S., Moran, J. M., Nieto-Castanon, A., Triantafyllou, C., Saxe, R., and Gabrieli, J. D. (2011). Associations and dissociations between default and self-reference networks in the human brain. *Neuroimage* 55, 225–232. doi: 10.1016/j.neuroimage.2010.11.048

Conflict of Interest: The authors declare that the research was conducted in the absence of any commercial or financial relationships that could be construed as a potential conflict of interest.

frontiers in Computational Neuroscience

ORIGINAL RESEARCH
published: 16 February 2021
doi: 10.3389/fncom.2021.565244

EEGs Vary Less Between Lab and Home Locations Than They Do Between People

Kaare B. Mikkelsen, Yousef R. Tabar, Christian B. Christensen and Preben Kidmose*

Department of Electrical and Computer Engineering, Aarhus University, Aarhus, Denmark

Given the rapid development of light weight EEG devices which we have witnessed the past decade, it is reasonable to ask to which extent neuroscience could now be taken outside the lab. In this study, we have designed an EEG paradigm well suited for deployment "in the wild." The paradigm is tested in repeated recordings on 20 subjects, on eight different occasions (4 in the laboratory, 4 in the subject's own home). By calculating the inter subject, intra subject and inter location variance, we find that the inter location variation for this paradigm is considerably less than the inter subject variation. We believe the paradigm is representative of a large group of other relevant paradigms. This means that given the positive results in this study, we find that if a research paradigm would benefit from being performed in less controlled environments, we expect limited problems in doing so.

Keywords: electroencephalogram, home recording, inter subject variability, intra subject variability, ear-EEG

OPEN ACCESS

Edited by:
Masaki Nakanishi,
University of California, San Diego, United States

Reviewed by:
Md. Kafiul Islam,
Independent University, Bangladesh, Bangladesh
Alexander James Casson,
The University of Manchester, United Kingdom

****Correspondence:***
Kaare B. Mikkelsen
mikkelsen.kaare@ece.au.dk

Received: *24 May 2020*
Accepted: *13 January 2021*
Published: *16 February 2021*

Citation:
Mikkelsen KB, Tabar YR, Christensen CB and Kidmose P (2021) EEGs Vary Less Between Lab and Home Locations Than They Do Between People. Front. Comput. Neurosci. 15:565244. doi: 10.3389/fncom.2021.565244

1. INTRODUCTION

With the advent of smart devices and wearable technologies, real life EEG recordings are getting increasingly feasible and potentially useful (Debener et al., 2012, 2015; Mullen et al., 2015). Applications include diagnosing and monitoring of epileptic patients (Gilliam et al., 1999; Askamp and van Putten, 2014; Zibrandtsen et al., 2017), decoding of auditory attention (Mirkovic et al., 2015; O'Sullivan et al., 2015; Das et al., 2018), brain-computer interfaces (Birbaumer and Cohen, 2007; De Vos et al., 2014), sleep monitoring (Shambroom et al., 2012; Younes et al., 2017; Mikkelsen et al., 2019), and monitoring of human behavior in extreme situations, such as cave exploration or space travel (Mogilever et al., 2018), to name a few. With the ongoing SARS-CoV-2 pandemic, the simple need to continue clinical investigations and EEG research outside laboratories has been added to the list.

However, given that the majority of existing EEG literature deals with single measurements on many subjects, there is limited data on the likely changes to results, or any decrease in data quality, that would come about from performing multiple measurements on the same subjects, in different locations, possibly outside of the laboratory and the immediate control of the investigator.

Looking at the literature, we find some studies focusing on intra- and inter-subject variability in the lab. Corsi-Cabrera et al. (1997, 2007) looked at patterns of correlation in scalp EEG in women, and found stable differences between subjects. Stastny et al. (2014) showed that inter-subject variability in the μ-rhythm could be used to identify subjects between sessions. Dalebout and Robey (1997) showed in 1997 that the P300 response varies more between subjects then within them, and in the late 80'ies Lauter et al. showed extensively that audiological responses follow the same pattern (Lauter and Karzon, 1990a,b).

More recently, Poulsen et al. (2017) showed that the amount of intersubject variability in a classroom setting could be used to gauge group engagement. Given that this is in itself an example of EEG recordings taken out of the laboratory setting, the comparison is particularly interesting.

Finally, Shen and Lin (2019) studied both inter and intra-subject variation in EEG during emotional responses. They found substantial inter- and intra-subject variation, not unlike what we show here.

In this study we present a paradigm designed to be both doable outside a laboratory, as well as reasonably comparable to a broad class of EEG paradigms. Second, we quantify the relationship between inter-subject, intra-subject (inter-session) and inter-location variability for this paradigm, and for each individual response invoked by it.

We tasked 20 subjects with performing the instructions in a 3-min long video on 8 separate occasions—4 in our EEG laboratory and 4 in their respective homes. All while wearing a combination of EEG, EOG, and chin EMG electrodes. By comparing the variation contribution from the different sources, we find clear inter-subject variability in all measures, and only little location-dependence. However, we do find that the unexplained variance generally increases for recordings performed outside the laboratory.

2. METHODS

2.1. Setup

The recording setup consisted of 25 iridium oxide electrodes (Kappel et al., 2019), connected to a TMSi Mobita amplifier.

The TMSi mobita amplifier is a mobile EEG amplifier with 24 bit resolution, individually shielded inputs, less than 0.4 micro V RMS noise in the 0.1–10 Hz band, greater than 10 GΩ input impedance, and greater than 100 dB CMRR.

The setup was a combination of ear-EEG (Mikkelsen et al., 2015), scalp EEG, EOG, and EMG electrodes: 12 positions within the ears (6 per ear, see **Figure 1**), 3 chin EMG electrodes, two EOG electrodes and 8 scalp electrodes (M1,M2,C3,C4,F3,F4,O1,O2) (see **Figure 1**). All electrodes were essentially identical, as seen in **Figures 1B–F**. To ensure good connections, all electrodes outside the ears (13 in total) were treated as wet electrodes and received electrode gel (Elefix from Nihon Kohden for electrodes on the scalp, Ten20 from Weaver and Company for face and mastoid). To ensure reliable connections on the scalp, liberal amounts of Elefix gel were used, in particular for subjects with long or curly hair (however, it was ensured that bridging between gel patches never occurred). All electrodes were embedded in soft silicone holders, and the cap was an EASYCAP EEG cap (EASYCAP GmbH, Germany), modified in-house. Ear-EEG ear pieces were costum made for the individual, ensuring a good and stable connection.

It is worth noting that the electrode gels were specifically chosen because they do not dry out (they are not hydrogels). Furthermore, as the dry electrodes, by design, can not dry out either, the electrode connections in the whole setup should be expected to be very stable over time.

The signals were sampled at 500 Hz, and a disposable electrode (Ambu, White Sensor, WS-00-S) placed on the neck was used as ground. The Mobita amplifier always uses an average reference during recording.

The EEG laboratory used in this study was a dedicated room in which we have successfully performed a host of different electrophysiological recordings, and which is used in teaching electrophysiological methods. During the recordings, no other activities took place in the room, leading to a quiet setting. The room has a sufficiently low amount of background electrical noise that additional electrical shielding has not been necessary.

The study was reviewed and approved by the Central Denmark Region Committees on Biomedical Research Ethics (Ref. nr. 1-10-72-413-17) as well as the Danish Medicines Agency (ref. nr. 2017111085).

2.2. Paradigm

Each recording consisted of two portions—one in a controlled laboratory in an EEG lab, and one in the subject's own home. The electrode setup was performed in the laboratory immediately prior to the first portion, and then kept on until the second portion at home. The setup was performed by an experienced EEG experimenter. The subjects were informed that they could take out the ear-EEG electrodes after the lab measurement and then put them back in before the home measurement. This option was used a total of 14 times (out of 80 possible). The time difference between first and second portion was, on average, 5 h and 9 min.

Each subject had 4 recording days, meaning that the video was viewed 8 times by each subject. On average, there was a 19 day gap between each recording day, though with considerable variation (25% were below 7 days, 51% below 14 days).

Behavioral Paradigm

While watching a video (accessible at `https://www.youtube.com/watch?v=4Uh2UeDzizk`), the participants were instructed to:

- Perform 5 jaw clenches
- Alternate between 20 s of open and closed eyes, with two repetitions
- Perform rhythmic, lateral eye motions.

The video takes 3 min and 9 s.

Please see **Figure 2** for a detailed diagram of experimental procedure.

It is worth noting that we took inspiration from the typical paradigms used for quality control of EEG setups in a clinical setting. This means that the expected responses in the recording are easy to recognize, and it is possible to positively identify whether the participant correctly followed the instructions.

2.3. Cohort

Twenty subjects were recruited, with ages between 22 and 36, mean 25.9 years. Thirteen were female. Subjects were a mixture of lay people (4), engineering students (15) and researchers (1).

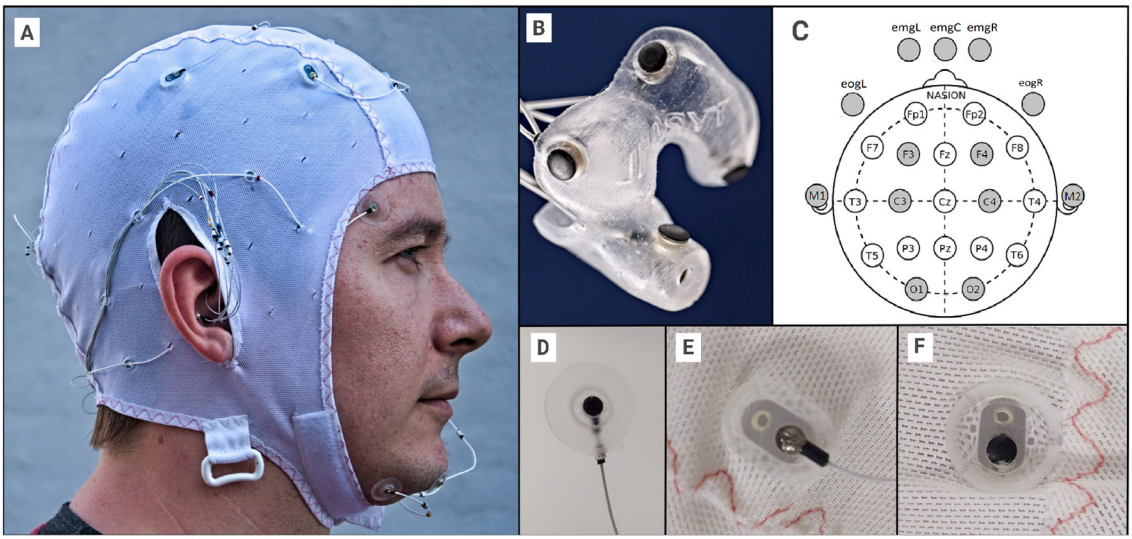

FIGURE 1 | (A) The EEG setup, with EEG cap, face electrodes and ear-EEG plugged in. **(B)** Close-up for single ear-EEG earplug (left in this case). **(C)** 10-20 reference diagram, showing the used scalp electrodes, including the 5 facial electrodes. **(D)** The EOG, EMG and M1/M2 electrodes were held in custom silicone holders. **(E)** Cap electrode holder from the outside. **(F)** Cap electrode holder from the inside. The diameter of the electrode is 3.5 mm and the diameter of the "cup" is approximately 10 mm. Written informed consent was obtained from the individual for the publication of any potentially identifiable images or data included in this article.

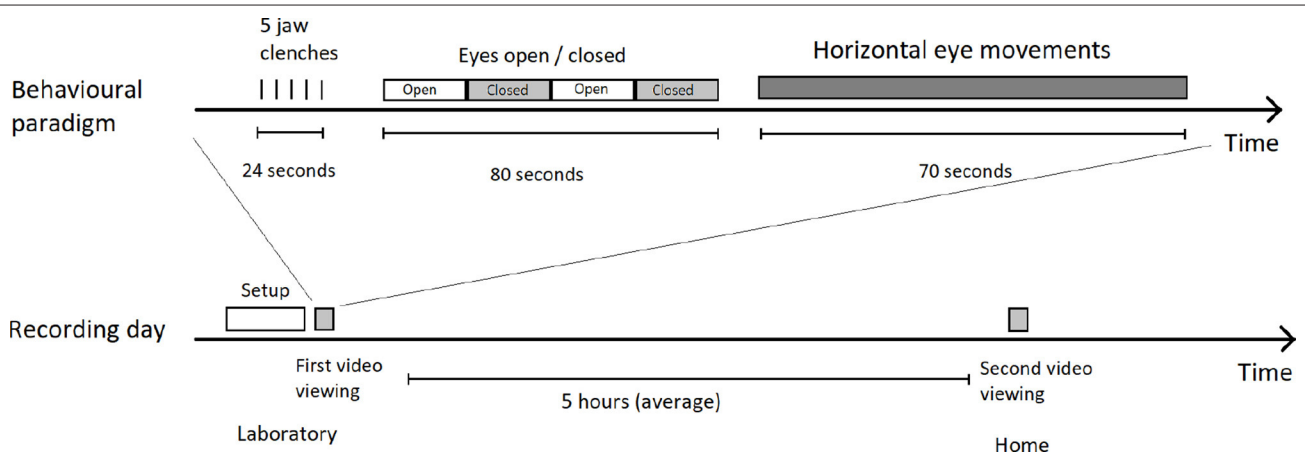

FIGURE 2 | Overview of a recording. **Top** shows the structure of the video and included instructions, **bottom** shows how the video was seen twice on the same day by the participant, once immediately after recording setup, and the second time several hours later in their own home (still wearing the recording equipment). The same video, with the same instructions, is viewed every time.

In total, 3 out of the 20 subjects could be considered to have prior EEG experience.

Subjects received monetary compensation for their participation.

2.4. Preprocessing

The timing between the EEG and the video instructions was determined by identifying the beginning of the lateral eye movements in the EOG, and extracting data up to 105 s prior to that as well as up to 85 s after.

As shown in **Figure 3**, the eye-movement dominated portion of the EEG is quite clear, and by using this it is possible to get an automatic, reproducible alignment at sub-second precision.

In preparing all EEG recordings, we employed a mixture of automatic and manual artifact rejection:

1. All channels in all recordings were band pass filtered to only keep activity in the 0.3 to 100 Hz band. This was done using a Hamming windowed sinc FIR filter of order 5500 [as implemented in EEGLAB (Delorme and Makeig, 2004)].
2. Instances where a single electrode had an amplitude larger than 350 μV were identified as artifacts, and the samples from

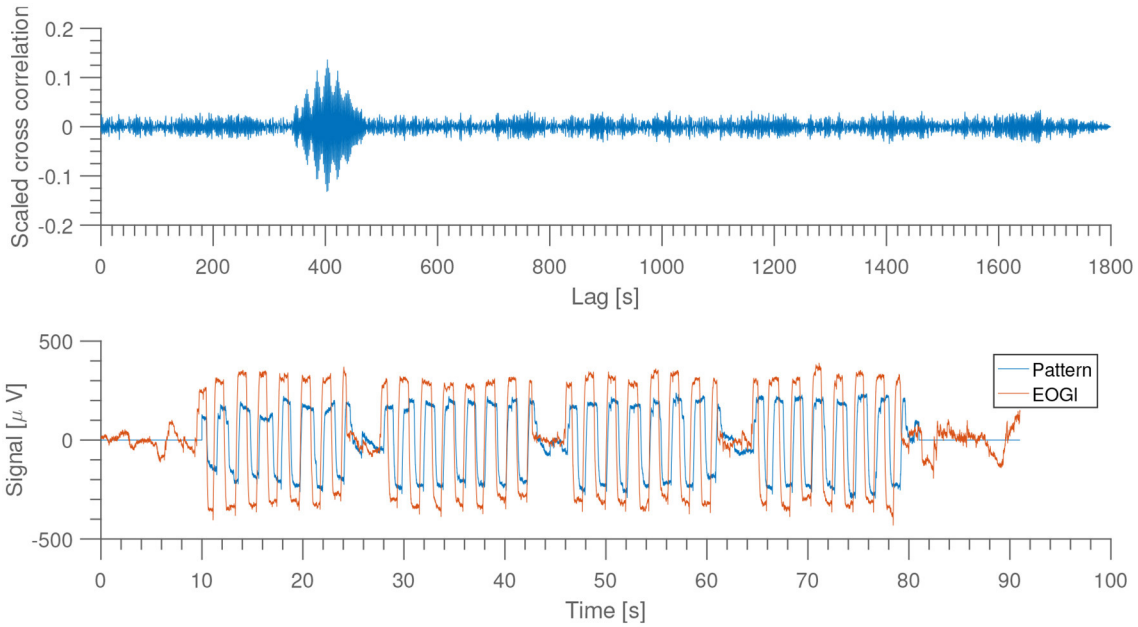

FIGURE 3 | Top: scaled version of the cross correlation between recorded signal from EOGl electrode and a sample recording used as "pattern." **Bottom**: comparison of EOGl and sample pattern at highest cross correlation. From subject 1, night 1, home recording.

that particular electrode was set to "nan" for a 2-s window around the event.

3. Finally, we used the fact that the ear electrodes have a high degree of redundancy between them, meaning that it should be possible to predict most of the signal from a healthy electrode using the signal from the neighboring electrodes. This was implemented by rejecting any ear electrode that had less than 0.4 Pearson correlation between itself and it's projection into the space of all other ear electrodes. The value of 0.4 was chosen to match rejection through visual inspection.

Due to the quite large signal amplitudes evoked by the eye-movement portion, the amplitude-thresholding was skipped for that part of the recordings.

Finally, the recordings were checked manually, to spot any additional channels to reject.

3. DATA MODELING

To maximize clarity and relevance of the analysis, for each part of the analysis of the paradigm, we focus on specific choices in modeling and specific electrodes (rather than report outputs from all possible electrode configurations). Thus, we do not restrict ourselves to a specific choice among the 25 electrodes, but have instead chosen to use the derivations that are most relevant for each sub analysis. See below for further details.

3.1. Jaw Clench Modeling

Jaw clenches are characterized by an increase in power at high frequencies (40–1,000 Hz), seen easily in electrodes placed close to the jaw muscles. Because of this, we extracted the power in the 40–80 Hz band for each ear electrode in windows of 0.5 s long, and calculated median power across electrodes for each window. By fitting the function:

$$f(t) = c + \sum_{i=1}^{5} a_i \cdot e^{(t-c_i)^2/w_i^2} \quad (1)$$

we may estimate the intensity of the clenching by the extracted amplitudes, a_i. Here, c, a_i, c_i, w_i are all free parameters determined through least squares fitting, and the index i represents the five jaw clenches (such that c_i is the timing and w_i the width of clench i). See **Figure 4** for an example. Prior to power estimation, the ear electrodes were referenced to their own average.

3.2. Alpha Power

The occipital alpha oscillation is present all over the head, but it is seen clearest in the occipital electrodes. Therefore, we estimated the power in the 8–12 Hz band averaged over electrodes O1 and O2, during the eyes open/closed portion of the paradigm. The two electrodes were referenced to the average of the scalp electrodes.

3.3. EOG Content

One way to characterize the EEG recordings is to specifically look at the different noise sources, to see whether they influence the recordings in the same manner across locations. An example of this is extracting eye movements using a single-sided ear-EEG device, which, besides its use in characterizing EEG recordings, could also be considered as a means to estimate visual attention (Favre-Félix et al., 2019).

To test this, we used a linear model, similar to what was used in Mikkelsen et al. (2017), to predict the activity in the EOGr-EOGl derivation during the "horizontal eye movements" portion of the behavioral paradigm. More precisely, the 70 s of eye movements were partitioned into two 35 s intervals, and a linear model (with a constant term) was trained to mimic the EOG activity using only the left or right ear electrodes. The model trained on the first 35 s was then applied to the second 35 s, and vise versa. For each ear, performance was recorded as the Pearson correlation between actual EOG signal and predicted.

From this point, we shall exclusively refer to this correlation as the "prediction quality."

3.4. Resting State Power Levels

It is generally interesting to know how the spontaneous, or "background" variation in the EEG data differs between locations and subjects, to infer whether paradigms known from recordings in the lab can be performed at home. In practice, this would be the main contribution to the "noise floor" in an ERP measurement.

We estimate the resting state EEG power by measuring the power for various electrode combinations (M1, avr. left ear, avr. right ear, C3, C4, F3, F4, all referenced to M2), and presenting both the full spectrum (up to 100 Hz) as well as the behavior of the average power in the 30–100 Hz band (excluding 50 Hz). We only used the "eyes open/closed" portion of the recordings for this analysis, and the power spectrum was calculated using Welch's algorithm with 3-s window widths.

3.5. Linear Mixed Models

A central question is to which extent variation in the independent variables causes variation in the results; it is very helpful when designing an experiment to know what alteration of study design may risk drowning out the signal.

In this study, the three most interesting sources of variation are that caused by adding subjects, that caused by repeating measurements, and that caused by changing location. In short, for $m = 1, ..., 20$ subjects, $n = 1, ..4$ repetitions and $l = 1, 2$ locations, the 80 observations, y_{mnl}, may be described as:

$$y_{mnl} \sim c + L_l + S_m \tag{2}$$

$$S_m \sim N(\mu_m, \sigma_1^2) \tag{3}$$

$$\mu_m \sim N(\mu, \sigma_2^2) \tag{4}$$

where $N(\mu, \sigma^2)$ is a normal distribution with mean μ and variance σ^2. In this terminology, σ_1^2 represents the intra subject variation, and σ_2^2 the inter-subject variation.

We apply our framework to the data using linear mixed effects models, letting "subject identity" be a "random effect" and everything else "fixed effects." Since we are doing the calculations in MATLAB (using `fitlme`), we describe the five models using Wilkinson notation (Wilkinson and Rogers, 1973):

Jaw Clench, alpha power:

$y \sim 1 + \text{location} + (1|\text{subject})$.

EOG content:

$y \sim 1 + \text{location} + \text{side-of-head} + (1|\text{subject})$.

Resting power levels:

$y \sim 1 + \text{location} + \text{channel} + (1|\text{subject})$.

Note that we add either "channel" or "side-of-head" dependencies in the last two, so as not to unduly add to the "intra subject variation."

By fitting the mixed effects models to the data, we can define the inter-subject, intra-subject and inter-location variation in the following ways:

Inter-subject: $std(\mu_i)$, where μ_i is the average response from subject i.

Intra-subject: The residual error, or root mean square error of the model fit. This can also be thought of as "day-to-day variation."

Inter-location: So as not to compare fixed-effects offsets to sums of squared errors, we represent the inter-location variation by the square root of the "squared error" term for the location-term, as calculated by "fitlme" in MATLAB.

We calculate these for each of the analyses described above, and rescale them such that the largest source of variation is 1 for each comparison, to make it easier to compare results from different paradigms.

3.6. Analysis of Location Influence

To specifically quantify the effects of doing measurements in multiple locations, we calculate p-values for both the differences in mean values between laboratory and home measurements, as well as the unexplained variances for each location (the "noise").

p-values for the significance of mean differences are extracted from the mixed linear model fits (the "ANOVA" field in the `fitlme` output) and for variation differences, we use permutation testing (by pairwise permutation of the location information) to estimate the probability of getting a greater difference than the one observed. All p-values are for two-tailed tests.

4. RESULTS

4.1. Data Quality

On five occasions, the behavioral data were lost. This happened on four occasions in the lab, and on one occasion at home. In the lab, it was due to human error in mismanagement of the recording, at home, the subject simply forgot to do it.

The automatic and manual artifact rejection resulted in 9% of the data samples being rejected (11% in lab, 7% at home). 1.5% of the data was rejected in the manual step. Viewing the setup as a whole, 2% of the time points were rejected (meaning that at 98% of the time, at least one electrode was recording). These numbers for lab vs. home were 4.6 vs. 0.2%. We have excluded the 5 missing recordings when calculating this.

4.2. Jaw Clenching

In **Figure 4** is seen an example of the extracted median gamma band power. The most common deviations from this pattern are either a missing first peak (some subjects forgot to do the

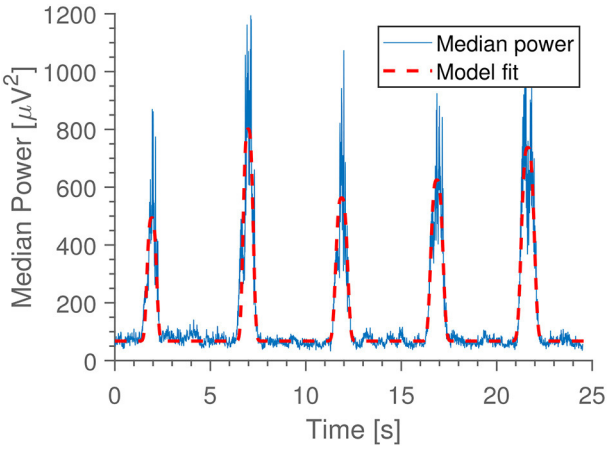

FIGURE 4 | Example of the MEG model [f in (1)] fitted to median gamma power.

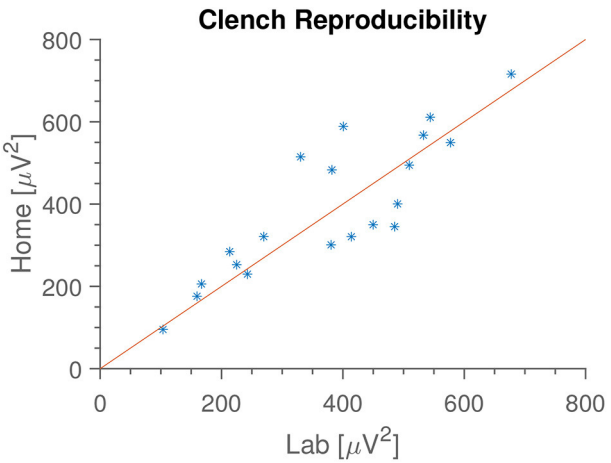

FIGURE 5 | Median median clench amplitude for each subject, in the two locations. Meaning that we calculate the median clench for each recording, and then find the median of those values. We see that median clench is very consistent between home and lab environments, and that the value varies between subjects. Identity line included for reference.

first clench) or some disturbance occurring halfway through (coughing, other movements). In **Figure 5** is shown the "median of medians" peak amplitude, meaning that first the median amplitude is calculated for each recording, and subsequently the median is taken for each subject's recording date. We see that this observable is very consistent within subjects between home and lab settings. Since the peak amplitude is influenced by how vigorously the subjects clench, we interpret this to mean that subjects were equally enthusiastic with and without direct supervision; they did not just go through the movements when at home, but strove to do the task as well as they had done in the laboratory.

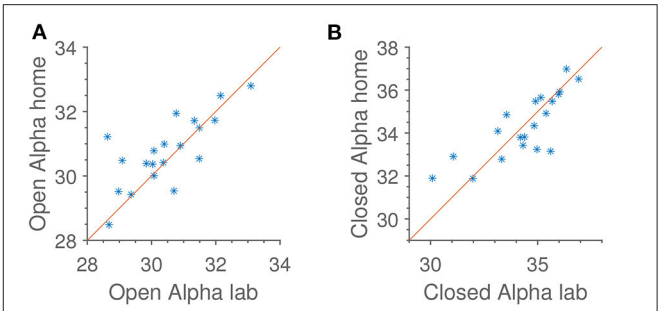

FIGURE 6 | Reproducibility of median alpha power in occipital electrodes, referenced to the average of the rest of the scalp electrodes. Identity line included for reference. Units are dB relative to 1[μV]^2. **(A)** Open eyes alpha scalp. **(B)** Closed eyes alpha scalp.

4.3. Alpha Power

In **Figure 6** is shown both alpha power for open and closed eyes. As with jaw clenching, we see that alpha powers measured at home and in the lab are very similar, but with some intersubject, reproducible variation.

Not shown in **Figure 6** is the subject-wise alpha modulation. When analyzing that, we find an average of 3.6 dB, or slightly more than a two-fold change in power. This is comparable to what is otherwise seen in the literature (Alloway et al., 1997).

4.4. EOG Prediction

Figure 7 shows an example of successful EOG prediction in the lab. **Figure 8** shows that EOG prediction works to the same extent at home as it does in the lab, though with a great deal of "noise" added.

We find no differences between the two ears. Instead, when calculating the Pearson correlation between prediction quality in left and right ear, we obtain a quite high value of 0.6, meaning that the performance in either ear tends to follow each other. On the other hand, we find very little correlation between performance at home and in the lab on the same day, at 0.11. By investigating the distribution of prediction performances, we find that the major variation in prediction quality is between "high" values that are between 0.5 and 1, and low values which are between 0 and 0.5. It appears that the variation between these two ranges is driven by variations in signal quality in both EOG and ear electrodes. In other words, if the prediction quality is not good (meaning below 0.5), it is most likely due to either many electrodes in the given ear having a bad connection, or one of the EOG electrodes being faulty. This is not particularly correlated between the two locations, which explains the low home vs. lab correlation.

4.5. Resting State Power Level

Figure 9 shows average power spectra in the EEG for different locations and electrode combinations. There are different observations to be made. (1) The relative difference in power is frequency dependent. For some reason, we see a higher level in the lab setting than home for frequencies below 10 Hz. We hypothesize that this is either due to some special circumstance in our laboratory (since it is unlikely that the noise environments

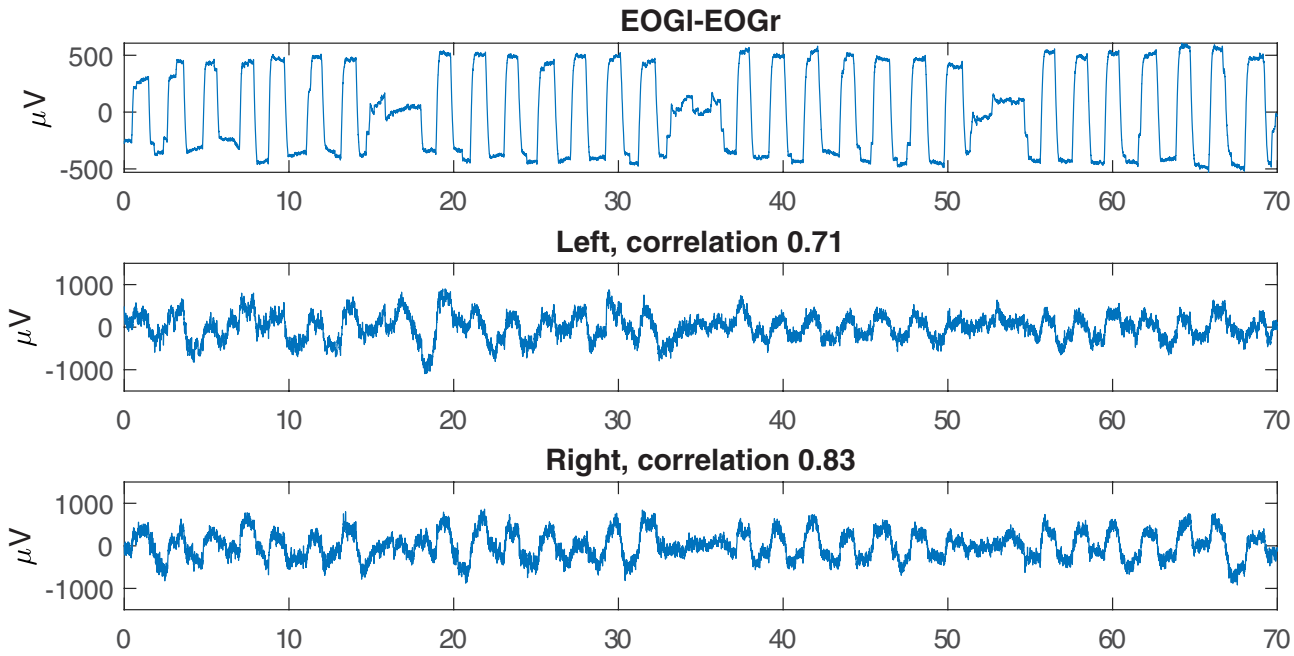

FIGURE 7 | Examples of EOG signals reproduced from the electrodes inside the left or right ear. This example is based on data recorded in the lab.

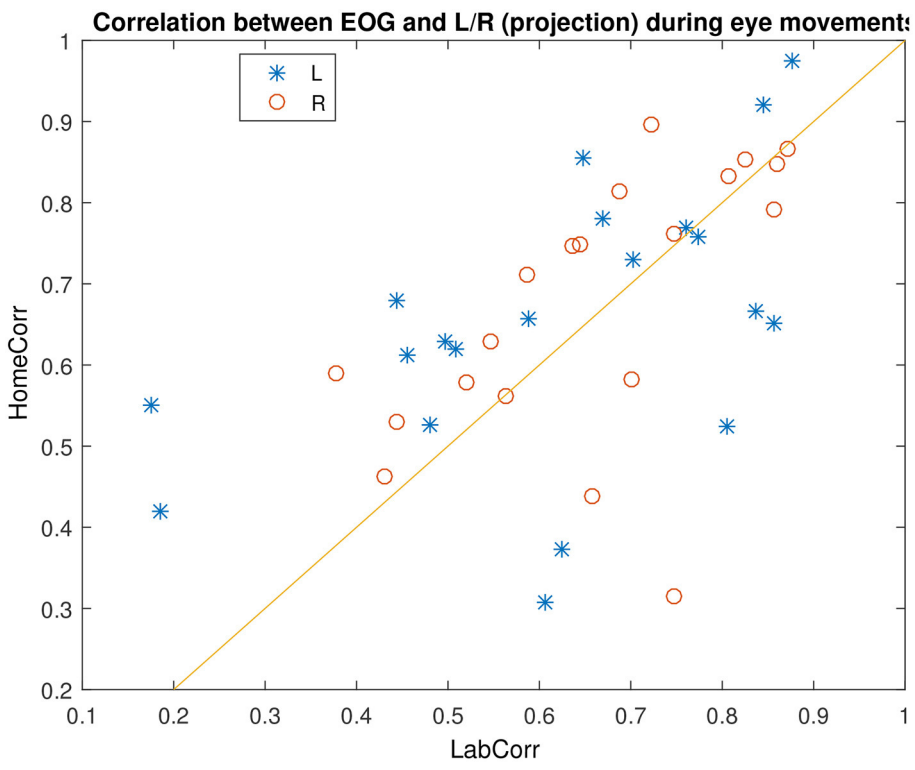

FIGURE 8 | Comparison of EOG prediction quality in the lab and at home, for different subjects. Identity line included for reference.

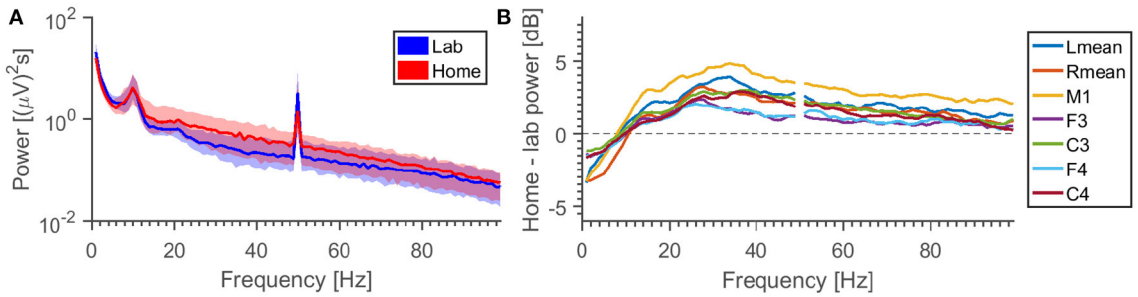

FIGURE 9 | (A) Grand average specters, for the M2-C3 EEG channel. For each frequency is calculated the distribution of power densities across all measurements, the region between 25th and 75h percentile is shown (colored area), together with the median (line). **(B)** Difference between median lab and home power specters for different measurement electrodes (all referenced to M2). Note that the specters (excluding the 50 Hz-peak) have been smoothed for added clarity.

of the test subjects should have some common bias) or long-term settling of the electrodes. (2) The variation in power density is greater than the difference caused by location. (3) The 50 Hz peak behaves differently from the surrounding noise floor—some combinations may have higher 50 Hz power in the laboratory, but lower noise in the surrounding frequency bins.

Performing an ANOVA on the average power between 30 and 100 Hz (excluding 50 Hz), with "subject" and "night" being random factors, the p-value for "location" is found to be 5% for all 7 EEG derivations plotted here. If we restrict the data to single EEG channels, the location p-value jumps between high ($> 18\%$) and low values ($< 3\%$).

4.6. Variational Analysis

Figure 10 shows an estimation of the relative contribution to total variation in the data from different sources. We see that in all cases, primary drivers are inter and intra-subject variation, with "location" being mostly a distant third. Note that this is not an estimate of significance—it is absolutely possible for a variable to have a very small, but very probable influence. For instance, it seems quite probable from the results in **Figure 9** that location has an influence. But from **Figure 10** we see that it contributes less uncertainty to the grand average than both the inter and intra-subject variation.

4.7. Significance of Location

In **Table 1** is shown differences in mean values and "unexplained error" between laboratory and home recordings. We see that for three of the sub paradigms, the unexplained error is significantly larger at home than in the laboratory, despite the fact that the difference in means is minimal.

It is worth noting that "EOG" is a clear outlier, with a smaller variation in home recordings than in the laboratory, and a quite large p-value. This is well explained by the observation made previously—that the main variation in EOG prediction quality is driven by electrode connection, which has no clear pattern between locations.

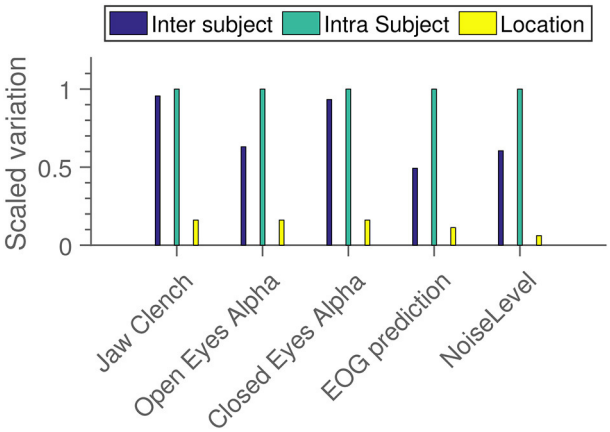

FIGURE 10 | Measures of how much variation is added to the EEG results from different independent variables. Within each subparadigm, the measured standard deviations have been scaled relative to the strongest component.

TABLE 1 | Analysis of location dependence for all sub paradigms.

	Clench	Open-alpha	Closed-alpha	EOG	Resting S.d.
Location offsets	14.65	0	−0.05	0.05	1.55
Location offsets p-values	0.54	0.94	0.15	0.04	0
Unexp. var. diff.	91.03	0.19	0.18	−0.02	1.35
Unexp. var. p-values	0	0	0	0.51	0

The units of offsets and standard deviations are, for column 1: $[\mu V]^2$, and for column 2 and 3: dB relative to 1 $[\mu V]^2$. Column 4 is dimensionless Pearson correlation. Positive values mean that the "home" value is larger.

5. DISCUSSION

By analyzing the evoked EEG from a behavioral EEG paradigm performed under many different conditions, we are able to compare the variation in response due to subject difference, location differences and that driven simply by the uncertainty of doing EEG measurements ("intra subject variation").

We find that for our paradigm, inter subject and intra subject variation contributes more to measurement noise than switching between laboratory and home measurements.

We also find that the signal quality as obtained in the home environment is decent; the rejection rate is actually lower for the home recordings than the lab recordings (7 vs. 11%). The signal to noise ratio is low enough that all parts of the paradigm could be shown to have reproducible results, as presented in **Figures 5**, **6**, **8**.

Note that this study does not conclude that location can not have a statistically significant effect on the measured EEG. Instead, we are concluding that the uncertainty added to the results from recording in multiple locations was less than both the intra subject and inter subject variation. Indeed, we do find that in most cases, the amount of unexplained variance (the "fitting error") is significantly greater (statistically speaking) outside the laboratory than inside it.

We also point out some decisions which had to be made in the design, and which could have changed the results in non-intuitive ways:

1. Some decisions had to be made regarding the definitions of both inter-subject, intra-subject and inter-location variation. Specifically, the choice of modeling "subject" as a *random* factor means that the "shrinkage" caused by "partial pooling" resulted in the inter-subject variability being roughly 85% of what we would have found if "subject" had been modeled as a *fixed* parameter. We have determined this by simply running both analyses.
2. We chose to use the estimated standard deviation of the location offset, rather than the offset itself, to represent the location-based effect. Had we chosen otherwise, the location-based variance would have been estimated at a much lower value.
3. It is likely that "intra-subject variability" could be defined in any number of ways, leading to smaller or larger estimates. However, we do believe that the unexplained variance, which we have chosen here, is a highly relevant quantity for comparison.
4. The "intra-subject" variation is, presumably, quite sensitive to the precise study design. Had the paradigm been longer, resulting in more data for each response calculation, it seems likely that "intra-subject" variation would have been less.

5.1. Limitations

In addition to the considerations listed above, there are certain circumstances which limit the generality of our results:

The main things to keep in mind when considering the general relevance of our results are:

1. While the "home" setting is presumably quite varied, the "lab" is not. If the laboratory conditions are somehow exceptional in this study, then that will bias the results. We do not think that this is the case.
2. The way the study was designed, the lab recording always preceded the home-recording. This means that certain time-based effects, such as long-term settling of the electrodes, necessarily influences the two locations differently. It is possible that this is part of the reason for the difference in background power spectra observed in **Figure 9**.
3. As is common in many neuroscience studies on healthy individuals, our subject cohort was not randomly drawn from the general population. The majority of the participants were engineering students, and it is possible that they would be better than average at carrying out instructions. As to the subset of participants with prior EEG experience, we do not think they biased the results. These subjects were considerably more likely to remove the ear-EEG electrodes between lab and home recordings, which is not the behavior we would expect from participants making an effort to maximize data quality.
4. The study does not include impedance measurements. This was no accident; to the best of our knowledge there are simply no commercially available EEG amplifiers which both have the necessary high input impedance and active shielding required for dry-contact EEG recording as well as the ability to measure electrode impedance. However, as we find that the signal quality (both in terms of automatic data rejection and in terms of recorded responses) is at least as good in the home setting as in the lab, in accordance with the design of the hardware (dry electrode and non-evaporating gels), we are convinced that our electrode connections are stable across both recording sessions.

Finally, we have specifically designed a paradigm which does not rely on precise alignment between recordings and stimuli. While we do believe that such a recording setup could be implemented, we did not attempt to do so in this study, and leave the solution of this problem to future works by either us or our colleagues.

6. CONCLUSION

We present a mixed EEG paradigm which is shown to be insensitive to moving the subject outside the laboratory and out of the direct control of the researcher.

On this basis, we believe that any researchers considering home measurements in a paradigm suited for it (our setup did not require strict control of sensory input, for instance), could do so without worrying that the lack of oversight would unduly contaminate their data. According to our results, if an EEG paradigm is known to work on a broad selection of subjects, it will also work on those subjects in their respective homes.

DATA AVAILABILITY STATEMENT

The data analyzed in this study were obtained as part of a clinical trial. The following restrictions apply: data can not be shared in any form until 5 years after the end of recordings, due to

a combination of Danish regulations on clinical trials and the GDPR. Requests to access these datasets should be directed to Kaare Bjarke Mikkelsen, mikkelsen.kaare@ece.au.dk.

ETHICS STATEMENT

The studies involving human participants were reviewed and approved by Videnskabetiske Komitéer Region Midt. The patients/participants provided their written informed consent to participate in this study.

AUTHOR CONTRIBUTIONS

KM designed the study, performed measurements, designed analysis, and wrote the manuscript. PK designed the study, build the hardware, and designed the analysis. YT designed the analysis. CC designed the study and the analysis. All authors contributed to the article and approved the submitted version.

FUNDING

This work was sponsored by the Innovation Fund Denmark, grant 7050-00007.

ACKNOWLEDGMENTS

The authors are grateful to Lars Nørvang Andersen at the Department of Mathematics at Aarhus University, for input on the statistical modeling. In addition, we appreciate the positive and constructive criticism from our two reviewers. Their input definitely improved this paper.

REFERENCES

Alloway, C. E. D., Ogilvie, R. D., and Shapiro, C. M. (1997). The alpha attenuation test: assessing excessive daytime sleepiness in narcolepsy-cataplexy. *Sleep* 20, 258–266. doi: 10.1093/sleep/20.4.258

Askamp, J., and van Putten, M. J. A. M. (2014). Mobile EEG in epilepsy. *Int. J. Psychophysiol.* 91, 30–35. doi: 10.1016/j.ijpsycho.2013.09.002

Birbaumer, N., and Cohen, L. G. (2007). Brain-computer interfaces: communication and restoration of movement in paralysis. *J. Physiol.* 579(Pt 3), 621–636. doi: 10.1113/jphysiol.2006.125633

Corsi-Cabrera, M., Galindo-Vilchis, L., del Rio-Portilla, Y., Arce, C., and Ramos-Loyo, J. (2007). Within-subject reliability and inter-session stability of EEG power and coherent activity in women evaluated monthly over nine months. *Clin. Neurophysiol.* 118, 9–21. doi: 10.1016/j.clinph.2006.08.013

Corsi-Cabrera, M., Solis-Ortiz, S., and Guevara, M. A. (1997). Stability of EEG inter-and intrahemispheric correlation in women. *Electroencephalogr. Clin. Neurophysiol.* 102, 248–255. doi: 10.1016/S0013-4694(96)95179-6

Dalebout, S. D., and Robey, R. R. (1997). Comparison of the intersubject and intrasubject variability of exogenous and endogenous auditory evoked potentials. *J. Am. Acad. Audiol.* 8, 342–354.

Das, N., Bertrand, A., and Francart, T. (2018). EEG-based auditory attention detection: boundary conditions for background noise and speaker positions. *J. Neural Eng.* 15:066017. doi: 10.1088/1741-2552/aae0a6

De Vos, M., Gandras, K., and Debener, S. (2014). Towards a truly mobile auditory brain-computer interface: exploring the P300 to take away. *Int. J. Psychophysiol.* 91, 46–53. doi: 10.1016/j.ijpsycho.2013.08.010

Debener, S., Emkes, R., De Vos, M., and Bleichner, M. (2015). Unobtrusive ambulatory EEG using a smartphone and flexible printed electrodes around the ear. *Sci. Rep.* 5:16743. doi: 10.1038/srep16743

Debener, S., Minow, F., Emkes, R., Gandras, K., and de Vos, M. (2012). How about taking a low-cost, small, and wireless EEG for a walk? *Psychophysiology* 49, 1617–1621. doi: 10.1111/j.1469-8986.2012.01471.x

Delorme, A., and Makeig, S. (2004). EEGLAB: an open source toolbox for analysis of single-trial EEG dynamics including independent component analysis. *J. Neurosci. Methods* 134, 9–21. doi: 10.1016/j.jneumeth.2003.10.009

Favre-Félix, A., Graversen, C., Bhuiyan, T. A., Skoglund, M. A., Rotger-Griful, S., Rank, M. L., et al. (2019). Absolute eye gaze estimation with biosensors in hearing aids. *Front. Neurosci.* 13:1294. doi: 10.3389/fnins.2019.01294

Gilliam, F., Kuzniecky, R., and Faught, E. (1999). Ambulatory EEG monitoring. *J. Clin. Neurophysiol.* 16, 111–115. doi: 10.1097/00004691-199903000-00003

Kappel, S. L., Rank, M. L., Toft, H. O., Andersen, M., and Kidmose, P. (2019). Dry-contact electrode ear-EEG. *IEEE Trans. Biomed. Eng.* 66, 150–158. doi: 10.1109/TBME.2018.2835778

Lauter, J. L., and Karzon, R. G. (1990a). Individual differences in auditory electric responses: comparisons of between-subject and within-subject variability. IV. Latency-variability comparisons in early, middle, and late responses. *Scand. Audiol.* 19, 175–182. doi: 10.3109/01050399009070769

Lauter, J. L., and Karzon, R. G. (1990b). Individual differences in auditory electric responses: comparisons of between-subject and within-subject variability. V. Amplitude-variability comparisons in early, middle, and late responses. *Scand. Audiol.* 19, 201–206. doi: 10.3109/01050399009070773

Mikkelsen, K. B., Kappel, S. L., Mandic, D. P., and Kidmose, P. (2015). EEG recorded from the ear: characterizing the Ear-EEG method. *Front. Neurosci.* 9:438. doi: 10.3389/fnins.2015.00438

Mikkelsen, K. B., Kidmose, P., and Hansen, L. K. (2017). On the keyhole hypothesis: high mutual information between ear and scalp EEG. *Front. Hum. Neurosci.* 11:341. doi: 10.3389/fnhum.2017.00341

Mikkelsen, K. B., Tabar, Y. R., Kappel, S. L., Christensen, C. B., Toft, H. O., Hemmsen, M. C., et al. (2019). Accurate whole-night sleep monitoring with dry-contact ear-EEG. *Sci. Rep.* 9, 1–12. doi: 10.1038/s41598-019-53115-3

Mirkovic, B., Debener, S., Jaeger, M., and De Vos, M. (2015). Decoding the attended speech stream with multi-channel EEG: implications for online, daily-life applications. *J. Neural Eng.* 12:046007. doi: 10.1088/1741-2560/12/4/046007

Mogilever, N. B., Zuccarelli, L., Burles, F., Iaria, G., Strapazzon, G., Bessone, L., et al. (2018). Expedition cognition: a review and prospective of subterranean neuroscience with spaceflight applications. *Front. Hum. Neurosci.* 12:407. doi: 10.3389/fnhum.2018.00407

Mullen, T. R., Kothe, C. A. E., Chi, Y. M., Ojeda, A., Kerth, T., Makeig, S., et al. (2015). Real-time neuroimaging and cognitive monitoring using wearable dry EEG. *IEEE Trans. Biomed. Eng.* 62, 2553–2567.doi: 10.1109/TBME.2015.2481482

O'Sullivan, J. A., Power, A. J., Mesgarani, N., Rajaram, S., Foxe, J. J., Shinn-Cunningham, B. G., et al. (2015). Attentional selection in a cocktail party environment can be decoded from single-trial EEG. *Cereb. Cortex.* 25, 1697–1706. doi: 10.1093/cercor/bht355

Poulsen, A. T., Kamronn, S., Dmochowski, J., Parra, L. C., and Hansen, L. K. (2017). EEG in the classroom: synchronised neural recordings during video presentation. *Sci. Rep.* 7:43916. doi: 10.1038/srep43916

Shambroom, J. R., Fábregas, S. E., and Johnstone, J. (2012). Validation of an automated wireless system to monitor sleep in healthy adults. *J. Sleep Res.* 21, 221–230. doi: 10.1111/j.1365-2869.2011.00944.x

Shen, Y.-W., and Lin, Y.-P. (2019). Challenge for affective brain-computer interfaces: non-stationary spatio-spectral EEG oscillations of emotional responses. *Front. Hum. Neurosci.* 13:366. doi: 10.3389/fnhum.2019.00366

Štastný, J., Sovka, P., and Kostilek, M. (2014). Overcoming inter-subject variability in BCI using EEG-based identification. *Radioengineering.* 23, 266–273.

Wilkinson, G. N., and Rogers, C. E. (1973). Symbolic description of factorial models for analysis of variance. *J. R. Stat. Soc. Ser. C* 22, 392–399.

Younes, M., Soiferman, M., Thompson, W., and Giannouli, E. (2017). Performance of a new portable wireless sleep monitor. *J. Clin. Sleep Med.* 13, 245–258. doi: 10.5664/jcsm.6456

Zibrandtsen, I. C., Kidmose, P., Christensen, C. B., and Kjaer, T. W. (2017). Ear-EEG detects ictal and interictal abnormalities in focal and generalized epilepsy—A comparison with scalp EEG monitoring. *Clin. Neurophysiol.* 128, 2454–2461. doi: 10.1016/j.clinph.2017.09.115

Conflict of Interest: The authors declare that the research was conducted in the absence of any commercial or financial relationships that could be construed as a potential conflict of interest.

frontiers in Computational Neuroscience

ORIGINAL RESEARCH
published: 04 August 2021
doi: 10.3389/fncom.2021.700467

Identifying Individuals With Mild Cognitive Impairment Using Working Memory-Induced Intra-Subject Variability of Resting-State EEGs

Thanh-Tung Trinh[1†], Chia-Fen Tsai[2,3†], Yu-Tsung Hsiao[4], Chun-Ying Lee[5], Chien-Te Wu[6] and Yi-Hung Liu[7*]*

[1] Neural Engineering and Smart Systems Laboratory, Graduate Institute of Manufacturing Technology, College of Mechanical and Electrical Engineering, National Taipei University of Technology (Taipei Tech), Taipei, Taiwan, [2] Department of Psychiatry, Division of Geriatric Psychiatry, Taipei Veterans General Hospital, Taipei, Taiwan, [3] Faculty of Medicine, National Yang Ming Chiao Tung University, Taipei, Taiwan, [4] Neural Engineering and Smart Systems Laboratory, Graduate Institute of Mechatronic Engineering, National Taipei University of Technology (Taipei Tech), Taipei, Taiwan, [5] Department of Mechanical Engineering, National Taipei University of Technology (Taipei Tech), Taipei, Taiwan, [6] International Research Center for Neurointelligence (WPI-IRCN), The University of Tokyo Institutes for Advanced Study (UTIAS), The University of Tokyo, Tokyo, Japan, [7] Department of Mechanical Engineering, National Taiwan University of Science and Technology (Taiwan Tech), Taipei, Taiwan

OPEN ACCESS

Edited by:
Masaki Nakanishi, University of California, San Diego, United States

Reviewed by:
Fei He, Coventry University, United Kingdom
Chunshu Wei, University of California, San Diego, United States

***Correspondence:**
Chien-Te Wu
wu.chiente@mail.u-tokyo.ac.jp
Yi-Hung Liu
lyh@mail.ntust.edu.tw

[†] These authors have contributed equally to this work

Received: 26 April 2021
Accepted: 30 June 2021
Published: 04 August 2021

Citation:
Trinh T-T, Tsai C-F, Hsiao Y-T, Lee C-Y, Wu C-T and Liu Y-H (2021) Identifying Individuals With Mild Cognitive Impairment Using Working Memory-Induced Intra-Subject Variability of Resting-State EEGs. Front. Comput. Neurosci. 15:700467. doi: 10.3389/fncom.2021.700467

Individuals with mild cognitive impairment (MCI) are at high risk of developing into dementia (e. g., Alzheimer's disease, AD). A reliable and effective approach for early detection of MCI has become a critical challenge. Although compared with other costly or risky lab tests, electroencephalogram (EEG) seems to be an ideal alternative measure for early detection of MCI, searching for valid EEG features for classification between healthy controls (HCs) and individuals with MCI remains to be largely unexplored. Here, we design a novel feature extraction framework and propose that the spectral-power-based task-induced intra-subject variability extracted by this framework can be an encouraging candidate EEG feature for the early detection of MCI. In this framework, we extracted the task-induced intra-subject spectral power variability of resting-state EEGs (as measured by a between-run similarity) before and after participants performing cognitively exhausted working memory tasks as the candidate feature. The results from 74 participants (23 individuals with AD, 24 individuals with MCI, 27 HC) showed that the between-run similarity over the frontal and central scalp regions in the HC group is higher than that in the AD or MCI group. Furthermore, using a feature selection scheme and a support vector machine (SVM) classifier, the between-run similarity showed encouraging leave-one-participant-out cross-validation (LOPO-CV) classification performance for the classification between the MCI and HC (80.39%) groups and between the AD vs. HC groups (78%), and its classification performance is superior to other widely-used features such as spectral powers, coherence, and the complexity estimated by Katz's method extracted from single-run resting-state EEGs (a common approach in previous studies). The results based on LOPO-CV, therefore, suggest that the spectral-power-based

task-induced intra-subject EEG variability extracted by the proposed feature extraction framework has the potential to serve as a neurophysiological feature for the early detection of MCI in individuals.

Keywords: intra-subject variability, electroencephalography, mild cognitive impairment, Alzheimer's disease, between-run similarity, brain-computer interface, machine learning

INTRODUCTION

Alzheimer's dementia has become the most prevalent type of neurodegenerative dementia. There are nearly 10 million new cases of dementia every year worldwide and 60–70% of these new cases are diagnosed with AD (World Health Organization, 2020). The prevalence of AD generally increases with age: the prevalence is 1% for people between 60 and 64 years, but it increases to 38% for people over 85 years (Ferrara et al., 2008). Although mild cognitive impairment (MCI), typically as a transitional state between normal aging and very early dementia, does not usually impact the daily life of individuals (Petersen, 2010), it may convert to AD or other types of dementia with a high risk. For example, a study reported that 15% of MCI in individuals older than 65 years old may develop into dementia (Alzheimer association, 2020), whereas another study reported that MCI of 32% of individuals developed into AD at the 5th-year follow-up (Chen Y. et al., 2020; Alzheimer association, 2021). Early detection and intervention for individuals with MCI will, therefore, be an important strategy in the fight to reduce the impact of AD on our community. However, early detection of MCI is challenging, as older adults with MCI are often not aware of the subtle decline in their cognitive function, which primarily prevents them from seeking medical advice or even interventions.

Several biomarkers have been proposed to help physicians verify the diagnosis of dementia due to AD; In contrast, the diagnosis of MCI heavily relies rather on neuropsychological assessments. For the diagnosis of AD, a common method is to detect human brain amyloid-beta (Aβ) deposition and abnormal aggregation of tau protein. The concentration ratio of Aβ42 to Aβ40 (Aβ42/40 ratio), the concentration of Aβ42 level and positive amyloid, and tau PET scan are considered as important biomarkers to detect AD (Hansson et al., 2019). However, these biomarkers are not ideal solutions for the community health care system, because they are expansive, time-consuming, invasive, and radiational in nature. In addition, although recently, there have been attempts to establish a biomarker-based guideline for the diagnosis of MCI (Ritchie et al., 2014; Martinez et al., 2017; Ross et al., 2021), there is still room for improvement in terms of accessibility, reliability, and validity of these biomarkers. Electroencephalography (EEG), on the other hand, is a promising alternative due to its non-invasive nature and relatively much lower costs. EEGs may, therefore, have great potential for assisting the clinical characterization of MCI and AD (Poza et al., 2014).

Resting-state EEGs, typically recorded while participants are not doing anything purposefully, has become a popular approach in clinical research with the patient population who has short attention span or difficulties performing a goal-directed task. Previously, a large body of literature based on single-session resting-state EEG has found differences in EEG features between AD and HC, such as spectral powers of different frequency bands, complexity, and connectivity. For example, compared with the HC group, individuals with AD showed lower signal complexity (Abasolo et al., 2005, 2006, 2008; Liu et al., 2015), a higher power of slow oscillations (delta, theta) and lower power of fast oscillation (alpha, beta, gamma) over the temporal, parietal, and occipital scalp regions (Huang et al., 2000; Rossini et al., 2007; Roh et al., 2011; Ishii et al., 2017), and lower electrode-to-electrode connectivity (Wang et al., 2014; Engels et al., 2015; Hata et al., 2016) in resting-state EEGs. Furthermore, the entropy-based complexity of EEG signals seems to gradually decrease with disease development (Sun et al., 2020). However, differences in resting-state EEGs between the MCI group and the HC group are relatively less studied. Few studies reported a non-significant trend for loss of complexity in individuals with MCI compared with HC (Park et al., 2007; Dauwels et al., 2011; Labate et al., 2013; Xu and Tao, 2013; Seker et al., 2021). Searching for a more distinguishing EEG signature based on resting-state recordings for the classification between MCI and HC appears to be a critical challenge.

In addition to altered resting-states, memory dysfunction can be another key clinical trait for inducing relevant EEG patterns to discriminate between AD/MCI and HC. Memory dysfunction is one of the critical diagnosis criteria for AD (American Psychiatric Association, 2013), and among all types of memory dysfunction, working memory impairment is often observed in both MCI and AD. Working memory refers to the ability to access and manipulate information that is stored in a short period of time (Baddeley et al., 2015). Most complex cognitive abilities, such as spatial orientation, problem solving, and reading, require working memory functions (Kirova et al., 2015). Specifically, individuals with MCI typically show performance declination in verbal/visual working memory (Saunders and Summers, 2010), sentence span, operation span (Gagnon and Belleville, 2011), digit span, letter-number sequencing, and arithmetic operation (Kessels et al., 2011). Since impaired working memory is commonly observed in individuals with MCI, working memory tasks can be a good candidate to induce task-relevant differences in resting-state EEGs between the MCI group and the HC group.

This study, therefore, aimed to capitalize on the spectral-power-based task-induced intra-subject variability of EEGs recorded in two separate runs of resting-states, before and after a challenging working memory task. Since working memory tasks are presumably more cognitively exhausted for the MCI or AD group than the HC group, we hypothesize that the difference in the neurophysiological patterns of the before-task

and after-task "resting-state" in the brain will be larger for the MCI group than the HC group, and such difference carries more discriminative information for classification in comparison with the approach using single-run resting-state EEGs that has been adopted in previous studies related to the MCI-HC classification. To achieve this goal, we designed a novel feature extraction framework in which we introduced the delayed matching-to-sample (DSTM) task as a cognitively challenging behavior test, applied a similarity-based approach (Chen G. et al., 2020) to quantitatively evaluate the task-induced intra-subject variation of resting-state EEG powers, and used it as a neural marker to classify between the MCI and HC groups. To the best knowledge of the authors, this is the first study that focuses on the analysis of task-induced intra-subject variability between two separate runs of resting-state EEGs for the detection of MCI. First, we investigated the group difference in between-run similarity of resting-state EEGs across different frequency bands and scalp regions between the AD, MCI, and HC groups. Second, we used machine-learning based feature selection methods to determine the best combination of intra-subject variability features for MCI-HC classification. The results showed that the proposed novel intra-subject variability feature can be a promising one to further develop an EEG-based computer-aided diagnosis method for the early detection of MCI.

METHOD

Participants

This study included 23 individuals with Alzheimer's disease (AD) (nine females, mean age of 71.65 ± 5.36 y/o), 24 individuals with mild cognitive impairment (MCI) (14 females, mean age of 70.96 ± 8.2 y/o) in the patient group and 27 participants in the healthy control (HC) group (17 females, mean age of 69.93 ± 4.98 y/o). Data collection was conducted from July 2017 to July 2020 at an outpatient memory clinic of a tertiary 2,700-bed referral center (**Table 1**). The diagnosis of participants from the patient group was based on the results of clinical interviews, neuropsychological examinations, laboratory findings, and image investigations (CT and/or MRI) and was confirmed at clinical consensus meetings by board-certified psychiatrists. The core clinical criteria recommended by National Institute on Aging and the Alzheimer's Association (NIA-AA) (Albert et al., 2011; McKhann et al., 2011) were used for the diagnosis of AD and MCI. Participants from the control group were enrolled *via* advertisement and confirmed as not having any condition for all-cause dementia listed in the NIA-AA criteria. Furthermore, the participants from the control group were all tested with neuropsychological battery, which resulted in the normal range on standardized neuropsychological batteries after adjustment for education (Tsai et al., 2012).

The exclusion criteria for all three groups were: (1) recent major psychiatric comorbidity (clinically diagnosed in the 6 months prior to the current neuropsychological evaluation), (2) motor and/or sensory deficits that constituted confounding variables in the assessment of cognitive functions, and (3) neurological illness or condition that may affect cognition.

The study protocol was reviewed and approved by the institutional review board of Taipei Veterans General Hospital (IRB No: 2017-06-009A). Before the experiment, written informed consents were obtained from all the participants or their legally authorized representatives according to the Declaration of Helsinki.

Experimental Procedure

In this experiment, all the participants underwent two sessions of resting-state condition (named resting run 1 and resting run 2) along with a working memory condition between two resting-state conditions (**Figure 1**). During each resting-state condition (90 s), the participants were instructed to gently keep their eyes fixated on a central fixation cross without doing/thinking anything purposefully. During the memory condition, the participants performed three types of delayed DMTS tasks (Sahakian et al., 1988; Fowler et al., 1995), with 10 trials for each type.

A DMTS trial included three phases. In the encoding phase (2 s), a set of sample stimuli was presented on the screen for the participants to remember. In the maintenance phase (3 s), the corresponding visual display was removed from the screen, and the participants were required to keep the information in their working memory. In the retrieval phase (3 s), a question display was presented on the screen, and the participants were required to judge if the contents of the question display match (both in terms of shape and position) those in the sample display. The participants were instructed to answer the question with a button press after the retrieval phase without a time limit. The three types of DMTS tasks varied in terms of contents to be remembered: 1. Type 1: the participants were required to remember the locations of three circles randomly placed on the screen, 2. Type 2: the participants were required to remember the locations of seven circles randomly placed on the screen. 3. Type 3: the participants were required to remember the locations of three different shapes (a circle, a square, and a star) randomly placed on the screen.

EEG Acquisition and Preprocessing

EEG signals were recorded with a 33-channel Quick-Cap connected to a 40-channel NuAmps (NeuroScan Amplifier, Compumedics Inc., Charlotte, NC, USA). The layout of the electrodes followed the International 10–20 system (**Figure 2**), where A1 and A2 were reference electrodes, the ground channel was at the forehead, and the remaining 30 electrodes were used for recording EEGs. Impedance was kept below 10 kOhm by applying Electro-Gel (Compumedics Inc., Charlotte, NC, USA) to the electrodes. Ocular activity (i.e., electrooculography, EOG) was monitored with two electrodes placed above the left eye and the right side of the right eye, respectively. The recorded EEG and EOG signals were amplified and filtered (0.5–100 Hz), and then digitized with a sampling rate of 500 Hz using the NuAmp amplifier from NeuroScan Inc. Ocular artifacts coming from blinking or eye movements were removed from the EEG signals using the artifact removal software from NeuroScan (Scan4.5). Afterward, the EEG signals were further filtered using a Finite Impulse Response (FIR) filter (0.5–50 Hz). Finally, other possible artifacts caused from generic discontinuities

TABLE 1 | Demographics and questionnaire data [Mean (SD)].

Variable	HC $n = 27$	MCI $n = 24$	AD $n = 23$	p	Effect size
Gender	17 F, 10 M	14 F, 10 M	9 F, 14 M	0.212	0.145
Age	69.93 (4.98)	70.96 (8.20)	71.65 (5.36)	0.621	0.013
Education (years)	13.44 (3.18)	12.13 (3.76)	11.43 (4.35)	0.132	0.050
MMSE	28.26 (1.79)	26.58 (1.89)	21.35 (5.77)	<0.001	0.412
MoCA	25.89 (3.29)	23.08 (4.11)	15.96 (6.43)	<0.001	0.447

F, female; M, male; HC, healthy controls; MCI, mild cognitive impairment; AD, Alzheimer's disease; MMSE, mini-mental state examination; MoCA, montreal cognitive assessment.
Gender: chi-square test of independence.
Age/Education year/MMSE/MoCA: one-way ANOVA.

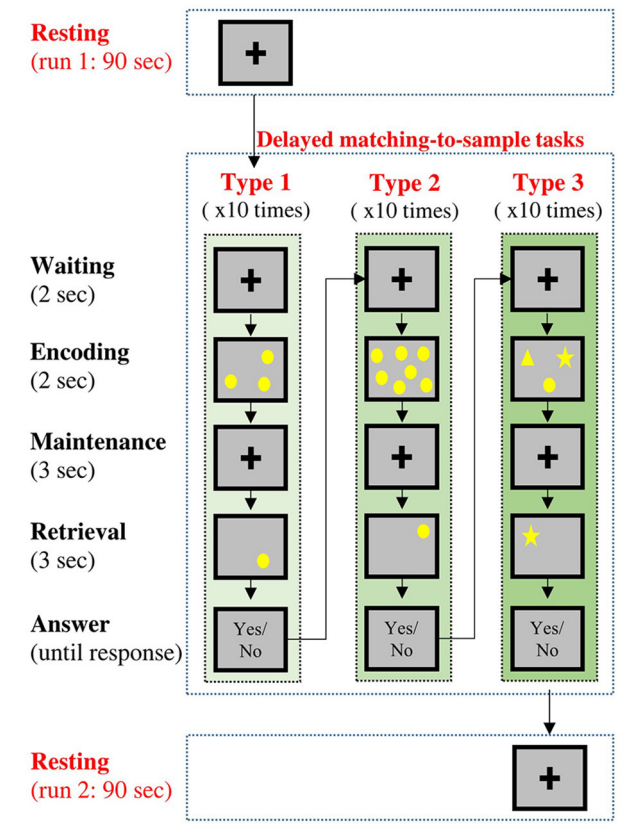

FIGURE 1 | Temporal sequence of the experimental procedures. Each participant would undergo two resting-state conditions and three delayed matching-to-sample (DMTS) tasks. Type 1 and Type 2 tasks requires the participants to remember the locations of stimuli, and Type 3 task requires the participants to remember both the contents and locations of stimuli.

and electromyography were removed using the independent component analysis (ICA) and ADJUST algorithm (Mognon et al., 2011) provided in the EEGLAB (Infomax ICA).

Feature Extraction: Between-Run Similarity Based on Spectral Powers

The purpose here was to quantify the intra-subject variability of the EEG signals between the two resting runs using a between-run similarity (BRS) of spectral powers. The calculation of the BRS consists of five steps.

Step 1: segmentation of the resting-state EEG signal into epochs

For each participant and for each run of resting state, the 90-s EEG signal was segmented into 36 epochs of 6-second length, and there is overlap of 60% between two consecutive epochs. Then, we visually inspected all the segmented EEG epochs to make sure that the data used for later analysis were noise- and artifact-free. Among the 74 participants, nine (three with AD, four with MCI, two HCs) had only 35 clean epochs for analyses in both runs or in one of the two runs. The rejected epochs had large-amplitude peaks in voltage, which could be due to some technical issue during recordings. Data of the remaining 65 participants were all clean (i.e., all 36 epochs per run were used for later analyses).

Step 2: calculation of band power for each epoch

For each participant, spectral band powers of delta (1–4 Hz), theta (4–8 Hz), low alpha (8–10 Hz), high alpha (10–13 Hz), low beta (13–20 Hz), high beta (20–30 Hz), and gamma (30–45 Hz) were extracted from each epoch using fast Fourier Transform (FFT). Considering a specific band, let BP_{ij}^{r} be the band power of the ith epoch recorded from the jth electrode of a specific scalp region, where $r \in \{1, 2\}$ denotes the rth run of the resting state, and, for example, $j = 1, 2, \ldots, 7$ for the frontal region. Note that $n = 35$ for some of the 74 participants (the nine aforementioned), and $n = 36$ for the remaining 65 participants.

Step 3: computation of the average power vector for each scalp region

Then, for each band and for each run, we extracted the averaged powers of each 6-s epoch across the electrodes in a given scalp region,

$$BP_{i}^{r} = \frac{1}{n_e} \sum_{j=1}^{n_e} BP_{ij}^{r} \tag{1}$$

where n_e is the number of electrodes in the scalp region of interest, and i denotes the ith epoch. Thus, for a given scalp region, the average scalp powers of the seven different bands corresponding to the ith epoch were then concatenated to form a power vector $\mathbf{p}_i^r$ of dimension 7, where r denotes the run number of resting-state EEG recordings (1 or 2 in this case).

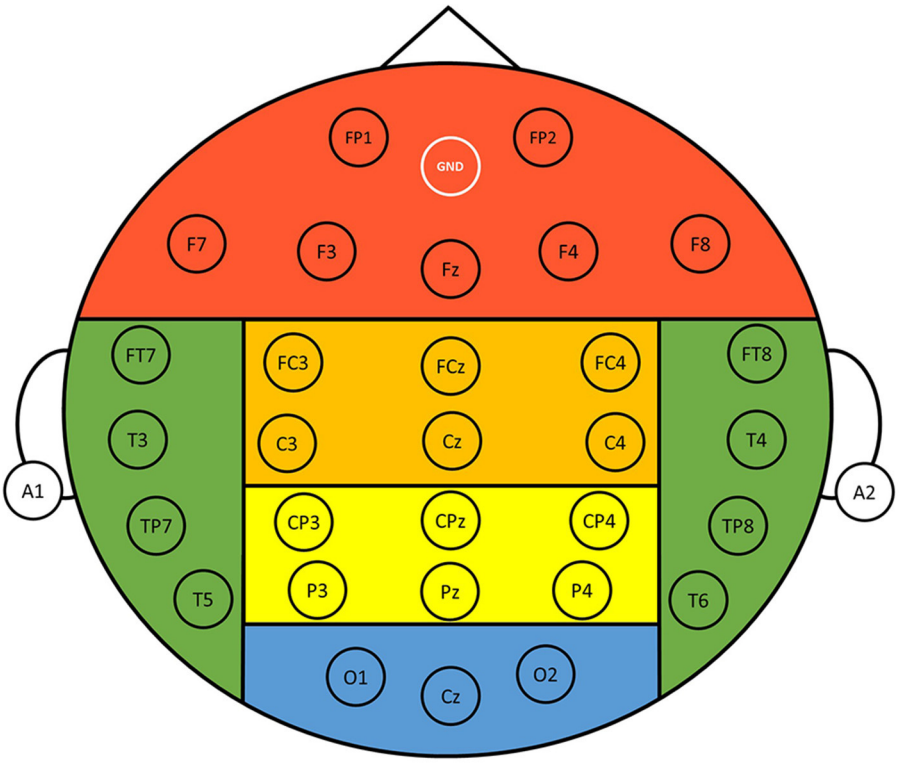

FIGURE 2 | Layout of the 30 recording electrodes. The positions of the electrodes follow the International 10-20 system. References were at A1 and A2 positions, and the ground electrode was at the forehead (GND). The entire scalp region was divided into six different regions for analysis, namely, frontal (FP1, FP2, F3, F4, F7, F8, Fz), central (FC3, FC4, FCz, C3, C4, Cz), parietal (CP3, CP4, CPz, P3, P4, Pz), occipital (O1, O2, Cz), left temporal (FT7, T3, TP7, T5), and right temporal (FT8, T4, TP8, T6) regions.

Step 4: calculation of between-run similarity for each participant and each scalp region

The aim here is to calculate the similarity between the EEG power vectors of the two runs for each scalp region and for each participant. Supposing that s_{ij} denotes the similarity between the average scalp powers of the ith ($i = 1, \ldots, n$) and jth ($i = 1, \ldots, m$) epochs in the 1st and the 2nd run of the resting-state EEGs, the similarity can be measured by the Euclidean distance as

$$s_{ij} = \frac{1}{\left\| \mathbf{p}_j^2 - \mathbf{p}_i^1 \right\|} \tag{2}$$

A higher value of s_{ij} corresponds to a higher between-run similarity between the vectors $\mathbf{p}_i^1$ and $\mathbf{p}_j^2$. Then, calculating the similarities between all possible pairs of $\mathbf{p}_i^1$ and $\mathbf{p}_j^2$ and then averaging all the similarities will yield the averaged between-run similarity for a specific scalp region,

$$S = \frac{1}{n \times m} \sum_{i=1}^{n} \sum_{j=1}^{m} s_{ij} \tag{3}$$

Step 5: standardization

The value of s_{ij} could be very small, because the distance between vectors ($\left\| \mathbf{p}_j^2 - \mathbf{p}_i^1 \right\|$) is considerably large in most cases. As a result, the value of the between-run similarity could approach to zero. Therefore, for the ith participant ($i = 1, 2, \ldots, 74$), we further standardize his/her BRS $S(i)$ using the HC group as the benchmark,

$$S(i) = \frac{S(i) - mean\ (HC)}{std\ (HC)} \tag{4}$$

where $mean\ (HC)$ and $std\ (HC)$stand for the mean and standard deviation of the between-run similarity values calculated from the HCs, respectively. There are two primary reasons behind performing standardization in this study. First, since the raw BRS values are generally small, standardization will help zoom in on the potential differences, if any, between groups. Second, in the field of clinical science, a common approach to quantitatively evaluate the level of dysfunction or impairments of individuals with clinical diagnosis is to perform standardization based on data from the healthy population (e.g., IQ, depression levels, cognitive declination, etc.). Accordingly, we apply the same concept to perform the study-driven standardization of the task-induced BRS based on data from HCs in the same study. In other words, data from healthy controls is treated as a distribution reference for estimating how far the task-induced BRS of individuals with MCI or AD deviates from the healthy population.

After performing the above five steps, six BRS values (i.e., six scalp regions) for each of the 74 participants were obtained. Each BRS represents the task-induced intra-subject variation of resting-state EEG power in a specific scalp region. A high between-run similarity corresponds to a low intra-subject variation between the two separate runs of resting states.

Classification

Two commonly used classifiers were adopted for classification, a linear discriminant analysis (LDA) and a support vector machine (SVM) classifier. LDA finds a linear decision boundary in the original space of patterns to separate classes. Its decision function is given by

$$D_{LDA}(\mathbf{x}) = (\mu_P - \mu_N)^t \Sigma^{-1}\mathbf{x} - \frac{1}{2}(\mu_P - \mu_N)^t \Sigma^{-1}(\mu_P + \mu_N) - \ln\left(\frac{C_P\pi_N}{C_N\pi_P}\right), \quad (5)$$

where $\mathbf{x} \in R^d$is test data, t denotes the transpose of a matrix, μ_P, and μ_N are is the mean vectors of the training data of the positive and negative classes, respectively, Σ is the covariance matrix of the training data, C_P and C_N are the penalty weight for the positive and negative classes, respectively, and π_P and π_N are the *a priori* probabilities of the positive and negative classes, respectively. Here, the penalty weights for both classes were set the same, i.e., $C_P = C_N$. Note that the feature dimension of the data d ($d \in [1, 6]$) represents how many between-run similarity features are used. For example, $d = 6$ if the between-run similarities of all the six scalp regions are used as the features, and $d = 1$ if only a between-run similarity of the scalp regions is adopted as the feature for classification.

SVM maps the training data $\{(\mathbf{x}_i, y_i)\}_{i=1}^{L}$, $y_i \in \{-1, +1\}$are is class labels, into a higher-dimensional feature space from the original space R^d *via* a non-linear mapping φ, and then finds a hyperplane $\mathbf{w}^t\varphi(\mathbf{x}) + b = 0$,which maximizes the margin of separation and minimizes the training errors, formulated as

$$\begin{aligned} &\text{Minimize} \quad \frac{1}{2}\|\mathbf{w}\|^2 + C\sum_{i=1}^{N}\xi_i \\ &\textit{subject to} \quad y_i\left(\mathbf{w}^t\varphi(\mathbf{x}_i) + b\right) - 1 + \xi_i \geq 0 \quad \forall i \\ &\qquad\qquad \xi_i \geq 0 \quad \forall i \end{aligned} \quad (6)$$

where $\mathbf{w}$ and b are the weight vector and the bias of the SVM hyperplane, respectively, ξ_i is slack variables representing the error measures of training data points, and $C$is a penalty weight. For an unseen data $\mathbf{x}$, its class label is predicted by the decision function

$$D_{SVM}(\mathbf{x}) = \sum_{\mathbf{x}_i \in SV} \alpha_i y_i K(\mathbf{x}_i, \mathbf{x}) + b, \quad (7)$$

where α_i are is Lagrange multipliers [obtained by solving the dual problem of (6)], SV denotes the set of support vectors (the training data points whose Lagrange multipliers satisfying $0 < \alpha_i \leq C$), and K is the kernel function. In this study, the radial basis function (RBF) function $K(\mathbf{x}_i, \mathbf{x}) = \exp(-\gamma\|\mathbf{x}_i - \mathbf{x}\|^2)$ was chosen as the kernel, where γ is the kernel parameter. The optimal value of the bias b can be determined by the Kuhn–Tucker condition. The test data $\mathbf{x}$ is classified as positive if $D_{SVM}(\mathbf{x}) > 0$; negative otherwise.

Performance Evaluation and Parameter Optimization

After performing feature extraction, we obtained 74 data (74 vectors) from the 74 participants, and each data consists of d between-run similarity values from d different scalp regions. Although the main goal of this study was to examine the feasibility of using between-run similarity features to achieve promising MCI-HC classification performance, we still performed three different binary classification tasks (AD vs. MCI, MCI vs. HC, and AD vs. HC) to see if such intra-subject variability could contribute to the classification between AD and MCI or between AD and HC.

Similar to previous EEG studies, the number of available EEG data in this study is limited, mainly because the time for recruiting participants was rather long. Performing the usual 10- or 5-fold cross validation is not appropriate, because the number of test data used for testing in each fold is considerably small: one misclassified set of data will result in a large error rate in each fold. Therefore, following the previous studies (Liao et al., 2017; Wu et al., 2018), LOPO-CV was adopted as the performance evaluation method to test the participant-independent accuracy, which predicts how well the results of the proposed method will generalize to unseen data. Take the classification of MCI (24 participants) vs. HC (27 participants) as an example. In each fold of LOPO-CV, data (d-dimensional vectors) from 50 participants were used to train the classifier, and then the d-dimensional data from the remaining participant served as the test data. This step was repeated until the data of every participant had been used as test data once. We then recorded the classification accuracy, computed as the number of correctly classified participants divided by the total number of participants from two groups. Hereafter, the classification accuracy or accuracy would be used to refer to those obtained by the LOPO-CV procedure.

Both the proposed between-run similarity feature and the LDA classifier involve no free parameter. SVM involves two parameters (C and γ). We optimized the parameters of SVM using the LOPO-CV and grid search methods. The values of C and γ were searched in the same set $\{2^{-29}, 2^{-27}, \ldots, 2^{27}, 2^{29}\}$, leading to 961 parameter grids. The best parameter grid results in the highest classification accuracy.

Feature Selection

The question now is how to determine the best feature subset to gain the highest classification accuracy. In other words, the goal is to determine the optimal value of the feature dimension d: which combination of the between-run similarities of the scalp regions is the best for classification. To this end, we adopted a commonly used wrapper-based feature selection method—the sequential forward selection (SFS) algorithm (Guyon and Elisseeff, 2003).

Let N_s be the number of scalp regions ($N_s = 6$). The optimal feature selection procedure based on the SFS algorithm initially finds the best single between-run similarity feature of a scalp

region, which gives the highest LOPO-CV classification accuracy. It is noted that here the LOPO-CV was performed on the data of the participants from two groups, as mentioned in section Performance Evaluation and Parameter Optimization (e.g., 51 data in MCI vs. HC). Subsequently, $N_s - 1$ pairs of features of the scalp regions are formed by combining each of the remaining features of the scalp regions with the best single feature, and the best pair (i.e., the pair that gives the highest LOPO-CV classification accuracy) is selected. Following the same logic, $N_s - 2$ triples of features are formed using each of the remaining features of the scalp regions and the best feature pair, and the best triple is selected (i.e., the triple that gives the highest LOPO-CV classification accuracy). This procedure is repeated until all the N_s features are tested. Finally, the best feature set is the one resulting in the highest LOPO-CV classification accuracy. In other words, we can rank these six features from the best to the worst after this SFS-based procedure. The top-n-ranked features giving the highest LOPO-CV classification accuracy form the optimal feature subset, where $1 \leq n \leq N_s$.

SFS is a wrapper-based greedy approach for feature selection, which has the advantage of achieving better accuracy than filter-based feature selection approach, but with the disadvantage of being more time-consuming (Guyon and Elisseeff, 2003). Fortunately, the number of the BRS feature candidates is only six, and thus the SFS algorithm used in this study is not computationally expensive. Wrapper approaches include the interaction between feature subset and classification model (Saeys et al., 2007). In other words, wrapper-based methods are classifier-specific in which the methods search for the best subset of features that optimizes the generalization classification accuracy of a chosen classifier (Kudo and Sklansky, 2000), and the generalization performance used for evaluating the features is often estimated by k-fold cross validation or LOPO-CV (Wu et al., 2018). Therefore, for the classifiers LDA and SVM, the optimal BRS feature subset selected by the SFS method could be different, as presented in the results (**Figure 6**). Even using the same SVM classifier, the optimal feature subset selected by the SFS algorithm could also be different for different SVM parameters (different values of C and γ), because the generalization performance of SVM varies with the parameter grid (C, γ). In summary, for the SVM classifier, the SFS-based feature selection and the grid-search-based parameter determination must be carried out together. The combination of the optimal BRS feature subset and the SVM classifier with the optimal hyperparameter gives the highest LOPO-CV classification accuracy. The SFS-based feature selection and the grid-search-based parameter determination procedure are summarized in **Figure 3**.

As illustrated in this figure, LOPO-CV is performed to estimate the generalization performance under the condition that a parameter grid and a feature subset have been given in advance. The calculated classification accuracy based on LOPO-CV is subsequently used for evaluating the chosen parameter grid and the feature subset. In other words, in each fold of the LOPO-CV process in this study, the test data (a BRS feature vector) from one participant is involved in the feature selection and the parameter optimization procedure. Accordingly, the test data in this LOPO-CV process are, in fact, validation data, not independent test data.

Statistical Analysis

Since the data of between-run similarities did not pass the Kolmogorov–Smirnov test, we performed the Wilcoxon rank sum test to statistically test three pre-planned between-group comparisons: AD vs. HC, MCI vs. HC, and AD vs. MCI. Since each between-group comparison included six tests (data of 6 scalp regions), we used a Bonferroni corrected α level of 0.0083 (0.05/6) to correct for multiple comparison.

RESULTS

Behavior Performance Among Groups in Different DMTS Tasks

Figure 4 reveals that the mean accuracy of DTMS tasks gradually increases from AD, MCI, to HC, except in Type 2 of the DMTS task where the MCI group showed higher mean accuracy than the HC group. All the three groups showed worst performance in Type 2 working memory task, as compared with the other two types. The between-group comparison in each type of working memory tasks revealed a significant difference in accuracy between the AD vs. HC group in Type 1 ($p = 0.003$) and Type 3 ($p = 0.012$), and AD vs. MCI group in Type 2 ($p = 0.038$).

Comparing the Between-Run Similarities Among the HC, MCI, and AD Groups

Figure 5A shows the EEG scalp topography of between-run similarities (non-standardized) of resting-state EEGs in each group. The HC group showed the highest between-run similarity over all the scalp regions. To further compare the group difference in between-run similarities, we perform statistical tests on the standardized between-run similarity (see Method for detailed calculation) on each scalp region across all groups. As shown in **Figure 5B**, the HC group shows the highest median values of between-run similarities (standardized) among the three groups at all the scalp regions (**Figure 5B**). However, there was significant group difference in the between-run similarity only in the frontal ($p = 0.006$, Bonferroni corrected alpha = 0.0083) and central ($p = 0.004$, Bonferroni corrected alpha = 0.0083) scalp regions in the MCI vs. HC comparison.

Figure 6 further illustrates the significant group difference in spectral power based BRS within each individual band (delta, theta, low alpha, high alpha, low beta, high beta, gamma) across the whole scalp region for the comparison of AD vs. HC, MCI vs. HC, and AD vs. MCI. The results show that the task-induced intra-subject variability of resting-state EEG is larger (lower BRS values) in the MCI group than the HC group over the frontal, central, and parietal scalp regions in low-beta, high-beta, and gamma bands; larger in the AD group than the HC group over the frontal, parietal, and occipital scalp regions in the delta and theta bands. Furthermore, in line with the results shown in **Figure 5A**, almost no statistically significant difference is found between the AD and MCI groups. These findings indicated that both low and high frequencies contribute to spectral power-based BRS

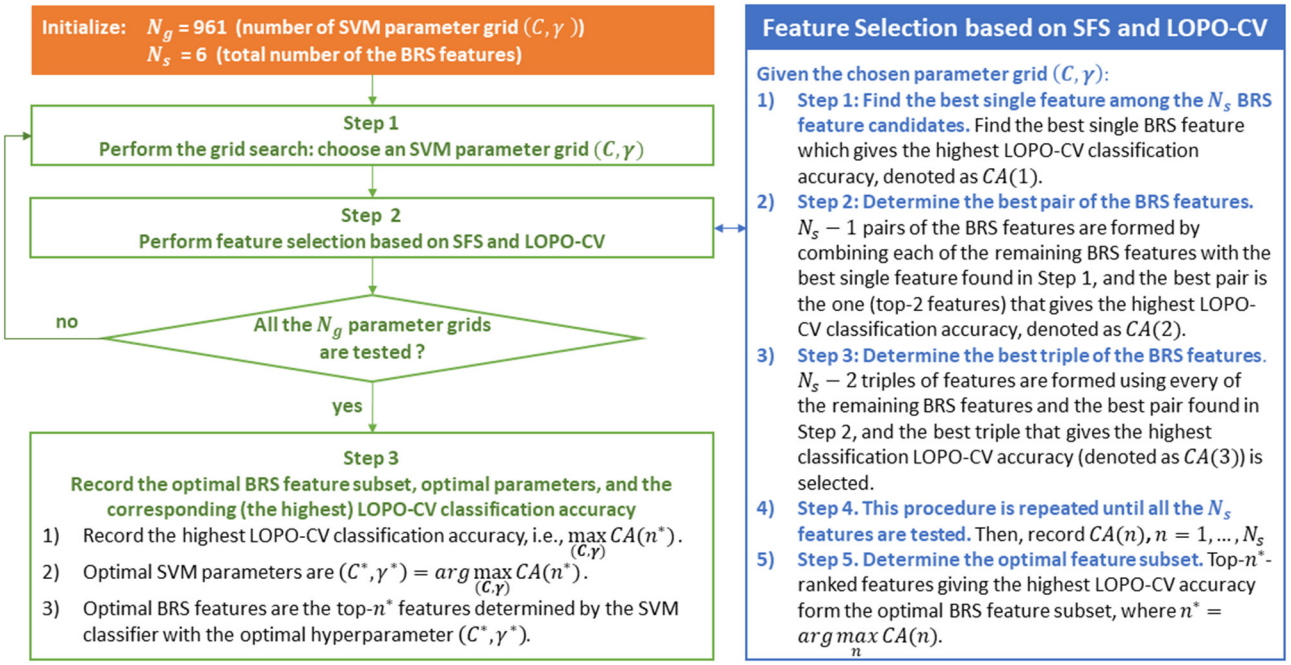

FIGURE 3 | SFS-based between-run similarity (BRS) feature selection and the grid-search-based parameter determination procedure based on the use of an SVM classifier.

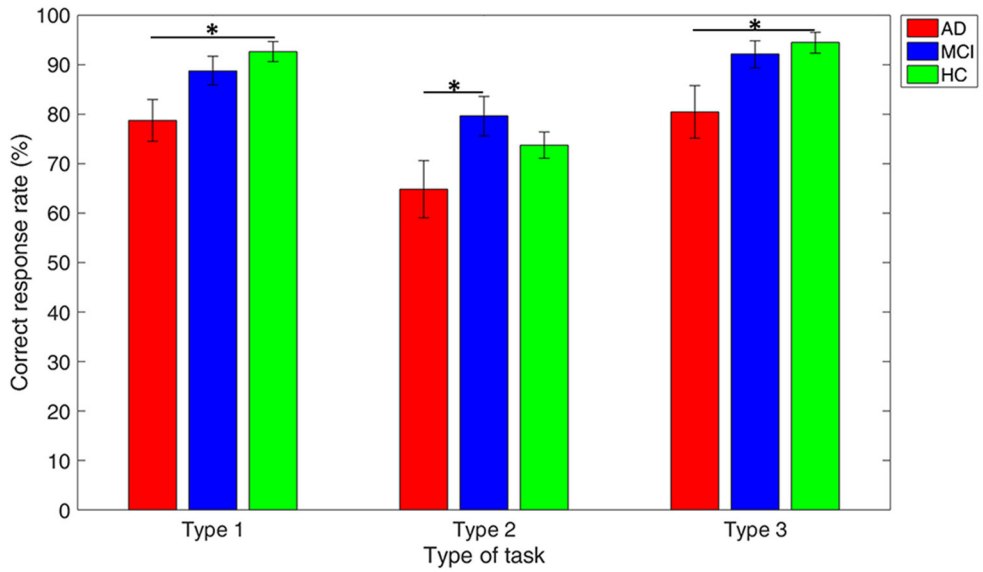

FIGURE 4 | Performance comparison among groups in each type of working memory tasks. Note: error bars indicate standard errors of the means of the correct response rate and * refers to $p < 0.05$.

difference between AD vs. HC or between MCI vs. HC but with different topographic distributions.

Comparing the Classification Accuracies Between the Three Binary Classifications

Classification results of the three binary classification tasks are shown in **Figure 6**, where for each classification task the SFS method was used to determine the best between-run similarity feature subset. The highest classification accuracy for the three classifications of AD vs. HC, MCI vs. HC, and AD vs. MCI, was 74.47, 80.39, and 78%, respectively, and these results were all achieved by SVM. The results indicate that the between-run similarity can be a good candidate to classify between different groups, especially between MCI vs. HC. Moreover, when the

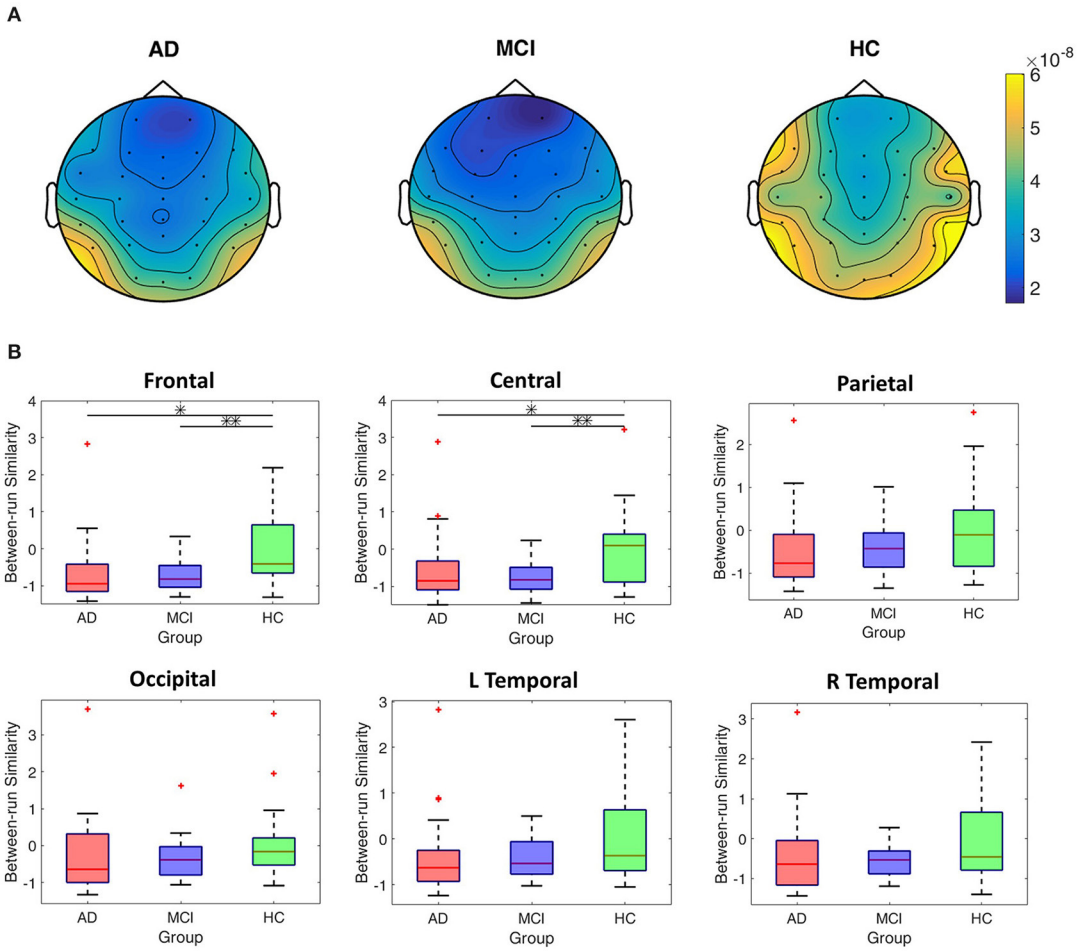

FIGURE 5 | Comparisons of between-run similarities across the AD, MCI, and HC groups. **(A)** The topographic distribution of the non-standardized between-run similarities of resting-state EEGs for each group. **(B)** Boxplots of the standardized between-run similarities for each group in different scalp regions. *$p < 0.05$; **$p < 0.05/6$.

SVM classifier was used, the highest accuracy 80.39% of the MCI-HC classification was achieved by only one feature (the between-run similarity of the parietal scalp region that includes six electrodes). Similarly, the highest accuracy of 74.47% of the AD-MCI classification was achieved when only one between-run similarity feature extracted from the four electrodes of the left temporal region was used. Considering the feasibility in the context of community healthcare, both classification accuracy and usability are critical. A small number of electrodes can largely shorten the time needed for preparation. Therefore, the results demonstrate the high usability of the proposed between-run similarity feature in both MCI-HC and AD-MCI classifications.

Comparing Classification Performances Between Other Features Extracted From Single-Run Resting-State EEGs and Between-Run Similarity Features

We further compared the classification performance of the proposed between-run similarity feature with other widely used features extracted from single-run (1st run) resting-state EEGs in different scalp regions in the three binary classification problems, namely, spectral power (SP), complexity, and connectivity features. Here, a simple LDA classifier was employed.

Fractal dimension (FD) has been widely used for measuring the complexity of an EEG signal. The FD of a signal can be estimated by different methods, such as those of Katz's and Higuchi's methods and the correlation dimension. Katz's FD (KFD) (Katz, 1988) has been a widely accepted approach, because it involves no free parameter and is, therefore, computationally cheap. Also, it is less sensitive to noise in comparison with the Higuchi's FD (Esteller et al., 2001), and has recently shown its high sensitivity to the change of in a mental state in various BCI applications, for example, the EEG-based detection of concentration level (Yeh et al., 2018). Coherence, a measure for the synchrony between two electrodes' EEG signals of two electrodes at a specific frequency band or point, is frequently-applied as an EEG connectivity feature (Liao et al., 2017). The feature extraction procedures for the three types of features to be compared are as follows.

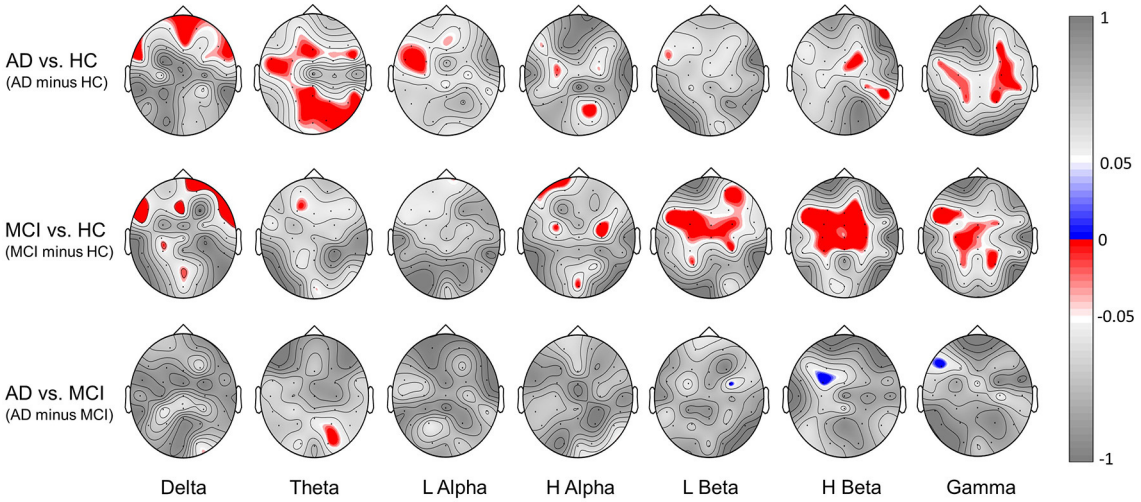

FIGURE 6 | Significant group difference in spectral power-based BRS values within individual bands (delta, theta, low alpha, high alpha, low beta, high beta, gamma) for the comparison of [AD minus HC], [MCI minus HC] and [AD minus MCI]. Here we showed the topography of *p*-values; red indicates a negative difference, and blue indicates a positive difference.

- Spectral power (SP). Take theta SP of the frontal region as an example. For each electrode, we first calculated the theta band power values from the n EEG epochs of the 1st run resting-state EEGs separately, and then averaged the n values. The seven average theta power features from the seven frontal electrodes were sent to the classifier for classification (i.e., $d = 7$).
- Katz's FD (KFD). As an example, the frontal-region KFD was calculated with the following steps: 1) for each electrode, we calculated the KFD values from the n EEG epochs of the 1st run resting-state EEGs separately; 2) then we averaged the nKFD values across epochs; 3) finally the seven averaged KFD features from the seven frontal electrodes were sent to the LDA classifier.
- Coherence (Coh). Take delta-band coherence in the frontal region as an example. For each pair of electrodes, we calculated the delta-band coherence values from the n EEG epochs of the 1st run resting-state EEGs separately, and then averaged the n values to obtain an average coherence feature. Since there were seven electrodes in the frontal region, we obtained totally $\frac{7\times(7-1)}{2} = 21$ coherence features of delta band, which form a 21-dimensional feature vector fed into the LDA classifier.

The results based on spectral power, KFD, and coherence features are listed in **Table 2**.

The spectral powers did not show satisfactory performance for any of the three classification problems. The highest accuracies for the AD-HC, MCI-HC, and AD-MCI classifications were 64, 64.71, and 61.7%, respectively, which were all slightly higher than the chance level (50%). Similar accuracies were also found for coherence. The best accuracies for the three binary classifications (AD-HC, MCI-HC, and AD-MCI), for example, were 64 (central), 64.71 (left temporal), and 62.34% (frontal). Compared with spectral power and coherence features, KFD performs relatively worse. All the accuracies from KFD were close to the chance level ($< 60\%$).

By further comparing the LDA-based results of the between-run similarity features shown in **Figure 7**, where the best accuracies are 68 (AD vs. HC: two features), 72.55 (MCI vs. HC: two features), and 51.06% (AD vs. MCI), we can see that the between-run similarity feature outperforms the three types of widely used features extracted from single-run resting-state EEGs in both the AD-HC and MCI-HC classifications.

DISCUSSION

In the brain-computer interface (BCI) community, intra-subject variability has been a challenge to be overcome. However, in this study, we have shown that in terms of classifying between individuals with MCI and healthy one, the intra-subject variability could be an advantage instead. We therefore proposed the between-run similarity feature to represent the task-induced intra-subject variability of the EEGs recorded in two separate runs of resting-states, before and after a challenging working memory task (i.e., the DMTS). The primary goal of this study was not to propose a novel EEG feature that can perform better than any other existing features but to propose a novel feature extraction framework by which the extracted feature (i.e., the tasked-induced intra-subject variability) can provide more discriminative information for identifying individuals with MCI, and perform better than the usual architecture of feature extraction from single-run resting-state EEGs. The results have demonstrated that the between-run similarity feature is indeed able to achieve high classification performance, especially in the MCI vs. HC classification (80.39%). It is believed that the accuracy can be further improved by combing the proposed between-run similarity feature and other features

TABLE 2 | Comparison of classification accuracies between different features and scalp regions using LDA classifier (in %).

Features		Frontal	Central	Parietal	Occipital	Left temporal	Right temporal
AD vs. HC	δ (SP/Coh)	58/58	52/**64**	46/54	38/36	**60**/**60**	44/58
	θ (SP/Coh)	**64**/**62**	56/54	56/38	**60**/**62**	54/**62**	50/**62**
	Lα(SP/Coh)	54/54	56/**64**	52/**62**	54/50	**60**/**64**	48/46
	Hα(SP/Coh)	58/**60**	54/**60**	54/54	48/48	58/58	50/**64**
	Lβ(SP/Coh)	58/**60**	54/52	44/52	54/40	58/48	50/48
	Hβ(SP/Coh)	**62**/58	**60**/52	50/52	48/42	**60**/52	44/56
	γ (SP/Coh)	**64**/52	44/34	42/42	42/42	**62**/38	46/54
	KFD	56	46	50	44	56	54
MCI vs. HC	δ (SP/Coh)	50.98/43.14	54.90/52.94	54.90/45.10	35.29/35.29	45.10/45.10	47.06/58.82
	θ (SP/Coh)	49.02/58.82	45.10/52.94	**62.75**/56.86	37.25/31.37	54.90/**60.78**	47.06/29.41
	Lα(SP/Coh)	47.06/41.18	43.14/45.10	54.90/43.14	45.10/43.14	52.94/50.98	54.90/37.25
	Hα(SP/Coh)	56.86/47.06	50.98/43.14	47.06/56.86	39.22/49.02	43.14/50.98	50.98/47.06
	Lβ(SP/Coh)	56.86/49.02	58.82/**60.78**	47.06/**62.75**	47.06/**62.75**	58.82/43.14	43.14/54.90
	Hβ(SP/Coh)	**64.71**/47.06	**60.78**/54.90	52.94/50.98	39.22/39.22	52.94/**64.71**	49.02/39.22
	γ (SP/Coh)	**64.71**/49.02	52.94/31.37	47.06/45.10	45.10/52.94	**62.75**/52.94	52.94/50.98
	KFD	58.82	56.86	54.90	50.98	56.86	43.14
AD vs. MCI	δ (SP/Coh)	36.17/46.81	44.68/55.32	40.43/46.81	36.17/31.91	40.43/57.45	57.45/36.17
	θ (SP/Coh)	55.32/46.81	59.57/59.57	**61.70**/53.19	44.68/51.06	57.45/53.19	42.55/53.19
	Lα(SP/Coh)	**61.70**/**62.34**	53.19/44.68	48.94/44.68	36.17/**62.34**	34.04/**61.70**	29.79/46.81
	Hα(SP/Coh)	**61.70**/46.81	**61.70**/34.04	53.19/31.91	31.91/61.70	38.30/42.55	34.04/59.57
	Lβ(SP/Coh)	46.81/51.06	57.45/42.55	48.94/38.30	38.30/**62.34**	34.04/48.94	29.79/59.57
	Hβ(SP/Coh)	40.43/55.32	55.32/48.94	48.94/38.30	40.43/51.06	31.91/59.57	36.17/**61.70**
	γ (SP/Coh)	38.30/40.43	40.43/31.91	44.68/34.04	42.55/59.57	42.55/48.94	44.68/**62.34**
	KFD	44.68	46.81	57.45	44.68	48.94	40.43

Spectral power and coherence features are based on different frequency bands, namely, delta (δ), theta (θ), low alpha (Lα), high alpha (Hα), low beta (Lβ), high beta (Hβ), and gamma. LOPO-CV classification accuracies higher than or equal to 60% were in boldface.

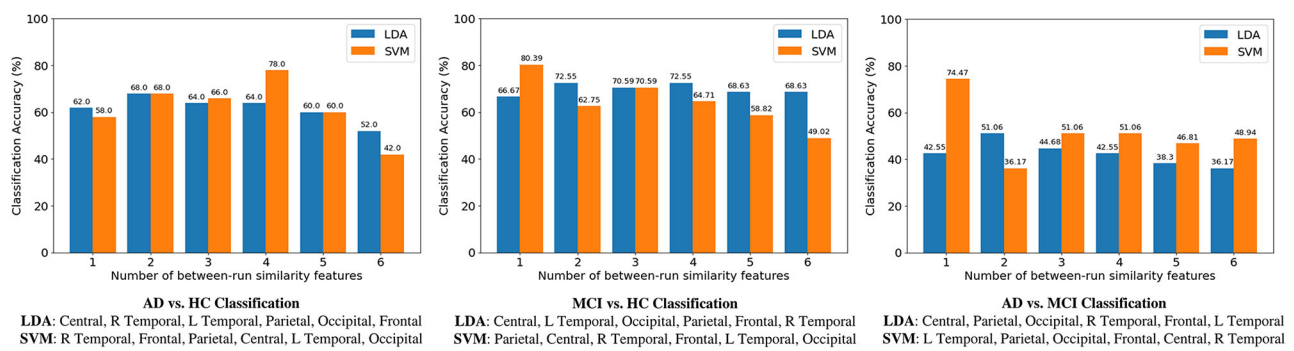

FIGURE 7 | Comparison of accuracies among three binary classifications. For each classification, the sequential forward selection (SFS) algorithm was used the find the optimal feature subset. Take AD-HC classification as an example. The best feature subset contains four features (the between-run similarities of right temporal, frontal, parietal, and central scalp regions) when a support vector machine (SVM) was used as the classifier. Accuracy decreases to 42% if all the six between-run similarity features were used, i.e., without feature selection.

that showed encouraging performance [e.g., multiscale entropy (MSE) Maturana-Candelas et al., 2019; Sun et al., 2020].

Previously, variants of the DMTS tasks have been tested in few recent EEG-based MCI studies. These few studies focused statistical analysis on the task-related EEG (EEGs recorded during performing the task) event-related potentials (e.g., Li et al., 2017). Task-related EEGs may contain discriminative information for classification. However, task-related EEGs sometimes suffer from signal contamination issue from great EOG/EMG artifacts because of excessive eye and body (especially the neck and facial actions) movements, which are not easy to remove completely. In contrast, resting-state EEGs are less likely to be contaminated by artifacts, and thus relatively easy to implement in clinical practice. The proposed feature

extraction framework records resting-state EEGs before and after the DMTS-based working memory task and extract task-induced intra-subject variability features. This "hybrid" approach is unique, because it not only preserves the advantage of the resting-state EEGs (i.e., cleaner signals), it also capitalizes on the clinical traits of working memory dysfunction of the MCI group, which is presumably more informative.

Few recent studies have also used spectral features to characterize MCI, such as band power (absolute power) (Rabbani et al., 2016; Ruiz-Gómez et al., 2018a; Kashefpoor et al., 2019) and relative power (Musaeus et al., 2018; Farina et al., 2020). The reported accuracies in these studies ranged between 60 and 80%. It is a bit unfair to compare the accuracy of the between-run similarity feature with the accuracies reported in those bodies of literature, because there were differences in terms of experimental settings as well as the inclusion and exclusion criteria of participants. Nevertheless, based on the same participants and settings, the results have indicated that, for both the MCI-HC and AD-HC classifications, the spectral power-based between-run similarity is superior to the spectral power feature extracted from a single run resting-state EEGs.

Working memory performance is an important indicator for evaluating memory ability. DMTS task has been largely used to evaluate working memory ability in animals, such as pigeons (Case et al., 2015; Zentall and Smith, 2016), monkey (Pontecorvo and Evans, 1985), and hens (Foster et al., 1995). In human participants, DMTS was also used to study working memory performance in alcohol-dependent (Bowden et al., 1992) and nicotine-dependent individuals (Janes et al., 2013). In addition, the voltage peak-based qEEG ratio of posterior parietal to the dorsolateral prefrontal cortex (DLPFC) extracted from task-induced EEG signals based on DMTS showed high performance for classification between normal aging individuals and patients with mild AD (94% specificity and 88% sensitivity) (Sneddon et al., 2005). As expected, this study demonstrated that working memory performance gradually decreases from the HC to MCI to AD group, except in the Type 2 task. All the three groups performed poorly in the Type 2 task, likely because of the larger memory loads of the Type 2 task (participants need to remember the locations of seven circles). A DMTS task with heavy memory loads can lead to decreases in accuracy (Adamson et al., 2000).

As **Figure 5** reveals, the lower between-run similarities in the AD and MCI groups than the HC group at the frontal and central scalp regions suggest a more noticeable difference between resting-state EEGs recorded before and after a challenging working memory task in the AD and MCI groups. The higher task-induced intra-subject variability suggests that performing cognitively exhausting working memory tasks causes greater disturbance to the degenerated brains in individuals with MCI or AD (Kirova et al., 2015), which then leads to greater difficulties to restore the same resting state as measured before performing the task. A useful analogy is comparing the difference of heart rate variability (HRV) or rhythm of breath during resting state before and after a 5K jogging between individuals with cardiovascular dysfunction and normal people. Although the spatial resolution of EEG makes it difficult to measure the exact signal source, the current frontally oriented results may very likely reflect the common findings on the critical role of prefrontal cortices in working memory and executive function (Guntekin et al., 2008; Papadaniil et al., 2016; Jiang et al., 2021).

The general patterns of lower between-run similarities in the AD and MCI groups than the HC group (**Figures 5A**, **6**) seems to also echo the observation of lower connectivity across electrodes in the AD and MCI groups than the HC group based on single-run resting-state EEGs (Michels et al., 2017; Ruiz-Gómez et al., 2018a,b). For example, results from cross-sample entropy-based connectivity (Ruiz-Gómez et al., 2018b) revealed that both the AD and MCI groups showed an overall lower electrode-to-electrode connectivity than the HC group in the frequency band of 14–19 Hz, which is very close to the low beta band in this study. Both the loss of electrode-to-electrode connectivity in previous studies and the decrease in task-induced intra-subject variation (i.e., a decreased capability to maintain stable resting-state EEG patterns after cognitively exhausting tasks) in this study could be associated with the reduction in cortical-cortical connections or gray matters observed in the brains of individuals with AD or MCI (Jeong, 2004; Maestu et al., 2021) compared to the HC group. Future studies combining structural and functional brain scans (e.g., voxel-based morphometry, white matter fiber tracking, or functional connectivity) and EEG recordings will be required to verify this link.

Somewhat counter-intuitively, the binary classification accuracy is higher for the MCI vs. HC classification than for the AD vs. HC classification. This result actually echoes the statistical results showing that the between-run similarity values over the frontal and central scalp regions were significant between MCI and HC but not between AD vs. HC. A possible explanation may attribute to the observation that some patients with AD were not able to keep up with the DMTS tasks because of high difficulties. Thus, the after-task resting EEGs could be quite similar to the before-task resting EEGs in these patients with AD, because they simply did not spend too much effort on the tasks, as compared with the MCI and HC group. This speculation could be partially supported by the significantly lower DMTS performance for the AD group as compares with the HC (Types 1 and 3) and MCI (Type 2) groups.

If we assumed that MCI was simply a mild AD, then the difference between them could follow a somewhat linear gradient from mild to moderate to severe in terms of the severity degrees of dementia. If this was true, it would be reasonable to predict that the classification problem of AD vs. MCI vs. HC may be more easily solved: there could exist a single EEG feature that covaries with severity degree, which can then be used for assessing cognitive dysfunction degree, with a higher degree corresponding to a higher probability/risk to be AD. Another possibility would be that there exists a feature set such that in the feature space, the class separability between AD and HC will be larger than that between MCI and HC. However, the results from previous studies were controversial and do not support the assumption above. Although some previous results have shown that AD-MCI classification accuracy is higher than the MCI-HC classification accuracy (Ieracitano et al., 2019; Meghdadi et al., 2021), some other studies have reported the opposite (Sharma

et al., 2019) or similar (Fiscon et al., 2018; Ieracitano et al., 2020) result patterns. The reported result in this study shows that MCI-HC (80.39%) is slightly higher than AD-HC (78%) in classification. However, such an accuracy drop of 2.3% reflects only one more misclassified participant in the LOPO-CV process, because in the AD-HC classification, misclassified data in a testing fold of the LOPO-CV resulted in an increase in error rate ($1/50 = 2\%$). Accordingly, in this study, the classification results on AD vs. HC and MCI vs. HC may be also viewed as similar.

From the view of psychopathology, there is no clear evidence either to assume that MCI and AD can be viewed as a gradient change or severity along the same clinical trait. First, according to the diagnostic criteria based on NINCDS-ADRDA and DSM-5, MCI is defined as a distinct syndrome of abnormal cognitive change deviating from the normal aging process, but is not grounded to dementia. In other words, MCI is not considered as early dementia (Bruscoli and Lovestone, 2004). Second, MCI in 32% of individuals developed into AD at the 5th-year follow-up, as aforementioned. In other words, MCI in about 70% of individuals would not process to become AD in 5 years. In contrast, many healthy elderly people develop AD directly without going through the MCI stage in clinical practice, meaning that the MCI stage is not necessarily the only transient state between healthy conditions and AD. Although MCI has a relative high risk of developing into AD, it is not the only risk factor. Other risk factors for AD include hypertension, type 2 diabetes mellitus, dyslipidemia, cardiovascular defects, and alteration of the apolipoprotein E4 (Livingston et al., 2020). All this evidence may help explain why AD-HC classification accuracy is not necessarily higher than the MCI-HC classification.

Being the first one to apply intra-subject variability in EEGs as features for the classification between AD/MCI vs, HC, this study suffers several limitations that can be further addressed in the near future. First, there are many different similarity-based measures. Although the Euclidean distance is a straight forward approach for measuring signal similarity, its application in high-dimensional data is more limited (Grootendorst, 2021). It may be possible to improve classification performance further using other types of similarity measures. For example, in a recent study, Hellinger distance and Bhattacharyya distance showed their effectiveness with highly noisy EEG signals (Chen G. et al., 2020). Although comparisons between different approaches of similarity measures are beyond the scope of this study, they certainly merit attention in evaluating the effectiveness of using different between-run similarity measures as neurophysiological features for classifying neurodegenerative diseases. Second, to be able to build a reliable classification model, we would certainly need a much larger sample size, especially in the context of clinical practices. Therefore, future studies with a much larger sample size would be necessary to further test the validity and reliability of task-induced intra-subject variability for the classification between AD, MCI, and HC groups.

Last but not least, the core concept behind this novel feature extraction framework is highly flexible to be integrated with other types of EEG features, complexity feature for example. In this study, since we hoped to focus the investigation on whether the new framework may lead to an improvement in the MCI-HC classification, we, therefore, decided to implement it with the more typical spectral power features and test the effectiveness of the spectral power-based BRS. On another note, other types of EEG feature can also be applied to quantify the signal similarity between the two separate runs of resting-state EEGs, as long as we replace the spectral powers with other EEG features in steps 2–4 in the calculation of the BRS. However, such a comparison is beyond the scope of this study. Nevertheless, based on the results of this study, it is expected that the task-induced intra-subject variability based on other types of features could also perform better than single-run resting-state EEGs and achieve even higher classification performance. In the future, further investigation on intra-subject variability based on other features may provide additional insights into how the EEG dynamics of individuals with MCI would change before and after performing working memory tasks (e.g., loss of complexity or irregularity in EEGs).

CONCLUSION

This study investigated the value of using intra-subject EEG variability between two separate runs of resting states, before and after a sequence of challenging working memory tasks, as a feature for the classification between individuals with MCI vs. healthy controls. We derived a between-run EEG power similarity as a measure of the intra-subject variability, and applied the machine learning methods (SFS-based feature selection and SVM classification) to determine the most sensitive scalp regions for classification. The main findings are 2-fold. First, the between-run similarity provided encouragingly high LOPO-CV classification accuracy (∼80%) for the MCI-HC and AD-HC classifications, and such performance was superior to the spectral power features extracted from single-run resting-state EEGs. Second, the feature selection results suggested that the 80% MCI-HC classification accuracy could be achieved using an SVM classifier and the six electrodes over the parietal scalp region. Moreover, the results were obtained by LOPO-CV. Because of the small EEG dataset, the LOPO-CV process was performed together with the feature selection and the parameter determination procedure. Follow-up studies will be needed to test the proposed methods on an independent dataset to further examine its generalization performance. Indeed, the intra-subject variability has been a challenging issue in terms of stability of BCI application. In contrast and counter-intuitively, the results reveal that the intra-subject variability between two resting-state EEG data collected before and after a challenging memory task can actually be a promising approach for MCI-HC classification. This study, therefore, shed new light on how we may transform the disadvantage

of intra-subject variability into an advantage in the field of BCI application.

DATA AVAILABILITY STATEMENT

The datasets presented in this article are not readily available because the current patient dataset cannot be shared in any form due to regulation of IRB and Personal Information protection Act. Requests to access the datasets should be directed to Yi-Hung Liu, lyh@mail.ntust.edu.tw.

ETHICS STATEMENT

The studies involving human participants were reviewed and approved by Institutional review board of Taipei Veterans General Hospital (IRB No: 2017-06-009A). The patients/participants provided their written informed consent to participate in this study.

AUTHOR CONTRIBUTIONS

T-TT participated in the algorithm design, EEG data recording, analysis, and drafting. C-FT participated in the study conception, participant recruitment, EEG data collection, and discussion. Y-TH helped process the EEG data and participated in the result analysis. C-YL participated in the analysis and discussion in critical points. C-TW conceptualized the study design, designed the memory task experiment, coordinated data collection, involved in data analyses, and participated in manuscript writing and revision. Y-HL was responsible for project coordination, conceptualized the study design, secured the researching funding, designed analyses protocols, and participated in paper writing and revision. All authors contributed to the article and approved the submitted version.

FUNDING

This work was supported by grant from Taipei Veterans General Hospital (V110C-199).

REFERENCES

Abasolo, D., Escudero, J., Hornero, R., Gomez, C., and Espino, P. (2008). Approximate entropy and auto mutual information analysis of the electroencephalogram in Alzheimer's disease patients. *Med. Biol. Eng. Comput.* 46, 1019–1028. doi: 10.1007/s11517-008-0392-1

Abasolo, D., Hornero, R., Espino, P., Alvarez, D., and Poza, J. (2006). Entropy analysis of the EEG background activity in Alzheimer's disease patients. *Physiol. Meas.* 27, 241–253. doi: 10.1088/0967-3334/27/3/003

Abasolo, D., Hornero, R., Espino, P., Poza, J., Sanchez, C. I., and de la Rosa, R. (2005). Analysis of regularity in the EEG background activity of Alzheimer's disease patients with approximate entropy. *Clin. Neurophysiol.* 116, 1826–1834. doi: 10.1016/j.clinph.2005.04.001

Adamson, C., Foster, T. M., and McEwan, J. S. A. (2000). Delayed matching to sample: the effects of sample-set size on human performance. *Behav. Processes* 49, 149–161. doi: 10.1016/s0376-6357(00)00087-5

Albert, M. S., DeKosky, S. T., Dickson, D., Dubois, B., Feldman, H. H., Fox, N. C., et al. (2011). The diagnosis of mild cognitive impairment due to Alzheimer's disease: recommendations from the National Institute on Aging-Alzheimer's Association workgroups on diagnostic guidelines for Alzheimer's disease. *Alzheimers Dement.* 7, 270–279. doi: 10.1016/j.jalz.2011.03.008

Alzheimer association (2020). 2020 Alzheimer's disease facts and figures. *Alzheimer's Dementia* 16:3. doi: 10.1002/alz.12068

Alzheimer association (2021). 2021 Alzheimer's disease facts and figures. *Alzheimer's Dementia* 17:3. doi: 10.1002/alz.12328

American Psychiatric Association (2013). *Diagnostic and Statistical mAnual of Mental Disorders* (5th ed.). Arlington, VA: American Psychiatric Association

Baddeley, A., Eysenck, M., and Anderson, M. C. (2015). *Memory*. New York, NY: Psychology Press.

Bowden, S. C., Benedikt, R., and Ritter, A. J. (1992). Delayed matching to sample and concurrent learning in nonamnesic humans with alcohol dependence. *Neuropsychologia* 30, 427–435. doi: 10.1016/0028-3932(92)90090-9

Bruscoli, M., and Lovestone, S. (2004). Is MCI really just early dementia? A systematic review of conversion studies. *Int. Psychogeriatr.* 16, 129–140. doi: 10.1017/s1041610204000092

Case, J. P., Laude, J. R., and Zentall, T. R. (2015). Delayed matching to sample in pigeons: effects of delay of reinforcement and illuminated delays. *Learn. Motiv.* 49, 51–59. doi: 10.1016/j.lmot.2015.01.001

Chen, G., Lu, G., Xie, Z., and Shang, W. (2020). Anomaly Detection in EEG Signals: A case study on Similarity. *Comput. Intell. Neurosci.* 2020:6925107. doi: 10.1155/2020/6925107

Chen, Y., Zhang, J. Y., Zhang, T. N., Cao, L., You, Y. Y., Zhang, C. J., et al. (2020). Meditation treatment of Alzheimer disease and mild cognitive impairment. *Medicine (Baltimore)* 99:10. doi: 10.1097/MD.0000000000019313

Dauwels, J., Srinivasan, K., Reddy, M. R., Musha, T., Vialatte, F. B., Latchoumane, et al. (2011). Slowing and loss of complexity in Alzheimer's EEG: Two sides of the same coin? *Int. J. Alzheimer's Dis.* 2011:539621. doi: 10.4061/2011/539621

Engels, M. M. A., Stam, C. J., van der Flier, W. M., Scheltens, P., de Waal, H., and van Straaten, E. C. W. (2015). Declining functional connectivity and changing hub locations in Alzheimer's disease: an EEG study. *BMC Neurol.* 15, 1–8. doi: 10.1186/s12883-015-0400

Esteller, R., Vachtsevanos, G., Echauz, J., and Litt, B. (2001). A comparison of waveform fractal dimension algorithms. *IEEE Transact. Circuits Syst. I: Fundamental Theory Appl.* 48, 177–183. doi: 10.1109/81.904882

Farina, F. R., Emek-Savaş, D. D., Rueda-Delgado, L., Boyle, R., Kiiski, H., Yener, G., et al. (2020). A comparison of resting state EEG and structural MRI for classifying Alzheimer's disease and mild cognitive impairment. *Neuroimage* 215:711465. doi: 10.1101/711465

Ferrara, M., Langiano, E., Brango, T. D., Vito, E. D., Cioccio, L. D., and Bauco, C. (2008). Prevalence of stress, anxiety and depression in with Alzheimer caregivers. *Health Qual. Life Outcomes* 6:93. doi: 10.1186/1477-7525-6-93

Fiscon, G., Weitschek, E., De Cola, M. C., Felici, G., and Bertolazzi, P. (2018). An integrated approach based on EEG signals processing combined with supervised methods to classify Alzheimer's disease patients. *2018 IEEE International Conference on Bioinformatics and Biomedicine (BIBM)* (Madrid).

Foster, T. M., Temple, W., Mackenzie, C., DeMello, L. R., and Poling, A. (1995). Delayed matching-to-sample performance of hens: effects of sample duration and response requirements during the sample. *J. Exp. Anal. Behav.* 64, 19–31. doi: 10.1901/jeab.1995.64-19

Fowler, K. S., Saling, M. M., Conway, E. L., Semple, J. M., and Louis, W. J. (1995). Computerized delayed matching to sample and paired associate performance in the early detection of dementia. *ApplBeuropsychol.* 2:4. doi: 10.1207/s15324826an0202_4

Gagnon, L. G., and Belleville, S. (2011). Working memory in mild cognitive impairment and Alzheimer's disease: contribution of forgetting and predictive value of complex span tasks. *Neuropsychology* 25, 226–236. doi: 10.1037/a0020919

Grootendorst, M. (2021). *9 Distance Measures in Data Science*. Available online at: https://towardsdatascience.com/9-distance-measures-in-data-science-918109d069fa (accessed February 1, 2021).

Guntekin, B., Saatçi, E., and Yener, G. (2008). Decrease of evoked delta, theta and alpha coherences in Alzheimer patients during a visual oddball paradigm. *Brain Res.* 1235, 109–116. doi: 10.1016/j.brainres.2008.06.028

Guyon, I., and Elisseeff, A. (2003). An introduction to variable and feature selection. *J. Mach. Learn. Res.* 3, 1157–1182. doi: 10.1162/153244303322753616

Hansson, O., Lehmann, S., Otto, M., Zetterberg, H., and Lewczuk, P. (2019). Advantages and disadvantages of the use of the CSF Amyloid β (Aβ) 42/40 ratio in the diagnosis of Alzheimer's Disease. *Alzheimers. Res. Ther.* 11:34. doi: 10.1186/s13195-019-0485-0

Hata, M., Kazui, H., Tanaka, T., Ishii, R., Canuet, L., Pascual-Marqui, R. D., et al. (2016). Functional connectivity assessed by resting state EEG correlates with cognitive decline of Alzheimer's disease – An eLORETA study. *Clin. Neurophysiol.* 127, 1269–1278. doi: 10.1016/j.clinph.2015.10.030

Huang, C., Wahlund, L.-O., Dierks, T., Julin, P., Winblad, B., and Jelic, V. (2000). Discrimination of Alzheimer's disease and mild cognitive impairment by equivalent EEG sources: a cross-sectional and longitudinal study. *Clin. Neurophysiol.* 111, 1961–1967. doi: 10.1016/s1388-2457(00)00454-5

Ieracitano, C., Mammone, N., Bramanti, A., Hussain, A., and Morabito, F. C. (2019). A Convolutional Neural Network approach for classification of dementia stages based on 2D-spectral representation of EEG recordings. *Neurocomputing* 323, 96–107. doi: 10.1016/j.neucom.2018.09.071

Ieracitano, C., Mammone, N., Hussain, A., and Morabito, F. C. (2020). A novel multi-modal machine learning based approach for automatic classification of EEG recordings in dementia. *Neural Netw.* 123, 176–190. doi: 10.1016/j.neunet.2019.12.006

Ishii, R., Canuet, L., Aoki, Y., Hata, M., Iwase, M., Ikeda, S., et al. (2017). Healthy and pathological brain aging: from the perspective of oscillations, functional connectivity, and signal complexity. *Neuropsychobiology* 75, 151–161. doi: 10.1159/000486870

Janes, A. C., Ross, R. S., Farmer, S., Frederick, B. B., Nickerson, L. D., Lukas, S. E., et al. (2013). Memory retrieval of smoking-related images induce greater insula activation as revealed by an fMRI-based delayed matching to sample task. *Addict. Biol.* 20, 349–356. doi: 10.1111/adb.12112

Jeong, J. (2004). EEG dynamics in patients with Alzheimer's disease. *Clin. Neurophysiol.* 115, 1490–1505. doi: 10.1016/j.clinph.2004.01.001

Jiang, Y., Li, J., Schmitt, F. A., Jicha, G. A., Munro, N. B., Zhao, X., et al. (2021). Memory-related frontal brainwaves predict transition to mild cognitive impairment in healthy older individuals five years before diagnosis. *J. Alzheimer's Dis.* 79, 531–541. doi: 10.3233/jad-200931

Kashefpoor, M., Rabbani, H., and Barekatain, M. (2019). Supervised dictionary learning of EEG signals for mild cognitive impairment diagnosis. *Biomed. Signal Process. Control* 53:101559. doi: 10.1016/j.bspc.2019.101559

Katz, M. J. (1988). Fractals and the analysis of waveforms. *Comput. Biol. Med.* 18, 145–156. doi: 10.1016/0010-4825(88)90041-8

Kessels, R. P. C., Molleman, P. W., and Oosterman, J. M. (2011). Assessment of working-memory deficits in patients with mild cognitive impairment and Alzheimer's dementia using Wechsler's Working Memory Index. *Aging Clin. Exp. Res.* 23, 487–490. doi: 10.1007/BF03325245

Kirova, A. M., Bays, R. B., and Lagalwar, S. (2015). Working memory and executive function decline across normal aging, mild cognitive impairment, and Alzheimer's disease. *Biomed Res. Int.* 6, 1–9.doi: 10.1155/2015/748212

Kudo, M., and Sklansky, J. (2000). Comparison of algorithms that select features for pattern classifiers. *Pattern Recognit.* 33, 25–41. doi: 10.1016/s0031-3203(99)00041-2

Labate, D., Foresta, F. L., Morabito, G., Palamara, I., and Morabito, F. C. (2013). Entropic measures of EEG complexity in Alzheimer's disease through a multivariate multiscale approach. *IEEE Sens. J.* 13, 3284–3292. doi: 10.1109/jsen.2013.2271735

Li, J., Broster, L. S., Jicha, G. A., Munro, N. B., Schmitt, F. A., and Abner, E. (2017). A cognitive electrophysiological signature differentiates amnestic mild cognitive impairment from normal aging. *Alzheimer's Res. Therapy* 9:3. doi: 10.1186/s13195-016-0229-3

Liao, S. C., Wu, C. T., Huang, H. C., Cheng, W. T., and Liu, Y. H. (2017). Major depression detection from EEG signals using kernel eigen-filter-bank common spatial patterns. *Sensors* 17:6. doi: 10.3390/s17061385

Liu, X., Zhang, C., Ji, Z., Ma, Y., Shang, X., Zhang, Q., et al. (2015). Multiple characteristics analysis of Alzheimer's electroencephalogram by power spectral density and Lempel–Ziv complexity. *Cogn. Neurodyn.* 10, 121–133. doi: 10.1007/s11571-015-9367-8

Livingston, G., Huntley, J., Sommerlad, A., Ames, D., Ballard, C., Banerjee, S., et al. (2020). Dementia prevention, intervention, and care: 2020 report of the lancet commission. *Lancet* 396, 413–446. doi: 10.1016/s0140-6736(20)30367-6

Maestu, F., de Haan, W., Busche, M. A., and DeFelipe, J. (2021). Neuronal excitation/inhibition imbalance: core element of a translational perspective on Alzheimer pathophysiology. *Ageing Res. Rev.* 69:101372. doi: 10.1016/j.arr.2021.101372

Martinez, G., Vernooij, R. W. M., Fuentes Padilla, P., Zamora, J., Flicker, L., and Bonfill Cosp, X. (2017). 18F PET with flutemetamol for the early diagnosis of Alzheimer's disease dementia and other dementias in people with mild cognitive impairment (MCI). *Cochrane Datab. Syst. Rev.* 11:CD012884. doi: 10.1002/14651858.cd012884

Maturana-Candelas, A., Gómez, C., Poza, J., Pinto, N., and Hornero, R. (2019). EEG characterization of THe Alzheimer's disease continuum by means of multiscale entropies. *Entropy* 21:544. doi: 10.3390/e21060544

McKhann, G. M., Knopman, D. S., Chertkow, H., Hyman, B. T., Jack, C. R., Kawas, C. H., et al. (2011). The diagnosis of dementia due to Alzheimer's disease: recommendations from the National Institute on Aging-Alzheimer's Association workgroups on diagnostic guidelines for Alzheimer's disease. *Alzheimers Dement.* 7:5. doi: 10.1016/j.jalz.2011.03.005

Meghdadi, A. H., StevanovicKaric, M., McConnell, M., Rupp, G., Richard, C., Hamilton, J., et al. (2021). Resting state EEG biomarkers of cognitive decline associated with Alzheimer's disease and mild cognitive impairment. *PLoS ONE* 16:e244180. doi: 10.1371/journal.pone.0244180

Michels, L., Muthuraman, M., Anwar, A. R., Kollias, S., Leh, S. E., Riese, F., et al. (2017). Changes of functional and directed resting-state connectivity are associated with neuronal oscillations, ApoE genotype and amyloid deposition in mild cognitive impairment. *Front. Aging Neurosci.* 9:304. doi: 10.3389/fnagi.2017.00304

Mognon, A., Jovicich, J., Bruzzone, L., and Buiatti, M. (2011). ADJUST: An automatic EEG artifact detector based on the joint use of spatial and temporal features. *Psychophysiology* 48:2. doi: 10.1111/j.1469-8986.2010.01061.x

Musaeus, C. S., Engedal, K., Hogh, P., Jelic, V., Mørup, M., Naik, M., et al. (2018). EEG theta power is an early marker of cognitive decline in dementia due to Alzheimer's disease. *J. Alzheimer's Dis.* 64, 1359–1371. doi: 10.3233/jad-180300

Papadaniil, C. D., Kosmidou, V. E., Tsolaki, A., Tsolaki, M., and Kompatsiaris, I. (2016). Cognitive MMN and P300 in mild cognitive impairment and Alzheimer's disease: A high density EEG-3D vector field tomography approach. *Brain Res.* 1648, 425–433. doi: 10.1016/j.brainres.2016.07.043

Park, J. H., Kim, S., Kim, C. H., Cichocki, A., and Kim, K. (2007). Multiscale entropy analysis of EEG from patients under different pathological conditions. *Fractals* 15, 399–404. doi: 10.1142/S0218348X07003691

Petersen, R. C. (2010). Alzheimer's disease: progress in prediction. *Lancet Neurol.* 9:1. doi: 10.1016/S1474-4422(09)70330-8

Pontecorvo, M. J., and Evans, H. L. (1985). Effects of aniracetam on delayed matching-to-sample performance of monkeys and pigeons. *Pharmacol. Biochem. Behav.* 22, 745–752. doi: 10.1016/0091-3057(85)90523-4

Poza, J., Gomez, C., García, M., Corralejo, R., Fernandez, A., and Hornero, R. (2014). Analysis of neural dynamics in mild cognitive impairment and Alzheimer's disease using wavelet turbulence. *J. Neural Eng.* 11:26010. doi: 10.1088/1741-2560/11/2/026010

Rabbani, H., Kashefpoor, M., and Barekatain, M. (2016). Automatic diagnosis of mild cognitive impairment using electroencephalogram spectral features. *J. Med. Signals Sensors* 6:175869. doi: 10.4103/2228-7477.175869

Ritchie, C., Smailagic, N., Noel-Storr, A. H., Takwoingi, Y., Flicker, L., Mason, S. E., et al. (2014). Plasma and cerebrospinal fluid amyloid beta for the diagnosis of Alzheimer's disease dementia and other dementias in people with mild cognitive impairment (MCI). *Cochrane Datab. Syst. Rev.* 2014:CD008782. doi: 10.1002/14651858.cd008782.pub4

Roh, J. H., Park, M. H., Ko, D., Park, K.-W., Lee, D.-H., Han, C., et al. (2011). Region and frequency specific changes of spectral power in Alzheimer's disease and mild cognitive impairment. *Clin. Neurophysiol.* 122, 2169–2176. doi: 10.1016/j.clinph.2011.03.023

Ross, D. A., Dag, A., John, O. B. T., Clive, B., Sube, B., Nick, F. C., et al. (2021). Mild cognitive impairment: the Manchester consensus. *Age Ageing* 50, 72–80. doi: 10.1093/ageing/afaa228

Rossini, P. M., Rossi, S., Babiloni, C., and Polich, J. (2007). Clinical neurophysiology of aging brain: from normal aging to neurodegeneration. *Prog. Neurobiol.* 83, 375–400. doi: 10.1016/j.pneurobio.2007.07.010

Ruiz-Gómez, S., Gómez, C., Poza, J., Gutierrez-Tobal, G., Tola-Arribas, M., Cano, M., et al. (2018a). Automated multiclass classification of spontaneous EEG activity in Alzheimer's disease and mild cognitive impairment. *Entropy* 20:e20010035. doi: 10.3390/e20010035

Ruiz-Gómez, S. J., Gómez, C., Poza, J., Martínez-Zarzuela, M., Tola-Arribas, M. A., Cano, M., et al. (2018b). Measuring alterations of spontaneous EEG neural coupling in Alzheimer's disease and mild cognitive impairment by means of cross-entropy metrics. *Front. Neuroinform.* 12:76. doi: 10.3389/fninf.2018.00076

Saeys, Y., Inza, I., and Larranaga, P. (2007). A review of feature selection techniques in bioinformatics. *Bioinformatics* 23, 2507–2517. doi: 10.1093/bioinformatics/ btm344

Sahakian, B. J., Morris, R. G., Evenden, J. L., Heald, A., Levy, R., Philpot, M., et al. (1988). A comparative study of visuospatial memory and learning in Alzheimer-type dementia and Parkinson's disease. *Comparative Study* 111:695. doi: 10.1093/brain/111.3.695

Saunders, N. L. J., and Summers, M. J. (2010). Attention and working memory deficits in mild cognitive impairment. *J. Clin. Exp. Neuropsychol.* 32, 350–357. doi: 10.1080/13803390903042379

Seker, M., Ozbek, Y., Yener, G., and Ozerdem, M. S. (2021). Complexity of EEG dynamics for early diagnosis of Alzheimer disease using permutation entropy neuromarker. *Comput. Methods Programs Biomed.* 206:106116. doi: 10.1016/j.cmpb.2021.106116

Sharma, N., Kolekar, M. H., Jha, K., and Kumar, Y. (2019). EEG and cognitive biomarkers based mild cognitive impairment diagnosis. *IRBM* 40, 113–121. doi: 10.1016/j.irbm.2018.11.007

Sneddon, R., Shankle, W. R., Hara, J., Rodriquez, A., Hoffman, D., and Saha, U. (2005). EEG detection of early Alzheimer's disease using psychophysical tasks. *Clin. EEG Neurosci.* 36, 141–150. doi: 10.1177/155005940503600304

Sun, J., Wang, B., Niu, Y., Tan, Y., Fan, C., Zhang, N., et al. (2020). Complexity analysis of EEG, MEG, and fMRI in mild cognitive impairment and Alzheimer's disease: a review. *Entropy* 22:239. doi: 10.3390/e22020239

Tsai, C. F., Lee, W. J., Wang, S. J., Shia, B. C., Nasreddine, Z., and Fuh, J. L. (2012). Psychometrics of the Montreal Cognitive Assessment (MoCA) and its subscales: validation of the Taiwanese version of the MoCA and an item response theory analysis. *IntPsychogeriatr.* 24:2298. doi: 10.1017/S1041610211002298

Wang, R., Wang, J., Yu, H., Wei, X., Yang, C., and Deng, B. (2014). Decreased coherence and functional connectivity of electroencephalograph in Alzheimer's disease. *Chaos* 24:033136. doi: 10.1063/1.4896095

World Health Organization (2020). *Dementia Key Facts*. Available online at: http://www.who.int/news-room/fact-sheets/detail/dementia (accessed September 21, 2020).

Wu, C. T., Dillon, D. G., Hsu, H. C., Huang, S., Barrick, E., and Liu, Y. H. (2018). Depression detection using relative EEG power induced by emotionally positive images and a conformal kernel support vector machine. *Appl. Sci.* 8:8. doi: 10.3390/app8081244

Xu, M., and Tao, H. (2013). Complexity analysis of electroencephalogram in patients with Alzheimer's disease and mild cognitive impairment. *Chin. J. Neurol.* 46, 687–691. doi: 10.3760/cma.j.issn.1006-7876.2013.10.010

Yeh, S. C., Hou, C. L., Peng, W. H., Wei, Z. Z., Huang, S., Kung, E. Y. C., et al. (2018). A multiplayer online car racing virtual-reality game based on internet of brains. *J. Syst. Archit.* 89, 30–40. doi: 10.1016/j.sysarc.2018.06.004

Zentall, T. R., and Smith, A. P. (2016). Delayed matching-to-sample: A tool to assess memory and other cognitive processes in pigeons. *Behav. Processes* 123, 26–42. doi: 10.1016/j.beproc.2015.07.002

Conflict of Interest: The authors declare that the research was conducted in the absence of any commercial or financial relationships that could be construed as a potential conflict of interest.

Publisher's Note: All claims expressed in this article are solely those of the authors and do not necessarily represent those of their affiliated organizations, or those of the publisher, the editors and the reviewers. Any product that may be evaluated in this article, or claim that may be made by its manufacturer, is not guaranteed or endorsed by the publisher.

Advantages of publishing in Frontiers

OPEN ACCESS
Articles are free to read for greatest visibility and readership

FAST PUBLICATION
Around 90 days from submission to decision

HIGH QUALITY PEER-REVIEW
Rigorous, collaborative, and constructive peer-review

TRANSPARENT PEER-REVIEW
Editors and reviewers acknowledged by name on published articles

Frontiers
Avenue du Tribunal-Fédéral 34
1005 Lausanne | Switzerland

Visit us: www.frontiersin.org
Contact us: frontiersin.org/about/contact

REPRODUCIBILITY OF RESEARCH
Support open data and methods to enhance research reproducibility

DIGITAL PUBLISHING
Articles designed for optimal readership across devices

FOLLOW US
@frontiersin

IMPACT METRICS
Advanced article metrics track visibility across digital media

EXTENSIVE PROMOTION
Marketing and promotion of impactful research

LOOP RESEARCH NETWORK
Our network increases your article's readership